



**HAL**  
open science

# Synthesis of magnetic polymer latex particles by reversible addition-fragmentation chain transfer (RAFT) polymerization in aqueous dispersed media

Thiago Rodrigues Guimarães

► **To cite this version:**

Thiago Rodrigues Guimarães. Synthesis of magnetic polymer latex particles by reversible addition-fragmentation chain transfer (RAFT) polymerization in aqueous dispersed media. Chemical engineering. Université de Lyon, 2017. English. NNT : 2017LYSE1107 . tel-01593363

**HAL Id: tel-01593363**

**<https://theses.hal.science/tel-01593363v1>**

Submitted on 26 Sep 2017

**HAL** is a multi-disciplinary open access archive for the deposit and dissemination of scientific research documents, whether they are published or not. The documents may come from teaching and research institutions in France or abroad, or from public or private research centers.

L'archive ouverte pluridisciplinaire **HAL**, est destinée au dépôt et à la diffusion de documents scientifiques de niveau recherche, publiés ou non, émanant des établissements d'enseignement et de recherche français ou étrangers, des laboratoires publics ou privés.



N°d'ordre NNT : 2017LYSE1107

## **THESE de DOCTORAT DE L'UNIVERSITE DE LYON**

opérée au sein de  
**l'Université Claude Bernard Lyon 1**

**Ecole Doctorale de Chimie ED206**

**Spécialité de doctorat : Chimie**

Soutenue publiquement le 19/06/2017, par :

**Thiago RODRIGUES GUIMARÃES**

---

# **Synthesis of magnetic polymer latex particles by reversible addition-fragmentation chain transfer (RAFT) polymerization in aqueous dispersed media**

---

Devant le jury composé de :

DELAIR, Thierry  
DUGUET, Etienne  
SAVE, Maud

Pr. Université Lyon 1  
Pr. Université Bordeaux 1  
Dr. Université de Pau et des  
Pays de l'Adour

JARY, Dorothée  
BOURGEAT-LAMI, Elodie  
LANSALOT, Muriel

Dr. CEA Grenoble  
Dr. Université Lyon 1  
Dr. Université Lyon 1

Président  
Rapporteur  
Rapporteuse  
Examinatrice  
Directrice de thèse  
Co-encadrante





# UNIVERSITE CLAUDE BERNARD - LYON 1

## Président de l'Université

Président du Conseil Académique

Vice-président du Conseil d'Administration

Vice-président du Conseil Formation et Vie Universitaire

Vice-président de la Commission Recherche

Directrice Générale des Services

**M. le Professeur Frédéric FLEURY**

M. le Professeur Hamda BEN HADID

M. le Professeur Didier REVEL

M. le Professeur Philippe CHEVALIER

M. Fabrice VALLÉE

Mme Dominique MARCHAND

## ***COMPOSANTES SANTE***

Faculté de Médecine Lyon Est – Claude Bernard

Faculté de Médecine et de Maïeutique Lyon Sud – Charles Mérieux

Faculté d'Odontologie

Institut des Sciences Pharmaceutiques et Biologiques

Institut des Sciences et Techniques de la Réadaptation

Département de formation et Centre de Recherche en Biologie Humaine

Directeur : M. le Professeur G.RODE

Directeur : Mme la Professeure C. BURILLON

Directeur : M. le Professeur D. BOURGEOIS

Directeur : Mme la Professeure C. VINCIGUERRA

Directeur : M. X. PERROT

Directeur : Mme la Professeure A-M. SCHOTT

## ***COMPOSANTES ET DEPARTEMENTS DE SCIENCES ET TECHNOLOGIE***

Faculté des Sciences et Technologies

Département Biologie

Département Chimie Biochimie

Département GEP

Département Informatique

Département Mathématiques

Département Mécanique

Département Physique

UFR Sciences et Techniques des Activités Physiques et Sportives

Observatoire des Sciences de l'Univers de Lyon

Polytech Lyon

Ecole Supérieure de Chimie Physique Electronique

Institut Universitaire de Technologie de Lyon 1

Ecole Supérieure du Professorat et de l'Education

Institut de Science Financière et d'Assurances

Directeur : M. F. DE MARCHI

Directeur : M. le Professeur F. THEVENARD

Directeur : Mme C. FELIX

Directeur : M. Hassan HAMMOURI

Directeur : M. le Professeur S. AKKOUCHE

Directeur : M. le Professeur G. TOMANOV

Directeur : M. le Professeur H. BEN HADID

Directeur : M. le Professeur J-C PLENET

Directeur : M. Y.VANPOULLE

Directeur : M. B. GUIDERDONI

Directeur : M. le Professeur E.PERRIN

Directeur : M. G. PIGNAULT

Directeur : M. le Professeur C. VITON

Directeur : M. le Professeur A. MOUGNIOTTE

Directeur : M. N. LEBOISNE



For my brother, Diego  
*Para meu irmão, Diego*



## ACKNOWLEDGMENTS

This work was performed in the C2P2 laboratory between June 2014 and June 2017 under the supervision of **Elodie BOURGEAT-LAMI** and **Muriel LANSALOT**. I would like first to thanks the director **Timothy MCKENNA** to provide the complete structure in the laboratory supporting me to develop this work.

I am deeply grateful for **Prof. Etienne DUGUET** and **Dr. Maud SAVE** for dedicating their time to read and review this thesis. The remarks and interesting discussions during the PhD defense have, undoubtedly, greatly contributed with my work. I would like to thank, in special, **Prof. Thierry DELAIR** who accepted to be the president of the defense committee.

I would like also to thank **Dr Dorothée JARY** who made such an effort to set a collaboration between our laboratory and CEA-Grenoble allowing the biological tests of our magnetic carriers to be performed. These tests have a significant contribution to the quality of this work. I am very grateful. Thank you **Dorothée** for spend your time training me, carrying out experiments, fixing the “*soucis administratifs*” and for serving as committee member as well.

I would like also to thanks the CNPQ, Brazilian research founding agency, for the scholarship which give me the opportunity to carry out my PhD in France. I would also like to thank the *Université Claude Bernard* and *Ecole Doctorale de Chimie* for provide me support during this three years, in special, **Prof. Jean-Marc LANCELIN** and **Prof. Stephan DANIELE** who presided the doctoral school during my PhD.

J'exprime toute ma gratitude à mes encadrantes **Elodie BOURGEAT-LAMI** et **Muriel LANSALOT**. Dès 2010, quand je suis arrivé à Lyon, **Elodie** a toujours été là pour m'aider. Je me rappelle que pour mon premier jour en France elle est venue me chercher à l'aéroport après un voyage atypique de plus de 36h de vol et connexions, valises perdues, grève, etc. Dès ce premier geste jusqu'à présent, j'ai toujours pu compter sur elle pour me donner des conseils et enseignements au niveau académique/scientifique bien que du côté personnel. Merci également pour tout le moment des partages au tour de discussions, réunions, voyage pour les congrès, diners et repas en salle pause. J'avoue qu'au début c'était dur de suivre ton français (parce-que le changement de sujet est assez fréquent pendant les discussions et également à cause du débit de mot par minute, ce qui c'est assez impressionnant). Par contre cela m'a bien aidé à avoir une bonne maîtrise de la langue française. Même des nouvelles sur la radio j'étais capable de suivre. Merci pour ta générosité

et la façon très humaine de conduire les étudiants. Si j'ai parlé de la vitesse de parler d'Elodie, alors **Muriel** accélère encore plus ce rythme, il avait des réunions avec toutes les deux que c'était un peu dur à suivre. Malgré la vitesse, pendant les réunions j'ai toujours apprécié l'enthousiasme de Muriel avec la science, en générale, et avec mon projet développé pendant ces trois ans de doctorat. J'ai appris beaucoup avec toi au niveau scientifique et bien que au niveau humain, j'ai beaucoup grandi avec toi. Merci pour tout. Et si un jour je reviens au labo vous faire une visite, je promets apporté un certain gâteau...

Je voudrais aussi remercier à tous les permanents qui rend ce laboratoire un endroit très agréable avec un ambiance bien conviviale. Merci à **Seb** pour ton bonne humeur et pour la patience en nous aider avec la partie bricolage de réacteurs et d'autres. **Jean-Pierre**, merci d'être cette personne fantastique et de faire notre vie plus doux, merci pour le cours de Bossa Nova dans le labo, dans lequel j'ai pu connaitre beaucoup d'artistes brésilien. Un merci spécial à **Franck D'Agosto**, qui a fait partie des '*Les quatre fantastiques*' encadrants avec **Elodie**, **Muriel** et **Amilton**, pendant mon stage en 2011, avec qui j'ai appris énormément sur la chimie, surtout sur la chimie RAFT, merci. Merci **Olivier**, **Manel** et **Franck Collas** pour tenir tous les équipements en route et aussi pour les agréables moments en salle de pause. Je remercie également **Vincent**, **Christophe**, **Damien** et **Jean** pour les moments de partages soit en salle de pause soit à la cantine.

**Nath** merci pour toute ta générosité et ta gentillesse. Merci pour le weekend dans le Beaujolais et de nous avoir présenté ta jolie région. Ce fut un vrai plaisir de pouvoir partager des bons moments à coté de vous. Merci aussi pour ton énorme efficacité en résoudre des soucis administratifs que nous, les étudiants, peuvent avoir/créer pendant notre période au labo. Merci aussi pour les gâteaux, même si j'ai pu manger juste 10% d'eux car 90% des gâteaux étaient au chocolat, je rigole, mais le clafoutis aux cerise est beaucoup mieux que le moelleux.

**Pierre-Yves**, merci pour tout l'amitié et l'apprentissage pendant ces années au tour de la science et la physique des analyses et surtout l'apprentissage en culture générale, que les terriens ne comprennent pas comme c'est possible estoquer tous ces infos et les faire sortir à un débit de mot par minute assez impressionnant. Même si l'on n'a jamais eu assez de temps pour finir nos conversations, car il avait besoin de laisser d'autres personnes parler aussi (pas souvent) toutes les discussions étaient très constructives... ok il avait quelques-unes qui n'étaient pas assez constructifs mais elles étaient toujours très intéressantes. Merci aussi à

**Kessy**, vous deux avez fait le période à Lyon plus agréable avec des bon moments des partages en soirées, crémaïversaire, restos, bar et d'autres.

Je tiens à remercier aussi **Fabrice** pour toute l'aide apporté avec la théorie au tour de diffusion de la lumière et de me faire comprendre que parfois, même si l'on obtient un résultat de 1000 nm de moyenne donné par la DLS, ça peut ne pas être la réalité. En vrai, c'est moi qui devrais regarder la « réalité » dans un autre angle, en utilisant d'autres techniques des caractérisations. Ce concept ne se résume pas au niveau scientifique, merci de m'avoir montré aussi un autre point de vue sur les problèmes plus profond de la société comme la politique, l'économie, les problèmes sociaux et d'autres. Tu m'as fait avoir un peu plus d'espoir au futur de la civilisation. Bien sûr que toutes ces discussions sérieuses (ou pas trop sérieuses, parfois) étaient souvent accompagnées d'un verre d'Islay ou d'une bonne Caipirinha.

Merci aussi a toutes les collègues du LCPP que j'ai croisé pendant ces 4 ans au labo. Tous les étudiants de *millésime 2010*: **Elsa, Fannie, Geoffroy, Etienne, Miloud, Estevan, Arash, Anne, Ian, Ari, Pierre, Céline, Weijing, Emilie Groison, Qiao, Jérôme, Thomas, Nancy, Francis, Ségolène**. Merci **Ana** de m'avoir beaucoup aidé avec l'intégration à la vie au labo et dehors aussi ☺. **Julien**, merci mon partenaire de dance et chant au laboratoire sur le rythme de RTL2. **Edgar** je te remercie également pour ta disponibilité et d'être toujours prêt à aider toute le monde. Un merci spécial à **Virginie, Elena** et **Isabelle** qui ont dédié leur temps à participer de ma thèse, 7 ans plus tard. **Isabelle** merci d'être venue exprès au jour de ma soutenance.

Je tiens à remercier également les étudiants du LCPP des *millésimes* plus récentes, les *AOC*: **Gisèle, James, Fannie, Eliana, Igor, João, Paulo, Rui, Margarida, Ana Rita, Duarte, Rodolfo, André** et **Nicolas**. *Les grand crus*: **Ali, Aaron, Islem, Cédric Bergerbit, Astrid, Lucie, Matthieu, Mathieu, Julliette, Magali, Yashmin, Fabiana, Rita, Amel** et **Daniel**. *Les premiers grands crus* : **Cédric Ysacco, Bashir, Benjamin, Amélie, Bastian, Dang, Emilie Velasquez, Benoît, Guilhem, Laura, Arthur, Isabelle, Yue, Winnie, Jennifer, Lionel, Ana Carolina, Solmaz, Sam, Ming, Arne, Barbara, Thaissa, Keran, Edgar** et **Anderson**. Je remercie également mes petits-enfants **Mathieu** et **Daniel**. Un merci spécial aux *aussies*: **Ming** (pour toute la patience avec l'entraînement en anglais et pour le Koala) et **Sam** de m'avoir montré que je suis un petit gamin au niveau sport et, particulièrement, un bébé au niveau vélo. Merci **Jennifer** pour ton amitié et merci d'être toujours présente pendant mes 3 ans de thèse, soit au labo, soit dehors en soirées, bars, restos, congrès et d'autres. **Laura** (et **Mathias**) je te remercie pour l'accueil dans ta ville de cœur, la Croix-Rousse. Au début je pensais que cela était juste un quartier, mais après j'ai compris que d'être un croix-roussien



va au-delà d'être juste née dans un quartier, c'est plutôt une façon de vivre. Et que le croix-roussien sont fier de l'être et aussi fier d'avoir un caillou ☺ (Ok, ok, un gros caillou...ops... pardon, en fait c'est « *Le Gros Caillou* »). Merci aussi **Magali**, qui a pris le rôle de Laura pour l'organisation des événements du labo, merci pour la patience et aussi pour les bonnes soirées ensemble (quand t'étais disponible, bien sûr, ce que n'était pas trop fréquent). Merci **Benoît** et **Guilhem**, pour la bonne ambiance amenée au labo depuis 2011. **Lionel SeBOSCO**, merci pour ta bonne humeur et pour rentre les jours passés au labo beaucoup plus marrant.

**Arthur**, tout au début je pensais que tu n'étais pas trop agréable avec les personnes que tu ne connaissais pas. Après t'avoir connu, ça a devenu clair et certain. Dans l'autre côté, quand on a l'opportunité de te connaître, on voit quel être humain exceptionnel tu es. Ton amitié au labo (spécialement pendant les derniers mois) m'a permis de connaître quelqu'un de vraiment spécial. Merci pour toutes les moments de partages au tour des quelques verres en soirées, bars, restos, piquenique, pétanque, barbecue et d'autres occasions, au final, il avait toujours une occasion pour un verre. Merci pour tout l'enseignement sur le système politique français et pour les occasions de discuter profondément des thèmes socioéconomiques. Je te remercie énormément pour ton amitié et pour les très bons moments passés à Lyon.

**Lucie**, je tiens à te remercier d'être cette personne fantastique avec qui j'ai pu échanger. Merci pour ton amitié, ton encouragement pendant ma rédaction, pour la camaraderie à chaque pause-café, pour tous les petits moments du jour à jour qui ont rendu mon temps au labo plus heureux. En dehors de la vie au labo, nous avons passé des moments inoubliables avec toi et **Laura**, et je suis sûr que si un jour on se retrouve à Lyon une autre fois, il ne faudra jamais retourner au Boston. Et n'oublie pas « l'essentiel est invisible pour les yeux », surtout quand l'essentiel est devant la porte d'entrée du labo et on ne voit pas car il est plus petit que la vitre (Ok... je rigole, on voit ton front, mais limite quand même). Merci encore Lucie, tu es comme une sœur pour moi et ça restera comme ça pour toujours.

**Aaron**, estoy más borracho que nacho, cariño. Gracias **Elena** et **Aaron** pour faire le période à Lyon plus cool et avec beaucoup de fiesta. Quel que soit le bar, le Flan's ou le Flan's, ou encore le Flan's, on a passé de très bons moments au Flan's. Vous deux, avec **Arne**, ont fait partie de nos quotidien, avec pleins de repas pendant les weekends ensemble et, c'est vrai que j'attends toujours le *Frango com Batatas* d'Elena. Obrigado, Gracias, Danke, à vous trois pour tout.

Avoir passé quelques années à Lyon m'a fait créer des forts liens avec des gens de la ville. Initialement je voudrais exprimer toute ma gratitude à **Bernard** que étais toujours

présent comme un oncle pour moi à Lyon. J'ai passé des très bons moments en ta compagnie et ça me fera des souvenirs pour la vie. Merci à toi pour tout ce que tu as fait pendant mon installation à Lyon (les deux fois). Tu seras toujours très bien venu chez-moi, à Lorena, ou ailleurs. Merci également à ta famille, **Martine, Jean-Claude, Marina, Christophe, Leane, Chloé et Sandrine** et bien sûr à tes amis, **Cathy, Patrick, Vincent, Mathieu et Antoine** qui m'ont toujours très bien accueilli chez-eux pour me introduire la culture et, principalement, la bouffe française.

Il y a des amis, que sont plus qu'ami, c'est de la famille qu'on peut choisir, **Laurent**, merci pour ta gentillesse, ton cœur généreux et pour ta façon souriante de vivre. Toi avec **Paula** ont fait mon séjour à Lyon moins dur quand le sujet était la distance de la famille, je vous remercie pour faire partie de notre famille française/latine !

Como não lembrar dos meus queridos conterrâneos do LCPP **Anderson, Gigi, Fabiana, Carlo** (vai... também já é bem brasileiro), **Yashmin, Toinho, João, Paulo e Ygoso**. Obrigado por todos os momentos juntos e por fazer o laboratório bem brasileiro, ajudando a suportar a saudades do Brasil. **Anderson e Gigi**, vocês são pessoas excepcionais e maravilhosas que eu vou levar para sempre em meu coração, que vocês continuem sempre assim. Muito obrigado por toda a alegria e risos proporcionados durante o período que passamos juntos em Lyon. **Paulo Marques**, obrigado por ter vindo da Bélgica para a minha tese e obrigado também pela excelente companhia para bebermos sempre bons drinks, seja em Lyon ou em Albi.

Bom não poderia deixar faltar meus padrinhos de batismo de laboratório, **Gizelda e Amilton**. Tudo que alcancei hoje na minha vida profissional foi graças a vocês. Vocês me ensinaram a dar os primeiros passos no laboratório e mesmo eu jogando no chão as primeiras pérolas da Gizelda, vocês continuaram confiando em mim e no meu potencial. Investiram tempo e dedicação na minha formação. Sou e serei eternamente grato a vocês pelos ensinamentos profissionais e muito além disso, pela participação de vocês na minha formação como ser humano. Obrigado pela amizade e companheirismo de sempre e continuem sendo essas pessoas maravilhosas que são, sempre promovendo o bem ao próximo.

Gostaria de agradecer também minha família. Obrigado a família **Rodrigues** e a **Guimarães** pelo incondicional apoio. Agradeço especialmente à minha **Mãe** e ao meu **Pai**, sem a força e a persistência de cada um de vocês, a transformação desse sonho de ser doutor em realidade não seria possível. Tudo que tenho e tudo que sou, devo a vocês dois, muito obrigado e amo vocês. **Diego**, meu irmão amado, dedico essa tese à sua memória.

Aos meus grandes amigos, meu muito obrigado, o apoio de vocês foi peça fundamental para a obtenção desse título. **Joyce, Juninho, Dias, Mayco, Leo, Camy e Carol**, cada um de vocês sabe a papel fundamental que exercem em minha vida. Obrigado por estarem sempre presentes.

**Thaissa**, obrigado amorzinho por ter feito o período do meu doutorado tão mais fácil. Sua presença em Lyon fez a distância e saudades do Brasil serem mais suaves. Afinal tudo com você parece ser mais suave e calmo. Tatynha, você é fantástica e nossa amizade será para a vida toda. Vou te guardar no meu coraçãozinho para sempre. Obrigado também pela paciência em me ajudar com o inglês para escrever a tese.

**Bárbara**, tem pessoas que são realmente transformadoras em nossas vidas, pessoas que são capazes de mudar nosso jeito de ser e alterar nossa natureza. Tratando a natureza com um olhar maniqueísta das coisas, podemos separar em pessoas que nos alteram negativamente e positivamente. Eu não consigo enxergar como você possa ter gerado algo de negativo em minha vida. Você é luz. Suas palavras, ou somente sua presença, são capazes de gerar pontinhos e luz no coração das pessoas próximas a ti que as transformam em pessoas melhores. Você é bondade pura. Eu sou muito grato por ter conhecido uma pessoa tão fenomenal quanto você, e de coração tão bom. Você foi capaz de me transformar em um ser humano melhor, com menos preconceito, menos discriminação contra *aspessoa* e com uma maior capacidade de amar, compreender melhor e aceitar o desconhecido. Você me ensinou o sentido (semântico e literal) de empatia e hoje tento passar isso adiante, sempre uso você como exemplo de pessoa empática na selvageria do mundo moderno. Você me ajudou a me amar mais também e passei momentos de muita superação ao seu lado, obrigado pela força. Coração, não se esqueça, você é vida, e vida não se destrói. Não se destrói, porque eu não vou deixar, estarei sempre ao seu lado para o que você precisar, obrigado por ser quem você é.

## ABSTRACT

In this work reversible addition-fragmentation chain transfer (RAFT) polymerization was exploited to synthesize magnetic latex particles decorated with *stimuli*-responsive polymer brushes. First, five hydrophilic (co)polymers with various compositions were successfully prepared by RAFT solution (co)polymerization of acrylic acid (AA) and 2-dimethylaminoethyl methacrylate (DMAEMA) for different AA to DMAEMA molar ratios. The obtained macromolecular RAFT agents (macroRAFTs), PAA or PDMAEMA homopolymers and P(AA-*co*-DMAEMA) copolymers, displayed interesting pH- and thermo-responsive properties. These hydrophilic macroRAFTs were then chain extended with styrene leading to the formation of well-defined amphiphilic block copolymers. An aqueous dispersion of iron oxide clusters was next prepared using a strategy based on emulsification/solvent evaporation in which the block copolymers were used as stabilizers. By varying the experimental conditions (sonication power, macroRAFT concentration and pH of the medium), the cluster size could be controlled from 45 up to 300 nm. These clusters were then used as seeds in styrene emulsion polymerization in the presence of a crosslinker. The iron oxide clusters were individually encapsulated into a polymer shell generating latex particles, stabilized by the hydrophilic segment of the block copolymers, and displaying interesting magnetic properties. At last, these magnetic beads were evaluated as carriers in the magnetic separation of bacteria. The magnetic latex particles decorated with P(AA-*co*-DMAEMA) copolymers were successfully employed for the capture and trigger release of bacteria, allowing their concentration in a biological sample.

## RESUME

Dans le cadre de ce travail de thèse, la polymérisation de type RAFT a été exploitée pour synthétiser des particules de latex magnétiques décorées de polymères stimulables. Cinq (co)polymères hydrophiles ont tout d'abord été préparés via la (co)polymérisation RAFT en solution d'acide acrylique (AA) et de méthacrylate de 2-diméthylaminoéthyle (MADAME). Les agents macromoléculaires obtenus (macroRAFT) : des homopolymères de PAA ou PMADAME ainsi que des copolymères P(AA-co-MADAME), présentent une sensibilité au pH et à la température. Ces macroRAFT hydrophiles ont ensuite été utilisés dans des réactions d'extension de chaîne avec du styrène conduisant à la formation de copolymères à blocs amphiphiles bien définis. Puis, des dispersions aqueuses d'agrégats (clusters) de nanoparticules d'oxyde de fer (OF) ont ensuite été préparées via un procédé de mini-émulsification/évaporation de solvant, en utilisant les copolymères à blocs comme stabilisants. Après optimisation des conditions expérimentales (sonication, concentration de macroRAFT, pH), des agrégats de taille contrôlée (45 à 300 nm) ont pu être obtenus. Ces clusters ont ensuite été utilisés comme semence lors de la polymérisation en émulsion du styrène, conduite en présence d'un agent de réticulation. Les clusters d'OF ont été individuellement encapsulés par une couche de polymère, formant des particules magnétiques stabilisées par le segment hydrophile des copolymères à blocs. Enfin, les particules magnétiques décorées de copolymères de P(AA-co-MADAME) ont été utilisées avec succès pour la capture et le relargage de bactéries grâce à la modulation de leurs propriétés de surface en fonction du pH.

## ABBREVIATIONS

<i>A</i>	interfacial area
AA	acrylic acid
AAm	<i>N</i> -Isopropylacrylamide
ACPA	4,4'-azobis(cyanovaleric acid)
ACS	American chemical society
ADIBA	2,2'-azobis[2-(2-imidazolin-2-yl)propane]dihydrochloride
AEMH	aminoethylmethacrylate
AIBN	azobisisobutyronitrile
APS	ammonium persulfate
ATRP	atom transfer radical polymerization
BA	butyl acrylate
CMC	critical micellar concentration
CNC	iron oxide clusters
CTA	chain transfer agent
CTPPA	4-cyano-4-thiothiopropylsulfanylpentanoic acid
CTX	chlorotoxin
DCM	dichloromethane
$D_i$	individual diameter measured by TEM
DLS	dynamic light scattering
DMAEA	2-dimethylaminoethyl acrylate
DMAEMA	2-dimethylaminoethyl methacrylate
DMF	dimethylformamide
DMSO	dimethyl sulfoxide
$D_n$	number-average diameter determined by TEM
DP	degree of polymerization
DTB	dithiobenzoate
DVB	divinyl benzene
$D_w$	weighted-average diameter determined by TEM
$D_z$	intensity-average diameter determined by TEM
EDC	(3-dimethylaminopropyl)carbodiimide methiodide
EGDMA	ethyleneglycol dimethacrylate
EMA	European medicines agency

EtO	diethyl ether
EVB	ethyl vinylbenzene
FA@IONP	fatty acid modified iron oxide nanoparticles
FDA	food and drug administration
FTIR	Fourier transform infrared spectroscopy
G	graphene
GMA	glycidyl methacrylate
HPMA	hydroxypropyl methacrylate
IOC <sup>TGA</sup>	iron oxide content
IONP	iron oxide nanoparticles
KPS	potassium persulfate
LAMs	less activated monomers
LCST	low critical solution temperature
LDH	layered double hydroxides
LDH	Layered double hydroxide
MAA	methacrylic acid
macroRAFT	macromolecular RAFT agents
MAMs	more activated monomers
MBA	<i>N,N'</i> -methylenebisacrylamide
MHWS	Mark-Houwink-Sakurada
MMA	methyl methacrylate
MPS	3-(trimethoxysilyl)propyl methacrylate
MRI	magnetic resonance imaging
<i>mSiO</i> <sub>2</sub>	mesoporous silica
<i>mTiO</i> <sub>2</sub>	mesoporous titania
$\bar{n}$	number of radical per particle
$N_A$	Avogadro's number
NiPAM	<i>N</i> -isopropylacrylamide
NMP	nitroxide-mediated radical polymerization
NMR	nuclear magnetic resonance
$N_p$	number of particles per volume
O/W	oil in water system
OA@IONP	oleic acid modified iron oxide nanoparticles

P4VP	poly(4-vinyl pyridine)
PC	polymer content
PDA	polydopamine
PEG	poly(ethylene glycol)
PEGA	poly(ethylene glycol) methyl ether acrylate
PEGMA	poly(ethylene glycol) methyl ether methacrylate
PEI	polyethyleneimine
PetEt	petroleum ether
PISA	polymerization induced self-assembly
PMA	poly(methyl acrylate)
PMAMVE	Poly(maleic anhydride-alt-methyl vinyl ether)
PpO	diisopropyl ether
PPO	poly(propylene glycol)
PS	polystyrene
PVA	poly(vinyl alcohol)
PVP	poly(vinylpyrrolidone)
RAFT	reversible addition-fragmentation chain transfer
RDRP	reversible-deactivation radical polymerization
REEP	macroRAFT-assisted encapsulating emulsion polymerization
RI	refractive index
R <sub>p</sub>	polymerization rate
S	styrene
SC	solids content
SDS	sodium dodecyl sulfate
SEC	size exclusion chromatography
SPION	superparamagnetic iron oxide nanoparticles
SQUID	superconducting quantum interference device
TEM	transmission electron microscopy
TEOS	tetraethoxysilane
TFMAA	2-(trifluoromethyl) acrylic acid
TGA	thermogravimetric analysis
THF	tetrahydrofuran
TTC	trithiocarbonate



UCST	upper critical solution temperature
VBK	9-(4-vinylbenzyl)-9H-carbazole
W/O	water in oil system
XRD	X-ray diffractometry
$Y_{IO}$	yield of iron oxide incorporation in the magnetic fraction
$Z_{av}$	Intensity-mean average diameter determined by DLS
$\gamma$	interfacial tension
$\omega_{free}$	fraction of free latex particles
$\omega_{mag}$	fraction of magnetic latex particles
$\nabla H$	magnetic gradient field
$\eta$	viscosity of the medium
$\nu_{as}$	asymmetric stretching vibrations bands
$\nu_s$	symmetric stretching vibrations bands
$M_r$	remanent magnetization
$M_s$	magnetization at saturation
$\Delta \bar{G}$	Gibbs energy

## TABLE OF CONTENTS

GENERAL INTRODUCTION .....	25
REFERENCES .....	31

### CHAPTER I - BIBLIOGRAPHIC REVIEW

1. Introduction .....	35
2. Iron oxide nanoparticles .....	35
3. Synthesis of iron oxide-based composite particles.....	37
3.1. Iron oxide encapsulation by an inorganic shell.....	37
3.2. Iron oxide/polymer composite particles.....	39
3.2.1. Mixture of pre-formed polymers and iron oxide nanoparticles .....	41
3.2.2. Simultaneous synthesis of polymer and iron oxide.....	43
3.2.3. Iron oxide formation in the presence of polymer particles .....	43
3.2.4. Polymerization in the presence of iron oxide.....	43
4. Applications of magnetic particles.....	46
4.1. Biomedical applications .....	46
4.1.1. In vitro applications .....	46
4.1.2. In vivo applications .....	48
4.2. Environmental applications.....	50
4.3. Support for catalysis.....	51
4.4. Miscellaneous .....	52
5. Conclusions .....	54
References .....	55

### CHAPTER II - SYNTHESIS OF MACROMOLECULAR RAFT AGENTS

1. Introduction .....	65
2. Bibliographic review .....	65
2.1. Free radical polymerization.....	65
2.2. Reversible-Deactivation Radical Polymerization (RDRP).....	67
2.2.1. Reversible addition-fragmentation chain transfer (RAFT) .....	68
2.2.2. Macromolecular design.....	71
2.2.3. Synthesis of block copolymers.....	72
3. Experimental Section .....	74
3.1. Materials.....	74

<b>3.2. Methods</b> .....	<b>75</b>
3.2.1. <i>Synthesis of hydrophilic macroRAFT agents</i> .....	75
3.2.2. <i>Chain extension reactions</i> .....	77
3.2.3. <i>Synthesis of amphiphilic macroRAFT agents</i> .....	77
3.2.4. <i>Determination of the cloud point temperature of the macroRAFT agents</i> .....	78
<b>3.3. Characterizations</b> .....	<b>78</b>
3.3.1. <i><sup>1</sup>H NMR</i> .....	78
3.3.2. <i>Size exclusion chromatography (SEC)</i> .....	79
<b>4. Results and Discussion</b> .....	<b>81</b>
<b>4.1. Synthesis of hydrophilic macroRAFT agents</b> .....	<b>81</b>
4.1.1. <i>Synthesis of poly(acrylic acid) macroRAFT agents: PAA-TTC</i> .....	82
4.1.2. <i>Synthesis of poly(2-dimethylaminoethyl methacrylate) macroRAFT agents: PDMAEMA-TTC</i> .....	84
4.1.3. <i>Synthesis of poly(2-dimethylaminoethyl methacrylate-co-acrylic acid) macroRAFT agents: P(DMAEMA-co-AA)-TTC</i> .....	88
4.1.4. <i>Chain extension reactions</i> .....	92
4.1.5. <i>Synthesis of amphiphilic block copolymers</i> .....	96
<b>4.2. Thermoresponsive properties of the different macroRAFTs</b> .....	<b>100</b>
4.2.1. <i>Effect of pH on the <math>T_{CP}</math> of the DMAEMA-based macroRAFT agents</i> .....	102
4.2.2. <i>Effect of ionic strength on the <math>T_{CP}</math> of PDMAEMA-TTC</i> .....	104
4.2.3. <i>Effect of the macroRAFT composition on the <math>T_{CP}</math></i> .....	105
<b>5. Conclusions</b> .....	<b>106</b>
<b>References</b> .....	<b>108</b>

## CHAPTER III - FORMATION OF IRON OXIDE CLUSTERS

<b>1. Introduction</b> .....	<b>118</b>
<b>2. Bibliographic review</b> .....	<b>118</b>
<b>2.1. Iron oxide nanoparticles</b> .....	<b>118</b>
2.1.1. <i>Structure of iron oxide</i> .....	118
2.1.2. <i>Properties of IONPs</i> .....	119
2.1.3. <i>Synthesis of IONPs</i> .....	122
2.1.4. <i>Surface modification</i> .....	125
<b>2.2. Cluster formation</b> .....	<b>126</b>
2.2.1. <i>Polyelectrolyte/iron oxide self-assembly</i> .....	126
2.2.2. <i>Solvent displacement</i> .....	127
2.2.3. <i>Emulsification/solvent evaporation</i> .....	128
<b>2.3. Selected synthetic strategy</b> .....	<b>130</b>

<b>3. Experimental Section .....</b>	<b>132</b>
<b>3.1. Materials.....</b>	<b>132</b>
<b>3.2. Methods .....</b>	<b>132</b>
3.2.1. <i>Small-scale preparation of IO clusters.....</i>	<i>132</i>
3.2.2. <i>Scale-up process for the preparation of IO clusters.....</i>	<i>133</i>
3.2.3. <i>Yield of cluster formation .....</i>	<i>133</i>
3.2.4. <i>Purification of the magnetic clusters.....</i>	<i>133</i>
<b>3.3. Characterization techniques .....</b>	<b>134</b>
3.3.1. <i>Dynamic light scattering (DLS) .....</i>	<i>134</i>
3.3.2. <i>Zeta potential measurements.....</i>	<i>135</i>
3.3.3. <i>Electron microscopy.....</i>	<i>135</i>
3.3.4. <i>Thermogravimetric analysis (TGA).....</i>	<i>136</i>
3.3.5. <i>Raman spectroscopy.....</i>	<i>136</i>
3.3.6. <i>Superconducting quantum interference device (SQUID) analysis.....</i>	<i>136</i>
3.3.7. <i>Fourier Transform Infrared (FTIR) spectroscopy .....</i>	<i>137</i>
3.3.8. <i>X-ray diffractometry (XRD).....</i>	<i>137</i>
<b>4. Results and Discussion.....</b>	<b>137</b>
<b>4.1. Characterization of the commercial iron oxide nanoparticles .....</b>	<b>137</b>
4.1.1. <i>Crystalline structure.....</i>	<i>137</i>
4.1.2. <i>Evaluation of chemical modification.....</i>	<i>138</i>
4.1.3. <i>Particle size and morphology.....</i>	<i>139</i>
4.1.4. <i>Magnetic properties .....</i>	<i>141</i>
<b>4.2. PDMAEMA-based iron oxide clusters.....</b>	<b>142</b>
4.2.1. <i>Effect of sonication time .....</i>	<i>144</i>
4.2.2. <i>Effect of sonication power.....</i>	<i>145</i>
4.2.3. <i>Effect of macroRAFT concentration.....</i>	<i>148</i>
4.2.4. <i>Effect of pH.....</i>	<i>154</i>
4.2.5. <i>Scale up experiments.....</i>	<i>157</i>
<b>4.3. PAA-based iron oxide clusters.....</b>	<b>158</b>
4.3.1. <i>Effect of macroRAFT concentration.....</i>	<i>158</i>
4.3.2. <i>Effect of the [NaOH]/[PAA-b-PS-TTC] ratio .....</i>	<i>162</i>
<b>4.4. Cluster preparation in the presence of hydrophilic macroRAFTs: influence of the PS block .....</b>	<b>165</b>
<b>4.5. P(AA-co-DMAEMA)-based clusters.....</b>	<b>168</b>
<b>4.6. Surface properties .....</b>	<b>171</b>
<b>5. Conclusions .....</b>	<b>172</b>
<b>References .....</b>	<b>175</b>

## CHAPTER IV - ENCAPSULATION OF IRON OXIDE CLUSTERS VIA EMULSION POLYMERIZATION

<b>1. Bibliographic review</b> .....	<b>183</b>
<b>1.1. Polymerization in dispersed media</b> .....	<b>183</b>
1.1.1. <i>Emulsion polymerization</i> .....	183
1.1.2. <i>Seeded emulsion polymerization</i> .....	186
1.1.3. <i>Miniemulsion polymerization</i> .....	187
<b>1.2. Polymer encapsulation of iron oxide nanoparticles</b> .....	<b>189</b>
1.2.1. <i>Miniemulsion polymerization</i> .....	189
1.2.2. <i>Emulsion polymerization</i> .....	191
<b>2. Experimental Section</b> .....	<b>195</b>
<b>2.1. Materials</b> .....	<b>195</b>
<b>2.2. Methods</b> .....	<b>195</b>
2.2.1. <i>Seeded emulsion polymerization</i> .....	195
2.2.2. <i>Magnetic separation</i> .....	196
<b>2.3. Characterizations</b> .....	<b>197</b>
2.3.1. <i>DLS</i> .....	197
2.3.2. <i>Electron microscopy</i> .....	198
2.3.3. <i>TGA</i> .....	198
<b>3. Results and Discussion</b> .....	<b>198</b>
<b>3.1. Encapsulation of PDMAEMA-based clusters</b> .....	<b>199</b>
3.1.1. <i>Effect of the polymerization process</i> .....	199
3.1.2. <i>Effect of the addition of a crosslinker for 10.0 wt% theoretical polymer content</i> .....	205
3.1.3. <i>Effect of the addition of a crosslinker for 2.6 wt% theoretical polymer content</i> .....	210
<b>3.2. Encapsulation of PAA-based clusters</b> .....	<b>212</b>
<b>3.3. Encapsulation of P(DMAEMA-co-AA)-based clusters</b> .....	<b>215</b>
<b>3.4. Magnetic properties of the the composite IO/polymer latex particles</b> .....	<b>217</b>
<b>4. Conclusions</b> .....	<b>221</b>
<b>References</b> .....	<b>223</b>

## CHAPTER V - USE OF MAGNETIC CARRIERS FOR BACTERIA CAPTURE AND TRIGGER RELEASE

<b>1. Introduction</b> .....	<b>231</b>
<b>2. Bibliographic review</b> .....	<b>231</b>
<b>2.1. Magnetic separation</b> .....	<b>231</b>

<b>2.2. Bacteria</b> .....	<b>234</b>
2.2.1. <i>Structure</i> .....	238
<b>3. Experimental Section</b> .....	<b>240</b>
<b>3.1. Materials</b> .....	<b>240</b>
<b>3.2. Methods</b> .....	<b>242</b>
3.2.1. <i>Preparation of bacteria samples</i> .....	242
3.2.2. <i>Magnetic separation</i> .....	242
<b>3.3. Characterizations</b> .....	<b>245</b>
3.3.1. <i>Optical microscopy</i> .....	245
3.3.2. <i>Electron microscopy</i> .....	246
<b>4. Results and Discussion</b> .....	<b>246</b>
<b>4.1. High bacteria concentrations</b> .....	<b>247</b>
4.1.1. <i>Effect of PDMAEMA-based magnetic latex particles and E. coli concentrations</i> .....	247
4.1.2. <i>Effect of PAA-based magnetic latex particles and E. coli concentrations</i> .....	249
4.1.3. <i>Effect of MLP surface composition on E. coli separation</i> .....	250
4.1.4. <i>Effect of MLP surface composition on Bs separation</i> .....	252
<b>4.2. Low bacteria concentrations</b> .....	<b>254</b>
4.2.1. <i>Use of amphoteric magnetic latex particle to increase the microbial cell concentration.</i>	254
<b>4.3. Electron microscopy</b> .....	<b>255</b>
<b>5. Conclusions</b> .....	<b>258</b>
<b>6. References</b> .....	<b>260</b>
<b>GENERAL CONCLUSION</b> .....	<b>264</b>
<b>PERSPECTIVES</b> .....	<b>269</b>
<b>ANNEXES</b> .....	<b>271</b>



## GENERAL INTRODUCTION

The elaboration of polymer/inorganic nanocomposites is attracting a continued interest from both industry and academia due to the benefits gained from the combination of polymers and inorganic solids.<sup>1</sup> Nanocomposite materials are composed of a matrix containing nanofillers that possess at least one of their dimensions smaller than 100 nm, and which can be nanoparticles, nanotubes or nanoplatelets.<sup>2</sup> The choice of the nanofiller and its compatibility with the matrix are crucial parameters to obtain materials with improved properties. For instance, carbon nanotubes can be employed to obtain reinforced materials in terms of mechanical properties, clay platelets can be used for the preparation of films with enhanced barrier properties, and cerium oxide nanoparticles are generally added to produce nanocomposites with better UV- or scratch resistance. Moreover, new properties can be also conferred to nanocomposites, such as magnetism or fluorescence, via the incorporation in the hybrid material of magnetic or fluorescent nanoparticles, respectively.

Transition metal oxide nanoparticles with magnetic properties can be used for the preparation of magnetic particles aiming at potential applications in catalysis, optics, drug delivery, magnetic resonance imaging (MRI) and *in vitro* or *in vivo* immunoassays.<sup>3-6</sup> Typically, iron oxide nanoparticles (IONPs) are used as magnetic materials due to their better biocompatibility and stability to oxidation than other metal oxides, such as cobalt and nickel, which are usually toxic.

Magnetic particles have been successfully employed as carriers in applications that require the isolation of specific targets from a fluid medium. Nonetheless, the use of bare iron oxide nanoparticles in the biological field is restricted as their hydrophilic surface can promote irreversible interactions with living organisms or tissues present in the nanoparticles surrounding environment. In addition, their small size (generally smaller than 20 nm) can lead to a low magnetic separation rate under a magnetic field, leading to time-consuming procedures. So the multi-encapsulation of these nanoparticles into a protective shell will not only avoid their contact with biological organisms, but it will also decrease the time for magnetic separation due to the higher concentration of the magnetic material. The protective coating can be either an inorganic shell such as silica (SiO<sub>2</sub>),<sup>7</sup> titania (TiO<sub>2</sub>)<sup>8</sup> or an organic shell like polymers.<sup>9, 10</sup> It is worth mentioning that particle functionalization is of key importance in applications involving magnetic particles, as the adsorption of targets onto the magnetic particle surface require the incorporation of appropriate functional groups.



## General Introduction

For *in vitro* immunoassays, magnetic composite particles can be advantageously used to overcome time-consuming and laborious steps of centrifugation or filtration.<sup>11, 12</sup> However, the time needed for the magnetic separation to be effective has to be short, a few seconds, otherwise this method can be considered less relevant than typical methods. The magnetic separation rate [ $v_x(x)$ ] is given by:

$$v_x(x) = \frac{2r^2 \cdot M_s \cdot \nabla H}{9\eta} \quad (1)$$

where  $r$  is the radius of the composite particle,  $M_s$  the magnetization at saturation,  $\nabla H$  the magnetic gradient field, and finally  $\eta$  the viscosity of the medium. In order to have high magnetic separation rates, only the size and  $M_s$  can be manipulated, as the magnetic gradient field depends on the magnet used while the viscosity of the medium is fixed by the nature of the sample. Therefore, the magnetic composite particles must fulfill some criteria as illustrated in Figure 1.

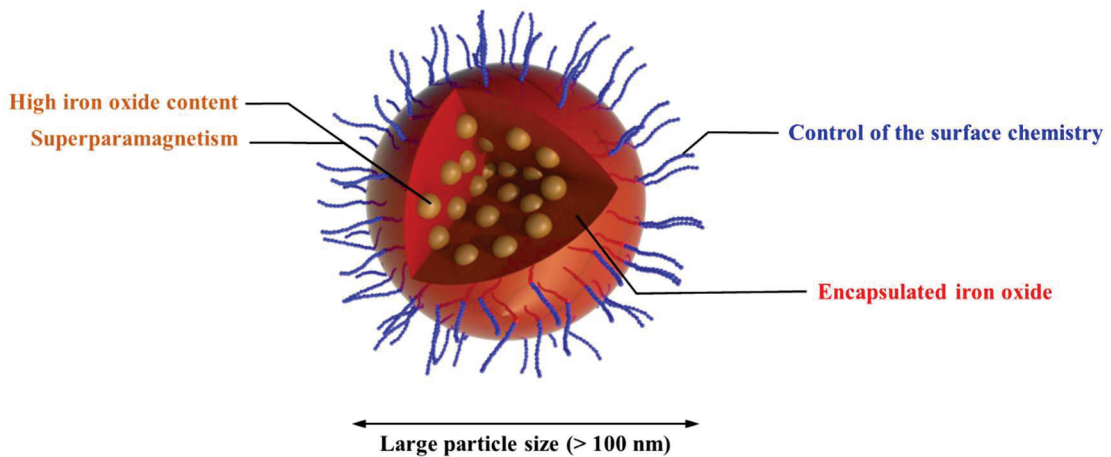


**Figure 1** – Schematic representation of composite magnetic particles and the characteristics required for their application in fields where magnetic separation is needed.

As demonstrated in equation (1), the larger is the particle size and the higher is the magnetization at saturation, the faster will be the separation. Besides, the magnetization at saturation is directly related to the magnetic content into the composite particle, *i.e.*  $M_s$  increases with increasing the iron oxide content.

Emulsion polymerization is a process widely applied for the synthesis of iron oxide/polymer particles<sup>9</sup> which can fulfill most of the criteria presented in Figure 1, since particles with relative large sizes ( $> 100$  nm) are obtained with a good control of particle surface functionalization depending on the stabilizer employed. In addition, by finely tuning the

compatibility between the inorganic and organic phases, magnetic particles exhibiting encapsulated morphology can be obtained. However, most of the examples described in the literature show hybrid particles with low magnetization at saturation due to low iron oxide content.<sup>13-15</sup> Alternatively, the formation of iron oxide clusters followed by emulsion polymerization to form a thin protective polymeric shell around these magnetic seeds has demonstrated to be a successful strategy to obtain particles with high iron oxide content.<sup>16, 17</sup> Iron oxide clusters formed from aggregates of superparamagnetic IONPs tend to maintain the superparamagnetism.<sup>a</sup> This is an important property in applications for which magnetic separation is needed. Indeed, if the particles would present a remanent magnetization after magnetic field removal, this would generate magnetic forces among the particles hindering their redispersion. This phenomenon would affect either the elution of the captured target or the recycling of the magnetic particles.

Polymer particles synthesized via emulsion polymerization are generally stabilized by conventional surfactants, which are small molecules with amphiphilic character. However, the presence of these molecules can negatively affect the properties of the final material. Alternatively, amphiphilic block copolymers can be used, not only to stabilize the colloids, but also to precisely control the surface functionality of the polymer particles. This functionalization depends on the chemical nature of the hydrophilic moiety of the amphiphilic block copolymers. The surface functionalization of the magnetic polymer particles is obviously a key parameter to afford suitable interactions with the biological targets during the magnetic separation.

Macromolecular design has been revolutionized by the advent of Reversible-Deactivation Radical Polymerization (RDRP) techniques, allowing the synthesis of a variety of block copolymers with predetermined structures and functionalities. Among the various RDRP processes, reversible addition–fragmentation chain transfer (RAFT) has received a lot of attention due its versatility allowing the successful synthesis of block copolymers from a wide range of monomers. This process associated to (mini)emulsion polymerizations has shown to be a powerful tool for the preparation of polymer particles with controlled surface functionalization.<sup>18</sup>

---

<sup>a</sup> Superparamagnetism can be explained as a “turn on/turn off” ability. When the nanoparticles are exposed to a magnetic field, a magnetization is observed (“turned-on”), but when this field is removed, there is no remanent magnetization ( $M_r \approx 0$ , “turned-off”).

The strategy applied in this work for the preparation of magnetic polymer particles is outlined in Figure 2. First, well-defined amphiphilic block copolymers were synthesized by RAFT polymerization in solution. In a first step, acrylic acid (AA) and 2-dimethylaminoethyl methacrylate (DMAEMA) monomers were homopolymerized to synthesize hydrophilic polymer chains carrying carboxylic acid or tertiary amine functions, respectively, or copolymerized to prepare hydrophilic chains carrying both functions. In a second step, amphiphilic block copolymers were synthesized using the hydrophilic macroRAFTs, carrying reactivatable trithiocarbonate groups, in a chain extension reaction with styrene. The resulting amphiphilic macroRAFTs, with controlled composition, were employed as stabilizer of iron oxide clusters obtained by an emulsification/solvent evaporation process. It is important to point out that the magnetic nanoparticles used in this work were superparamagnetic, and so were the resulting clusters. Then, seeded-emulsion polymerization was carried out to form a protective polymeric outer shell around the clusters, which are used as seeds in the polymerization process, leading to their encapsulation. Furthermore, by changing the monomer composition of the hydrophilic part of the amphiphilic macroRAFTs, it is possible to tune the particles surface properties, allowing the employment of these particles in magnetic separation of different targets. Finally, particles with different surface functionalities were tested in the magnetic separation of bacteria via capture and trigger release processes, with the aim of isolating and concentrating these species from complex biological fluids as schematically represented in Figure 2.

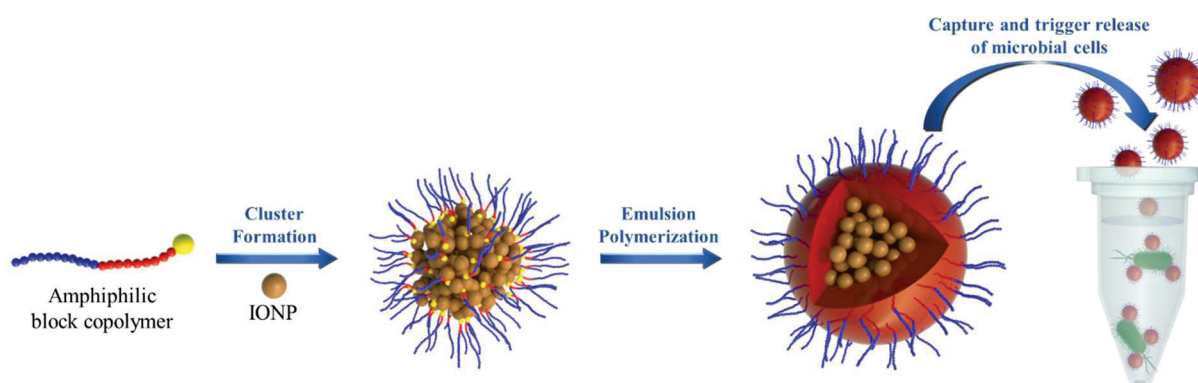


**Figure 2** – Synthetic route employed for the synthesis of iron oxide/polymer composite particles. Amphiphilic block copolymers were prepared via RAFT polymerization and applied as stabilizer of iron oxide clusters obtained by an emulsification/solvent evaporation process. Magnetic polymer particles were then formed via seeded emulsion polymerization using the clusters as seeds. The final magnetic particles were employed to increase bacteria concentration in a biological medium via a capture and trigger release process

The manuscript is divided into five chapters.

In **Chapter 1**, a bibliographic study is presented, reviewing the main approaches to prepare iron oxide-based composite particles. Their applications in many fields such as biomedicine, environment and catalysis, are also presented giving a brief description of each application and the required properties of the magnetic particles for the intended application.

**Chapter 2** is dedicated to the synthesis of amphiphilic block copolymers via RAFT polymerization. First, a brief overview about RDRP processes is given, focusing on RAFT polymerization. The synthesis of the hydrophilic macroRAFT agents with variable monomer compositions (AA, DMAEMA or both) is then investigated. The preparation of amphiphilic block copolymers via chain extension reactions of the hydrophilic macroRAFTs with styrene is presented next. Finally, the thermosensitive properties of PDMAEMA-based macroRAFTs are studied as a function of pH, ionic strength and monomer composition.

The formation of iron oxide clusters using amphiphilic block copolymers as stabilizers is described in **Chapter 3**. The chapter begins with a bibliographic study covering the main approaches used for the synthesis of iron oxide (IO) nanoparticles and the various strategies for preparing IO clusters. An in-depth study of the emulsification/solvent evaporation process used to form aqueous dispersions of iron oxide clusters was then carried out. More specifically, effects of sonication power and time, macroRAFT concentration and composition, and pH on cluster size and size distribution were studied. The surface properties of the clusters were then evaluated by means of zeta potential measurements under different pH and ionic strength conditions.

**Chapter 4** focuses on the formation of the magnetic particles via emulsion polymerization using iron oxide clusters as seeds. First, the main concepts of emulsion polymerization are introduced. The synthesis of iron oxide/polymer composite particles via (mini)emulsion polymerization processes was also reviewed. The production of the targeted magnetic particles was then investigated, using aqueous dispersion of the clusters in styrene/divinylbenzene emulsion copolymerization. The influence of the polymerization process and of the crosslinker content was firstly studied. By varying the composition of the hydrophilic moiety of the amphiphilic macroRAFT, different surface functionalizations have been imparted to the composite particles. Finally, their magnetic properties have been

evaluated in terms of magnetization at saturation, iron oxide content and magnetic separation time.

In **Chapter 5**, the magnetic particles are tested to increase bacteria concentration from biological samples using the capture-and-release technology. First, a brief bibliographic study about bacteria is presented and, then, the use of magnetic separation for *in vitro* immunoassays is described. Different magnetic particles functionalized with PDMAEMA or PAA have been tested for the concentration of E. Coli samples. The ability of the functionalized magnetic latex particles to capture and trigger release a wide range of bacteria was also evaluated in a next part.

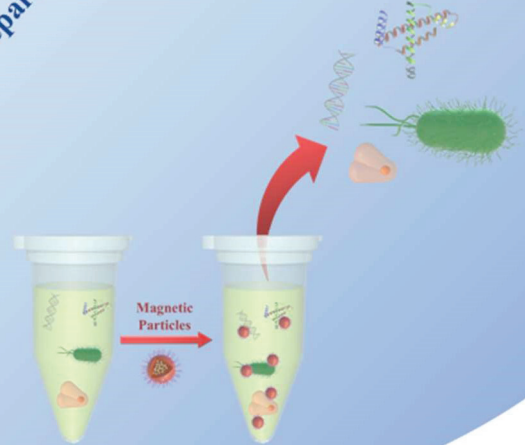
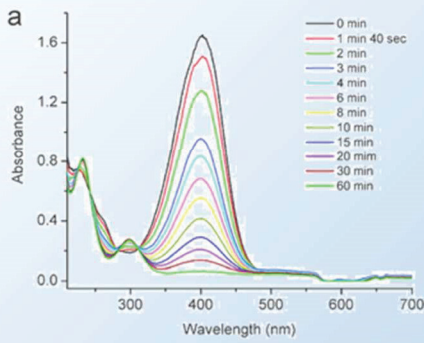
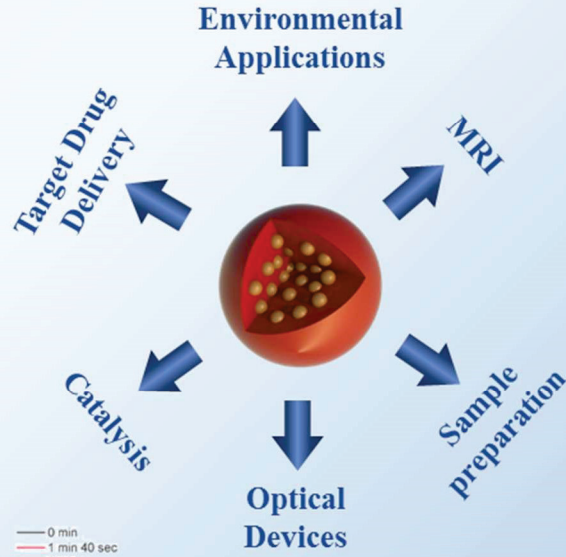
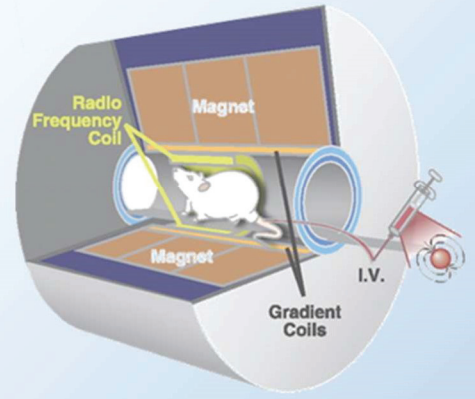
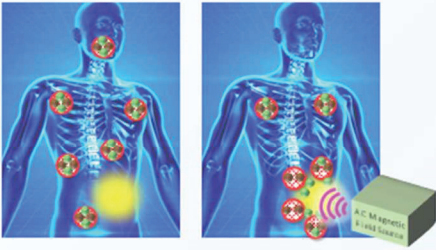
Finally, conclusions and perspectives for future works are given in the last part of the manuscript.

## REFERENCES

1. Mittal, V., *Polymer nanocomposites by emulsion and suspension polymerization*. Royal Society of Chemistry: 2010.
2. Mittal, V., *Synthesis techniques for polymer nanocomposites*. John Wiley & Sons: 2014.
3. Laurent, S.; Forge, D.; Port, M.; Roch, A.; Robic, C.; Vander Elst, L.; Muller, R. N., Magnetic iron oxide nanoparticles: synthesis, stabilization, vectorization, physicochemical characterizations, and biological applications. *Chemical Reviews* **2008**, *108* (6), 2064-2110.
4. Lee, N.; Hyeon, T., Designed synthesis of uniformly sized iron oxide nanoparticles for efficient magnetic resonance imaging contrast agents. *Chemical Society Reviews* **2012**, *41* (7), 2575-2589.
5. Teja, A. S.; Koh, P.-Y., Synthesis, properties, and applications of magnetic iron oxide nanoparticles. *Progress in crystal growth and characterization of materials* **2009**, *55* (1), 22-45.
6. Wu, W.; Wu, Z.; Yu, T.; Jiang, C.; Kim, W.-S., Recent progress on magnetic iron oxide nanoparticles: synthesis, surface functional strategies and biomedical applications. *Science and Technology of Advanced Materials* **2016**.
7. Philipse, A. P.; van Bruggen, M. P. B.; Pathmamanoharan, C., Magnetic silica dispersions: preparation and stability of surface-modified silica particles with a magnetic core. *Langmuir* **1994**, *10* (1), 92-99.
8. Ma, W.-F.; Zhang, Y.; Li, L.-L.; You, L.-J.; Zhang, P.; Zhang, Y.-T.; Li, J.-M.; Yu, M.; Guo, J.; Lu, H.-J., Tailor-made magnetic Fe<sub>3</sub>O<sub>4</sub>@ mTiO<sub>2</sub> microspheres with a tunable mesoporous anatase shell for highly selective and effective enrichment of phosphopeptides. *ACS Nano* **2012**, *6* (4), 3179-3188.
9. Bourgeat-Lami, E.; Lansalot, M., Organic/Inorganic Composite Latexes: The Marriage of Emulsion Polymerization and Inorganic Chemistry. In *Hybrid Latex Particles*, VanHerk, A. M.; Landfester, K., Eds. Springer-Verlag Berlin: Berlin, 2010; Vol. 233, pp 53-123.
10. Rahman, M. M.; Elaissari, A., Organic-inorganic hybrid magnetic latex. In *Hybrid Latex Particles*, VanHerk, A. M.; Landfester, K., Eds. Springer-Verlag Berlin: Berlin, 2010; Vol. 233, pp 237-281.
11. Gupta, A. K.; Gupta, M., Synthesis and surface engineering of iron oxide nanoparticles for biomedical applications. *Biomaterials* **2005**, *26* (18), 3995-4021.
12. Olsvik, O.; Popovic, T.; Skjerve, E.; Cudjoe, K. S.; Hornes, E.; Ugelstad, J.; Uhlen, M., Magnetic separation techniques in diagnostic microbiology. *Clinical microbiology reviews* **1994**, *7* (1), 43-54.
13. Chen, K.; Zhu, Y.; Zhang, Y.; Li, L.; Lu, Y.; Guo, X., Synthesis of magnetic spherical polyelectrolyte brushes. *Macromolecules* **2011**, *44* (3), 632-639.
14. Hoffmann, D.; Landfester, K.; Antonietti, M., Encapsulation of magnetite in polymer particles via the miniemulsion polymerization process. *Magneto hydrodynamics* **2001**, *37* (217-221), 58.
15. Landfester, K.; Ramirez, L. P., Encapsulated magnetite particles for biomedical application. *Journal of Physics: Condensed Matter* **2003**, *15* (15), S1345.

16. Xu, S.; Ma, W.-F.; You, L.-J.; Li, J.-M.; Guo, J.; Hu, J. J.; Wang, C.-C., Toward designer magnetite/polystyrene colloidal composite microspheres with controllable nanostructures and desirable surface functionalities. *Langmuir* **2012**, *28* (6), 3271-3278.
17. Paquet, C.; Page, L.; Kell, A.; Simard, B., Nanobeads highly loaded with superparamagnetic nanoparticles prepared by emulsification and seeded-emulsion polymerization. *Langmuir* **2010**, *26* (8), 5388-96.
18. Zetterlund, P. B.; Thickett, S. C.; Perrier, S. b.; Bourgeat-Lami, E.; Lansalot, M., Controlled/living radical polymerization in dispersed systems: an update. *Chemical Reviews* **2015**, *115* (18), 9745-9800.





# Chapter I

## BIBLIOGRAPHIC REVIEW



TABLE OF CONTENTS

<b>1. Introduction</b> .....	<b>35</b>
<b>2. Iron oxide nanoparticles</b> .....	<b>35</b>
<b>3. Synthesis of iron oxide-based composite particles</b> .....	<b>37</b>
<b>3.1. Iron oxide encapsulation by an inorganic shell</b> .....	<b>37</b>
<b>3.2. Iron oxide/polymer composite particles</b> .....	<b>39</b>
3.2.1. <i>Mixture of pre-formed polymers and iron oxide nanoparticles</i> .....	41
3.2.2. <i>Simultaneous synthesis of polymer and iron oxide</i> .....	43
3.2.3. <i>Iron oxide formation in the presence of polymer particles</i> .....	43
3.2.4. <i>Polymerization in the presence of iron oxide</i> .....	43
<b>4. Applications of magnetic particles</b> .....	<b>46</b>
<b>4.1. Biomedical applications</b> .....	<b>46</b>
4.1.1. <i>In vitro applications</i> .....	46
4.1.2. <i>In vivo applications</i> .....	48
<b>4.2. Environmental applications</b> .....	<b>50</b>
<b>4.3. Support for catalysis</b> .....	<b>51</b>
<b>4.4. Miscellaneous</b> .....	<b>52</b>
<b>5. Conclusions</b> .....	<b>54</b>

## 1. INTRODUCTION

Magnetic iron oxide nanoparticles have attracted extensive interest due to their magnetic properties and their potential applications in many fields such as catalysis, drug delivery, magnetic resonance imaging (MRI) and *in vitro* or *in vivo* immunoassays.<sup>1,2</sup> In this chapter, we will first give a general introduction about iron oxide nanoparticles and their properties. Then, a bibliographic study covering the main approaches used for the synthesis of iron oxide-based composite particles will be presented with special focus on preparation of magnetic polymer particles. Finally, the main applications of magnetic particles will be defined including some examples and the properties required for their employment.

## 2. IRON OXIDE NANOPARTICLES

The magnetic properties of iron oxide nanoparticles strongly depend on the size (typically between 1 and 100 nm)<sup>1</sup> and shape<sup>2</sup> of the nanoparticles, which are directly related to the methods used for their synthesis. These methods can be either classified as “*top-down*”, for the physical procedures, or “*bottom-up*”, for the chemical ones. Physical methods are based on size reduction of already formed iron oxide bulk material, using grinders to obtain small nanoparticles.<sup>3</sup> Despite the high energy and the long process deployed in these methods, the final products have broad size distributions and irregular morphologies. Furthermore, the milling process can lead to iron oxide amorphization and it can also introduce some impurities to the final material. On the other hand, in the chemical methods, the nanoparticles are built from precursor molecules allowing a better control of their characteristics. Indeed, there are many *bottom-up*-based techniques, such as co-precipitation,<sup>4, 5</sup> thermo-decomposition,<sup>6, 7</sup> solvothermal process,<sup>8, 9</sup> sol-gel process<sup>10</sup> and microemulsion.<sup>11</sup> The main difference among these approaches is related to the final characteristics of the nanoparticles such as their shape, size and polydispersity. Among them, the co-precipitation can be considered as an easy, robust and rapid method to synthesize iron oxide nanoparticles leading to the formation of nano-objects with irregular morphology but with acceptable control of the size. Hence, it is one of the most applied procedures, generating nanoparticles that meet the requirements of the majority of applications. However, there are some specific applications, such as magnetic storage,<sup>12</sup> for which a fine control of size and shape is required. Hence, more laborious methods, such as thermo-decomposition, are needed to generate well-defined nanocrystals.<sup>12</sup>

Among the eight types of known iron oxides ( $\text{Fe}_x\text{O}_y$ ),<sup>13</sup> magnetite ( $\text{Fe}_3\text{O}_4$ ), maghemite ( $\gamma\text{-Fe}_2\text{O}_3$ ) and hematite ( $\alpha\text{-Fe}_2\text{O}_3$ ) have attracted particular interest due to their polymorphic temperature induced phase transitions.<sup>14</sup> However, hematite has a weak ferromagnetism at room temperature with magnetization at saturation ( $M_s$ ) often smaller than  $1 \text{ emu g}^{-1}$ , while  $M_s$  reaches  $76 \text{ emu g}^{-1}$ <sup>15</sup> for maghemite and  $92 \text{ emu g}^{-1}$ <sup>4</sup> for magnetite (*bulk materials*). Therefore, magnetite and maghemite are very often employed as magnetic nanoparticles.

Bare iron oxide nanoparticles will tend to aggregate leading to their precipitation. Thereby, colloidal stability must be ensured during the synthesis, storage and application of these nano-objects. In order to improve their stability, surface modifiers are commonly used such as surfactants, fatty acids and short polymer chains.<sup>1</sup> These modifiers can also act as protective coatings reducing the oxidation process, and hence reinforcing their chemical stability. In addition, surface functionalization is crucial for many applications, such as magnetic separations or targeted drug delivery, and the chemical nature of the surface modifiers can be tuned to favor the interaction between the nanoparticles and the targeted biocompound.<sup>16</sup>

The determination of magnetic properties is also crucial for the applications of iron oxide nanoparticles. Hence, iron oxide nanoparticles (IONP) with superparamagnetic properties at room temperature are required for many biomedical applications.<sup>16</sup> Superparamagnetism can be explained as a “turn on/turn off” ability, *i.e.* nanoparticles under a magnetic field exhibit a magnetization ( $M \neq 0$ , “turned-on”), but when the field is removed, there is no remanent magnetization ( $M_r \approx 0$ , “turned-off”). For instance, magnetic particles with superparamagnetic properties are essential for applications in magnetic separation to ensure particles redispersion. Otherwise, if a remanent magnetization is observed ( $M_r > 0$ ), particles can stay stacked together, due to interparticle magnetic forces, hindering their redispersion.<sup>17</sup> It is important to point out that there is a close correlation between the particle size and the magnetic properties; IONPs are generally superparamagnetic when their size (diameter) is smaller than typically 15-20 nm.<sup>14, 16</sup>

However, there are some limitations in using superparamagnetic iron oxide nanoparticles with such small particles size ( $< 20 \text{ nm}$ ) in applications where magnetic separation is required. Indeed, small particles generate long-time separation, up to several hours. Therefore, a way of reducing the separation time consists in the preparation of larger composite particles highly loaded with IONP.

### 3. SYNTHESIS OF IRON OXIDE-BASED COMPOSITE PARTICLES

As aforementioned in the Introduction part, the direct use of superparamagnetic iron oxide nanoparticles with unmodified surface can be a limitation in the biological field, due to their charged surface, which can generate non-specific interactions with organisms. In addition, their small particle size normally results in long magnetic separation. As an alternative to the chemical modifiers presented in the previous section, individual- or multi-encapsulation of magnetic nanoparticles within a shell can provide a mean to protective coating to these inorganic materials. This process will avoid direct contact of the iron oxide nanoparticles with the biological target and also enhance their chemical resistance. In addition, the multi-encapsulation approach can also generate larger magnetic composite particles (100-300 nm) reducing drastically the separation time from several hours to a few seconds compared to individually encapsulated IONPs. Magnetic composite particles can be classified based on the chemical nature of the shell: inorganic such as silica ( $\text{SiO}_2$ )<sup>18</sup> or titania ( $\text{TiO}_2$ )<sup>19</sup> or organic such as carbon<sup>20</sup> or polymers.<sup>3, 21</sup>

#### 3.1. Iron oxide encapsulation by an inorganic shell

In addition to the already cited advantages in protecting iron oxide particles within an inorganic shell (e.g.,  $\text{TiO}_2$  or  $\text{SiO}_2$ ), one can mention an easy post-modification of the surface, in which the well-known chemistry of silane-based molecules is exploited.<sup>22</sup>

Silica is widely applied to encapsulate iron oxide particles and thus form composite magnetic particles, and three main approaches have been reported. The first one is based on the Stöber process, in which silica is formed from the hydrolysis and condensation of a precursor, commonly tetraethoxysilane (TEOS).<sup>23-25</sup> This method was applied by Pinho *et al.*<sup>23</sup> for the encapsulation of 10 nm maghemite nanoparticles into a silica shell, whereby the shell thickness was controlled by varying the TEOS amount. The authors showed that the shell thickness had a significant impact on  $r_1/r_2$  relaxivity ratio, important parameters to be considered in MRI when magnetic particles are used as contrast agents. A second method is based on silica deposition from silicic acid solution.<sup>26</sup> In this approach, water-soluble silica precursors, commonly salts, are condensed via alkalization of the medium and the resulting silica is deposited on iron oxide surface. The third one is based on water-in-oil microemulsion, in which inverse micelles are used to confine silica precursors and to control the shell thickness.<sup>27, 28</sup> Pfaff *et al.*<sup>28</sup> applied this process to synthesize  $\gamma\text{-Fe}_2\text{O}_3/\text{SiO}_2$  particles,

which were post-modified with 3-(trimethoxysilyl)propyl methacrylate (MPS) for the latter incorporation of a fluorescent glycopolymer on their surface via the grafting-to method. These multifunctional particles were tested for biological imaging within mammalian cells (A549 cells) by fluorescence microscopy showing that glycopolymer-modified particles seem to have an effect on internalization of the particles into the cells when compared to the non-functionalized magnetic particles.

Nonetheless, as mentioned above, hybrid particles obtained by individual encapsulation of superparamagnetic IONPs generally result in systems with long separation times due to their small size. An alternative to the preparation of magnetic composite particles with larger particle size and higher iron oxide content consists in first forming iron oxide clusters which are next encapsulated with a protecting inorganic shell, as outlined in Figure 3. This strategy was applied by Ge *et al.*<sup>29</sup>, in which submicronic iron oxide clusters (ca. 100 nm in diameter) and low polydispersity were first prepared via the solvothermal method.<sup>b</sup> Despite their large dimensions, these objects present superparamagnetic properties as they are obtained by aggregation of superparamagnetic iron oxide nanoparticles. Using these clusters as seeds, a sol-gel process was carried out to encapsulate them within a silica shell (Figure 4A). Their superparamagnetic properties and short separation time, associated to the protective silica coating make these composite particles good candidates for applications in fields in which magnetic separation is needed such as support for catalysis or biological separation.

In a similar approach,<sup>19</sup> iron oxide clusters were encapsulated into a titanium dioxide shell forming composite particles with a core-shell morphology (Figure 4B). A hydrothermal treatment was carried out on the titania shell leading to the formation of a mesoporous TiO<sub>2</sub> shell, which increased the specific surface area of the final particles. They were successfully used for selective enrichment of phosphopeptides.

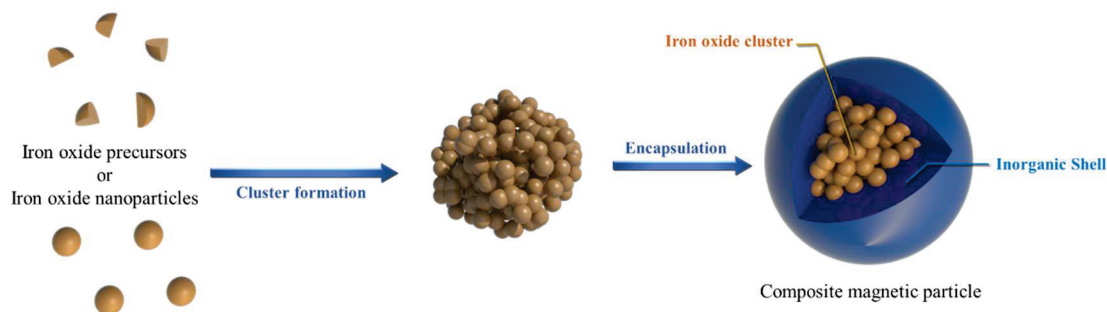


**Figure 3** – Scheme illustrating the formation of iron oxide clusters and their encapsulation with an outer inorganic shell.

<sup>b</sup> A description of the solvothermal process will be given in Chapter 3.

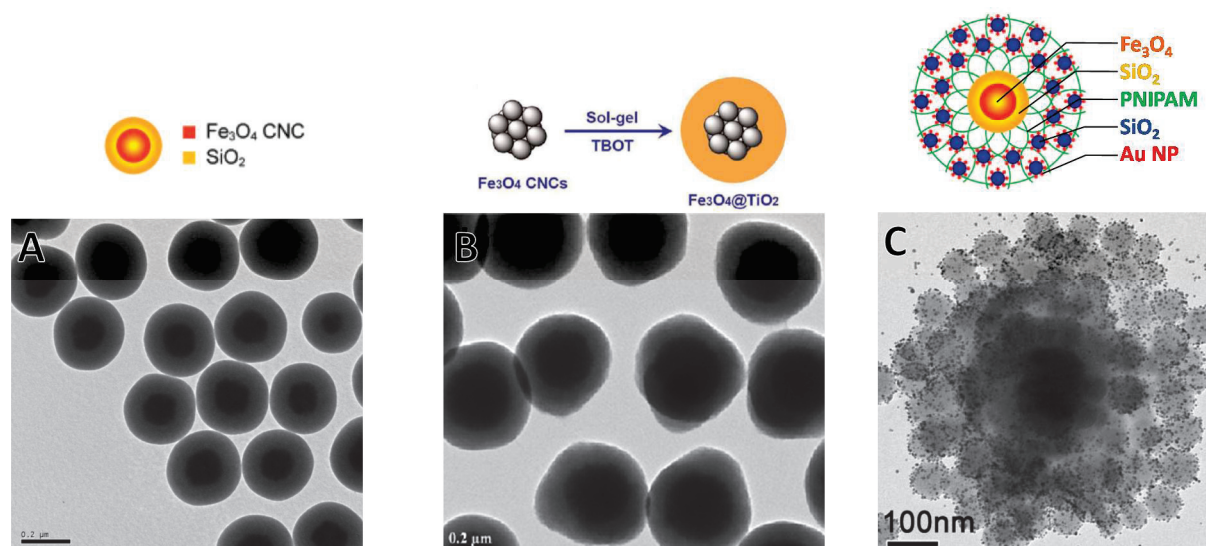


**Figure 4** – TEM micrographs and scheme of iron oxide clusters encapsulated within an inorganic shell: (A) silica<sup>29</sup>, (B) titania<sup>19</sup> and (C) silica.<sup>30</sup> Reprinted from Refs (A)<sup>29</sup>, (B)<sup>19</sup> and (C)<sup>30</sup> with permission from the respective publishers.

Finally, it is important to point out that post-modification of silica particles with silane-based molecules is a procedure commonly reported in the literature allowing the surface functionalization with primary amines,<sup>31</sup> methacrylate groups,<sup>32</sup> bromine<sup>33</sup>. Ge *et al.*<sup>30</sup> reported the elaboration of Fe<sub>3</sub>O<sub>4</sub>/SiO<sub>2</sub>/poly(*N*-isopropylacrylamide)/SiO<sub>2</sub>-Au particles (Figure 4C) through a multi-step synthesis. First, Fe<sub>3</sub>O<sub>4</sub>/SiO<sub>2</sub> core-shell composite particles were prepared, as described above for Ge's work.<sup>29</sup> Then, a polymerizable methacrylate silane was grafted at the particle surface. Copolymerization of *N*-isopropylacrylamide and *N,N'*-methylenebisacrylamide (MBA), used as crosslinker agent, in the presence of the modified composite particles led to the formation of a polymer network surrounding the Fe<sub>3</sub>O<sub>4</sub>/SiO<sub>2</sub> particles. Ag nanoparticles were then fixed at the polymer network and an additional sol-gel process was carried out forming satellite silica particles by using the Ag nanoparticles as template. An additional sol-gel process was next carried out to form gold nanoparticles, which were labeled with at surface of silica particles (at the satellite- and central-localized silica particles). The system was then tested in Au-nanoparticle catalyzed reduction of 4-nitrophenol with NaBH<sub>4</sub> and the catalytic system showed an excellent activity up to eight cycles of use.

### 3.2. Iron oxide/polymer composite particles

Iron oxide nanoparticles can be also encapsulated into an organic shell leading to the formation of iron oxide/polymer composite particles. However, the incorporation of iron



oxide into polymer particles may be highly challenging depending on the chemical nature of the polymer. Indeed, the hydrophilic character of IONPs provided by the ionic charges present at their surface is not compatible with the hydrophobic character of most of the polymers. So, organic modifiers must be attached to the iron oxide surface in order to increase their hydrophobicity generating better affinity between  $\text{Fe}_x\text{O}_y$  and the polymer. Alternatively, more hydrophilic polymer chains with higher compatibility with iron oxide surface can also be employed for the synthesis of magnetic polymer particles. The main approaches reported in the literature to synthesize magnetic polymer particles can be classified in four groups, as outlined in Figure 5 and as listed below:

- A) Iron oxide formation in the presence of polymer particles.
- B) Polymerization in the presence of iron oxide.
- C) Mixture of pre-formed polymers and iron oxide nanoparticles.
- D) Simultaneous synthesis of polymer and iron oxide.

These different approaches are presented in the following sections.

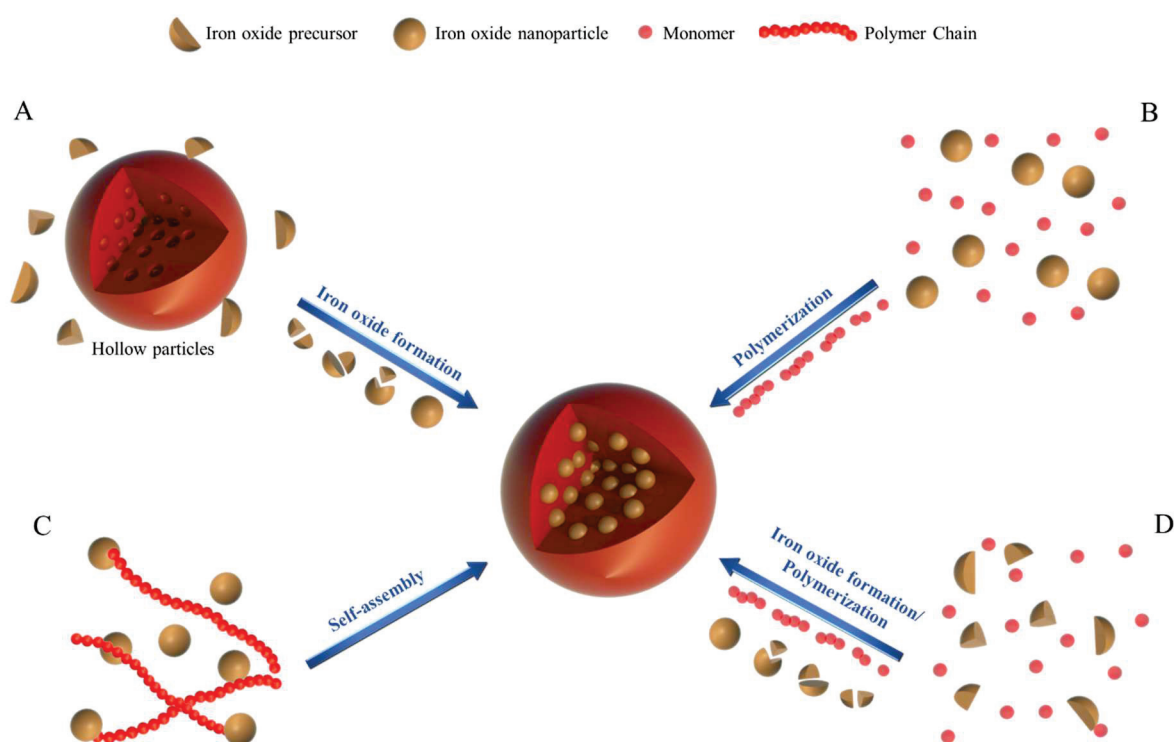


**Figure 5** – Schematic representation of the synthetic strategies used for the preparation of iron oxide/polymer composite particles.

Furthermore, the advent of Reversible-Deactivation Radical Polymerization (RDRP)<sup>c</sup> processes has revolutionized the macromolecular design, allowing the synthesis of new polymers or copolymers with predetermined structures and functionalities. Indeed, well-defined polymer chains of predetermined molar mass can be synthesized through the three main RDRP processes: Atom Transfer Radical Polymerization (ATRP),<sup>34</sup> Nitroxide-Mediated radical Polymerization (NMP)<sup>35</sup> and Reversible Addition-Fragmentation chain Transfer (RAFT).<sup>36</sup> Among these techniques, RAFT is likely the more versatile, affording the controlled polymerization of a wide range of monomers. Combining the benefits of RDRP for the design of controlled polymer chains, with the magnetic properties of iron oxide nanoparticles, provides the opportunity to finely tune the surface functionalization of the magnetic polymer particles with potential applications in biomedicine,<sup>37</sup> aerospace<sup>38</sup> and environment.<sup>39</sup>

### *3.2.1. Mixture of pre-formed polymers and iron oxide nanoparticles*

Through the assembly of iron oxide nanoparticles and polymer chains, in a controlled physical process, well-defined magnetic polymer particles can be obtained. Three main strategies can be distinguished: the emulsification/solvent evaporation process,<sup>40-42</sup> the solvent displacement method<sup>43</sup> and the grafting-to approach.<sup>44, 45</sup>

The emulsification/solvent evaporation process can be considered as an easy and robust method enabling the synthesis of magnetic polymer particles from pre-formed polymer and IONPs. To obtain a good dispersion of the nanoparticles into the polymeric phase, the two phases need to be compatible between them. In a typical procedure, either a water-in-oil (W/O)<sup>40, 46</sup> or an oil-in-water (O/W)<sup>41, 42</sup> emulsion is formed using a high energy homogenization process (e.g. vigorous agitation or ultra-sounds). The droplets, which can be either organic (O/W) or aqueous (W/O), are composed of a polymer solution loaded with iron oxide nanoparticles. After elimination of the solvent by washing or evaporation, magnetic polymer particles are obtained with however a broad size distribution. This approach has been exploited by the German Company Chemagen Biopolymer-Technologie<sup>d</sup> for the production of commercial magnetic particles for applications in magnetic separation of biotargets.<sup>40</sup> Iron oxide was first dispersed in a water solution of poly(vinyl alcohol), and the resulting aqueous

---

<sup>c</sup> The concept of RDRP processes will be presented in the bibliographic review of Chapter 2 with emphasis on the RAFT polymerization process.

<sup>d</sup> Acquired by PelkinElmer in 2011<sup>47</sup>



dispersion was introduced in a highly viscous vegetal oil phase under high shear mechanical stirring (700 rpm), leading to the formation of a colloidal suspension. A crosslinker was next introduced to the system forming a polymer network which will fix the structure.<sup>48</sup> Micron-sized magnetic particles were then obtained with a broad size distribution (1 to 50  $\mu\text{m}$ ) and a high iron oxide content (50-60 wt%), and were easily re-dispersable in aqueous solutions due to the nature of the polymer.

The preparation of magnetic particles from pre-formed polymer and iron oxide can also be carried out via solvent displacement. Pavia-Sanders *et al.*<sup>43</sup> prepared magnetic particles aiming at an environmental application: oil capture from contaminated water. The preparation of the magnetic particles is outlined in Figure 6. First, an amphiphilic block copolymer: poly(acrylic acid)-*block*-polystyrene was synthesized by ATRP. The block copolymers and the iron oxide were then dispersed/solubilized in DMF:THF (1:1 vol:vol) mixture which were then added dropwise to water, a selective solvent to PAA block, leading to the formation of magnetomicelles. The micelles were then crosslinked via amidation reaction between the carboxylic group of acrylic acid and the amine group of the crosslinker (2,2'-(ethylenedioxy)bis(ethylamine)) in the presence of 1-(3-(dimethylamino)propyl)-3-ethylcarbodiimide methiodide (EDCI). The resulting crosslinked magnetic particles (Figure 6) were then successfully applied to oil sequestration for water purification.

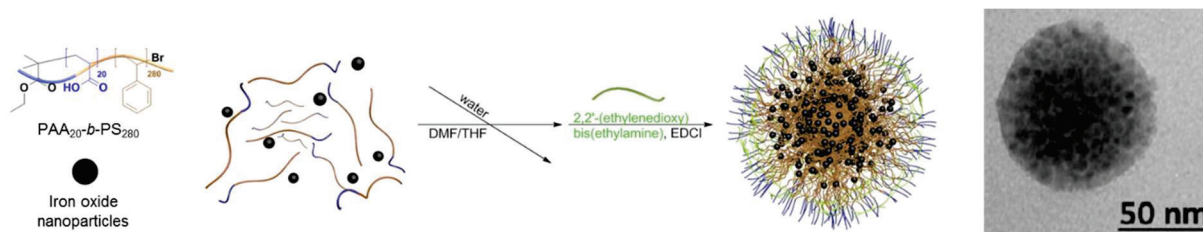


**Figure 6** – Synthetic approach to iron oxide/polymer particle formation via solvent displacement method. Adapted from Ref<sup>43</sup> with permission from ACS.

A last approach leading to the formation of magnetic polymer particles from preformed IONPs and polymer chains is the grafting-to process. Grafting-to consists in the synthesis of polymer chains with a specific functionalization able to be grafted at the iron oxide surface. By using this approach, Basuki *et al.*<sup>37, 44</sup> synthesized poly(pentafluorophenyl acrylate)-*block*-poly(oligoethylene glycol acrylate) block copolymers via RAFT polymerization. The RAFT agent employed in this synthesis carried a phosphonic acid group in order to functionalize one end of the block copolymer. In a one-pot reaction, the phosphonic acid functionalization was used to graft the block copolymers onto the surface of iron oxide nanoparticles, and the

pentafluorophenyl groups from block copolymer were partially replaced by amines such as *L*-arginine and *L*-histidine. This system was evaluated as carrier for targeted drug delivery. Fluorescence lifetime imaging microscopy was used to follow the release behavior of Rhodamine 6G dye embedded onto magnetic polymer particles.

### 3.2.2. Simultaneous synthesis of polymer and iron oxide

An advantage of this approach is the simultaneous formation and *in situ* functionalization of magnetic particles. Lu *et al.*<sup>49</sup> have reported the thermodecomposition of ferric triacetylacetonate using *N*-vinylpyrrolidone as reaction medium. Iron oxide nanoparticles (particle size of around 20 nm), containing at their surface stabilizing poly(*N*-vinylpyrrolidone) (PVP) chains, were thus synthesized in a one-pot process.

### 3.2.3. Iron oxide formation in the presence of polymer particles

The synthesis of iron oxide in the presence of preformed polymer particles is a widespread strategy to produce iron oxide/polymer particles. This approach is the one exploited for the synthesis of the commercial particles, Dynabeads<sup>®</sup>, for applications in the biomedical field. The method was first reported in 1983 by Ughelstad *et al.*<sup>50, 51</sup> and involves 3 steps: 1) synthesis of porous polystyrene particles functionalized with nitro or nitrate groups located in the particle core, 2) addition of Fe<sup>+2</sup>/Fe<sup>3+</sup> ions in the porous particle dispersion, and 3) coprecipitation of the cations leading to *in situ* formation of iron oxide upon increasing pH and temperature. The resulting magnetic particles contain ca. 30 wt% of iron oxide leading to a magnetization at saturation of 23.5 emu g<sup>-1</sup>.

### 3.2.4. Polymerization in the presence of iron oxide

Magnetic polymer particles obtained via *in situ* polymerizations - *i.e.* the polymerization reaction is carried out in the presence of magnetic nanoparticles - is a strategy extensively exploited for the preparation of magnetic polymer particles. The approaches reported in the literature can be classified into two main groups.

The first one is based on surface-initiated polymerization in homogeneous media, also known as grafting-from. In this process, an active compound such as an initiator<sup>39, 52</sup> or a chain transfer agent (CTA)<sup>52-55</sup> is adsorbed and/or grafted on the nanoparticle surface, and polymer chains are then grown in from this active group. Well-defined polymer brushes can also be

obtained via RDRP processes, by which composition and molar masses are both controlled, allowing a fine tuning of surface functionalization. Dong *et al.*<sup>39</sup> have reported the preparation of Fe<sub>3</sub>O<sub>4</sub>@Br/PDMAEMA particles via surface-initiated ATRP. The phosphate acid group of the ATRP initiator provides a good interaction with the iron oxide surface while the bromine group is involved in the polymerization, leading to the formation of PDMAEMA brushes. Surface-initiated ATRP was also explored by other authors to synthesize iron oxide composite particles with poly(9-(4-vinylbenzyl)-9H-carbazole)-*block*-poly(oligoethylene glycol methyl ether methacrylate) (PVBK<sup>e</sup>-*b*-PEGMA),<sup>56</sup> PS,<sup>57</sup> and PDMAEMA<sup>58</sup> polymer brushes. These hybrid systems were developed aiming at different applications, namely as MRI contrast agent,<sup>56</sup> for the formation of nanostructured films<sup>57</sup> and for nonviral gene delivery.<sup>58</sup>

The grafting-from method can also be applied using RAFT agent as both surface modifier and control agent of the polymerization.<sup>52-54</sup> In a first step, RAFT agent is adsorbed at the surface of iron oxide via R or Z group complexation<sup>f</sup>. The main difference between these strategies is associated to the growth direction of polymer chains. In which, R-group anchoring lead to chain growth from the nanoparticle surface and Z-group anchoring lead chains growth to the iron oxide nanoparticles. Nevertheless, some studies with Z-group complexation is often described as a grafting-to approach instead of grafting-from. Xiao *et al.*<sup>52</sup> employed grafting-from approach to prepare thermoresponsive magnetic particles. First, RAFT agent was complexed by a carboxylic R-group onto the IONP surface via ligand exchange. Then, surface-controlled copolymerization of NiPAM and acrolein were carried out forming thermoresponsive polymer brushes. Finally, bovine serum albumin (BSA) was successfully immobilized onto the surface of the smart particles, which could be latter isolated from the medium via magnetic separation.

The second approach consists on polymerizations carried out in the presence of iron oxide nanoparticles in heterogeneous systems. These polymerization reactions are conducted in dispersed media such as precipitation,<sup>59</sup> dispersion,<sup>60</sup> suspension,<sup>61</sup> emulsion<sup>62-64</sup> or miniemulsion<sup>15, 65</sup> polymerization processes. These processes lead to the formation of particles of different sizes, with dispersion and suspension polymerizations resulting in micron-sized particles, and (mini)emulsion polymerizations in particles generally smaller than 300 nm in diameter. The preparation of magnetic particles via (mini)emulsion polymerization

---

<sup>e</sup> VBK: fluorescent monomer.

<sup>f</sup> R and Z group composing the RAFT agent structure will be presented in Chapter 2

processes will be briefly described below and a detailed description of these approaches will be given in Chapter 4.

Miniemulsion polymerization has been largely used for the preparation hybrid particle system including magnetic latex particles.<sup>15, 66-74</sup> In a typical experiment, organically modified iron oxide nanoparticles are first dispersed into the monomer to form a ferrofluid. This organic phase is then mixed with an aqueous phase containing the stabilizer, and homogenized by ultrasound or any other high-energy process, to form monomer droplets generally smaller than 300 nm in diameter. In a next step, the monomer droplets loaded with the inorganic particles, are polymerized via miniemulsion polymerization to form composite latex particles.

Miniemulsion polymerization is undoubtedly a powerful tool for the encapsulation of iron oxide nanoparticles.<sup>75-77</sup> However, the formation of monomer dispersions incorporating well-dispersed IONPs was shown to be a limiting step when targeting high iron oxide contents. For instance, for the preparation of oleic acid-modified IONP/PS composite particles via miniemulsion polymerization, the content of IONPs in the hybrid material is limited to about 15 wt%.<sup>66, 68, 78</sup> The authors have attributed this low content to the difficulty encountered in dispersing high amounts of iron oxide in the monomer phase, resulting in magnetic particles with low magnetization at saturation, which is a limitation for most applications. In some cases, the iron oxide content in the final polymer particles can be higher than expected, *i.e.*, the final particles are richer in iron oxide than the amount initially introduced in the monomer, which can be attributed to the formation of secondary-nucleated particles devoid of IONPs or to low monomer conversions.<sup>79</sup>

The use of iron oxide clusters, as shown in Figure 3, followed by their encapsulation within a polymer shell via miniemulsion polymerization<sup>69, 73</sup> can be a valid alternative for the preparation of magnetic polymer particles with high iron oxide content. Ramirez et al.<sup>69</sup> reported a procedure based on, firstly, the formation of iron oxide clusters via an emulsification/solvent evaporation approach, followed by a second step of miniemulsion polymerization of styrene in the presence of the cluster dispersion. The resulting magnetic polymer particles present up to 39 wt% of iron oxide.

Approaches developed in emulsion polymerization suffer from the same limitation regarding the content of iron oxide generating particles with poor magnetic content.<sup>80, 81</sup> One way to circumvent this problem consists also in using iron oxide clusters as seeds in the emulsion polymerization, resulting in magnetic polymer particles with higher iron oxide content.<sup>82, 83</sup>

The use of preformed iron oxide clusters seems to be a relevant strategy to obtain particles with high iron oxide content. Indeed, the resulting hybrid particles are good candidates to be used in applications in which magnetic separation is needed. Their considerable large sizes (around 100 nm) associated to high iron oxide content leads to the formation of particles with low magnetic separation time. Moreover, the preparation of well-defined polymer chains via RDRP process to decorate these magnetic particles allow a fine tuning of surface functionalization opening many possibilities for their application in different fields.

## **4. APPLICATIONS OF MAGNETIC PARTICLES**

The development of magnetic particles for specific applications have been largely reviewed in the literature with the focus placed on biomedical analyses,<sup>14, 16, 84-87</sup> drug delivery,<sup>88</sup> biological tests,<sup>1, 17, 89</sup> environment<sup>85</sup> and optical devices.<sup>90</sup> The following sections provide a brief overview of the main applications.

### **4.1. Biomedical applications**

Biomedical applications relying on the use of iron oxide/polymer particles can be classified as *in vitro* and *in vivo* applications. *In vivo* means that the magnetic particles will be in contact with living organisms, e.g. being injected as MRI agent or for targeted drug delivery. On the other hand, in *in vitro* applications, the magnetic particles are used for biological diagnostics or sample preparation in a laboratory.

#### *4.1.1. In vitro applications*

The use of magnetic particles for the preparation of samples in biomedical diagnostics via magnetic separation can replace time-consuming and laborious separation steps by centrifugation for instance.<sup>17, 87</sup> Moreover, magnetic separation can be used for biological samples collected directly on site, which can be a secluded region such as rainforests or deserts, where conventional separation methods are not available.

The magnetic separation of biological targets using iron oxide/polymer particles is outlined in Figure 7. First the magnetic particles are added into the biological sample, which can contain peptides,<sup>19</sup> proteins,<sup>31, 91</sup> nucleic acids,<sup>58</sup> cells<sup>92</sup> or bacteria.<sup>93</sup> After an incubation time, the sample is exposed to a magnetic field leading to the separation of the magnetic particles with the bio-targets attached to them. The supernatant is then collected and the magnetic particles

re-dispersed in a medium allowing elution of the bio-compound. Finally, a second magnetic separation is carried out to recycle the magnetic particles and to collect the supernatant containing the biological targets that will be further analyzed.

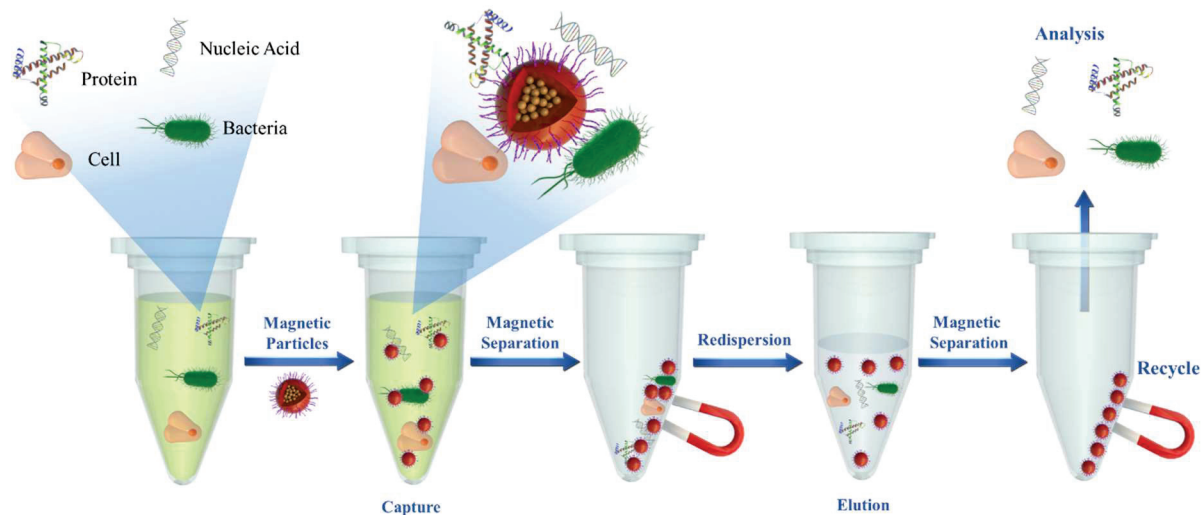


**Figure 7** – Scheme of magnetic separation for sample preparation in biomedical diagnostics.

Surface functionalization of the magnetic particles is a key parameter to have a good interaction with biological targets. The separation can be classified as either direct, in which the functionalization of particle surface is used for interaction with the bio-targets, or indirect, in which bio-ligands such as oligonucleotides or antibodies<sup>89</sup> are first attached to the particle surface before being placed in contact with the bio-targets. It is worth mentioning that a good choice of the surface functionalization is also crucial to favor the elution of the bio-compounds, otherwise bio-targets could stay attached at the magnetic particle surface.

As discussed above, magnetic particles have to fulfill a number of requirements to observe an efficient magnetic separation, *i.e.* they must contain a high amount of iron oxide encapsulated into large particles (typically higher than 100 nm), while showing superparamagnetic properties. Commercial magnetic particles that meet the aforementioned criteria are available on the market for the magnetic separation of bio-compounds. PelkinElmer®, Ademtech, Dynal®, Merck are suppliers of magnetic beads which can be used for separation of nucleic acids, viruses, antibodies, proteins, marked cells, etc. For instance, Ademtech commercialize *Adembeads* functionalized with carboxylic acid, which allow the post-modification with oligonucleotides, peptides or proteins for a specific bio-target isolation. Magnetic separation is widely applied in sample preparation for biomedical diagnostics, in which the magnetic nanoparticles have been successfully used as solid support for the purification, extraction, and



concentration of biomolecules.<sup>21</sup> Further details on magnetic separations by using magnetic particles will be presented in Chapter 5.

#### *4.1.2. In vivo applications*

Magnetic particles can be used in therapeutic processes, for example hyperthermia, MRI or targeted drug delivery.<sup>3, 94</sup> To this end, all the components comprised in the final magnetic particles must be biocompatible<sup>g</sup>. The evaluation of the compounds to be applied in *in vivo* applications is made by regulatory agencies such as Food and Drug Administration (FDA) and European Medicines Agency (EMA). Some examples of FDA-approved polymers<sup>96</sup> are poly(ethylene glycol) (PEG), poly(vinylpyrrolidone) (PVP) and poly(vinyl alcohol) (PVA), which have been widely studied in the preparation of iron oxide/polymer particles for *in vivo* applications.<sup>16, 96</sup> On the other hand, iron oxide nanoparticles are classified as non toxic or harmful, and are also approved by FDA and EMA, in particular for MRI applications.<sup>96, 97</sup>

As defined by Lee and Hyeon:<sup>98</sup> “a MRI typically consists of pixels or voxels representing the nuclear magnetic resonance (NMR) signal intensity of the hydrogen atoms in water or fat of living organisms”. A scheme of magnetic resonance imaging is presented in Figure 8A. Firstly the organism is arranged inside the scanner apparatus and submitted to a strong magnetic field (1.5~3.0 T). The hydrogen spin present in water or in fat molecules of its tissues will be aligned parallel or anti-parallel to the magnetic field.<sup>99</sup> Then, a resonance radiofrequency wave is produced by a coil changing the spin orientation to an excited state. The time to the longitudinal and transverse magnetization back towards equilibrium is known as  $T_1$  (longitudinal) and  $T_2$  (transverse) relaxation times.<sup>h</sup> Each animal tissue has a different susceptibility to be imaged by  $T_1$  and  $T_2$  weighted-images, e.g., skeletal muscles have short  $T_2$  value compared to gray matter. Stanisz *et al.*<sup>100</sup> provided a list in their work with  $T_1/T_2$  relaxation times for several tissues.

The use of contrast agent in MRI is applied to improve the image quality. A local magnetic field gradient can be induced by using iron oxide nanoparticles which accelerate the dephasing of protons spins.<sup>98</sup> This can generate images where the regions in which the magnetic particles are concentrated will appear more highlighted (Figure 8B, bottom). This magnetic property associated to a good control of surface functionalization, e.g. by attaching

---

<sup>g</sup> *Biocompatibility: the quality of not having toxic or injurious effects on biological systems*<sup>94</sup>

<sup>h</sup> *The magnetic relaxometry will be described in Chapter 3*

bio-compounds, enable the synthesis of magnetic particles able to interact with a specific tissue in a process known as targeted magnetic resonance imaging. For instance, Sun *et al.*<sup>101</sup> have prepared magnetic nanoparticles labeled with chlorotoxin (CTX), a peptide with a binding affinity for tumors of the neuroectodermal origin, and demonstrated their successful use for mapping of the tumor cells in a rat (Figure 8B, “Targeted” image). The “Non-targeted” image in Figure 8B illustrates the use of magnetic particles without the CTX attached on their surface.

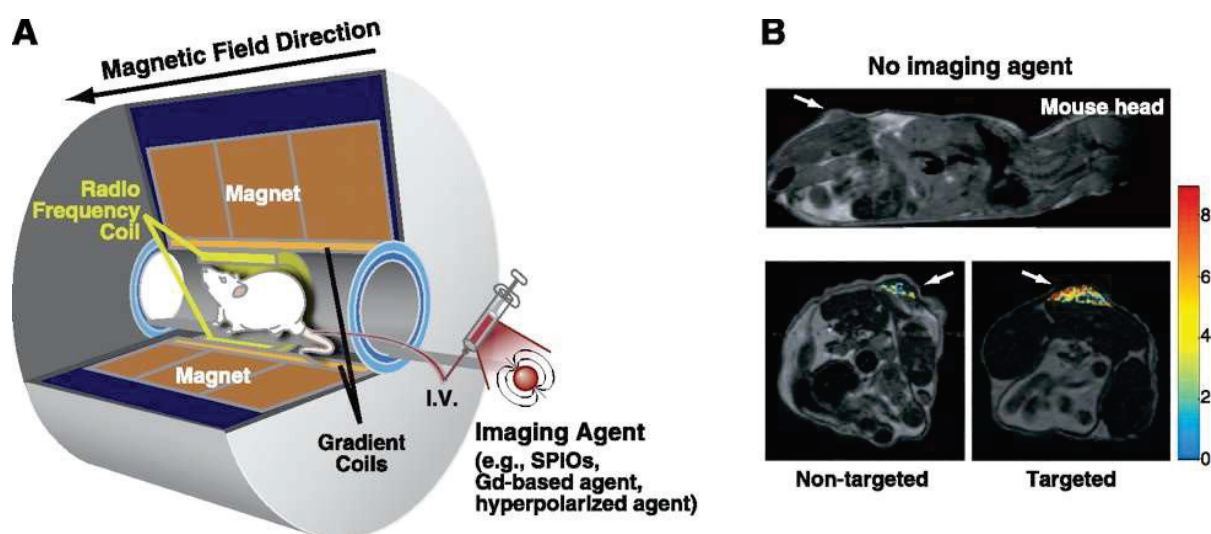


**Figure 8** – Small animal MRI using superparamagnetic iron oxide nanoparticles using superparamagnetic IONPs as contrast agent. (A) Scheme of the MRI scanner apparatus adapted from<sup>99</sup> and (B) anatomical image of a mouse whereby the tumor is highlighted with arrows,<sup>101</sup> bottom images were obtained after injection of non-labeled (i.e., non-targeted) and chlorotoxin (CTX) labeled (i.e. targeted) IONPs, respectively.

Magnetic polymer particles can also be used in systems developed for targeted drug delivery. In typical procedures of drug administration, either via oral ingestion or intravenous injection, due to drug spreading in the body, the administration of a high concentration of active ingredient is necessary to guarantee an effective concentration at the disease site (Figure 9). This overdosing can increase the amount of drug uptaken into healthy cells inducing side effects to the organism. The use of magnetic micro- or nanoparticles as carriers for drugs has the potential to mitigate the side effects and to control the drug distribution on the target site.<sup>3</sup> The strategy is illustrated in Figure 9. Magnetic particles with a high response to a magnetic field and controlled surface functionalization are first synthesized. The drug molecule is then introduced into/onto the magnetic particles. Finally, a gradient magnetic field is generated conducting the particles to the site to be treated.



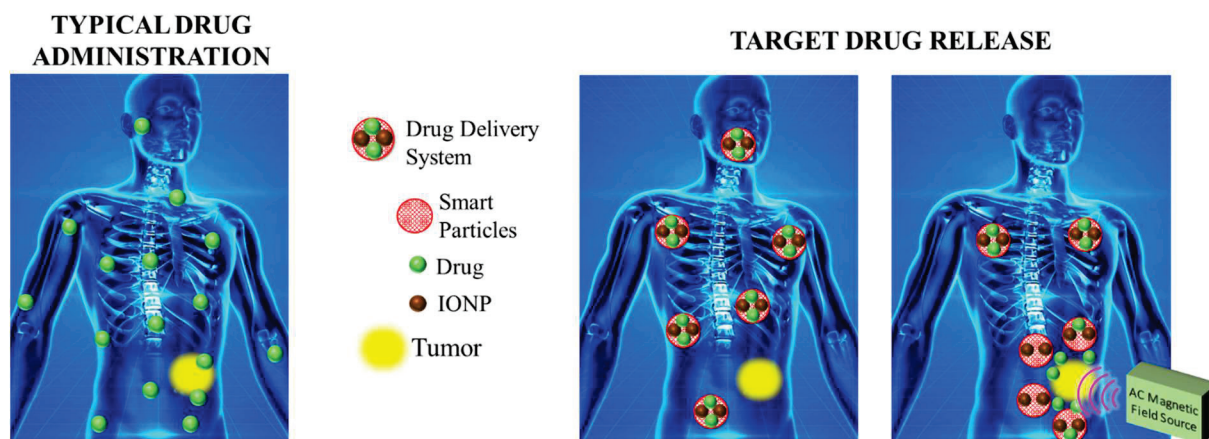


**Figure 9** – Scheme illustrating the concept of drug administration and targeted drug release using magnetic particles.<sup>102</sup>

Furthermore, tumor cells normally have a temperature slightly higher than that of healthy cells due to the higher activity to reproduce themselves. They can also have a pH slightly different from healthy cells. Based on these concepts, a lot of works on sensitive polymers<sup>i</sup> have been exploited in order to design nanoparticles able to release drugs directly on the target.<sup>88</sup> To do so, multi-functional magnetic polymer particles containing superparamagnetic nanoparticles and drugs encapsulated into a sensitive polymer shell are designed. Then, a gradient magnetic field is employed conducting these particles to the target as shown in Figure 9. Based on hyperthermia process, *i.e.* the ability to heat iron oxide nanoparticles under an alternating current magnetic field, the multifunctional particle can be heated *in situ*. This mechanism associated with the thermosensitivity of the polymer shell allows releasing the drug directly on the affected site.

#### 4.2. Environmental applications

The use of iron oxide nanoparticles in the environmental field has also been reported in the literature.<sup>85</sup> IONPs can be used in purification processes to remove heavy metals and ions,<sup>104</sup> oil,<sup>43</sup> toxic dyes<sup>20</sup> or microorganisms<sup>39</sup> from their surrounding environment.

Pavía-Sanders *et al.*<sup>43</sup> have prepared iron oxide/polymer particles via the solvent displacement method detailed in section 3.2.1. These particles were used for the purification of oil-contaminated water via magnetic separation (Figure 10). The particles were first dispersed in the contaminated water. Due to the hydrophobic character of their core, the oil tends to be

<sup>i</sup> Sensitive polymers are polymers that exhibit a drastic and discontinuous change of their physical properties upon applying an external stimulus such as pH, temperature or ionic strength<sup>102</sup>

absorbed by the particles until a thermodynamic equilibrium is reached. Then, by applying an external magnetic field, more than 80% of the oil contaminant was removed. Moreover, the magnetic polymer particles can be recycled after purification via ethanol washes exhibiting again high oil-capture efficiency.

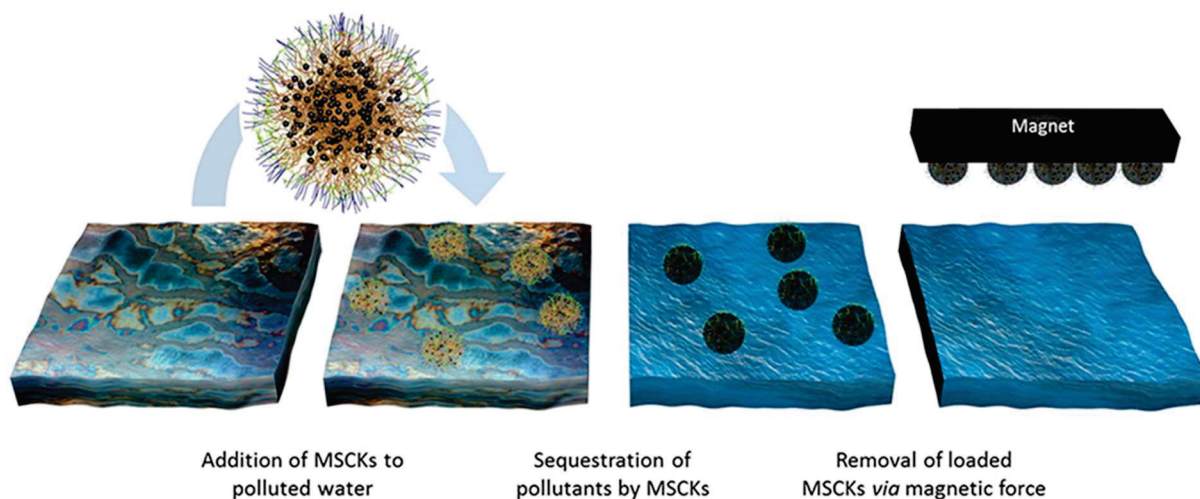


**Figure 10** – Application of magnetic polymer particles to the purification of oil-contaminated water. Adapted from Ref<sup>43</sup> with permission from ACS.

A similar system was developed by Dong *et al.*<sup>39</sup> to purify contaminated water from microorganisms such as bacteria. The authors synthesized  $\text{Fe}_3\text{O}_4@\text{Br}/\text{PDMAEMA}$  via surface initiated ATRP, as described above in Section 3.2.4. The PDMAEMA brushes were then quaternized to have a positive charge independent of the pH of the medium, allowing the capture of bacteria under different conditions. *E. Coli*, which is a typical contaminant in the food industry, was chosen as microorganism to be captured by the magnetic particles. The cationic character at surface of magnetic carriers played an important role in the bacteria capture showing a very high capture efficiency. In addition, the magnetic particles could be recycled, showing high efficiencies for up to 8 purification cycles.

### 4.3. Support for catalysis

Silica particles are widely used as support for catalysis in both industrial and academic fields. However, additional purification steps as filtration and centrifugation are necessary to recycle the catalytic system. Alternatively, magnetic composite particles encapsulated with a silica outer shell can be employed,<sup>30, 105</sup> in which the catalytic system can be easily removed from the reaction medium by using a magnet.

Using a sequential sol-gel process, Ge *et al.*<sup>30</sup> synthesized a catalytic system based on gold nanoparticles supported on magnetic silica particles (see section 3.1). The catalytic system was tested in Au-catalyzed reduction of 4-nitrophenol with NaBH<sub>4</sub> (Figure 10). UV-vis spectroscopy was employed to monitor the consumption of 4-nitrophenol ( $\lambda = 400$  nm), as shown in Figure 11B. The authors reported that without the Au catalyst, the reaction did not proceed. In the presence of the catalytic system, the peak at 400 nm was gradually reduced and an adsorption at 295 nm increased (Figure 11B), indicating the successful formation of 4-aminophenol. Moreover, the system could be easily recovered by magnetic separation showing an excellent activity for up to eight cycles.

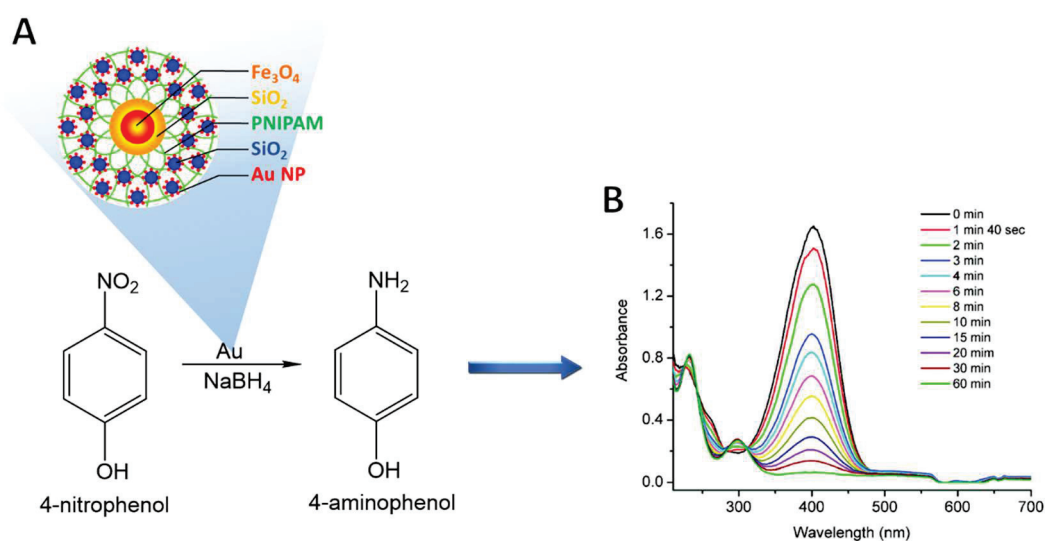


**Figure 11** – Au-catalyzed reduction of 4-nitrophenol with NaBH<sub>4</sub> using magnetic silica particles as catalytic support. (A) Chemical reaction scheme and (B) monitoring of the reaction kinetics by UV-vis spectroscopy. Adapted from Ref<sup>30</sup> with permission from ACS.

#### 4.4. Miscellaneous

As described above, magnetic properties of iron oxide nanoparticles have been largely exploited in biomedical, environmental and catalytic fields. In addition, these nanoparticles can be used in other fields of applications such as aerospace, optics and storage media. In the Aerospace applications, they are used to form ferrofluids, which can be applied either in spacecraft's fluid dynamics, where gravity force is equivalent to zero, or as microscale ion thrusters for spacecraft propulsion.<sup>38</sup> Iron oxide nanocrystals with controlled morphology and monodisperse size distribution can be also applied in multi-terabit magnetic storage media.<sup>6</sup> Bragg diffraction is the process involved in the color appearance of crystalline materials, which is observed when the periodicity of the particles matches the wavelength of the incident

light. Based on this concept, iron oxide particles can be applied in the development of optical devices in which the emitted color can be changed by varying the strength of external magnetic field and the particle size.<sup>106</sup> Ge, Yin and coworkers<sup>107-109</sup> have synthesized iron oxide clusters via a solvothermal process, with controlled sizes between 90 and 190 nm. As can be seen in Figure 12B, the peak resulting from the diffraction of (111) plane shifts to higher values of wavelengths with the magnetic field strength, leading to color changes of the cluster dispersion (Figure 12A).

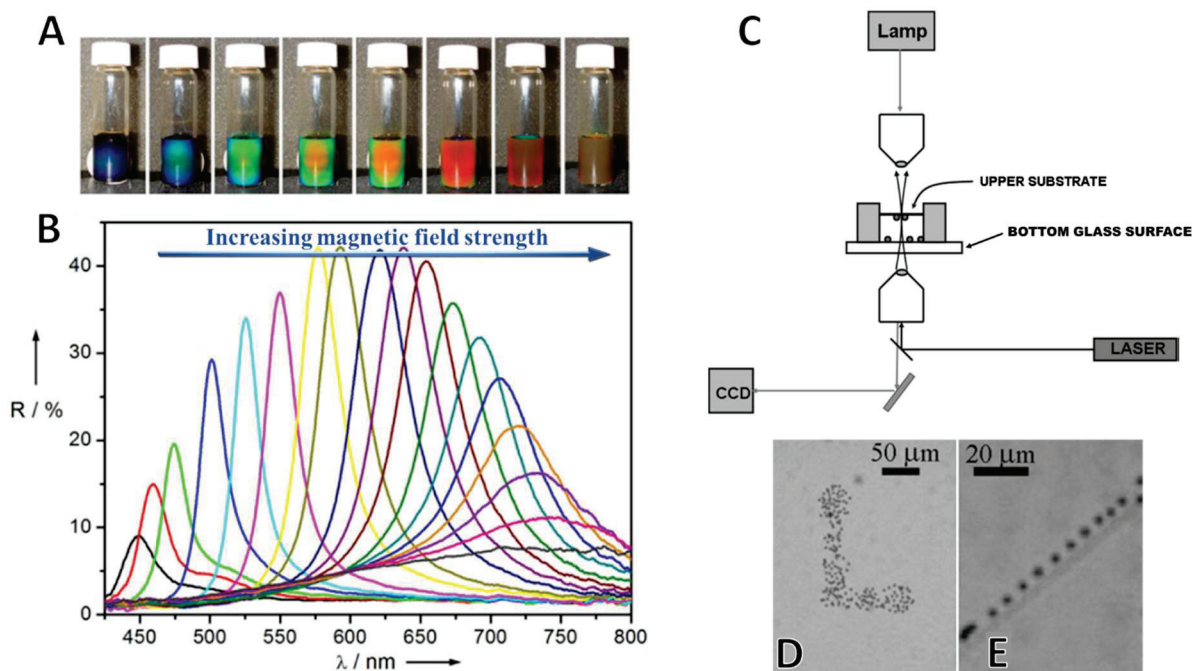


**Figure 12** – Application of magnetic particles in the development of (A and B) optical devices and (C, D and E) colloidal printers. Reproduced from Refs (A, B)<sup>107</sup> and (C-E)<sup>90</sup> with permission from the respective publishers.

The ability of manipulating particles with a laser beam has been applied in biological and physical science to manipulate, pump and sort particles. Helseth<sup>90</sup> has developed a colloidal printer as illustrated in Figure 12C. First, commercial magnetic polymer particles, Dynabeads®, were deposited on a bottom glass surface. Then, a laser beam with a wavelength of 532 nm was applied, transporting the magnetic particles to upper substrates. Two substrates were printed: a polymeric film positively charged, in which particles were fixed via opposite electrostatic interaction (the Dynabeads® particles used in this work are negatively charged) or a magnetic film, with the particles fixed through intermagnetic forces. The author showed that it is possible to control the deposition of the magnetic particles on both films, as illustrated in Figure 12D for the cationic polymeric film, and in Figure 12E for the magnetic

film. Colloidal printers have potential applications in printing of chemical and biological patterns, in which small colloidal particles functionalized with, e.g. proteins, can be printed accurately on a suitable material.

## **5. CONCLUSIONS**

The synthesis of magnetic particles and their potential applications have been reviewed in this chapter. In the biomedical field, magnetic particles can be applied as contrast agent in magnetic resonance imaging or as carriers in drug delivery systems assisted by magnetic field. By using magnetic separation to replace conventional separation methods, magnetic particles can be employed as catalytic support, for the enrichment of bio-compounds and for water purification. In addition, these particles have potential application for the development of specific devices in optics, aerospace and colloidal printer.

In applications involving magnetic separation, particles with a fast response to the magnetic field are required, to ensure short separation times when compared to conventional methods, such as centrifugation or filtration. In order to obtain particles with high magnetic separation rate, the particles must have a relatively large size and high iron oxide content. Superparamagnetism properties are also needed to re-disperse the particles, favoring the elution of targeted objects and later recycling of the magnetic particles. A protective coating surrounding the magnetic particles is also required to avoid irreversible interactions between the particles and the targets. Moreover, by a fine-tuning of the surface functionalization, these particles can be used in the capture and trigger release of specific target.

Many efforts have been employed to obtain magnetic particles that fulfill all the aforementioned criteria, but despite these efforts, a few number of works have actually achieved it. In this work, we report a novel strategy to meet these requirements. RAFT polymerization will be first used to synthesize amphiphilic block copolymers with different compositions. These well-defined copolymers will be then used for the stabilization of iron oxide clusters formed via an emulsification/solvent evaporation process. The iron oxide clusters will be next used as seed in emulsion polymerization to form polymer-encapsulated IO clusters. The chemical surface of the magnetic polymer particles will be tuned by changing the monomer composition in the hydrophilic moiety of the amphiphilic block copolymer. Finally, the control of the surface functionality of the magnetic carriers associated with their fast response when exposed to a magnetic field will be employed in capture and trigger release of bacteria.



## REFERENCES

1. Laurent, S.; Forge, D.; Port, M.; Roch, A.; Robic, C.; Vander Elst, L.; Muller, R. N., Magnetic iron oxide nanoparticles: synthesis, stabilization, vectorization, physicochemical characterizations, and biological applications. *Chemical Reviews* **2008**, *108* (6), 2064-2110.
2. Chalasani, R.; Vasudevan, S., Form, content, and magnetism in iron oxide nanocrystals. *The Journal of Physical Chemistry C* **2011**, *115* (37), 18088-18093.
3. Rahman, M. M.; Elaissari, A., Organic–inorganic hybrid magnetic latex. In *Hybrid Latex Particles*, VanHerk, A. M.; Landfester, K., Eds. Springer-Verlag Berlin: Berlin, 2010; Vol. 233, pp 237-281.
4. Lee, J.; Isobe, T.; Senna, M., Preparation of ultrafine Fe<sub>3</sub>O<sub>4</sub> particles by precipitation in the presence of PVA at high pH. *Journal of Colloid and Interface Science* **1996**, *177* (2), 490-494.
5. Kang, Y. S.; Risbud, S.; Rabolt, J. F.; Stroeve, P., Synthesis and characterization of nanometer-size Fe<sub>3</sub>O<sub>4</sub> and  $\gamma$ -Fe<sub>2</sub>O<sub>3</sub> particles. *Chemistry of Materials* **1996**, *8* (9), 2209-2211.
6. Park, J.; An, K.; Hwang, Y.; Park, J.-G.; Noh, H.-J.; Kim, J.-Y.; Park, J.-H.; Hwang, N.-M.; Hyeon, T., Ultra-large-scale syntheses of monodisperse nanocrystals. *Nature materials* **2004**, *3* (12), 891-895.
7. Sun, S.; Zeng, H., Size-Controlled Synthesis of Magnetite Nanoparticles. *Journal of the American Chemical Society* **2002**, *124* (28), 8204-8205.
8. Ge, J.; Yin, Y., Magnetically responsive colloidal photonic crystals. *Journal of Materials Chemistry* **2008**, *18* (42), 5041-5045.
9. Liu, J.; Sun, Z.; Deng, Y.; Zou, Y.; Li, C.; Guo, X.; Xiong, L.; Gao, Y.; Li, F.; Zhao, D., Highly water-dispersible biocompatible magnetite particles with low cytotoxicity stabilized by citrate groups. *Angew Chem Int Ed Engl* **2009**, *48* (32), 5875-9.
10. Albornoz, C.; Jacobo, S. E., Preparation of a biocompatible magnetic film from an aqueous ferrofluid. *Journal of Magnetism and Magnetic Materials* **2006**, *305* (1), 12-15.
11. Chin, A. B.; Yaacob, I. I., Synthesis and characterization of magnetic iron oxide nanoparticles via w/o microemulsion and Massart's procedure. *Journal of materials processing technology* **2007**, *191* (1), 235-237.
12. Hyeon, T., Chemical synthesis of magnetic nanoparticles. *Chemical Communications* **2003**, (8), 927-934.
13. Cornell, R. M.; Schwertmann, U., *The iron oxides: structure, properties, reactions, occurrences and uses*. John Wiley & Sons: 2003.
14. Wu, W.; Wu, Z.; Yu, T.; Jiang, C.; Kim, W.-S., Recent progress on magnetic iron oxide nanoparticles: synthesis, surface functional strategies and biomedical applications. *Science and Technology of Advanced Materials* **2016**.
15. Joumaa, N.; Toussay, P.; Lansalot, M.; Elaissari, A., Surface modification of iron oxide nanoparticles by a phosphate-based macromonomer and further encapsulation into submicrometer polystyrene particles by miniemulsion polymerization. *Journal of Polymer Science Part A: Polymer Chemistry* **2008**, *46* (1), 327-340.

16. Demirer, G. S.; Okur, A. C.; Kizilel, S., Synthesis and design of biologically inspired biocompatible iron oxide nanoparticles for biomedical applications. *Journal of Materials Chemistry B* **2015**, *3* (40), 7831-7849.
17. Olsvik, O.; Popovic, T.; Skjerve, E.; Cudjoe, K. S.; Hornes, E.; Ugelstad, J.; Uhlen, M., Magnetic separation techniques in diagnostic microbiology. *Clinical microbiology reviews* **1994**, *7* (1), 43-54.
18. Philipse, A. P.; van Bruggen, M. P. B.; Pathmamanoharan, C., Magnetic silica dispersions: preparation and stability of surface-modified silica particles with a magnetic core. *Langmuir* **1994**, *10* (1), 92-99.
19. Ma, W.-F.; Zhang, Y.; Li, L.-L.; You, L.-J.; Zhang, P.; Zhang, Y.-T.; Li, J.-M.; Yu, M.; Guo, J.; Lu, H.-J., Tailor-made magnetic Fe<sub>3</sub>O<sub>4</sub>@ mTiO<sub>2</sub> microspheres with a tunable mesoporous anatase shell for highly selective and effective enrichment of phosphopeptides. *ACS Nano* **2012**, *6* (4), 3179-3188.
20. Yang, N.; Zhu, S.; Zhang, D.; Xu, S., Synthesis and properties of magnetic Fe<sub>3</sub>O<sub>4</sub>-activated carbon nanocomposite particles for dye removal. *Materials Letters* **2008**, *62* (4), 645-647.
21. Bourgeat-Lami, E.; Lansalot, M., Organic/Inorganic Composite Latexes: The Marriage of Emulsion Polymerization and Inorganic Chemistry. In *Hybrid Latex Particles*, VanHerck, A. M.; Landfester, K., Eds. Springer-Verlag Berlin: Berlin, 2010; Vol. 233, pp 53-123.
22. Iler, R. K., *The chemistry of silica: solubility, polymerization, colloid and surface properties, and biochemistry*. John Wiley & Sons Inc: Canada, 1979.
23. Pinho, S. L. C.; Pereira, G. A.; Voisin, P.; Kassem, J.; Bouchaud, V.; Etienne, L.; Peters, J. A.; Carlos, L.; Mornet, S.; Geraldes, C. F. G. C.; Rocha, J.; Delville, M.-H., Fine Tuning of the Relaxometry of  $\gamma$ -Fe<sub>2</sub>O<sub>3</sub>@SiO<sub>2</sub> Nanoparticles by Tweaking the Silica Coating Thickness. *ACS Nano* **2010**, *4* (9), 5339-5349.
24. Wang, X.; Shi, Y.; Graff, R. W.; Lee, D.; Gao, H., Developing recyclable pH-responsive magnetic nanoparticles for oil–water separation. *Polymer* **2015**, *72*, 361-367.
25. Vincent Maurice; Thomas Georgelin; Jean-Michel Siaugue; Cabuil, V., Synthesis and characterization of functionalized core–shell gamma Fe<sub>2</sub>O<sub>3</sub>–SiO<sub>2</sub> nanoparticles. *Journal of Magnetism and Magnetic Materials* **2009**, *321*, 1408–1413.
26. Liu, X.; Ma, Z.; Xing, J.; Liu, H., Preparation and characterization of amino–silane modified superparamagnetic silica nanospheres. *Journal of Magnetism and Magnetic Materials* **2004**, *270* (1–2), 1-6.
27. Yi, D. K.; Selvan, S. T.; Lee, S. S.; Papaefthymiou, G. C.; Kundaliya, D.; Ying, J. Y., Silica-Coated Nanocomposites of Magnetic Nanoparticles and Quantum Dots. *Journal of the American Chemical Society* **2005**, *127* (14), 4990-4991.
28. Pfaff, A.; Schallon, A.; Ruhland, T. M.; Majewski, A. P.; Schmalz, H.; Freitag, R.; Müller, A. H. E., Magnetic and Fluorescent Glycopolymer Hybrid Nanoparticles for Intranuclear Optical Imaging. *Biomacromolecules* **2011**, *12* (10), 3805-3811.
29. Ge, J.; Hu, Y.; Zhang, T.; Yin, Y., Superparamagnetic Composite Colloids with Anisotropic Structures. *Journal of the American Chemical Society* **2007**, *129* (29), 8974-8975.

30. Ge, J.; Huynh, T.; Hu, Y.; Yin, Y., Hierarchical Magnetite/Silica Nanoassemblies as Magnetically Recoverable Catalyst-Supports. *Nano Letters* **2008**, *8* (3), 931-934.
31. Liu, Q.; Shi, J.; Cheng, M.; Li, G.; Cao, D.; Jiang, G., Preparation of graphene-encapsulated magnetic microspheres for protein/peptide enrichment and MALDI-TOF MS analysis. *Chemical Communications* **2012**, *48* (13), 1874-1876.
32. Chen, H.; Deng, C.; Zhang, X., Synthesis of Fe<sub>3</sub>O<sub>4</sub>@ SiO<sub>2</sub>@ PMMA Core-Shell-Shell Magnetic Microspheres for Highly Efficient Enrichment of Peptides and Proteins for MALDI-ToF MS Analysis. *Angewandte Chemie International Edition* **2010**, *49* (3), 607-611.
33. Xiong, Z.; Zhao, L.; Wang, F.; Zhu, J.; Qin, H.; Wu, R. a.; Zhang, W.; Zou, H., Synthesis of branched PEG brushes hybrid hydrophilic magnetic nanoparticles for the selective enrichment of N-linked glycopeptides. *Chemical Communications* **2012**, *48* (65), 8138-8140.
34. Matyjaszewski, K., Atom Transfer Radical Polymerization (ATRP): Current Status and Future Perspectives. *Macromolecules* **2012**, *45* (10), 4015-4039.
35. Nicolas, J.; Guillauneuf, Y.; Lefay, C.; Bertin, D.; Gimes, D.; Charleux, B., Nitroxide-mediated polymerization. *Progress in Polymer Science* **2013**, *38* (1), 63-235.
36. Barner-Kowollik, C., *Handbook of RAFT Polymerization*. Wiley-VCH: Weinheim, 2008.
37. Basuki, J. S.; Jacquemin, A.; Esser, L.; Li, Y.; Boyer, C.; Davis, T. P., A block copolymer-stabilized co-precipitation approach to magnetic iron oxide nanoparticles for potential use as MRI contrast agents. *Polymer Chemistry* **2014**, *5* (7), 2611-2620.
38. King, L. B.; Meyer, E.; Hopkins, M. A.; Hawckett, B. S.; Jain, N., Self-Assembling Array of Magneto-electrostatic Jets from the Surface of a Superparamagnetic Ionic Liquid. *Langmuir* **2014**, *30* (47), 14143-14150.
39. Dong, H.; Huang, J.; Koepsel, R. R.; Ye, P.; Russell, A. J.; Matyjaszewski, K., Recyclable antibacterial magnetic nanoparticles grafted with quaternized poly (2-(dimethylamino) ethyl methacrylate) brushes. *Biomacromolecules* **2011**, *12* (4), 1305-1311.
40. Muller-Schulte, D. Magnetic polymer particles on the basis of polyvinyl alcohol, process for the production and use. US 20010014468 A1, 2000.
41. Hamoudeh, M.; Al Faraj, A.; Canet-Soulas, E.; Bessueille, F.; Léonard, D.; Fessi, H., Elaboration of PLLA-based superparamagnetic nanoparticles: characterization, magnetic behaviour study and in vitro relaxivity evaluation. *International journal of pharmaceuticals* **2007**, *338* (1), 248-257.
42. Hamoudeh, M.; Fessi, H., Preparation, characterization and surface study of poly-epsilon caprolactone magnetic microparticles. *Journal of Colloid and Interface Science* **2006**, *300* (2), 584-590.
43. Pavia-Sanders, A.; Zhang, S.; Flores, J. A.; Sanders, J. E.; Raymond, J. E.; Wooley, K. L., Robust magnetic/polymer hybrid nanoparticles designed for crude oil entrapment and recovery in aqueous environments. *ACS Nano* **2013**, *7* (9), 7552-7561.
44. Basuki, J. S.; Duong, H. T.; Macmillan, A.; Whan, R.; Boyer, C.; Davis, T. P., Polymer-grafted, nonfouling, magnetic nanoparticles designed to selectively store and release molecules via ionic interactions. *Macromolecules* **2013**, *46* (17), 7043-7054.



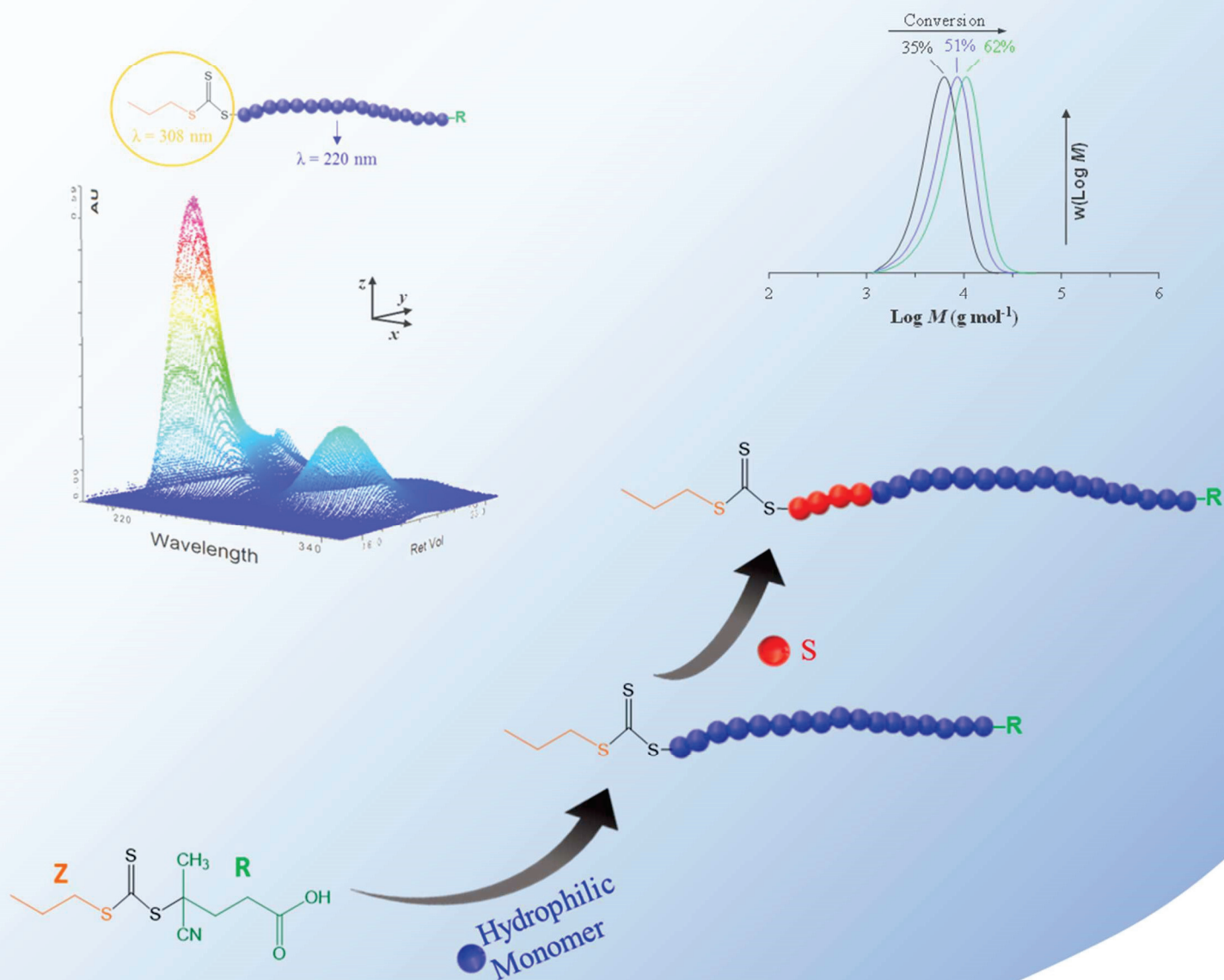
45. Chen, T.; Shukoor, M. I.; Wang, R.; Zhao, Z.; Yuan, Q.; Bamrungsap, S.; Xiong, X.; Tan, W., Smart multifunctional nanostructure for targeted cancer chemotherapy and magnetic resonance imaging. *ACS Nano* **2011**, *5* (10), 7866-7873.
46. Urban, M.; Musyanovych, A.; Landfester, K., Fluorescent superparamagnetic polylactide nanoparticles by combination of miniemulsion and emulsion/solvent evaporation techniques. *Macromolecular Chemistry and Physics* **2009**, *210* (11), 961-970.
47. <http://ir.perkinelmer.com/releasedetail.cfm?ReleaseID=584487> (accessed December 2016).
48. Müller-Schulte, D.; Brunner, H., Novel magnetic microspheres on the basis of poly (vinyl alcohol) as affinity medium for quantitative detection of glycosylated haemoglobin. *Journal of Chromatography A* **1995**, *711* (1), 53-60.
49. Lu, X.; Niu, M.; Qiao, R.; Gao, M., Superdispersible PVP-Coated Fe<sub>3</sub>O<sub>4</sub> Nanocrystals Prepared by a “One-Pot” Reaction†. *The Journal of Physical Chemistry B* **2008**, *112* (46), 14390-14394.
50. John Ughelstad, T. E., Arvid Berge, Bertil Helgée Magnetic polymer particles and process for the preparation thereof. WO 1983003920 A1, 1983.
51. Ugelstad, J.; Berge, A.; Ellingsen, T.; Aune, O.; Kilaas, L.; Nilsen, T.; Schmid, R.; Stenstad, P.; Funderud, S.; Kvalheim, G. In *Monosized magnetic particles and their use in selective cell separation*, Makromolekulare Chemie. Macromolecular Symposia, Wiley Online Library: 1988; pp 177-211.
52. Zhou, W.-H.; Lu, C.-H.; Guo, X.-C.; Chen, F.-R.; Yang, H.-H.; Wang, X.-R., Mussel-inspired molecularly imprinted polymer coating superparamagnetic nanoparticles for protein recognition. *Journal of Materials Chemistry* **2010**, *20* (5), 880-883.
53. Qin, S.; Wang, L.; Zhang, X.; Su, G., Grafting poly (ethylene glycol) monomethacrylate onto Fe<sub>3</sub>O<sub>4</sub> nanoparticles to resist nonspecific protein adsorption. *Applied Surface Science* **2010**, *257* (3), 731-735.
54. Wang, W. C.; Neoh, K. G.; Kang, E. T., Surface functionalization of Fe<sub>3</sub>O<sub>4</sub> magnetic nanoparticles via RAFT-mediated graft polymerization. *Macromolecular rapid communications* **2006**, *27* (19), 1665-1669.
55. Xiao, L.-H.; Wang, T.; Zhao, T.-Y.; Zheng, X.; Sun, L.-Y.; Li, P.; Liu, F.-Q.; Gao, G.; Dong, A., Fabrication of magnetic-antimicrobial-fluorescent multifunctional hybrid microspheres and their properties. *International Journal of Molecular Sciences* **2013**, *14* (4), 7391-7404.
56. Liu, J.; He, W.; Zhang, L.; Zhang, Z.; Zhu, J.; Yuan, L.; Chen, H.; Cheng, Z.; Zhu, X., Bifunctional nanoparticles with fluorescence and magnetism via surface-initiated AGET ATRP mediated by an iron catalyst. *Langmuir* **2011**, *27* (20), 12684-12692.
57. Xie, Y.; Sougrat, R.; Nunes, S. P., Synthesis and characterization of polystyrene coated iron oxide nanoparticles and asymmetric assemblies by phase inversion. *Journal of Applied Polymer Science* **2015**, *132* (5).
58. Majewski, A. P.; Stahlschmidt, U.; Jérôme, V. r.; Freitag, R.; Müller, A. H.; Schmalz, H., PDMAEMA-grafted core-shell-corona particles for nonviral gene delivery and magnetic cell separation. *Biomacromolecules* **2013**, *14* (9), 3081-3090.

59. Li, Y.; Dong, M.; Kong, J.; Chai, Z.; Fu, G., Synthesis of Fe<sub>3</sub>O<sub>4</sub>@ poly(methacrylic acid) core-shell submicrospheres via RAFT precipitation polymerization. *Journal of Colloid and Interface Science* **2013**, *394*, 199-207.
60. Niu, M.; Du, M.; Gao, Z.; Yang, C.; Lu, X.; Qiao, R.; Gao, M., Monodispersed magnetic polystyrene beads with excellent colloidal stability and strong magnetic response. *Macromolecular Rapid Communications* **2010**, *31* (20), 1805-1810.
61. Ozalp, V. C.; Bayramoglu, G.; Erdem, Z.; Arica, M. Y., Pathogen detection in complex samples by quartz crystal microbalance sensor coupled to aptamer functionalized core-shell type magnetic separation. *Analytica Chimica Acta* **2015**, *853*, 533-540.
62. Haladjova, E.; Rangelov, S.; Tsvetanov, C. B.; Posheva, V.; Peycheva, E.; Maximova, V.; Momekova, D.; Mountrichas, G.; Pispas, S.; Bakandritsos, A., Enhanced Gene Expression Promoted by Hybrid Magnetic/Cationic Block Copolymer Micelles. *Langmuir* **2014**, *30* (27), 8193-8200.
63. Rahman, M. M.; Chehimi, M. M.; Fessi, H.; Elaissari, A., Highly temperature responsive core-shell magnetic particles: synthesis, characterization and colloidal properties. *Journal of Colloid and Interface Science* **2011**, *360* (2), 556-564.
64. Li, K.; Dugas, P.-Y.; Lansalot, M.; Bourgeat-Lami, E., Surfactant-Free Emulsion Polymerization Stabilized by Ultrasmall Superparamagnetic Iron Oxide Particles Using Acrylic Acid or Methacrylic Acid as Auxiliary Comonomers. *Macromolecules* **2016**, *49* (20), 7609-7624.
65. Zhang, F.; Yu, S.; Hou, G.; Xu, N.; Wu, Z.; Yue, L., Miniemulsion-based assembly of iron oxide nanoparticles and synthesis of magnetic polymer nanospheres. *Colloid and Polymer Science* **2015**, *293* (7), 1893-1902.
66. Chen, K.; Zhu, Y.; Zhang, Y.; Li, L.; Lu, Y.; Guo, X., Synthesis of magnetic spherical polyelectrolyte brushes. *Macromolecules* **2011**, *44* (3), 632-639.
67. Kaewsaneha, C.; Tangboriboonrat, P.; Polpanich, D.; Eissa, M.; Elaissari, A., Anisotropic janus magnetic polymeric nanoparticles prepared via miniemulsion polymerization. *Journal of Polymer Science Part A: Polymer Chemistry* **2013**, *51* (22), 4779-4785.
68. Landfester, K.; Ramirez, L. P., Encapsulated magnetite particles for biomedical application. *Journal of Physics: Condensed Matter* **2003**, *15* (15), S1345.
69. Ramirez, L. P.; Landfester, K., Magnetic polystyrene nanoparticles with a high magnetite content obtained by miniemulsion processes. *Macromolecular Chemistry and Physics* **2003**, *204* (1), 22-31.
70. Ramos, J.; Forcada, J., Surfactant-free miniemulsion polymerization as a simple synthetic route to a successful encapsulation of magnetite nanoparticles. *Langmuir* **2011**, *27* (11), 7222-7230.
71. Tan, C. J.; Chua, H. G.; Ker, K. H.; Tong, Y. W., Preparation of bovine serum albumin surface-imprinted submicrometer particles with magnetic susceptibility through core-shell miniemulsion polymerization. *Analytical chemistry* **2008**, *80* (3), 683-692.
72. Teo, B. M.; Suh, S. K.; Hatton, T. A.; Ashokkumar, M.; Grieser, F., Sonochemical synthesis of magnetic Janus nanoparticles. *Langmuir* **2010**, *27* (1), 30-33.
73. Xu, Y.; Xu, H.; Gu, H., Controllable preparation of epoxy-functionalized magnetic polymer latexes with different morphologies by modified miniemulsion polymerization. *Journal of Polymer Science Part A: Polymer Chemistry* **2010**, *48* (11), 2284-2293.

74. Yoon, H.-J.; Lim, T. G.; Kim, J.-H.; Cho, Y. M.; Kim, Y. S.; Chung, U. S.; Kim, J. H.; Choi, B. W.; Koh, W.-G.; Jang, W.-D., Fabrication of multifunctional layer-by-layer nanocapsules toward the design of theragnostic nanoplatform. *Biomacromolecules* **2014**, *15* (4), 1382-1389.
75. Qi, D.; Cao, Z.; Ziener, U., Recent advances in the preparation of hybrid nanoparticles in miniemulsions. *Advances in Colloid and Interface Science* **2014**, *211*, 47-62.
76. Weiss, C. K.; Landfester, K., Miniemulsion polymerization as a means to encapsulate organic and inorganic materials. In *Hybrid Latex Particles*, Springer: 2010; pp 185-236.
77. Bourgeat-Lami, E.; D'Agosto, F.; Lansalot, M., Synthesis of nanocapsules and polymer/inorganic nanoparticles through controlled radical polymerization at and near interfaces in heterogeneous media. In *Controlled Radical Polymerization at and from Solid Surfaces*, Springer: 2015; pp 123-161.
78. Hoffmann, D.; Landfester, K.; Antonietti, M., Encapsulation of magnetite in polymer particles via the miniemulsion polymerization process. *Magneto hydrodynamics* **2001**, *37* (217-221), 58.
79. Chakraborty, S.; Jähnichen, K.; Komber, H.; Basfar, A. A.; Voit, B., Synthesis of magnetic polystyrene nanoparticles using amphiphilic ionic liquid stabilized RAFT mediated miniemulsion polymerization. *Macromolecules* **2014**, *47* (13), 4186-4198.
80. Feyen, M.; Weidenthaler, C.; Schüth, F.; Lu, A.-H., Synthesis of structurally stable colloidal composites as magnetically recyclable acid catalysts. *Chemistry of Materials* **2010**, *22* (9), 2955-2961.
81. Yanase, N.; Noguchi, H.; Asakura, H.; Suzuta, T., Preparation of magnetic latex particles by emulsion polymerization of styrene in the presence of a ferrofluid. *Journal of Applied Polymer Science* **1993**, *50* (5), 765-776.
82. Xu, S.; Ma, W.-F.; You, L.-J.; Li, J.-M.; Guo, J.; Hu, J. J.; Wang, C.-C., Toward designer magnetite/polystyrene colloidal composite microspheres with controllable nanostructures and desirable surface functionalities. *Langmuir* **2012**, *28* (6), 3271-3278.
83. Paquet, C.; Page, L.; Kell, A.; Simard, B., Nanobeads highly loaded with superparamagnetic nanoparticles prepared by emulsification and seeded-emulsion polymerization. *Langmuir* **2010**, *26* (8), 5388-96.
84. Gao, J.; Gu, H.; Xu, B., Multifunctional magnetic nanoparticles: design, synthesis, and biomedical applications. *Accounts of chemical research* **2009**, *42* (8), 1097-1107.
85. Kalia, S.; Kango, S.; Kumar, A.; Haldorai, Y.; Kumari, B.; Kumar, R., Magnetic polymer nanocomposites for environmental and biomedical applications. *Colloid and Polymer Science* **2014**, *292* (9), 2025-2052.
86. Yan, D.; Zhao, Y.; Wei, M.; Liang, R.; Lu, J.; Evans, D. G.; Duan, X., *RSC Advances*. **2013**.
87. Gupta, A. K.; Gupta, M., Synthesis and surface engineering of iron oxide nanoparticles for biomedical applications. *Biomaterials* **2005**, *26* (18), 3995-4021.
88. Brazel, C. S., Magneto thermally-responsive Nanomaterials: Combining Magnetic Nanostructures and Thermally-Sensitive Polymers for Triggered Drug Release. *Pharmaceutical Research* **2009**, *26* (3), 644-656.

89. He, J. C.; Huang, M. Y.; Wang, D. M.; Zhang, Z. M.; Li, G. K., Magnetic separation techniques in sample preparation for biological analysis: A review. *Journal of Pharmaceutical and Biomedical Analysis* **2014**, *101*, 84-101.
90. Helseth, L. E., Colloidal printer based on an optical micropump. *Applied Physics Letters* **2007**, *90* (9).
91. Shao, M.; Ning, F.; Zhao, J.; Wei, M.; Evans, D. G.; Duan, X., Preparation of Fe<sub>3</sub>O<sub>4</sub>@SiO<sub>2</sub>@layered double hydroxide core-shell microspheres for magnetic separation of proteins. *Journal of the American Chemical Society* **2012**, *134* (2), 1071-1077.
92. Song, E.-Q.; Hu, J.; Wen, C.-Y.; Tian, Z.-Q.; Yu, X.; Zhang, Z.-L.; Shi, Y.-B.; Pang, D.-W., Fluorescent-magnetic-biotargeting multifunctional nanobioprobes for detecting and isolating multiple types of tumor cells. *ACS Nano* **2011**, *5* (2), 761-770.
93. El-Boubbou, K.; Gruden, C.; Huang, X., Magnetic glyco-nanoparticles: a unique tool for rapid pathogen detection, decontamination, and strain differentiation. *Journal of the American Chemical Society* **2007**, *129* (44), 13392-13393.
94. Cheng, Z.; Al Zaki, A.; Hui, J. Z.; Muzykantov, V. R.; Tsourkas, A., Multifunctional nanoparticles: cost versus benefit of adding targeting and imaging capabilities. *Science* **2012**, *338* (6109), 903-910.
95. Dorland, W. A. N., *Dorland's medical dictionary*. Saunders: 1968.
96. Lee, H.; Shin, T.-H.; Cheon, J.; Weissleder, R., Recent developments in magnetic diagnostic systems. *Chemical Reviews* **2015**, *115* (19), 10690-10724.
97. Cheng, L.; Wang, C.; Feng, L. Z.; Yang, K.; Liu, Z., Functional Nanomaterials for Phototherapies of Cancer. *Chemical Reviews* **2014**, *114* (21), 10869-10939.
98. Lee, N.; Hyeon, T., Designed synthesis of uniformly sized iron oxide nanoparticles for efficient magnetic resonance imaging contrast agents. *Chemical Society Reviews* **2012**, *41* (7), 2575-2589.
99. James, M. L.; Gambhir, S. S., A molecular imaging primer: modalities, imaging agents, and applications. *Physiological Reviews* **2012**, *92* (2), 897-965.
100. Stanisz, G. J.; Odrobina, E. E.; Pun, J.; Escaravage, M.; Graham, S. J.; Bronskill, M. J.; Henkelman, R. M., T1, T2 relaxation and magnetization transfer in tissue at 3T. *Magnetic resonance in medicine* **2005**, *54* (3), 507-512.
101. Sun, C.; Veiseh, O.; Gunn, J.; Fang, C.; Hansen, S.; Lee, D.; Sze, R.; Ellenbogen, R. G.; Olson, J.; Zhang, M., In vivo MRI detection of gliomas by chlorotoxin-conjugated superparamagnetic nanoprobes. *Small* **2008**, *4* (3), 372-379.
102. <https://pixabay.com> (free images database) (accessed December 2016).
103. Hoffman, A. S. In "Intelligent" polymers in medicine and biotechnology, Macromolecular Symposia, Wiley Online Library: 1995; pp 645-664.
104. Tavares, D. S.; Daniel-da-Silva, A. L.; Lopes, C. B.; Silva, N. J.; Amaral, V. S.; Rocha, J.; Pereira, E.; Trindade, T., Efficient sorbents based on magnetite coated with siliceous hybrid shells for removal of mercury ions. *Journal of Materials Chemistry A* **2013**, *1* (28), 8134-8143.

105. Shokouhimehr, M.; Piao, Y.; Kim, J.; Jang, Y.; Hyeon, T., A magnetically recyclable nanocomposite catalyst for olefin epoxidation. *Angewandte Chemie International Edition* **2007**, *46* (37), 7039-7043.
106. Yin, Y., Magnetically responsive photonic nanostructures. *SPIE Newsroom* **2011**.
107. Ge, J.; Hu, Y.; Yin, Y., Highly Tunable Superparamagnetic Colloidal Photonic Crystals. *Angewandte Chemie International Edition* **2007**, *46* (39), 7428-7431.
108. Ge, J.; Hu, Y.; Zhang, T.; Huynh, T.; Yin, Y., Self-Assembly and Field-Responsive Optical Diffractions of Superparamagnetic Colloids. *Langmuir* **2008**, *24* (7), 3671-3680.
109. Ge, J.; Lee, H.; He, L.; Kim, J.; Lu, Z.; Kim, H.; Goebel, J.; Kwon, S.; Yin, Y., Magnetochromatic Microspheres: Rotating Photonic Crystals. *Journal of the American Chemical Society* **2009**, *131* (43), 15687-15694.



# Chapter II

## SYNTHESIS OF MACROMOLECULAR RAFT AGENTS



TABLE OF CONTENTS

<b>1. INTRODUCTION</b> .....	<b>65</b>
<b>2. BIBLIOGRAPHIC REVIEW</b> .....	<b>65</b>
<b>2.1. Free radical polymerization</b> .....	<b>65</b>
<b>2.2. Reversible-Deactivation Radical Polymerization (RDRP)</b> .....	<b>67</b>
2.2.1. <i>Reversible addition-fragmentation chain transfer (RAFT)</i> .....	68
2.2.1.1. <i>Mechanism</i> .....	68
2.2.1.2. <i>Impact of R and Z groups</i> .....	69
2.2.2. <i>Macromolecular design</i> .....	71
2.2.3. <i>Synthesis of block copolymers</i> .....	72
<b>3. EXPERIMENTAL SECTION</b> .....	<b>74</b>
<b>3.1. Materials</b> .....	<b>74</b>
<b>3.2. Methods</b> .....	<b>75</b>
3.2.1. <i>Synthesis of hydrophilic macroRAFT agents</i> .....	75
3.2.2. <i>Chain extension reactions</i> .....	77
3.2.3. <i>Synthesis of amphiphilic macroRAFT agents</i> .....	77
3.2.4. <i>Determination of the cloud point temperature of the macroRAFT agents</i> .....	78
<b>3.3. Characterizations</b> .....	<b>78</b>
3.3.1. <i><sup>1</sup>H NMR</i> .....	78
3.3.2. <i>Size exclusion chromatography (SEC)</i> .....	79
<b>4. RESULTS AND DISCUSSION</b> .....	<b>81</b>
<b>4.1. Synthesis of hydrophilic macroRAFT agents</b> .....	<b>81</b>
4.1.1. <i>Synthesis of poly(acrylic acid) macroRAFT agents: PAA-TTC</i> .....	82
4.1.2. <i>Synthesis of poly(2-dimethylaminoethyl methacrylate) macroRAFT agents: PDMAEMA-TTC</i> 84	
4.1.3. <i>Synthesis of poly(2-dimethylaminoethyl methacrylate-co-acrylic acid) macroRAFT agents: P(DMAEMA-co-AA)-TTC</i> .....	88
4.1.4. <i>Chain extension reactions</i> .....	92
4.1.5. <i>Synthesis of amphiphilic block copolymers</i> .....	96
<b>4.2. Thermoresponsive properties of the different macroRAFTs</b> .....	<b>100</b>
4.2.1. <i>Effect of pH on the cloud point of the DMAEMA-based macroRAFT agents</i> .....	102
4.2.2. <i>Effect of ionic strength on the LCST of PDMAEMA-TTC</i> .....	104
4.2.3. <i>Effect of the macroRAFT composition on the T<sub>CP</sub></i> .....	105
<b>5. CONCLUSIONS</b> .....	<b>106</b>
<b>REFERENCES</b> .....	<b>108</b>

## 1. INTRODUCTION

In this chapter, the synthesis of amphiphilic block copolymers will be investigated by RAFT polymerization. First, a brief overview about RDRP processes is given, focusing on RAFT polymerization. Then, the synthesis of five hydrophilic macroRAFTs aiming at different molar fractions of DMAEMA/AA: 100/0, 75/25, 50/50, 25/75, 0/100 will be presented. This variation in composition will generate polymer chains with different thermo- and/or pH-responsive properties. PAA polymer chains are negatively charged at basic pH and uncharged under acidic conditions (pka value close to 5),<sup>1</sup> while PDMAEMA is positively charged at acidic pH and uncharged under alkaline conditions (pka value close to 7).<sup>2</sup> On the other hand, macroRAFT copolymers composed of AA and DMAEMA display both characteristics, being positively charged at acidic pH and negatively charged in basic conditions. Therefore, these macroRAFT copolymers will be referred to hereafter as amphoteric macroRAFTs. In a second step, amphiphilic block copolymers will be prepared via chain extension reaction of the five hydrophilic macroRAFTs with styrene. The thermo-responsive properties of all PDMAEMA-based macroRAFTs will be further investigated. The amphiphilic block copolymers will be later on employed for the stabilization of iron oxide clusters and magnetic latex particles (Chapters 3 and 4, respectively). The control of the monomer composition of the macroRAFT is thus of prime importance to prepare particles with well-defined surface chemistries.

## 2. BIBLIOGRAPHIC REVIEW

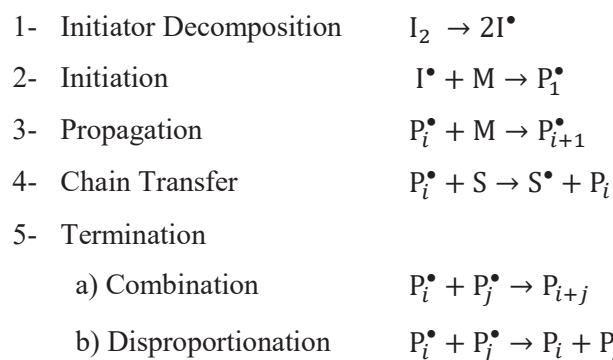
### 2.1. Free radical polymerization

Free radical polymerization is one of the most studied polymerization processes,<sup>3</sup> both in academia and industry. It enables the production of ca. 100 millions tons of polymer per year<sup>4</sup> corresponding to a range of 50% of all manufactured plastic materials and synthetic rubbers.<sup>5</sup>

The general mechanism of free radical polymerization<sup>6</sup> is presented in Scheme 1. The first step involves the *initiator decomposition*, in which a radical is formed from an initiator. Generally, these radicals are formed by thermal decomposition of either organic (e.g. azo compounds, diacyl peroxides) or inorganic (e.g. persulfate salts) compounds. They can also be generated from light-induced decomposition of photoinitiators or from redox systems at low temperatures. After *initiator decomposition*, the formed radicals ( $I^\bullet$ ) react with a few monomer units generating an oligoradical ( $P_1^\bullet$ , Scheme 1). During the *propagation* step, the active species ( $P_i^\bullet$ ) successively react with monomer units leading to the formation of polymer



chains. The propagating macromolecules ( $P_i^\bullet$ ) increase their size until the occurrence of an event leading to the loss of their activity: *termination* or *chain transfer*. The termination step occurs basically by two ways: (1) *termination by combination*, when two growing chains react between them forming a single chain, and (2) *termination by disproportionation* when the termination results in two inactive polymer chains. Chain transfer occurs when the propagating radical reacts with a compound (S) to form an inactive polymer chain and a new radical ( $S^\bullet$ ) able to initiate a new chain. S can be a solvent, a monomer, a polymer chain, an initiator or a chain transfer agent (CTA). Moreover, in conventional radical polymerization, all steps described above occur in less than one second resulting in polymer chains with a broad molar mass distribution and various chain end-functionalizations.



**Scheme 1** – Mechanism of free radical polymerization

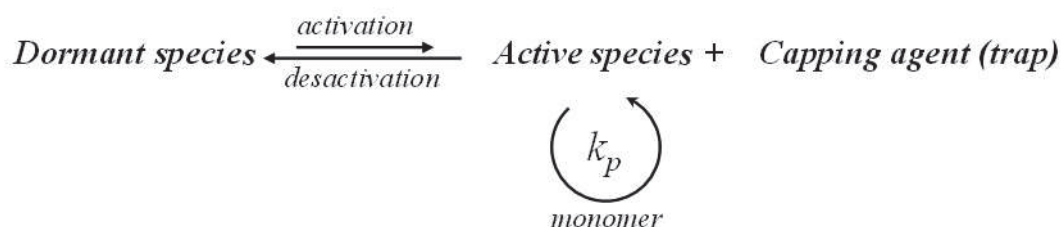
Indeed, polymers with a large variety of chemical compositions can be synthesized via free radical polymerization. Nonetheless, the architectural control of these polymer chains is limited. Since termination and chain transfer steps are not controlled, polymer chains presenting different chain end-functionalization will be obtained. Furthermore, in copolymerization systems, the difference of the monomers reactivity ratio can lead to the formation of heterogeneous materials, thus negatively impacting their final properties. The advent of reversible-deactivation radical polymerization (RDRP) techniques about 20 years ago has however revolutionized the macromolecular design. Well-defined polymer chains of predetermined molar mass and narrow molar mass distribution can now be synthesized, with a controlled chain-end functionalization and well-defined monomer compositions allowing the production of various macromolecular architectures (e.g. block copolymers, star polymers).

## 2.2. Reversible-Deactivation Radical Polymerization (RDRP)

Since the pioneering works published in the 90's about the main RDRP techniques of nitroxide-mediated polymerization (NMP),<sup>7</sup> atom transfer radical polymerization (ATRP)<sup>8, 9</sup> and reversible addition-fragmentation chain transfer (RAFT) polymerization,<sup>10</sup> these techniques have demonstrated to be powerful tools for the synthesis of polymers with new macromolecular architectures.

RDRP relies on the use of a controlling agent, which will react with the oligoradicals to form dormant chains. The key of the process is the ability to reactivate the dormant chains allowing the propagation to be restarted. These activation-deactivation cycles generate an equilibrium between the dormant and propagating chains,<sup>11</sup> as illustrated in Scheme 2. This equilibrium has to be shifted to the dormant side ( $k_{\text{activation}} \ll k_{\text{deactivation}}$ ) allowing the control of the polymer chains. When these conditions are reached, the polymerization is controlled and is characterized by the following features:

- First-order kinetic behavior
- Linear evolution of molar masses with conversion
- Narrow molar mass distribution
- Long-lived polymer chains with preserved end functionalities



**Scheme 2** – Main equilibrium involved in reversible-deactivation radical polymerizations

RDRP techniques can be divided into two main classes depending on the reaction used to control the radical polymerization: reversible termination or reversible chain transfer. The first class is based on the control of the termination process (step 5 in Scheme 1). There are two main techniques relying on this approach, NMP and ATRP. In NMP, the dormant species is an alkoxyamine thermally activated via a homolytic cleavage of the C-O bond, generating the propagating radical and the nitroxide. In ATRP, the dormant species is an alkyl halide, which can be activated by transition metal complexes. For the second class, the control of the growing chains operates through reversible chain transfer reactions. In this case the

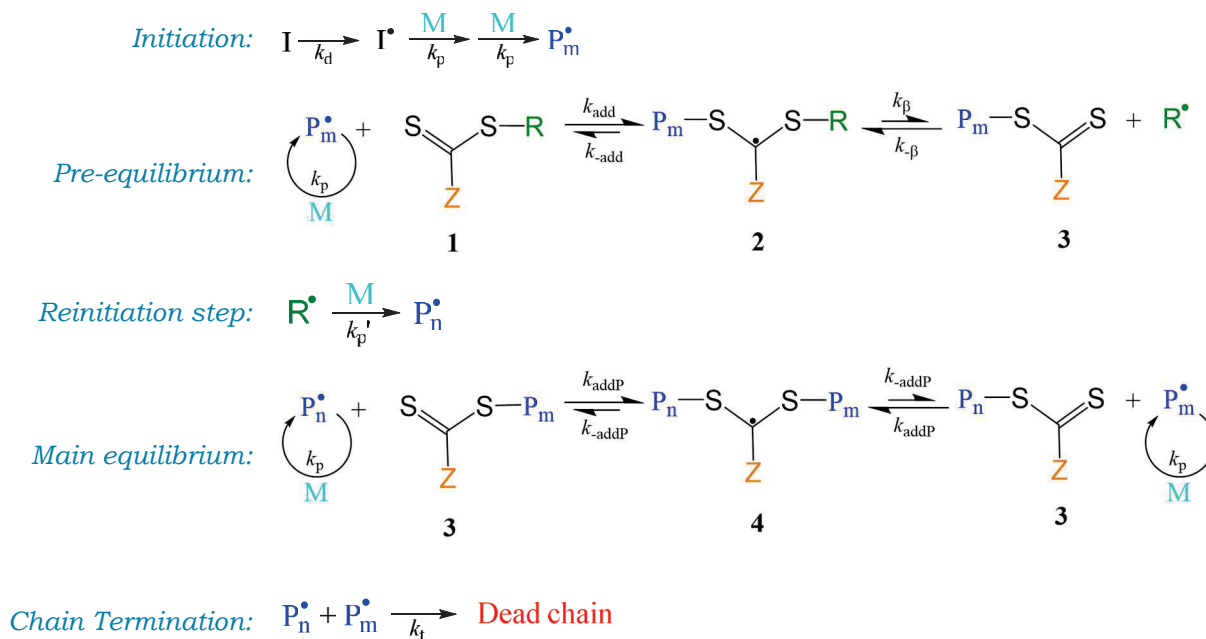
mechanism proceeds via a degenerative chain transfer process, in which the propagating species are in equilibrium with the dormant ones. As degenerative chain transfer is not able to create radicals, the reaction thus requires addition of an external source of radicals to maintain a constant rate of polymerization. The most relevant technique based on this mechanism is the RAFT polymerization that will be described in the next section.

### *2.2.1. Reversible addition-fragmentation chain transfer (RAFT)*

The RAFT technique can be considered as the most versatile of all RDRP processes, allowing the polymerization of most vinyl monomers to be controlled. It also offers further advantages: the reaction can be carried out under mild conditions, non-toxic chemicals are used, minimal process development is required compared to conventional radical polymerization and it is compatible with a wide variety of reaction media, even water. This technique is also known as MADIX polymerization when a xanthate-based CTA is used as controlling agent.

#### *2.2.1.1. Mechanism*

The RAFT mechanism is presented in Scheme 3. Unlike ATRP and NMP, RAFT requires the use of a radical initiator. The *initiation* step is similar to that reported above for conventional radical polymerization. In a step known as the *pre-equilibrium*, the resulting oligoradical ( $P_m^\bullet$ ) will transfer its radical to the RAFT agent **1** generating an intermediate radical **2**, which will then fragment to release a dormant species (**3**) and the radical  $R^\bullet$  coming from the RAFT agent. This radical will be able to initiate the polymerization, generating other growing polymer chains,  $P_n^\bullet$ , which will be deactivated in the next step, the so-called *main equilibrium*, forming the intermediate radical **4**, which, similarly to what is observed in the pre-equilibrium, will then fragment to release a dormant species **3** and a propagating one. The recurring reactivation of the dormant species **3** followed by fast deactivation, allows the controlled addition of monomer units, one-by-one, generating a linear increase of the molar mass *vs* conversion. Associated to this chemical equilibrium, the control over the polymerization process is possible if all chains are offered an equal opportunity to grow ( $k_{\text{addP}} \gg k_p$  and  $k_\beta \gg k_p$ ). Simultaneously, irreversible termination reactions can also occur, but using a very low amount of initiator should minimize these reactions. If all these requirements are met, well-defined polymer chains will be obtained with controlled number of monomer units, narrow molar mass distributions and preserved chain end functionality.



Scheme 3 – RAFT polymerization mechanism. Adapted from Ref. <sup>12</sup>

### 2.2.1.2. Impact of R and Z groups

To obtain optimal control over a RAFT polymerization, the design of the RAFT agent is of prime importance, as outlined in Figure 13. The Z group plays an important role in the reactivity of the RAFT agent. Indeed, both the addition and fragmentation rates, *i.e.*  $k_{add}$  and  $k_\beta$ , respectively (Scheme 3) can be varied over 5 orders of magnitude through manipulation of Z.<sup>12</sup> The R group must be a good homolytic leaving group in order to efficiently reinitiate the radical polymerization.

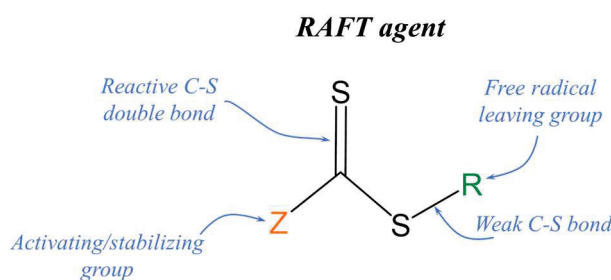


Figure 13 – General structure of a RAFT agent adapted from Ref. <sup>13</sup>

As aforementioned, a successful RAFT polymerization is closely related to the good selection of Z group. It is important to point out that monomers can be classified as belonging to one of two broad classes:<sup>12</sup> more activated monomers (MAMs) and less activated monomers (LAMs). RAFT polymerization of MAMs, such as styrenic, (meth)acrylamides and

(meth)acrylates monomers, requires the use of CTAs with high reactivity towards radical addition such as dithioesters or trithiocarbonates RAFT agents (see Figure 14) with Z-groups based on sulfur or carbons. While Z-groups based on oxygen (xanthates) or nitrogen (dithiocarbamates) have lower reactivity toward radical addition allowing the control of low activated monomers as vinyl esters or vinyl amides. As recently reported in the literature,<sup>14</sup> even ethylene, which is considered as a non-activated monomer, can be successfully polymerized by RAFT using xanthate-based RAFT agents. The versatility of the RAFT process in controlling the polymerization of a wide range of monomer classes is shown in Figure 14.

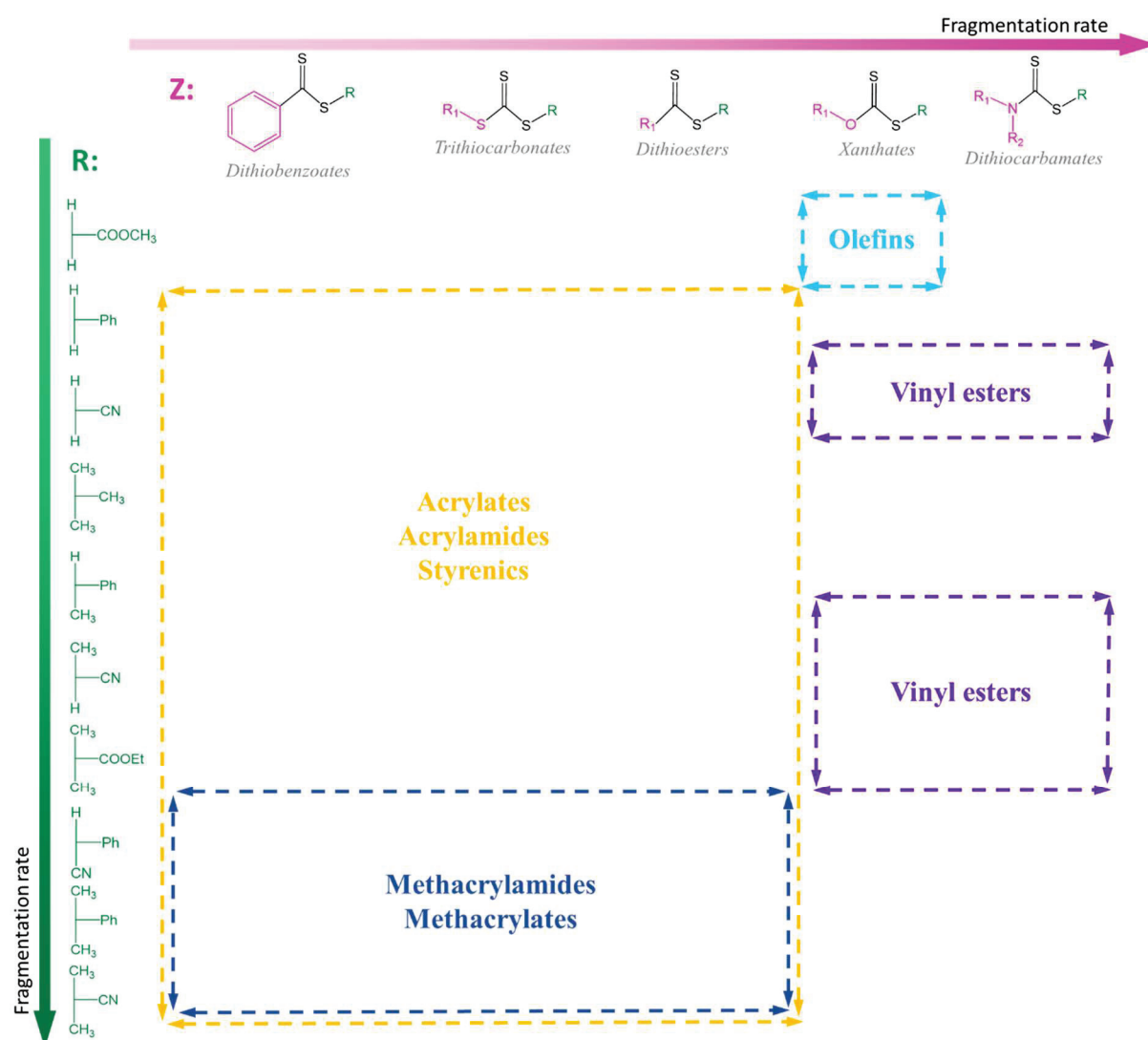


Figure 14 – Impact of R and Z groups on RAFT polymerization of various types of monomers.

The R group must be a good homolytic leaving group, which can be released in the pre-equilibrium step (Scheme 3) instead of liberating  $P_m^\bullet$  again, which means that the formation of

$R^\bullet$  and **3** have to be favored during the *pre-equilibrium* step ( $k_\beta > k_{-add}$ ). The expelled radical ( $R^\bullet$ ) must also be able to efficiently reinitiate the polymerization reaction. Selecting the R group based only on its chemical similarity with the monomer propagating radical is not sufficient to guarantee the successful re-initialization because the penultimate unit effect is substantial.<sup>12</sup> For example, Chong *et al.* reported that the use of a RAFT agent with ethylpropionate ( $C(CH_3)_2CO_2Et$ ) as R group, a monomeric analogue of poly(methyl methacrylate) (PMMA), led to a poor control over the polymerization of MMA because R is a poor homolytic leaving group with respect to PMMA propagating radicals.<sup>15</sup> Figure 14 presents a guideline to select the R group depending on the nature of the monomer.<sup>12</sup>

Commercial RAFT agents are now available primarily for research purposes, from Sigma Aldrich<sup>®</sup>, Boron Molecular<sup>©</sup> or Wako<sup>©</sup>. Generally these suppliers provide guide to selection of a given RAFT agent based on its R and Z groups to optimize the control over the polymerization. Furthermore, the scale-up to industrial production of RAFT agents has been announced by Rhodia<sup>16</sup>, Arkema<sup>17</sup> and Lubrizol<sup>18</sup>, with the commercial names of Rhodixan-A1 (xanthate), Blocbuilder BD and CTA-1 (trithiocarbonates), respectively.

RAFT polymerizations can be conducted via all main polymerization techniques such as bulk, solution, emulsion, miniemulsion or dispersion polymerizations. There is an extensive literature about RAFT polymerization that can be found summarized in some recent reviews<sup>12, 19-24</sup> and books.<sup>25</sup>

### 2.2.2. *Macromolecular design*

The benefits of RDRP for the development of new polymers or copolymers with predetermined structures and functionalities have revolutionized the macromolecular design. Synthesis of block copolymers, gradient copolymers, graft copolymers and stars can now be achieved (Figure 15), opening the door to new materials with new properties, once thought impossible to obtain via free radical processes.<sup>26</sup> The next section will focus on the preparation of block copolymers via the RAFT process, as this is the polymer structure targeted in this thesis.

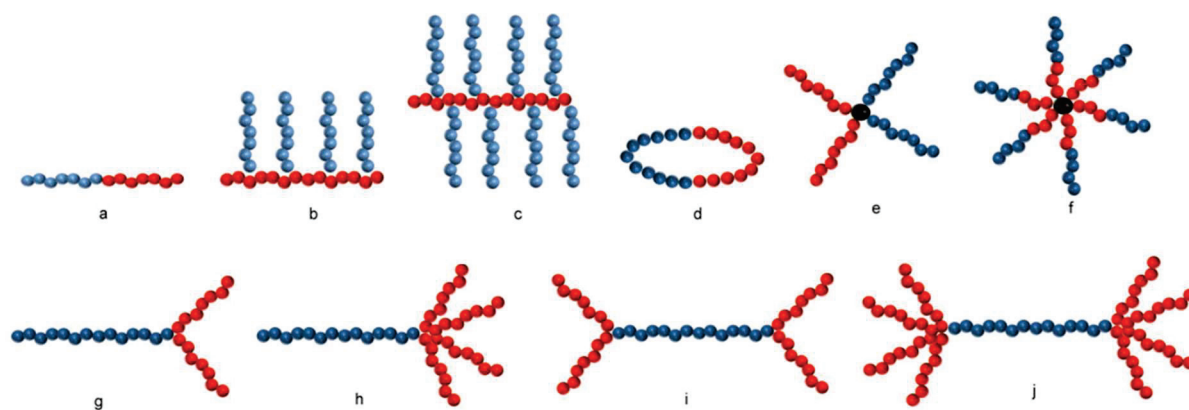


**Figure 15** - Examples of various complex architectures that can be achieved via RAFT-mediated polymerization: (a) linear; (b) graft; (c) brush or comb; (d) ring; (e) star  $A_nB_n$ ; (f) star-block  $(AB)_n$ ; (g)  $AB_2$  star; (h) palm tree  $AB_n$ ; (i) H-shaped and (j) dumbbell (pom-pom). Reproduced with permission from Elsevier ©2012.<sup>27</sup>

### 2.2.3. Synthesis of block copolymers

In RDRP processes, the reactivation of dormant chains in a chain extension reaction, with the same or with another monomer, can be exploited to prepare a wide range of hard-soft, hydrophilic-hydrophobic and other types of block copolymers<sup>28</sup> (Figure 15a). Until the advent of RDRP, block copolymers were prepared via anionic or cationic polymerization techniques, which require stringent reaction conditions and are restricted to a limited range of monomers. RDRP now allows the preparation of a broad range of new polymeric materials due to its high versatility in terms of experimental conditions (*e.g.* tolerance to water or oxygen), and to its compatibility with a broad range of functional monomers or reaction media (including polymerization in dispersed media). Among the main RDRP processes, RAFT is the most versatile one, which explains why it has received a great deal of attention for the preparation of block copolymers.<sup>26</sup>

In a typical procedure to synthesize block copolymers, monomer A is first polymerized by RAFT resulting in well-defined polymer chains with end groups composed of the RAFT moiety. The product of this first polymerization is also referred to as a macromolecular RAFT agent or macroRAFT. After purification, the macroRAFT is employed as a macromolecular chain transfer agent to control the polymerization of monomer B, in a chain extension reaction, resulting in an AB block copolymer.

In a similar way as for homopolymers, the proper selection of an adequate RAFT agent is of prime importance for successful synthesis of block copolymers. The Z-group has to be chosen so as to adequately control the polymerization of the two monomers forming the block



copolymer. A guideline is provided in Figure 14 in order to select the appropriate Z-group with respect to the type of monomer. Moreover, there are two additional key points to take into account:<sup>26</sup>

- *The order of monomer addition:* Similarly to what is described above for the R group of the molecular RAFT agent (section 2.2.1.1), the macro-R group has to be a good homolytic leaving group in order to favor the formation of dormant species and of macroradicals in the *pre-equilibrium step* (Scheme 3). In addition, the macroradicals also have to be able to efficiently reinitiate the polymerization of the second monomer.
- *The effect of radical initiator concentration:* The use of high concentrations of initiator during the synthesis of the first block can affect the chain-end functionalization of the polymer chains hindering the subsequent chain extension reaction (presence of dead chains). This is of course also true for the second step. On the other hand, a too low concentration of initiator may result, in both steps, in low polymerization rates. The optimal molar ratio between the (macro)RAFT agent and the initiator depends on the nature of the monomer. It is typically higher than 3, more often close to 10.

The composition of the resulting block copolymers and the number of monomer units in each segment can be easily controlled by the RAFT process. These innovative copolymers have been employed in various applications such as drug delivery,<sup>29</sup> mediator for the elaboration of polymer/inorganic nanocomposites<sup>30</sup> and compatibilizing agents of polymer melts.<sup>31</sup> Moreover, RAFT polymerization is a powerful tool for the preparation of block copolymers composed of hydrophilic and hydrophobic segments resulting in macromolecules with an amphiphilic character. These amphiphilic compounds can be successfully applied as polymeric-based stabilizers for emulsion or miniemulsion polymerizations,<sup>32, 33</sup> in which they will not only provide colloidal stability, but also allow functionalizing the polymer particle surface via their hydrophilic part. Therefore, depending on the functional groups carried by the hydrophilic monomer, the final properties of the materials can be improved, such as film adhesion<sup>34</sup> or barrier properties.<sup>35</sup> Even more, particles with new properties such as thermo-,<sup>36</sup> pH-<sup>37</sup> and CO<sub>2</sub>-responsiveness<sup>38</sup> can be prepared.

Block copolymers are usually synthesized in homogeneous media via solution or bulk polymerization.<sup>26</sup> However, the synthesis of block copolymers via RAFT-mediated emulsion polymerization has also been recently reported in the literature<sup>39-42</sup> using the so-called polymerization-induced self-assembly (PISA) process. Among the advantages of this strategy is the possibility to reach very high solid contents and the use of “green” solvent such as



water. But one of the most interesting features of the PISA system lies in the possibility to synthesize directly in water (sometimes in one-pot/two-step processes as reported below) amphiphilic block copolymers.

Indeed, a simple, direct and very powerful strategy was reported by Chaduc *et al.*<sup>39, 43</sup> and Zhang *et al.*<sup>40</sup> for the synthesis of amphiphilic block copolymers via a one-pot polymerization process in water. First, hydrophilic monomers were polymerized in water in the presence of 4-cyano-4-thiothiopropylsulfanylpentanoic acid (CTPPA) as RAFT agent, forming PAA, PMAA or poly(methacrylic acid-*co*-poly(ethylene oxide) methyl ether methacrylate) (P(MAA-*co*-PEO<sub>18</sub>MA)) (*co*)polymers. Styrene and an additional amount of initiator were then added in the same reactor and the polymerization relaunched. The size exclusion chromatograms showed that the great majority of the hydrophilic chains were reactivated. This resulted in block copolymers with narrow molar mass distributions. This strategy was then exploited<sup>40</sup> for the synthesis of P(MAA-*co*-PEO<sub>18</sub>MA)-*b*-PS block copolymers of various compositions. Hence, the hydrophobic/hydrophilic balance of the resulting amphiphilic block copolymers was affected, leading to various morphologies depending on the experimental conditions: spheres, vesicles and fibers. The different morphologies of the obtained objects resulted in different rheological behaviors of the latexes.<sup>44</sup>

### 3. EXPERIMENTAL SECTION

#### 3.1. Materials

4-cyano-4-thiothiopropylsulfanylpentanoic acid (CTPPA) RAFT agent (Figure 16) was synthesized as described elsewhere.<sup>45</sup> The monomers, acrylic acid (AA, anhydrous, 99%, Sigma-Aldrich), 2-dimethylaminoethyl methacrylate (DMAEMA, 99%, Sigma-Aldrich) and styrene (S, 99%, Acros Organics) were all used as received. The initiator, 4,4'-azobis(4-cyanopentanoic acid) (ACPA, 99%), the salts lithium bromide (LiBr, 99%) and sodium nitrate (NaNO<sub>3</sub>, 99%) and the solvents, 1,3,5-trioxane (>99%), 1,4-dioxane (puriss. p.a., >99.5%), dimethyl sulfoxide-*d*<sub>6</sub> (DMSO-*d*<sub>6</sub>, 99%), chloroform (CHCl<sub>3</sub>, 99%), diethyl ether (Et<sub>2</sub>O, 99.5%) and petroleum ether (PetEt) were all purchased from Sigma-Aldrich, and used with no further purification. THF (VWR Rectapur, stabilized) for methylation, acetone (>99%, VWR), diisopropyl ether (*i*Pr<sub>2</sub>O, >99%, Across), dichloromethane (DCM, 99%, Carlo Erba Reagents) and dimethyl sulfoxide (DMSO, 99.9%, VWR) were used as received. Tetrahydrofuran (THF, HPLC, stabilized/BHT, Sigma Aldrich), dimethylformamide (DMF,

HPLC, Biosolve) and dimethyl sulfoxide (DMSO, HPLC, Biosolve) were used for SEC analyses.

### 3.2. Methods

#### 3.2.1. Synthesis of hydrophilic macroRAFT agents

As shown in Figure 16, five different hydrophilic macroRAFT agents were prepared: PAA, PDMAEMA and three P(DMAEMA-*co*-AA) copolymers with various DMAEMA to AA molar ratios, all of them carrying a reactivatable trithiocarbonate end group (TTC).

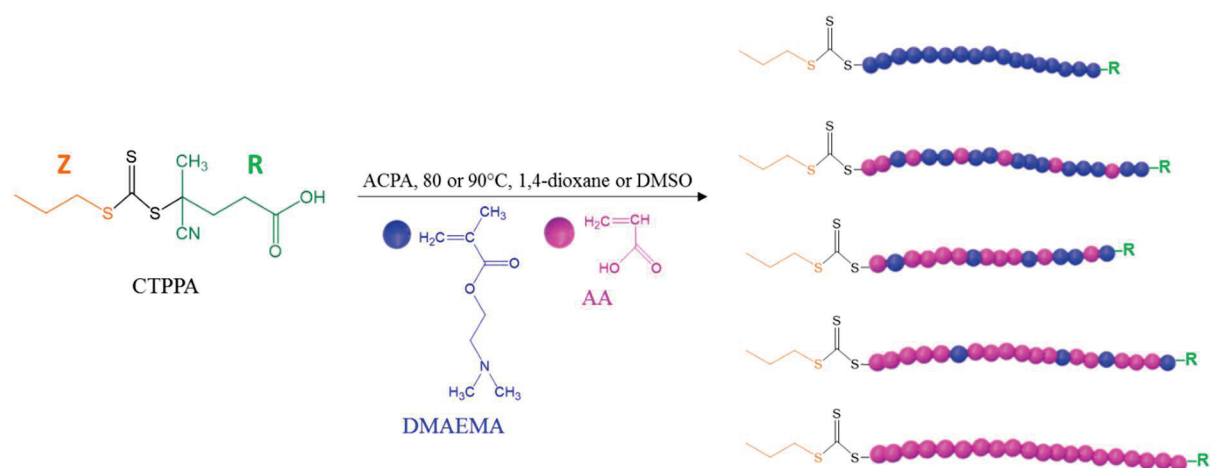


**Figure 16** – Scheme illustrating the synthesis of hydrophilic macroRAFT agents via RAFT polymerization in solution using CTPPA as RAFT agent and ACPA as initiator. Each sphere in the macroRAFT structure represents approximately 2.5 monomer units.

In a typical run (TRG42, Table 4), 0.18 mmol of RAFT agent (CTPPA), 1.2 mmol of 1,3,5-trioxane, 14.4 mmol of AA and 0.018 mmol of ACPA were introduced in a round-bottom flask. The mixture was diluted with 6 mL of 1,4-dioxane and the flask was purged with nitrogen for 30 minutes and sealed. The glass bottle was immersed in an oil bath at 80°C. The reaction was conducted during 6 hours. The procedure was similar for DMAEMA polymerization and AA/DMAEMA copolymerization; except that DMAEMA polymerizations were performed at 90°C in 1,4-dioxane (Table 5), while AA/DMAEMA copolymerizations were conducted at 80°C in DMSO (Table 6).

For each experiment, samples were taken during the polymerization to determine the evolution of conversion as a function of time (by  $^1\text{H}$  NMR), and that of molar masses and molar mass distributions versus conversion (by size exclusion chromatography). The theoretical number-average molar masses ( $M_{n,\text{th}}$ ) were calculated using the following equation:

$$M_{n,th} = \frac{(X_A \cdot [\text{Mon}_A]_0 \cdot M_{\text{Mon}_A}) + (X_B \cdot [\text{Mon}_B]_0 \cdot M_{\text{Mon}_B})}{[\text{RAFT}]_0} + M_{\text{RAFT}} \quad (2)$$

where  $M_{\text{Mon}}$ ,  $[\text{Mon}]_0$  and  $M_{\text{RAFT}}$ ,  $[\text{RAFT}]_0$  are the molar masses and the initial concentrations of the monomer(s) (A and B for copolymers or only A for homopolymer) and the RAFT agent, respectively, and X is the (individual) molar conversion of monomer(s) determined by  $^1\text{H NMR}$ .

Before synthesizing each macroRAFT, polymerizations were carried out to follow the reaction kinetics. Then, this experiment was scaled up ten times and stopped at a moderate conversion, *i.e.* around 50%, to guarantee a high chain-end functionality and avoid irreversible termination reactions often observed at high conversions (further descriptions will be given in section 4.1.1). All macroRAFTs synthesized at higher scale were precipitated, at least 3 times, in a large volume of non-solvent, until the total elimination of the residual monomer, as evaluated by  $^1\text{H NMR}$ . In the particular case of the P(DMAEMA-*co*-AA)-TTC macroRAFT copolymers, we first needed to perform precipitation tests in order to found appropriate conditions for their purification. Indeed, as shown in Table 1, these copolymers are insoluble in many solvents. DMSO was the best solvent and it was therefore used to solubilize the macroRAFT copolymers. It is important to point out that DMSO is a solvent that requires laborious manipulation. First it is difficult to evaporate because of its high boiling point (191°C). In addition it is highly polar and immiscible with most of the organic solvents typically used as non-solvent to precipitate the polymer, such as pentane, hexane, heptane and diethyl ether. Therefore, tests were also carried to select the most appropriate non-solvent. The results are shown in Table 2.

**Table 1** – Solubility of hydrophilic macroRAFT agents in organic solvents.

MacroRAFT	Solubilization					
	<i>1,4-dioxane</i>	$\text{CHCl}_3$	<i>THF</i>	<i>Acetone</i>	<i>DMF</i>	<i>DMSO</i>
PAA <sub>50</sub> -TTC	S	-	-	-	-	-
PDMAEMA <sub>45</sub> -TTC	S	-	-	-	-	-
P(AA <sub>34</sub> - <i>co</i> -DMAEMA <sub>36</sub> )-TTC	I	I	I	I	PS	S

S – Soluble    PS – Partially soluble    I – Insoluble

**Table 2** – Precipitation tests of hydrophilic macroRAFT agent solutions in different non-solvents.

MacroRAFT solution	Precipitation					
	<i>PetEt</i>	<i>THF</i>	<i>iPr<sub>2</sub>O</i>	<i>DCM</i>	<i>DCM/iPr<sub>2</sub>O</i> 50/50	<i>DCM/Et<sub>2</sub>O</i> 50/50
PAA <sub>50</sub> -TTC in 1,4-dioxane	G	-	-	-	-	-
PDMAEMA <sub>45</sub> -TTC in 1,4-dioxane	G	-	-	-	-	-
P(AA <sub>34-co</sub> -DMAEMA <sub>36</sub> )-TTC in DMSO	I	I	A	A	G	A

G – Good precipitation    color: red;">A – Acceptable    color: red;">I – Insufficient

As seen in Table 1 and Table 2, the PAA-TTC and PDMAEMA-TTC macroRAFT homopolymers were solubilized in 1,4-dioxane and then precipitated in petroleum ether. On the other hand, for the macroRAFT copolymers composed of AA and DMAEMA units, which were synthesized in DMSO, the DCM/*iPr*<sub>2</sub>O mixture (50/50 by volume) was found to be the best non-solvent composition, and was used to precipitate the macroRAFT copolymers. Finally, the precipitates were dried overnight under vacuum at 40 °C resulting in yellow fine powders, and stored at 2-4 °C.

### 3.2.2. Chain extension reactions

Chain extension experiments were carried out in order to verify the livingness of the hydrophilic macroRAFT agents. To do so, RAFT polymerization of the same monomer as that used for the synthesis of the macroRAFT agent was conducted using a procedure similar to that described above (section 3.2.1). Theoretical molar masses were also predicted by means of equation 1 but replacing  $M_{\text{RAFT}}$  and  $[\text{RAFT}]_0$  by the molar mass and initial concentration of the macroRAFT agents, respectively.

### 3.2.3. Synthesis of amphiphilic macroRAFT agents

The strategy employed for the synthesis of the amphiphilic block copolymers is outlined in Figure 17. The reactions were carried out following a protocol similar to that described above in section 3.2.1 for the synthesis of the hydrophilic macroRAFTs. RAFT polymerizations of styrene were conducted at 80°C in the presence of the previously synthesized hydrophilic macroRAFT agents either in 1,4-dioxane for PAA-TTC and PDMAEMA-TTC or in DMSO for amphoteric macroRAFTs. Theoretical molar masses were obtained using again equation 1,

where  $M_{\text{RAFT}}$  and  $[\text{RAFT}]_0$  are the molar mass and the initial concentrations of the hydrophilic macroRAFT agents, respectively.

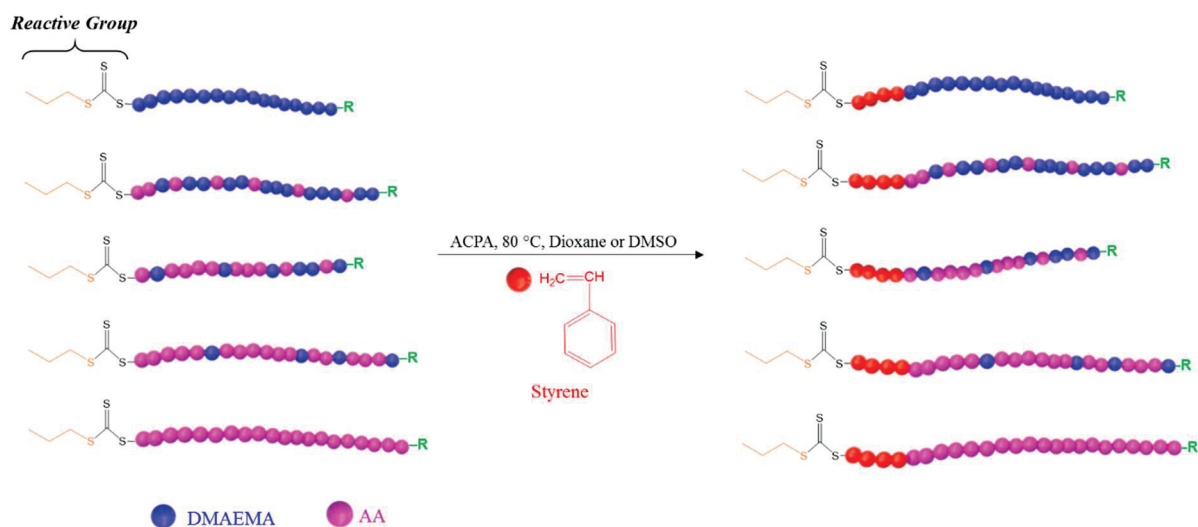


**Figure 17** – Scheme illustrating the synthesis of amphiphilic macroRAFT agents via chain extension reaction with styrene using hydrophilic macroRAFTs as macromolecular chain transfer agents. Each sphere in the macroRAFT structure represents approximately 2.5 monomer units.

### 3.2.4. Determination of the cloud point temperature of the macroRAFT agents

The thermosensitivity of the PDMAEMA macroRAFTs was evaluated by the determination of cloud point temperature via UV-visible spectroscopy. A macroRAFT solution ( $20 \text{ g L}^{-1}$ ) was first prepared and the pH was then adjusted by addition of 0.1 M HCl or 0.1 M NaOH solutions. After pH correction, water was added to fix the final concentration of macroRAFT at  $10 \text{ g L}^{-1}$ . The polymer solution was transferred in a 1 cm path length quartz-cell, and the transmittance at 650 nm was monitored as a function of temperature (from 15 to 90 °C with a heating ramp of  $0.5 \text{ °C min}^{-1}$ ) using an Evolution 220 UV-visible spectrophotometer (Thermo Scientific) coupled with a Peltier thermocontroller PCCU1 (Thermo Scientific). The cloud point temperature of the macroRAFT agents was defined as the temperature corresponding to 50% transmittance (T50%).

## 3.3. Characterizations

### 3.3.1. <sup>1</sup>H NMR

Samples taken during polymerizations were characterized by <sup>1</sup>H liquid NMR spectroscopy (300 MHz Bruker) in DMSO-d<sub>6</sub> at room temperature to determine the individual conversion

from the relative integration of the vinylic protons and the protons of 1,3,5-trioxane. The global conversion for copolymers was determined according to relationship:  $X = X_{AA} \cdot f_{AA,0} + X_{DMAEMA} \cdot f_{DMAEMA,0}$  where  $f_{AA,0}$ ,  $f_{DMAEMA,0}$  are the molar fractions of AA and DMAEMA on initial monomer mixture. The degree of polymerization of the polystyrene block in the amphiphilic macroRAFT copolymers was determined from the relative integration of the aromatic peak from polystyrene and the characteristic peaks of PAA or PDMAEMA (ANNEX 2. 3.).

### 3.3.2. *Size exclusion chromatography (SEC)*

Before analyses of the homopolymers or block copolymers composed of AA units, the carboxylic acid groups were methylated in a THF/H<sub>2</sub>O (90/10) mixture using tri(methylsilyl)diazomethane methylation agent to prevent interactions between these polar groups and the stationary phase.<sup>46, 47</sup> All samples were filtered through a 0.45 μm pore size membrane and analyzed at 4 mg mL<sup>-1</sup>.

#### *DMF-SEC*

SEC analyses in DMF (LiBr, 0.01 mol L<sup>-1</sup>) were performed at 70 °C with a flow rate of 1.0 mL min<sup>-1</sup> using an Eco-SEC semi-micro SEC system from Tosoh. The separation was carried out using two PSS GRAM columns (7 μm, 300 × 7.5 mm). The setup was equipped with a dual flow refractive index (RI) detector and a UV detector. The average molar masses (number-average molar mass  $M_n$  and weight-average molar mass  $M_w$ ) and the molar mass distributions ( $D = M_w/M_n$ ) were derived from the RI signal using a calibration curve based on PMMA standards from Polymer Laboratories.

#### *DMSO-SEC*

SEC measurements in DMSO (NaNO<sub>3</sub>, 0.01 mol L<sup>-1</sup>) were performed at 60 °C at a flow rate of 0.6 mL min<sup>-1</sup> using device (1260 Infinity Series) from Agilent. The separation was carried out using three PSS GRAM columns (7 μm, 300 × 7.5 mm). The setup was equipped with a refractive index detector and a UV detector.  $M_n$  and  $D$  were derived from the RI signal by a calibration curve based on PMMA standards.

#### *THF-SEC*

SEC measurements in THF were carried out at 40 °C with a flow rate of 1 mL min<sup>-1</sup>. The separation was carried out on three columns from PSS Instruments [PSS SDV analytical

(8x300 mm)]. The device (Viscotek TDA305) was equipped with RI detector ( $\lambda = 670$  nm). To determine the average molar masses and the molar mass distributions, the RI signal was derived from a calibration curve traced using the Mark-Houwink-Sakurada (MHWS) equations:

$$[\eta] = K \cdot M^\alpha \quad (3)$$

$$K_1 \cdot M_1^{1+\alpha_1} = K_2 \cdot M_2^{1+\alpha_2} \quad (4)$$

To do so, conventional calibration curves based either on PMMA or on polystyrene (PS from Polymer Laboratories) standards were first established (see Figure 19). By using the equation 3 and the MHWS parameters listed in Table 1, new calibration curves were then established based either on poly(methyl acrylate) (PMA) for the analysis of methylated PAA-TTC or on PDMAEMA for the analysis of PDMAEMA-TTC macroRAFTs (Figure 19).

**Table 3** – MHWS parameters for PDMEMA, PMA, PMMA and PS used to re-calculate the SEC calibration curves.

Polymer	$K$	$\alpha$	Solvent	T (°C)	Ref.
PDMAEMA	$4.98 \cdot 10^{-5}$	0.73	THF	35	48
PMA	$3.81 \cdot 10^{-4}$	0.63	THF	35	49
PMMA	$1.28 \cdot 10^{-4}$	0.69	THF	30	50
PS	$1.60 \cdot 10^{-4}$	0.71	THF	25	50

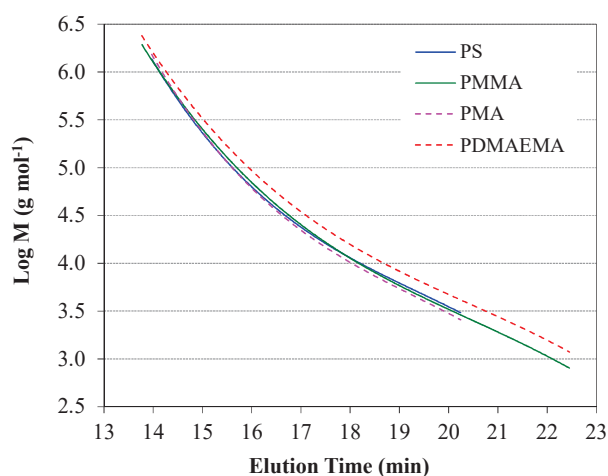


**Figure 18** – SEC calibration curves of commercial polymer standards fitted to a third degree polynomial (—, straight lines) and re-calculated by using the MHWS equations (- - -, dashed lines).



## 4. RESULTS AND DISCUSSION

### 4.1. Synthesis of hydrophilic macroRAFT agents

This section is dedicated to the synthesis of the macroRAFT agents using CTPPA as RAFT agent. This molecule was successfully synthesized as evidenced by  $^1\text{H}$  NMR (ANNEX 2. 1.) following the protocol described elsewhere.<sup>45</sup> We will first report the synthesis of five hydrophilic macroRAFTs based on AA and DMAEMA with various compositions. Then, the livingness of the macroRAFT polymers and their chain-end functionalization will be assessed. Finally, chain extension reactions with styrene will be carried out using the purified hydrophilic macroRAFTs in order to prepare amphiphilic block copolymers.

The pathway of the polymerization reaction, which begins by the synthesis of the hydrophilic block and is continued by chain extension with styrene as the hydrophobic monomer, was selected based on the ability of the resulting macroradical to efficiently re-initiate the polymerization. Indeed, for PDMAEMA-based block copolymers, it is recommended to start with the polymerization of DMAEMA, because their methacrylyl tertiary radicals have greater leaving capability than styryl radicals. Hence, the fragmentation toward the formation of species **3** in the *pre-equilibrium step* is favored (see RAFT mechanism in Scheme 3).<sup>26, 51</sup> However, for some systems in which the sequence of polymerizations is not straightforward, the pathway should be defined via experimental assessment.<sup>52</sup> Therefore, for the synthesis of poly(acrylic acid)-*block*-polystyrene, the polymerization of AA was first carried out based on protocols previously reported in the literature,<sup>32, 33, 53, 54</sup> in which well-defined block copolymer were obtained by respecting this pathway, i.e., AA polymerized first. Analogously, for the synthesis of P(DMAEMA-*co*-AA)-*b*-PS-TTC amphiphilic block copolymers, the hydrophilic moieties composed of AA and DMAEMA were first synthesized followed by the chain extension with styrene.

As presented above in section 2.2.3, the one-pot PISA process is a powerful tool for the synthesis of diblock copolymers but, unfortunately, it could not be applied in this work for the following reasons:

- 1) *Hydrolysis of DMAEMA*: the amino-based meth(acrylate) monomers are rather unstable towards hydrolysis in aqueous solution leading to the formation of amines (*i.e.* trimethylamine, di(methyl)ethylamine) and of acrylic or methacrylic acid.<sup>55 56</sup> The decomposition kinetics strongly depends on the pH and the nature of the monomer. In general, acrylate-based monomers are more susceptible to hydrolysis than methacrylate ones. For example, the degradation process of 2-



(dimethylamino)ethyl acrylate (DMAEA) is 5-7 times faster than that of DMAEMA.<sup>55</sup> However, hydrolysis of DMAEMA was effectively observed during its RAFT polymerization in water at pH 7 using CTPPA as RAFT agent.<sup>56</sup> Therefore, this degradation process limits the synthesis of pure PDMAEMA macroRAFTs in water. It is worth mentioning that PDMAEMA polymer chains are more stable than the monomer. Bout *et al.*<sup>57</sup> observed that PDMAEMA chains were stable after 6 months of incubation at 37°C, during which no degradation was observed. Van der Wetering *et al.*<sup>55</sup> confirmed this tendency and showed that even in harsh conditions (T = 80°C and pH = 1 or 7), PDMAEMA degradation was about only 15% and 4%, respectively.<sup>55</sup>

- 2) To circumvent the hydrolysis issue encountered for the RAFT polymerization of DMAEMA in water, a two step synthesis of PDMAEMA-*b*-PS could have been envisioned, with the synthesis of the hydrophilic block in organic solvent and the chain extension with styrene in water. However, this strategy was not applicable as experiments performed in our team has shown that PDMAEMA is not able to efficiently reinitiate styrene polymerization in emulsion.

On the other hand, the successful one-pot synthesis of PAA-*b*-PS diblock copolymers in water has already been reported<sup>43</sup> and leads at acidic pH to formation of spherical micelles with a hydrophobic PS core (lowest DP reported: *ca.* 200) and a hydrophilic PAA outer-layer. The same strategy could *a priori* be used for the synthesis of the PAA-*b*-PS copolymers targeted in our study. However, to rely on similar synthetic protocols, all the amphiphilic block copolymers were synthesized via two-step solution polymerization as it is a strategy well adapted to all the systems envisioned in this thesis. For the five hydrophilic macroRAFT agents targeted, kinetic studies were performed in order to be able to stop the polymerization at around 50% conversion in the scale-up experiments thus preserving the living character of the polymer chains.

### 4.1.1. Synthesis of poly(acrylic acid) macroRAFT agents: PAA-TTC

Poly(acrylic acid) homopolymers end-functionalized with a trithiocarbonate group (schematically represented in Figure 19A) were synthesized by RAFT-mediated solution polymerization. The experimental conditions and the results of these syntheses are summarized in Table 4.

**Table 4** – Synthesis of PAA-TTC homopolymers via RAFT polymerization of AA in 1,4-dioxane using CTPPA as RAFT agent.

Exp.	[AA] (mol L <sup>-1</sup> ) <sup>a</sup>	[Mon]/ [RAFT]	[RAFT]/ [ACPA]	X (NMR) (%)	$M_{n,th}^b$ (g mol <sup>-1</sup> )	$M_{n,exp}$ (THF-SEC) <sup>c</sup> (g mol <sup>-1</sup> )/ $\bar{D}$
TRG42	2.3	81	9	92	5650	5950/1.19
TRG50	2.3	80	9	62	3850	3650/1.11

<sup>a</sup>Based on 1,4-dioxane, volume: 6 and 60 mL for TRG42 and TRG50, respectively. Theoretical  $M_n$  calculated based on monomer conversion. <sup>b</sup>Experimental number-average molar mass and dispersity ( $\bar{D} = M_w/M_n$ ) determined by SEC in THF based on PMA calibration by using the MWHS equations.  $M_n$  values have been recalculated to show the non-methylated mass of the polymer.

We first performed an experiment (TRG42) to determine the kinetics behavior (Figure 19B). This experiment was then scaled up (TRG50) and the polymerization was quenched at 62% conversion resulting in a macroRAFT composed of 50 units of acrylic acid, which is a good agreement with the 40 units initially targeted.

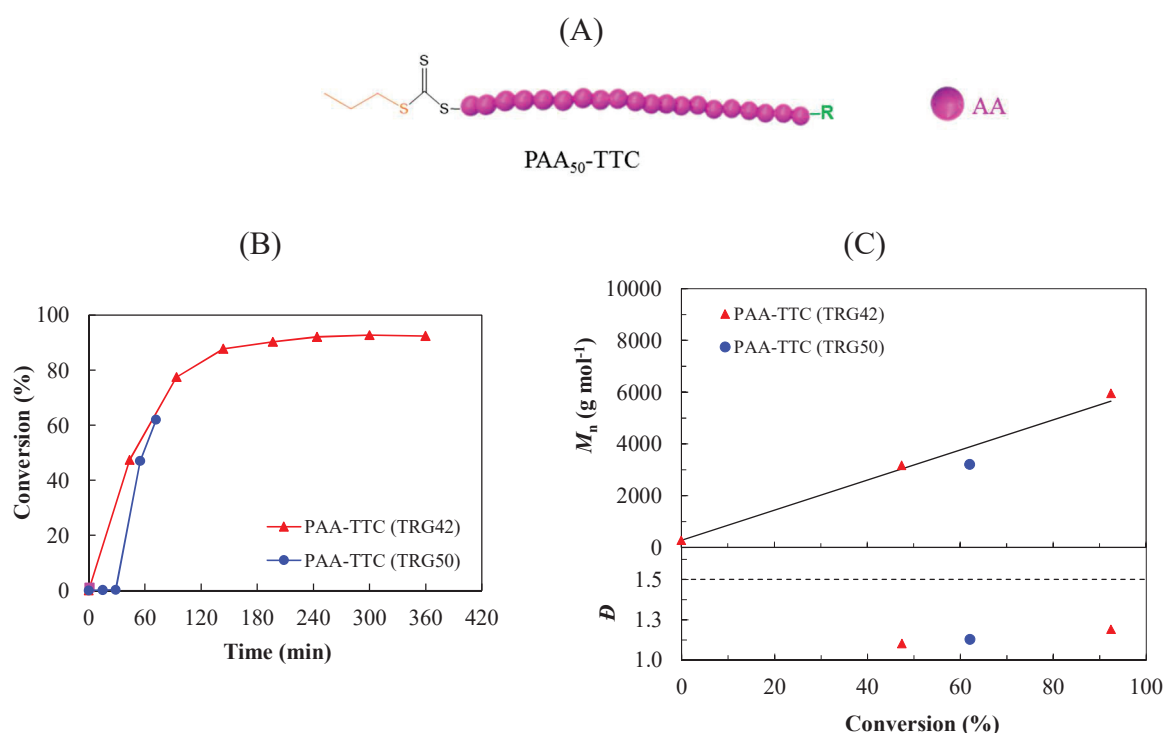


**Figure 19** – RAFT polymerization of AA in 1,4-dioxane using CTPPA as RAFT agent. (A) Schematic representation of PAA-TTC macroRAFT. Evolutions of (B) monomer conversion versus time and (C)  $M_n$  and  $\bar{D}$ , calculated from PMA calibration curves using the MWHS equation, versus conversion. The straight line corresponds to the theoretical evolution of  $M_n$  with conversion.

As can be seen in Figure 19C, the number-average molar mass of the polymer chains increases with conversion as expected for a RAFT polymerization. Moreover, the resulting  $M_n$  recalculated using MWHS parameters fit well with the theoretical values (straight line in

Figure 19C). However, the presence of polymer chains resulting from bimolecular (and irreversible) termination by recombination was observed at 92% conversion on the SEC trace (Figure 20A). Indeed, at 47% of conversion those chains were not observed as evidenced by a well-defined and symmetric peak. Based on this kinetic study, the experiment was then scaled up (TRG50) 10 times and the polymerization was quenched at 62% conversion resulting in a macroRAFT composed of 50 units of acrylic acid ( $M_n = 3650 \text{ g mol}^{-1}$  and  $D = 1.11$ , Figure 8B), which is a good agreement with the 40 units initially targeted. This macroRAFT will be then used for the synthesis of the PAA-*b*-PS-TTC amphiphilic block copolymers.

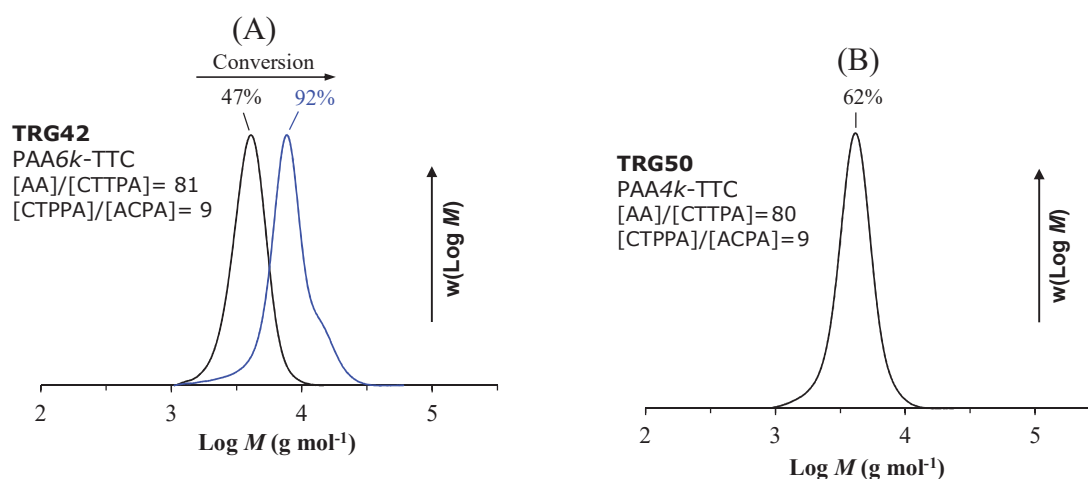


**Figure 20** – THF-SEC chromatograms of: (A) run TRG42 and (B) run TRG50 (Table 4) based on PMA calibration curve re-calculated from the MHWS equations.

#### 4.1.2. Synthesis of poly(2-dimethylaminoethyl methacrylate) macroRAFT agents: PDMAEMA-TTC

PDMAEMA macroRAFT homopolymers were synthesized via RAFT polymerization of DMAEMA still using CTPPA as RAFT agent. As before, an experiment (run TRG45) was carried out to determine the kinetics behavior and then three scaled-up experiments, TRG48, TRG61 and TRG87, were performed, as detailed in Table 5, in order to obtain higher amounts of macroRAFT.

**Table 5** – Synthesis of PDMAEMA-TTC via RAFT polymerization of DMAEMA in 1,4-dioxane using CTPPA as RAFT agent.

Exp.	[DMAEMA] (mol L <sup>-1</sup> ) <sup>a</sup>	[Mon]/ [RAFT]	[RAFT]/ [Ini]	X (NMR) (%)	$M_{n,th}^b$ (g mol <sup>-1</sup> )	$M_{n,exp}$ (g mol <sup>-1</sup> )/ $\mathcal{D}$		
						THF-SEC <sup>c</sup>	DMF-SEC <sup>d</sup>	DMSO-SEC <sup>d</sup>
<b>TRG45</b>	1.2	77	5	62	7800	7770/1.29	n.d.	n.d.
<b>TRG48</b>	1.2	80	5	56	7300	6950/1.36	5300/1.33	4750/1.18
<b>TRG61</b>	1.2	80	5	54	7150	n.d.	5150/1.31	4450/1.21
<b>TRG87</b>	1.2	80	5	53	6950	n.d.	n.d.	4400/1.24

<sup>a</sup>Based on 1,4-dioxane, volume: 60 mL except for TRG45 where 12 mL were used. <sup>b</sup>Theoretical  $M_n$  calculated based on monomer conversion. Experimental number-average molar mass and dispersity determined either by: <sup>c</sup>SEC in THF based on PDMAEMA calibration by using the MWHS equations or by <sup>d</sup>SEC in DMF or in DMSO using PMMA calibration.

As can be seen in Figure 21B, RAFT polymerization of DMAEMA was quite fast, and reached 50% conversion in less than 2 hours (TRG45). The conversion was however limited to around 60%, and reached a pseudo-plateau (Figure 21B). The limited conversion can be associated to the low initial concentration of DMAEMA used in these polymerizations (*i.e.* typically 1.2 mol L<sup>-1</sup>). Generally, a way to improve the final conversion consists in increasing the initial monomer concentration. Sahnoun *et al.*<sup>58</sup> reported the RAFT polymerization of DMAEMA in 1,4-dioxane, and observed that the final conversions increased from 68 to 75 and then 85%, when increasing the initial monomer concentration from 2.0 to 4.2 and then 5.9 mol L<sup>-1</sup>, the last concentration corresponding to bulk polymerization. On the other hand, increasing monomer concentration can increase the viscosity of the solution, which in turn can affect the control of the polymerization, resulting in polymers with broader molar mass distributions. This limited conversion at 60% is however not a limitation for our system as the scale-up experiment(s) are stopped at around 50% of conversion to maintain the livingness of the polymer chains. Hence, in order to keep the control over the polymerization and narrow molar mass distributions, the monomer concentration was set at 1.2 mol L<sup>-1</sup> for the scale-up experiments. Indeed, THF-SEC chromatograms of run TRG45 (Figure 22A) show narrow molar mass distributions indicating an excellent control over the RAFT polymerization. Furthermore, as can be seen in Figure 21C, the experimental  $M_n$  determined by using conventional PMMA calibration curves were lower than the theoretical values. However, a much better agreement was obtained when  $M_n$  was determined by using the MWHS parameters for PDMAEMA as detailed in section 3.3.2.

Following this kinetic study, 3 batches of macroRAFT were prepared, the reaction being stopped when the conversion was close to 50% (TRG48, TRG61 and TRG87, Table 5). A good reproducibility of the polymerization kinetics was observed (Figure 21B) and the final conversions were 56, 54 and 53% respectively, leading to the formation of macroRAFT agents with similar chain lengths (Table 5).

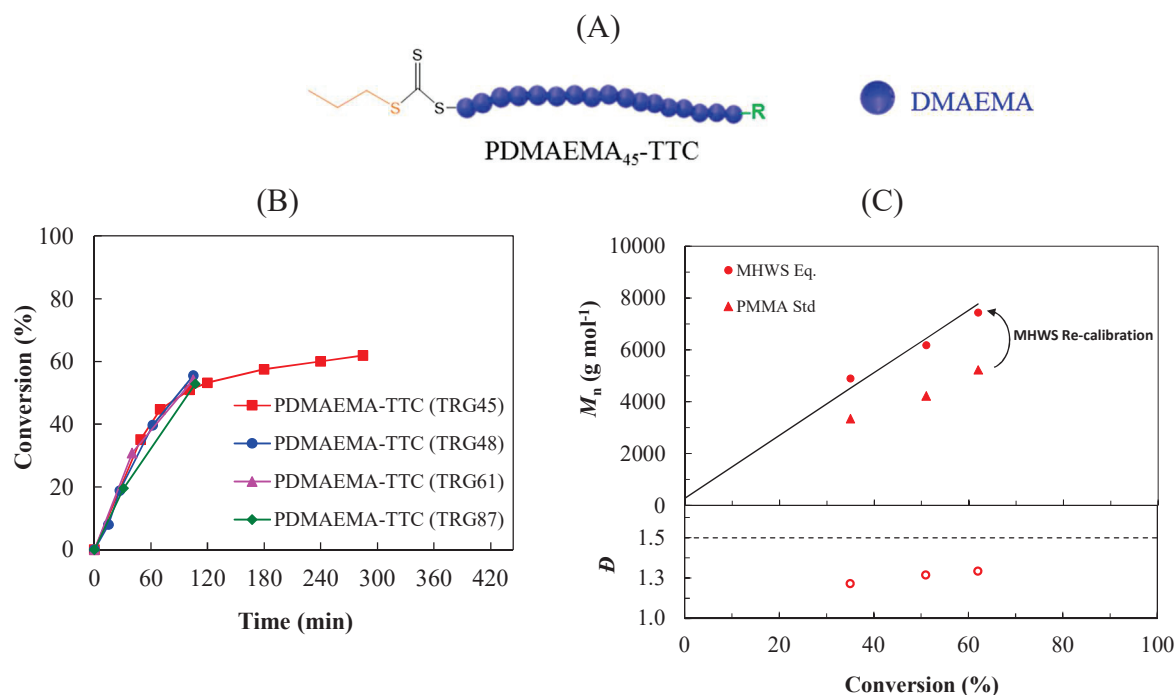


**Figure 21** – RAFT polymerizations of DMAEMA in 1,4-dioxane using CTPPA as RAFT agent. (A) Schematic representation of PDMAEMA-TTC macroRAFT. Evolutions of: (B) monomer conversion versus time and (C)  $M_n$  and  $D$  determined by THF-SEC, versus conversion (TRG45, Table 5). The straight line corresponds to the theoretical evolution of  $M_n$  with conversion. The triangles ( $\blacktriangle$ ) correspond to  $M_n$  and  $D$  calculated from PMMA calibration and the circles ( $\bullet$ ) to  $M_n$  and  $D$  calculated from PDMAEMA calibration as established using the MWHS equations.

The same good agreement between the molar masses was observed for the first scaled-up experiment (TRG48, Table 5), in which the experimental  $M_n$  obtained by THF-SEC using MHKS parameters was 6950 against 7300 g mol<sup>-1</sup> determined by using the equation 1. However, for the second and third scaled-up batches (TRG61 and TRG87), it was not possible to analyze the polymers by THF-SEC as in the meantime, the column pack was changed and no peak could be identified after sample injection. This was associated with undesirable interaction between the polar groups of PDMAEMA and the new chromatographic columns. The analyses were thus performed in DMF with LiBr salt,<sup>59</sup> and nice chromatograms were obtained with good elution peaks. They were integrated using a calibration curve based on PMMA standards resulting in the chromatograms shown in Figure 22B and C. On the other

hand, discrepancies between experimental and theoretical  $M_n$  values were observed, which can be associated with the use of a conventional calibration curve based on polymer standards different from the analyzed polymer. Unfortunately MWHS parameters for PDMAEMA in DMF are not available in the literature.

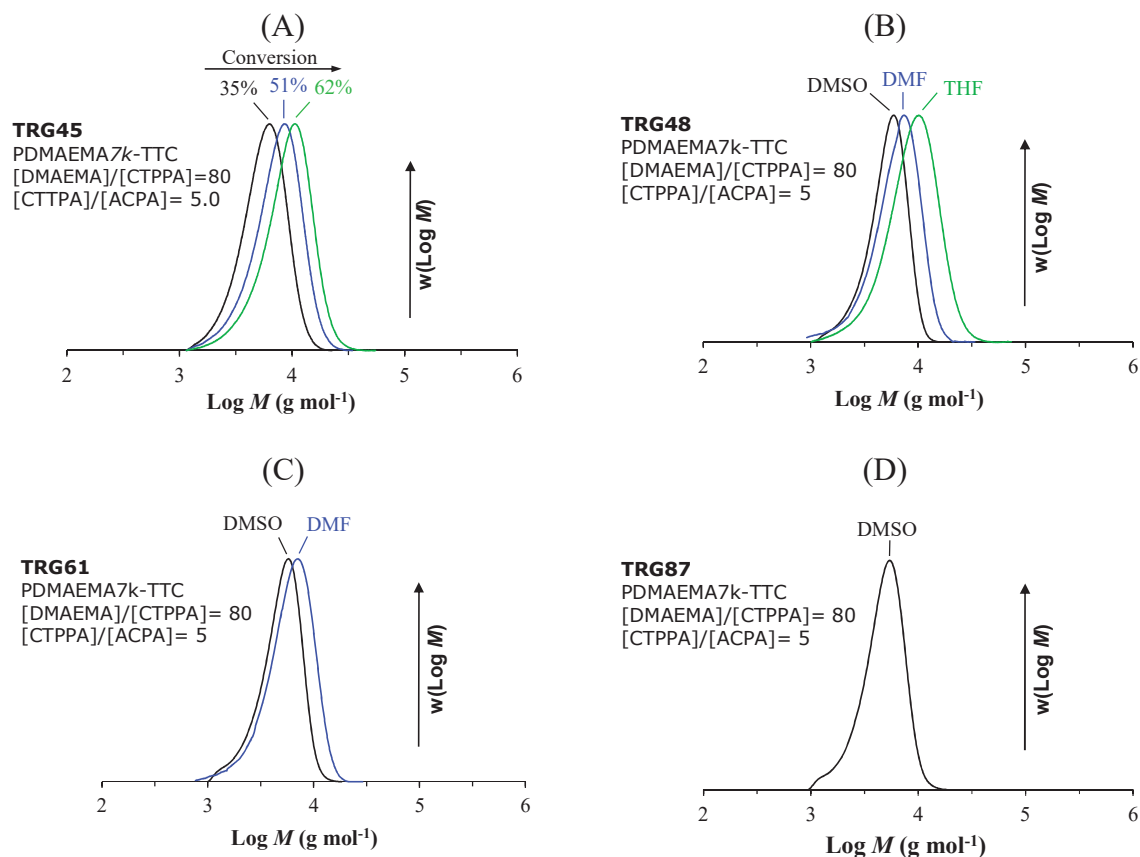


**Figure 22** – SEC chromatograms of: (A) run TRG45 in THF-SEC and scaled-up experiments: (B) TRG48, (C) TRG61 and (D) TRG87. The SEC-traces were derived from the RI signal using PMMA calibration when performed in DMF and DMSO and from the PDMAEMA calibration curve calculated from the MWHS equations in the case of THF-SEC.

PDMAEMA chains were also analyzed by SEC using DMSO as eluent. The obtained chromatograms are nice (Figure 22B, C and D), but the  $M_n$  values obtained from PMMA calibration still present some discrepancies with the theoretical ones (Table 5).

When comparing  $M_n$  and  $D$  values obtained for each scaled-up batch (entries TRG48, TRG61 and TRG87 in Table 5), the values are really close for a given SEC system, confirming the good reproducibility of the experiments. Whatever the SEC system used, these narrow molar mass distributions indicate an excellent control over the RAFT polymerization.

4.1.3. Synthesis of poly(2-dimethylaminoethyl methacrylate-co-acrylic acid) macroRAFT agents: P(DMAEMA-co-AA)-TTC.

Amphoteric macroRAFT agents were synthesized via RAFT copolymerization of DMAEMA and AA for various AA to DMAEMA ratios, still using CTPPA as RAFT agent. A schematic representation of the macroRAFT copolymers is shown in Figure 23A, B and C.

The first series of experiments was carried out in 1,4-dioxane (runs TRG97 and TRG99, Table 6), the same solvent previously employed for the synthesis of the corresponding PAA and PDMAEMA homopolymers. However, through the polymerization, polymer precipitation was observed. Polymer precipitation usually occurs when intermolecular forces between the polymer chains predominate with respect to polymer-solvent interactions.<sup>60</sup> In our case, polymer-polymer interaction can be associated with hydrogen bonding between the COOH groups from AA and the tertiary amines from DMAEMA. H-bonding between amine groups and carboxylic acid side-groups have been described by many authors<sup>60-64</sup> and this interaction has been demonstrated useful for the preparation of polymer blends<sup>60</sup> or hydrogels.<sup>63, 65, 66</sup> It is important to point out that in aqueous solution, these monomers can also interact between them by other intermolecular forces, such as electrostatic interactions and ion pairing (salt-bridging).<sup>63</sup> Moreover, by varying the pH of the medium, intermolecular forces can be tuned

**Table 6** –Synthesis of P(DMAEMA-co-AA)-TTC via RAFT polymerization in 1,4-dioxane or DMSO using CTPPA as RAFT agent.

Exp.	[DMAEMA] <sub>0</sub> (mol L <sup>-1</sup> )	[AA] <sub>0</sub> (mol L <sup>-1</sup> )	Solvent	X <sub>DMAEMA</sub> / DP <sub>DMAEMA</sub> / X <sub>AA</sub> (%) <sup>a</sup>		M <sub>n,th</sub> <sup>b</sup> (g mol <sup>-1</sup> )	M <sub>n,exp</sub> (g mol <sup>-1</sup> )/Đ	
					DP <sub>AA</sub>		THF-SEC <sup>c</sup>	DMSO-SEC <sup>d</sup>
TRG97	0.61	0.61	1,4- dioxane					
TRG99	0.31	0.91						
TRG102	0.61	0.61	DMSO	98/55	39/22	9150	-	-
TRG103	0.31	0.92		100/61	21/39	7250	-	-
TRG106	0.15	1.08		100/82	10/59	6800	-	-
TRG112	0.59	0.60		82/40	33/16	6650	-	7650/1.15
TRG126	0.30	0.89		39/56	16/23	4450	-	8200/1.24
TRG110	0.15	1.06		100/57	10/39	4700	2850/1.36	5800/1.17

[RAFT]/[Ini] = 5;<sup>a</sup> Individual conversion of each monomer determined via <sup>1</sup>H NMR. <sup>b</sup> Theoretical M<sub>n</sub> calculated based on individual monomer conversions. Experimental number-average molar mass and dispersity based on PMMA calibration via SEC in <sup>c</sup>THF or in <sup>d</sup>DMSO.



or even totally suppressed, which can be exploited for the preparation of reversible hydrogels.<sup>63</sup> Nonetheless, in our system, polymer-polymer interactions cannot be considered as an advantage as they lead to polymer precipitation, preventing the preparation of amphoteric macroRAFT agents in 1,4-dioxane.

Alternatively, RAFT copolymerization of AA and DMAEMA was carried out in DMSO and no precipitation was observed during the polymerization. As before, three experiments were first carried out to determine the kinetic behavior for different AA to DMAEMA ratios (runs TRG102, TRG103 and TRG106, Table 6), and the polymerization was next scaled up 10 times to obtain higher amounts of macroRAFT agents (entries TRG110, TRG112 and TRG126 in Table 6).

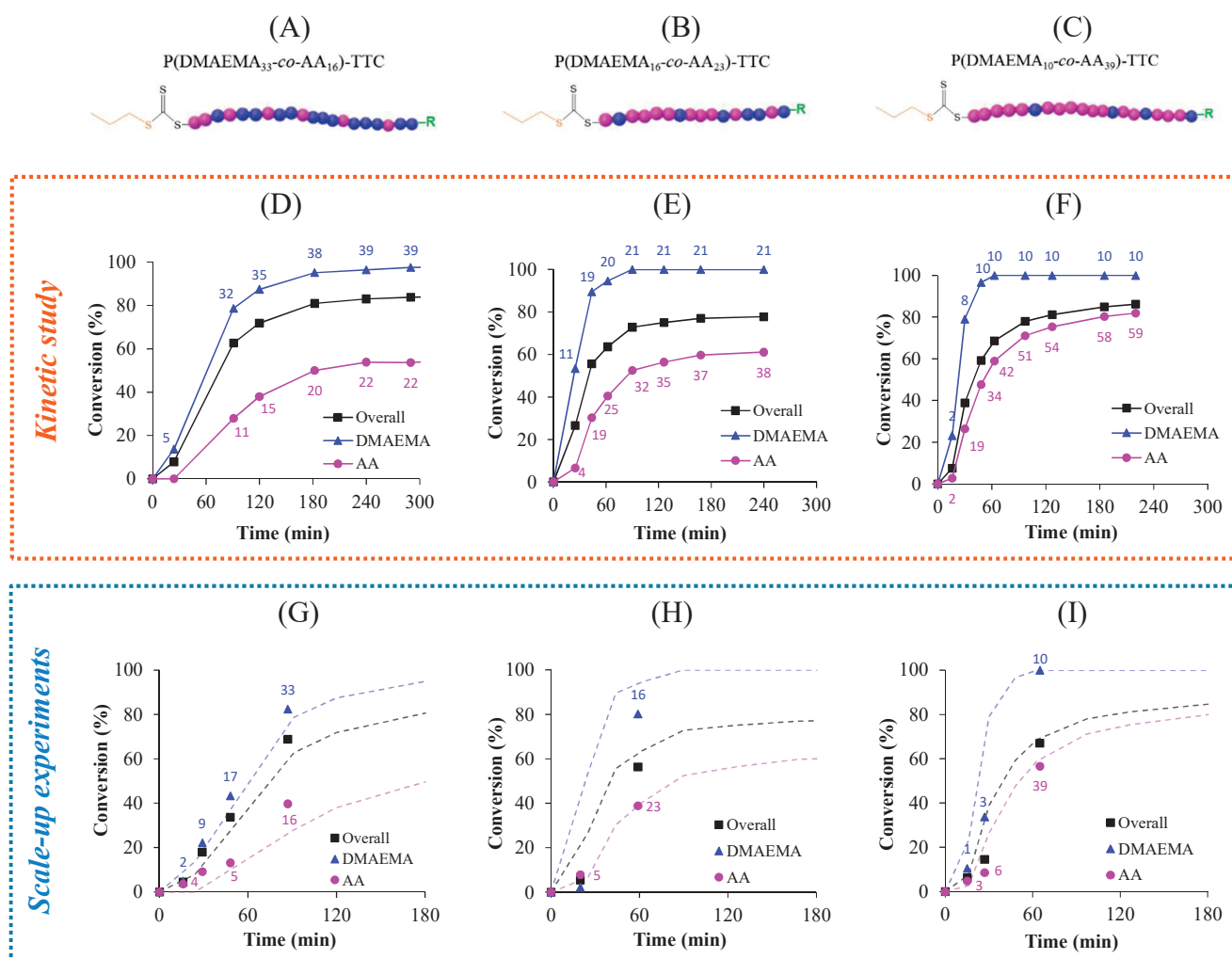


**Figure 23** – RAFT copolymerization of AA and DMAEMA in DMSO using CTPPA as RAFT agent. (A, B, C) Schematic representation of P(DMAEMA-co-AA)-TTC macroRAFT agents. Evolution of individual (data labels represent the number of units for each monomer) and overall monomer conversion versus time for the runs (D) TRG102, (E) TRG103 and (F) TRG106; and for the scaled-up experiments (dashed line represents the kinetic study): (G) TRG112, (H) TRG126 and (I) TRG110.

The evolution of the individual and overall monomer conversions as a function of time for the three AA/DMAEMA ratios tested, are presented in Figure 23D, E and F. As seen in Figure 23, DMAEMA is consumed faster than AA. This can be associated to the well-known difference in reactivity ratio between methacrylate and acrylate monomers.<sup>26, 51</sup> Generally, the more stable methacrylyl tertiary radicals (DMAEMA) will favor the insertion of methacrylate-based units in the copolymer chains over that of this acrylate monomer (AA). It is important to point out that the ability of these monomers to form intermolecular interaction between them could affect their reactivity ratios. Unfortunately, we did not find in the literature the reactivity ratios for the AA/DMAEMA couple.

It is important to stress out here the difference between RDRP and conventional free radical polymerization regarding composition drift. In free radical polymerization, the polymer chains are formed in a fraction of a second, *i.e.* initiation, propagation and termination occur simultaneously during the polymerization reaction, generating polymer chains richer in the more reactive monomer first and latter polymer chains richer in the less reactive monomer. This composition drift generates heterogeneous materials, which can negatively impact their final applications. In contrast, during RAFT polymerization (a RDRP process), polymer chains are formed by one-by-one addition of monomer units, which will generate similar polymer chains with a compositional gradient, *i.e.* polymer chains with an intramolecular composition drift.<sup>67</sup> It is important to point out that the schematic representations of Figure 23A-C were elaborated taking into account the data from the kinetic study. The DMAEMA units, which are consumed faster, are thus represented close to the R-group, while the acrylic acid units, which are reacted later, are shown closer to the Z-group.

Scale-up experiments were then carried out with good reproducibility (Figure 23G-I) resulting in gradient copolymers with varying DMAEMA to AA ratios (entries TRG112, TRG126, TRG110 in Table 6).

As mentioned above, SEC measurements of polar polymers is sometimes quite challenging due to possible interactions with the chromatographic columns. In addition, intermolecular forces between the polymer chains can prevent their complete solubilization. It becomes even more complicated if the polymers have two or more different polar functions, in our case carboxylic acid and amine functions, situation that can further promote interaction with the packing materials. Among the three amphoteric P(DMAEMA-*co*-AA) macroRAFTs, only the polymer the richest in acrylic acid (TRG110), after methylation to form methyl acrylate units, shows an elution peak (RI signal) in THF-SEC (Figure 24A). Unfortunately, for the sample

(TRG110) the whole peak could not be properly integrated due to an overlay with a second peak at longer retention time. SEC-DMSO was thus performed for all amphoteric macroRAFTs. The chromatograms (Figure 24A-C) show the formation of well-defined polymers indicating a good control over the RAFT polymerization. It is important to point out that in the chromatogram of Figure 24C a secondary peak at lower molar masses than the main peak was observed. This could be associated with some polymer chains with a partial methylation of the AA units leading to a potential interaction with the column packing. They were not considered as dead chains as the main and the secondary peak both present a signal at wavelength of 310 nm (see ANNEX 2.2.), which is a strong indication that the chains are end-functionalized with trithiocarbonate group. Further information concerning the evaluation of end functionalization of the macroRAFTs will be presented in the next section.

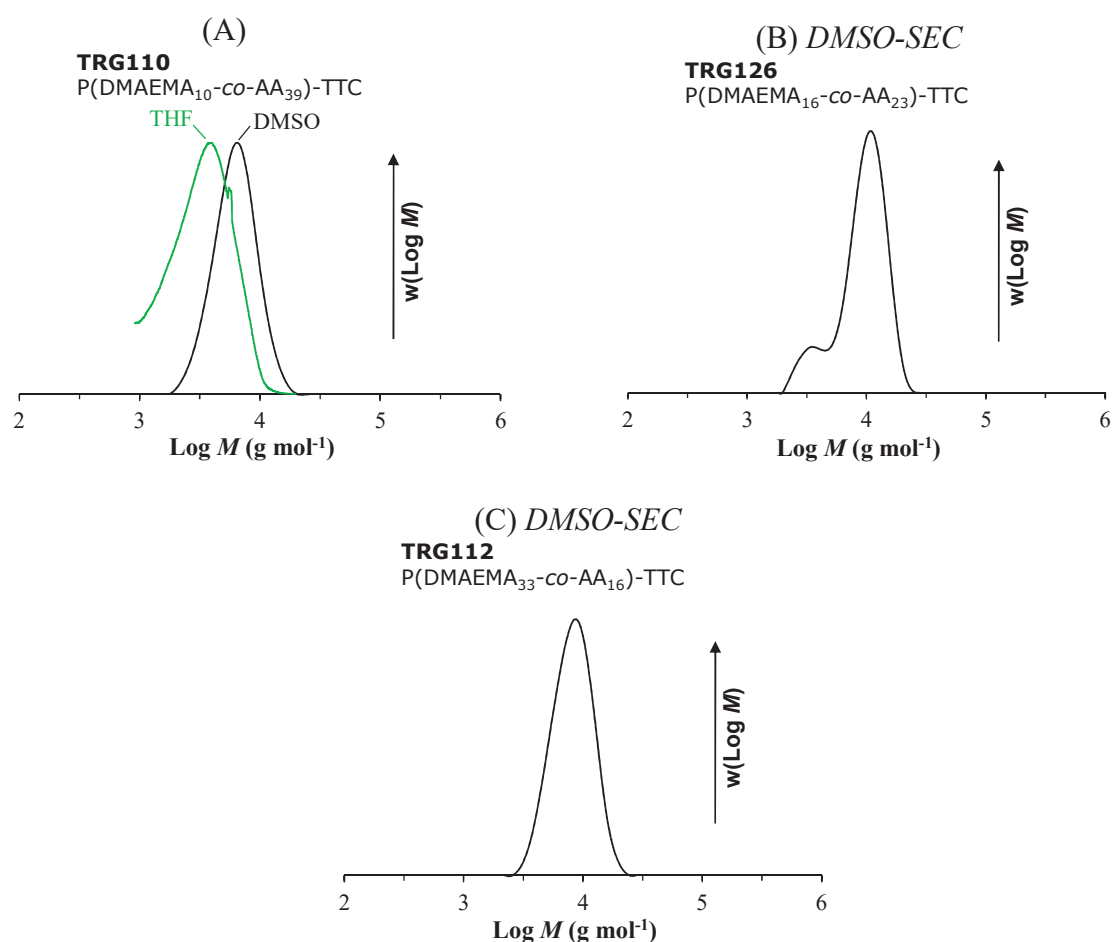


**Figure 24** – SEC chromatograms derived from the RI signal using PMMA calibration of: (A) P(DMAEMA<sub>10</sub>-co-AA<sub>39</sub>)-TTC (TRG110) in THF and in DMSO, (B) P(DMAEMA<sub>16</sub>-co-AA<sub>23</sub>)-TTC (TRG126) in DMSO and (C) P(DMAEMA<sub>33</sub>-co-AA<sub>16</sub>)-TTC (TRG112) in DMSO.

As demonstrated above, the SEC analysis of amphoteric copolymers is not an easy task. However, the results obtained from DMSO-SEC point towards the successful formation of macroRAFTs with three different compositions in AA and DMAEMA.

Our ultimate goal is to chain extend the PAA and PDMAEMA homopolymers as well as the P(DMAEMA-*co*-AA) copolymers with a PS segment to form amphiphilic block copolymers for use as stabilizers first in the cluster preparation and then in emulsion polymerization. Previously, the livingness of two of these hydrophilic macroRAFTs (namely PAA-TTC and PDMAEMA-TTC) was evaluated by chain extension experiments using the same monomer as in the first block.

#### *4.1.4. Chain extension reactions*

Chain extension reactions are relevant experiments to check the livingness of the hydrophilic macroRAFT agents, and assess their ability to initiate a second RAFT polymerization. To do so, the majority of the polymer chains composing the macroRAFT agent have to be end-functionalized with a reactivatable trithiocarbonate group. This function is known to be a UV-absorbing chromophore group with an absorption maximum at around 305-310 nm.<sup>30</sup> Therefore, by using the UV-detector of the SEC device, 3D graphs can be plotted for the PDMAEMA-TTC and PAA-TTC macroRAFT agents (Figure 25A and Figure 26A, respectively), with the wavelength on X axis, the retention volume on Y axis (equivalent to retention time as elution rate = 1 mL min<sup>-1</sup>) and the UV-vis absorbance on Z axis.

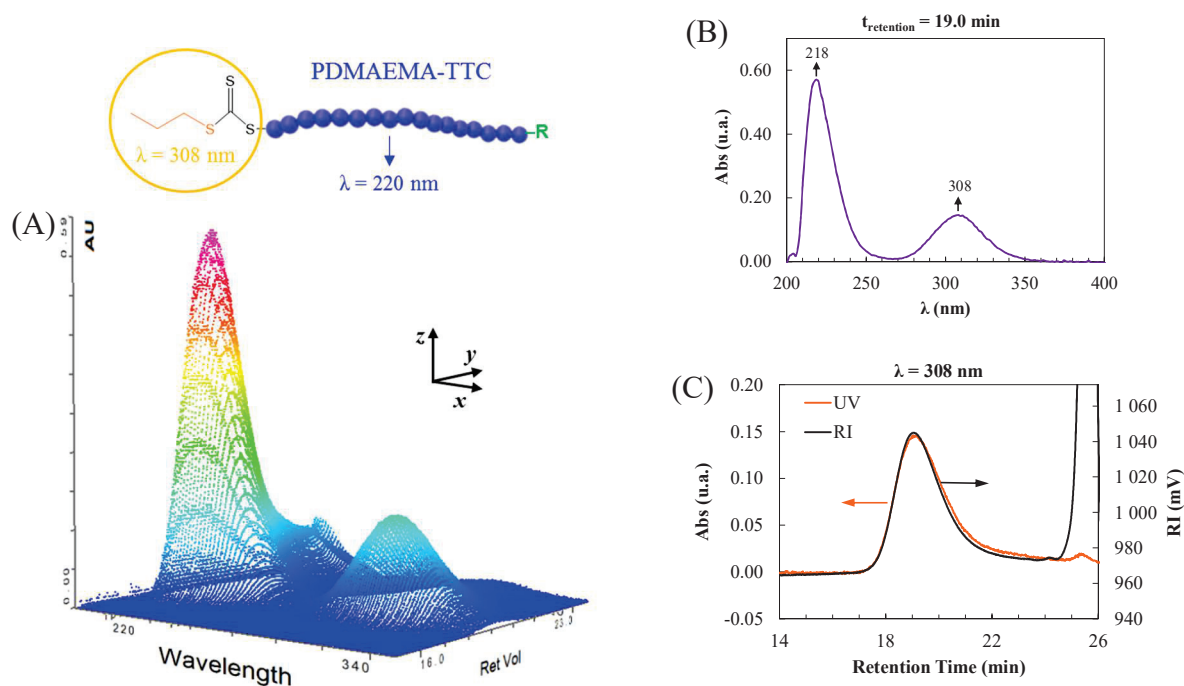


**Figure 25** – THF-SEC of PDMAEMA-TTC macroRAFT (run TRG48) using UV-detection. (A) Surface plot with wavelength on X axis, retention volume on Y axis and UV-vis absorbance on Z axis; (B) cross-section in XZ-plane at a fixed retention time of 19.0 min and (C) cross-section in YZ-plane at a fixed wavelength of 308 nm, corresponding to TTC chain end-functionalization.

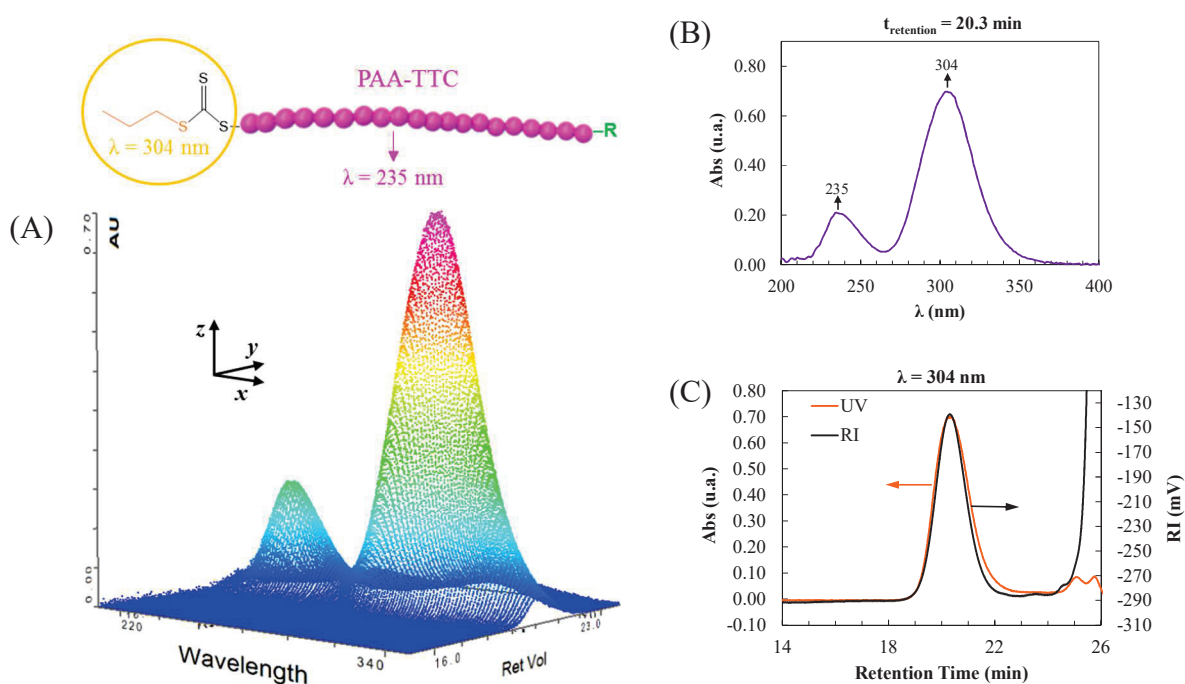


**Figure 26** – THF-SEC of PAA-TTC macroRAFT (run TRG50) using UV-detection. (A) Surface plot with wavelength on X axis, retention volume on Y axis and UV-vis absorbance on Z axis; (B) cross-section on XZ-plane at a fixed retention time of 20.3 min and (C) cross-section on YZ-plane at a fixed wavelength of 304 nm, corresponding to TTC chain-end functionalization.

Two peaks can clearly be evidenced in the surface plots of Figure 25A and Figure 26A: a first one at 218 nm for PDMAEMA, and at 235 nm for PAA-TTC, which can be attributed to the carbonyl groups present on the side-groups of both hydrophilic macroRAFTs, and another one at ca. 305 nm (present for both macroRAFTs) which can be attributed to the trithiocarbonate end-group. In the XY cross-section representation of Figure 25B, the peak at around 218 nm is more intense than the peak at 310 nm corresponding to the TTC end groups. On the contrary Figure 26B shows that the peak of the RAFT end-group in PAA-TTC is more intense than the peak of the carbonyl one, which can be attributed to the difference of molar masses between the two macroRAFTs. Finally, the chromatograms were traced at a fixed absorbance of 305 nm in Figure 25C and Figure 26C (cross-sections in the YZ plane of the surface plots of Figure 25A and Figure 26A), and an excellent correlation between the RI and UV signals was observed for both macroRAFTs, indicating that most of the polymer chains are carrying the reactivable trithiocarbonate end-group.

Chain extension experiments of the hydrophilic macroRAFTs were then carried out using the same monomer as that used for the synthesis of each respective macroRAFT agent. As seen in Figure 27A, the polymerization was fast with more than 50% of monomer consumed in less than one hour for both experiments, but a conversion limited to approximately 70% was observed for the PDMAEMA system. As explained above, this limitation in conversion can

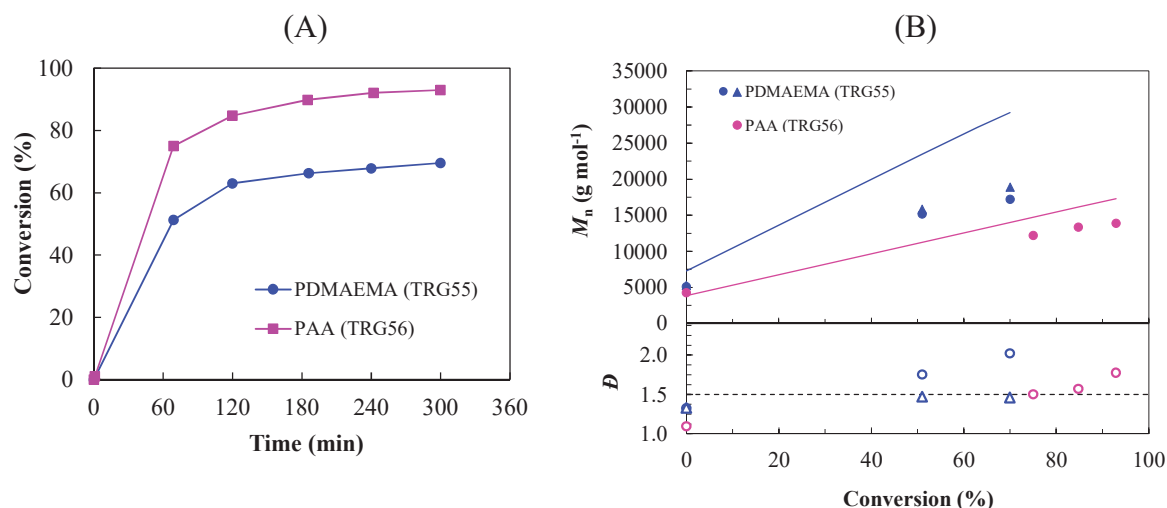


**Figure 27** – Chain extension experiments. Evolution of (A) monomer conversion versus time and (B)  $M_n$  and  $D$  versus conversion. The straight line corresponds to the theoretical evolution of  $M_n$  with conversion. The blue symbols correspond to the "PDMAEMA" (TRG55) SEC-analysis performed either in THF-SEC (●) or in DMF-SEC (▲), and the pink one (●) to the "PAA" -TTC performed in THF-SEC.

be associated to the (low) concentration of monomer employed in this system ( $[\text{DMAEMA}]_0 = 2 \text{ mol L}^{-1}$ ). Indeed, a similar value of conversion was reported in the literature, 68%, for the RAFT solution polymerization of DMAEMA at concentration of 2 M in dioxane.<sup>58</sup>

The shift of the SEC traces with conversion for AA- and DMAEMA-based macroRAFT agents (Figure 28) indicates a good livingness for both series of polymers, demonstrating that the hydrophilic macroRAFT agents can be successfully reactivated. The molar masses effectively increased with conversion, but in both cases the experimental  $M_n$  were lower than the theoretical ones (Figure 27B). This can be attributed to the presence of short polymer chains formed by irreversible termination (dead chains from the first step) or by chain transfer (potential transfer to the solvent or formation of new chains coming from the initiator in the chain extension step).

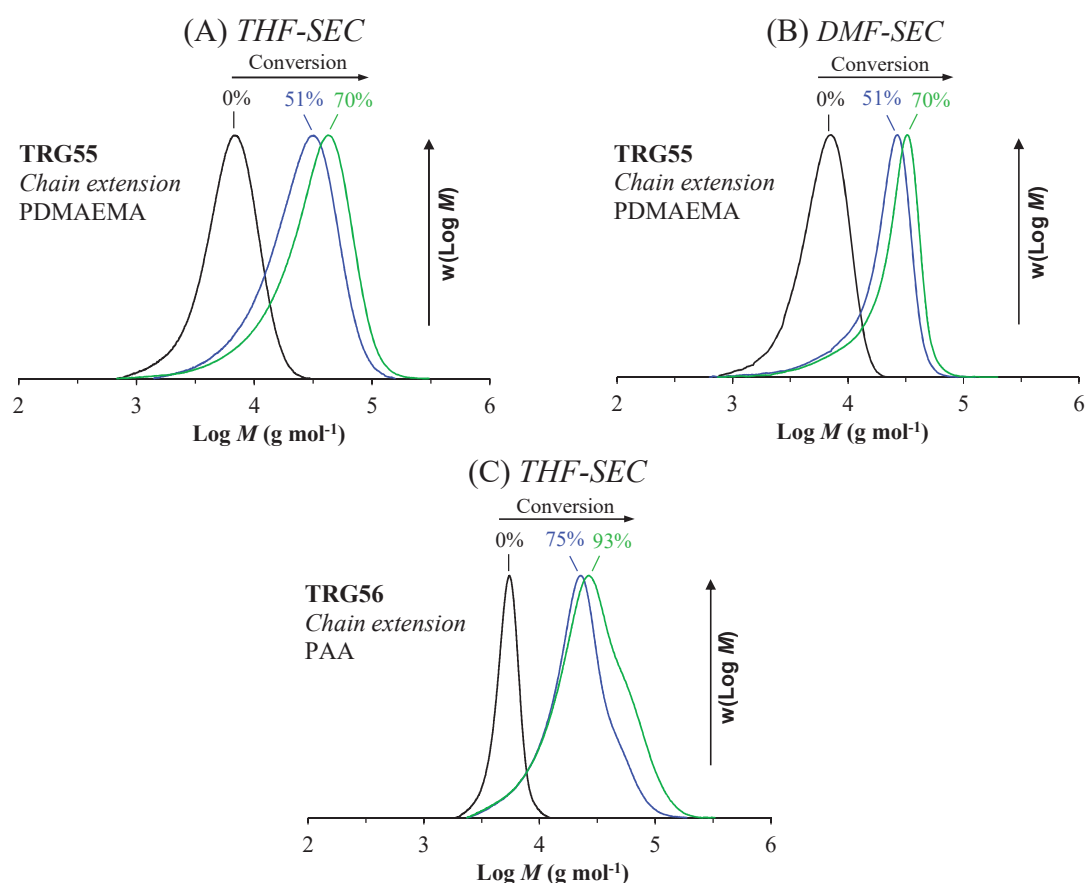


**Figure 28** – SEC chromatograms of PDMAEMA-TTC (run TRG55) performed in (A) THF-SEC and (B) DMF-SEC. Chromatogram evolution with conversion of (C) PAA-TTC (TRG56) performed in THF-SEC.

Furthermore, SEC traces of Figure 28A and 28B show that the tailoring effect was less remarkable in DMF-SEC than in THF-SEC indicating that the SEC analysis in DMF was



more appropriated to PDMAEMA-based macroRAFTs than THF-SEC. This difference results in lower  $D$  values for SEC-DMF (Figure 27B).

The livingness of the hydrophilic macroRAFT agents will be exploited in the next series of experiments to synthesize amphiphilic block copolymer via chain extension reactions using styrene as hydrophobic monomer.

#### 4.1.5. Synthesis of amphiphilic block copolymers

In this section, chain extension reactions of hydrophilic macroRAFTs with styrene will be carried out in order to synthesize amphiphilic macroRAFT containing on average ten units of styrene per macroRAFT. The experimental conditions and the results are summarized in Table 7. The experiments carried out from PDMAEMA-TTC were performed three times to obtain higher amounts of amphiphilic macroRAFT (run TRG59, TRG88 and TRG117)

**Table 7** – Synthesis of amphiphilic block copolymers via RAFT polymerization of styrene in the presence of hydrophilic macroRAFT agents.

Exp.	Hydrophilic macroRAFT (-TTC)	[ACPA] (mM)	[Mon]/[RAFT]	X NMR (%)/ $DP_{S-theo}^a$	$DP_{S-exp}^{RMN}^b$	$M_{n,th}^c$ (g mol <sup>-1</sup> )	$M_{n,exp}^d$ (g mol <sup>-1</sup> )/ $D$
TRG60	PAA <sub>50</sub>	12	30	38/11	12	5100	6000/1.14 <sup>e</sup>
TRG62	PAA <sub>50</sub>	7	30	26/8	10	4700	5300/1.17 <sup>e</sup>
TRG66	PAA <sub>50</sub>	12	30	32/10	9	4900	6250/1.19 <sup>e</sup>
TRG59	PDMAEMA <sub>45</sub>	17	20	28/6	8	7900	6850/1.24 <sup>f</sup> 4650/1.18 <sup>g</sup>
TRG88	PDMAEMA <sub>42</sub>	11	30	27/8	9	7950	4900/1.18 <sup>g</sup>
TRG117	PDMAEMA <sub>42</sub>	11	30	26/8	nd	7950	4800/1.19 <sup>g</sup>
TRG122	P(DMAEMA <sub>33</sub> -co-AA <sub>16</sub> )	11	26	40/10	nd	7650	-
TRG133	P(DMAEMA <sub>16</sub> -co-AA <sub>23</sub> )	11	27	42/11	nd	5650	-
TRG121	P(DMAEMA <sub>10</sub> -co-AA <sub>39</sub> )	12	27	41/11	nd	5900	3900/1.28 <sup>d</sup>

*1,4-dioxane was used as solvent except for TRG122, TRG133 and TRG121 in which DMSO was used. [macroRAFT]/[Ini] = 3, except for TRG62 which was 5. <sup>a</sup>Theoretical degree of polymerization of styrene calculated from conversion; <sup>b</sup>Experimental degree of polymerization of styrene determined by <sup>1</sup>H NMR from the relative integration of the aromatic peak to the characteristic peak of the hydrophilic macroRAFTs (ANNEX 2. 3)*

The first experiment (TRG59 in Table 7) was carried out with  $[\text{Mon}]/[\text{RAFT}] = 20$  aiming at a polymerization degree of styrene of about 10 units in the final amphiphilic macroRAFT. However, the maximum conversion reached for this polymerization was around 30%, lower than the 50% conversion needed to synthesize the targeted amphiphilic block copolymer. Therefore, for the next experiments, the  $[\text{Mon}]/[\text{RAFT}]$  ratio was fixed at 30 and the reactions quenched at around 30% conversion. This conversion was effectively reached after 4 hours for all chain experiments, even if the polymerizations were quite slow (Figure 29).

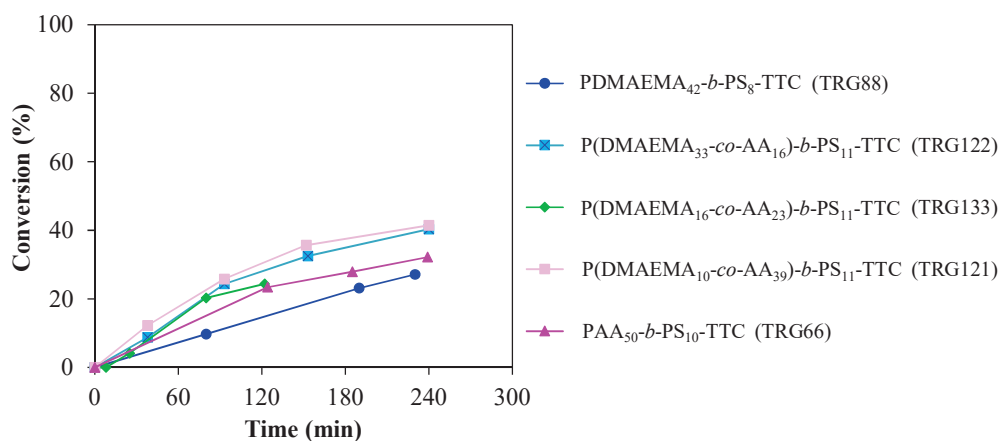


**Figure 29** – Monomer conversion versus time during RAFT polymerizations of styrene in 1,4-dioxane (TRG88 and TRG66) or in DMSO (TRG122, TRG133 and TRG121) using hydrophilic macroRAFTs as macromolecular chain transfer agents.

### PAA-*b*-PS-TTC

The PAA-*b*-PS-TTC amphiphilic macroRAFT agent was characterized by SEC in THF (TRG60, Figure 30A). The shift of the main peak towards higher molar masses indicates successful chain extension. However, a shoulder on high molar mass side of the main peak is observed, which can be attributed to irreversible termination reactions by recombination. A similar behavior was observed during chain extension of PAA-TTC in section 4.1.4. On the other hand, one additional peak of low molar mass can also be observed on the chromatogram, which can likely be associated with impurities of the reaction medium such as initiator fragments. In order to decrease the amount of dead chains, an additional experiment was carried out in which the initiator concentration was decreased from 12 to 7 mM (TRG62, Table 7). However, the termination process was still observed (Figure 30A). Hence, the scaled-up experiment (TRG66, Table 7) was based on the formulation of run TRG60. It is worth mentioning that for the scaled-up experiment (TRG66 in Table 7), the sample was purified by precipitation prior to injection, and the peak at low molar mass was no longer observed (Figure 30A).

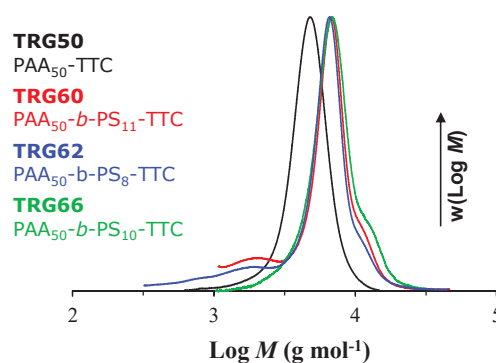


**Figure 30** – SEC chromatograms of PAA-TTC (TRG50) and PAA-*b*-PS-TTC (TRG60, TRG62 and TRG66) performed in THF-SEC.

To confirm the formation of PAA-*b*-PS-TTC amphiphilic block copolymers, UV detection from THF-SEC was exploited. Indeed, polystyrene absorbs UV light at a specific wavelength of 260 nm<sup>68</sup> (see SEC traces for PS in Figure 31A at a fixed wavelength of 265 nm) while for the PAA-TTC, the absorption at 265 nm is almost absent (Figure 31B). However, as can be seen on the chromatogram of PAA-*b*-PS-TTC (Figure 31C), an absorption peak at 265 nm can be clearly evidenced, confirming the successful reactivation of PAA-TTC to form amphiphilic macroRAFT copolymers. Moreover, a second peak at around 20 min was observed at 265 nm (PS) but not at 310 nm (TTC function), supporting the assumption that the polymer chains corresponding to this peak result from irreversible termination (as already discussed in the section 4.1.1.). In addition, the signals observed on UV- and RI-detectors at retention time higher than 26 min can be associated to impurities as explained above (run TRG60 was not purified prior to injections).

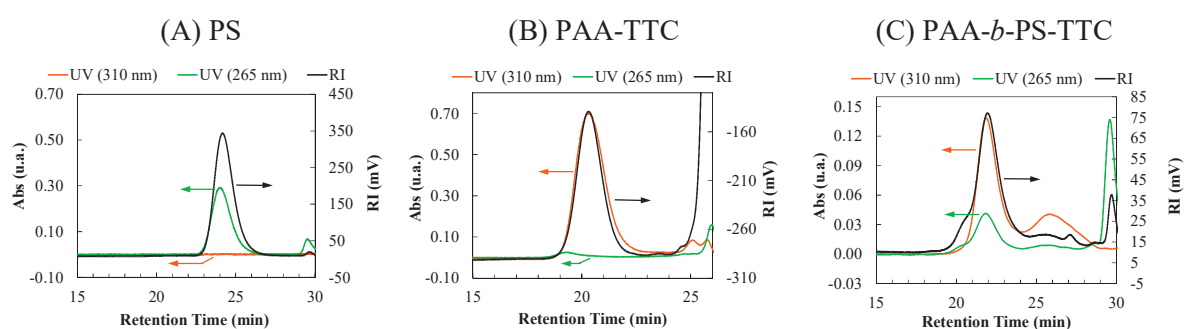


**Figure 31** – THF-SEC chromatograms using double-detection by UV at 265 nm (green line) and 310 nm (orange line), and RI signal (black line) of (A) commercial standard of polystyrene; (B) PAA-TTC (TRG50) and (C) PAA-*b*-PS-TTC (TRG60).

PDMAEMA-*b*-PS-TTC

Regarding the PDMAEMA-based macroRAFT agents, DMF-SEC was carried out resulting in the chromatograms of Figure 32A. The shift of the main peak towards higher molar masses indicates successful chain extension. However the DMF-SEC was not available to analyse the additional batches of macroRAFT (TRG88 and TRG117), so DMSO-SEC was performed for these runs and chromatograms are shown in Figure 32B. Well-defined peaks were obtained for all samples, hydrophilic and amphiphilic macroRAFTS, resulting in narrow molar mass distributions. However, no peak displacement was obtained for SEC performed in DMSO, which can be associated to the insolubility of the PS block in DMSO, which could lead to a polymer coil contraction or even association of the block copolymers, affecting the retention time of these species. Obviously, DMSO-SEC is not appropriate for the analysis of such copolymers.

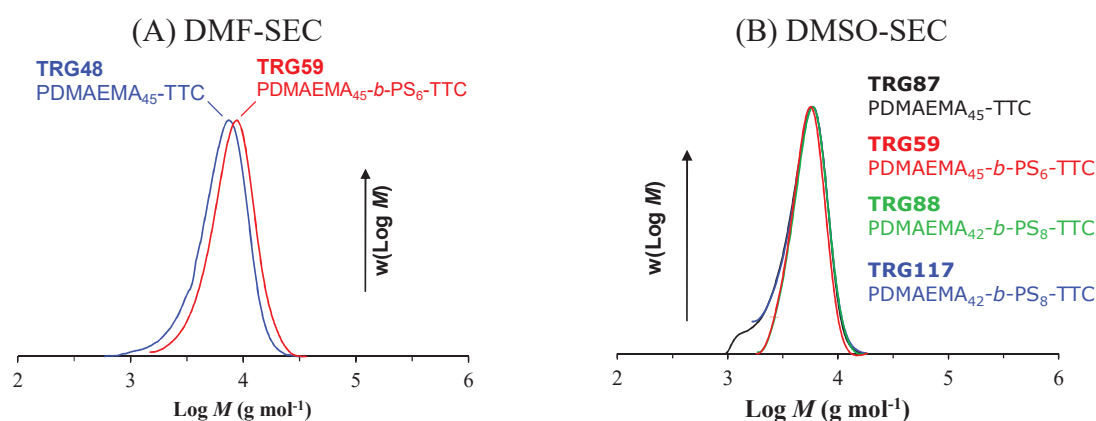


**Figure 32** – SEC chromatograms of PDMAEMA-TTC (TRG48 and TRG87) and PDMAEMA-*b*-PS-TTC (TRG59, TRG88 and TRG117) performed in (A) DMF-SEC and (B) DMSO-SEC.

P(DMAEMA-*co*-AA)-*b*-PS-TTC

The amphiphilic block copolymers prepared from the amphoteric macroRAFTs were also analyzed by SEC. The addition of some styrene units to the amphoteric macroRAFT P(DMAEMA<sub>10</sub>-*co*-AA<sub>39</sub>)-TTC led to a better elution of the polymer as evidenced in the chromatogram of Figure 33A characterized by a well-defined and narrow peak ( $\bar{D} = 1.28$ , Table 7). It is worth mentioning that no dead chains from irreversible termination reactions were observed in the chromatograms resulting in a good fit between the UV at 310 nm (TTC end functionalization) and RI signals. To further evidence the chain extension, the UV signals at 265 and 310 nm were compared to the RI trace. The nice overlay of the three signals (Figure 33B) confirms the successful formation of a block copolymer.

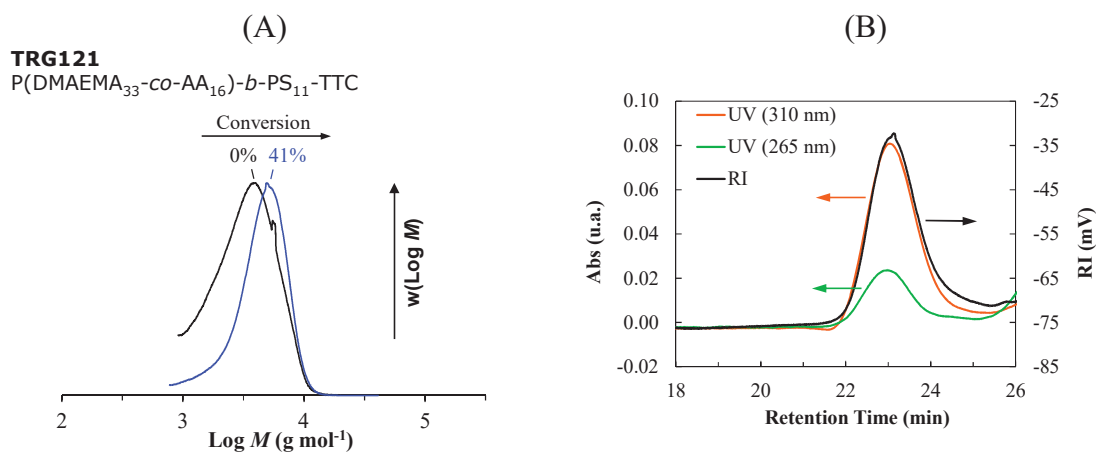


**Figure 33** – THF-SEC chromatograms of P(DMAEMA<sub>10</sub>-co-AA<sub>39</sub>)-b-PS<sub>11</sub>-TTC (TRG121) (A) SEC traces derived from the RI signal by using PMMA calibration, and (B) UV-signal at wavelength of 265 nm (green line) and 310 nm (orange line), and RI signal (black line) as a function of retention time.

Unfortunately, for the amphoteric amphiphilic macroRAFTs with higher DMAEMA contents (TRG122 and TRG133, see Table 7), the RI signal could not be integrated to determine the molar masses. Indeed, the elution peaks (likely) corresponding to these macroRAFTs were too close to the peak associated to the salt (NaNO<sub>3</sub>) used in DMSO (onset at 64 min), disturbing the whole assessment of the peak (Figure 34). On the other hand, for both systems no shoulders were observed at the onset of the peaks, which is an indication that the formation of dead chains via irreversible termination process can be neglected.

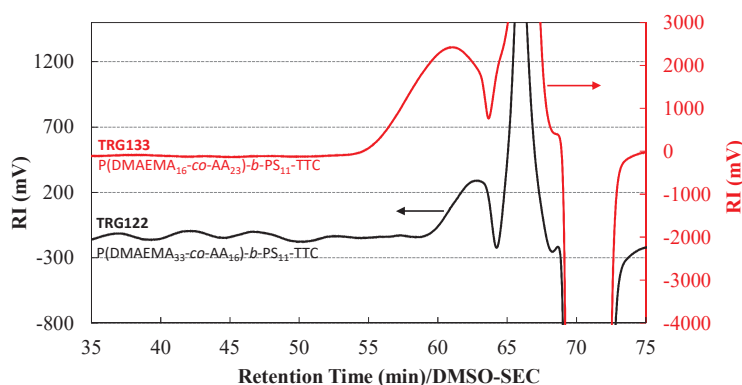


**Figure 34** – RI signals of SEC-chromatograms in DMSO of P(DMAEMA<sub>16</sub>-co-AA<sub>23</sub>)-b-PS<sub>11</sub>-TTC (TRG122) and of P(DMAEMA<sub>33</sub>-co-AA<sub>16</sub>)-b-PS<sub>11</sub>-TTC (TRG133).

#### 4.2. Thermoresponsive properties of the different macroRAFTs

Stimuli-responsive polymers are able to change their conformation in solution under variations in their local environment, such as pH, temperature, ionic strength or presence of a

gas. They have been largely explored<sup>69, 70</sup> for the development of new carriers for targeted drug delivery,<sup>71</sup> bioadhesion mediators,<sup>36, 72</sup> sensors for very small concentration of analytes<sup>73</sup> and microfluidic devices.<sup>74</sup>

Thermosensitive polymers are a sub-class of materials that change their conformation in solution when the temperature varies. The most common transition is the lower critical solution temperature or LCST, which is the temperature, or the range of temperature, for which the polymer chains become insoluble in water, precipitating on themselves (Figure 35). The LCST value corresponds to a given concentration of the polymer, where the cloud point temperature is actually the lowest. This phase transition is generally observed when the enthalpic contribution of hydrogen bonds between polymer chains and water becomes less important than the entropic gain of the system during a heating process. The LCST can be determined by the measurement of the cloud point, which corresponds to the temperature at which the polymer chains are collapsing as determined by UV-spectroscopy, light scattering or visual inspection. Examples of polymers that present a LCST are PDMAEMA, poly(ethylene glycol) (PEO), poly(propylene glycol) (PPO) or poly(*N*-isopropylacrylamide) (PNIPAm) which is the most studied thermosensitive polymer with a LCST of 32 °C.<sup>75</sup> The LCST of PNIPAm can be easily tuned around 37 °C, near to human body temperature, by copolymerizing it with other monomers making it a suitable polymer for use in the biomedical field.<sup>76</sup>

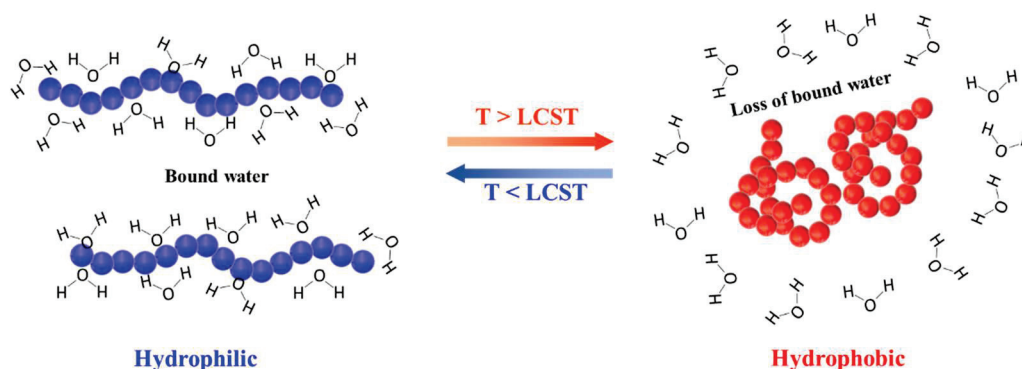


**Figure 35** – Schematic representation of phase transition of polymer chains presenting LCST.

In addition, some polymers can also present a multi-responsive character, *i.e.* their conformation in solution depends on two or more external stimuli. PDMAEMA is an example of multi-responsive polymer, in which the LCST can be varied with the pH, from around 40 °C in alkaline conditions to 80 °C in neutral conditions, being totally soluble at acidic pH.<sup>77</sup>

These multi-responsive polymers have been employed in systems with potential biomedical applications as for example cancer treatment.<sup>78</sup>

In the next sections, we will report the thermosensitive properties of the DMAEMA-based macroRAFT agents. The cloud point temperature ( $T_{CP}$ ) of the macroRAFT solutions will be measured by monitoring the UV-vis transmittance or light scattering with temperature, and some experimental conditions will be varied such as the pH, the ionic strength and the macroRAFT composition.

### 4.2.1. Effect of pH on the cloud point of the DMAEMA-based macroRAFT agents

As mentioned above, PDMAEMA exhibits a LCST, which is pH-dependent. This is due to its tertiary amine side groups, which can be protonated at low pH or deprotonated under basic conditions. Hence, at acidic pH, the hydrophilicity of the polymer chains will be increased, improving their solubility in water shifting the LCST to higher temperatures. This phenomenon was evidenced in our study. As shown in Figure 36a, no phase transition was observed at neutral pH and slightly basic conditions (*i.e.* pH = 7.4) as the amine was protonated. However, when the pH was increased,  $T_{CP}$  decreased from 69 °C (at pH 8) to around 45 °C (for pH  $\geq$  9) (Figure 36a). The cloud point of PDMAEMA-TTC at pH 9 was also determined by DLS by following the evolution of the particle size ( $Z_{av}$ ) with temperature (Figure 36B). Similar results were obtained (*i.e.*  $T_{CP} = 43.5$  °C *vs* 45.4 °C by UV-vis spectroscopy), confirming the thermo-responsive property of PDMAEMA-TTC.

As seen in Table 8, different  $T_{CP}$  values have been reported in the literature for PDMAEMA. Indeed, cloud point temperatures are strongly influenced by experimental conditions such as concentration, heating ramp and ionic strength, and also depend on intrinsic characteristics of the polymer chains, such as chain-end functionalization and molar masses. For instance, Plamper *et al.*<sup>77</sup> showed that the  $T_{CP}$  of PDMAEMA (stars and linear chains) decreases with increasing molar mass. This effect is more pronounced for polymer chains with molar masses lower than 100 000 g mol<sup>-1</sup>, and can be associated to their higher solubility. The  $T_{CP}$  values obtained in our experiments (TRG87 in Table 8) were always higher than the values reported in the literature at the same pH, which can be associated to the low molar mass of the PDMAEMA chains synthesized in our work.



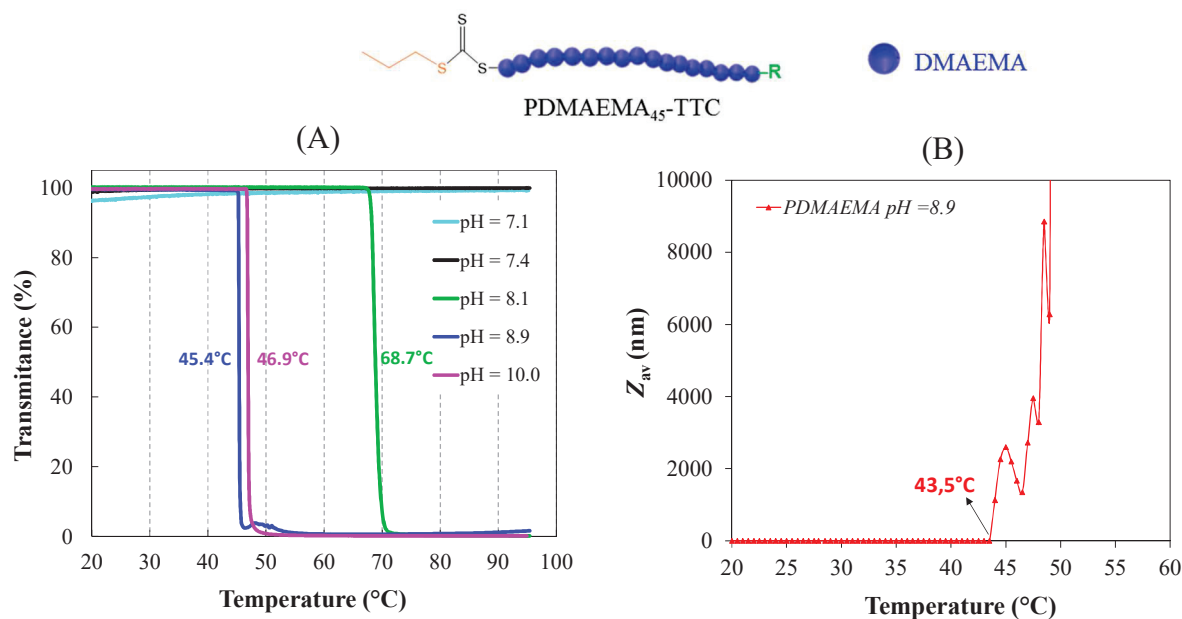


**Figure 36** – Effect of pH on the cloud point temperature of PDMAEMA-TTC (TRG87 in Table 5) as determined by (A) UV-vis spectroscopy at 650 nm and (B) DLS analysis ( $Z_{av}$ ).

**Table 8** –Thermosensitive properties of PDMAEMA. Cloud point measurements obtained at different pHs for PDMAEMA-TTC (TRG87) compared with literature values.

Exp.	Polymer	T <sub>CP</sub> (°C) for different pH values						Ramp (°C min <sup>-1</sup> )	C (g L <sup>-1</sup> )
		4.0	7.0	7.5	8.0	9.0	10.0		
TRG87	PDMAEMA <sub>42</sub> -TTC ( $M_n = 3400 \text{ g mol}^{-1}$ ) <sup>a</sup>	-	no	no	69	45	47	0.5	10
Loh <sup>79</sup>	PDMAEMA-Br <sup>d</sup> ( $M_n = 6540 \text{ g mol}^{-1}$ ) <sup>a</sup>	69.4	44.7	-	-	38.4	-	2.0	10
Fournier et al. <sup>80</sup>	PDMAEMA-DTB <sup>f</sup> ( $M_n = 9500 \text{ g mol}^{-1}$ ) <sup>a</sup>	no	46.6	-	-	-	34.7	1.0	5
Plamper et al. <sup>77</sup>	PDMAEMA <sub>108</sub> -Br <sup>d</sup> ( $M_n = 16500 \text{ g mol}^{-1}$ ) <sup>a</sup>	-	76.0	-	53.0	42.3	38.7	1.0	1
Yuk et al. <sup>81</sup>	PDMAEMA <sup>e</sup> ( $M_w = 28000 \text{ g mol}^{-1}$ ) <sup>b</sup>	no	-	54	-	-	-	0.2	50

Cloud point temperature determined by UV-vis spectroscopy. <sup>a</sup>Based on PMMA calibration. <sup>b</sup>Determined by DLS. PDMAEMA synthesized via: <sup>d</sup>ATRP, carrying a bromine as chain-end functionalization, <sup>e</sup>free radical polymerization and <sup>f</sup>RAFT polymerization mediated by a dithiobenzoate (DTB) RAFT agent.

Furthermore, the T<sub>CP</sub> values of PDMAEMA-*b*-PS-TTC amphiphilic block copolymers were also determined for different pH values (Figure 37). However, no clear phase transitions were observed for all pH studied, and only an onset of phase transition was evidenced at pH 8.0 and 10.1, between 70 and 80°C. This was unexpected, as the incorporation of hydrophobic monomer units into PDMAEMA should increase the hydrophobicity of the polymer chains leading to a decrease of the LCST. Many authors have reported a diminution of the LCST of

PDMAEMA by copolymerization with hydrophobic monomers, in for instance block copolymers with methyl methacrylate,<sup>82</sup> star copolymers with (meth)acrylates<sup>83</sup> or statistical copolymers with styrene.<sup>84</sup> The reason for that observation remains unclear and further investigations would be necessary to elucidate it, such as variation of the heating ramp or complementary analyses by DLS.

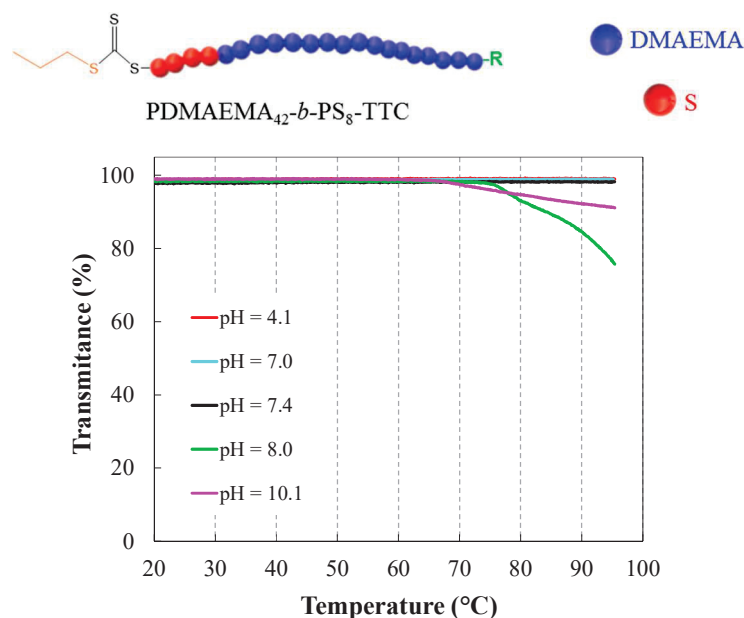


**Figure 37** – Effect of pH on the cloud point temperature of PDMAEMA-*b*-PS-TTC (TRG88 in Table 5) as determined by UV-vis spectroscopy at 650 nm.

#### 4.2.2. Effect of ionic strength on the LCST of PDMAEMA-TTC

The ionic strength is an important parameter to be taken into account when the behavior of polymers in solution is evaluated. In Figure 38, the ionic strength was varied by changing the NaCl concentration while maintaining the pH at 9. No significant change of T<sub>CP</sub> was observed for low NaCl concentrations (ca. 46°C for 10 mM and 100 mM). However, a decrease of the cloud point temperature of around 10°C was evidenced for the highest salt concentration (34.9°C at 1 M).

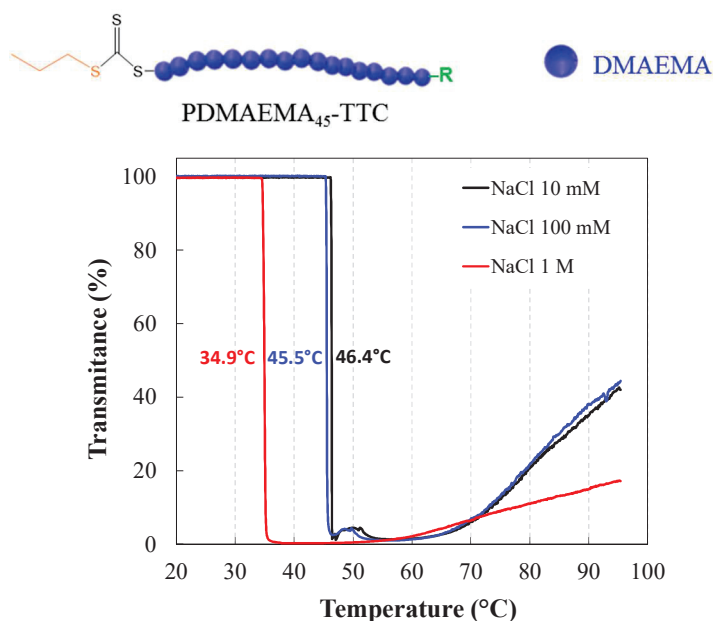


**Figure 38** – Effect of ionic strength at pH 9 on the cloud point of PDMAEMA-TTC (TRG87 in Table 5) as determined by UV-vis spectroscopy at 650 nm.

#### 4.2.3. Effect of the macroRAFT composition on the $T_{CP}$

The thermosensitivity of the two amphoteric macroRAFTs composed of DMAEMA and AA for different AA to DMAEMA molar ratios was also evaluated (Figure 39). No phase transition was evidenced for both macroRAFTs, either with high AA (TRG110) or high DMAEMA (TRG112) contents, under basic (pH 10) or acidic conditions (pH 4). As aforementioned, at acidic pH the tertiary amine side-groups of PDMAEMA becomes protonated and positively charged increasing the hydrophilicity of the macroRAFT hindering the phase transition. On the other hand, under basic conditions, where is expected a cloud point for PDMAEMA-based copolymers, the carboxylic acid groups of AA units become deprotonated and negatively charged increasing the hydrophilicity of the amphoteric macroRAFT hindering the phase transition as well. Perhaps, at intermediary pH, the polymer chains become completely uncharged and a phase transition could be observed. However, further investigations with a fine variation of pH would be necessary to confirm that expected trend.

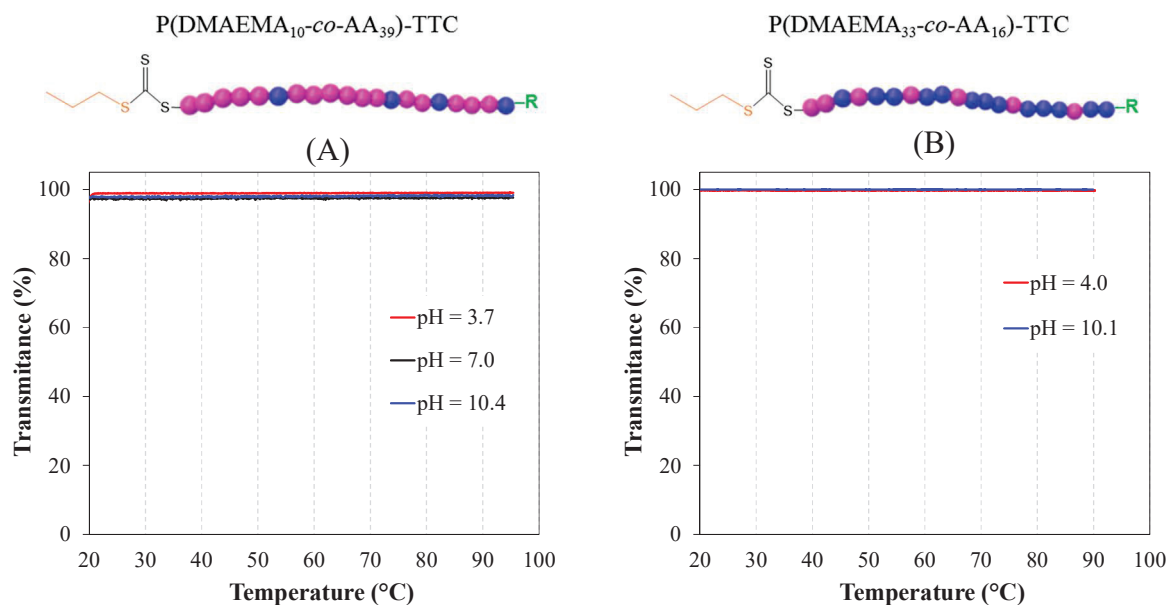


**Figure 39** – Effect of pH on the cloud point temperatures of the amphoteric macroRAFT agents. (A) P(DMAEMA<sub>10</sub>-co-AA<sub>39</sub>)-TTC and (B) P(DMAEMA<sub>33</sub>-co-AA<sub>16</sub>)-TTC (TRG110 and TRG112, respectively, Table 5) as determined by UV-vis spectroscopy at 650 nm.

## 5. CONCLUSIONS

RAFT polymerization was successfully employed to synthesize well-defined hydrophilic PAA-TTC and PDMAEMA-TTC macroRAFT agents. SEC analysis by using MHWS recalibration curves showed an excellent agreement between the theoretical and experimental molar masses for both polymers. Chain-end functionalization was evaluated by using UV detection during the SEC analysis showing that most of the polymer chains carry the reactivatable trithiocarbonate end-group. The living character of the chains was confirmed by successful chain extension experiments. Amphiphilic block copolymers were then synthesized by chain extension reaction of PAA-TTC and PDMAEMA-TTC with styrene. SEC measurements with UV detection confirmed the formation of well-defined block copolymers with narrow molar mass distributions ( $D < 1.25$ ).

Amphoteric polymers were synthesized by RAFT copolymerization of AA and DMAEMA at different molar ratio in DMSO. Solubilization of the resulting copolymers in organic solvent proved to be quite challenging probably due to intramolecular interactions between the polar groups in the chains. In addition, such interactions can also account for the difficulties encountered in analyzing these polymers by THF-SEC. Well-defined peaks were however obtained for amphoteric macroRAFTs in DMSO-SEC indicating their successful synthesis via RAFT polymerization. Amphiphilic block copolymers were also prepared via chain extension

reaction of amphoteric macroRAFTs with a PS segment. THF-SEC chromatograms showed the successful synthesis of P(DMAEMA<sub>10-co-AA<sub>39</sub></sub>)-*b*-PS<sub>11</sub>-TTC. However, no peak was observed for the amphiphilic macroRAFTs the richest in DMAEMA: P(DMAEMA<sub>16-co-AA<sub>23</sub></sub>)-*b*-PS<sub>11</sub>-TTC and P(DMAEMA<sub>33-co-AA<sub>16</sub></sub>)-*b*-PS<sub>11</sub>-TTC. Unfortunately, DMSO-SEC chromatography also led to unsatisfactory results for these two amphiphilic macroRAFTs.

The thermoresponsive properties of the PDMAEMA-based macroRAFTs were next evaluated. As reported in the literature, the LCST of PDMAEMA solutions increases with decreasing pH. In our work, the cloud point temperature shifted from *ca.* 45 °C for pH > 9 to around 70 °C at pH = 8 and it was completely absent at pH lower than 7.5 in the range of temperature studied (*i.e.* from 15 to 90 °C). In contrast, no phase transition was evidenced for the amphiphilic block copolymers based on styrene regardless of the pH, which is in disagreement with the literature, as a decrease of LCST was expected due to the increase of macroRAFT hydrophobicity. No phase transition was observed either for the amphoteric macroRAFT agents composed of AA and DMAEMA, both in basic and acidic conditions. This can be associated to an antagonistic effect of pH on the solubility of AA and DMAEMA, in which AA units are negatively charged at basic pH while the DMAEMA ones are positively charged under acidic conditions. Therefore, the macroRAFT will be charged over a wide range of pH values leading to a higher hydrophilicity, hindering the phase transition.

In summary, ten macroRAFT agents were synthesized in this chapter. Five hydrophilic macroRAFTs: PAA-TTC and PDMAEMA-TTC homopolymers and three amphoteric copolymers with various AA to DMAEMA ratios were successfully obtained via RAFT polymerization in solution. Chain extension experiments of these hydrophilic macroRAFTs with styrene led to the formation of five amphiphilic block copolymers completing our macroRAFT library.

These amphiphilic macroRAFT agents will play a determinant role during the preparation of magnetic polymer particles in which the hydrophilic moiety will provide the stabilization to the particles. The role of the amphiphilic macroRAFTs on cluster formation and stabilization will be presented in the following chapter.

## REFERENCES

1. Li, G.; Song, S.; Guo, L.; Ma, S., Self-assembly of thermo-and pH-responsive poly(acrylic acid)-*b*-poly(N-isopropylacrylamide) micelles for drug delivery. *Journal of Polymer Science Part A: Polymer Chemistry* **2008**, *46* (15), 5028-5035.
2. Bütün, V.; Armes, S.; Billingham, N., Synthesis and aqueous solution properties of near-monodisperse tertiary amine methacrylate homopolymers and diblock copolymers. *Polymer* **2001**, *42* (14), 5993-6008.
3. Vana, P.; Barner-Kowollik, C.; Davis, T. P.; Matyjaszewski, K., Radical polymerization. *Encyclopedia of Polymer Science and Technology* **2003**.
4. Matyjaszewski, K., Atom Transfer Radical Polymerization (ATRP): Current Status and Future Perspectives. *Macromolecules* **2012**, *45* (10), 4015-4039.
5. Braun, D., Origins and development of initiation of free radical polymerization processes. *International Journal of Polymer Science* **2010**, *2009*.
6. Moad, G.; Solomon, D. H., *The chemistry of radical polymerization*. Elsevier: 2006.
7. Georges, M. K.; Veregin, R. P.; Kazmaier, P. M.; Hamer, G. K., Narrow molecular weight resins by a free-radical polymerization process. *Macromolecules* **1993**, *26* (11), 2987-2988.
8. Kato, M.; Kamigaito, M.; Sawamoto, M.; Higashimura, T., Polymerization of methyl methacrylate with the carbon tetrachloride/dichlorotris-(triphenylphosphine) ruthenium (II)/methylaluminum bis (2, 6-di-tert-butylphenoxide) initiating system: possibility of living radical polymerization. *Macromolecules* **1995**, *28* (5), 1721-1723.
9. Wang, J.-S.; Matyjaszewski, K., Controlled/" living" radical polymerization. Atom transfer radical polymerization in the presence of transition-metal complexes. *Journal of the American Chemical Society* **1995**, *117* (20), 5614-5615.
10. Chiefari, J.; Chong, Y.; Ercole, F.; Krstina, J.; Jeffery, J.; Le, T. P.; Mayadunne, R. T.; Meijs, G. F.; Moad, C. L.; Moad, G., Living free-radical polymerization by reversible addition-fragmentation chain transfer: the RAFT process. *Macromolecules* **1998**, *31* (16), 5559-5562.
11. Braunecker, W. A.; Matyjaszewski, K., Controlled/living radical polymerization: Features, developments, and perspectives. *Progress in Polymer Science* **2007**, *32* (1), 93-146.
12. Keddie, D. J.; Moad, G.; Rizzardo, E.; Thang, S. H., RAFT Agent Design and Synthesis. *Macromolecules* **2012**, *45* (13), 5321-5342.
13. Chaparro, T. C. Synthesis of nanocomposites with anisotropic properties by controlled radical emulsion polymerization. Universidade de São Paulo and Université Claude Bernard Lyon 1, 2016.
14. Dommange, C.; D'Agosto, F.; Monteil, V., Polymerization of Ethylene through Reversible Addition-Fragmentation Chain Transfer (RAFT). *Angewandte Chemie International Edition* **2014**, *53* (26), 6683-6686.
15. Chong, Y.; Krstina, J.; Le, T. P.; Moad, G.; Postma, A.; Rizzardo, E.; Thang, S. H., Thiocarbonylthio compounds [SC (Ph) S- R] in free radical polymerization with reversible addition-fragmentation chain transfer (RAFT Polymerization). Role of the free-radical leaving group (R). *Macromolecules* **2003**, *36* (7), 2256-2272.

16. Destarac, M., Controlled radical polymerization: industrial stakes, obstacles and achievements. *Macromolecular Reaction Engineering* **2010**, 4 (3-4), 165-179.
17. Couvreur, L.; Guerret, O.; Laffitte, J.-A.; Magnet, S., Dibenzyltrithiocarbonate (DBTTC) performances overview of a commercially available RAFT agent. *Polym. Prepr. (Am. Chem. Soc., Div. Polym. Chem.)* **2005**, 46, 219.
18. Brzytwa, A. J.; Johnson, J., Scaled Production of RAFT CTA– a STAR Performer. *Polym. Prepr. Am. Chem. Soc. Div. Polym. Chem* **2011**, 52, 533-534.
19. Zetterlund, P. B.; Thickett, S. C.; Perrier, S. b.; Bourgeat-Lami, E.; Lansalot, M., Controlled/living radical polymerization in dispersed systems: an update. *Chemical Reviews* **2015**, 115 (18), 9745-9800.
20. Moad, G.; Rizzardo, E.; Thang, S. H., RAFT polymerization and some of its applications. *Chemistry—An Asian Journal* **2013**, 8 (8), 1634-1644.
21. Cenacchi-Pereira, A.; Grant, E.; D’Agosto, F.; Lansalot, M.; Bourgeat-Lami, E., Encapsulation with the use of controlled radical polymerization. In *Encyclopedia of Polymeric Nanomaterials*, Springer: 2015; pp 718-729.
22. Moad, G., Reversible addition–fragmentation chain transfer (co)polymerization of conjugated diene monomers: butadiene, isoprene and chloroprene. *Polymer International* **2017**, 66 (1), 26-41.
23. Moad, G.; Keddie, D.; Guerrero-Sanchez, C.; Rizzardo, E.; Thang, S. H. In *Advances in switchable RAFT polymerization*, Macromolecular Symposia, Wiley Online Library: 2015; pp 34-42.
24. Moad, G.; Rizzardo, E.; Thang, S. H., Living radical polymerization by the RAFT process—a third update. *Australian Journal of Chemistry* **2012**, 65 (8), 985-1076.
25. Barner-Kowollik, C., *Handbook of RAFT Polymerization*. Wiley-VCH: Weinheim, 2008.
26. Keddie, D. J., A guide to the synthesis of block copolymers using reversible-addition fragmentation chain transfer (RAFT) polymerization. *Chemical Society Reviews* **2014**, 43 (2), 496-505.
27. Gregory, A.; Stenzel, M. H., Complex polymer architectures via RAFT polymerization: From fundamental process to extending the scope using click chemistry and nature's building blocks. *Progress in Polymer Science* **2012**, 37 (1), 38-105.
28. Chong, Y.; Le, T. P.; Moad, G.; Rizzardo, E.; Thang, S. H., A more versatile route to block copolymers and other polymers of complex architecture by living radical polymerization: the RAFT process. *Macromolecules* **1999**, 32 (6), 2071-2074.
29. Schilli, C. M.; Zhang, M.; Rizzardo, E.; Thang, S. H.; Chong, Y.; Edwards, K.; Karlsson, G.; Müller, A. H., A New Double-Responsive Block Copolymer Synthesized via RAFT Polymerization: Poly(*N*-isopropylacrylamide)-*block*-poly(acrylic acid). *Macromolecules* **2004**, 37 (21), 7861-7866.
30. Guimarães, T. R.; de Camargo Chaparro, T.; D’Agosto, F.; Lansalot, M.; Dos Santos, A. M.; Bourgeat-Lami, E., Synthesis of multi-hollow clay-armored latexes by surfactant-free emulsion polymerization of styrene mediated by poly(ethylene oxide)-based macroRAFT/Laponite complexes. *Polymer Chemistry* **2014**, 5 (22), 6611-6622.



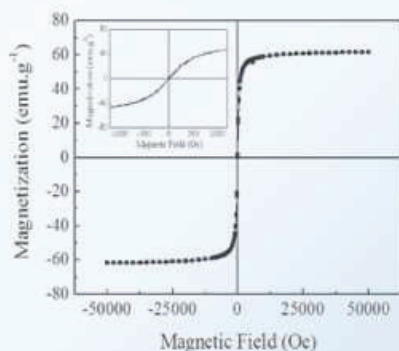
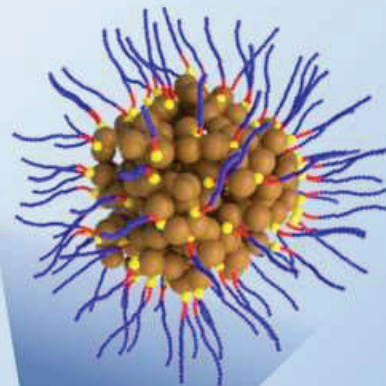
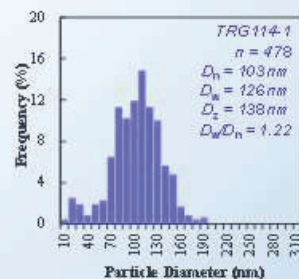
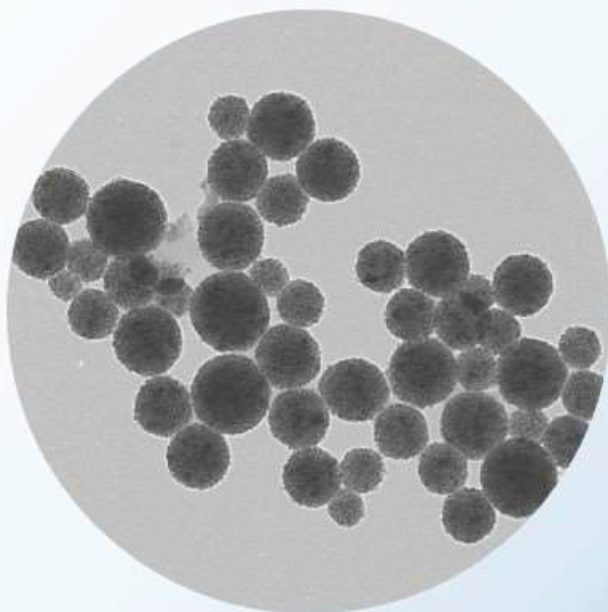
31. Wang, H.; Zhou, H.; Chen, Y.; Zhang, C., Synthesis of fluorinated gradient copolymers by RAFT emulsifier-free emulsion polymerization and their compatibilization in copolymer blends. *Colloid and Polymer Science* **2014**, *292* (11), 2803-2809.
32. Pham, B. T.; Nguyen, D.; Ferguson, C. J.; Hawckett, B. S.; Serelis, A. K.; Such, C. H., Miniemulsion polymerization stabilized by amphiphilic macro RAFT agents. *Macromolecules* **2003**, *36* (24), 8907-8909.
33. Pham, B. T.; Zondanos, H.; Such, C. H.; Warr, G. G.; Hawckett, B. S., Miniemulsion polymerization with arrested Ostwald ripening stabilized by amphiphilic RAFT copolymers. *Macromolecules* **2010**, *43* (19), 7950-7957.
34. Dreyer, J. K.; Nylander, T.; Karlsson, O. J.; Piculell, L., Spreading dynamics of a functionalized polymer latex. *ACS applied materials & interfaces* **2011**, *3* (2), 167-176.
35. Kim, H.; Lee, J.; Lee, D.; Kim, J., Film properties of reactive latexes modified with epoxy and carboxyl surface functional groups. *POLYMER-KOREA* **1999**, *23* (6), 852-860.
36. Cunliffe, D.; de las Heras Alarcón, C.; Peters, V.; Smith, J. R.; Alexander, C., Thermoresponsive surface-grafted poly(*N*-isopropylacrylamide) copolymers: effect of phase transitions on protein and bacterial attachment. *Langmuir* **2003**, *19* (7), 2888-2899.
37. Hu, Y.; Wang, J.; Zhang, H.; Jiang, G.; Kan, C., Synthesis and characterization of monodispersed P(St-*co*-DMAEMA) nanoparticles as pH-sensitive drug delivery system. *Materials Science and Engineering: C* **2014**, *45*, 1-7.
38. Zhang, Q.; Yu, G.; Wang, W.-J.; Yuan, H.; Li, B.-G.; Zhu, S., Switchable block copolymer surfactants for preparation of reversibly coagulatable and redispersible poly(methyl methacrylate) latexes. *Macromolecules* **2013**, *46* (4), 1261-1267.
39. Chaduc, I.; Girod, M.; Antoine, R.; Charleux, B.; D'Agosto, F.; Lansalot, M., Batch emulsion polymerization mediated by poly(methacrylic acid) macroRAFT agents: one-pot synthesis of self-stabilized particles. *Macromolecules* **2012**, *45* (15), 5881-5893.
40. Zhang, W.; D'Agosto, F.; Boyron, O.; Rieger, J.; Charleux, B., Toward a better understanding of the parameters that lead to the formation of nonspherical polystyrene particles via RAFT-mediated one-pot aqueous emulsion polymerization. *Macromolecules* **2012**, *45* (10), 4075-4084.
41. Lansalot, M.; Rieger, J.; D'Agosto, F., Polymerization-Induced Self-Assembly: The Contribution of Controlled Radical Polymerization to The Formation of Self-Stabilized Polymer Particles of Various Morphologies. *Macromolecular Self-assembly* **2016**, 33-82.
42. Canning, S. L.; Smith, G. N.; Armes, S. P., A critical appraisal of RAFT-mediated polymerization-induced self-assembly. *Macromolecules* **2016**, *49* (6), 1985-2001.
43. Chaduc, I.; Zhang, W.; Rieger, J.; Lansalot, M.; D'Agosto, F.; Charleux, B., Amphiphilic Block Copolymers from a Direct and One-pot RAFT Synthesis in Water. *Macromolecular Rapid Communications* **2011**, *32* (16), 1270-1276.
44. Zhang, W.; Charleux, B.; Cassagnau, P., Viscoelastic properties of water suspensions of polymer nanofibers synthesized via RAFT-mediated emulsion polymerization. *Macromolecules* **2012**, *45* (12), 5273-5280.
45. Lai, J. T.; Filla, D.; Shea, R., Functional polymers from novel carboxyl-terminated trithiocarbonates as highly efficient RAFT agents. *Macromolecules* **2002**, *35* (18), 6754-6756.

46. Couvreur, L.; Lefay, C.; Belleney, J.; Charleux, B.; Guerret, O.; Magnet, S., First nitroxide-mediated controlled free-radical polymerization of acrylic acid. *Macromolecules* **2003**, *36* (22), 8260-8267.
47. Kühnel, E.; Laffan, D. D.; Lloyd-Jones, G. C.; Martínez del Campo, T.; Shepperson, I. R.; Slaughter, J. L., Mechanism of methyl esterification of carboxylic acids by trimethylsilyldiazomethane. *Angewandte Chemie International Edition* **2007**, *46* (37), 7075-7078.
48. Kockler, K. B.; Fleischhaker, F.; Barner-Kowollik, C., Free Radical Propagation Rate Coefficients of N-Containing Methacrylates: Are We Family? *Macromolecules* **2016**.
49. Zhang, C.; Zhou, Y.; Liu, Q.; Li, S.; Perrier, S.; Zhao, Y., Facile synthesis of hyperbranched and star-shaped polymers by RAFT polymerization based on a polymerizable trithiocarbonate. *Macromolecules* **2011**, *44* (7), 2034-2049.
50. Heitz, C.; Rawiso, M.; François, J., X-ray scattering study of a poly(methacrylic acid) sample as a function of its neutralization degree. *Polymer* **1999**, *40* (7), 1637-1650.
51. Stenzel, M. H., Complex architecture design via the RAFT process: scope, strengths and limitations. *Handbook of RAFT Polymerization* **2008**, 315-372.
52. Such, G. K.; Evans, R. A.; Davis, T. P., The use of block copolymers to systematically modify photochromic behavior. *Macromolecules* **2006**, *39* (26), 9562-9570.
53. Pham, B. T.; Such, C. H.; Hawket, B. S., Synthesis of polymeric janus nanoparticles and their application in surfactant-free emulsion polymerizations. *Polymer Chemistry* **2015**, *6* (3), 426-435.
54. Lu, F.; Luo, Y.; Li, B., A Facile Route to Synthesize Highly Uniform Nanocapsules: Use of Amphiphilic Poly(acrylic acid)-block-polystyrene RAFT Agents to Interfacially Confine Miniemulsion Polymerization. *Macromolecular Rapid Communications* **2007**, *28* (7), 868-874.
55. Van de Wetering, P.; Zuidam, N.; Van Steenberg, M.; Van der Houwen, O.; Underberg, W.; Hennink, W., A mechanistic study of the hydrolytic stability of poly(2-(dimethylamino) ethyl methacrylate). *Macromolecules* **1998**, *31* (23), 8063-8068.
56. Carlsson, L.; Fall, A.; Chaduc, I.; Wågberg, L.; Charleux, B.; Malmström, E.; D'Agosto, F.; Lansalot, M.; Carlmark, A., Modification of cellulose model surfaces by cationic polymer latexes prepared by RAFT-mediated surfactant-free emulsion polymerization. *Polymer Chemistry* **2014**, *5* (20), 6076-6086.
57. Bout, A.; Valerio, D.; Scholte, B., In vivo transfer and expression of the lacZ gene in the mouse lung. *Experimental Lung Research* **1993**, *19* (2), 193-202.
58. Sahnoun, M.; Charreyre, M. T.; Veron, L.; Delair, T.; D'Agosto, F., Synthetic and characterization aspects of dimethylaminoethyl methacrylate reversible addition fragmentation chain transfer (RAFT) polymerization. *Journal of Polymer Science Part A: Polymer Chemistry* **2005**, *43* (16), 3551-3565.
59. Dutertre, F.; Boyron, O.; Charleux, B.; Chassenieux, C.; Colombani, O., Transforming Frozen Self-Assemblies of Amphiphilic Block Copolymers Into Dynamic pH-Sensitive Micelles. *Macromolecular Rapid Communications* **2012**, *33* (9), 753-759.
60. Goh, S.; Liu, Y.; Lee, S.; Huan, C., Miscibility and Interactions in Blends and Complexes of Poly(*N*-acryloyl-*N'*-phenylpiperazine) with Acidic Polymers. *Macromolecules* **1999**, *32* (25), 8595-8602.

61. Zhai, M.; Chen, Y.; Yi, M.; Ha, H., Swelling behaviour of a new kind of polyampholyte hydrogel composed of dimethylaminoethyl methacrylate and acrylic acid. *Polymer International* **2004**, *53* (1), 33-36.
62. Khutoryanskiy, V. V.; Mun, G. A.; Nurkeeva, Z. S.; Dubolazov, A. V., pH and salt effects on interpolymer complexation via hydrogen bonding in aqueous solutions. *Polymer International* **2004**, *53* (9), 1382-1387.
63. Bajomo, M.; Robb, I.; Steinke, J. H.; Bismarck, A., Fully Reversible pH-Triggered Network Formation of Amphoteric Polyelectrolyte Hydrogels. *Advanced Functional Materials* **2011**, *21* (1), 172-176.
64. Zhang, X.; Xiao, Y.; Lang, M., Hydrogen bonding interaction induced complexation of mPEG-b-PAA and star PDMAEMA-*b*-poly(HEMA-*g*-PCL) hybrid micelles in water. *Journal of Macromolecular Science, Part A* **2014**, *51* (1), 63-75.
65. Liu, Y.-Y.; Shao, Y.-H.; Lü, J., Preparation, properties and controlled release behaviors of pH-induced thermosensitive amphiphilic gels. *Biomaterials* **2006**, *27* (21), 4016-4024.
66. Deng, L.; Zhai, Y.; Guo, S.; Jin, F.; Xie, Z.; He, X.; Dong, A., Investigation on properties of P(MAA-co-DMAEMA)-*g*-EG polyampholyte nanogels. *Journal of Nanoparticle Research* **2009**, *11* (2), 365-374.
67. Moad, G.; Barner-Kowollik, C., The Mechanism and Kinetics of the RAFT Process: Overview, Rates, Stabilities, Side Reactions, Product Spectrum and Outstanding Challenges. *Handbook of RAFT Polymerization* **2008**.
68. Li, T.; Zhou, C.; Jiang, M., UV absorption spectra of polystyrene. *Polymer Bulletin* **1991**, *25* (2), 211-216.
69. Stuart, M. A. C.; Huck, W. T.; Genzer, J.; Müller, M.; Ober, C.; Stamm, M.; Sukhorukov, G. B.; Szleifer, I.; Tsukruk, V. V.; Urban, M., Emerging applications of stimuli-responsive polymer materials. *Nature Materials* **2010**, *9* (2), 101-113.
70. De las Heras Alarcón, C.; Pennadam, S.; Alexander, C., Stimuli responsive polymers for biomedical applications. *Chemical Society Reviews* **2005**, *34* (3), 276-285.
71. Hoffman, A. S., The origins and evolution of “controlled” drug delivery systems. *Journal of Controlled Release* **2008**, *132* (3), 153-163.
72. Ista, L.; Lopez, G., Lower critical solubility temperature materials as biofouling release agents. *Journal of Industrial Microbiology & Biotechnology* **1998**, *20* (2), 121-125.
73. Anker, J. N.; Hall, W. P.; Lyandres, O.; Shah, N. C.; Zhao, J.; Van Duyne, R. P., Biosensing with plasmonic nanosensors. *Nature Materials* **2008**, *7* (6), 442-453.
74. Barker, S. L.; Ross, D.; Tarlov, M. J.; Gaitan, M.; Locascio, L. E., Control of flow direction in microfluidic devices with polyelectrolyte multilayers. *Analytical Chemistry* **2000**, *72* (24), 5925-5929.
75. Schild, H. G., Poly(N-isopropylacrylamide): experiment, theory and application. *Progress in Polymer Science* **1992**, *17* (2), 163-249.
76. Yamato, M.; Utsumi, M.; Kushida, A.; Konno, C.; Kikuchi, A.; Okano, T., Thermo-responsive culture dishes allow the intact harvest of multilayered keratinocyte sheets without disperse by reducing temperature. *Tissue Engineering* **2001**, *7* (4), 473-480.

77. Plamper, F. A.; Ruppel, M.; Schmalz, A.; Borisov, O.; Ballauff, M.; Müller, A. H., Tuning the thermoresponsive properties of weak polyelectrolytes: aqueous solutions of star-shaped and linear poly(*N,N*-dimethylaminoethyl methacrylate). *Macromolecules* **2007**, *40* (23), 8361-8366.
78. Zhuang, J.; Gordon, M. R.; Ventura, J.; Li, L.; Thayumanavan, S., Multi-stimuli responsive macromolecules and their assemblies. *Chemical Society Reviews* **2013**, *42* (17), 7421-7435.
79. Loh, X. J., Poly(DMAEMA-*co*-PPGMA): Dual-responsive “reversible” micelles. *Journal of Applied Polymer Science* **2013**, *127* (2), 992-1000.
80. Fournier, D.; Hoogenboom, R.; Thijs, H. M.; Paulus, R. M.; Schubert, U. S., Tunable pH-and temperature-sensitive copolymer libraries by reversible addition-fragmentation chain transfer copolymerizations of methacrylates. *Macromolecules* **2007**, *40* (4), 915-920.
81. Yuk, S. H.; Cho, S. H.; Lee, S. H., pH/temperature-responsive polymer composed of poly(*N,N*-dimethylamino) ethyl methacrylate-*co*-ethylacrylamide). *Macromolecules* **1997**, *30* (22), 6856-6859.
82. de Souza, J. C. P.; Naves, A. F.; Florenzano, F. H., Specific thermoresponsiveness of PMMA-block-PDMAEMA to selected ions and other factors in aqueous solution. *Colloid and Polymer Science* **2012**, *290* (13), 1285-1291.
83. Xue, Y.; Wei, D.; Zheng, A.; Guan, Y.; Xiao, H., Study of Stimuli-Sensitivities of Amphiphilic Modified Star Poly [*N, N*-(Dimethylamino) ethyl Methacrylate] and Its Ability of DNA Complexation. *Journal of Macromolecular Science, Part A* **2014**, *51* (11), 898-906.
84. Zhang, C.; Maric, M., Synthesis of stimuli-responsive, water-soluble poly[2-(dimethylamino) ethyl methacrylate/styrene] statistical copolymers by nitroxide mediated polymerization. *Polymers* **2011**, *3* (3), 1398-1422.





# Chapter III

## FORMATION OF IRON OXIDE CLUSTERS



TABLE OF CONTENTS

<b>1. Introduction</b> .....	<b>118</b>
<b>2. Bibliographic review</b> .....	<b>118</b>
<b>2.1. Iron oxide nanoparticles</b> .....	<b>118</b>
2.1.1. <i>Structure of iron oxide</i> .....	118
2.1.2. <i>Properties of IONPs</i> .....	119
2.1.3. <i>Synthesis of IONPs</i> .....	122
2.1.3.1. <i>Co-precipitation</i> .....	123
2.1.3.2. <i>Thermodecomposition</i> .....	123
2.1.3.3. <i>Hydrothermal and solvothermal processes</i> .....	124
2.1.4. <i>Surface modification</i> .....	125
<b>2.2. Cluster formation</b> .....	<b>126</b>
2.2.1. <i>Polyelectrolyte/iron oxide self-assembly</i> .....	126
2.2.2. <i>Solvent displacement</i> .....	127
2.2.3. <i>Emulsification/solvent evaporation</i> .....	128
<b>2.3. Selected synthetic strategy</b> .....	<b>130</b>
<b>3. Experimental Section</b> .....	<b>132</b>
<b>3.1. Materials</b> .....	<b>132</b>
<b>3.2. Methods</b> .....	<b>132</b>
3.2.1. <i>Small-scale preparation of IO clusters</i> .....	132
3.2.2. <i>Scale-up process for the preparation of IO clusters</i> .....	133
3.2.3. <i>Yield of cluster formation</i> .....	133
3.2.4. <i>Purification of the magnetic clusters</i> .....	133
<b>3.3. Characterization techniques</b> .....	<b>134</b>
3.3.1. <i>Dynamic light scattering (DLS)</i> .....	134
3.3.2. <i>Zeta potential measurements</i> .....	135
3.3.3. <i>Electron microscopy</i> .....	135
3.3.4. <i>Thermogravimetric analysis (TGA)</i> .....	136
3.3.5. <i>Raman spectroscopy</i> .....	136
3.3.6. <i>Superconducting quantum interference device (SQUID) analysis</i> .....	136
3.3.7. <i>Fourier Transform Infrared (FTIR) spectroscopy</i> .....	137
3.3.8. <i>X-ray diffractometry (XRD)</i> .....	137
<b>4. Results and Discussion</b> .....	<b>137</b>
<b>4.1. Characterization of the commercial iron oxide nanoparticles</b> .....	<b>137</b>
4.1.1. <i>Crystalline structure</i> .....	137
4.1.2. <i>Evaluation of chemical modification</i> .....	138
4.1.3. <i>Particle size and morphology</i> .....	139



4.1.4. Magnetic properties .....	141
<b>4.2. PDMAEMA-based iron oxide clusters.....</b>	<b>142</b>
4.2.1. Effect of sonication time .....	144
4.2.2. Effect of sonication power .....	145
4.2.3. Effect of macroRAFT concentration.....	148
4.2.4. Effect of pH.....	154
4.2.5. Scale up experiments .....	157
<b>4.3. PAA-based iron oxide clusters.....</b>	<b>158</b>
4.3.1. Effect of macroRAFT concentration.....	158
4.3.2. Effect of the $[NaOH]/[PAA-b-PS-TTC]$ ratio .....	162
<b>4.4. Cluster preparation in the presence of hydrophilic macroRAFTs: influence of the PS block</b>	<b>165</b>
<b>4.5. P(AA-co-DMAEMA)-based clusters.....</b>	<b>168</b>
<b>4.6. Surface properties .....</b>	<b>171</b>
<b>5. Conclusions .....</b>	<b>172</b>
<b>References .....</b>	<b>175</b>

## **1. INTRODUCTION**

The formation of iron oxide clusters using amphiphilic block copolymers as stabilizers is described in this chapter. A bibliographic review covering the main approaches used for the synthesis of iron oxide nanoparticles and the various strategies for preparing IO clusters is first presented. Among these approaches, the emulsification/solvent evaporation process appeared to be a straightforward method and was selected for our work. Hence aqueous dispersions of iron oxide clusters were then prepared using the amphiphilic macroRAFTs previously synthesized as stabilizers. More specifically, the effects of sonication power and time, macroRAFT concentration and composition, and pH on cluster size and size distribution were studied. The surface properties of the clusters were then evaluated by means of zeta potential measurements under different pH and ionic strength conditions.

## **2. BIBLIOGRAPHIC REVIEW**

### **2.1. Iron oxide nanoparticles**

Iron oxide nanoparticles (IONPs) are particles with diameters between about 1 and 100 nanometers. Among the various crystalline forms of iron oxide, the three main ones found in nature are magnetite ( $\text{Fe}_3\text{O}_4$ ) and its oxidized forms maghemite ( $\gamma\text{-Fe}_2\text{O}_3$ ) and hematite ( $\alpha\text{-Fe}_2\text{O}_3$ ). Magnetite and maghemite have attracted extensive interest due to their stronger magnetism and their potential applications in many fields, for instance as new supports for catalysts, in drug delivery, or for magnetic resonance imaging (MRI) and *in vitro* or *in vivo* immunoassays.<sup>1-3</sup>

#### *2.1.1. Structure of iron oxide*

Iron oxide structure can be described as an arrangement of close-packed planes of oxygen or hydroxide anions, with iron cations in octahedral or tetrahedral interstitial sites (Figure 40). In hematite, Fe(III) ions are occupying octahedral sites surrounded by four oxygen atoms in an hexagonal close-packed arrangement.<sup>4</sup> For magnetite and maghemite, the oxygen anions will be close-packed in a cubic arrangement with Fe cations filling the gaps. Magnetite,  $\text{Fe}_3\text{O}_4$ , has an inverse spinel structure in which Fe(III) ions are randomly distributed in octahedral and tetrahedral sites, and Fe(II) ions arranged in octahedral sites.  $\gamma\text{-Fe}_2\text{O}_3$  can be considered as a Fe(II) deficient structure of magnetite, presenting a spinel structure with vacancies in cation

sublattice, with two filled sites being followed by one vacant site, and Fe(III) regularly arranged at tetrahedral sites.<sup>5</sup>

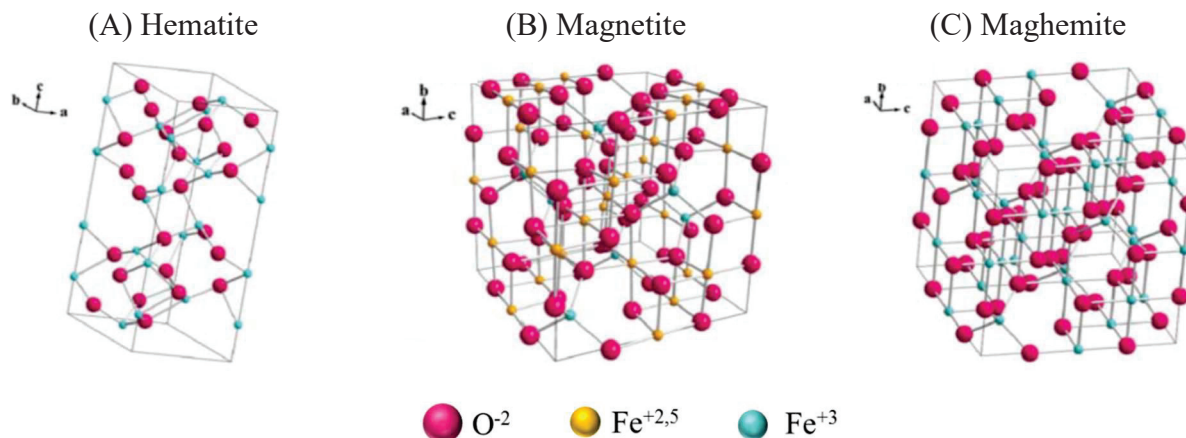


**Figure 40** – Crystal structure of: (A) hematite, (B) magnetite and (C) maghemite. Reprinted from Ref<sup>6</sup> with permission from RCS.

### 2.1.2. Properties of IONPs

Iron oxide nanoparticles are materials with interesting optical, thermal and especially magnetic properties, which have been studied for many years and largely exploited in the optical, biological and biomedical fields.<sup>1-3</sup>

Optical properties of iron oxide nanoparticles are very important for the development of solar radiation filters, electrochromic devices and photoelectrochemical generation of hydrogen. An example among these optical properties is the Bragg diffraction phenomenon, which consists in color appearance in crystalline materials when the periodicity of IO particles matches the wavelength of the incident light. Based on this concept, iron oxide particles have been employed for the development of multi-color optical devices, in which the emitted color can be changed by varying the strength of the external magnetic field and the particle size.<sup>7</sup>

The magnetic property is the most exploited feature of IONPs, and this is true in diverse fields. This characteristic is linked to the iron atom, which has a strong magnetic moment due to four unpaired electrons in its 3d orbitals. There are various forms of magnetism depending on magnetic dipole arrangements as shown in Figure 41. When an iron oxide crystal is exposed to a magnetic field, the magnetic dipoles will align showing a net magnetic moment. If, after magnetic field removal, the magnetic dipoles stay aligned and still exhibit a net magnetic moment (Figure 41B), these materials are classified as ferromagnetic. On the other hand, materials that present anti-ferromagnetism possess no net magnetic moment due to anti-parallel alignment of the magnetic dipoles with the same magnitude (Figure 41C). When an

anti-parallel alignment of magnetic dipoles of different intensities is obtained, the material is defined as ferrimagnetic showing a small net magnetic moment (Figure 41D).

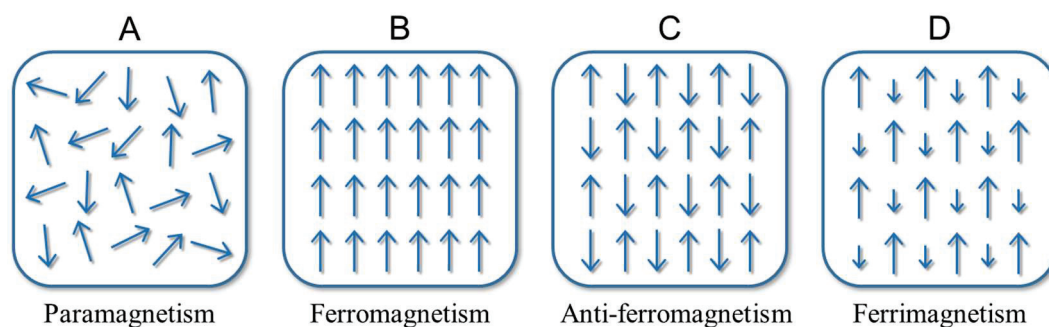
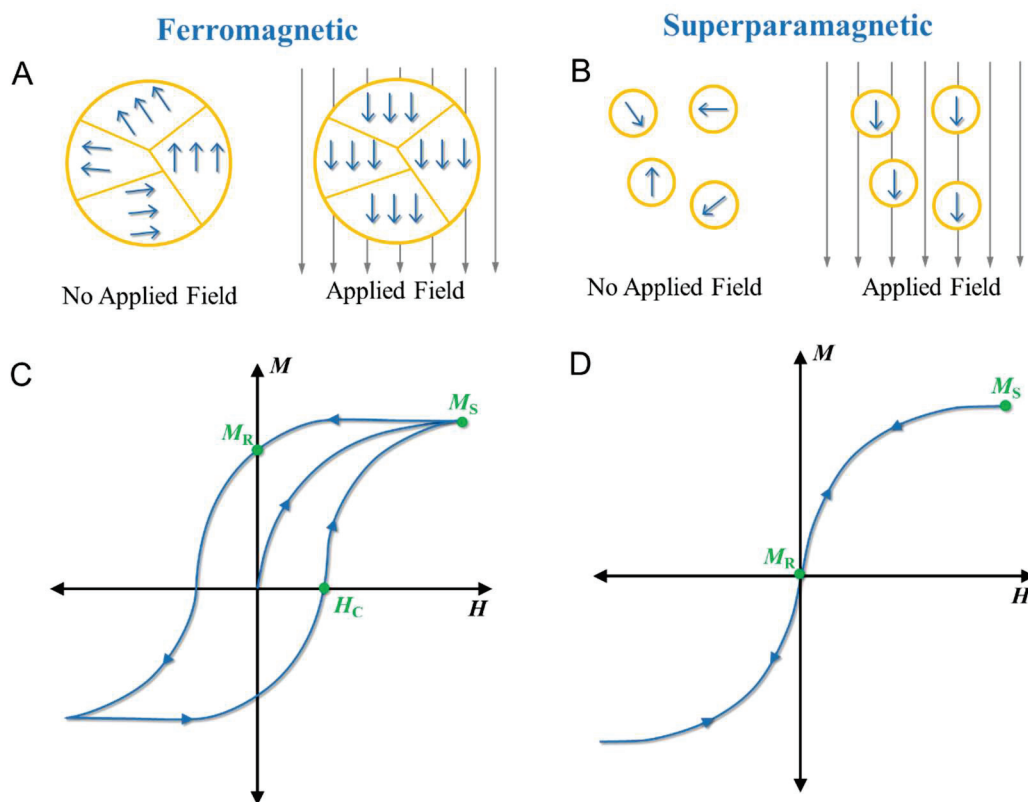


Figure 41 – Different arrangements of individual atomic magnetic moments.

Magnetization,  $M$ , is defined by the vector sum of all magnetic moments of the atoms per unit of volume (or mass) of the material. A bulk magnetic material is composed of domains that present their magnetization in a multi-domain structure, as schematically represented in Figure 42A.<sup>4</sup> When this bulk material presents ferromagnetism and is exposed to a magnetic field ( $H$ ), the domains will be aligned with the magnetic field reaching a magnetization at saturation ( $M_s$ ) (Figure 42C). Once the field removed, a remanent magnetization is still present, but less intense than  $M_s$  due to the individual rearrangement of each domain, leading to a hysteresis loop in the magnetization curves as shown in Figure 42C. Nanoparticles with a small size, under the superparamagnetism size ( $< D_s$ ), present a single domain structure (Figure 42B). At sufficiently high temperature (above the blocking temperature,  $T_B$ ), the thermal energy leads to a rotation of the nanoparticles, enough to reach the net loss of magnetization in the absence of magnetic field.<sup>8</sup> Therefore, no hysteresis is observed for the magnetization curve in the superparamagnetic case, with the magnetization dropping to its initial value after removal of the magnetic field (Figure 42D). Superparamagnetism is an important property for the use of magnetic particles, notably in biological applications, because once the magnetic field is removed the intermagnetic forces among the particles are also suppressed, preventing their agglomeration, and allowing their redispersion in the suspension medium.<sup>9</sup>

Furthermore, IONPs have interesting thermal properties that have been exploited for therapeutical purposes. Hyperthermia is the ability of IONPs to produce heat when exposed to an oscillating magnetic field.<sup>10</sup> Indeed, this property can be exploited for *in vivo* treatments, in which the increment of temperature on the site of the tumor tissue will destroy the pathological cells, because diseased cells are usually more sensitive to temperature than

healthy tissues. It is important to point out that the nanoparticles employed in *in vivo* systems have to be biocompatible.<sup>4</sup>



**Figure 42** – Scheme of a magnetic material presenting either (A) multi-domain or (B) single-domain structures. Typical magnetization curves of materials with either (C) ferromagnetic or (D) superparamagnetic properties.

Magnetic properties of IONPs can also be exploited in application such as MRI where IONPs act as contrast agents. As defined by Lee and Hyeon<sup>11</sup> a “magnetic resonance image typically consists of pixels or voxels representing the nuclear magnetic resonance (NMR) signal intensity of the hydrogen atoms in water and fat of living organisms”. The technique is based on first applying a strong magnetic field (1.5~3.0 T) to the organism, which will induce the alignment of almost all nuclear spins of hydrogen from water or fat parallel to the magnetic field, as illustrated in Figure 43A (spins aligning in the same direction Z than the magnetic field  $B_0$ ). The nuclei are then excited by a resonant radiofrequency (RF) pulse wave in an instant time represented as  $t = 0$  in the graphs of Figure 43C and 43D, which generates a transverse magnetization ( $M_{xy}$ ) and, at the same time, decreases the longitudinal ( $M_z$ ) magnetization. The instant after the pulse is represented by yellow circles in Figure 43C and 43D, leading to spin conformation shown in the yellow scheme in Figure 43B. When the

radiofrequency wave is removed, the excited nuclear spins tend to return to their initial state (highlighted in light-pink in Figure 43B). The time of relaxation for the longitudinal magnetization to recover 63% of their initial state is represented by  $T_1$  (Figure 43C). As shown in Figure 3D,  $T_2$  is the time for the transverse magnetization to reach 37% of the excited state.

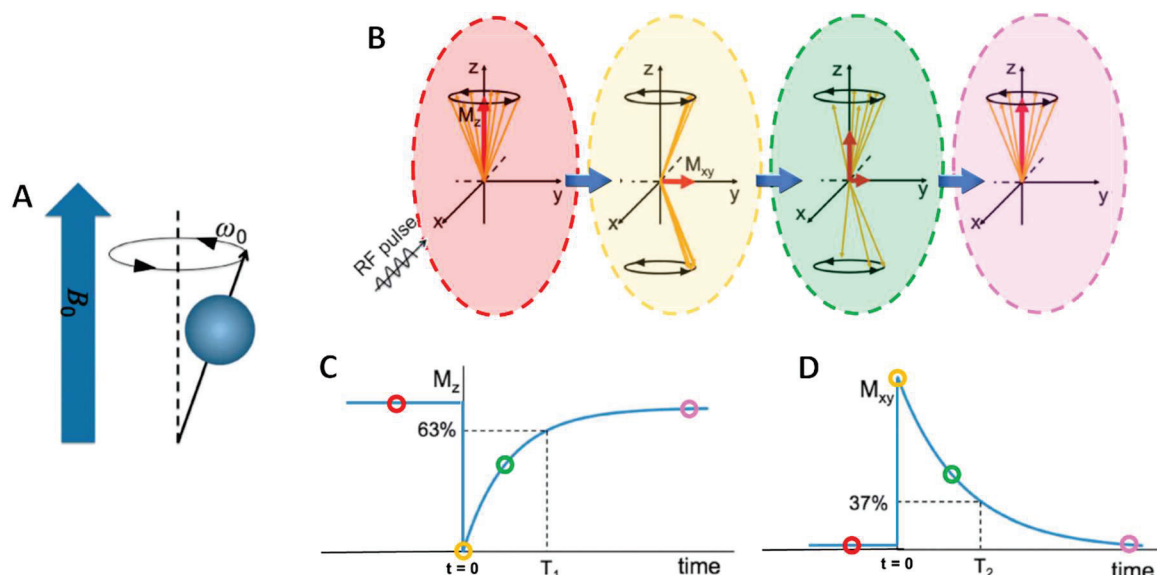


**Figure 43** – Principles of MRI. (A) Hydrogen nuclear spin oriented under a strong magnetic field  $B_0$ . (B) Schematic representation of hydrogen nuclear spins in relaxation instants before (red) and after excitation by a resonant radiofrequency pulse wave (yellow, green and pink) showing the longitudinal and transverse magnetizations. Determination of: (C)  $T_1$  and (D)  $T_2$  relaxation times. Adapted from Ref<sup>11</sup>.

Superparamagnetic nanoparticles have been employed as contrast agent in MRI diagnostics. Under a magnetic field the magnetized nanoparticles induce local magnetic field inhomogeneities, which accelerate the dephasing rate of surrounding water.<sup>11</sup> Hence, the contrast will be enhanced at vicinity of the particles. Furthermore, the possibility of functionalization of the IONP surface, e.g. via immobilization of biomolecules or incorporation of a responsive polymer, can lead to specific interaction with a targeted tissue. This approach, also known as targeted MRI, is a promising diagnostic technique to precisely identify the position of tumor cells.<sup>12</sup>

### 2.1.3. Synthesis of IONPs

Iron oxide nanoparticles can be synthesized by two main ways using top-down or bottom-up approaches. The top-down approach is a physical method based on size reduction of a

material to form smaller particles, commonly using a high-energy crusher. Briefly, bulk magnetic iron oxide is mixed with an organic solvent and high amounts of surfactant (10-20 vol %). This mixture is milled for a long period (typically a few weeks) to achieve the expected size reduction. The surfactant plays an important role, not only in preventing particle agglomeration, but also by enhancing the efficiency of the grinding process. However, the obtained particles have a broad size distribution and the method is not very cost-effective.

The bottom-up approach is based on the synthesis of iron oxide nanoparticles from precursory molecules and it is most commonly used. Nanoparticles with better controlled sizes and narrower size distributions are usually obtained by this technique. In this bibliographic review, we will focus on bottom-up methods due to their relevance, describing the main strategies applied to synthesize IONPs.

#### *2.1.3.1. Co-precipitation*

The co-precipitation technique to synthesize IONPs was developed by Massart *et al.*<sup>13</sup> The Massart's method is widely applied due to its simplicity and the mild conditions required for the reaction, which can be carried out in water, under air atmosphere, at room temperature and ambient pressure. The strategy is based on the co-precipitation of iron II and iron III salts in alkali media. The Fe(II):Fe(III) concentration ratio, as well as the concentration and the nature of the base, are critical parameters. The resulting nanoparticles have, in general, small sizes, *i.e.* less than 10 nm in diameter, and satisfactory size distributions.

#### *2.1.3.2. Thermodecomposition*

This synthetic method is based on the decomposition of organometallic complexes in solvents, such as aromatic ethers or hydrocarbons, at high temperatures typically comprised between 200 and 300°C.<sup>14-16</sup> Some examples of precursory molecules are iron(III) acetylacetonate, iron(III) *N*-nitroso-*N*-phenylhydroxylamine and iron pentacarbonyl. This technique usually leads to particles with a narrower size distribution than the ones obtained by the co-precipitation method.

One promising application of iron oxide nanoparticles concerns the next generation of multi-terabit magnetic storage media.<sup>17</sup> However, for this application, well-defined monodisperse nanocrystals are required. Park *et al.*<sup>18</sup> have reported a strategy to synthesize, in a large scale reaction, monodisperse iron oxide nanoparticles. The TEM micrographs of Figure 44 show the monodisperse nanocrystals obtained by this method. Typically, a metal-oleate complex



was first obtained by the reaction of iron(III) chloride and sodium-oleate. Then the resulting complex was slowly heated up to 320°C and aged for 30 min to afford spherical IONPs. The authors observed that at higher temperature, 380°C, 20 nm cube-shaped iron nanocrystals were produced (Figure 44B). The size of the nanoparticles could be controlled by varying the nature of the solvent, *i.e.* the higher the boiling point the bigger the average sizes. Thus, particles from 5 up to 22 nm were successfully prepared. The strategy was also exploited for other transition metal oxides such as manganese and cobalt.

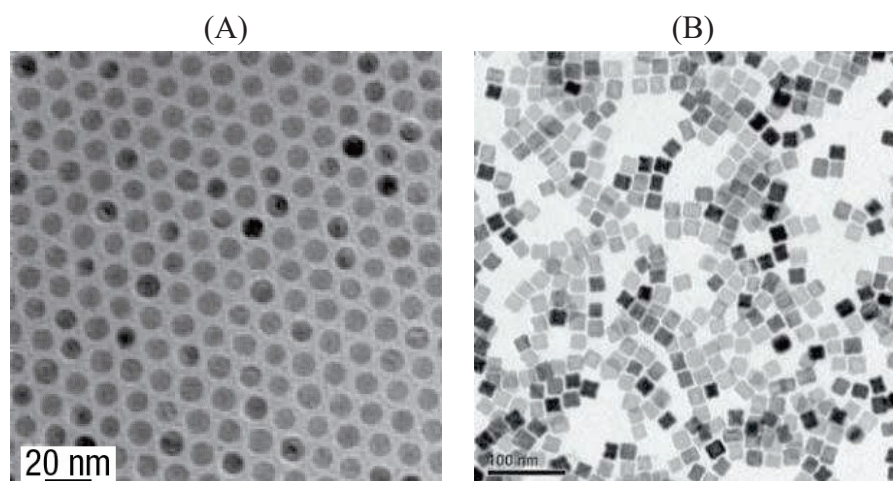


**Figure 44** - TEM micrographs of monodisperse iron oxide nanocrystals synthesized via the thermodecomposition method. (A) Iron oxide nanoparticles and (B) Fe nanocubes prepared from thermodecomposition of iron-oleate complex at 320°C for (A) and 380°C for (B). Reproduced from Ref<sup>18</sup> with permission from Nature Publishing Group.

### 2.1.3.3. *Hydrothermal and solvothermal processes*

The solvothermal method allows the preparation of nanoparticles with controlled size and narrow dispersity. The reaction is performed at high temperatures, typically between 130 and 400 °C, and well above the boiling point of the solvent in a pressurized bottle.<sup>19-22</sup> In such conditions, an equilibrium is established among the solid, liquid and gas phases. Iron oxide formation occurs preferentially at the interfaces, enabling the control of the particle growth, generating well-defined particles. This technique can be considered slow, as the reaction generally runs from 8 up to 72 hours. Usually iron(III) chloride is used as precursor component.<sup>19-22</sup>

Water can also be employed as the solvent in this strategy. In that case, the method is entitled hydrothermal. The temperature of the reaction is lower (100 up to 140 °C) than mentioned above for the solvothermal process. The precursor molecules can be iron chlorides and the

reaction is carried out under alkali conditions.<sup>23, 24</sup> There are also strategies that use precursor molecules able to *in situ* release the alkali, for instance ammonium ferric citrate.<sup>25</sup>

Among the advantages of the solvothermal method is the possibility of *in situ* formation of iron oxide clusters. These clusters are aggregates of iron oxide nanoparticles (magnetite or maghemite) with diameters ranging from 50 to 800 nm. For instance, using this method Deng *et al.*<sup>19</sup> reported the synthesis of IO clusters with sizes varying from 200 nm to 800 nm, which were used for the preparation of multi-color optical devices.<sup>26, 27</sup> Liu *et al.*<sup>20</sup> have also reported the synthesis of iron oxide clusters, ca. 230 nm in diameter, composed of 5 nm iron oxide nanoparticles stabilized by citrate ions. It is important to point out that the solvothermal method employed for cluster preparation has great advantages over conventional methods of iron oxide synthesis, such as thermodecomposition or co-precipitation, as big particles (100-300 nm) with superparamagnetic properties can be obtained. Indeed, the size of the magnetic particles is a crucial parameter in regards to the targeted application in which magnetic separation is needed: the bigger is the particle, the higher is the separation rate.

Iron oxide clusters have been demonstrated to be a good alternative for the preparation of composite particles with high iron oxide content. These composite particles generally present a core-shell morphology with a core of iron oxide cluster and a protective shell coating. The outer-shell can be an inorganic compound, such as silica or titanium dioxide, or an organic polymer.

#### 2.1.4. Surface modification

Despite the high density ( $> 4 \text{ g cm}^{-3}$ ) of iron oxide, it is possible to obtain stable dispersions in water. Their stability is provided by electrostatic repulsion of the ionic charges present at their surface, due to the presence of hydroxyl functions (OH). Indeed, above the isoelectric point, which is around pH 7, the particles are negatively charged due to the formation of  $\text{-O}^-$  groups, whereas below pH 7, the particles are positively charged due to the protonation of the OH groups forming  $\text{-OH}_2^+$ . This pH-dependent surface charge also permits the stabilization of the nanoparticles in water via a wide range of stabilizers such as citrate ions, surfactants, fatty acids in a double-layered conformation, and polymers such as poly(acrylic acid) (PAA) and poly(*N*-vinylpyrrolidone), which provide steric stabilization.<sup>3</sup>

Furthermore, the incorporation of polymers at the surface of iron oxide can not only provide better colloidal stabilization but can also generate smart magnetic particles with additional properties such as thermo-,<sup>28</sup> pH-<sup>29</sup> and  $\text{CO}_2$ -responsiveness<sup>30</sup> depending on the nature of the

polymer. IONPs with stimuli-responsive properties have recently attracted considerable attention because of their great potential in cancer-therapy or diagnostics (MRI),<sup>31</sup> in which *in vivo* tests are carried out.<sup>32</sup> Moreover, the employment of polymers to decorate iron oxide nanoparticles can also be exploited to control their surface properties for biological applications. For instance, biocompounds can be attached to their surface allowing the selective enrichment of enzymes, bacteria, cells or peptides.<sup>33</sup>

## 2.2. Cluster formation

As aforementioned the formation of clusters composed of superparamagnetic iron oxide nanoparticles has been demonstrated to be an important strategy to obtain big particles with superparamagnetic properties. In addition to the solvothermal process described above, physical methods have also been reported for the formation of IO clusters. The main strategies to assemble iron oxide nanoparticles into clusters will be described in the following paragraphs.

### 2.2.1. Polyelectrolyte/iron oxide self-assembly

The formation of iron oxide clusters via self-assembly using polyelectrolytes is schematically represented in Figure 45A. This approach is first based on the modification of bare iron oxide nanoparticles with an anionic polyelectrolyte, e.g. PAA or poly(sodium styrene sulfonate).<sup>34</sup> In a second step, a solution of a cationic polymer is added to the IO dispersion. Cluster formation can be induced either by direct interaction between the cationic and the anionic polyelectrolytes<sup>34</sup> under appropriate pH conditions or by a gradual change of the physicochemical properties of the surrounding solution such as ionic strength<sup>35, 36</sup> or pH<sup>37</sup> in order to destabilize the IO particles and promote cluster formation.

The group of Berret has extensively studied the formation of IO clusters by polyelectrolyte complexation.<sup>35, 36, 39-46</sup> The strategy reported by Fresnais *et al.*<sup>35, 36</sup> relies on, first, modification of iron oxide nanoparticles with PAA ( $2 \text{ kg mol}^{-1}$ ). Then, a solution of poly(trimethylammonium ethylacrylate)-*b*-poly(acrylamide) (PTEA<sub>11K</sub>-*b*-PAM<sub>30K</sub>) block copolymers is added to the IO dispersion and the ionic strength adjusted with ammonium chloride to 1 M. With this high ionic strength, the electrostatic charges of the polyelectrolyte are screened and stabilization is ensured by steric repulsion. The salt concentration is then gradually decreased via either dilution or dialysis restoring the charges of the polyelectrolytes.

Hence, electrostatic interaction between these polymers gradually increases leading to precipitation of the individual IONPs into clusters as shown in the TEM micrographs of Figure 45B. This strategy was also exploited to generate iron oxide rods, as shown in Figure 45C, in which the desalting process was carried out under a magnetic field.<sup>38, 47</sup>

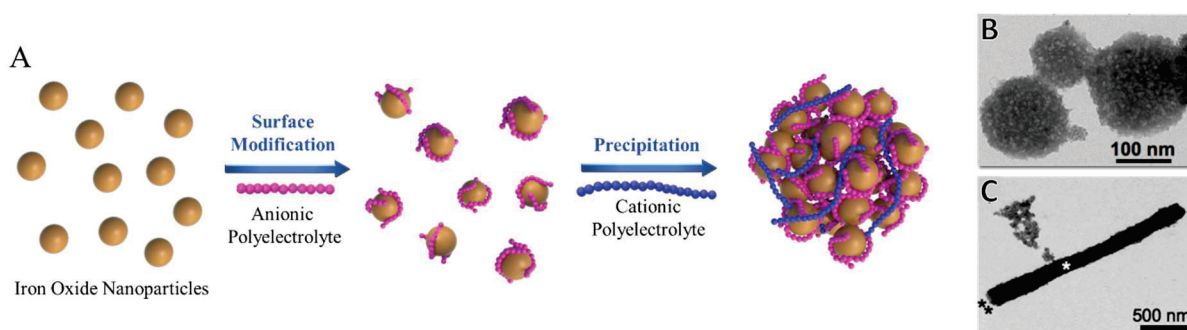


**Figure 45** – Preparation of iron oxide clusters via polyelectrolyte complexation. (A) Schematic representation of the overall process, and (B, C) TEM micrographs of the clusters formed in absence (B) or in presence (C) of a magnetic field. Reproduced with permission from (B) Wiley<sup>35</sup> and (C) RCS.<sup>38</sup>

### 2.2.2. Solvent displacement

The technique of solvent displacement has been widely employed for the preparation of block copolymer assemblies with different morphologies such as micelles, vesicles, fibers, lamellar crystals, among others.<sup>48</sup> The polymer is first solubilized in a good solvent, such as THF or DMF. The polarity of the medium is then increased, either via dialysis or by addition of a co-solvent of higher polarity (e.g., water), leading to a controlled precipitation of the polymer in nano- or micro-objects presenting different morphologies. This approach has been also exploited for the preparation of iron oxide clusters.<sup>37, 49, 50</sup> For example, Kim *et al.*<sup>49</sup> have reported the use of the solvent displacement strategy (outlined in Figure 46A) for the preparation of clusters (so-called magnetomicelles by the authors) composed of  $\gamma$ -Fe<sub>2</sub>O<sub>3</sub> nanoparticles ( $D_n = 11$  nm) and PS<sub>250</sub>-*b*-PAA<sub>13</sub> amphiphilic block copolymers. The IO nanoparticles and the amphiphilic block copolymer were first dispersed in a mixture of DMF and THF. Water was then added to the system leading to self-assembly of PS-*b*-PAA into micelles loaded with IONPs. A crosslinking reaction between the carboxylic groups of PAA and the crosslinker 2,2-(ethylenedioxy)bis(ethylamine), in the presence of (3-dimethylaminopropyl)carbodiimide methiodide as activator, was then carried out fixing permanently the structure. The authors showed that by varying the PS-*b*-PAA/IONP ratio, it

was possible to control the number of IONPs into the micelle core, from 3 up to 60 nanoparticles per micelle.

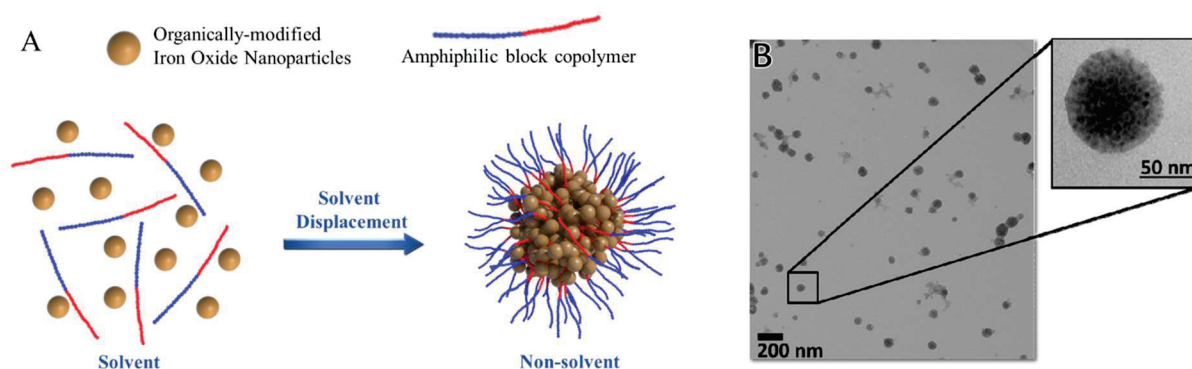


**Figure 46** – Magnetomicelles prepared via amphiphilic block copolymers self-assembly using the solvent displacement method. (A) Schematic representation of the assembly process and (B) TEM micrographs of  $\gamma$ -Fe<sub>2</sub>O<sub>3</sub> clusters prepared via the self-assembly of PS-*b*-PAA. Reproduced from Ref<sup>50</sup> with permission from ACS.

The solvent displacement method has also been employed by Pavia-Sanders *et al.*<sup>50</sup> for the preparation of magnetomicelles, shown in the TEM micrographs of Figure 46B. The resulting clusters were employed in the purification, via magnetic separation, of oil-contaminated water. In a similar strategy Rocha *et al.*<sup>51</sup> have synthesized magnetic micelles via the self-assembly of poly(ethylene glycol)-*b*-poly(4-vinylpyridine) (PEG-*b*-P4VP) in the presence of IONPs. The self-assembly was conducted via two different methods: (1) basic titration in which micelles were formed at pH higher than 4.5 or (2) solvent displacement via dialysis. The magnetic properties of the resulting clusters were evaluated by relaxometry measurements showing that the aggregates possessed larger relativity ratios ( $r_1/r_2$ ) than single IONPs. It is important to point out that the solvent displacement strategy is generally carried out in dilute conditions (IO contents typically lower than about 1 wt%), and is time-consuming, which is one strong limitation of the process.

### 2.2.3. Emulsification/solvent evaporation

Nanoemulsions are usually prepared by high-energy methods using mechanical devices able to break the oil phase into small droplets, namely high-pressure homogenizers, rotor–stators or ultrasound generators. The use of high-energy homogenization processes has been largely exploited in the synthesis of latex particles via miniemulsion polymerization.<sup>52, 53</sup> In miniemulsion polymerization, hydrophobic monomer droplets (< 300 nm) stabilized by



amphiphilic molecules, are first prepared by emulsification, and subsequently polymerized leading to the formation of polymer latex particles. Miniemulsions are kinetically stable systems, which are subject to various destabilization mechanisms. One of these mechanisms is known as Ostwald ripening. During ripening, molecules from the small droplets diffuse to the larger ones through the continuous phase. This diffusional degradation can occur in a short interval of time (typically a few minutes), broadening the dispersity of droplet sizes or even leading to complete loss of stability. For direct miniemulsion systems, the use of an hydrophobe, such as a long chain hydrocarbon (e.g. hexadecane or dodecyl acrylate), allows building up an osmotic pressure inside the droplets retarding the Ostwald ripening process up to several months.<sup>52</sup> By analogy with miniemulsion polymerization, miniemulsification procedures have also been used recently to form iron oxide clusters. Such clusters can be further engaged in a polymerization process where they act as seeds.<sup>54-60</sup> In a typical procedure, schematically represented in Figure 47A, a ferrofluid<sup>j</sup> is first prepared by dispersing organically-modified iron oxide nanoparticles in a non-polar solvent, such as toluene or octane. This ferrofluid is then introduced in an aqueous solution containing a stabilizer, such as SDS, resulting in a two-phase system, which is next emulsified using high-energy methods, resulting in solvent droplets loaded with iron oxide nanoparticles. In a second step, the organic solvent is eliminated resulting in an aqueous suspension of iron oxide clusters stabilized by the surfactant molecules that were initially used to stabilize the oil droplets. Several authors have employed the (mini)emulsification/solvent evaporation method for the preparation of iron oxide clusters.

For instance Ramirez *et al.*<sup>60</sup> reported the formation of iron oxide clusters with diameters comprised between 40 and 200 nm using this method. First, oleic acid (OA)-modified IONPs were dispersed in octane forming an organic ferrofluid. Then, the ferrofluid was sonicated in presence of an aqueous solution of SDS forming the miniemulsion droplets. The iron oxide cluster aqueous dispersion was formed after solvent evaporation.<sup>60</sup> The diameter of the IO aggregates was controlled by the amount of oleic acid present in the ferrofluid and the SDS concentration. Paquet *et al.*<sup>55, 56</sup> reported a similar strategy for the preparation of iron oxide cluster dispersions but using toluene instead of octane. After toluene evaporation, well-defined iron oxide clusters were obtained showing a spherical morphology (Figure 47B). The

---

<sup>j</sup> Ferrofluids contain nanometer sized superparamagnetic particles dispersed in aqueous or organic media which has no net magnetic moment except when it is under the influence of an applied field.<sup>5</sup>

cluster dispersion was then used as seed in an emulsion polymerization resulting in core-shell particles composed of a magnetic core surrounded by a protective polymeric shell.

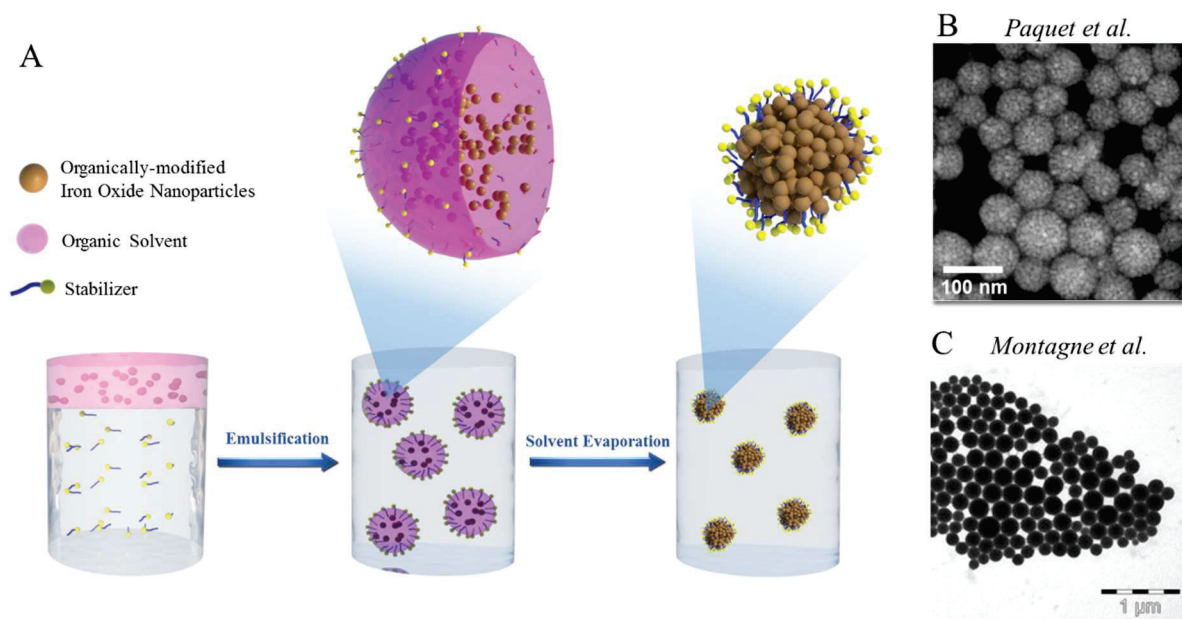


**Figure 47** – Preparation of iron oxide clusters by emulsification/solvent evaporation. (A) Synthetic route and (B, C) TEM micrographs of typical examples of IO clusters obtained by this method. Reproduced with permission from (B) ACS<sup>56</sup> and (C) Wiley.<sup>61</sup>

Montagne *et al.*<sup>54, 61</sup> employed the same strategy for the preparation of iron oxide/polystyrene composite particles. A magnetic emulsion obtained from the dispersion of an octane-based ferrofluid into an aqueous solution of nonyl phenol ether surfactant (NP10) was first formed by using a high-energy mixing process (Figure 47C).<sup>54</sup> Styrene and initiator were then added to the magnetic emulsion and the polymerization was conducted at 80°C resulting in highly loaded iron oxide magnetic particles.<sup>61</sup>

### 2.3. Selected synthetic strategy

Among the various strategies described above, the emulsification/solvent evaporation process appears to be the most appropriate method to achieve our goal. This method indeed presents several advantages. First, compared to the solvent displacement technique, the emulsification/solvent evaporation process allows cluster suspensions to be obtained at much higher solids content. Second, it requires milder temperature conditions compared to the solvothermal process. Moreover the high temperatures (> 130°C) employed in the solvothermal method could degrade the RAFT moiety of the amphiphilic macroRAFT agent. At last, this technique can be considered as a straightforward and efficient method, easy to



implement at the lab scale, and which can be completed in a few hours (the solvent displacement process may take several days).

On the other hand, most of the emulsification/solvent evaporation processes reported in the literature for the preparation of iron oxide clusters involve the use of conventional surfactants (e.g., SDS) to stabilize the emulsion droplets and the resulting clusters. However, molecular surfactants are undesirable for many applications as they can negatively affect the properties of the final material. In addition, as mentioned in Chapter 1 of this thesis, controlling the surface properties of the magnetic beads is of prime importance for biological applications. Hence, by using conventional surfactants, the assessment of different surface functionalizations can be considered limited. To address this issue, we propose to use amphiphilic macroRAFT agents as stabilizers. As presented in Chapter 2, the versatility of RAFT polymerization allows the synthesis of well-defined amphiphilic macroRAFT copolymers. It is expected that the hydrophobic part of the block copolymer will be buried into the toluene droplets and will precipitate onto the surface of the clusters after solvent evaporation, while the hydrophilic part will provide colloidal stability to the formed clusters. Besides, using this strategy, IO clusters with different surface functionalizations can be formed by varying the nature of the hydrophilic block (namely PAA, PDMAEMA and copolymers of DMAEMA and AA) as illustrated in Figure 48. In particular, the

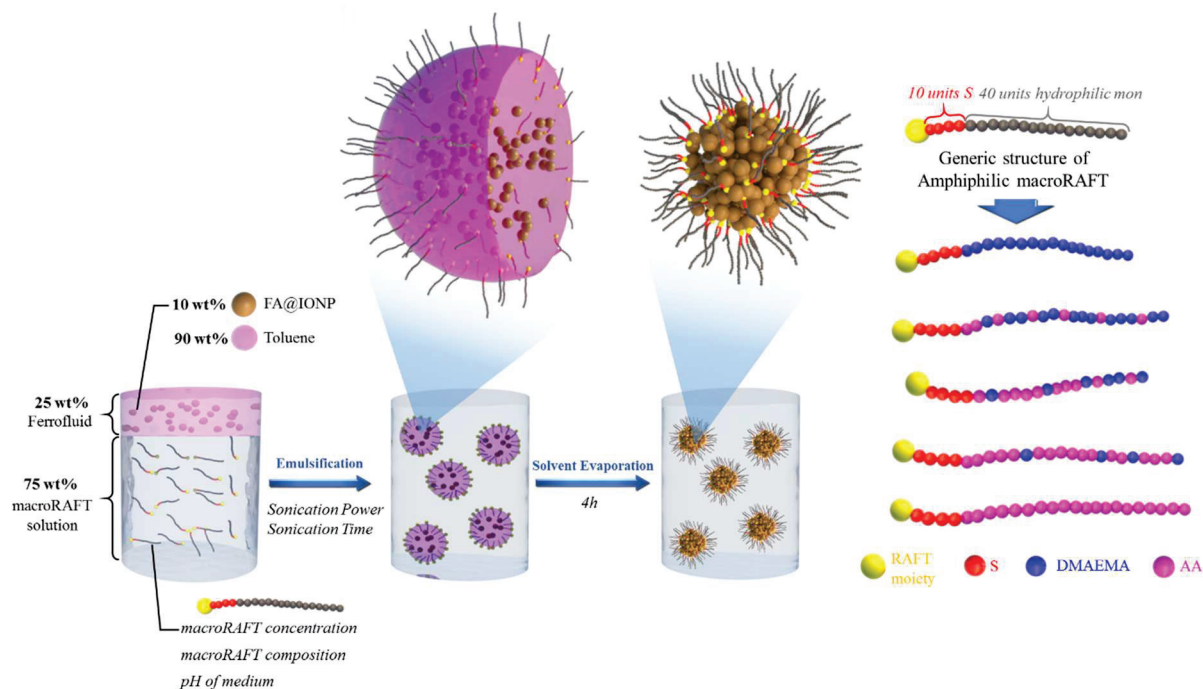


**Figure 48** – Synthetic representation of our strategy. Formation of iron oxide clusters stabilized with macroRAFT agents via emulsification/solvent evaporation (FA@IONPs: fatty acid-modified iron oxide nanoparticles).

pH-responsiveness of the hydrophilic part of the macroRAFT copolymers can lead to the formation of smart clusters with pH-responsive properties. This property will be exploited in Chapter 5 for the capture and trigger release of bacteria via magnetic separation.

### **3. EXPERIMENTAL SECTION**

#### **3.1. Materials**

The fatty acid-modified iron oxide nanoparticles (hereafter denoted as FA@IONPs, commercial name: EMG1200) were purchased from Ferrotec and characterized as described in section 4.1. The macroRAFT agents were synthesized as described in Chapter 2. Toluene (> 99%) was purchased from Biosolve and used without further purification.

#### **3.2. Methods**

##### *3.2.1. Small-scale preparation of IO clusters*

The strategy developed for the formation of iron oxide clusters, schematically represented in Figure 48, is based on the emulsification/solvent evaporation technique reported by *Paquet et al.*<sup>55, 56</sup> The authors have studied and optimized a wide range of parameters and based on their work, we fixed the experimental conditions as follows: toluene/aqueous phase (wt/wt ratio) = 0.25 and concentration of iron oxide nanoparticles: 10 wt% based on toluene. Initially, the FA@IONPs were dispersed in toluene at a concentration of 100 g L<sup>-1</sup> forming an organic ferrofluid. The macroRAFT agents were solubilized at different concentrations in a 37 mM NaCl solution to maintain a constant ionic strength. Unless stated otherwise, the ferrofluid (1.25 g) was introduced in the macroRAFT solution (5.0 g) and emulsified during 240 s using an Ultrasonic processor (output power of 75 W) with a microprobe (tip diameter = 3 mm). A small aliquot was withdrawn from the suspension for determination of the droplet diameter ( $Z_{av-Droplet}$ ) by dynamic light scattering (DLS). The miniemulsions were then heated at 90 °C for 4 h to allow toluene evaporation. FTIR and GC analyses confirmed that no toluene was remaining in the samples after that time (ANNEX 3. 1). Water was added intermittently to maintain a constant volume. The resulting cluster suspension was characterized by DLS, TEM and gravimetry. Different experimental parameters such as the sonication time, the macroRAFT agent concentration, the ultrasound power and the macroRAFT composition have been varied. The detailed conditions of these experiments will be provided below in section 4 (results and discussion).

### 3.2.2. *Scale-up process for the preparation of IO clusters*

Scale-up experiments were carried out using an Ultrasonic Processor (maximum output power of 750 W) with a standard probe (12 mm). In a typical procedure, 24.0 g of the toluene ferrofluid was introduced into 95.0 g of the macroRAFT solution and the mixture was sonicated during 240 s with an output power of 150 W. A small aliquot was collected and characterized by DLS to determine the droplet diameter. Toluene was then extracted by rota-evaporation under vacuum at a maximum temperature of 45 °C instead of 90 °C to prevent premature degradation of the RAFT agent. Water was added intermittently in the round-bottom flask to maintain a constant volume.

### 3.2.3. *Yield of cluster formation*

The ability of the macroRAFT agents to effectively stabilize the iron oxide clusters was evaluated by gravimetric analysis. At the end of the solvent evaporation process, the cluster suspension was filtered onto a 160 mesh grid to remove the big aggregates and isolate the stable part. The solids content of this new suspension was determined gravimetrically ( $SC_{clu}$ ) and the yield of cluster formation ( $f_{clu}$ ) was then determined according to:

$$f_{clu} = \frac{SC_{clu}}{SC_{th}} \cdot 100 \quad (5)$$

where  $SC_{th}$  is the theoretical solids content (IONPs, NaCl and macroRAFT) calculated taking into account the initial amount of solid and the sample weight after the evaporation process.

### 3.2.4. *Purification of the magnetic clusters*

Some of the suspensions were purified by magnetic separation in order to remove the free macroRAFT and the small IO particles that were not incorporated into the IO clusters, as schematically represented in Figure 49. In a typical experiment, 1.0 g of the iron oxide clusters suspension was placed in an Eppendorf tube and exposed to a magnetic field using a strong magnet (Dynamag – 2<sup>TM</sup> from ThermoFisher Scientific) for 600 s. The supernatant was collected and the solids content determined gravimetrically ( $SC_{free}$ ). The recovered solid was re-dispersed in a buffer solution (37 mM NaCl at pH = 4), until the total weight of the dispersion reached 1.0 g, and the solids content was again determined gravimetrically ( $SC_{sep}$ ).

Then the magnetically separated fraction ( $f_{sep}$ ) and the supernatant fraction ( $f_{free}$ ) were determined using equations 2 and 3 below.

$$f_{free} = \frac{SC_{free}}{SC_{clu}} \times 100 \quad (2)$$

$$f_{sep} = \frac{SC_{sep}}{SC_{clu}} \times 100 \quad (3)$$

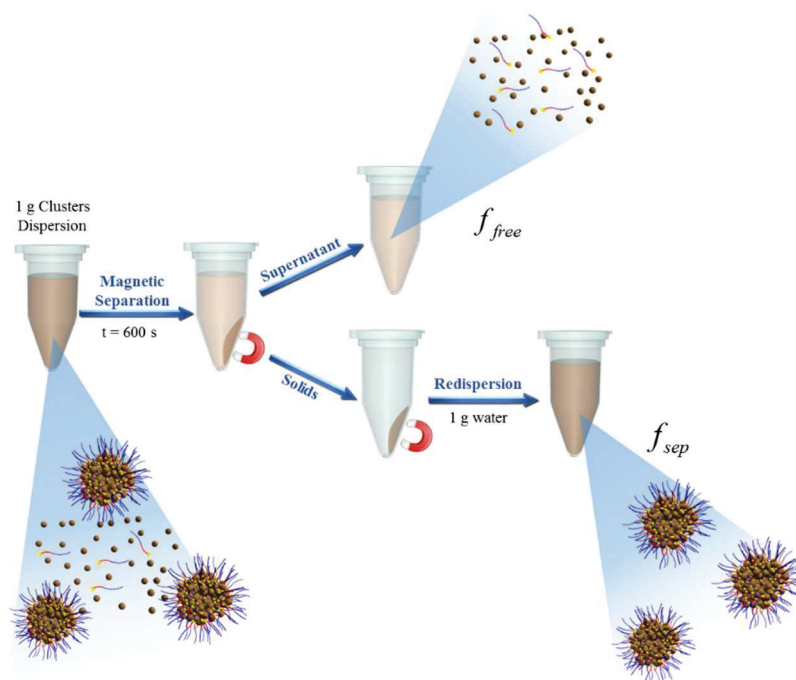


**Figure 49** – Scheme illustrating the procedure used to separate the free macroRAFT and the free iron oxide from the IO clusters.

### 3.3. Characterization techniques

#### 3.3.1. Dynamic light scattering (DLS)

Average hydrodynamic diameters ( $Z_{av}$ ) were measured by DLS using the Zetasizer NanoZS instrument from Malvern. The data were collected at  $173^\circ$  scattering angle using the fully automatic mode of the Zetasizer system and fitted with monomodal cumulant analysis. The broadness of the distribution was given by a dimensionless number called *Poly* (the higher this value, the broader the size distribution).

### 3.3.2. Zeta potential measurements

Zeta potential measurements were performed with the Zetasizer Nano ZS instrument from Malvern. The measurements were performed after dilution (1/10000) of the cluster suspension in a  $10^{-3}$  mol L<sup>-1</sup> KCl aqueous solution. The pH was adjusted within the range of pH = 4 to pH = 10 by using  $10^{-3}$  mol L<sup>-1</sup> HCl or NaOH aqueous solutions.

### 3.3.3. Electron microscopy

The morphology and particle size of the commercial FA@IONPs and of the iron oxide clusters were evaluated by either transmission electron microscopy (TEM) or *cryogenic* TEM (*cryo*TEM). For TEM analysis, a drop of the IONPs dispersed in hexane was deposited on a silicon monoxide-coated 200-mesh copper grid and allowed to evaporate under air. The clusters suspended in water were deposited on a formvar-carbon 200-mesh copper grid. For *cryo*TEM, a drop of the cluster suspension was deposited without dilution onto 300 mesh holey carbon films (Quantifoil R2/1) and quench-frozen in liquid ethane using a cryo-plunge workstation (made at LPS Orsay). The specimens were then mounted on a precooled Gatan 626 specimen holder. All observations were made using a Philips CM120 microscope operating at an accelerating voltage of 120 kV (Centre Technologique des Microstructures (CTμ), platform of the University Claude Bernard Lyon 1, Villeurbanne, France).

Statistical analyses of particle size were performed on 800 to 1200 particles from TEM micrographs. The measurements were semi-automatically performed by using the Image J free-software with a plug-in called macro Particle Size Analyzer (macroPSA) developed by Ralph Sperling from Institut Català de Nanotecnologia (ICN), Spain.<sup>62</sup> The particles were automatically identified from TEM micrographs generating a table of results with the measured diameters ( $D_i$ ), then used for the determination of the number- ( $D_n$ ), weight- ( $D_w$ ) and intensity- ( $D_z$ ) average diameters as follows:

$$D_n = \frac{\sum_{i=1}^n n_i \cdot D_i}{\sum_{i=1}^n n_i} \quad (4)$$

$$D_w = \frac{\sum_{i=1}^n n_i \cdot D_i^4}{\sum_{i=1}^n n_i \cdot D_i^3} \quad (5)$$

$$D_z = \frac{\sum_{i=1}^n n_i \cdot D_i^6}{\sum_{i=1}^n n_i \cdot D_i^5} \quad (6)$$

where  $n_i$  is the number of particles with diameter  $D_i$ . Histograms of particle size were plotted with the frequency based on number (% num) and intensity (% int.) distribution calculated by using the equations:

$$\%num_i = \frac{n_i \cdot D_i}{\sum_{i=1}^n D_i \cdot n_i} \cdot 100 \quad (7)$$

$$\%int_i = \frac{n_i \cdot D_i^6}{\sum_{i=1}^n D_i^6 \cdot n_i} \cdot 100 \quad (8)$$

#### 3.3.4. Thermogravimetric analysis (TGA)

TGA was carried out using a TGA/DSC1 STARe system from Mettler Toledo. The samples (5-15 mg) were heated from room temperature to 900 °C under a nitrogen or air atmosphere with a heating rate of 10 °C min<sup>-1</sup>.

#### 3.3.5. Raman spectroscopy

Raman analyses were performed on a Labram HR800 vis Jobin Yvon Horiba spectrograph with the kind support of Gilles Montagnac (Laboratoire de Géologie de Lyon, UMR 5276 CNRS, ENS de Lyon). An Ar<sup>+</sup>/Kr<sup>+</sup> laser with 514.5 nm wavelength at power output of 280 μW (3% of the maximum power) was used as the excitation source. The spectrometer was calibrated using the 520.7 cm<sup>-1</sup> Raman band of a standard silicon sample.

#### 3.3.6. Superconducting quantum interference device (SQUID) analysis

Magnetic measurements were made with a SQUID MPMS-XL5 (Quantum Design) equipped with an integrated helium liquefier magnetometer. The analysis was performed with the kind support of Ruben Checa from the *Laboratoire des Multimatériaux et Interfaces*, UMR CNRS 5615, *Claude Bernard University*.

### 3.3.7. *Fourier Transform Infrared (FTIR) spectroscopy*

Fatty acid modification of the commercial iron oxide nanoparticles was verified by FTIR. Attenuated Total Reflectance FTIR (ATR-FTIR) spectra were acquired in the range 400-4000  $\text{cm}^{-1}$  with a FTIR Nicolet 5700 spectrometer (Thermo Electron Corporation) equipped with a Smart Orbit accessory.

### 3.3.8. *X-ray diffractometry (XRD)*

XRD analyses were performed on a PANalyticalX'Pert Pro diffractometer equipped with a X'Celerator Scientific detector and a Cu anticathode (K1/K2). The instrument was used in the theta/theta reflection mode, fitted with a nickel filter, 0.04 radian Soller slits, 10 mm mask,  $1/2^\circ$  fixed divergence slit, and  $1^\circ$  fixed antiscatter slit. The diffraction data (detector active length =  $2.122^\circ$  ( $2\Theta$ )) were collected over the  $2\Theta$  range  $5-70^\circ$  with a step size of  $0.0167^\circ$  and a counting time of 350 s/step.

## 4. RESULTS AND DISCUSSION

### 4.1. Characterization of the commercial iron oxide nanoparticles

The commercial fatty acid-modified iron oxide nanoparticles (FA@IONPs) was supplied as a dry product that could be easily re-dispersed in toluene, forming an organic ferrofluid. The crystalline structure, size and morphology of the nanoparticles as well as their magnetic properties were all evaluated as presented in the following sections.

#### 4.1.1. *Crystalline structure*

Raman spectroscopy was used to characterize the crystalline structure of the particles (Figure 50). All observed peaks (350, 512, 664, 726 and  $1330 \text{ cm}^{-1}$ ) are in agreement with the characteristics bands of maghemite.<sup>63</sup> Noteworthy also is the absence of the characteristics peaks of hematite at 225 and  $245 \text{ cm}^{-1}$ , which could be a by-product of maghemite synthesis (oxidation process). This is an important result as maghemite has much better magnetic properties than hematite:  $M_s = 76 \text{ emu g}^{-1}$  for maghemite, whereas  $M_s < 1 \text{ emu g}^{-1}$  for hematite at room temperature.<sup>64</sup>



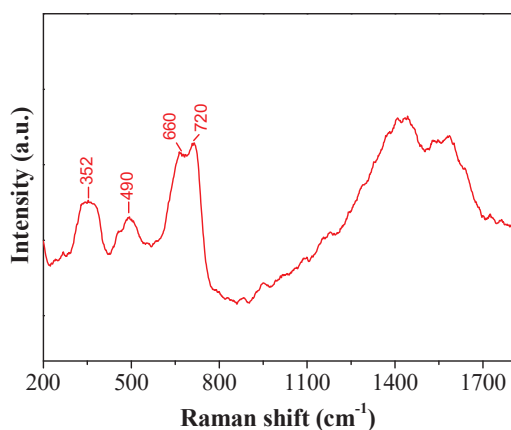


**Figure 50** – Raman spectrum of the commercial fatty acid modified iron oxide nanoparticles from Ferrotec<sup>®</sup>. The original signal was smoothed with Origin software.

#### 4.1.2. Evaluation of chemical modification

Surface modification of the FA@IONPs was evaluated by ATR-FTIR and Raman spectroscopy, and quantified by TGA. In the ATR-FTIR spectrum (Figure 51A), the characteristic band at  $535\text{ cm}^{-1}$  of stretching vibrations of the Fe-O bond can be observed. The presence of  $\text{CH}_2$  asymmetric and symmetric stretching vibrations at  $2915$  and  $2847\text{ cm}^{-1}$ , respectively, indicates the presence of hydrocarbon chains in the modified iron oxide. In addition, the complexation of carboxylic acid groups on the nanoparticle surface can be confirmed by the shifting of the asymmetric and symmetric stretching vibrations bands of the carbonyl group, in which peaks of  $\nu_{\text{as}}(\text{COO}^-)$  and  $\nu_{\text{s}}(\text{COO}^-)$  are observed at  $1516\text{ cm}^{-1}$  and  $1404\text{ cm}^{-1}$ , respectively, resulting in a wavenumber difference of  $112\text{ cm}^{-1}$ . For the non-complexed ionic form of carboxylic acid, the difference reported in the literature is usually comprised between  $130$  and  $140\text{ cm}^{-1}$ . This reduction, from  $130$ - $140\text{ cm}^{-1}$  to  $112\text{ cm}^{-1}$ , can be associated with the complexation of the carboxylic acid groups onto the inorganic surface through the formation of chelating (bidentate) complexes.<sup>65</sup> The iron oxide surface modification was also evidenced by Raman spectroscopy. The Raman spectrum of Figure 51C shows a peak at  $2900\text{ cm}^{-1}$  characteristic of C-H bonds, confirming the presence of organic material on the iron oxide surface. Finally, the organic material content was determined by TGA (Figure 51C). The analyses were carried out under two different atmospheres, oxidative (air) and non-oxidative ( $\text{N}_2$ ), and the same result was found: the modified iron oxides incorporate  $14\text{ wt}\%$  of organic material.

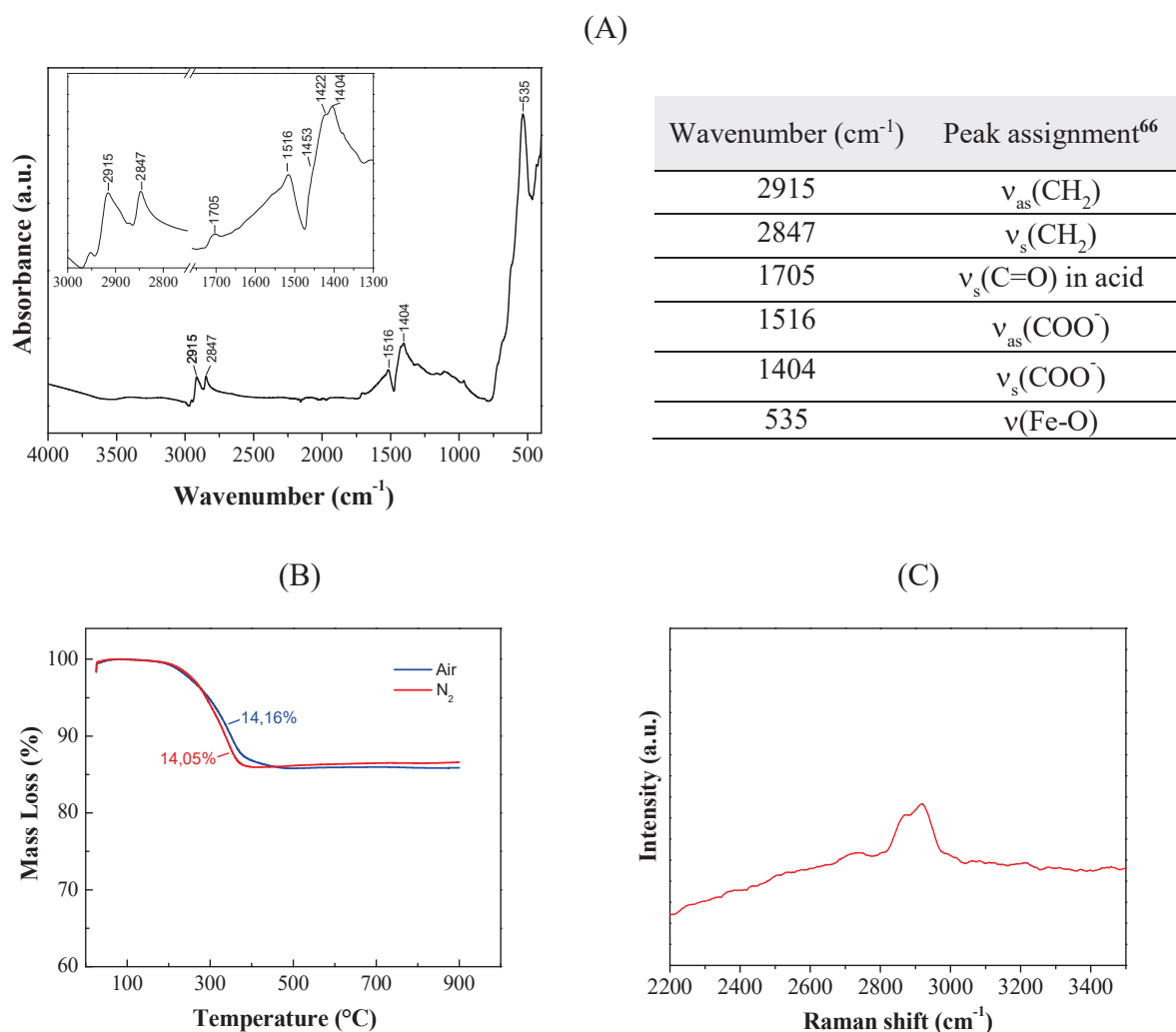


**Figure 51** – Characterizations of the commercial iron oxide nanoparticles by: (A) ATR-FTIR spectroscopy, (B) TGA analysis and (C) Raman spectroscopy.

#### 4.1.3. Particle size and morphology

DLS, TEM and XRD were employed in order to evaluate the morphology, average particle size and size distribution of the iron oxide nanoparticles. As seen in Figure 52, the FA@IONPs exhibit an irregular shape. A statistical analysis was carried out on these images, resulting in the histogram shown in Figure 53B. The particles are small with a high dispersity ( $D_n = 10$  nm and  $D_w/D_n = 1.18$ ). Moreover, DLS measurement was carried out after suspending the particles in toluene (Figure 53A). A single peak ( $Z_{av} = 31$  nm and Poly = 0.25) was evidenced, indicating a good dispersability of the organically modified iron oxide nanoparticles in this solvent. A minor population of big particles, between 1000 and 10 000 nm, was also detected. However, the number of these large particles is likely negligible since

the graph is represented in intensity and as can be seen in Figure 53A, these large particles are not observed in the corresponding number distribution.

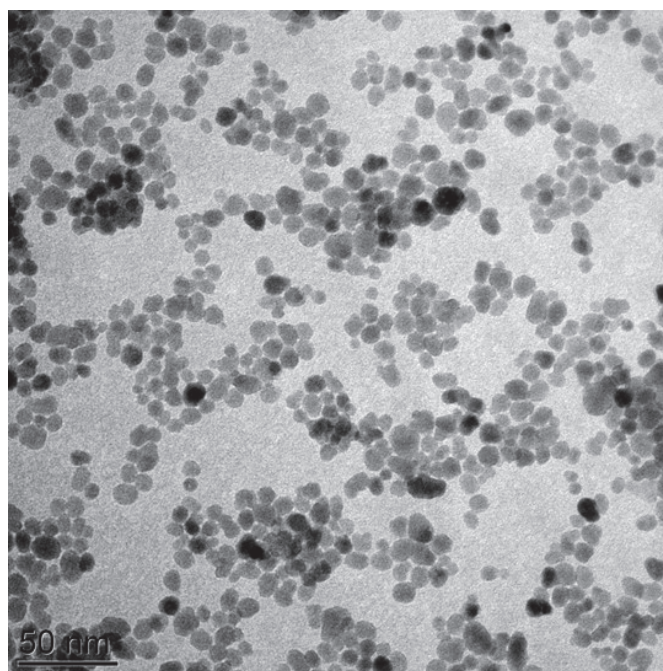


Figure 52 - TEM image of the commercial iron oxide nanoparticles.

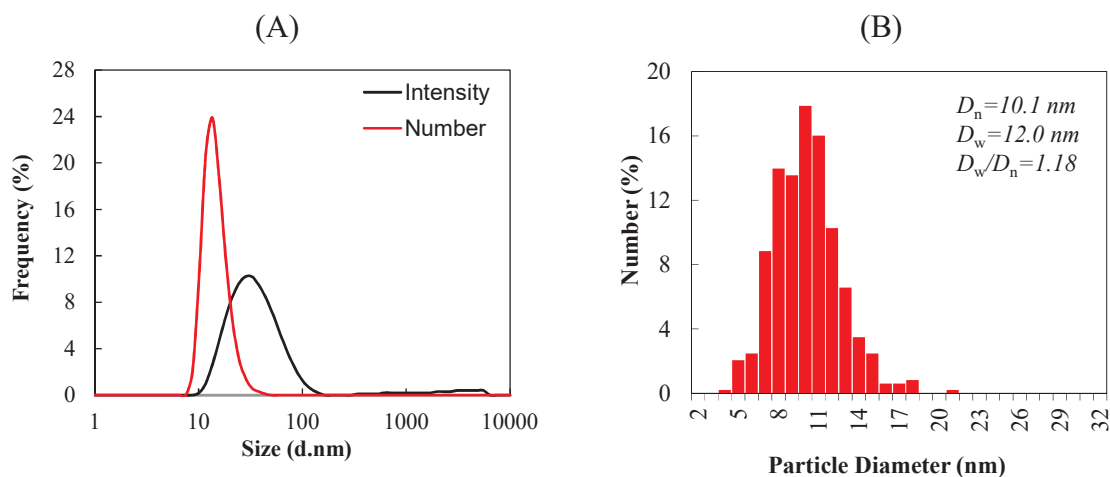
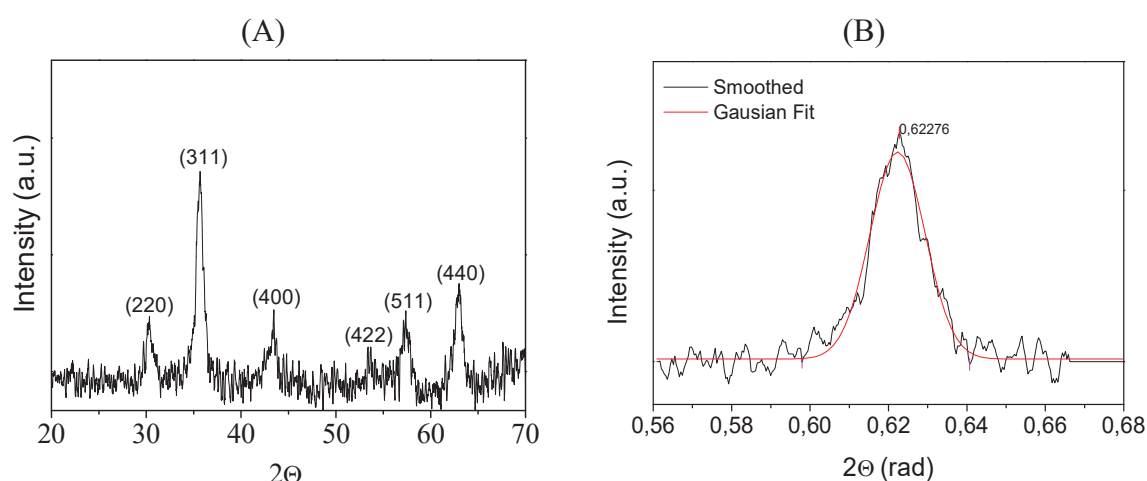


Figure 53 – Particle size distribution of FA@IONPs as determined by (A) DLS and (B) TEM.

The particles were also characterized by XRD (Figure 54). The diffractogram shows the characteristics peaks of maghemite in accordance with literature.<sup>67</sup> Moreover, the Gaussian law was applied to the most representative peak at 311 fitting the resulting signal. The half-area of the integrated peak (311) was used in the Debye-Scherrer equation to determine the particle size. The obtained value, 10 nm, is in good agreement with the number-average diameter determined by TEM. On the other hand, the value obtained by DLS was 3 times

higher than the diameter determined by TEM or DRX. This difference can be attributed to the calculation made in DLS to determine  $Z_{av}$ , which is more sensitive to the presence of big particles than TEM and XRD measurements, which can lead to bigger values (further discussions about differences in size measurements from DLS and TEM will be given in section 4.2.1). In addition, the non-spherical morphology of the nanoparticles can generate inaccurate data because mathematic treatment of DLS is based on spherical particles. In terms of particle size, the results obtained from TEM and DRX are thus more reliable.



**Figure 54** – XRD analysis of FA@IONPs. (A) Diffractogram and (B) Gaussian fit of the 311 peak.

#### 4.1.4. Magnetic properties

For utilization in biological separation, the particles must be easily separated from the whole medium by the simple application of a magnet. Their magnetic behavior will come from the magnetic properties of the iron oxide nanoparticles, which are expected to be superparamagnetic. In this case the hysteresis phenomenon, which is a remaining magnetization at zero field, should not be evidenced. This property has a well-known dependence with the size of iron oxide nanoparticles, i.e. when they are smaller than about 20 nm the nanoparticles often display superparamagnetic behavior at room temperature.<sup>5</sup> Despite the irregular morphology of the iron oxide nanoparticles shown in Figure 52, all particles have a diameter smaller than typically 20 nm. Consequently, superparamagnetic properties are expected, which was assessed by SQUID measurements. As can be seen in Figure 55, no remaining magnetization at zero field was observed after two cycles of analysis, confirming the superparamagnetic behavior of the particles. Noteworthy is the high value of the magnetization at saturation, 62 emu per gram of the organically modified iron oxide.

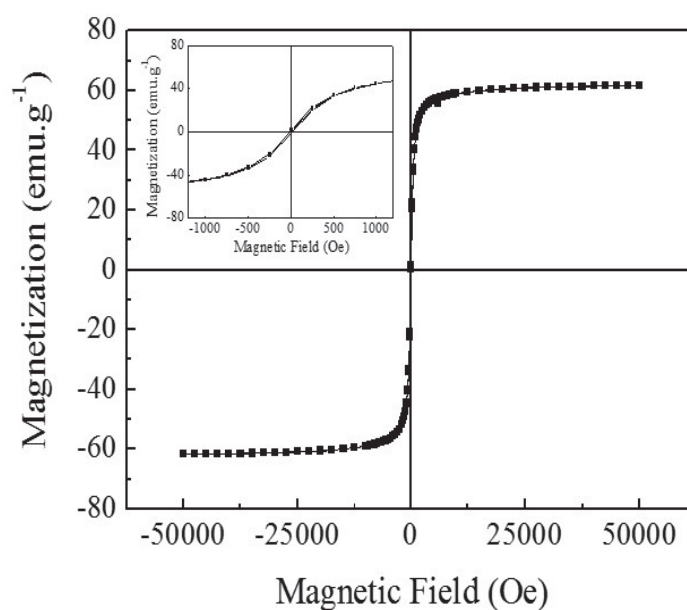


Figure 55 – SQUID analysis of the commercial FA@IONPs.

#### 4.2. PDMAEMA-based iron oxide clusters

The strategy used in this work for the formation of IO clusters is based on Paquet's work<sup>56</sup> and involve the following steps: (i) dispersion of iron oxide nanoparticles in toluene to form an organic ferrofluid, (ii) emulsification of the ferrofluid in an aqueous solution of macroRAFT, and (iii) evaporation of toluene leading to the formation of the IO clusters. The SDS surfactant used by Paquet *et al.*<sup>56</sup> was replaced by the reactive amphiphilic macroRAFT agents. First, an optimization of the system was carried out by varying the following conditions: the sonication time, the ultrasound power and the concentration of PDMAEMA-*b*-PS-TTC. The experimental conditions and some results from these preliminary studies are presented in Table 9. The best conditions were then employed in scale-up experiments. Finally, the effect of the initial pH of the macroRAFT solution was also studied.

**Table 9** – Experimental conditions and results for the preparation of cluster suspensions in the presence of PDMAEMA-*b*-PS-TTC macroRAFT agent.

Run	$C_{\text{macroRAFT}}$ (mol L <sup>-1</sup> ) <sup>a</sup>	P (W)/ (%)	$t^b$ (s)	$SC_{\text{th}}^c$ (%)	$f_{\text{clu}}^d$ (%)	$Z_{\text{av-Droplets}}$ (nm)/Poly <sup>e</sup>	$Z_{\text{av-Clusters}}$ (nm)/Poly <sup>e</sup>	$D_n$ (nm)/ $D_w/D_n^f$
<i>Sonication time series</i>								
TRG69-1	1.0 10 <sup>-4</sup>	75/15%	<u>60</u>	-	-	474/0.35	-	-
TRG69-2	1.0 10 <sup>-4</sup>	75/15%	<u>120</u>	-	-	430/0.34	-	-
TRG69-3	1.0 10 <sup>-4</sup>	75/15%	<u>240</u>	-	-	310/0.21	-	-
TRG69-4	1.0 10 <sup>-4</sup>	75/15%	<u>420</u>	-	-	312/0.27	-	-
TRG69-5	1.0 10 <sup>-4</sup>	75/15%	<u>600</u>	2.00	90	325/0.29	318/0.34	-
TRG80-1	2.5 10 <sup>-4</sup>	75/15%	<u>60</u>	-	-	236/0.22	-	-
TRG80-2	2.5 10 <sup>-4</sup>	75/15%	<u>120</u>	-	-	418/0.32	-	-
TRG80-3	2.5 10 <sup>-4</sup>	75/15%	<u>240</u>	-	-	224/0.13	-	-
TRG80-4	2.5 10 <sup>-4</sup>	75/15%	<u>420</u>	-	-	217/0.16	-	-
TRG80-5	2.5 10 <sup>-4</sup>	75/15%	<u>600</u>	2.75	94	226/0.19	194/0.13	-
<i>Sonication power series</i>								
TRG75-5	2.5 10 <sup>-4</sup>	<u>25/5%</u>	240	3.00	9	153/0.12	148/0.12	45/2.72
TRG75-4	2.5 10 <sup>-4</sup>	<u>50/10%</u>	240	3.16	46	160/0.04	151/0.05	74/1.40
TRG75-3	2.5 10 <sup>-4</sup>	<u>60/12%</u>	240	3.14	65	226/0.22	163/0.08	82/1.37
TRG70-7	2.5 10 <sup>-4</sup>	<u>75/15%</u>	240	2.85	84	183/0.07	172/0.06	94/1.32
TRG75-1	2.5 10 <sup>-4</sup>	<u>100/20%</u>	240	2.70	89	199/0.10	192/0.11	114/1.68
<i>PDMAEMA-<i>b</i>-PS-TTC concentration series</i>								
TRG70-4	<u>1.0 10<sup>-6</sup></u>	75/15%	240	2.20	7	576/0.31	1773/0.54	-
TRG70-3	<u>1.0 10<sup>-5</sup></u>	75/15%	240	2.31	8	429/0.43	487/0.50	-
TRG70-2	<u>1.0 10<sup>-4</sup></u>	75/15%	240	1.72	53	344/0.20	455/0.31	-
TRG70-8	<u>1.5 10<sup>-4</sup></u>	75/15%	240	1.93	82	243/0.16	249/0.23	124/1.82
TRG70-7	<u>2.5 10<sup>-4</sup></u>	75/15%	240	2.08	84	183/0.07	172/0.06	94/1.32
TRG70-6	<u>5.1 10<sup>-4</sup></u>	75/15%	240	2.16	83	156/0.03	146/0.05	59/1.60
TRG70-5	<u>7.6 10<sup>-4</sup></u>	75/15%	240	2.28	85	153/0.04	142/0.07	57/1.57
TRG70-1	<u>1.0 10<sup>-3</sup></u>	75/15%	240	2.86	95	148/0.06	139/0.05	66/1.58

FA@IONP concentration in toluene = 100 g L<sup>-1</sup>; Ferrofluid/aqueous phase wt/wt ratio = 0.25; Toluene evaporation at 90 °C. <sup>a</sup>Concentration of PDMAEMA-based macroRAFTs in a 37 mM NaCl solution at pH 4; <sup>b</sup>Sonication time; <sup>c</sup>Theoretical solids contents; <sup>d</sup>Yield of cluster formation calculated from Equation 1; <sup>e</sup>Determined by DLS; <sup>f</sup>Number-average particle size and dispersity obtained by statistical analysis of 600-1200 particles from TEM images.

## 4.2.1. Effect of sonication time

In a first series of experiments, the ferrofluid was miniemulsified in the macroRAFT solution for 10 min at a fixed power of 75 W. Two PDMAEMA-*b*-PS-TTC concentrations were investigated:  $1 \cdot 10^{-4}$  M and  $2.5 \cdot 10^{-4}$  M (TRG69 and TRG80 series, Table 9). Samples were periodically withdrawn to analyze the evolution of droplet size ( $Z_{av-Droplets}$ , DLS) with sonication time (Figure 56). The energy transferred from the ultrasound waves to the droplets has sheared them reducing the average droplet sizes and dispersity up to 240 s of sonication, and at this point a plateau was reached. Hence, the sonication time will be fixed at 240 s in the next series of experiments. It is important to point out that the sample corresponding to 60 s of sonication time in the TRG80 series was unstable with clear phase separation between the organic phase (black dispersion on the top) and the aqueous macroRAFT solution (light-yellow translucent solution in the bottom), which could lead to inaccurate measurement of the particle size (Figure 56).

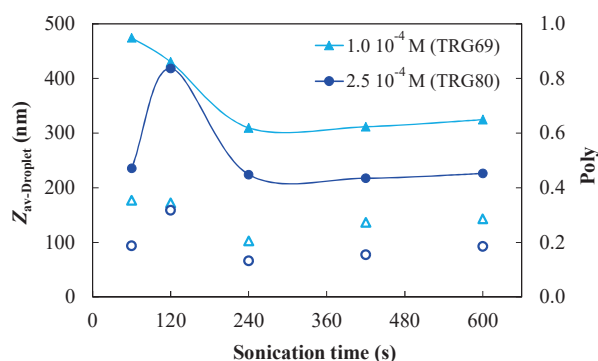


**Figure 56** – Effect of sonication time on the evolution of  $Z_{av}$  (full symbols) and  $Poly$  values (open symbols) of toluene droplets loaded with iron oxide nanoparticles before solvent evaporation, for two different macroRAFT concentrations:  $1 \cdot 10^{-4}$  (TRG69 series) and  $2.5 \cdot 10^{-4}$  M (TRG80 series) and a fixed sonication power of 75 W

As explained above, in a typical miniemulsion system, a hydrophobic agent is usually introduced in the oil phase to prevent or minimize Ostwald ripening.<sup>52</sup> However we have not considered the addition of a hydrophobe to be necessary in the present system for two reasons. First, Ostwald ripening was effectively observed by Paquet *et al.*<sup>56</sup> during the formation of toluene droplets loaded with FA@IONPs using SDS as surfactant. However, according to the authors, solvent migration had not influence on the final cluster size and size distribution as the iron oxide nanoparticles could not diffuse in this process (indeed, only the oil phase can migrate and the composition of the droplets remained therefore unchanged). On the other hand, Ramirez and co-workers<sup>60</sup> did not observe diffusional degradation of



miniemulsion droplets, composed of styrene and oleic acid-modified IONPs, still stabilized by SDS. The authors proposed that the absence of diffusional degradation was related to the hydrocarbon segments of oleic acid, which can play the role of the hydrophobic agent.

#### 4.2.2. Effect of sonication power

The sonication power was varied from 25 to 100 W using a fixed PDMAEMA-*b*-PS-TTC concentration of  $2.5 \cdot 10^{-4}$  M. Figure 57B shows the evolution of the droplet size with sonication power and an unexpected behavior was observed. Indeed, the particle size increased with increasing sonication power. Actually, increasing the ultrasound power leads to more energy transferred to the system and the forces exerted on the droplets are more important, which should lead to the generation of more droplets with smaller size. However, the formation of these new droplets will generate an enormous surface area to be stabilized and in absence of enough stabilizer, the droplets will coalesce generating bigger ones, which explains the increasing of droplet size with sonication power.

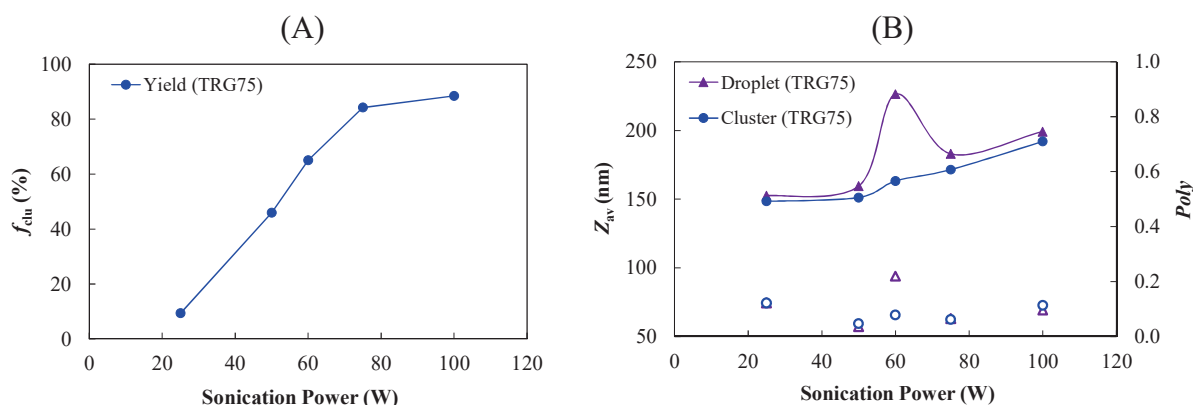


**Figure 57** - Effect of sonication power on: (A) the yield of cluster formation and (B) the evolution of droplet and cluster sizes (full symbols) and Poly values (open symbols) determined by DLS. Sonication time = 240 s and [PDMAEMA-*b*-PS-TTC] =  $2.5 \cdot 10^{-4}$  M.

It is important to point out that after toluene evaporation, the diameter of the resulting clusters was almost the same as the droplet size before evaporation (Figure 57B). We will come back to this point later in the discussion (section 4.2.3).

Furthermore, high yields of cluster formation were obtained when the sonication power employed was higher than 60 W, as can be evidenced in Figure 57A, indicating that a minimum power of 75 W was necessary to generate stable systems with high yields.

The TEM images of Figure 58 show the formation of spherical clusters regardless of the sonication power. In order to analyze the particles size and size dispersity from the TEM

images, statistical analyses of particle diameter were performed by using ImageJ free software and the resulting histograms are presented in Figure 58 (*right column*) showing a relatively broad but unimodal particle size distributions, except for the lowest sonication power ( Figure 58A) which showed a left skewed pattern. The broad particle size distribution was not considered however to be a limiting factor for the final application targeted in this thesis, i.e. the magnetic separation of bacteria.

Figure 59B shows the evolution of the particle diameters determined by TEM and DLS as a function of the sonication power. Although the hydrodynamic diameter determined by DLS ( $Z_{av}$ ) and the number-average diameter determined by TEM ( $D_n$ ) followed a similar trend, a closer look at the figure shows that the particle diameters obtained by the two techniques are different: the DLS diameter ( $Z_{av} = 172$  nm) being two times higher than the TEM diameter ( $D_n = 94$  nm) for a fixed sonication power of 75 W. This can be explained by the equations used to determine the particle size, which varie from one technique to another. Indeed,  $Z_{av}$  is an intensity-weighted mean diameter derived from the cumulant analysis based on the Rayleigh light scattering equation (Eq. 9):

$$I = I_0 \frac{1 + \cos^2 \theta}{2R^2} \left( \frac{2\pi}{\lambda} \right)^4 \left( \frac{n^2 - 1}{n^2 + 2} \right)^2 \left( \frac{d}{2} \right)^6 \quad (9)$$

where  $R$  is the distance from the source of the incident light to the particles,  $\theta$  is the scattering angle,  $n$  the refractive index of the particle,  $d$  the particle diameter,  $\lambda$  the wavelength of light and  $I_0$  the unpolarized light intensity. According to equation (9), the intensity ( $I$ ) varies as the sixth power of the particle diameter ( $d$ ). Hence, the DLS average diameters will be strongly affected by the presence of big particles, which can explain the difference between  $Z_{av}$  and  $D_n$  (Figure 59B). As a matter of fact, a relatively good agreement was observed between  $Z_{av}$  and  $D_z$ , as according to Equation (6),  $D_z$  is also an intensity-average diameter, which scales as the sixth power of the diameter. Hence, a good fit between the DLS results and the intensity frequency-based histograms was obtained for this series of samples as shown in ANNEX 3. 2. However, in the following the intensity-based histograms will not be presented and we will only give the corresponding  $D_z$  value. Despite relatively good agreement between the two values,  $Z_{av}$  was systematically higher than  $D_z$ , which can be due to two main factors: (1) the number of particles measured by these two techniques is significantly different, as DLS analysis takes into account a lot more particles to calculate  $Z_{av}$  than a statistical analysis from TEM images; and (2) the attenuator of the DLS apparatus is automatically adjusted in a step-

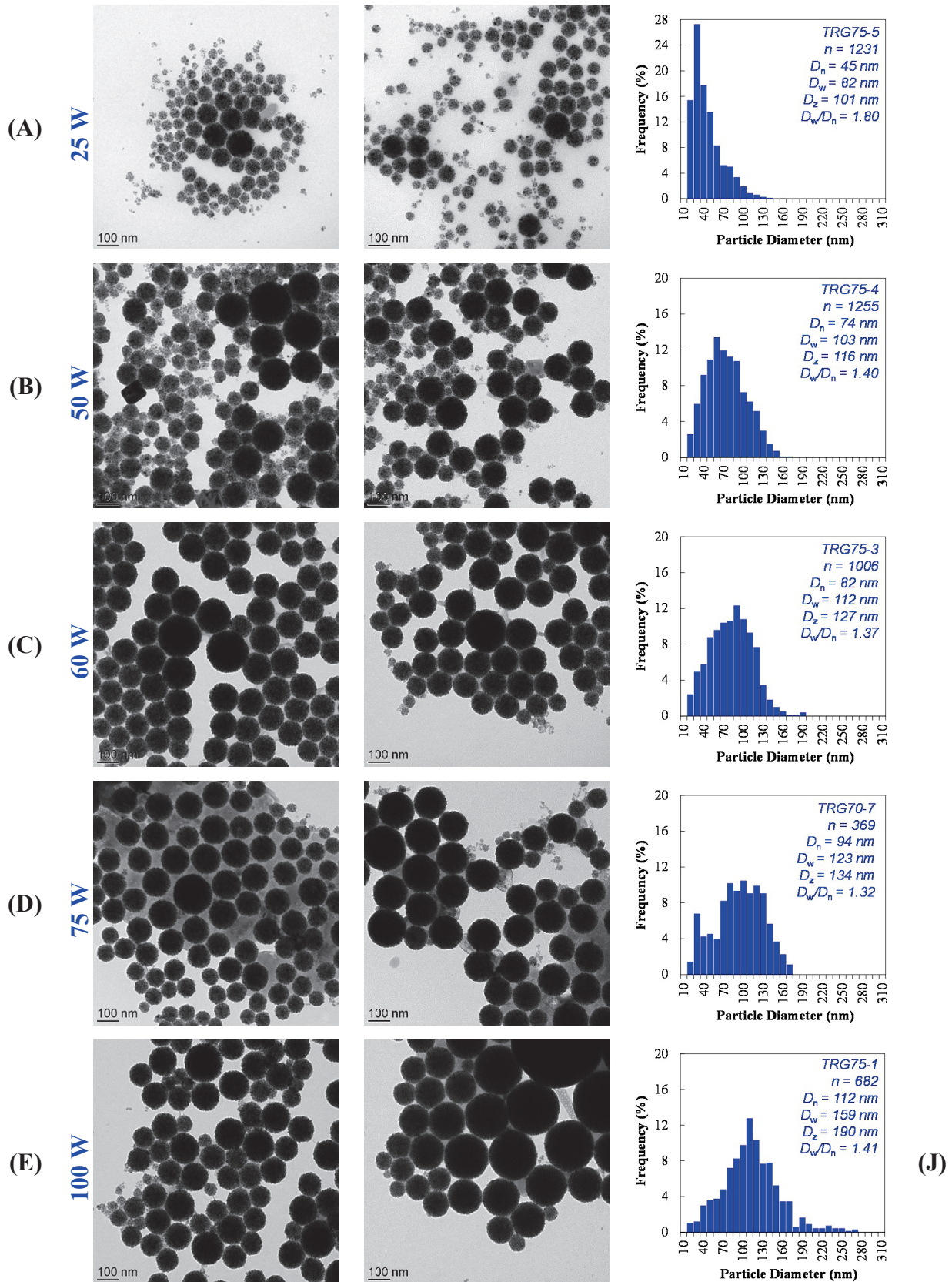


**Figure 58** – Effect of sonication power on the size and size distribution of the IO clusters. (A) 25 W, (B) 50 W, (C) 60 W, (D) 75 W and (E) 100 W. *Left and middle*: TEM micrographs at a fixed magnification of 56000x and *right*: corresponding number frequency size-distribution histograms. Sonication time = 240 s and [PDMAEMA-*b*-PS-TTC] =  $2.5 \cdot 10^{-4}$  M.

size to have a good measurement of the particles with the higher intensity (the biggest ones), which leads to a less accurate detection of the small particles, and hence an increase of the particle size.

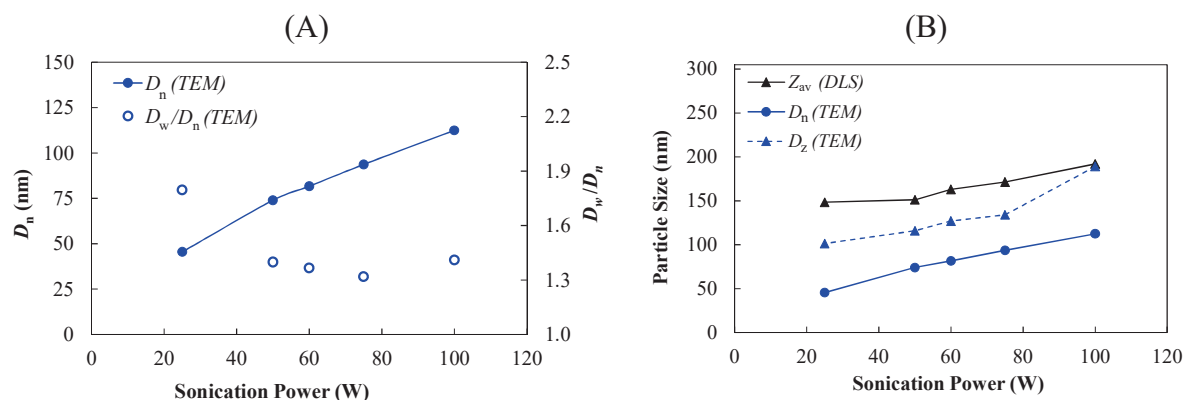


**Figure 59** – Effect of sonication power on cluster size and size distribution. (A)  $D_n$  (full symbols) and dispersity ( $D_w/D_n$ , open symbols) determined by TEM and (B)  $Z_{av}$  measured by DLS and number and intensity-mean diameter ( $D_n$  and  $D_z$ ) calculated from TEM images using Equations 4 and 6, respectively. Sonication time = 240 s and [PDMAEMA-*b*-PS-TTC] =  $2.5 \cdot 10^{-4}$  M.

For the next series of experiments, the power was fixed at 75 W, which provided the best compromise between the cluster yield ( $f_{clu} = 90\%$ ), the particle size ( $D_n = 100$  nm) and the dispersity ( $D_w/D_n = 1.3$ ) in the ultrasound power range studied.

#### 4.2.3. Effect of macroRAFT concentration

The concentration of the amphiphilic macroRAFT agent is a key parameter that requires particular attention. The PDMAEMA-*b*-PS-TTC concentration was varied from  $1.0 \cdot 10^{-6}$  M to  $1.0 \cdot 10^{-3}$  M (TRG70-1 to TRG70-8, Table 9) to see its effect on droplet and cluster stabilization. As seen in Figure 60B, unstable suspensions were obtained for macroRAFT concentrations lower than  $1.0 \cdot 10^{-4}$  M. This was corroborated by the DLS measurements of Figure 60D, which showed the formation of big clusters typically larger than 500 nm in diameter with high poly values, confirming the poor colloidal stability of the suspensions. This poor stability was concurrently accompanied by a very low yield of cluster formation (lower than typically 10%, Figure 60C and Table 9). In contrast, stable systems were obtained for higher concentrations:  $1.0 \cdot 10^{-4}$  M to  $1.0 \cdot 10^{-3}$  M (Figure 60B). The particle size and the *Poly* value decreased with increasing macroRAFT concentration. This behavior was expected as the amphiphilic macroRAFT is the stabilizer of the system. Indeed, increasing the macroRAFT concentration enabled to stabilize a greater interfacial area leading to the



formation of smaller droplets and, consequently, smaller clusters as well. Moreover the yield of cluster formation reached values higher than 80% for concentrations higher than  $1.5 \cdot 10^{-4}$  M, indicating that a minimum amount of macroRAFT agent was necessary to stabilize the toluene droplets and form stable clusters.

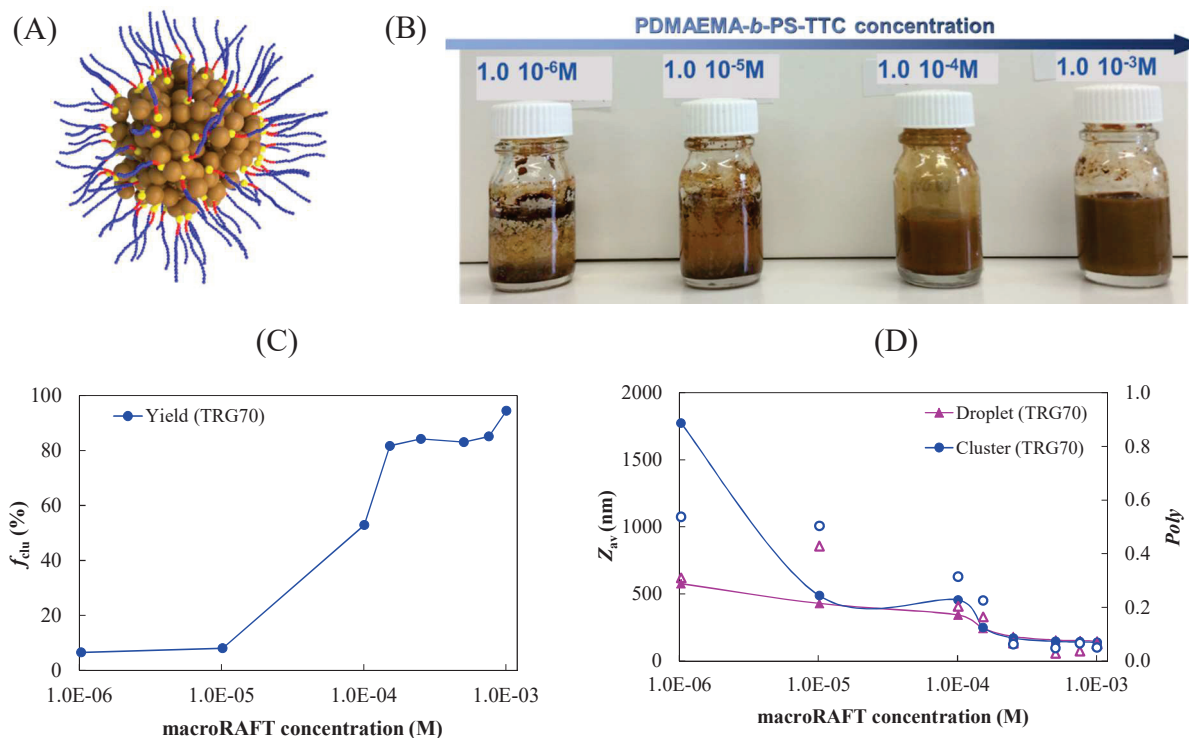


**Figure 60** – Effect of macroRAFT concentration on cluster formation. (A) Schematic representation of the PDMAEMA-*b*-PS-TTC-stabilized IO clusters, (B) photographs of IO cluster suspensions after toluene evaporation, (C) yield of cluster formation and (D) evolution of cluster and droplet sizes (full symbols) and *Poly* values (open symbols) measured by DLS. Sonication power = 75 W and sonication time = 240 s (see Table 4 for detailed experimental conditions).

The TEM micrographs of Figure 61 and Figure 63 confirmed these results. Low macroRAFT concentrations led to the formation of large and ill-defined clusters (Figure 61) whereas higher concentrations resulted in spherical clusters with however a broad size distribution (Figure 63). As shown in Figure 62A, the higher the macroRAFT concentration the lower was the TEM diameter in agreement with DLS measurements. The average particle diameter determined by DLS ( $Z_{\text{av}} = 172$  nm for  $[\text{macroRAFT}] = 2.5 \cdot 10^{-4}$  M) was however still higher than the number average TEM diameter ( $D_n = 94$  nm) and a closer agreement was found between  $Z_{\text{av}}$  and  $D_z$  for the same reasons as were mentioned above for the effect of the sonication power.

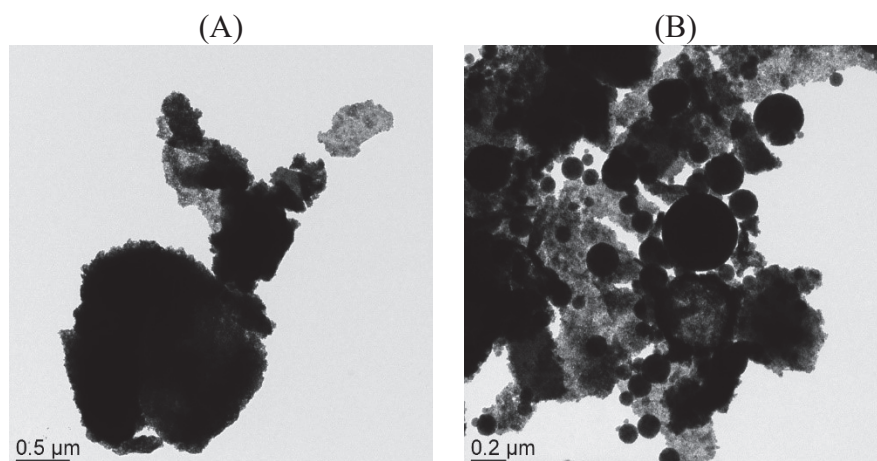


**Figure 61** – Effect of PDMAEMA-*b*-PS-TTC concentration on cluster formation. TEM images of the IO clusters for: (A) [macroRAFT] =  $1.0 \times 10^{-6}$  M and (B)  $1.0 \times 10^{-5}$  M. Sonication power = 75 W and sonication time = 240 s (see Table 4 for detailed experimental conditions).

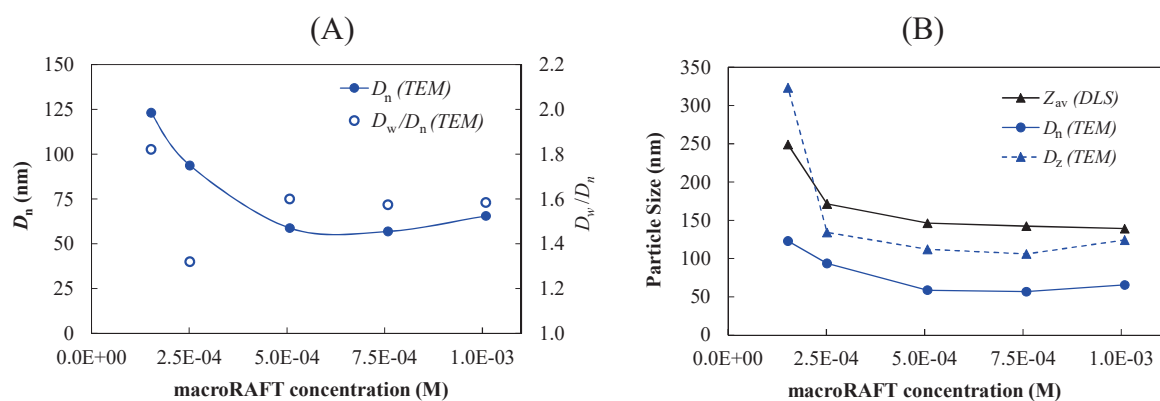


**Figure 62** – Effect of macroRAFT concentration on cluster size and size distribution. (A)  $D_n$  (full symbols) and dispersity ( $D_w/D_n$ , open symbols) determined by TEM and (B)  $Z_{av}$  measured by DLS and number and intensity-mean diameter ( $D_n$  and  $D_z$ ) from TEM determined using Equations 4 and 6, respectively. Sonication power = 75 W and sonication time = 240 s.

It is important to point out that the TEM images shown in Figure 58 and Figure 63 were obtained from dried cluster dispersions previously deposited onto a TEM grid. However, the solvent evaporation could affect the size and size distribution of the clusters. In order to investigate the potential impact of the drying step, *cryo*-TEM observations of the cluster dispersion (TRG70-1, Table 9) were carried out. The resulting micrographs are presented in Figure 64A while the corresponding histogram is shown in Figure 64B. The two techniques gave very similar  $D_n$  values (TEM:  $D_n = 65$  nm, Figure 63E and *cryo*-TEM:  $D_n = 62$  nm, Figure 64B). The polydispersities were however slightly different ( $D_w/D_n = 1.58$  for TEM and 2.02 for *cryo*-TEM), which is likely due to the lower number of particles which has been analyzed by *cryo*-TEM (245) compared to TEM (1189). These observations confirm that the drying process did not affect the size and size distribution of the IO clusters.

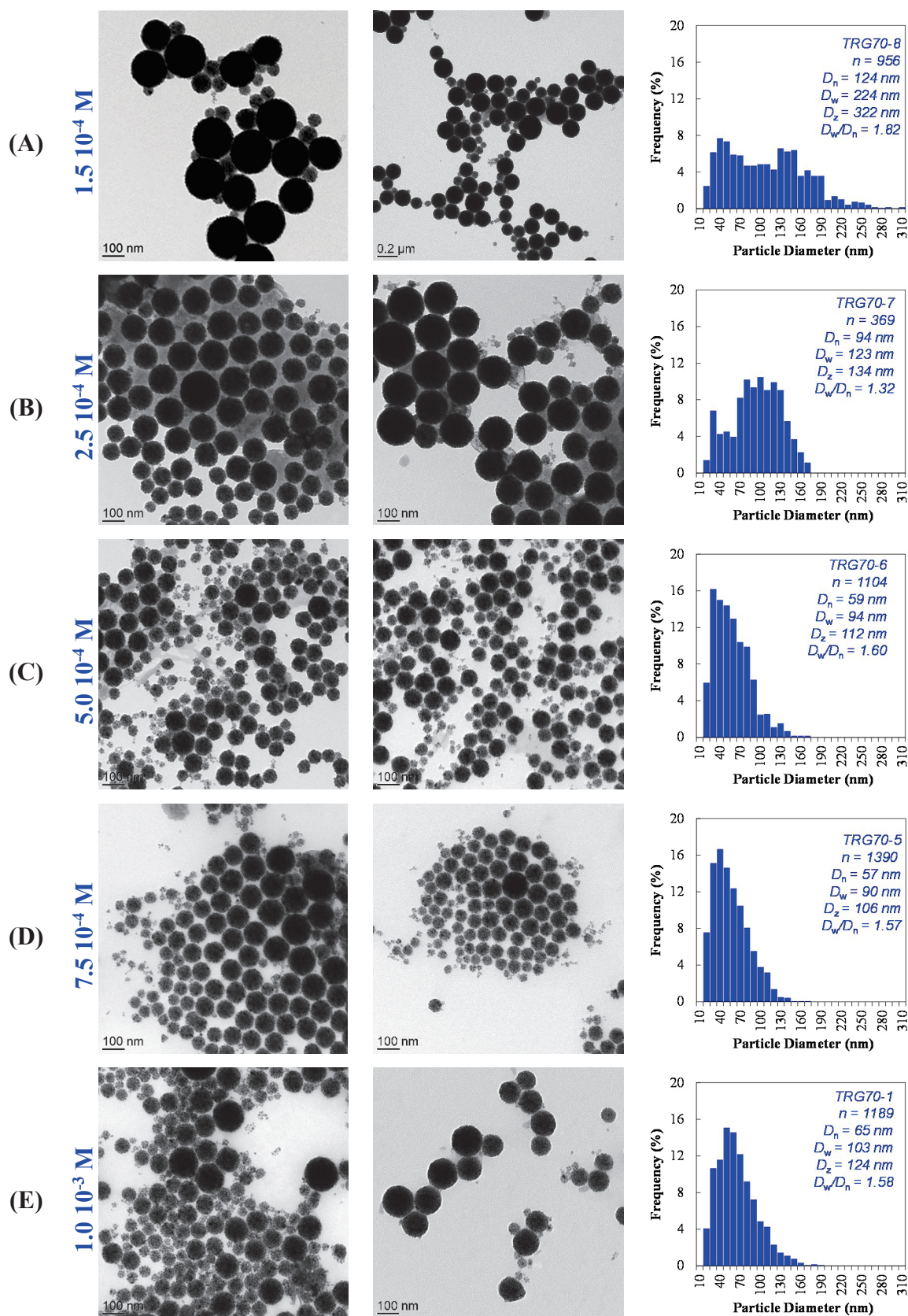


**Figure 63** – Effect of the PDMAEMA-*b*-PS-TTC concentration on the size and size distribution of the IO clusters. (A) 1.5 10<sup>-4</sup> M, (B) 2.5 10<sup>-4</sup> M, (C) 5.0 10<sup>-4</sup> M, (D) 7.5 10<sup>-4</sup> M and (E) 1.0 10<sup>-3</sup> M. *Left and middle*: TEM micrographs at a fixed magnification of 56000x and *right*: corresponding number frequency size distribution histograms. Sonication power = 75 W and sonication time = 240 s.



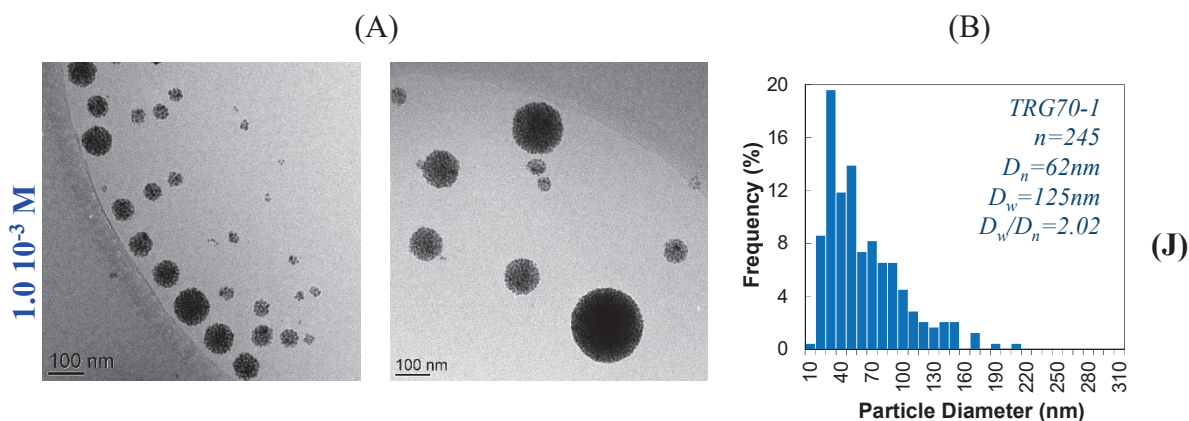


**Figure 64** – (A) *cryo*-TEM images and (B) corresponding number frequency size distribution histograms of iron oxide clusters prepared at [PDMAEMA-*b*-PS-TTC] =  $1.0 \cdot 10^{-3}$  M (TRG70-1 in Table 2). Sonication power = 75 W and sonication time = 240 s.

Another point that also deserves our attention is the small difference between the droplet and cluster sizes determined by DLS (Figure 60D). This was unexpected as the droplets contain only 10 wt% of iron oxide, which should result in a significant volume contraction after toluene evaporation, and hence to much lower cluster sizes. However, some toluene droplets may not contain any IONPs, as represented in Figure 65B, which would completely change the picture. Indeed, Bourgeat-Lami *et al.*<sup>68</sup> studied the mechanism of formation of monomer droplets loaded with organically modified silica particles by *cryo*-TEM, and showed that the majority (in number) of droplets did not contain any inorganic particle. We also attempted to observe our toluene miniemulsion droplets loaded with FA@IONPs via *cryo*-TEM, but unfortunately no clear images could be obtained (see ANNEX 3. 4). This may be explained by a poor contrast between toluene and water. Hence, a second strategy was employed to verify this hypothesis. This strategy consists in the estimation of the droplet diameter,  $D_{i-Droplet}$ , from the cluster size determined by TEM, using the fraction  $\phi$  of droplets effectively loaded with IONPs as an adjustable parameter.

The droplet diameter is given by:

$$D_{i-Droplet} = \sqrt[3]{\frac{6 \cdot V_{i-Droplet}}{\pi}} \quad (10)$$

where  $V_{i-Droplet}$  is the volume of one toluene droplet estimated based on volume contraction during the toluene evaporation as follows:

$$V_{i-Droplet} = \frac{V_{i-Cluster} \cdot \rho_{Cluster}}{10 \cdot \rho_{Droplet}} \cdot \left( \frac{\phi}{100} \right) \quad (11)$$

where  $V_{i-Cluster}$  is the volume of one iron oxide cluster calculated from the diameter measured by TEM ( $D_i$ ), IO is the content of IONPs in toluene (ca. 10 wt%),  $\rho_{Cluster}$  the cluster density,  $\rho_{Droplet}$  the droplet density and  $\varphi$  the fraction of toluene droplets loaded with IONPs. The intensity-average droplet diameter ( $D_{z-Droplet}$ ) was then estimated using equation 6 (section 3.3.3), but replacing  $D_i$  by  $D_{i-Droplet}$ .

The graph of Figure 65A shows the plot of the estimated  $D_{z-Droplets}$  as a function of macroRAFT concentration for various  $\varphi$  values, as well as the experimental values of  $Z_{av}$  for the droplets and clusters (DLS) and of  $D_z$  for the clusters (TEM).

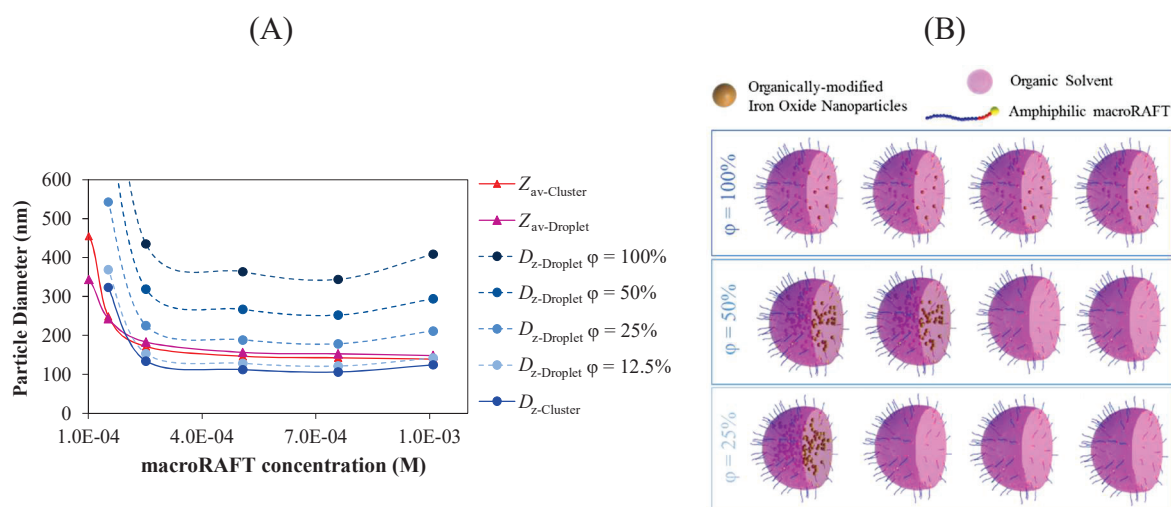


**Figure 65** – Effect of volume contraction during toluene evaporation. (A) Evolution of  $Z_{av-Droplets}$  and  $Z_{av-Clusters}$  by DLS,  $D_{z-Clusters}$  of IO clusters determined from TEM, and  $D_{z-Droplets}$  calculated from equations 10, 11 and 12 considering different fractions ( $\varphi$ ) of droplets loaded with IONPs and (B) schematic representation of the composite droplets for variable  $\varphi$  values.

As shown in Figure 65A, the estimated droplet size ( $D_{z-droplets}$ ) decreases with decreasing  $\varphi$ . This behavior can be associated to the concomitant increase of iron oxide content in the loaded droplets (as represented in Figure 65B). Consequently, these droplets will contain less toluene, leading to a smaller volume contraction during the evaporation process. Hence, the lower is the fraction  $\varphi$ , the closer will be the droplet and cluster sizes. For most of the macroRAFT concentrations studied, the droplet size determined by DLS is between the estimated  $D_{z-Droplets}$  for  $\varphi = 25$  and 12.5%, indicating that most of the droplets were unloaded, which is in agreement with the previous observations in the literature.<sup>68</sup> It is worth mentioning that this is a fairly rough estimation of the number of droplets loaded with iron oxide nanoparticles, because there are some effects that were not considered such as the higher viscosity of the loaded droplets compared to the unloaded ones, which should affect the size and size distributions, resulting for instance in loaded droplets bigger than unloaded ones.

The number of amphiphilic macroRAFT agents per cluster surface area is another important parameter to be considered. A way to determine this number consists in measuring the amount of free macroRAFT in water, the adsorbed amount being determined by difference between the initial and the equilibrium concentrations. However, unfortunately we did not succeed to properly separate the free macroRAFT from the IO clusters for various reasons detailed in ANNEX 3. 4.

#### 4.2.4. Effect of pH

As described in Chapter 2, the PDMAEMA chains can be considered as pH-responsive. This phenomenon is related to the tertiary amine groups present on the side chains, which are protonated below pKa (i.e.  $\text{pH} < 7.0\text{-}7.5$ )<sup>69, 70</sup> conferring a cationic character to the PDMAEMA chains. In this section, different macroRAFT solutions were prepared for various [HCl]/[macroRAFT] ratios to target different pH values, and used to stabilize the IO clusters (Table 10).

**Table 10** – Experimental conditions and results for the preparation of cluster suspensions in the presence of PDMAEMA-*b*-PS-TTC macroRAFT agent at different pHs.

Run	pH <sub>0</sub> <sup>b</sup>	[HCl]/ [macroRAFT]	SC <sub>th</sub> <sup>c</sup> (%)	$f_{\text{clu}}$ <sup>d</sup> (%)	$Z_{\text{av-Droplets}}$ (nm)/Poly <sup>e</sup>	$Z_{\text{av-Clusters}}$ (nm)/Poly <sup>e</sup>	$D_n$ (nm)/ $D_w/D_n$ <sup>f</sup>
TRG128-3	10.0	<u>0</u>	2.97	7	1290/0.67	904/0.74	-
TRG128-1	8.5	<u>0</u>	2.86	6	573/0.25	801/0.70	-
TRG130-1	7.0	<u>10</u>	2.98	56	452/0.25	322/0.27	386/1.44
TRG130-2	-	<u>20</u>	1.91	91	371/0.17	349/0.19	312/1.48
TRG130-3	5.8	<u>30</u>	1.95	92	278/0.17	243/0.18	71/4.46
TRG70-7	4.0	<u>30</u>	2.24	84	183/0.07	172/0.06	94/1.32

$C_{\text{macroRAFT}}$  (mol L<sup>-1</sup>) =  $2.5 \cdot 10^{-4}$ ; FA@IONP concentration in toluene = 100 g L<sup>-1</sup>; Ferrofluid/aqueous phase wt/wt ratio = 0.25; Toluene evaporation at 90 °C. <sup>a</sup>Concentration of PDMAEMA-based macroRAFTs in a 37 mM NaCl solution; <sup>b</sup>pH of the macroRAFT solution; <sup>c</sup>Theoretical solids content; <sup>d</sup>Yield of cluster formation calculated from Equation 1; <sup>e</sup>Determined by DLS; <sup>f</sup>Number-average particle size and dispersity obtained by statistical analysis of 800-1200 particles from TEM images.

Unstable systems were obtained for low [HCl]/[macroRAFT] ratios (pH = 8.5 and 10.0) resulting in yields lower than 10% (TRG128-1 and TRG128-3, Table 10). Indeed, at such high pH values, the PDMAEMA segments are not charged resulting in poor stabilization of

the IO clusters. Furthermore, it is worth reminding also that PDMAEMA has a thermo-responsive behavior, which is pH-dependent. The LCST of the PDMAEMA homopolymer was determined in Chapter 2 and was found to decrease from 69 to 47 °C with increasing pH from 8.0 to 10. These phase transition temperatures were always below 90 °C, the temperature set during toluene evaporation. Therefore, precipitation of the PDMAEMA segments likely occurred, which can also account for the poor stability of the clusters under basic conditions.

When increasing the HCl concentration (i.e., when decreasing pH), more stable systems were obtained resulting in higher yields of cluster formation as shown in Figure 66A. In addition, the droplet and cluster size determined by DLS decreased with increasing [HCl] confirming the positive effect of polymer chains protonation on cluster stabilization

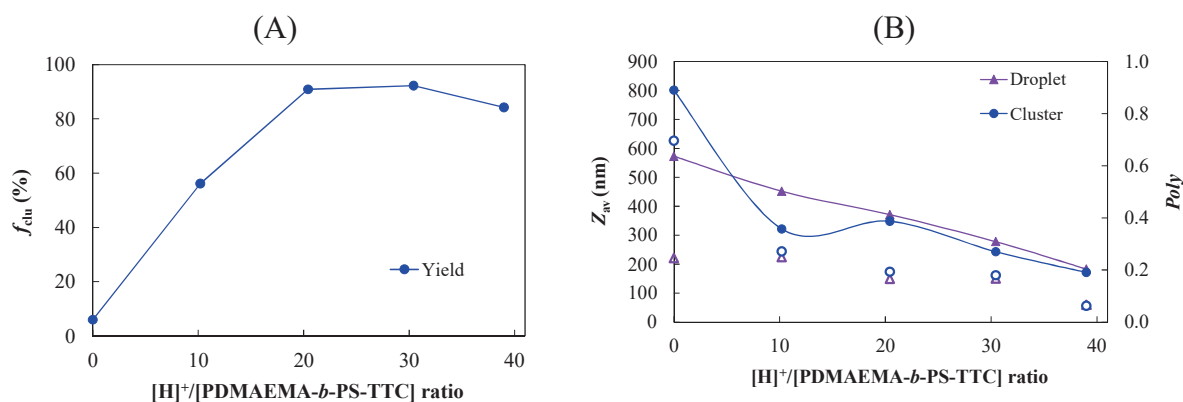


**Figure 66** – Effect of the [HCl]/[macroRAFT] ratio on cluster formation. (A) Yield of cluster formation and (B) evolution of cluster and droplet sizes (full symbols) and *Poly* value (open symbols) by DLS. Sonication power = 75 W, sonication time = 240 s and [PDMAEMA-*b*-PS-TTC] = 2.5 10<sup>-4</sup> M (see Table 10 for detailed experimental conditions).

As shown in the TEM micrographs of Figure 67, spherical clusters were obtained in all cases. The lowest [HCl]/[macroRAFT] ratios (i.e.,  $r = 10$  and  $20$ ) led to relatively big clusters with number-average diameters around 350 nm and dispersities lower than 1.5 in agreement with DLS analysis. This is an important result, demonstrating that it is possible to obtain clusters with a relatively big size and an acceptable dispersity. As magnetic properties depend on the particle size, these big clusters are expected to display a fast response in a magnetic field. On the other hand, the clusters obtained for  $r = 30$  had a very broad size distribution with the presence of small and big clusters whereas relatively small clusters with an acceptable size distribution ( $D_n = 94$  nm and  $D_w/D_n = 1.32$ ) were obtained for  $r = 40$  which is again in agreement with DLS analysis



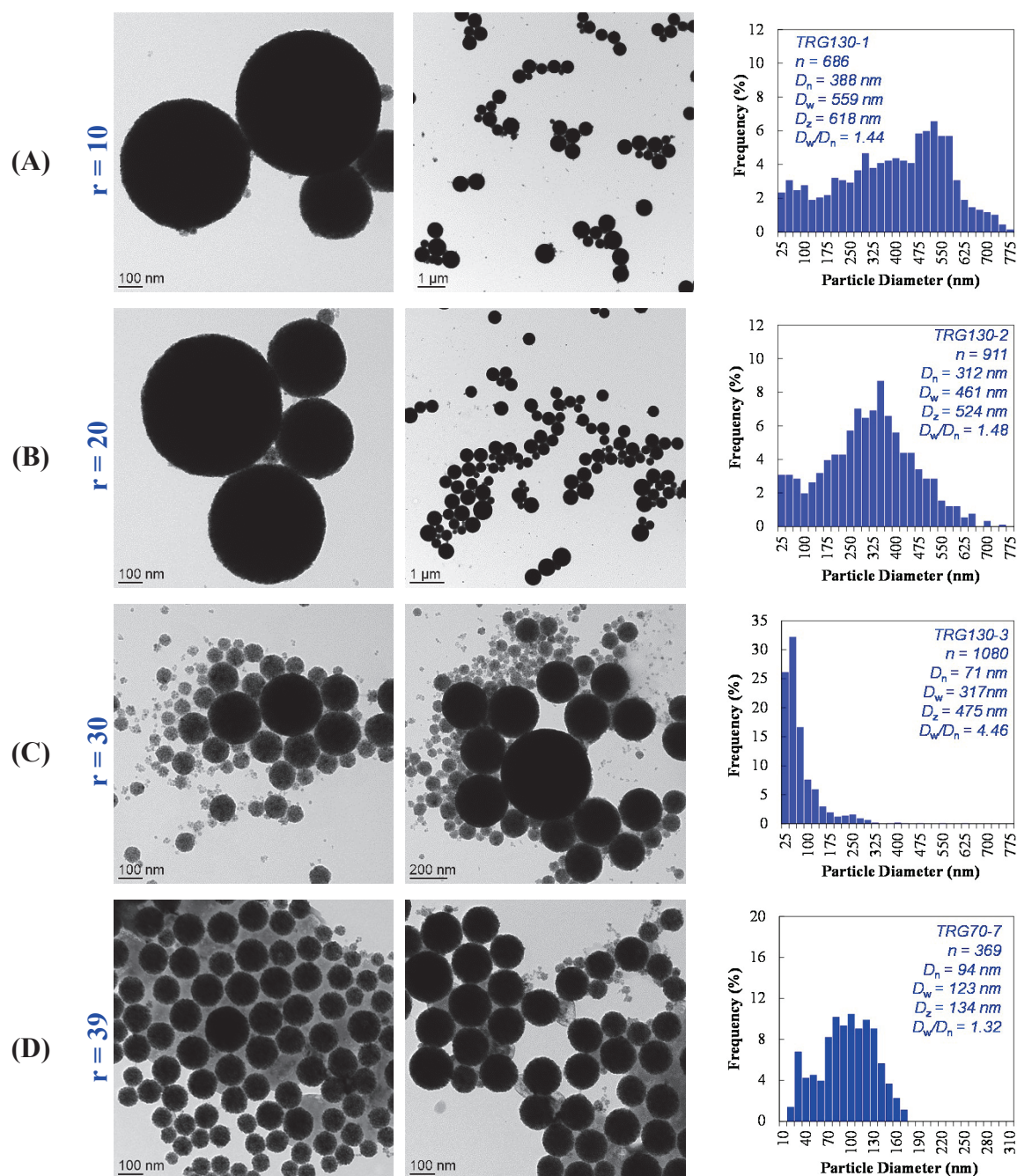


**Figure 67** – Effect of the  $[HCl]/[macroRAFT]$  ratio on the size and size distribution of the IO clusters. (A)  $r = [H^+]/[PDMAEMA-b-PS-TTC] = 10$ , (B)  $r = 20$ , (C)  $r = 30$  and (D)  $r = 39$ . *Left and middle*: TEM images of the IO cluster and *right*: corresponding number frequency size distribution histograms. Sonication power = 75 W, sonication time = 240 s and  $[PDMAEMA-b-PS-TTC] = 2.5 \cdot 10^{-4}$  M.

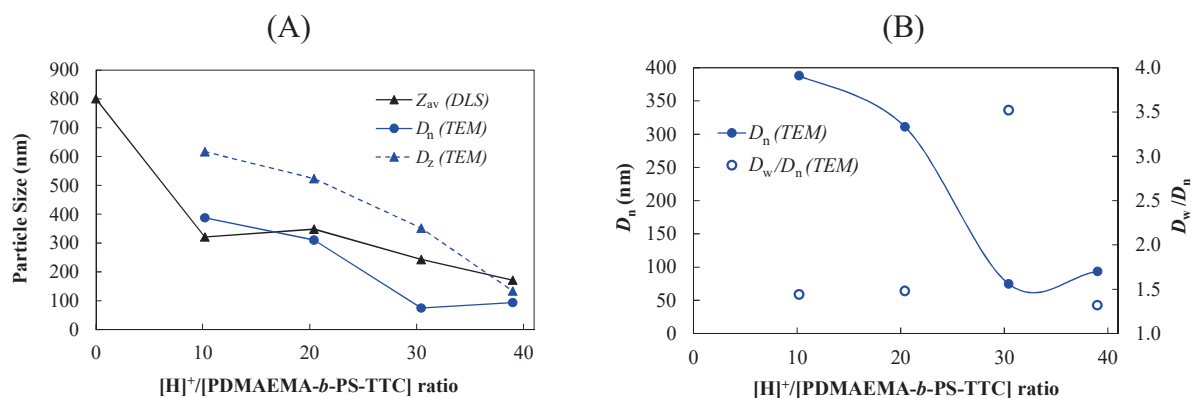


**Figure 68** – Effect of protonation degree of the tertiary amine from PDMAEMA-*b*-PS macroRAFT. (A)  $Z_{av}$  measured by DLS and number and intensity-mean diameter ( $D_n$  and  $D_z$ ) from TEM determined using Equation 4 and 6 and (B) ( $D_n$ , full symbols) and dispersity ( $D_w/D_n$ , open symbols) determined by TEM ( $t = 240$  s and  $P = 75$  W).

#### 4.2.5. Scale up experiments

The experimental conditions optimized in the previous sections (*i.e.* [macroRAFT] =  $2.5 \cdot 10^{-4}$  M and  $\text{pH}_0 = 4$ ; run TRG70-7) were applied to prepare a larger amount of clusters to be used in Chapter 4. Indeed, these conditions gave the highest particle diameter and the lowest dispersity of the series. The results of these scale-up experiments are summarized in Table 11.

**Table 11** – Experimental conditions and results for the scale-up experiments performed to prepare cluster suspensions in the presence of PDMAEMA-*b*-PS-TTC macroRAFT agent

Run	$\text{SC}_{\text{th}}^{\text{a}}$ (%)	$f_{\text{clu}}(\%)^{\text{b}}$	$Z_{\text{av-Droplets}}$ (nm)/ $\text{Poly}^{\text{c}}$	$Z_{\text{av-Clusters}}$ (nm)/ $\text{Poly}^{\text{c}}$	$D_n$ (nm)/ $D_w/D_n^{\text{d}}$	$\text{SC}_{\text{sep}}^{\text{e}}$ (%)	$f_{\text{sep}}(\%)^{\text{f}}$
<i>Scaled-up series</i>							
TRG78	2.94	70	261/0.22	244/0.20	80/2.02	-	-
TRG89	2.74	86	187/0.12	180/0.05	82/1.61	2.08	89
TRG107	2.68	83	240/0.24	196/0.11	77/1.78	1.97	89
TRG119	2.67	86	194/0.13	184/0.10	71/1.58	2.00	87
TRG134	2.79	83	197/0.15	181/0.10	81/1.82	2.13	93

IONP@FA concentration in toluene =  $100 \text{ g L}^{-1}$ ; Ferrofluid/aqueous phase wt/wt ratio = 0.25; Toluene evaporation at  $45 \text{ }^\circ\text{C}$  by rota-evaporation under vacuum conditions; [PDMAEMA-*b*-PS-TTC] =  $2.5 \text{ mM}$  in  $37 \text{ mM NaCl}$  solution at  $\text{pH } 4$ ; Sonication time =  $240 \text{ s}$ ; <sup>a</sup>Theoretical solids content; <sup>b</sup>Yield of cluster formation calculated from Equation 1; <sup>c</sup>Determined by DLS; <sup>d</sup>Number-average particle size and dispersity obtained by statistical analysis of 800-1200 particles from TEM images (see ANNEX 3. 5); <sup>e</sup>Solids content after magnetic separation; <sup>f</sup>Yield of cluster separation calculated from Equation 3.

A good reproducibility was observed among the different batches prepared during the project. Moreover, the fraction of iron oxide clusters with a fast response to the magnetic field was also high for all batches, around 90% (Table 11). Additional results about the time of magnetic separation will be presented in Chapter 4.

### **4.3. PAA-based iron oxide clusters**

The same strategy as that described above for PDMAEMA-based macroRAFT agents was used in this section for the preparation of iron oxide clusters stabilized with the amphiphilic PAA-*b*-PS-TTC macroRAFT copolymers.

#### *4.3.1. Effect of macroRAFT concentration*

As observed in the previous section, the concentration of the amphiphilic macroRAFT agent is a key parameter that requires particular attention. Iron oxide clusters were thus prepared at different PAA-*b*-PS-TTC concentrations as presented in Table 12.



**Table 12** – Experimental conditions and results for the preparation of cluster suspensions in the presence of PAA-*b*-PS-TTC macroRAFT agent.

Run	$C_{\text{macroRAFT}}$ (mol L <sup>-1</sup> ) <sup>a</sup>	$SC_{\text{th}}$ <sup>b</sup> (%)	$f_{\text{clu}}$ (%) <sup>c</sup>	$Z_{\text{av-Droplets}}$ (nm)/Poly <sup>d</sup>	$Z_{\text{av-Clusters}}$ (nm)/Poly <sup>d</sup>	$D_n$ (nm)/ $D_w/D_n$ <sup>e</sup>
<i>PAA-b-PS-TTC concentration series</i>						
TRG115-4	$1.0 \cdot 10^{-6}$	1.79	7	165/0.08	2947/1.00	-
TRG115-3	$1.0 \cdot 10^{-5}$	1.71	7	253/0.22	2313/1.00	-
TRG115-2	$1.0 \cdot 10^{-4}$	2.13	53	156/0.05	674/0.62	95/1.32
TRG115-8	$1.5 \cdot 10^{-4}$	2.10	72	153/0.12	250/0.25	77/1.70
TRG115-7	$2.5 \cdot 10^{-4}$	2.18	82	207/0.25	149/0.09	65/1.74
TRG115-6	$5.1 \cdot 10^{-4}$	2.39	93	135/0.06	139/0.06	73/1.47
TRG115-5	$7.5 \cdot 10^{-4}$	2.77	95	131/0.06	134/0.07	74/1.50
TRG115-1	$1.0 \cdot 10^{-3}$	2.27	88	138/0.04	133/0.09	63/1.50
<i>Scale-up series</i>						
TRG132	$2.5 \cdot 10^{-4}$	2.26	84	145/0.08	143/0.07	66/1.78
TRG140	$2.5 \cdot 10^{-4}$	2.62	95	142/0.13	161/0.13	71/1.55
TRG152	$2.5 \cdot 10^{-4}$	2.78	94	148/0.08	148/0.06	-
TRG156	$2.5 \cdot 10^{-4}$	2.78	96	146/0.08	145/0.08	52/1.97

*IONP@FA concentration in toluene = 100 g L<sup>-1</sup>; Ferrofluid/aqueous phase wt/wt ratio = 0.25; Toluene evaporation at 90 °C. <sup>a</sup>Concentration of PAA-*b*-PS-TTC in a 37 mM NaCl solution at pH 10; <sup>b</sup>Theoretical solids content; <sup>c</sup>Yield of cluster formation calculated from Equation 1; <sup>d</sup>Determined by DLS; <sup>e</sup>Number-average particle size and dispersity obtained by statistical analysis of 600-1200 particles from TEM images.*

As shown in Figure 69B, low PAA-*b*-PS concentrations ( $\leq 1 \cdot 10^{-5}$  M) led to unstable suspensions. As discussed above for PDMAEMA-*b*-PS-TTC, this result indicates that a minimum amount of macroRAFT agent is necessary to ensure droplet/cluster stabilization. In addition, by increasing the PAA-*b*-PS-TTC the size and size distribution of the droplets/clusters decreased (Figure 69C), leading to the formation of more stable systems, and thus to higher yields (Figure 69D).

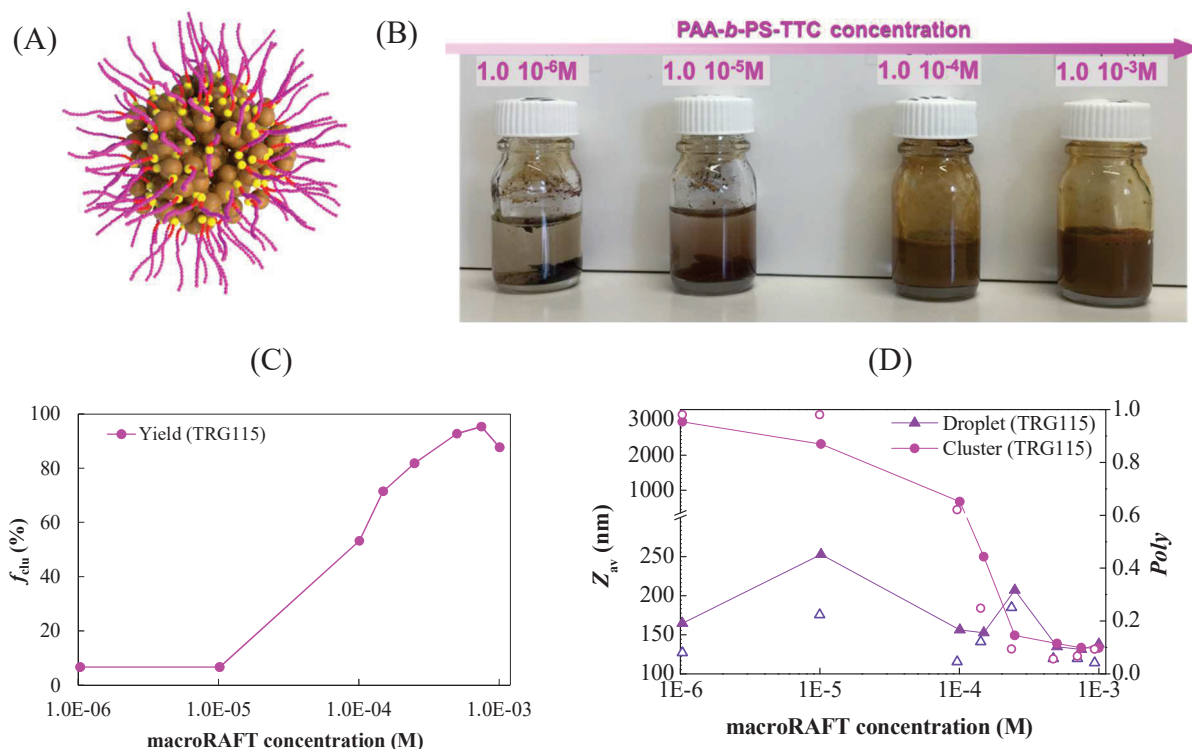


**Figure 69** – Effect of PAA-*b*-PS-TTC concentration on cluster formation. (A) Schematic representation of the PAA-*b*-PS-TTC-stabilized IO clusters, (B) photographs of IO cluster suspensions after toluene evaporation, (C) yield of cluster formation and (D) evolution of droplet and cluster sizes (full symbols) and *Poly* value (open symbols, DLS) with macroRAFT concentration. Sonication power = 75 W and sonication time = 240 s (see Table 4 for detailed experimental conditions).

The TEM images of Figure 70 show the formation of spherical clusters. The corresponding size histograms of Figure 70 indicate that the concentration of PAA-*b*-PS-TTC plays an important role on cluster size, as can be also verified in the graphs of particle size evolution with concentration shown in Figure 71A and B. The cluster size decreased with increasing the macroRAFT concentration, as reported above for PDMAEMA-*b*-PS.  $D_n$  (TEM) was again smaller than  $Z_{\text{av}}$ , which showed a better agreement with  $D_z$ .

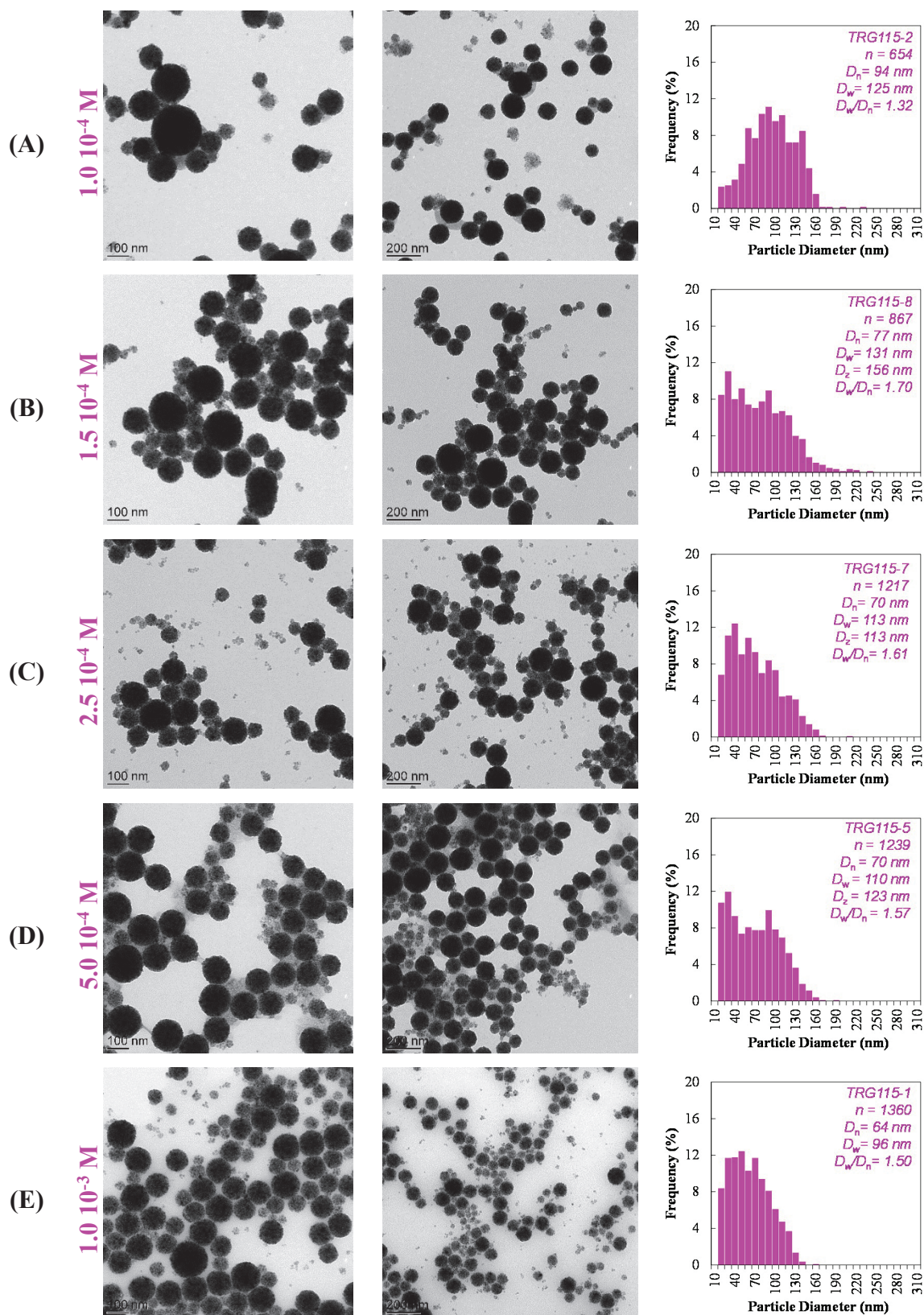


**Figure 70** – Effect of PAA-*b*-PS-TTC concentration on the size and size distribution of the IO clusters. (A) 1.0 10<sup>-4</sup> M, (B) 1.5 10<sup>-4</sup> M, (C) 2.5 10<sup>-4</sup> M, (D) 5.0 10<sup>-4</sup> M and (E) 1.0 10<sup>-3</sup> M. *Left*: TEM micrographs at fixed magnification of 56000x, *middle*: additional micrographs at different magnifications, and *right*: corresponding number frequency size distribution histograms. Sonication power = 75 W and sonication time = 240 s.

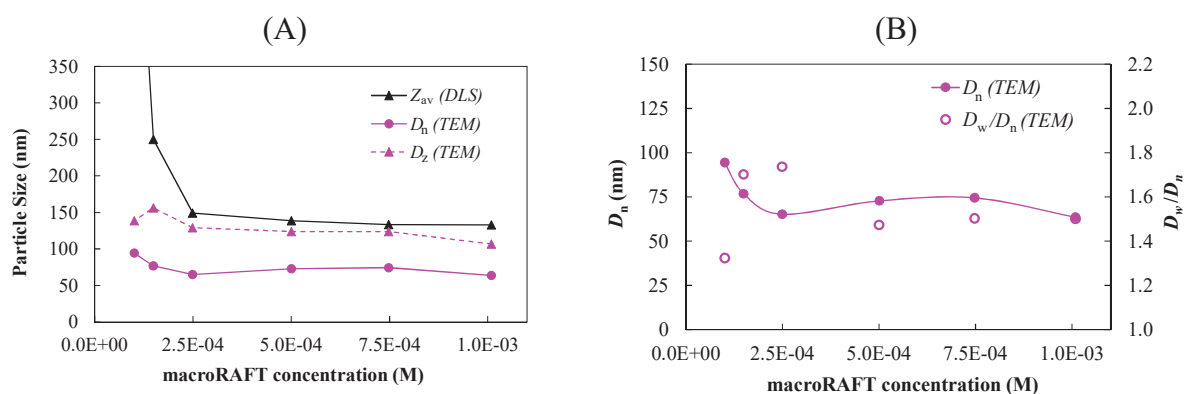


**Figure 71** – Effect of PAA-*b*-PS-TTC concentration on cluster size and size distribution. (A)  $D_n$  (full symbols) and dispersity ( $D_w/D_n$ , open symbols) determined by TEM and (B)  $Z_{av}$  measured by DLS and number and intensity-mean diameter ( $D_n$  and  $D_z$ ) from TEM determined using Equations 4 and 6. Sonication power = 75 W and sonication time = 240 s.

#### 4.3.2. Effect of the $[NaOH]/[PAA-b-PS-TTC]$ ratio

Like PDMAEMA, PAA is a pH-responsive polymer, following however an opposite behavior. PDMAEMA becomes positively charged with protonation of the amino groups, whereas PAA becomes negatively charged with deprotonation of the carboxylic acid groups. In the following series of experiments, we varied the NaOH concentration in order to see its effect on cluster formation (Table 13).

**Table 13** – Experimental conditions and results for the preparation of cluster suspensions in the presence of PAA-*b*-PS-TTC macroRAFT agent at different pHs.

Run	$C_{macroRAFT}$ (mol L <sup>-1</sup> ) <sup>a</sup>	pH <sub>0</sub> <sup>b</sup>	$[NaOH]/$ $[macroRAFT]$	SC <sub>th</sub> <sup>c</sup> (%)	$f^d$ (%)	$Z_{av-Droplets}$ (nm)/Poly <sup>e</sup>	$Z_{av-Clusters}$ (nm)/Poly <sup>e</sup>	$D_n$ (nm)/ $D_w/D_n^f$
<i>pH series</i>								
TRG127-1	2.5 10 <sup>-4</sup>	3.3	=	2.06	94	228/0.21	277/0.38	89/1.85
TRG127-3	2.5 10 <sup>-4</sup>	4.0	2	2.00	95	178/0.13	360/0.42	-
TRG129-1	2.5 10 <sup>-4</sup>	5.8	10	1.74	97	191/0.20	242/0.28	103/1.63
TRG129-2	2.5 10 <sup>-4</sup>	6.7	20	2.04	90	179/0.12	177/0.10	-
TRG127-2	2.5 10 <sup>-4</sup>	7.0	26	2.41	79	214/0.19	164/0.09	86/1.58
TRG115-7	2.5 10 <sup>-4</sup>	10.0	40	2.18	81	207/0.25	149/0.09	65/1.74

FA@IONP concentration in toluene = 100 g L<sup>-1</sup>; Ferrofluid/aqueous phase wt/wt ratio = 0.25; Toluene evaporation at 90 °C. <sup>a</sup>Concentration in a 37 mM NaCl solution at pH 10; <sup>b</sup>pH of the macroRAFT solution; <sup>c</sup>Theoretical solids content; <sup>d</sup>Yield of cluster formation calculated from Equation 1; <sup>e</sup>Determined by DLS; <sup>f</sup>Number-average particle size and dispersity obtained by statistical analysis of 900-1200 particles from TEM images.



As shown in Figure 72A, high yields of cluster formation (>80%) were attained in the whole range of  $[\text{OH}^-]/[\text{PAA-}b\text{-PS-TTC}]$  ratios investigated (*i.e.* 0 to 40). This is an interesting result which demonstrates that the PAA segments are able to stabilize the clusters not only via electrosteric repulsion at high pH, but also by providing steric stabilization to the clusters at low  $[\text{OH}^-]/[\text{PAA-}b\text{-PS-TTC}]$  ratios. As expected, the cluster diameter decreased with increasing the NaOH concentration (Figure 72B).

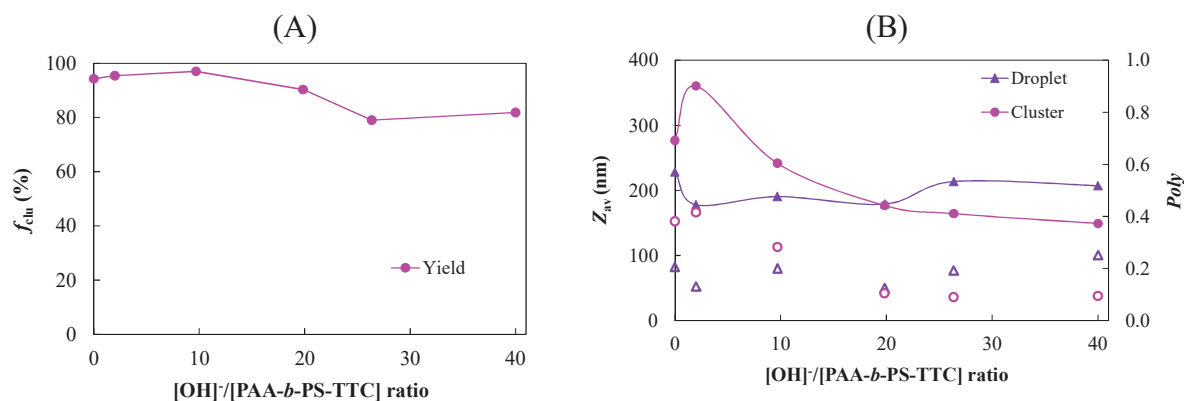


**Figure 72** – Effect of the  $[\text{OH}^-]/[\text{PAA-}b\text{-PS-TTC}]$  ratio on: (A) the yield of cluster formation and (B) cluster and droplet size (full symbols) and *Poly* value (open symbols, DLS). Sonication power = 75 W, sonication time = 240 s and  $[\text{PAA-}b\text{-PS-TTC}] = 2.5 \cdot 10^{-4}$  M (see Table 13 for detailed experimental conditions).

Nevertheless, the histograms shown in Figure 73 indicate that the  $[\text{OH}^-]/[\text{PAA-}b\text{-PS-TTC}]$  ratio did not have such a strong effect on the cluster size and size distribution. These results are in disagreement with those obtained by DLS (Figure 72B), which showed that the cluster size was smaller at high pH indicating a better contribution of electrosteric repulsion for cluster stabilization. Actually, both results are correct. Indeed, a closer look at the histograms of Figure 73A and B shows the presence of a small fraction of particles with size higher than 200 nm. This small population of particles will induce a shift of  $Z_{\text{av}}$  to higher values as the DLS technique is sensitive to the presence of big particles. This effect can be clearly evidenced in Figure 74A, in which  $D_z$  from TEM fits quite well with the  $Z_{\text{av}}$  from DLS, and both values decreased as the pH increased, whereas  $D_n$  stayed almost constant for all  $[\text{OH}^-]$  concentrations. These results further demonstrate the importance of particle size analysis by TEM and how the DLS results can be affected by a small fraction of big particles. Finally, the almost constant  $D_n$  values obtained in the whole range of pH investigated indicate that the PAA-*b*-PS-TTC macroRAFT agent is able to successfully stabilize IO clusters by steric or electrosteric stabilization.

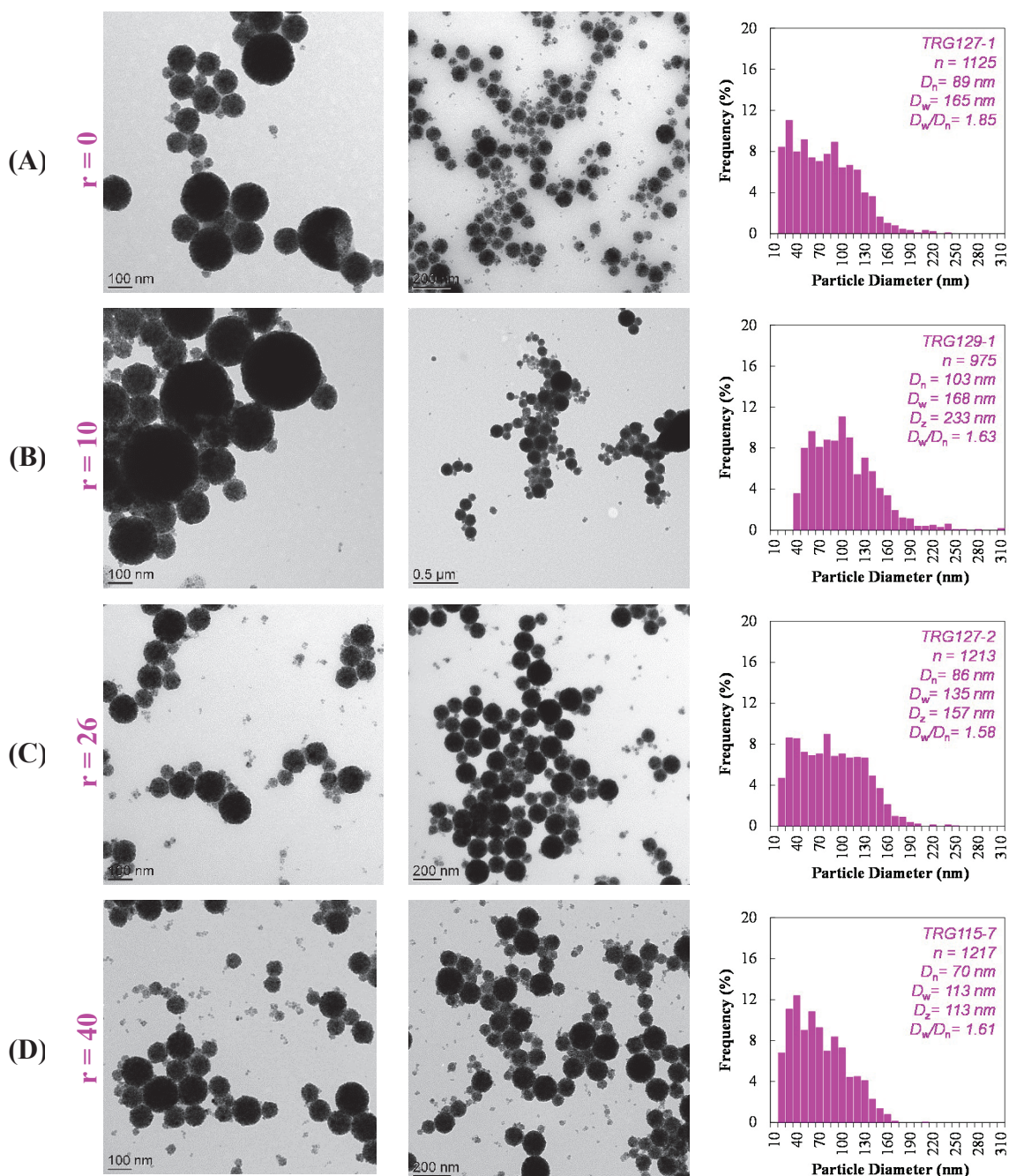


**Figure 73** – Effect of the  $[\text{OH}^-]/[\text{PAA-}b\text{-PS-TTC}]$  ratio on the size and size distribution of the IO clusters. (A)  $r = [\text{OH}^-]/[\text{PAA-}b\text{-PS-TTC}] = 0$ , (B)  $r = 10$ , (C)  $r = 26$  and (D)  $r = 40$  *Left*) TEM micrographics at a fixed magnification of 56000x, *middle*: additional micrographics at different magnifications and *right*: corresponding number frequency size distribution histograms. Sonication power = 75 W, sonication time = 240 s and  $[\text{PAA-}b\text{-PS-TTC}] = 2.5 \cdot 10^{-4}$  M.



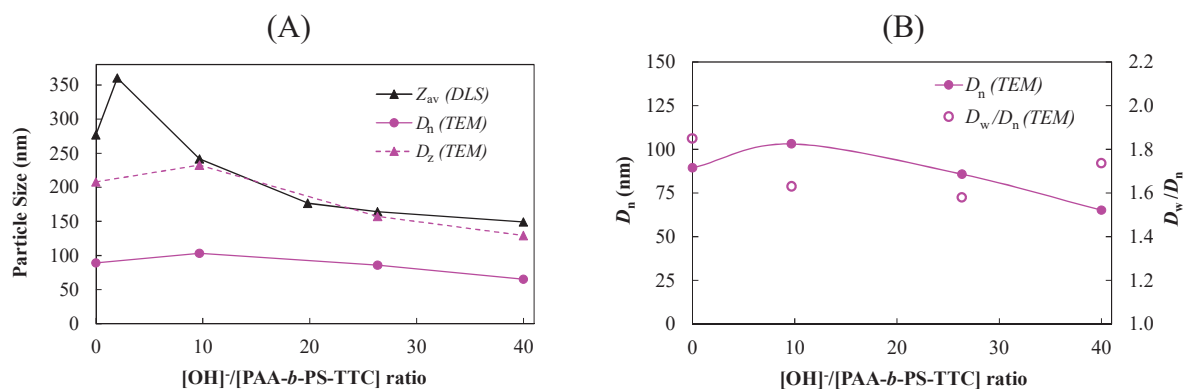


**Figure 74** – Effect of the  $[\text{OH}^-]/[\text{PAA-}b\text{-PS-TTC}]$  ratio on cluster size and size distribution. (A)  $D_n$  (full symbols) and dispersity ( $D_w/D_n$ , open symbols) determined by TEM and (b)  $Z_{av}$  measured by DLS and number and intensity-mean diameter ( $D_n$  and  $D_z$ ) from TEM determined using Equation 4 and 6, respectively. Sonication power = 75 W, sonication time = 240 s and  $[\text{PAA-}b\text{-PS-TTC}] = 2.5 \cdot 10^{-4}$  M.

Furthermore, the ability of the PAA chains to stabilize the clusters over a wide range of pH supports the hypothesis that the poor stability of the clusters obtained for PDMAEMA at high pH, is due to the thermo-responsiveness of the PDMAEMA segments.

#### 4.4. Cluster preparation in the presence of hydrophilic macroRAFTs: influence of the PS block

In order to assess the role of the hydrophobic polystyrene block on cluster formation and stabilization, a series of experiments was carried out using the hydrophilic macroRAFT agents (*i.e.* without the hydrophobic block, either PAA-TTC or PDMAEMA-TTC). Table 14 summarizes the experimental conditions and the results of these experiments.

The graphs of Figure 75 show the effect of hydrophilic and amphiphilic macroRAFT concentrations on the preparation of IO clusters. As observed in Figure 75A the yield of cluster formation in the presence of PDMAEMA-TTC is systematically lower than that attained when using PDMAEMA-*b*-PS-TTC. These results indicate that the PS hydrophobic segment played an important role in cluster stabilization. Nonetheless, this behavior was not observed for the PAA-based clusters. Indeed, the yield of cluster formation was similar, even higher for one concentration, when using PAA-TTC instead of PAA-*b*-PS-TTC. It has been reported in the literature that with fatty acid-modified iron oxide nanoparticles, in which the interaction between the nanoparticles and the fatty acid is ensured by the complexation of the carboxylic groups, the fatty acid modifier agent can be replaced by other carboxylic acid containing species present in the medium. This effect could explain why the PAA-TTC

hydrophilic macroRAFT was able to stabilize the clusters, the fatty acid of the commercial IONP being replaced by PAA-TTC around the cluster surface giving to them higher hydrophilicity and, consequently, better stability in water phase (Figure 75B). However, further characterizations would be necessary to support this scenario.

**Table 14** – Experimental conditions and results for the preparation of cluster suspensions in the presence of hydrophilic macroRAFT agents: PAA-TTC and PDMAEMA-TTC.

Run	$C_{\text{macroRAFT}}$ (mol L <sup>-1</sup> ) <sup>a</sup>	pH <sub>0</sub> <sup>b</sup>	SC <sub>th</sub> <sup>c</sup> (%)	$f_{\text{clu}}$ (%) <sup>d</sup>	$Z_{\text{av-Droplets}}$ (nm)/Poly <sup>e</sup>	$Z_{\text{av-Clusters}}$ (nm)/Poly <sup>e</sup>	$D_n$ (nm)/ $D_w/D_n$ <sup>f</sup>
<i>PDMAEMA-TTC concentration series</i>							
TRG114-4	$1.0 \cdot 10^{-6}$	4	2.61	7	571/0.24	3059/1.00	-
TRG114-3	$1.0 \cdot 10^{-5}$	4	2.21	8	767/0.23	5064/1.00	-
TRG114-2	$1.0 \cdot 10^{-4}$	4	1.69	24	330/0.30	494/0.42	209/1.73
TRG114-1	$1.0 \cdot 10^{-3}$	4	2.59	53	171/0.13	992/0.75	103/1.22
<i>PAA-TTC concentration series</i>							
TRG116-4	$1.0 \cdot 10^{-6}$	10	2.07	4	181/0.10	727/0.59	-
TRG116-3	$1.0 \cdot 10^{-5}$	10	1.56	4	177/0.11	2296/1.00	-
TRG116-2	$1.0 \cdot 10^{-4}$	10	2.01	83	159/0.11	159/0.09	86/1.52
TRG116-1	$1.0 \cdot 10^{-3}$	10	2.43	84	137/0.09	132/0.08	67/1.50

FA@IONP concentration in toluene = 100 g L<sup>-1</sup>; Ferrofluid/aqueous phase wt/wt ratio = 0.25; Toluene evaporation at 90 °C. <sup>a</sup>Concentration in a 37 mM NaCl solution; <sup>b</sup>pH of macroRAFT solution; <sup>c</sup>Theoretical solids content; <sup>d</sup>Yield of cluster formation calculated from Equation 1; <sup>e</sup>Determined by DLS; <sup>f</sup>Number-average particle size and dispersity obtained by statistical analysis of 500-1200 particles from TEM images.

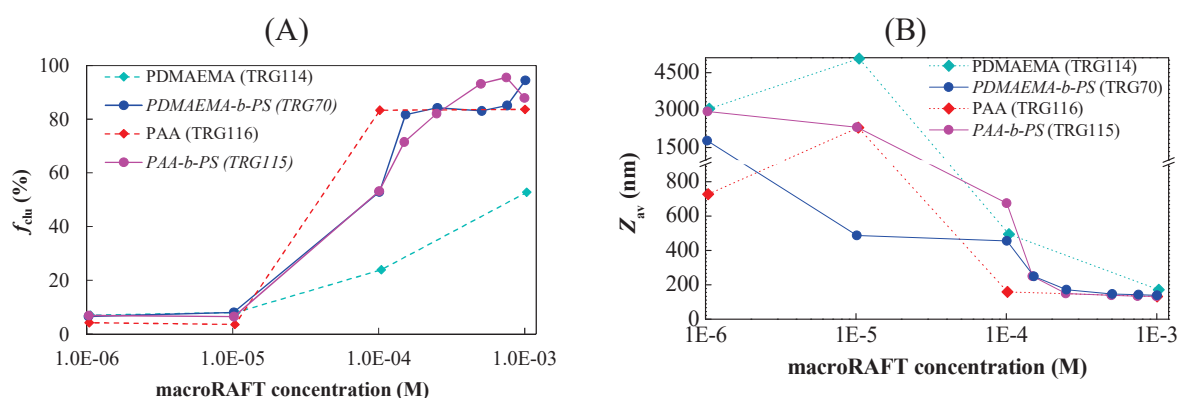


**Figure 75** – Effect of macroRAFT composition and concentration on the formation of IO clusters. (A) Yield of cluster formation and (B) cluster size (DLS). Sonication power = 75 W and sonication time = 240 s (see Table 11, Table 12 and Table 14 for detailed experimental conditions).

Furthermore, iron oxide clusters stabilized with hydrophilic PDMAEMA macroRAFT present narrower size distribution (e.g.  $D_w/D_n = 1.22$  for  $[\text{macroRAFT}] = 1 \cdot 10^{-3} \text{ M}$ , Table 9) than those obtained for PDMAEMA-*b*-PS-TTC stabilized clusters (e.g.  $D_w/D_n = 1.58$  for

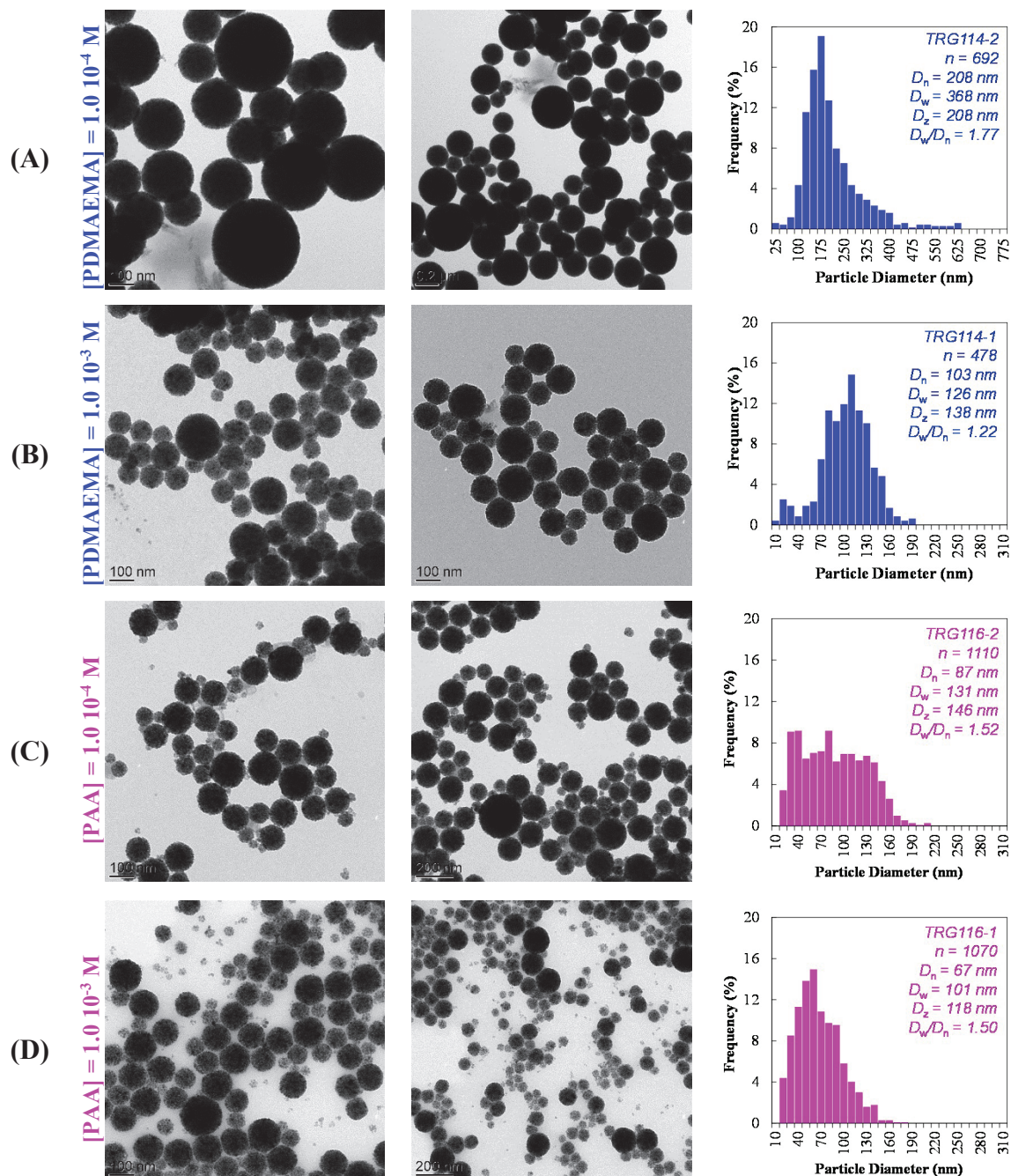


**Figure 76** – Effect of macroRAFT composition and concentration on the size and size distribution of the IO clusters. (A)  $[\text{PDMAEMA-TTC}] = 1.0 \cdot 10^{-4} \text{ M}$ , (B)  $[\text{PDMAEMA-TTC}] = 1.0 \cdot 10^{-3} \text{ M}$ , (C)  $[\text{PAA-TTC}] = 1.0 \cdot 10^{-4} \text{ M}$  and (D)  $[\text{PAA-TTC}] = 1.0 \cdot 10^{-3} \text{ M}$ . *Left*: TEM micrographs at a fixed magnification of 56000x, *middle*: additional micrographs at different magnifications and *right*: corresponding number frequency size distribution histograms. Sonication power = 75 W and sonication time = 240 s (see Table 14 for detailed experimental conditions).

[macroRAFT] =  $1 \cdot 10^{-3}$  M, Table 14). Indeed, in the histograms of Figure 76A and B it can be observed that the fraction of small particles ( $D_i < 75$  nm) is lower than that observed for the clusters stabilized with the amphiphilic block copolymer at the same concentration (see histograms of Figure 63). This can be related to the lower efficiency of PDMAEMA hydrophilic chains for the stabilization of small iron oxide clusters leading to the formation of narrow particle size distribution at concentration of  $1 \cdot 10^{-3}$  M ( $D_w/D_n = 1.22$ ). Nonetheless, the yields of cluster formation for PDMAEMA-TTC systems were always lower than 60 % restricting their employment as optimized system for the scaled-up experiments. It is worth mentioning that the PDMAEMA-TTC system was not extensively studied, but by changing the sonication conditions such as time and power, or employing a wide range of macroRAFT concentration, higher yield could probably be achieved.

#### **4.5. P(AA-*co*-DMAEMA)-based clusters**

As detailed in Chapter 2, the versatility of RAFT polymerization was exploited by preparing different macroRAFTs with various compositions in AA and DMAEMA. As mentioned above, PAA and PDMAEMA display opposite pH-responsive properties, PAA being negatively charged under basic conditions while PDMAEMA is positively charged under acidic conditions. Based on these concepts, IO clusters were prepared in the presence of amphiphilic macroRAFT agents, varying the DMAEMA/AA composition of the hydrophilic moiety, as schematically represented in Figure 78A. Optimized experimental conditions (Table 15) were set-up based on the results presented in the previous sections.

The macroRAFT agents were first dissolved in water at either  $\text{pH}_0 = 4$  or  $\text{pH}_0 = 10$ , as indicated in Table 15. After the emulsification process with the toluene-based ferrofluid and toluene evaporation, cluster suspensions with yields often higher than 80% were obtained (Figure 77A). The evolution of the cluster size with the AA molar fraction is plotted in Figure 77B. The lower  $Z_{av}$  values were obtained for the systems prepared under basic conditions. This effect is confirmed by TEM micrographs (Figure 78), which show the presence of big particles (300-500 nm) for the clusters prepared with macroRAFT solutions at  $\text{pH} = 4$ . Even if the fraction of big particles is not significant for these systems (see histograms of Figure 78) the  $Z_{av}$  value is strongly affected as can be observed in Figure 77B. This behavior at low pH can be associated with inter-/intramolecular interaction between AA units, related to H-bond formation between the hydrogen atoms from carboxylic acid groups.<sup>71-73</sup> However, at higher pH these groups are deprotonated preventing the H-bonding formation.<sup>73</sup> The clusters



prepared at pH = 10 present a narrower distribution (Figure 78). Nonetheless, the clusters stabilized by the amphoteric macroRAFT with the lower AA content (P(DMAEMA<sub>33</sub>-co-AA<sub>16</sub>)-b-PS<sub>10</sub>-TTC) and prepared at pH 10 (TRG151, Figure 78) present a broad size distribution, which can be explained by the few number of AA units in the hydrophilic moiety, which seems to be not enough to provide good colloidal stability to the system, leading to the formation of big particles.

**Table 15** – Experimental conditions and results for the preparation of cluster suspensions in the presence of P(DMAEMA-co-AA)-b-PS macroRAFT agents with various AA to DMAEMA ratios.

Run	$C_{\text{macroRAFT}}$ (mol L <sup>-1</sup> ) <sup>a</sup>	pH <sub>0</sub> <sup>b</sup>	pH <sub>f</sub> <sup>c</sup>	SC <sub>th</sub> <sup>d</sup> (%)	$f^e$ (%)	$Z_{\text{av-Droplets}}$ (nm)/Poly <sup>f</sup>	$Z_{\text{av-Clusters}}$ (nm)/Poly <sup>f</sup>	$D_n$ (nm)/ $D_w/D_n^g$
<i>P(DMAEMA<sub>33</sub>-co-AA<sub>16</sub>)-b-PS<sub>10</sub>-TTC</i>								
TRG139	2.5 10 <sup>-4</sup>	4.0	5.6	2.71	90	370/0.26	319/0.20	96/2.75
TRG151	2.5 10 <sup>-4</sup>	10.0	8.0	2.78	78	396/0.40	277/0.22	108/1.98
<i>P(DMAEMA<sub>16</sub>-co-AA<sub>23</sub>)-b-PS<sub>11</sub>-TTC</i>								
TRG144	2.5 10 <sup>-4</sup>	4.0	-	2.61	66	1307/0.21	666/0.23	109/5.81
TRG148	2.5 10 <sup>-4</sup>	10.0	-	2.57	100	175/0.08	177/0.08	91/1.53
<i>P(DMAEMA<sub>10</sub>-co-AA<sub>39</sub>)-b-PS<sub>11</sub>-TTC</i>								
TRG143	2.5 10 <sup>-4</sup>	10.0	7.4	2.62	96	140/0.08	137/0.07	77/1.4

FA@IONP concentration in toluene = 100 g L<sup>-1</sup>; Ferrofluid/aqueous phase wt/wt ratio = 0.25; Toluene evaporation at 90 °C. <sup>a</sup>Concentration in a 37 mM NaCl solution; <sup>b</sup>pH of macroRAFT solution; <sup>c</sup>pH of cluster dispersion after toluene evaporation; <sup>d</sup>Theoretical solids content; <sup>e</sup>Yield of cluster formation calculated from Equation 1; <sup>f</sup>Determined by DLS; <sup>g</sup>Number-average particle size and dispersity obtained by statistical analysis of 1000-2000 particles from TEM images.

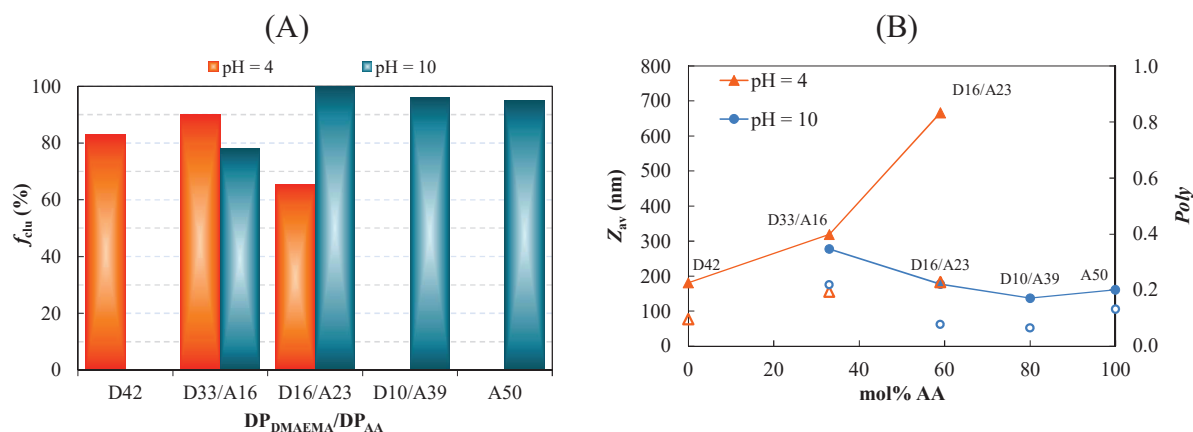


**Figure 77** – Effect of the composition of the hydrophilic segment of the macroRAFT agent on cluster formation. (A) Yield of cluster formation and (B) cluster and droplet size (full symbols) and Poly value (open symbols, DLS) in basic or acidic condition. Sonication power = 75 W and sonication time = 240 s (see Table 15 for detailed experimental conditions).

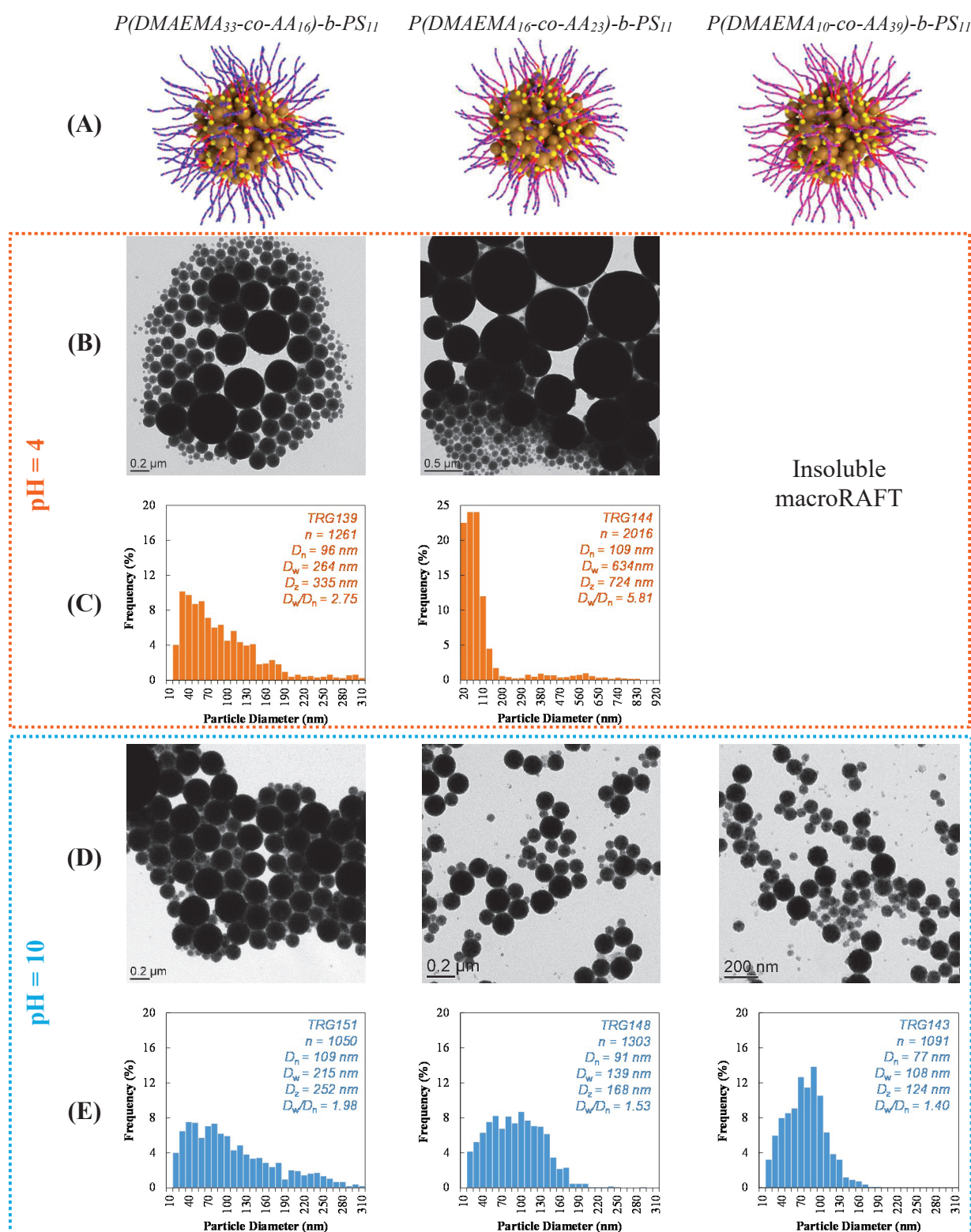


**Figure 78** – Effect of the composition of the hydrophilic segment of the amphiphilic macroRAFTs. (A) Schematic representation of IO clusters stabilized by amphiphilic macroRAFTs with variable compositions. (B, D) TEM images and (C, E) corresponding number frequency size distribution histograms of IO clusters stabilized with: *left*:  $P(\text{DMAEMA}_{33}\text{-co-AA}_{16})\text{-b-PS}_{11}\text{-TTC}$ , *middle*:  $P(\text{DMAEMA}_{16}\text{-co-AA}_{23})\text{-b-PS}_{11}\text{-TTC}$  and *right*:  $P(\text{DMAEMA}_{10}\text{-co-AA}_{39})\text{-b-PS}_{11}\text{-TTC}$ . (B, C) pH = 4 and (D, E) pH = 10. Sonication power = 75 W and sonication time = 240 (see Table 15 for detailed experimental conditions).



#### 4.6. Surface properties

The pH-responsive properties of the clusters stabilized by the amphiphilic macroRAFT agents were evaluated by  $\zeta$ -potential measurements at different pHs. Figure 79 clearly shows the pH-dependent behavior of the cluster surface, which is directly related to the composition of the hydrophilic part of the amphiphilic macroRAFT. Hence, a gradual deprotonation of the carboxylic acid groups of the AA units as the pH increases led to a better contribution of the anionic charges to cluster stabilization, as evidenced by the evolution of the  $\zeta$ -potential. On the opposite, the protonation of the DMAEMA units when decreasing the pH will increase the contribution of the cationic charges. Nevertheless, the zeta potential of the clusters stabilized by PDMAEMA<sub>42</sub>-*b*-PS<sub>8</sub>-TTC also became negative at pH higher than 9, which was an unexpected behavior. One possible explanation may come from the carboxylic acid chain-end functionalization of the macroRAFT, originating from the R group of the molecular RAFT agent used for its synthesis (the structure of the CTPPA RAFT agent is shown in Chapter 2). This observation is in accordance with some works reported in the literature,<sup>74, 75</sup> which have shown that the zeta-potential of polymer particles decorated with PDMAEMA became negative under basic conditions. The authors have associated this behavior with the anionic sulfate group present at the polymer chain ends, coming from the persulfate initiator. It is worth mentioning that DMAEMA monomer can be partially hydrolyzed in aqueous solution resulting in the formation of methacrylic acid,<sup>76</sup> which could also explain the negative  $\zeta$ -potential observed in basic conditions for the iron oxide clusters. However, after polymerization, PDMAEMA is much more stable than its monomer. Bout *et al.*<sup>77</sup> have reported that PDMAEMA chains were stable after 6 months of incubation at 37°C and Wettering *et al.*<sup>76</sup> have observed that even at 80°C and pH 7 only 4% of PDMAEMA units were hydrolyzed. Therefore, it is very unlikely that hydrolysis is taking place during the few minutes needed to adjust the pH before zeta-potential measurement, at room temperature. Furthermore, no significant variation of cluster size was observed in the range of pH studied for all systems, except for the PAA-stabilized clusters that were unstable at pH 3.

It is worth mentioning that the clusters stabilized by the amphoteric P(DMAEMA<sub>16</sub>-*co*-AA<sub>23</sub>)-*b*-PS<sub>11</sub>-TTC displayed an interesting behavior as a function of pH. Their surface charges turn from positive in acidic conditions (pH = 4) to negative at pH 5.5. Such behavior in surface properties in mild pH conditions is an important result for an application in the biomedical field, as some organisms are not resistant to harsh pH conditions.

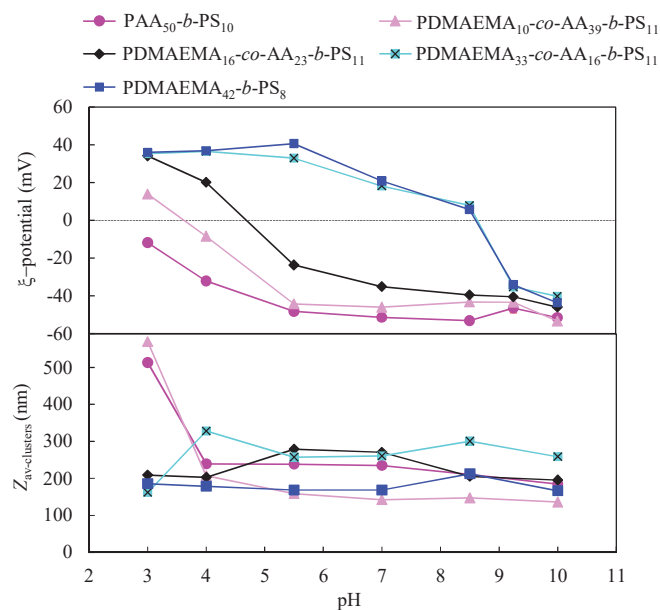


**Figure 79** – Surface properties of the IO clusters. Evolution of  $\zeta$ -potential and  $Z_{av-Clusters}$  as a function of pH for various macroRAFT copolymers.

## 5. CONCLUSIONS

The preparation of IO clusters stabilized by amphiphilic diblock copolymers has been presented in this chapter. The composition of both blocks was controlled via RAFT polymerization, allowing in particular a fine control of the composition of the hydrophilic moiety leading to different surface chemistries for the final iron oxide clusters.

After a brief survey of the literature regarding the synthesis and properties of IONPs and the preparation of IO clusters, the first part of this chapter was dedicated to the characterization of commercial fatty acid-functionalized iron oxide nanoparticles. RAMAN spectroscopy indicated that the nanoparticles were mainly composed of maghemite ( $\gamma$ -Fe<sub>2</sub>O<sub>3</sub>). FTIR and RAMAN spectroscopy combined with TGA showed that some fatty acid molecules (15-20 wt%) were effectively chemically bonded to the inorganic surface. Moreover the morphology of the IONPs was investigated by TEM, showing a number-average diameter of 10 nm (all nanoparticles having a size lower than 20 nm) and an irregular shape. The resulting average diameter was in agreement with the particle size determined by XRD. Finally, as expected for such small particle sizes, the  $\gamma$ -Fe<sub>2</sub>O<sub>3</sub> nanoparticles displayed superparamagnetic properties as evidenced by SQUID measurements.

Toluene droplets loaded with IONPs and stabilized with the macroRAFT copolymers were formed via an emulsification process using ultrasounds for homogenization. Toluene was then evaporated leading to the formation of well-defined IO clusters with a spherical shape, as

evidenced by TEM. The effect of sonication time, sonication power and macroRAFT concentration was studied using PDMAEMA<sub>45</sub>-*b*-PS<sub>9</sub>-TTC as stabilizer. The best conditions (sonication time = 240 s and [PDMAEMA-*b*-PS-TTC] = 2.5 10<sup>-4</sup> M) were then applied in scale-up experiments. The pH of the macroRAFT solution was also varied, demonstrating an important effect on cluster stabilization, with the formation of clusters bigger than 300 nm around pH 7 ( $r = 10$  or 20). Two explanations were proposed for the formation of these big clusters. The first one is based on a lower efficiency of steric stabilization compared to electrosteric one. Indeed, at pH 7 the tertiary amines from DMAEMA units become deprotonated and cationic charges contributing to stabilization are no longer present. The second explanation is associated with the thermo-responsiveness of PDMAEMA. Clusters stabilized by PAA-*b*-PS were also prepared and a similar effect of the macroRAFT concentration was evidenced, showing that a minimum concentration of PAA-*b*-PS-TTC was needed to ensure cluster stabilization (*ca.* 2.5 10<sup>-4</sup> M). PAA-TTC and PDMAEMA-TTC macroRAFTs were also evaluated for cluster formation showing that the lone hydrophilic block can also lead to stable IO clusters. Finally, the composition of the hydrophilic part of the amphiphilic macroRAFTs was varied by varying the DMAEMA to AA ratio, allowing the formation of pH-responsive IO clusters as demonstrated by the evolution of  $\zeta$ -potential with pH.

As described in the bibliographic review, the size of the IO clusters is a key parameter for the final applications, either in the development of optical devices or in the biomedical field. The graph shown in

Figure 80A demonstrates the ability of our strategy to provide clusters stabilized by PDMAEMA segments with a wide range of sizes, from 60 nm up to 400 nm and with a fine control between 60 and 120 nm ( $D_w/D_n$  between 1.2-1.8). The particle size was mainly tuned by the experimental conditions. In addition, high yields were obtained for most of the systems. The preparation of clusters stabilized with PAA-TTC could also be controlled, again mainly by playing with the experimental conditions, but with less amplitude, the particle sizes staying in the range of 60 to 100 nm. These are interesting results showing that we can easily control the size and the surface properties of the clusters, which are crucial parameters for the biomedical application aimed at in this work, *i.e.* the magnetic separation of bacteria.

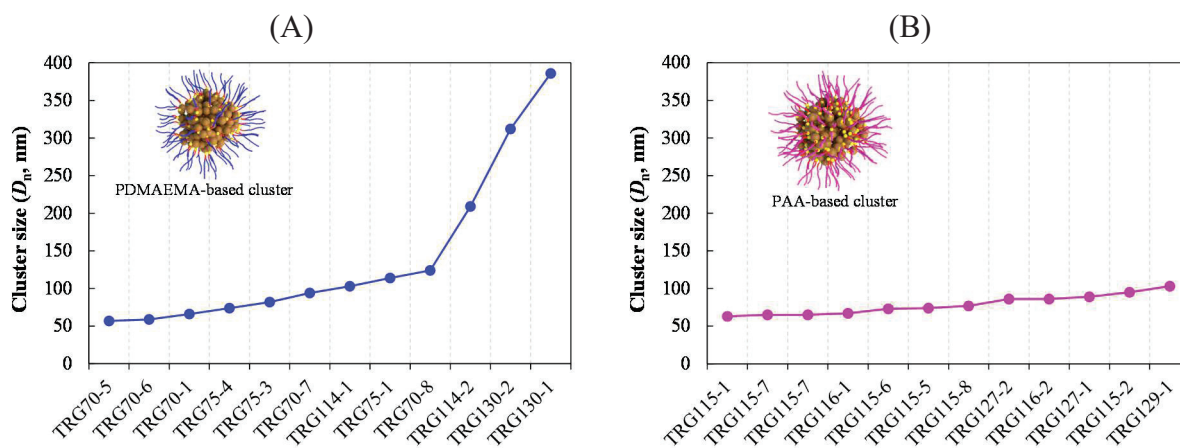


**Figure 80** – Plots of the diameter of IO clusters obtained for different experimental conditions (on X-axis is presented the reference of the experiment). (A) PDMAEMA- and (B) PAA-stabilized clusters.

## REFERENCES

1. Demirer, G. S.; Okur, A. C.; Kizilel, S., Synthesis and design of biologically inspired biocompatible iron oxide nanoparticles for biomedical applications. *Journal of Materials Chemistry B* **2015**, 3 (40), 7831-7849.
2. Gao, J.; Gu, H.; Xu, B., Multifunctional magnetic nanoparticles: design, synthesis, and biomedical applications. *Accounts of Chemical Research* **2009**, 42 (8), 1097-1107.
3. Laurent, S.; Forge, D.; Port, M.; Roch, A.; Robic, C.; Vander Elst, L.; Muller, R. N., Magnetic iron oxide nanoparticles: synthesis, stabilization, vectorization, physicochemical characterizations, and biological applications. *Chemical Reviews* **2008**, 108 (6), 2064-2110.
4. Teja, A. S.; Koh, P.-Y., Synthesis, properties, and applications of magnetic iron oxide nanoparticles. *Progress in Crystal Growth and Characterization of Materials* **2009**, 55 (1), 22-45.
5. Cornell, R. M.; Schwertmann, U., *The iron oxides: structure, properties, reactions, occurrences and uses*. John Wiley & Sons: 2003.
6. Zhang, X.; Niu, Y.; Meng, X.; Li, Y.; Zhao, J., Structural evolution and characteristics of the phase transformations between  $\alpha$ -Fe<sub>2</sub>O<sub>3</sub>, Fe<sub>3</sub>O<sub>4</sub> and  $\gamma$ -Fe<sub>2</sub>O<sub>3</sub> nanoparticles under reducing and oxidizing atmospheres. *CrystEngComm* **2013**, 15 (40), 8166-8172.
7. Yin, Y., Magnetically responsive photonic nanostructures. *SPIE Newsroom* **2011**.
8. Hudson, R., Coupling the magnetic and heat dissipative properties of Fe<sub>3</sub>O<sub>4</sub> particles to enable applications in catalysis, drug delivery, tissue destruction and remote biological interfacing. *RSC Advances* **2016**, 6 (5), 4262-4270.
9. Dave, S. R.; Gao, X., Monodisperse magnetic nanoparticles for biodetection, imaging, and drug delivery: a versatile and evolving technology. *Wiley Interdisciplinary Reviews: Nanomedicine and Nanobiotechnology* **2009**, 1 (6), 583-609.
10. Jordan, A.; Wust, P.; Fähling, H.; John, W.; Hinz, A.; Felix, R., Inductive heating of ferrimagnetic particles and magnetic fluids: physical evaluation of their potential for hyperthermia. *International Journal of Hyperthermia* **2009**, 25 (7), 499-511.
11. Lee, N.; Hyeon, T., Designed synthesis of uniformly sized iron oxide nanoparticles for efficient magnetic resonance imaging contrast agents. *Chemical Society Reviews* **2012**, 41 (7), 2575-2589.
12. Sun, C.; Veisoh, O.; Gunn, J.; Fang, C.; Hansen, S.; Lee, D.; Sze, R.; Ellenbogen, R. G.; Olson, J.; Zhang, M., In vivo MRI detection of gliomas by chlorotoxin-conjugated superparamagnetic nanopores. *Small* **2008**, 4 (3), 372-379.
13. Massart, R.; Dubois, E.; Cabuil, V.; Hasmonay, E., Preparation and properties of monodisperse magnetic fluids. *Journal of Magnetism and Magnetic Materials* **1995**, 149 (1-2), 1-5.
14. Sun, S.; Zeng, H., Size-Controlled Synthesis of Magnetite Nanoparticles. *Journal of the American Chemical Society* **2002**, 124 (28), 8204-8205.
15. Pinna, N.; Grancharov, S.; Beato, P.; Bonville, P.; Antonietti, M.; Niederberger, M., Magnetite nanocrystals: nonaqueous synthesis, characterization, and solubility. *Chemistry of Materials* **2005**, 17 (11), 3044-3049.

16. Sun, S.; Zeng, H.; Robinson, D. B.; Raoux, S.; Rice, P. M.; Wang, S. X.; Li, G., Monodisperse  $MFe_2O_4$  ( $M = Fe, Co, Mn$ ) Nanoparticles. *Journal of the American Chemical Society* **2004**, *126* (1), 273-279.
17. Sun, S.; Murray, C.; Weller, D.; Folks, L.; Moser, A., Monodisperse FePt nanoparticles and ferromagnetic FePt nanocrystal superlattices. *Science* **2000**, *287* (5460), 1989-1992.
18. Park, J.; An, K.; Hwang, Y.; Park, J.-G.; Noh, H.-J.; Kim, J.-Y.; Park, J.-H.; Hwang, N.-M.; Hyeon, T., Ultra-large-scale syntheses of monodisperse nanocrystals. *Nature Materials* **2004**, *3* (12), 891-895.
19. Deng, H.; Li, X.; Peng, Q.; Wang, X.; Chen, J.; Li, Y., Monodisperse magnetic single-crystal ferrite microspheres. *Angewandte Chemie* **2005**, *117* (18), 2842-2845.
20. Liu, J.; Sun, Z.; Deng, Y.; Zou, Y.; Li, C.; Guo, X.; Xiong, L.; Gao, Y.; Li, F.; Zhao, D., Highly water-dispersible biocompatible magnetite particles with low cytotoxicity stabilized by citrate groups. *Angew Chem Int Ed Engl* **2009**, *48* (32), 5875-9.
21. Luo, B.; Song, X. J.; Zhang, F.; Xia, A.; Yang, W. L.; Hu, J. H.; Wang, C. C., Multi-functional thermosensitive composite microspheres with high magnetic susceptibility based on magnetite colloidal nanoparticle clusters. *Langmuir* **2010**, *26* (3), 1674-1679.
22. Ge, J.; Hu, Y.; Biasini, M.; Beyermann, W. P.; Yin, Y., Superparamagnetic magnetite colloidal nanocrystal clusters. *Angewandte Chemie International Edition* **2007**, *46* (23), 4342-4345.
23. Cai, H.; An, X.; Cui, J.; Li, J.; Wen, S.; Li, K.; Shen, M.; Zheng, L.; Zhang, G.; Shi, X., Facile hydrothermal synthesis and surface functionalization of polyethyleneimine-coated iron oxide nanoparticles for biomedical applications. *ACS Applied Materials & Interfaces* **2013**, *5* (5), 1722-1731.
24. Russo, P.; Acierno, D.; Palomba, M.; Carotenuto, G.; Rosa, R.; Rizzuti, A.; Leonelli, C., Ultrafine magnetite nanopowder: synthesis, characterization, and preliminary use as filler of polymethylmethacrylate nanocomposites. *Journal of Nanotechnology* **2012**, *2012*.
25. de Tercero, M. D.; Bruns, M.; Martínez, I. G.; Türk, M.; Fehrenbacher, U.; Jennewein, S.; Barner, L., Continuous hydrothermal synthesis of in situ functionalized iron oxide nanoparticles: a general strategy to produce metal oxide nanoparticles with clickable anchors. *Particle & Particle Systems Characterization* **2013**, *30* (3), 229-234.
26. Ge, J.; Hu, Y.; Zhang, T.; Huynh, T.; Yin, Y., Self-assembly and field-responsive optical diffractions of superparamagnetic colloids. *Langmuir* **2008**, *24* (7), 3671-3680.
27. Ge, J.; Yin, Y., Magnetically responsive colloidal photonic crystals. *Journal of Materials Chemistry* **2008**, *18* (42), 5041-5045.
28. Cunliffe, D.; de las Heras Alarcón, C.; Peters, V.; Smith, J. R.; Alexander, C., Thermoresponsive surface-grafted poly(*N*-isopropylacrylamide) copolymers: effect of phase transitions on protein and bacterial attachment. *Langmuir* **2003**, *19* (7), 2888-2899.
29. Hu, Y.; Wang, J.; Zhang, H.; Jiang, G.; Kan, C., Synthesis and characterization of monodispersed P (St-co-DMAEMA) nanoparticles as pH-sensitive drug delivery system. *Materials Science and Engineering: C* **2014**, *45*, 1-7.

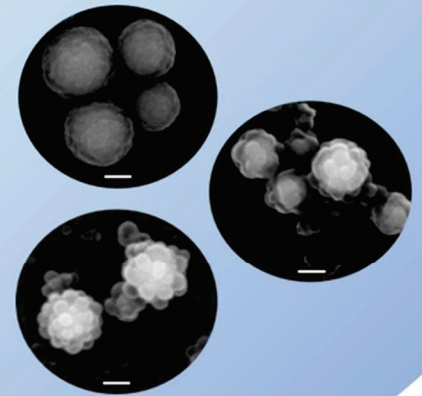
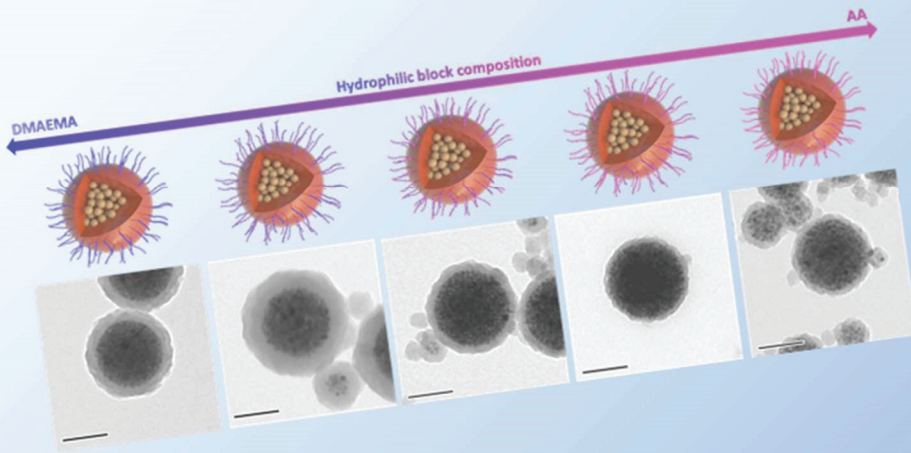
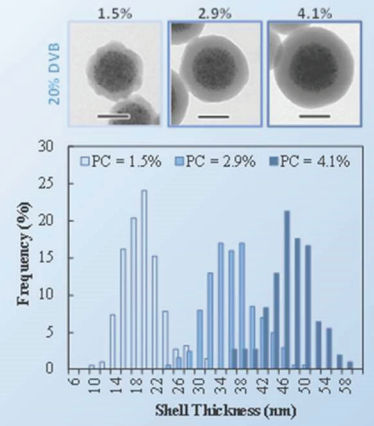
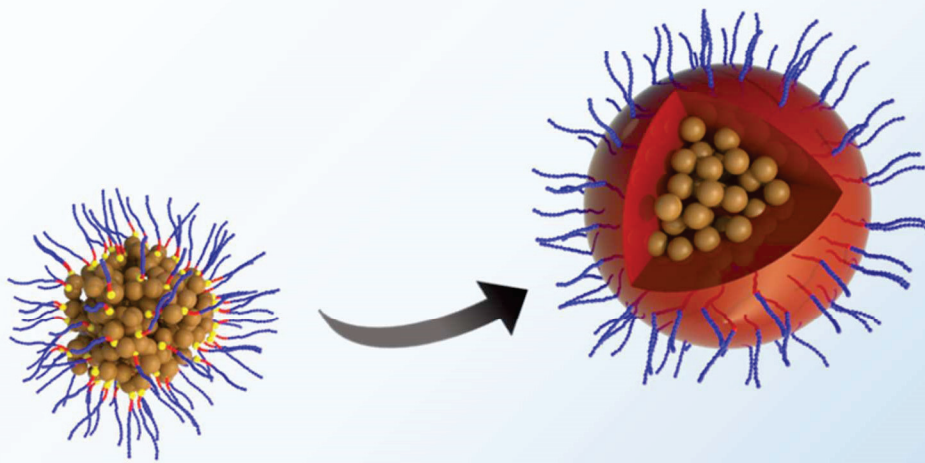


30. Zhang, Q.; Yu, G.; Wang, W.-J.; Yuan, H.; Li, B.-G.; Zhu, S., Switchable block copolymer surfactants for preparation of reversibly coagulatable and redispersible poly (methyl methacrylate) latexes. *Macromolecules* **2013**, *46* (4), 1261-1267.
31. Brazel, C. S., Magnetothermally-responsive Nanomaterials: Combining Magnetic Nanostructures and Thermally-Sensitive Polymers for Triggered Drug Release. *Pharmaceutical Research* **2009**, *26* (3), 644-656.
32. Weissleder, R.; Nahrendorf, M.; Pittet, M. J., Imaging macrophages with nanoparticles. *Nature Materials* **2014**, *13* (2), 125-138.
33. He, J. C.; Huang, M. Y.; Wang, D. M.; Zhang, Z. M.; Li, G. K., Magnetic separation techniques in sample preparation for biological analysis: A review. *Journal of Pharmaceutical and Biomedical Analysis* **2014**, *101*, 84-101.
34. Ditsch, A.; Laibinis, P. E.; Wang, D. I.; Hatton, T. A., Controlled clustering and enhanced stability of polymer-coated magnetic nanoparticles. *Langmuir* **2005**, *21* (13), 6006-18.
35. Fresnais, J.; Berret, J. F.; Frka-Petesic, B.; Sandre, O.; Perzynski, R., Electrostatic Co-Assembly of Iron Oxide Nanoparticles and Polymers: Towards the Generation of Highly Persistent Superparamagnetic Nanorods. *Advanced Materials* **2008**, *20* (20), 3877-3881.
36. Fresnais, J.; Lavelle, C.; Berret, J.-F., Nanoparticle aggregation controlled by desalting kinetics. *Journal of Physical Chemistry* **2009**, (113), 16371-16379.
37. Rocha, N.; Mendes, J.; Durães, L.; Maleki, H.; Portugal, A.; Geraldès, C. F. G. C.; Serra, A.; Coelho, J., Poly(ethylene glycol)-*block*-poly(4-vinyl pyridine) as a versatile block copolymer to prepare nanoaggregates of superparamagnetic iron oxide nanoparticles. *Journal of Materials Chemistry B* **2014**, *2* (11), 1565.
38. Yan, M.; Fresnais, J.; Berret, J. F., Growth mechanism of nanostructured superparamagnetic rods obtained by electrostatic co-assembly. *Soft Matter* **2010**, *6* (9), 1997.
39. Berret, J. F., Stoichiometry of Electrostatic Complexes Determined by Light Scattering. *Macromolecules* **2007**, *40*, 4260-4266.
40. Berret, J. F., Controlling electrostatic co-assembly using ion-containing copolymers: From surfactants to nanoparticles. *Advances in Colloid and Interface Science* **2011**, *167* (1–2), 38-48.
41. Berret, J. F.; Sehgal, A.; Morvan, M.; Sandre, O.; Vacher, A.; Airiau, M., Stable oxide nanoparticle clusters obtained by complexation. *Journal of Colloid and Interface Science* **2006**, *303* (1), 315-318.
42. Berret, J.-F.; Schonbeck, N.; Gazeau, F.; El Kharrat, D.; Sandre, O.; Vacher, A.; Airiau, M., Controlled Clustering of Superparamagnetic Nanoparticles Using Block Copolymers: Design of New Contrast Agents for Magnetic Resonance Imaging. *Journal of the American Chemical Society* **2006**, *128* (5), 1755-1761.
43. Chapel, J. P.; Berret, J. F., Versatile electrostatic assembly of nanoparticles and polyelectrolytes: Coating, clustering and layer-by-layer processes. *Current Opinion in Colloid & Interface Science* **2012**, *17* (2), 97-105.
44. Fresnais, J.; Berret, J. F.; Frka-Petesic, B.; Sandre, O.; Perzynski, R., Reorientation kinetics of superparamagnetic nanostructured rods. *Journal of Physics: Condensed Matter* **2008**, *20* (49), 494216.

45. Fresnais, J.; Berret, J. F.; Qi, L.; Chapel, J. P.; Castaing, J. C.; Sandre, O.; Frka-Petescic, B.; Perzynski, R.; Oberdisse, J.; Cousin, F., Universal scattering behavior of coassembled nanoparticle-polymer clusters. *Physical Review E* **2008**, 78 (4).
46. Fresnais, J.; Yan, M.; Courtois, J.; Bostelmann, T.; Bée, A.; Berret, J.-F., Poly (acrylic acid)-coated iron oxide nanoparticles: Quantitative evaluation of the coating properties and applications for the removal of a pollutant dye. *Journal of Colloid and Interface Science* **2013**, 395, 24-30.
47. Yan, M.; Chevry, L.; Berret, J.-F., Fabrication of magnetic clusters and rods using electrostatic co-assembly. *Prog. Colloid Polym. Sci.* **2010**, 137, 35-39.
48. Blanz, A.; Armes, S. P.; Ryan, A. J., Self-assembled block copolymer aggregates: from micelles to vesicles and their biological applications. *Macromolecular Rapid Communications* **2009**, 30 (4-5), 267-277.
49. Kim, B.-S.; Qiu, J.-M.; Wang, J.-P.; Taton, T. A., Magnetomicelles: composite nanostructures from magnetic nanoparticles and cross-linked amphiphilic block copolymers. *Nano Letters* **2005**, 5 (10), 1987-1991.
50. Pavia-Sanders, A.; Zhang, S.; Flores, J. A.; Sanders, J. E.; Raymond, J. E.; Wooley, K. L., Robust magnetic/polymer hybrid nanoparticles designed for crude oil entrapment and recovery in aqueous environments. *ACS Nano* **2013**, 7 (9), 7552-7561.
51. Rocha, N.; Mendes, J.; Durães, L.; Maleki, H.; Portugal, A.; Geraldés, C. F.; Serra, A.; Coelho, J., Poly(ethylene glycol)-*block*-poly(4-vinyl pyridine) as a versatile block copolymer to prepare nanoaggregates of superparamagnetic iron oxide nanoparticles. *Journal of Materials Chemistry B* **2014**, 2 (11), 1565-1575.
52. Weiss, C. K.; Landfester, K., Miniemulsion polymerization as a means to encapsulate organic and inorganic materials. In *Hybrid Latex Particles*, Springer: 2010; pp 185-236.
53. Asua, J. M., Challenges for industrialization of miniemulsion polymerization. *Progress in Polymer Science* **2014**, 39 (10), 1797-1826.
54. Montagne, F.; Mondain-Monval, O.; Pichot, C.; Mozzanega, H.; Elaissari, A., Preparation and characterization of narrow sized (o/w) magnetic emulsion. *Journal of Magnetism and Magnetic Materials* **2002**, 250, 302-312.
55. Paquet, C.; de Haan, H. W.; Leek, D. M.; Lin, H.-Y.; Xiang, B.; Tian, G.; Kell, A.; Simard, B., Clusters of Superparamagnetic Iron Oxide Nanoparticles Encapsulated in a Hydrogel: A Particle Architecture Generating a Synergistic Enhancement of the T2 Relaxation. *ACS Nano* **2011**, 5 (4), 3104-3112.
56. Paquet, C.; Page, L.; Kell, A.; Simard, B., Nanobeads highly loaded with superparamagnetic nanoparticles prepared by emulsification and seeded-emulsion polymerization. *Langmuir* **2010**, 26 (8), 5388-96.
57. Bibette, J., Monodisperse ferrofluid emulsions. *Journal of Magnetism and Magnetic Materials* **1993**, 122 (1), 37-41.
58. Qiu, P.; Jensen, C.; Charity, N.; Towner, R.; Mao, C., Oil Phase Evaporation-Induced Self-Assembly of Hydrophobic Nanoparticles into Spherical Clusters with Controlled Surface Chemistry in an Oil-in-Water Dispersion and Comparison of Behaviors of Individual and Clustered Iron Oxide Nanoparticles. *Journal of the American Chemical Society* **2010**, 132 (50), 17724-17732.

59. Xu, H.; Cui, L.; Tong, N.; Gu, H., Development of High Magnetization Fe<sub>3</sub>O<sub>4</sub>/Polystyrene/Silica Nanospheres via Combined Miniemulsion/Emulsion Polymerization. *Journal of the American Chemical Society* **2006**, *128* (49), 15582-15583.
60. Ramirez, L. P.; Landfester, K., Magnetic polystyrene nanoparticles with a high magnetite content obtained by miniemulsion processes. *Macromolecular Chemistry and Physics* **2003**, *204* (1), 22-31.
61. Montagne, F.; Mondain-Monval, O.; Pichot, C.; Elaïssari, A., Highly magnetic latexes from submicrometer oil in water ferrofluid emulsions. *Journal of Polymer Science Part A: Polymer Chemistry* **2006**, *44* (8), 2642-2656.
62. <https://code.google.com/archive/p/psa-macro/> (accessed 03/03/2017).
63. Hanesch, M., Raman spectroscopy of iron oxides and (oxy) hydroxides at low laser power and possible applications in environmental magnetic studies. *Geophysical Journal International* **2009**, *177* (3), 941-948.
64. Wu, W.; Wu, Z.; Yu, T.; Jiang, C.; Kim, W.-S., Recent progress on magnetic iron oxide nanoparticles: synthesis, surface functional strategies and biomedical applications. *Science and Technology of Advanced Materials* **2016**.
65. Nakamoto, K., Applications in coordination chemistry. *Infrared and Raman Spectra of Inorganic and Coordination Compounds: Part B: Applications in Coordination, Organometallic, and Bioinorganic Chemistry, Sixth Edition* **2009**, 1-273.
66. Potapova, E.; Carabante, I.; Grahn, M.; Holmgren, A.; Hedlund, J., Studies of collector adsorption on iron oxides by in situ ATR-FTIR spectroscopy. *Industrial & Engineering Chemistry Research* **2010**, *49* (4), 1493-1502.
67. Lu, X.; Niu, M.; Qiao, R.; Gao, M., Superdispersible PVP-Coated Fe<sub>3</sub>O<sub>4</sub> Nanocrystals Prepared by a “One-Pot” Reaction. *The Journal of Physical Chemistry B* **2008**, *112* (46), 14390-14394.
68. Bourgeat-Lami, E.; Farzi, G.; David, L.; Putaux, J.-L.; McKenna, T., Silica encapsulation by miniemulsion polymerization: distribution and localization of the silica particles in droplets and latex particles. *Langmuir* **2012**, *28* (14), 6021-6031.
69. Fournier, D.; Hoogenboom, R.; Thijs, H. M.; Paulus, R. M.; Schubert, U. S., Tunable pH-and temperature-sensitive copolymer libraries by reversible addition-fragmentation chain transfer copolymerizations of methacrylates. *Macromolecules* **2007**, *40* (4), 915-920.
70. Bütün, V.; Armes, S.; Billingham, N., Synthesis and aqueous solution properties of near-monodisperse tertiary amine methacrylate homopolymers and diblock copolymers. *Polymer* **2001**, *42* (14), 5993-6008.
71. Zhai, M.; Chen, Y.; Yi, M.; Ha, H., Swelling behaviour of a new kind of polyampholyte hydrogel composed of dimethylaminoethyl methacrylate and acrylic acid. *Polymer international* **2004**, *53* (1), 33-36.
72. Goh, S.; Liu, Y.; Lee, S.; Huan, C., Miscibility and Interactions in Blends and Complexes of Poly(*N*-acryloyl-*N'*-phenylpiperazine) with Acidic Polymers. *Macromolecules* **1999**, *32* (25), 8595-8602.

73. Bajomo, M.; Robb, I.; Steinke, J. H.; Bismarck, A., Fully Reversible pH-Triggered Network Formation of Amphoteric Polyelectrolyte Hydrogels. *Advanced Functional Materials* **2011**, *21* (1), 172-176.
74. Amalvy, J.; Unali, G.-F.; Li, Y.; Granger-Bevan, S.; Armes, S.; Binks, B.; Rodrigues, J.; Whitby, C., Synthesis of sterically stabilized polystyrene latex particles using cationic block copolymers and macromonomers and their application as stimulus-responsive particulate emulsifiers for oil-in-water emulsions. *Langmuir* **2004**, *20* (11), 4345-4354.
75. Muñoz-Bonilla, A.; van Herk, A. M.; Heuts, J. P., Adding stimuli-responsive extensions to antifouling hairy particles. *Polymer Chemistry* **2010**, *1* (5), 624-627.
76. Van de Wetering, P.; Zuidam, N.; Van Steenberg, M.; Van der Houwen, O.; Underberg, W.; Hennink, W., A mechanistic study of the hydrolytic stability of poly(2-(dimethylamino) ethyl methacrylate). *Macromolecules* **1998**, *31* (23), 8063-8068.
77. Bout, A.; Valerio, D.; Scholte, B., In vivo transfer and expression of the lacZ gene in the mouse lung. *Experimental lung research* **1993**, *19* (2), 193-202.



# Chapter IV

## ENCAPSULATION OF IRON OXIDE CLUSTERS VIA EMULSION POLYMERIZATION



TABLE OF CONTENTS

<b>1. Bibliographic review</b> .....	<b>183</b>
<b>1.1. Polymerization in dispersed media</b> .....	<b>183</b>
1.1.1. <i>Emulsion polymerization</i> .....	183
1.1.1.1. <i>Mechanism of ab initio emulsion polymerization</i> .....	184
1.1.2. <i>Seeded emulsion polymerization</i> .....	186
1.1.3. <i>Miniemulsion polymerization</i> .....	187
<b>1.2. Polymer encapsulation of iron oxide nanoparticles</b> .....	<b>189</b>
1.2.1. <i>Miniemulsion polymerization</i> .....	189
1.2.2. <i>Emulsion polymerization</i> .....	191
<b>2. Experimental Section</b> .....	<b>195</b>
<b>2.1. Materials</b> .....	<b>195</b>
<b>2.2. Methods</b> .....	<b>195</b>
2.2.1. <i>Seeded emulsion polymerization</i> .....	195
2.2.2. <i>Magnetic separation</i> .....	196
<b>2.3. Characterizations</b> .....	<b>197</b>
2.3.1. <i>DLS</i> .....	197
2.3.2. <i>Electron microscopy</i> .....	198
2.3.3. <i>TGA</i> .....	198
<b>3. Results and Discussion</b> .....	<b>198</b>
<b>3.1. Encapsulation of PDMAEMA-based clusters</b> .....	<b>199</b>
3.1.1. <i>Effect of the polymerization process</i> .....	199
3.1.2. <i>Effect of the addition of a crosslinker for 10% theoretical polymer contents</i> .....	205
3.1.3. <i>Effect of the addition of a crosslinker for 2.6 wt% theoretical polymer content</i> .....	210
<b>3.2. Encapsulation of PAA-based clusters</b> .....	<b>212</b>
<b>3.3. Encapsulation of P(DMAEMA-co-AA)-based clusters</b> .....	<b>215</b>
<b>3.4. Magnetic properties of the the composite IO/polymer latex particles</b> .....	<b>217</b>
<b>4. Conclusions</b> .....	<b>221</b>
<b>References</b> .....	<b>223</b>



## **1. BIBLIOGRAPHIC REVIEW**

### **1.1. Polymerization in dispersed media**

Polymerizations in dispersed media include all polymerization processes conducted in a continuous phase in which the resulting polymeric material is not soluble.<sup>1</sup> The main techniques of polymerization in dispersed media are precipitation, dispersion, suspension, emulsion, miniemulsion and microemulsion polymerization. The obtained product consists of a colloidal dispersion of polymer particles in a liquid (what is called a latex), and depending on the process, the particle sizes range from 10 nm up to 10.000  $\mu\text{m}$ . Generally water is used as the continuous phase leading to the formation of oil-in-water (O/W) systems. However, organic solvent can also be used as continuous medium for the polymerization of hydrophilic monomers using W/O systems. In this case, the techniques are referred to as inverse emulsion, inverse miniemulsion or inverse suspension polymerization.

In this bibliographic review, we will focus on emulsion and miniemulsion polymerization processes. Among their advantages compared to other polymerization processes, one can mention: i) the relatively high polymer content of the resulting latexes (up to 75%),<sup>2</sup> ii) the possibility to synthesize polymer chains with high molar masses and iii) the use of water as continuous medium, an environmental friendly solvent, which allows good heat transfer and low viscosity of the final product. Moreover, miniemulsion and emulsion polymerization techniques are widely employed for the preparation of composite latex particles incorporating inorganic compounds.<sup>3</sup> For instance, the use of iron oxide nanoparticles as inorganic material has been largely reported for the preparation of magnetic latex particles with potential applications in biomedical and optical fields.<sup>4,5</sup>

#### *1.1.1. Emulsion polymerization*

The emulsion polymerization process is applied for producing over than 10 million tons of dry polymer per year,<sup>6</sup> representing around 4% of the overall polymer global production. The latexes obtained by this process are widely applied in coating technologies for instance. Indeed, synthetic latexes are largely employed in areas such as paints, adhesives and paper coatings. Furthermore, this polymerization process has been also widely exploited in the academic area for the development of new materials such as composite particles incorporating inorganic fillers,<sup>4</sup> magnetic particles,<sup>7</sup> stimuli-responsive particles,<sup>8</sup> and nano-objects with particular morphologies (fibers or vesicles).<sup>9</sup>

There are four basic ingredients required for an emulsion polymerization reaction: water, monomer(s), surfactant and a water-soluble initiator. However, in some recipes, some other compounds such as buffers, chain transfer agents or fillers can also be added. Surfactants play an important role in emulsion polymerization providing colloidal stability to the system. In general, they are amphiphilic molecules that adsorb onto the surface of the polymer particles, reducing the polymer/water interfacial tension, and causing the particles to be repelled from each other, leading to the formation of stable latex particles with diameters ranging from 50 to 500 nm. The mechanism of emulsion polymerization has been reviewed by many authors,<sup>1, 10, 11</sup> and is presented in the next section.

#### 1.1.1.1. Mechanism of *ab initio* emulsion polymerization

The progress of an *ab initio* emulsion polymerization can be divided in three distinct stages: (I) nucleation, (II) particle growth and (III) end of reaction. These stages are schematically represented in Figure 81.

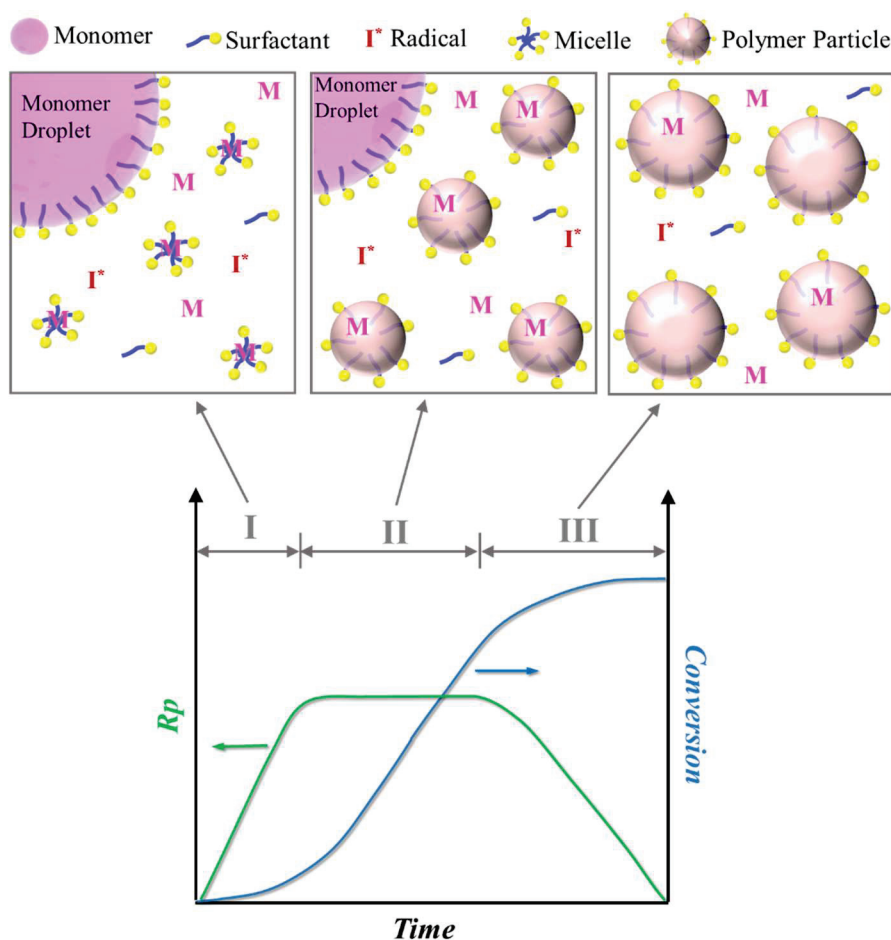


**Figure 81** – Scheme illustrating the mechanism of emulsion polymerization showing the three stages: (I) nucleation, (II) particle growth and (III) end of reaction.

The reaction medium is composed of water, a surfactant, a water-soluble initiator and monomer droplets as illustrated in Figure 81. Initially, the initiator is decomposed in the aqueous phase forming the radicals ( $I^*$ ). These radicals will then react with the small amount of monomer soluble in the water phase, generating oligoradicals. After initiation, polymer particle nucleation, will occur following the mechanisms presented below:

- *Micellar nucleation*: this mechanism was first proposed by Harkins<sup>12</sup> and Smith and Ewart.<sup>13</sup> The previously formed oligoradicals will add a few monomer units becoming hydrophobic enough to enter into monomer-swollen micelles (Figure 81). This mechanism is the one usually put forward for monomers with low solubility in water such as styrene, butadiene or 2-ethylhexyl acrylate. Their original contributions have been used from 1940s as basis for fundamental study about emulsion polymerization mechanism.
- *Homogeneous and coagulative nucleation*: the homogeneous nucleation was studied by many authors,<sup>1</sup> in particular by Roe.<sup>14</sup> This nucleation process was proposed to explain the particle formation from monomer with higher water solubility such as methyl methacrylate, vinyl acetate or vinyl chloride, and also to explain particle nucleation in the absence of micelles. In this case, the oligoradical will grow until a critical length leading to its precipitation. The polymerization can continue inside this precursor particle (not stable from a colloidal point of view), swollen with monomer, which will be stabilized by the adsorption of surfactant molecules. The oligoradical can also penetrate in a particle already formed. Later on Gilbert and co-workers<sup>15</sup> proposed the homogeneous-coagulative nucleation mechanism, which can be considered as an extension of homogeneous nucleation. The author proposed that the precursor particles will agglomerate due to their poor colloidal stability and low ability to swell with monomer, forming new particles via a coagulation process.
- *Monomer droplet nucleation*: this mechanism is very unlikely in conventional emulsion polymerization, as the surface area of the monomer droplets (diameter of few micrometers) is significantly lower than that of the micelles and/or polymer particles (size often less than 100 nm).

It is worth mentioning that the main reaction locus in emulsion polymerization is inside the particles. Hence, the concentration of radicals per particle ( $\bar{n}$ ) and the monomer concentration inside the particles ( $[M]_p$ ) are key parameters influencing the polymerization kinetics. During the nucleation step (Phase I), the number of particles ( $N_p$ ) gradually increases leading to an

increase of the polymerization rate ( $R_p$ ), as demonstrated by Equation 1 and illustrated in Figure 81.

$$R_p = \frac{k_p \cdot [M]_p \cdot N_p \cdot \tilde{n}}{N_A} \quad (1)$$

The ending of the phase I is evidenced when most of the surfactant added to the system is covering the surface of the polymer particles (*i.e.* when  $N_p$  is constant), which occurs at approximately 10% of conversion. During phase II, monomer diffusion from the droplets to the particles through the water phase is constant, maintaining the thermodynamic equilibrium, which results in a constant monomer concentration inside the swollen particles. During phase II, monomer diffusion from the droplets to the particles through the water phase is constant, maintaining a constant monomer concentration inside the swollen particles. In addition, if the number of radicals per particle is also constant (which is usually true in the case of styrene for instance), a stationary regime is attained during which  $R_p$  is constant (Figure 81). Phase II will take place up to 40 to 90% of conversion, which depends mainly on the polymer solubility in the monomer. Once the droplets no longer exist (which marks the beginning of phase III), the monomer concentration inside the particles will continuously decrease and, consequently, so will the polymerization rate (Figure 1). In some cases (e.g. MMA), an increase of the polymerization rate can however be observed in phase III, which can be associated to a gel effect. This phenomenon is due to the formation of polymer chains with high molecular weight, which increases considerably the viscosity inside the particles retarding the termination of the macroradicals.

### *1.1.2. Seeded emulsion polymerization*

Seeded emulsion polymerization is based on the use of previously formed particles as “seeds” for the polymerization. This approach has been widely employed for the production of hybrid particles, e.g. polymer-polymer or inorganic-polymer<sup>16</sup> which allows the combination of the different properties from the different phases.

In a typical polymer-polymer hybrid system, a two-step emulsion polymerization process is commonly used. Initially, a dispersion of latex particles is synthesized via emulsion polymerization. This dispersion is later used as reaction medium in a second emulsion polymerization, generally carried out in a semi-batch process. The formed hybrid polymer-polymer particles can exhibit different morphologies such as core-shell, raspberry,

hemispherical particles, among others.<sup>17</sup> Indeed this morphology variation will depend on polymerization kinetics and/or thermodynamics involved in the different phases composing the hybrid system.<sup>18</sup> The ability to control the morphology associated to the different polymer compositions in the two polymer phases makes this approach a powerful tool for the development of materials for applications in paper coatings,<sup>2</sup> catalysis,<sup>19</sup> energy storage<sup>20</sup> or biology.<sup>21</sup>

As mentioned above, inorganic-organic hybrid systems have also been prepared via seeded emulsion polymerization. This approach is based on *in situ* polymerization of hydrophobic monomers in the presence of inorganic particles, such as inorganic pigments, aluminosilicates, metallic particles and metal oxides, which are generally hydrophilic. Thus, modification of the surface of these inorganic particles is necessary to improve the interaction between the two phases. To do so, molecules reactive in the free radical polymerization process, such as macromonomers, initiators or functional monomers, are often used to modify their surface.<sup>22, 23</sup>

### *1.1.3. Miniemulsion polymerization*

Miniemulsion polymerization can be considered as a variant of emulsion polymerization in which droplet nucleation plays a key role. The idea is to strongly favor this type of nucleation (over micellar or homogeneous ones) by considerably reducing the droplet size, thus favoring radical entry into the droplets. Thus, unlike the droplets formed in emulsion polymerization, those considered in miniemulsion polymerization are quite small (typically lower than 500 nm, versus micrometer-sized in the emulsion process). In a typical recipe, two separate phases are prepared, an aqueous phase containing the surfactant and an organic phase composed of monomer and a hydrophobic agent. Both organo- and water-soluble initiators can be used in miniemulsion polymerization. These two phases are then mixed using high energy emulsification devices such as rotor–stators, ultrasound probes or high-pressure homogenizers resulting in small monomer droplets (< 300 nm). These sub-micronic droplets will act as “nanoreactors” for the polymerization. It is important to point out that the concentration of surfactant in the aqueous phase has to be lower than the CMC, preventing the micellar nucleation and consequently, favoring droplet nucleation. In addition, due to the partial solubility of the organic phase in water, oil diffusion from the droplets to the aqueous phase can take place. This diffusional degradation, also known as Ostwald ripening, can occur in a short interval of time (typically a few minutes), broadening the dispersity of droplet size or

even leading to droplet coalescence. The use of a hydrophobic agent is therefore required to improve the droplet stabilization, retarding up to several months the process of Ostwald ripening. Hence, an ideal miniemulsion polymerization can be obtained, *i.e.* neither re-nucleation nor diffusional degradation processes are observed. In that case the miniemulsion is so-called a “one to one copy” process, in which each droplet formed during emulsification results in a polymer particle of similar composition.

Miniemulsion polymerization has been largely employed for the preparation of hybrid particles, allowing the encapsulation of various inorganic compounds into polymer particles.<sup>5, 24, 25</sup> Indeed, there are several works<sup>5, 26</sup> in the literature reporting the efficient encapsulation of silica,<sup>27</sup> iron oxide nanoparticles,<sup>28</sup> golden nanoparticles,<sup>28</sup> clay platelets<sup>29</sup> (as illustrated in Figure 82) and other inorganic compounds using this approach. The only difference with the procedure described above is the introduction in the hydrophobic phase of an organically-modified nanofiller which has to be easily oil-dispersable, *i.e.* displaying a hydrophobic character, which is often given by modifier agents such as organic salts, fatty acids or polymers.

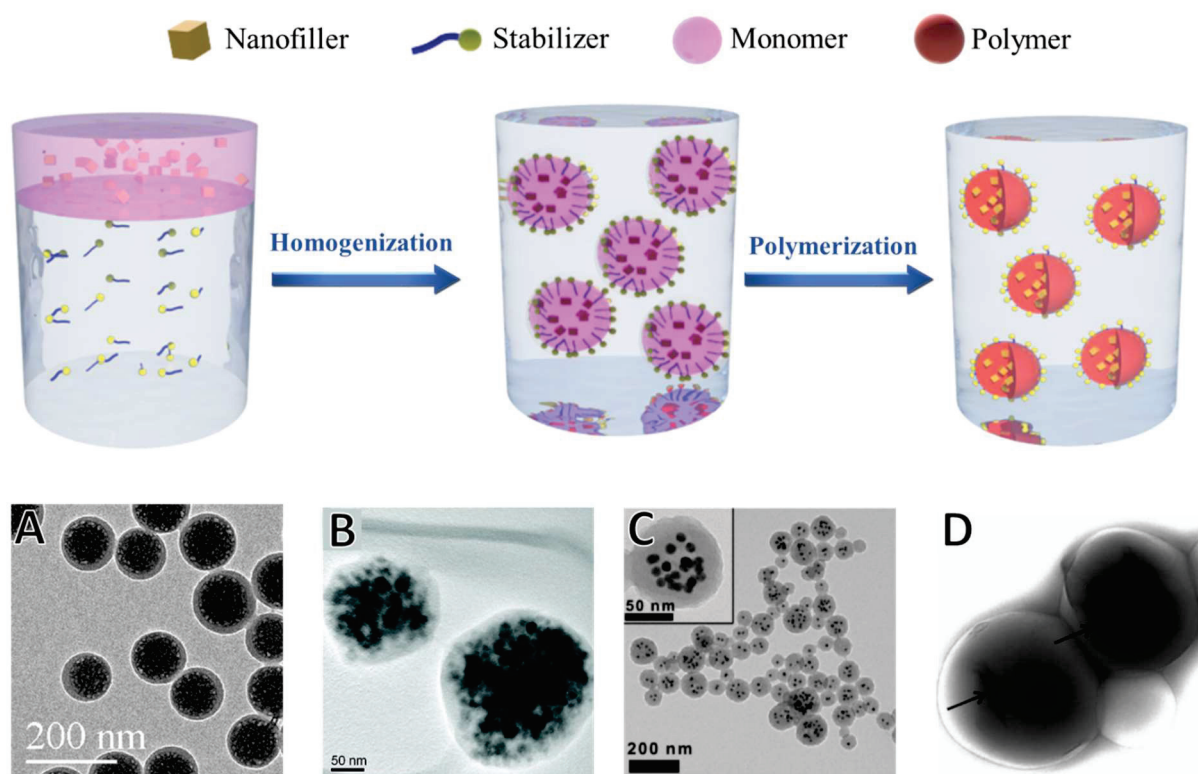


**Figure 82** – Scheme illustrating the encapsulation of nanofillers by miniemulsion polymerization. TEM micrographs showing the encapsulation of: (A) silica,<sup>27</sup> (B) iron oxide,<sup>28</sup> (C) golden nanoparticles,<sup>30</sup> and (D) clay nanoplatelets<sup>29</sup> (reproduced with permission from respective publishers).



Miniemulsion polymerization is undoubtedly a powerful tool for the encapsulation of inorganics. Thus, in the following section, we will focus on the preparation of IO/polymer composite particle.

## **1.2. Polymer encapsulation of iron oxide nanoparticles**

The synthesis of polymer particles in the presence of magnetic nanoparticles can be performed by precipitation,<sup>31, 32</sup> dispersion,<sup>33, 34</sup> suspension,<sup>35, 36</sup> emulsion,<sup>4</sup> or miniemulsion polymerization processes.<sup>5</sup> The main differences among these processes are related to monomer and polymer solubility in the continuous phase and the size of the final iron oxide/polymer composite particles. In the following sections, we will focus on the synthesis of magnetic latex particles via emulsion and miniemulsion polymerization, showing some selected examples

### *1.2.1. Miniemulsion polymerization*

Miniemulsion polymerization has been largely exploited for the preparation of magnetic latexes.<sup>28, 37-45</sup> Nevertheless, some drawbacks are often observed, such as phase separation between the inorganic particles and the polymer, low iron oxide content in the final magnetic particles and/or nucleation of new polymer particles, limitations which will obviously negatively impact their direct use.<sup>42</sup>

As mentioned in the previous chapters of this thesis, the preparation of magnetic polymer particles with high iron oxide content is an important requirement for many applications. However, the difficulty in dispersing high amounts of iron oxide nanoparticles into monomers was shown to be one of the main limitations encountered to generate magnetic particles with a high IO content. Ramirez *et al.*<sup>41</sup> reported an approach based on multi-step emulsification to prepare highly loaded iron oxide/polystyrene particles. First, oleic acid-modified IONPs were dispersed in octane forming an organic ferrofluid. Then, the ferrofluid was sonicated in the presence of an aqueous solution of SDS forming a first miniemulsion followed by solvent evaporation, resulting in the formation of iron oxide clusters (the clustering process was described in Chapter 3). In a separate flask, a similar emulsification process was carried out to prepare a second miniemulsion composed of styrene, water, hexadecane and SDS. The cluster dispersion was then mixed with this second miniemulsion and an additional sonication

process was performed. Finally a radical initiator, KPS, was added and the system heated at 80°C during 18 h, resulting in magnetic latex particles containing up to 40 wt% of iron oxide. It is important to point out that the formation of a protective coating surrounding the iron oxide core is an important characteristic if one aims to use the magnetic particles for biological purposes. Nonetheless, some incompatibility between the organic and inorganic phases can lead to phase separation, even after hydrophobization of the IO surface and after polymerization. Thus, crosslinking agents have been added in the miniemulsion recipe in order to prevent phase separation by physically entrapping the IONPs. Ramos and Forcada<sup>46</sup> reported the preparation of magnetic latex particles via miniemulsion polymerization in the presence of crosslinking agents (either hydrophobic or hydrophilic). The authors showed that in the absence of crosslinker, phase separation occurred, with the organically-modified IONP accumulating at the particle surface forming a “Janus”-like morphology which can be associated to the well-known chemical incompatibility between the hydrocarbon chains from oleic acid and the polystyrene. On the other hand, the use of a crosslinking agent enabled to successfully encapsulate the IONPs. In addition, the authors observed an effect of the nature of the crosslinker on particle morphology. When a water-soluble crosslinking agent was used, the IONPs were uniformly distributed in the polymer particles whereas the use of an organo-soluble crosslinker led to the formation of core-shell hybrid particles, with a IO-rich core.<sup>42</sup>

RAFT-mediated miniemulsion polymerization has also been employed for the preparation of magnetic latex particles. Recently Chakraborty *et al.*<sup>47</sup> reported the synthesis of hybrid polystyrene latexes incorporating oleic acid-modified IONPs. The nanocomposite latex particles were synthesized by miniemulsion polymerization in the presence of a carboxylic RAFT agent and an amphiphilic ionic liquid as stabilizer. Firstly, the efficiency of two ionic liquids with varied compositions was studied in the stabilization of miniemulsified monomer droplets in the absence of iron oxide. Both compounds were able to confer colloidal stability to the system. Despite a broad particle size distribution, good stability was reported. Then, in a second series of experiments, iron oxide nanoparticles were used as inorganic compounds and the authors showed that in the absence of RAFT agent, the IONPs were located at the particle surface forming a “Janus”-like morphology, as illustrated in Figure 83. As explained above, the phase separation can be associated to chemical incompatibility between oleic acid and PS. Nevertheless, by using the carboxylic RAFT agent, this incompatibility was minimized. The entrapment of IONPs into the core of the particles can be probably associated to the strong interaction between the carboxylic groups of the RAFT agent and iron oxide. On

the other hand, a fine tuning of the AIBN:RAFT agent molar ratio allowed the formation of rather stable magnetic PS particles incorporating up to 27 wt% (with respect to polymer) of iron oxide nanoparticles, providing interesting magnetic properties to these composite particles.

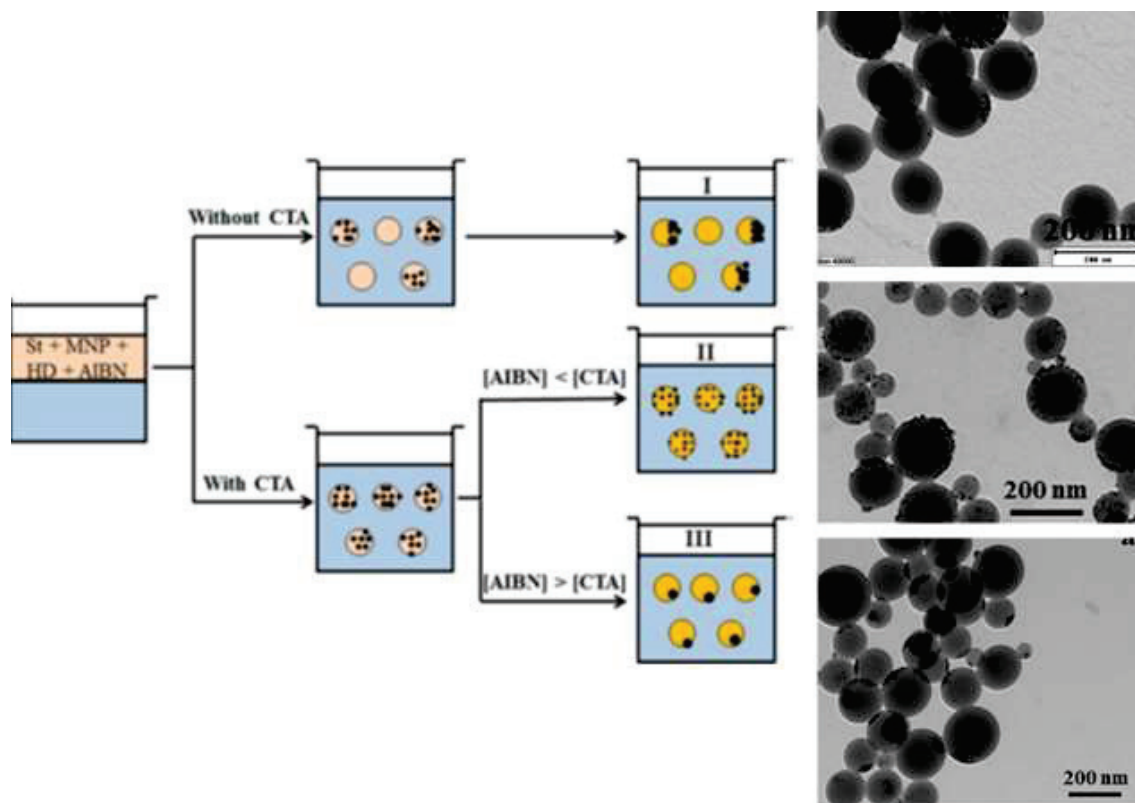


**Figure 83** – Representation of the different morphologies I–III that are possible to develop through ionic liquid-stabilized miniemulsion polymerization in the absence and presence of RAFT agent (CTA) with their respective TEM images. Adapted from <sup>47</sup>.

### 1.2.2. Emulsion polymerization

Magnetic latex particles have also been prepared by emulsion polymerization.<sup>46, 48-59</sup> However, the same drawbacks as those generally observed in miniemulsion polymerization can also be evidenced here such as: poor magnetic properties of the final composite material, phase separation and nucleation of new polymer particles.

Using a strategy quite similar to that followed by Ramirez *et al.*<sup>41</sup> in miniemulsion polymerization, Montagne *et al.*<sup>53, 60</sup> obtained PS particles highly loaded in IO. The strategy is based on the formation of magnetic O/W emulsions by using a high energy mixing process. To do so, an octane-based ferrofluid was sheared against an aqueous solution of nonyl phenol ether surfactant leading to the formation of IO-loaded solvent droplets.<sup>60</sup> The monomer (styrene) and the initiator was then added to the magnetic emulsion, and the polymerization

was conducted at 80°C resulting in magnetic particles with high IO contents.<sup>53</sup> Later on, the same group studied the effect of the addition of a crosslinking agent (divinyl benzene, DVB) in various amounts, showing that the later had a direct impact on the morphology of the obtained magnetic particles. A well-defined core-shell morphology was obtained for high concentrations as illustrated in Figure 84H.<sup>48, 49</sup>

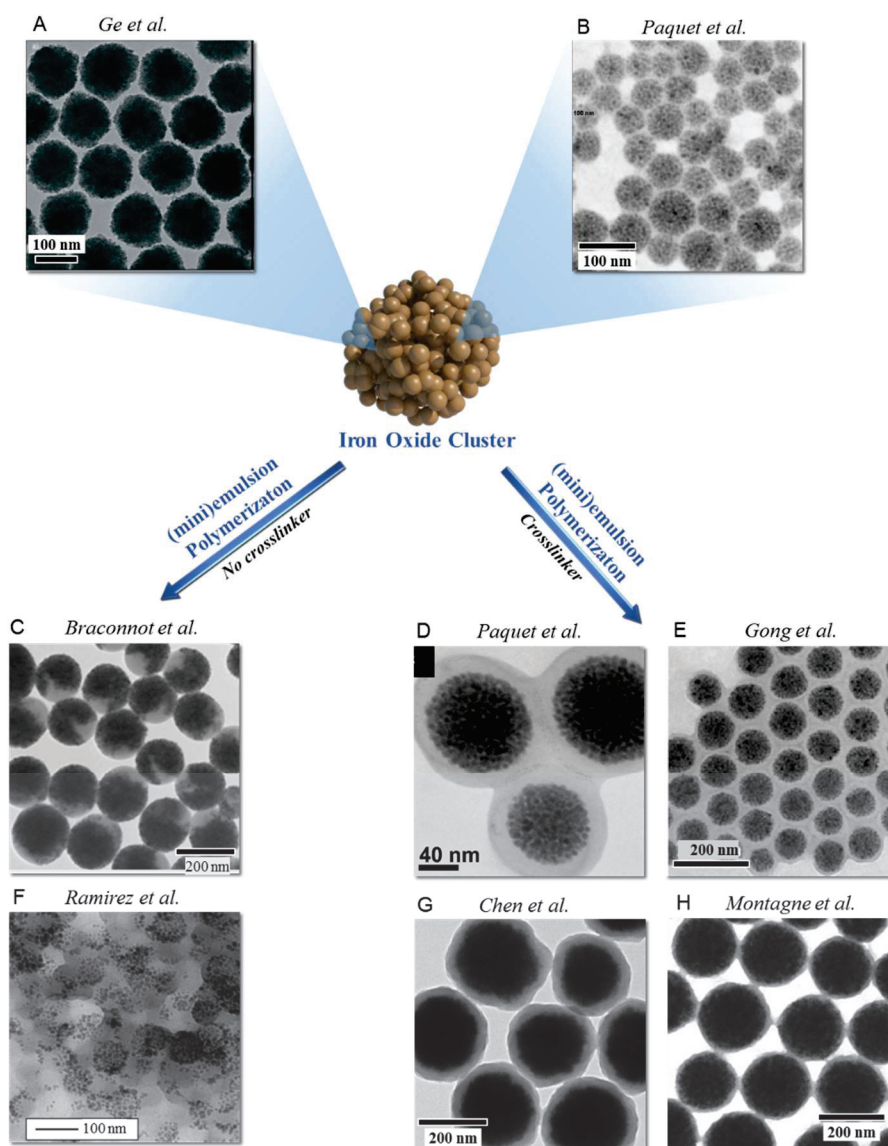


**Figure 84** – Schematic representation of iron oxide cluster encapsulation via *in situ* polymerization. TEM micrographs of the initial clusters obtained via: (A) solvothermal method or (B) emulsification/solvent evaporation process. TEM images of iron oxide/polymer hybrid particles prepared via: (C, D, E, H) emulsion, (F) miniemulsion or (G) solution polymerization. Reproduced with permission from refs: (A);<sup>61</sup> (B);<sup>54</sup> (C);<sup>48</sup> (D);<sup>54</sup> (E);<sup>46</sup> (F);<sup>41</sup> (G)<sup>62</sup> and (H).<sup>53</sup>

Recently, several strategies based on the formation of IO clusters and the use of a crosslinker have been reported by different authors in order to generate magnetic latex particles with high iron oxide content and presenting an encapsulated morphology. The most relevant works are

192

summarized in Figure 84, where the effect of crosslinker agent on particle morphology can be clearly evidenced with crosslinked system resulting in core-shell morphology while non-crosslinked systems lead to phase separation.

Although the strategy based on *in situ* polymerization using iron oxide clusters as seeds results in particles with high iron oxide contents, composite particles with poor control of their surface properties are often obtained due to the use of conventional surfactants (e.g. SDS) for particle stabilization. However, for the intended application of this thesis, that is to say bio-separation using magnetic particles, surface functionalization is of key importance. RDRP-based processes have demonstrated to be a powerful tool to finely control surface functionalization by the preparation of polymers of controlled composition later used for the preparation of particles.<sup>9</sup>

In that context, RAFT-assisted emulsion polymerization has been successfully used for the preparation of inorganic-organic hybrid materials. Recently, a strategy called REEP, for *macroRAFT-assisted encapsulating emulsion polymerization*, has been developed for the encapsulation of different inorganic materials. Initially, macroRAFT agents are carefully designed containing functional monomers with lateral groups able to promote their adsorption at the inorganic surface and also some hydrophobic monomer units to encourage the polymerization to take place at the inorganic surface. After adsorption of the macroRAFT at the inorganic surface, starved-emulsion polymerization is carried out in the presence of the functionalized inorganic particles leading to their encapsulation. This approach was first reported by the group of Hawket for the encapsulation of inorganic pigments<sup>63</sup> and Gibbsite clay platelets,<sup>64</sup> and subsequently employed by our group with success for the encapsulation of a large variety of inorganic particles such as cerium oxide,<sup>65</sup> silica,<sup>66</sup> Ge-imogolite,<sup>67</sup> layered double hydroxide (LDH) clay platelets.<sup>68</sup> Very recently Li *et al.*<sup>69</sup> reported the use of REEP for the preparation of magnetic latex particles. The authors show that the monomer composition play an important role on the final particle morphology, and encapsulated systems were successfully observed when monomer composition resulted in polymer with low glass transition temperature ( $T_g$ ). In addition, due to the pH-responsiveness of the macroRAFT, composed of butyl acrylate and acrylic acid units, the initial pH of the reaction medium was an important parameter impacting the particle size of final magnetic latex particles. In the same period, Hawket's group also reported<sup>70</sup> the employment of REEP for the encapsulation of iron oxide nanoparticles using also a macroRAFT composed of BA and AA. The resulting carboxylic acid functions at the surface of magnetic particles were



exploited to conjugate a fluorescent dye, Rhodamine B isothiocyanate, and the resulting dye-conjugate system was successfully employed for cell labeling displaying no cytotoxicity. As interesting as it is, the REEP approach was however not investigated in this thesis. Indeed, the size of the IONP/macroRAFT clusters, obtained after direct macroRAFT adsorption and then used as seed in emulsion polymerization, has been quite limited ( $< 50$  nm), thus limiting somehow the size of the final magnetic particles ( $< 70$  nm) as well as the IO content in those particles. However, as mentioned in Introduction of this thesis the larger the size and the higher the IO content, the faster will be the magnetic separation. Besides, the nature of the macroRAFT allowing a successful encapsulation has been so far limited to BA/AA copolymers, restricting the surface functionalization of the final particles. Our strategy is thus based on the formation of iron oxide clusters stabilized by various amphiphilic block copolymers macroRAFTs, clusters which are then used as seeds in emulsion polymerization. By varying the composition of the hydrophilic part of the amphiphilic macroRAFTs (represented as grey spheres in Figure 85), magnetic latex particles with different surface functionalizations will be obtained. This chapter presents the *seeded* emulsion polymerization of styrene (copolymerized in some cases with DVB) using as seeds the clusters prepared with different amphiphilic macroRAFT agents in Chapter 3.

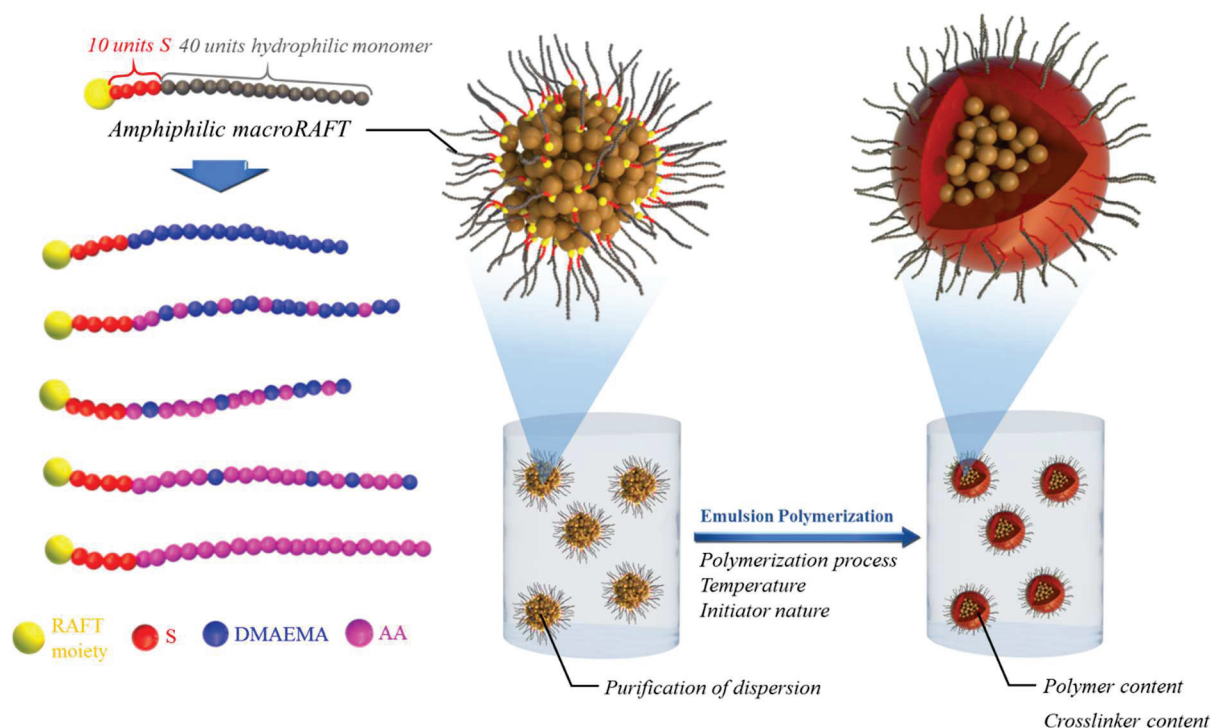


**Figure 85** – Synthetic representation of our strategy. *Seeded* emulsion polymerization in the presence of iron oxide clusters stabilized by amphiphilic macroRAFT agents with varied compositions of the hydrophilic block.



## **2. EXPERIMENTAL SECTION**

### **2.1. Materials**

Iron oxide cluster dispersions were prepared as described in Chapter 3. The initiators, 4,4'-azobis(cyanovaleric acid) (ACPA,  $\geq 98\%$ , Sigma-Aldrich) and 2,2'-azobis[2-(2-imidazolin-2-yl)propane] dihydrochloride (ADIBA, 99%, Wako) were used without further purification. Sodium hydroxide (NaOH 0.1 M, standard, Acros Organics), hydrochloric acid (HCl 0.1 M, standard, Acros Organics) and styrene (S, 99%, Acros Organics) were all used as received. The crosslinking agent, divinyl benzene (DVB, 80%, Sigma-Aldrich) was composed of a mixture of four isomers. In order to quantify the proportion of each isomer, gas chromatography analysis was performed (see ANNEX 4. 1) resulting in the following composition: 57.0 vol% *m*-DVB, 26.7 vol% *p*-DVB, 9.3 vol% *m*-ethyl vinylbenzene (EVB) and 7.0 vol% *p*-EVB.

### **2.2. Methods**

#### *2.2.1. Seeded emulsion polymerization*

Surfactant-free emulsion polymerization of styrene (with or without DVB) was carried out using iron oxide clusters as seeds in batch or semi-continuous experiments. 15 g of the cluster dispersion ( $SC \approx 2\%$ ) was introduced in a 50 mL double-jacket round-bottom reactor equipped with a condenser, a nitrogen inlet, an infusion syringe pump and a mechanical agitation system, (Figure 86). Then, the initiator ( $1.7 \cdot 10^{-3}$  M) and a minimum amount of monomer (0.06 g) were introduced in the reactor. The dispersion was deoxygenated with nitrogen for 30 min. After this interval, water at 60°C was recirculated through the double jacket marking the beginning of the reaction. Styrene or the monomer mixture, styrene/DVB, was fed into the reactor at  $0.3 \text{ g h}^{-1}$  during 4 h (unless stated otherwise), except for batch polymerization in which the overall monomer content was added at the initial stage. The polymerization reactions were conducted during 6 h. Samples were periodically withdrawn to follow monomer conversion, particle size and particle morphology as a function of time.

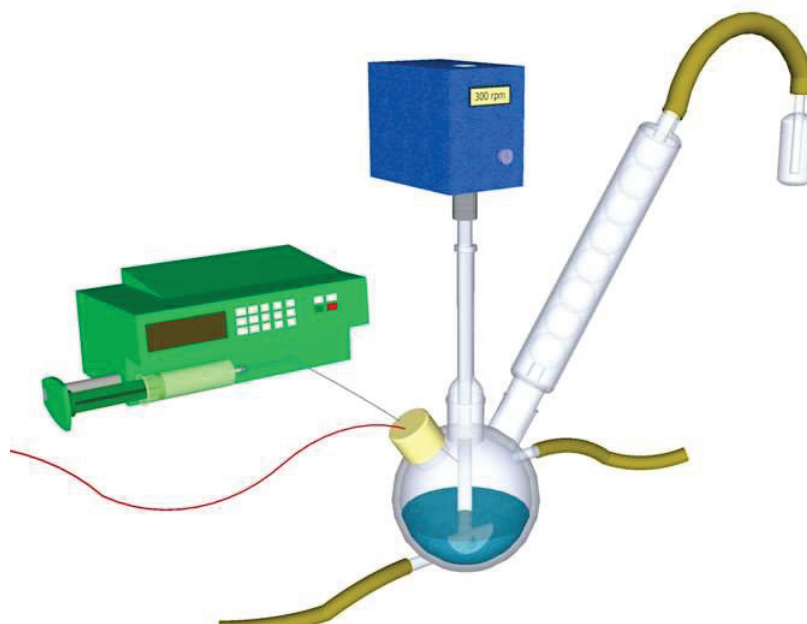


Figure 86 – Scheme illustrating the reaction system used for *seeded* emulsion polymerization.

### 2.2.2. Magnetic separation

The resulting hybrid latexes were characterized in order to determine the fraction of magnetic latex particles and the fraction of free latex particles (formed by secondary nucleation) as schematically shown in Figure 87. Firstly, the hybrid latexes were exposed to a magnetic field using a magnet (Dynamag – 2 from ThermoFisher Scientific) during different times: 10, 30, 60 or 600 s, to separate the magnetic fraction from the non-magnetic latex fraction (which may contain both polymer particles and hybrid particles with a very low amount of IONP). The supernatant was collected and the solids content was determined gravimetrically ( $SC_{free}$ ). The magnetic fraction was re-dispersed in water while maintaining the same volume as the initial sample and the solids content was also determined gravimetrically ( $SC_{mag}$ ). The fractions of magnetic latex particles ( $\omega_{mag}$ , wt%) and of free latex particles ( $\omega_{free}$ , wt%) were then determined using equations 1 and 2, where  $SC_{\text{hybrid latex}}$  is the experimental solids content of the hybrid latex before separation. At last, the magnetic fraction was dried and characterized by TGA in order to determine the iron oxide content ( $IOC^{\text{TGA}}$ , wt%).

$$\omega_{free} = \frac{SC_{free}}{SC_{\text{hybrid-latex}}} \cdot 100 \quad (1)$$

$$\omega_{mag} = \frac{SC_{mag}}{SC_{\text{hybrid-latex}}} \cdot 100 \quad (2)$$

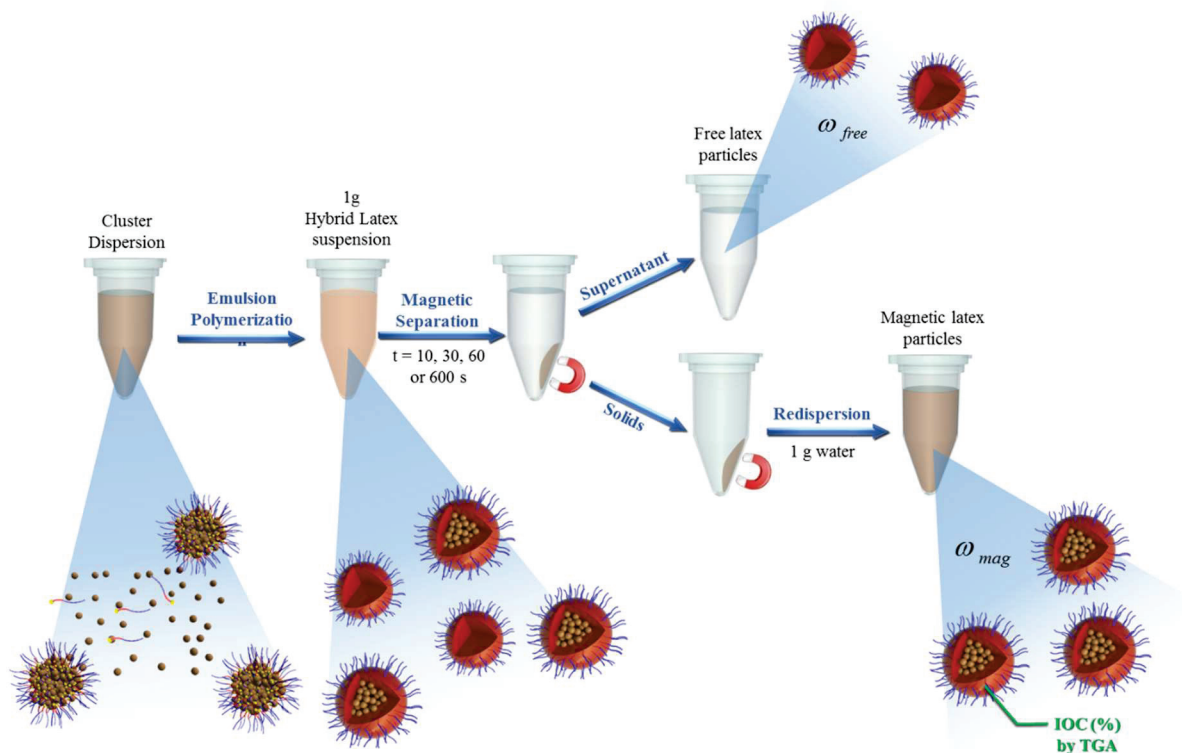


Figure 87 – Scheme of magnetic separation of iron oxide/polymer composite latex particles.

The yield of iron oxide incorporation in the magnetic fraction,  $Y_{IO}$  (%), was then calculated as follows:

$$Y_{IO} = \frac{\omega_{mag} \cdot m_{solids} \cdot IOC^{TGA}}{100 \cdot m_{IO}} \quad (3)$$

where  $m_{IO}$  and  $m_{solids}$  are respectively the mass of iron oxide and of total solid in the latex suspension.

## 2.3. Characterizations

### 2.3.1. DLS

Average hydrodynamic diameters ( $Z_{av}$ ) were measured via dynamic light scattering (DLS) using the Zetasizer NanoZS instrument from Malvern. The data were collected at  $173^\circ$  scattering angle using the fully automatic mode of the Zetasizer system and fitted with monomodal cumulant analysis. The broadness of the distribution was given by a dimensionless number called *Poly* (the higher this value, the broader the size distribution).

2.3.2. *Electron microscopy*

*TEM*

The morphology and particle size of the hybrid latexes were evaluated by transmission electron microscopy (TEM). The hybrid latex suspensions were diluted 20 times in water, and then deposited on a formvar-carbon 200-mesh copper grid. The observations were made using a Philips CM120 microscope operating at an accelerating voltage of 120 kV (Centre Technologique des Microstructures (CT $\mu$ ), Claude Bernard University, Villeurbanne, France).

*SEM*

The morphology of hybrid particle was also evaluated via Scanning Electron Microscopy (SEM). The hybrid latex suspensions were diluted 20 times in water, and then deposited on a formvar-carbon 200-mesh copper grid, dried and covered by a thin layer of copper (Sputtering Cu with Baltec MED020 - 10nm). The observations were made in a FEI QUANTA 250 FEG scanning electron microscope at an acceleration voltage of 10 kV (CT $\mu$ ).

2.3.3. *TGA*

Thermogravimetric analysis (TGA) was performed on a TGA/DSC1 STARe system from Mettler Toledo. In a typical experiment, the samples (5-15 mg) were heated under a nitrogen or air atmosphere from room temperature to 900 °C with a heating rate of 10 °C min<sup>-1</sup>.

### **3. RESULTS AND DISCUSSION**

In this Chapter, the macroRAFT-stabilized iron oxide clusters prepared in Chapter 3 were used as *seeds* in emulsion polymerization of styrene in order to form a polymer shell on their surface. In a first part, the effect of process conditions and of the addition of a crosslinking agent (DVB) was studied using PDMAEMA-based clusters as seeds. The best conditions, with some adjustments, were then used to encapsulate PAA- and amphoteric-based clusters. Finally, the magnetic properties of the resulting iron oxide-based composite particles were investigated.

### 3.1. Encapsulation of PDMAEMA-based clusters

The main characteristics of the different batches of PDMAEMA-based clusters used in this chapter are summarized in Table 16.

**Table 16** – Characteristics of the IO clusters prepared at a large scale using PDMAEMA-*b*-PS-TTC as stabilizer, for their use as seeds in the emulsion polymerization of styrene

Run	SC <sub>th</sub> <sup>a</sup> (%)	f <sub>clu</sub> (%) <sup>b</sup>	Z <sub>av-clusters</sub> (nm)/Poly <sup>c</sup>	D <sub>n</sub> (nm)/ D <sub>w</sub> /D <sub>n</sub> <sup>d</sup>	D <sub>z</sub> (nm) <sup>d</sup>	SC <sub>sep</sub> <sup>e</sup> (%)	f <sub>sep</sub> (%) <sup>f</sup>
<b>TRG78</b>	2.94	70	244/0.20	80/2.02	206	1.80	88
<b>TRG89</b>	2.74	86	180/0.05	82/1.61	155	2.08	89
<b>TRG107</b>	2.68	83	196/0.11	77/1.78	198	1.97	89
<b>TRG119</b>	2.67	86	184/0.10	71/1.58	139	2.00	87
<b>TRG134</b>	2.79	83	181/0.10	81/1.82	194	2.13	93

<sup>a</sup> Theoretical solids contents; <sup>b</sup> Yield of cluster formation calculated from Equation 1 in Chapter 3; <sup>c</sup> Determined by DLS; <sup>d</sup> Determined by statistical analysis of 800-1200 particles from TEM images; <sup>e</sup> Experimental solids contents after magnetic separation; <sup>f</sup> Yield of cluster separation calculated using Equation 3 in Chapter 3;

It is worth mentioning that some cluster dispersions were purified by magnetic separation before use. In this case the suffix *sep* was added to the name of the experiment: for instance, TRG78sep (see Table 17).

#### 3.1.1. Effect of the polymerization process

The emulsion polymerization reaction was first performed in batch (entry TRG79, Table 17) using the TRG78 cluster dispersion as seed. After 3 hours of reaction, a total consumption of styrene was observed as shown in Figure 88. However, a large amount of free polymer particles (*i.e.* devoid of inorganic particles) could be observed in the TEM images of Figure 89A (the dark spots represent the iron oxide nanoparticles due to their higher capacity to absorb electrons while the polymer matrix appears in light grey). The formation of free polymer particles indicates the occurrence of secondary nucleation, which was quantified by magnetic separation giving a value of 64 wt% of free polymer particles (Table 17).

**Table 17** – Experimental conditions and results for seeded emulsion polymerization of styrene using PDMAEMA-*b*-PS-stabilized IO clusters as seeds.

Ref.	Cluster	PC <sub>th</sub> (%) <sup>a</sup>	IO <sub>0</sub> (%) <sup>b</sup>	X (%) <sup>c</sup> /t (h) <sup>c</sup>	Z <sub>av</sub> (nm)/ Poly <sup>d</sup>	ω <sub>free</sub> (%) <sup>e</sup>	IOC <sup>TGA</sup> (%) <sup>f</sup>	Y <sub>IO</sub> (%) <sup>g</sup>	Coag. (%) <sup>h</sup>
<i>Batch process</i>									
<b>TRG79</b>	TRG78	10.0	13	100/5	355/0.21	64	22	71	none
<b>TRG108</b>	TRG107sep	10.1	12	63/6	382/0.22	n.d.	n.d.	n.d.	0.47 (4.0)
<b>TRG174*</b>	TRG134sep	5.1	27	90/8	-	30	32	87	0.04 (0.6)
<b>TRG200**</b>	TRG134sep	2.5	55	66/7	-	12	47	91	0.02 (0.5)
<i>Semi-batch process</i>									
<b>TRG83</b>	TRG78	13.7	9	91/6	186/0.21	86	38	62	none
<b>TRG90</b>	TRG89sep	11.1	12	81/6	589/0.35	-	-	-	n.d.
<b>TRG118</b>	TRG107sep	11.8	10	72/23	562/0.40	15	14	97	0.8 (6.0)

Temperature = 60°C; cluster suspension = 15 g; ADIBA = 0.5 wt% based on Sty except for \*1.1 wt% and \*\*2.1 wt%. For semi-batch systems: initial amount of monomer = 0.05 g (3 wt% based on overall monomer mass), flow rate = 0.4 g h<sup>-1</sup>; Onset of monomer addition = 30 min; Endset = 270 min. <sup>a</sup>Theoretical polymer content at 100% conversion; <sup>b</sup>Iron oxide content based on overall monomer mass; <sup>c</sup>Monomer conversion/reaction time; <sup>d</sup>Determined by DLS; <sup>e</sup>Determined using Equation 1 after 10 minutes of magnetic separation; <sup>f</sup>IO content in the magnetic fraction determined by TGA; <sup>g</sup>Yield of iron oxide incorporation in the magnetic fraction calculated using Equation 3, <sup>h</sup>Coagulum content based either on overall latex mass or on the total amount of solid (in brackets), determined after latex filtration on a 160 mesh grid.

In order to decrease the fraction of free polymer particles observed in batch, the next reaction was carried out using a semi-continuous process (TRG83) expecting a reduction of the secondary nucleation. Indeed, secondary nucleation may be linked to the presence of free macroRAFTs in the continuous phase, which may be organized as micelles that can be swollen by monomer and thus become competitive nucleation sites. However, secondary nucleation was also observed in semi-batch conditions resulting in the formation of a very high amount of free latex particles (ω<sub>free</sub> = 86 wt%, entry TRG83 in Table 17).

Furthermore, Figure 88A shows a longer inhibition period in the semi-continuous experiment compared to the batch one, which can be associated to a longer nucleation period. Indeed, for the semi-batch system, a low monomer amount was introduced in the initial load (3 g L<sup>-1</sup>), which can partition between 3 phases: the IO clusters, the macroRAFT aggregates (“micelles”) and water. It is important to point out that the concentration of clusters in the aqueous phase, *ca.* 20 g L<sup>-1</sup>, is initially much higher than that of styrene (3 g L<sup>-1</sup>), which could affect the amount of styrene available in water (styrene solubility in water = 0.3 g L<sup>-1</sup>). This low monomer concentration in the water phase would lead to a lower polymerization rate



during the initiation step, as at this stage the latter only depends on the radical and monomer concentrations. As the radical concentration was the same in both cases, a lower initiation rate and hence a longer inhibition period was observed for the semi-batch system compared to the batch one, for which the initial styrene concentration was much larger (*i.e.* 100 g L<sup>-1</sup>).

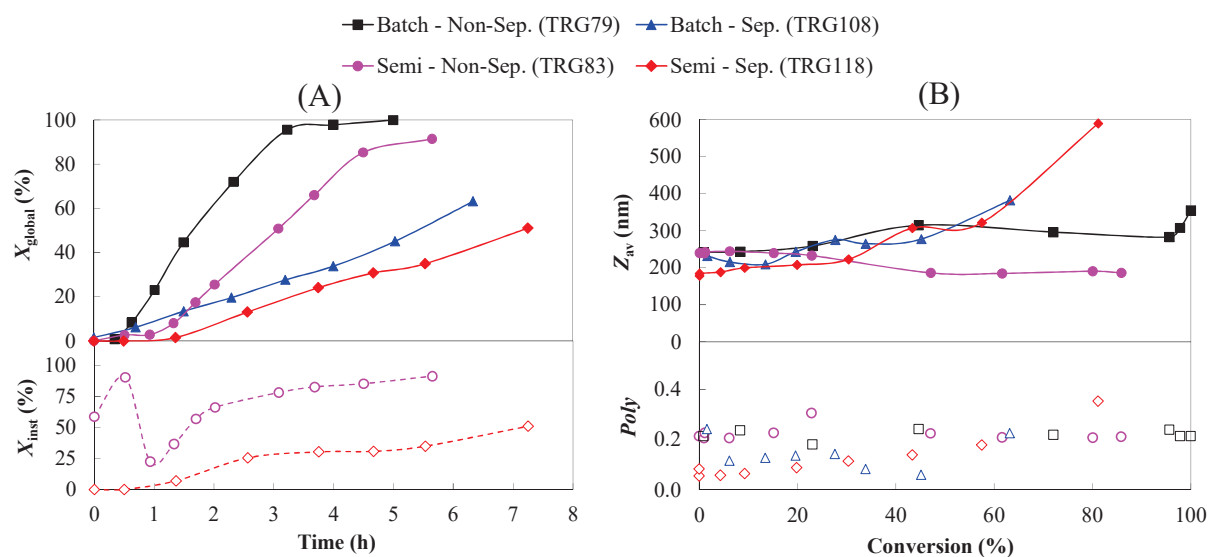


**Figure 88** – Effect of polymerization conditions (batch *versus* semi-batch) on the evolutions of: (A) instantaneous and global conversions with time and (B) particle size and *Poly* value (DLS) with overall conversion during seeded emulsion polymerization of styrene using PDMAEMA-based IO clusters as seeds.

In order to decrease the fraction of free macroRAFT and avoid the formation of secondary-nucleated particles, the cluster dispersions were purified via magnetic separation/redispersion in water and the resulting suspension was used as seed in a semi-batch emulsion polymerization (TRG118). As expected, the extent of secondary nucleation was significantly reduced:  $\omega_{\text{free}}$  decreased from 86 to 15 wt% (Table 17), indicating that in this case nucleation preferentially occurred into the clusters leading to a higher fraction of magnetic latex particles ( $\omega_{\text{mag}} = 85$  wt%). In addition, Figure 88A shows that a lower polymerization rate was observed in the presence of the purified cluster when compared to the non-purified ones (with still an induction period). The same observation stands true when the polymerization was performed under batch conditions (TRG108). This is likely due to the difference in the number of particles formed in the two systems. Indeed, the polymerization conducted in the presence of non-purified clusters led to the formation of new polymer particles by secondary nucleation resulting in a higher number of particles, and consequently in higher polymerization rates (see Equation 1).

For both processes (batch and semi-batch), the size of the particles synthesized in the presence of the purified clusters increased significantly after 40% conversion (Figure 88B) suggesting a loss of colloidal stability. Probably, the gradual increase of the total surface area associated with a deficit in macroRAFT agent could result in partial flocculation of the particles (Coag. = 6.0% based on monomer mass, entry TRG118 in Table 17).

The morphology of the resulting hybrid particles was characterized by TEM (Figure 89). Compared to the original clusters shown in Chapter 3, the encapsulated clusters clearly did not maintain their initial spherical morphology. The clusters indeed appear shattered with the IONP being either located at the surface of the hybrid particles indicating a phase separation (Figure 89A and C, non-purified clusters) or homogeneously distributed in the polymer particles (Figure 89B and D, purified clusters). As already mentioned, phase separation between fatty acid modified iron oxide nanoparticles and polystyrene has already been reported in the literature,<sup>39, 42, 47, 49</sup> and is usually attributed to some incompatibility between the hydrocarbon chains of the fatty acid and the polymer. However, for the reactions carried out using the purified clusters as seeds (TRG108 and TRG118), phase separation was not evidenced, as the inorganic nanoparticles were homogeneously distributed in the polymeric matrix (Figure 89B and D). Nevertheless, these results must be considered with care. Indeed, the experimental runs TRG108 and TRG118 were performed with clusters synthesized from a different batch of commercial IONP than TRG79 and TRG83. In addition, when an experiment (TRG90) using the same conditions of run TRG118 was carried but using the same batch of clusters than the runs TRG79 and TRG83, the phase separation phenomenon was observed as well (TEM micrographs of TRG90 shown in ANNEX 4. 2). Hence, the different morphologies observed for these systems are likely associated to a potential variation in the chemical nature of the modifier used for the preparation of the commercial IONP (the only indication from the supplier is *fatty acid modified IONP*), rather than to the fact that the clusters were first separated from free macroRAFTs. These aspects could deserve more investigation but were not the focus of the present work.

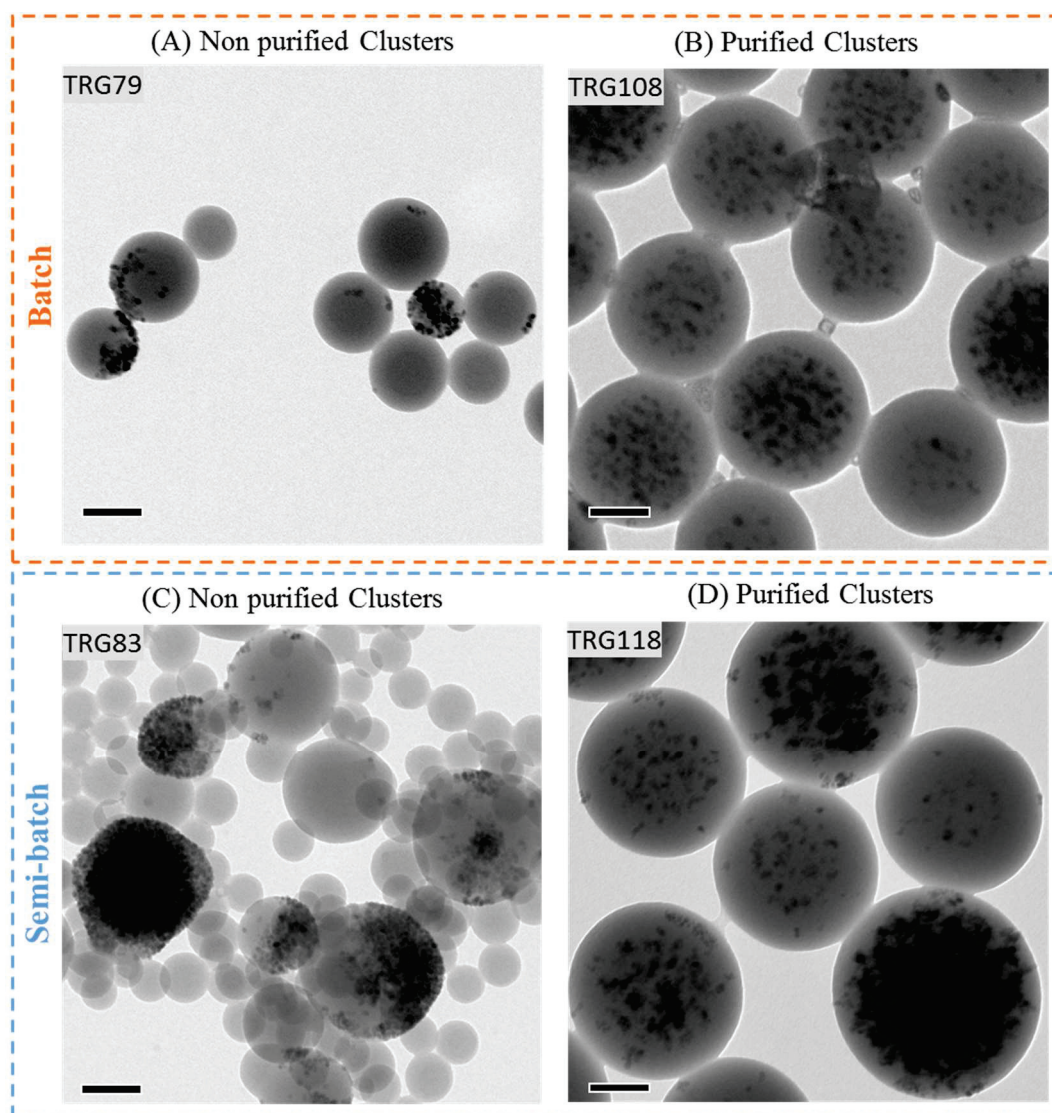


**Figure 89** – TEM micrographs of IO/polymer composite particles (without magnetic separation) prepared via batch (A, B) or semi-batch (C, D) emulsion polymerization of styrene using the as synthesized (A, C) or the separated (B, D) IO clusters as seeds

*Effect of the polymer content in batch experiments*

As mentioned earlier, the iron oxide content in the hybrid particles is a key parameter to obtain magnetic carriers with high magnetic separation rates. Therefore, in the next series of experiments, we tried to increase the IO content by varying the initial amount of monomer while maintaining a fixed amount of clusters in water (entries TRG174 and TRG200 in Table 17). For these experiments, the clusters were purified and the reactions were carried out in batch.

The TEM micrographs of Figure 90 show that the reaction carried out with 2.5% of styrene resulted in hybrid particles presenting a hemispherical morphology. However, by increasing the initial amount of styrene, an encapsulated morphology was gradually obtained. Two

hypotheses can be proposed to explain the evolution of particle morphology with increasing the monomer concentration: IO migration dynamics and interfacial tension. These two hypotheses are discussed below.

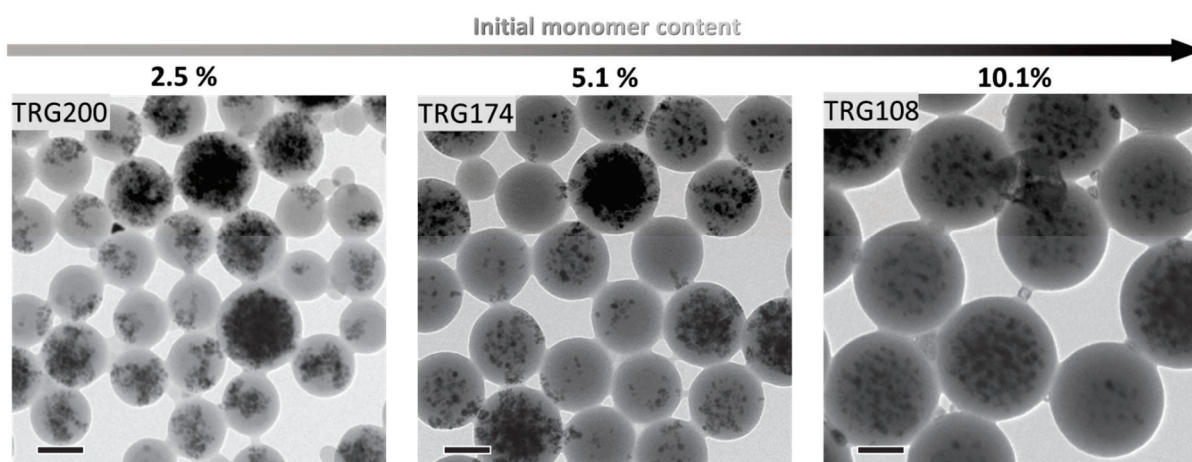


**Figure 90** - TEM micrographs of iron oxide/polymer composite particles prepared via seeded emulsion polymerization of styrene in batch for various theoretical polymer contents.  $PC_{th}$ ): 2.5 wt% (TRG200), 5.1 wt% (TRG174) and 10.1 wt% (TRG108), respectively.

#### *IO migration dynamics*

The rate of diffusion of the organically-modified IONP toward the particle surface depends on the viscosity of the polymer particles. As the monomer is consumed, the viscosity of the polymer particles gradually increases, which could slow down the diffusion of the inorganic particles toward the surface. If we consider that the number of clusters is approximately the same from one experiment to another, the amount of styrene per cluster gradually decreases with the initial styrene concentration. Hence, as the monomer concentration increases, the IONP will have more time to homogeneously diffuse into the particle, to finally lead to the expected encapsulated morphology.

#### *Interfacial tension*

By increasing the initial styrene concentration, the molar mass of the polymer chains is expected to increase as the cluster concentration, and thus the macroRAFT concentration, should approximately remain the same from one experiment to another. Asua<sup>71</sup> proposed a morphology map for polymer-inorganic hybrid particles prepared via miniemulsion polymerization (Figure 91). According to the authors, the equilibrium morphology ( $E$ ) is given by:

$$E = A_{PW} \cdot \gamma_{PW} + A_{IW} \cdot \gamma_{IW} + A_{IP} \cdot \gamma_{IP} + A_{II} \cdot \gamma_{II} \quad (4)$$



where  $A_{ij}$  and  $\gamma_{ij}$  are respectively the interfacial area and interfacial tension between phases  $i$  and  $j$  with P, I and W representing the polymer, inorganic and aqueous phases, respectively. An increase of the molar mass of the polymer will generate polymer chains that are more hydrophobic resulting in a better affinity of the polymer phase for the organically-modified IONPs, which will decrease the I/P interfacial tension. In addition, more hydrophobic polymer chains will generate a higher  $\gamma_{PW}$ . These two combined effects should lead to a decrease of the  $\gamma_{IP}/\gamma_{PW}$  ratio, and thus to a change of particle morphology from hemispherical to core-shell particles as illustrated in Figure 91.

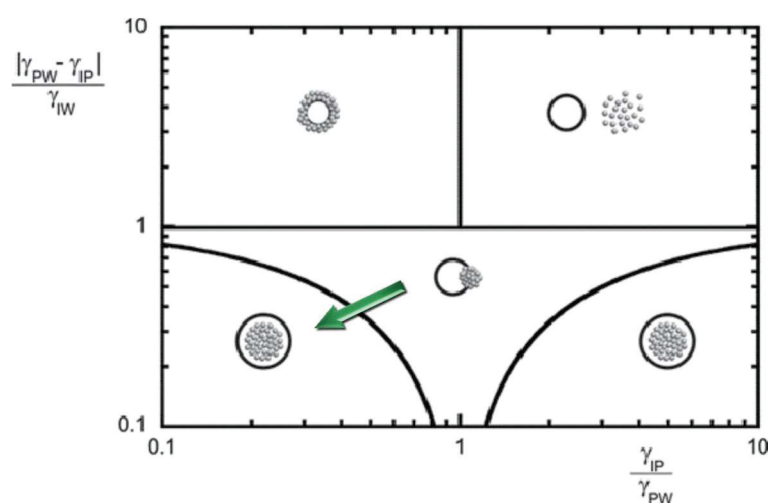


**Figure 91** – Predicted equilibrium morphologies of polymer/inorganic composite particles as a function of the interfacial tension ( $\gamma$ ) between the inorganic (I), polymer (P) and aqueous (W) phases, respectively. Adapted from<sup>71</sup> with permission of Wiley.

In summary, the above results in batch or semi-batch for various IO contents showed that in all cases, the clusters lost their original spherical shape. Therefore we next investigated the effect of the addition of a crosslinker on particle morphology with the hope that crosslinking will enable to maintain the integrity of the clusters.

### *3.1.2. Effect of the addition of a crosslinker for 10% theoretical polymer contents*

The effect of a crosslinking agent, DVB, was first studied during seeded emulsion polymerization of styrene in the presence of PDMAEMA-stabilized clusters targeting 10 wt% of polymer content (Table 18). To avoid the excess of monomer (including crosslinking agent) in the reaction medium during the initial stages of the polymerization, the polymerizations were carried out in semi-batch conditions.

**Table 18** - Experimental conditions and results for seeded semi-batch emulsion polymerization of styrene in the presence of DVB using PDMAEMA-*b*-PS-stabilized IO clusters as seeds.

Ref.	Cluster	DVB (%) <sup>a</sup>	IO <sub>0</sub> (%) <sup>b</sup>	X (%) <sup>c</sup> /t (h) <sup>c</sup>	Z <sub>av</sub> (nm)/Poly <sup>d</sup>	ω <sub>free</sub> (%) <sup>e</sup>	IOC <sup>TGA</sup> (%) <sup>f</sup>	Y <sub>IO</sub> (%) <sup>g</sup>	Coag. (%) <sup>h</sup>
TRG90	TRG89sep	0	12	81/6	589/0.35	15	14	97	n.d.
TRG94*	TRG89sep	5	11	12/7	589/0.35	12	22	30	1.96 (14.5)
TRG91	TRG89sep	10	10	26/7	462/0.24	9	14	52	n.d.
TRG101	TRG89sep	20	11	34/6	596/0.21	11	44	89	0.02 (0.86)

\*Unstable latexes; Temp. = 60°C; 15g of cluster dispersion; ADIBA = 0.5 wt% of overall monomer mass; PC<sub>th</sub> ≈ 10 wt% based on latex mass; 0.05 g of monomer introduced initially (3 wt% based on overall mon mass), flow rate= 0.4 g h<sup>-1</sup>; Onset = 30 min; Endset = 270 min. <sup>a</sup>DVB content based on overall monomer mass; <sup>b</sup>Iron oxide content based on overall monomer mass; <sup>c</sup>Monomer conversion/reaction time; <sup>d</sup>Determined by DLS; <sup>e</sup> Determined using Equation 1 after 10 minutes of magnetic separation; <sup>f</sup>Iron oxide content in the magnetic fraction determined by TGA; <sup>g</sup>Yield of iron oxide incorporation in the magnetic fraction calculated using Equation 3, <sup>h</sup>Coagulum content based either on overall latex mass or on the total amount of solid (in brackets).

The first experiment was carried out in the presence of 20 wt% of DVB based on overall monomer mass. The resulting latex was stable presenting a low coagulum content. The conversion was however significantly lower than in absence of DVB. To better understand this phenomenon, the next series of experiments consisted in studying the effect of DVB content in the monomer phase on the polymerization kinetics and particle morphology. As can be seen in Figure 92, the presence of DVB systematically led to low polymerization rates and limited conversions. This can be explained by the thermodynamic balance involved in the stabilization of swollen crosslinked particles in emulsion polymerization. The Gibbs energy balance involved in this equilibrium was proposed as follows:<sup>72</sup>

$$\Delta\bar{G}^* = \Delta\bar{G}_m + \Delta\bar{G}_t + \Delta\bar{G}_{el} \quad (5)$$

where  $\Delta\bar{G}^*$  is the molar free energy,  $\Delta\bar{G}_m$  is the contribution of monomer-polymer mixing forces,  $\Delta\bar{G}_t$  is the particle-water interfacial tension force and  $\Delta\bar{G}_{el}$  the polymer network elastic-retractile force. In a conventional emulsion polymerization, only the two first parameters of equation 5 are present.<sup>73</sup> Indeed, the solvent is generally a good solvent for the polymer, which maintains a negative  $\Delta\bar{G}^*$  value over the polymerization keeping the system energetically favorable to polymer-monomer mixing. In crosslinked emulsion polymerization, the additional term  $\Delta\bar{G}_{el}$  is added to the energy balance to take into account the changes in polymer network configuration.<sup>74</sup> This elastic force is directly affected by the crosslinking degree and the increment (positive) of  $\Delta\bar{G}_{el}$  leads to a less energetically favorable solvation of



the polymer particles. This induces a gradual decrease of the monomer concentration into the polymer particles resulting in lower polymerization rates. Indeed, at high crosslinker content the particles become solid, which means that no solvent (in this case the monomer) can diffuse inside the particles and the polymerization is thus quenched, which limits the final conversion. Errede *et al.*<sup>75</sup> reported that for a styrene/DVB system, the critical crosslinking degree is attained for 20 mol% of DVB in the polymer chains. In our case, taking into account the high reactivity of the first double bond of DVB, the first chains generated are likely rapidly reaching this critical value.

Moreover, a sharp increase of particle size can be observed in Figure 92B for conversions higher than 20%. As explained above, this behavior is likely due to a gradual increase of particle size with increasing conversion, which would result in an insufficient surface coverage by the amphiphilic macroRAFT (the used clusters being first purified), leading to partial flocculation. This behavior may also be linked to the events explained above. Indeed, the high degree of crosslinking of the clusters leads to the generation of pure polymer particles which cannot be efficiently stabilized as the amount of macroRAFT in the continuous phase is expected to be very low. These particles would actually correspond to the ca. 10% of free polymer particles detected in these samples (Table 3).

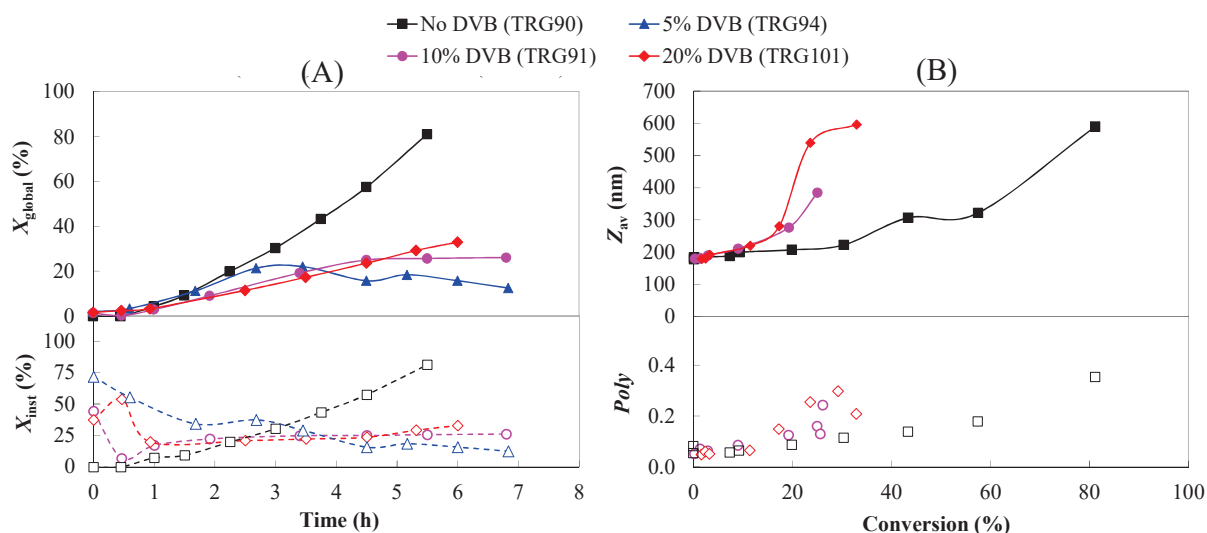


**Figure 92** – Effect of DVB content on the evolutions of: (A) instantaneous and global conversion with time and (B) particle size and *Poly* value (DLS) with global conversion during seeded semi-batch emulsion polymerization of styrene using PDMAEMA-stabilized clusters as seeds. The particle size analyses of the experiment performed with 5% of DVB were not conclusive with big variation from one sample to another, and the data are not shown.

The TEM images of the composite particles are shown in Figure 93. It can be clearly seen that the DVB content had a direct impact on the hybrid particle morphology leading to the

formation of well-defined core-shell particles for high DVB contents. As explained above, there are two possible interpretations: variation of interfacial tensions and a reduced mobility. Increasing the DVB content will lead to an increase of the hydrophobicity of the polymer shell, which should decrease the  $\gamma_{IP}/\gamma_{PW}$  ratio and favor the formation of core-shell particles (Figure 91). In addition, by increasing the crosslinking density, the viscosity of the hybrid particle will significantly increase, which should slow down the migration of the IONPs towards the surface. The TEM images of Figure 93 show that for the initial stages of the polymerization (*i.e.* for low and similar PC: 0.9, 1.4, 1.2 and 1.4%), the spherical structure of iron oxide clusters tend to be better preserved as the DVB content increases. For the polymerization with no DVB, the phase separation was observed in the early stage of the polymerization. With 5 wt% of DVB the IONPs tend to migrate to the polymer surface, but stay concentrated in the inner core of the particles. However, at 10 and 20% the initial

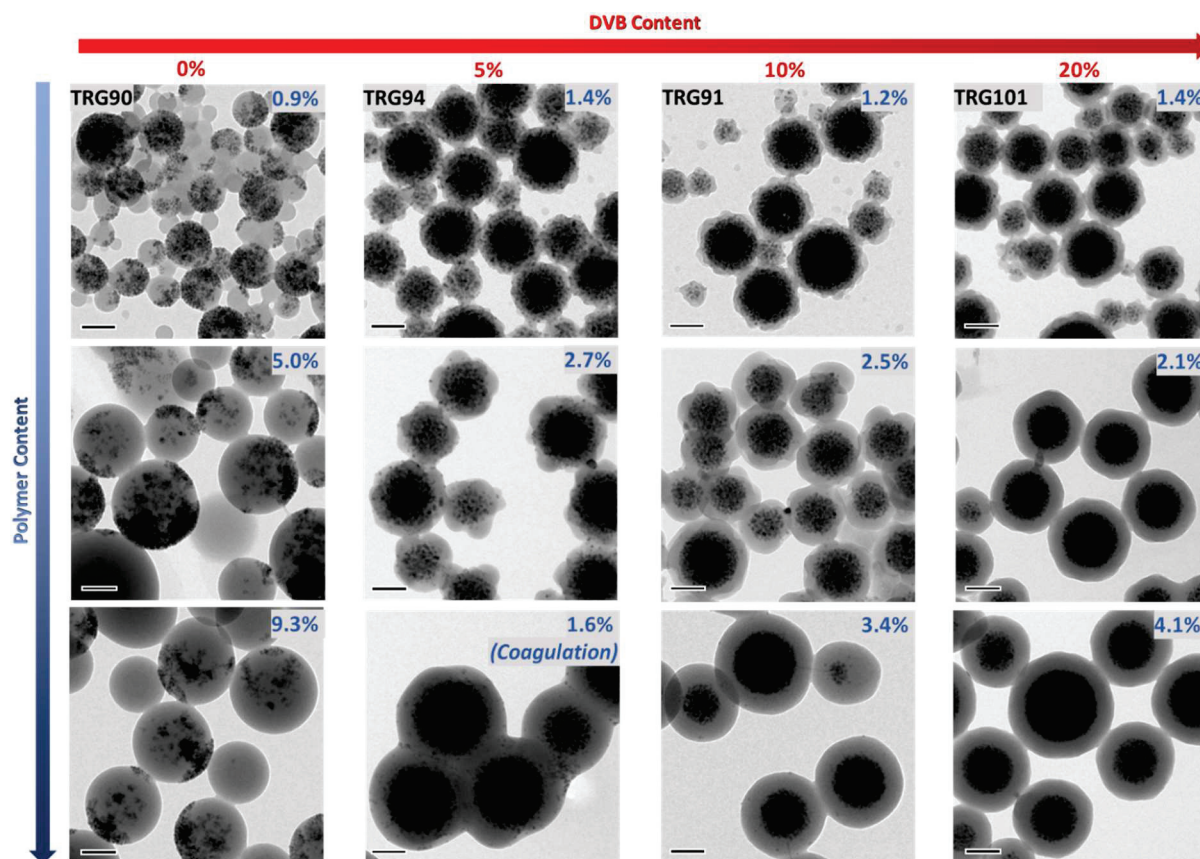


**Figure 93** – TEM micrographs of IO/polymer composite particles synthesized by seeded semi-batch emulsion polymerization of styrene in the presence of increasing amounts of DVB (based on overall monomer mass): 0 wt% (TRG90), 5 wt% (TRG94), 10 wt% (TRG91) and 20 wt% (TRG101), for increasing polymer contents.

spherical morphology of the clusters was completely maintained. These observations have also been reported by other authors, who associate this behavior to the relatively high viscosity in the polymer phase (and essentially in the inner core of the particles), which strongly restricts the movement of the IONPs toward the surface of the hybrid particles.<sup>58, 76, 77</sup> We have plotted in Figure 94 the evolution of the thickness of the polymer shell with the polymer content. This value was determined by statistical analyses of the TEM images on *ca.* 300 particles. The shell thickness steadily increased with increasing polymer content, indicating that it can be easily modulated by varying the amount of monomer introduced in the reactor. However, the experimental values were always lower than the expected ones, which can be explained by three factors: i) uncertainties associated with the determination of the initial number of clusters due to a limited accuracy in the determination of their size and/or density; ii) the assumption that all the monomer added was consumed to form the polymeric shell (whereas some of the polymer is obviously located in the inner core) and iii) uncertainties linked to the value of polymer shell density used in the calculation (*i.e.* the PS value,  $1.05 \text{ g cm}^{-3}$ ), whereas the density will be likely impacted by the presence of DVB.

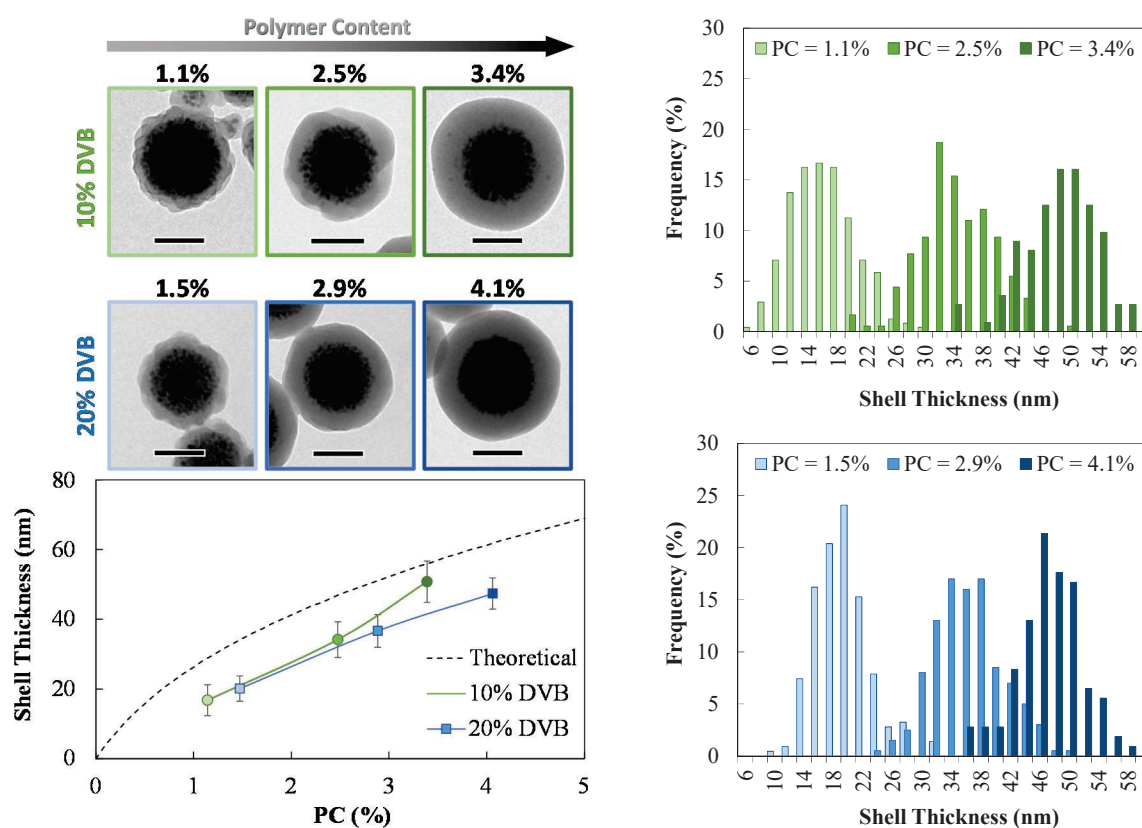


**Figure 94** – Shell thickness of core-shell hybrid particles prepared via seeded emulsion polymerization of styrene in the presence of PDMAEMA-stabilized clusters and 10 (TRG91) or 20 wt% (TRG101) of DVB as crosslinking agent as a function of polymer content.

In addition, as the amount of DVB increases, the yield of iron oxide incorporation in the magnetic fraction significantly increases, from 30 (5 wt% DVB) to 89% (20 wt% DVB) (Table 18).

As mentioned above, the shell thickness can be modulated by varying the amount of monomer introduced in the reactor. According to Figure 94, a thin polymeric shell surrounding the iron oxide seed was notably observed for a PC close to 2%, resulting in the formation of composite particles with a very high IO content. Hence, in the next series of experiments, the theoretical polymer content was decreased from 10 to 2 wt%.

### 3.1.3. Effect of the addition of a crosslinker for 2.6 wt% theoretical polymer content

The first experiment carried out to reach the goals mentioned above (thin shell/high IO content) relied on the addition of a high amount of DVB (21mM, TRG123, Table 4), only present in the initial monomer load to rapidly entrap the iron oxide clusters, followed by the feeding of styrene to avoid the formation of too highly crosslinked chains in the outer polymeric shell. Indeed, in the previous experiments DVB was present in both the initial charge and the feed (see TRG101, Table 4).

**Table 19** – Experimental conditions and results for seeded semi-batch emulsion polymerization of styrene in the presence of DVB using PDMAEMA-*b*-PS-stabilized iron oxide clusters as seeds.

Ref.	Cluster	DVB <sup>IC</sup> (mM)/(%) <sup>a</sup>	DVB <sup>FED</sup> (mM)/(%) <sup>b</sup>	X (%) <sup>c</sup> /t (h) <sup>c</sup>	Z <sub>av</sub> (nm)/Poly <sup>d</sup>	ω <sub>free</sub> (%) <sup>e</sup>	IOC <sup>TGA</sup> (%) <sup>f</sup>	Y <sub>IO</sub> (%) <sup>g</sup>	Coag. (%) <sup>h</sup>
TRG101*	TRG89sep	8/20	178/20	34/6	596/0.21	11	44	89	0.02 (0.9)
TRG123	TRG119sep	21/40	0	66/7	228/0.09	-	-	-	0.01 (0.3)
TRG124	TRG119sep	42/80	0	63/7	290/0.17	6	46	95	0.02 (0.5)
TRG131	TRG119sep	46/80	26/20	53/7	353/0.23	6	54	85	0.21 (4.8)

15 g of cluster dispersion; PC<sub>th</sub> ≈ 2.6 % except for \*10.1%; IO<sub>0</sub> (%) = 55; Temp. = 60°C; [ADIBA] = 1.7 mM; 0.1 g of monomer introduced initially (30 wt% based on overall monomer mass), flow rate = 0.4 g·h<sup>-1</sup>; Onset = 30 min; Endset = 80 min. <sup>a,b</sup> DVB concentration based on latex volume and content based on monomer mass of either initial charge (IC) or feed (FED); <sup>c</sup> Monomer conversion/reaction time; <sup>d</sup> Determined by DLS; <sup>e</sup> Determined using Equation 1 after 10 minutes of magnetic separation; <sup>f</sup> Iron oxide content in the magnetic fraction determined by TGA; <sup>g</sup> Yield of iron oxide incorporation in the magnetic fraction calculated Equation 3, <sup>h</sup> Coagulum content based either on overall latex mass or on solidbrackets.

Actually, this strategy based on the addition of DVB only in the initial load ([DVB<sup>IC</sup>] = 21 mM) resulted in a higher conversion: 66% for TRG123 against 34% for TRG101 (Table 19). Moreover, the initial spherical morphology of the IO clusters was



preserved as shown in Figure 95 (run TRG123). However, a raspberry-like morphology was observed instead of a well-defined core-shell morphology as obtained for run TRG101 (Figure 95), which is our target morphology. Then, a second reaction was carried out using twice the amount of DVB in the initial load ( $[DVB^{IC}] = 42 \text{ mM}$ ) but again a raspberry-like morphology was obtained, with however a smoother shell. Finally, a higher total amount of DVB was used ( $[DVB^{IC}] + [DVB^{FED}] = 72 \text{ mM}$ ; TRG131) leading to formation of a well-defined core-shell morphology (Figure 95). This morphology evolution, from raspberry to core-shell, can again be associated with difference in the hydrophobicity of the polymer shell: the higher is the DVB content, the more hydrophobic will be the polymeric shell. Hence, the surface tension between the polymer and water phases will increase. In order to reach an energetically favorable equilibrium, *i.e.* to decrease the surface tension, the surface area tends to be the smallest as possible, forming a regular spherical polymeric shell. Hence, TRG131 which displays a core-shell morphology and a thin polymer shell was selected as the optimized experiment.

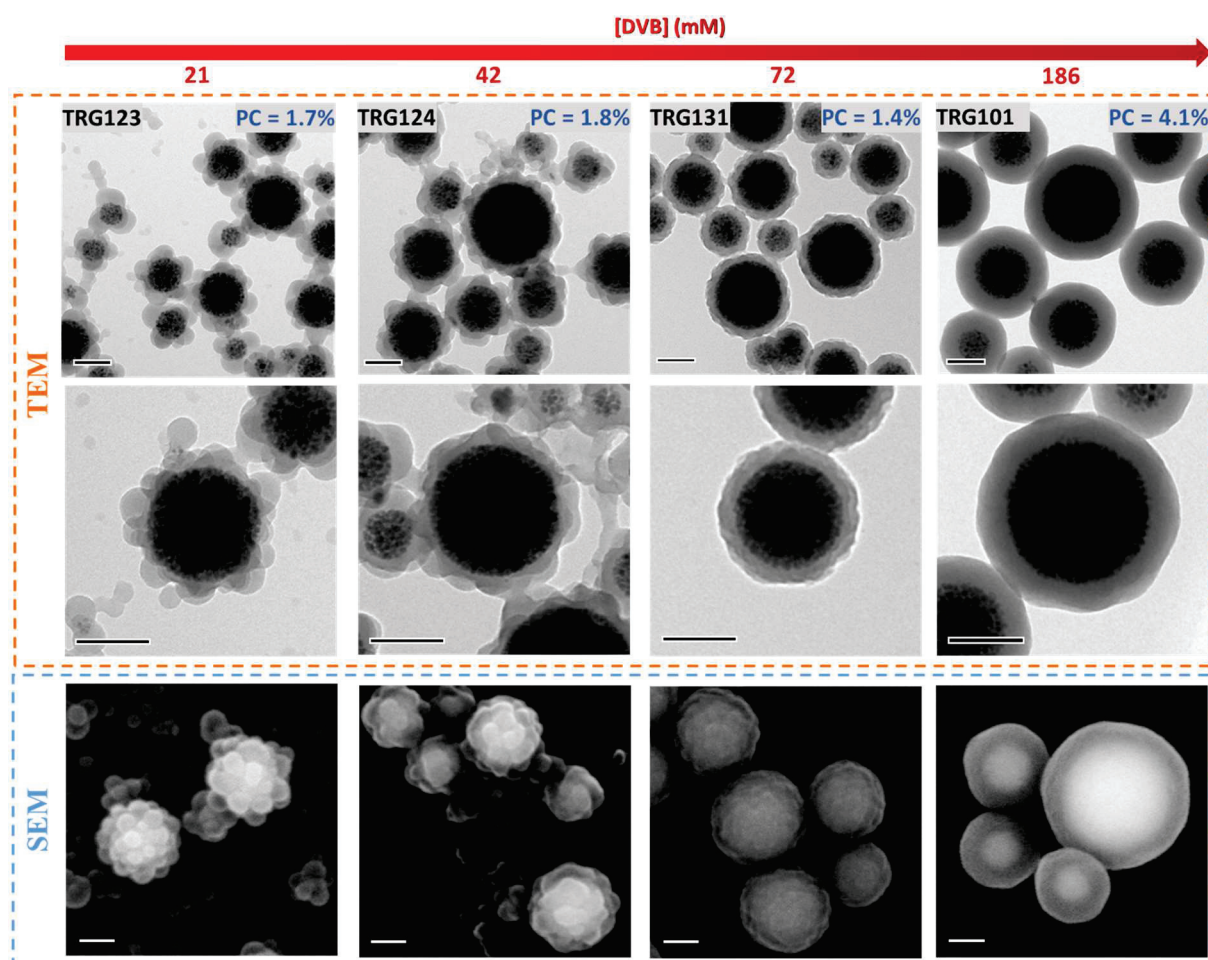


Figure 95 – TEM (*top*) and SEM (*bottom*) micrographs of IO/polymer composite particles synthesized by seeded emulsion polymerization of styrene using IO cluster as seeds, for increasing

DVB concentrations: [DVB] = 21 mM (TRG123), 42 mM (TRG124), 72 mM (TRG131) and 186 mM (TRG101).

### 3.2. Encapsulation of PAA-based clusters

In this section, the strategy described above for the PDMAEMA-based clusters was extrapolated to the encapsulation of iron oxide clusters stabilized by the PAA-*b*-PS-TTC macroRAFT. The characteristics of the IO clusters are summarized in Table 20 while the experimental conditions used for the emulsion polymerization of styrene are shown in Table 21.

**Table 20** – Characteristics of the IO clusters prepared at a large scale using PAA-*b*-PS-TTC as stabilizer, for their use as seeds in the emulsion copolymerization of styrene and DVB.

Run	SC <sub>th</sub> <sup>a</sup> (%)	f <sub>clu</sub> (%) <sup>b</sup>	Z <sub>av-clusters</sub> (nm)/Poly <sup>c</sup>	D <sub>n</sub> (nm)/ D <sub>w</sub> /D <sub>n</sub> <sup>d</sup>	D <sub>z</sub> (nm) <sup>d</sup>	SC <sub>sep</sub> <sup>e</sup> (%)	f <sub>sep</sub> (%) <sup>f</sup>
<b>TRG132</b>	2.26	84	143/0.07	66/1.78	141	2.03	91
<b>TRG140</b>	2.62	95	161/0.13	71/1.55	131	2.41	99
<b>TRG152</b>	2.78	94	148/0.06	-	-	2.07	96
<b>TRG156</b>	2.78	96	145/0.08	52/1.97	127	2.00	87

<sup>a</sup> Theoretical solids contents; <sup>b</sup> Yield of cluster formation calculated from Equation 1 of Chapter 3; <sup>c</sup> Determined by DLS; <sup>d</sup> Determined by statistical analysis of 800-1200 particles from TEM images; <sup>e</sup> Experimental solids contents after magnetic separation; <sup>f</sup> Yield of cluster separation calculated using Equation 3 in Chapter 3;

**Table 21** – Experimental conditions and results for semi-batch emulsion polymerization of styrene in the presence of DVB using PAA-*b*-PS-stabilized iron oxide clusters as seeds and different initiators.

Ref.	Cluster	Initiator/T (°C)	pH <sub>0</sub>	X (%) / t (h) <sup>a</sup>	Z <sub>av</sub> (nm) / Poly <sup>b</sup>	Coag. (%) <sup>c</sup>
<b>TRG135*</b>	TRG132sep	ADIBA/60	7.5	*	4495/1.00	1.31 (48.2)
<b>TRG136*</b>	TRG132sep	ACPA/70	7.5	*	3239/0.92	0.46 (21.7)
<b>TRG145</b>	TRG140sep	ACPA/70	9.6	41/22	203/0.11	0.01 (0.3)
<b>TRG149</b>	TRG140sep	ACPA/80	9.5	47/22	650/0.43	0.16 (3.5)
<b>TRG154*</b>	TRG152sep	APS/75	7.4	*	-	0.87 (31.5)
<b>TRG157</b>	TRG156sep	APS-NaHCO <sub>3</sub> /75	7.3	43/21	441/	0.13 (2.8)

Cluster dispersion = 15 g; PC<sub>th</sub> ≈ 2.6 %; IO<sub>0</sub> (%) = 55; [Initiator] = 1.7 mM; 0.1 g of monomer introduced initially (30 wt% based on overall monomer mass), flow rate = 0.4 g h<sup>-1</sup>; Onset = 30 min; Endset = 80 min. S:DVB (all isomers including EVB) wt:wt ratio were 20:80 and 80:20 in the initial load and in the feed, respectively. <sup>a</sup> Monomer conversion/reaction time; <sup>b</sup> Determined by DLS; <sup>c</sup> Coagulum content based either on overall latex mass or on the total amount of solid (in brackets).



A first experiment (TRG135, Table 21) was performed under the optimized experimental conditions obtained previously for the PDMAEMA-based clusters (TRG131, Table 19), leading to an unstable latex. This is likely due to the nature of the initiator, ADIBA, which is of opposite charge to that of the macroRAFT stabilizer at pH = 7.5. ADIBA was thus replaced by an anionic initiator, ACPA, and the polymerization was performed at 70°C. However, this also led to an unstable latex (TRG136, Table 21). Hence, in a third attempt, the suspension pH was increased to 9.6 to ensure that all the carboxylic acid groups of ACPA and PAA were deprotonated, resulting in a stable latex with almost no coagulum, and an average particle diameter of 203 nm (TRG145, Table 21).

The conversion was however quite low (41% after 22h). Therefore different strategies were tested aiming at improving the monomer-to-polymer conversion. It is known that the rate of initiator decomposition depends on temperature. Figure 96 shows the decomposition profiles of APS, ADIBA and ACPA for different temperatures. To ensure an initiator consumption (and hopefully a radical flux) similar to that of run of TRG131 (with ADIBA at 60°C), the temperature was increased to 80°C using ACPA (TRG149, Table 21). The conversion was slightly increased to 47% (41% at 70°C), which is similar to that obtained previously for the PDMAEMA-*b*-PS system using ADIBA as initiator ( $X = 53\%$ , TRG131 in Table 19).

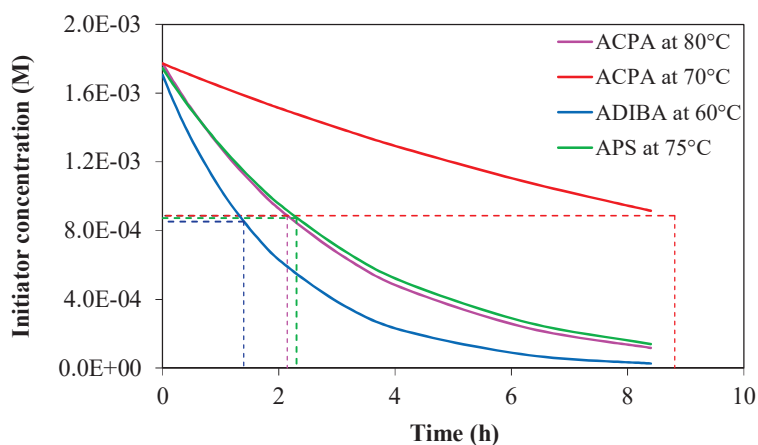


**Figure 96** – Radical initiator decomposition kinetic profiles. The dashed lines represent the half-life time.

An inorganic initiator was then tested, APS. Again, the temperature was set at 75°C in order to have a similar decomposition profile as for ADIBA (Figure 96). This led however to an unstable latex (TRG154, Table 21), which is likely due to the decrease of pH induced by persulfate decomposition. Therefore, a buffer ( $\text{NaHCO}_3$ ) was introduced in the suspension

medium to maintain a pH around 7 resulting in a stable latex with low coagulum content (TRG157, Table 21).

Figure 97 shows the morphology of the obtained hybrid particles. There is no major influence of the type of initiator. The differences of shell thickness observed among the samples are likely due to differences in the polymer content. As mentioned above, the high reactivity of DVB likely favors a quick "frozen state" of the inner particle core (section 3.1.2). The TEM images of Figure 97 (TRG145 and TRG157) support this hypothesis. Indeed, the polymer shell was hardly visible at low polymer content indicating that the polymerization is initially located into the particles and progressed outward from the core as the monomer was consumed.

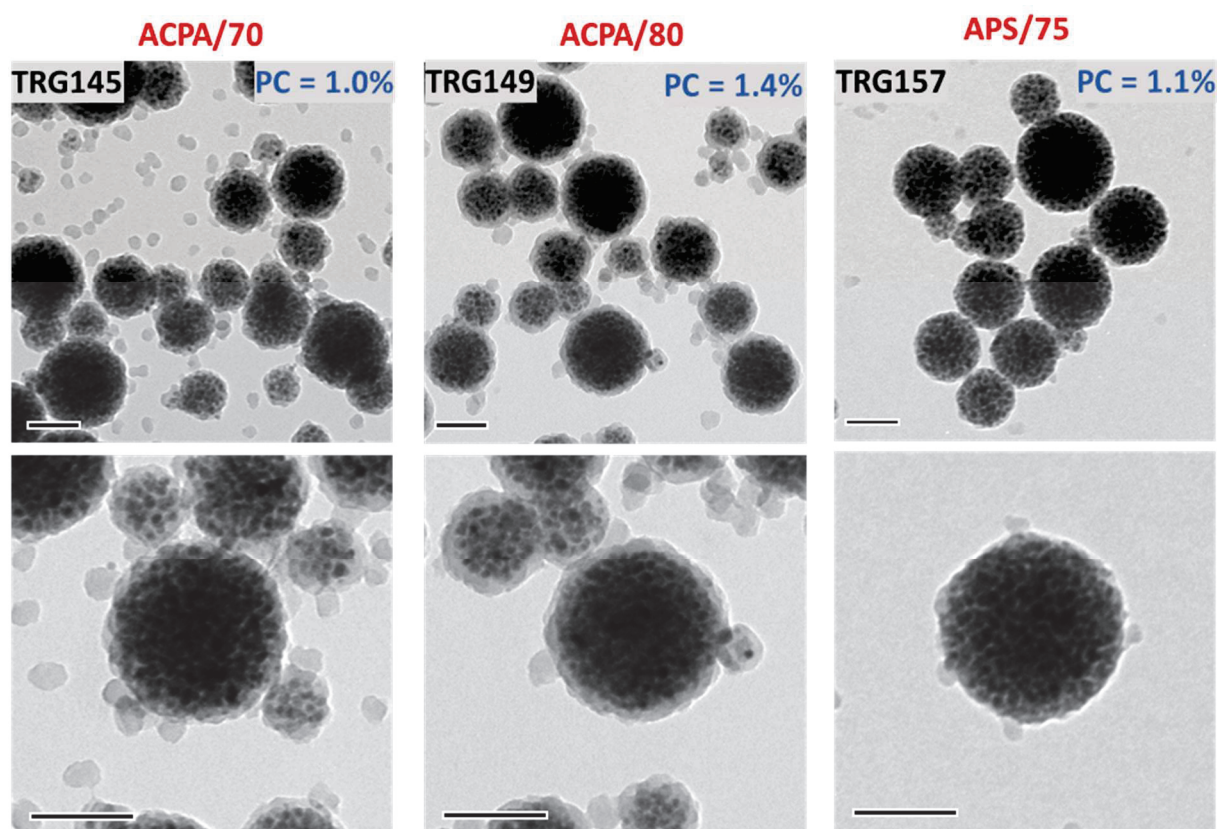


**Figure 97** – TEM images of IO/polymer composite particles synthesized by seeded semi-batch emulsion polymerization of styrene in the presence of DVB using different initiators: ACPA at 70°C (TRG145), ACPA at 80°C (TRG149) and APS at 75°C (TRG157) and PAA-*b*-PS-stabilized iron oxide clusters as seeds.

Due to the good colloidal stability of the resulting latex associated to the regular core-shell morphology of the hybrid particles, the experimental conditions of TRG149 (ACPA/80°C) were selected for the following section, which will investigate the use of P(DMAEMA-*co*-

AA)-stabilized clusters as seeds. For the sake of comparison, some experiments were also performed with ADIBA at 60°C.

### 3.3. Encapsulation of P(DMAEMA-co-AA)-based clusters

This section deals with the encapsulation of IO clusters stabilized by P(DMAEMA-co-AA)-TTC macroRAFT agents. Table 22 summarizes the main characteristics of the clusters while the experimental conditions and results of the emulsion polymerization experiments are shown in Table 23. For each experiment, the composition of the macroRAFT is also recalled.

**Table 22** – Characteristics of the IO clusters prepared at a large scale using P(DMAEMA-co-AA)-b-PS-TTC as stabilizer, for their use as seeds in the emulsion copolymerization of styrene and DVB

Run	DP <sub>DMAEMA</sub> /DP <sub>AA</sub>	pH <sub>f</sub>	Z <sub>av-cluster</sub> (nm)/Poly <sup>c</sup>	D <sub>n</sub> (nm)/D <sub>w</sub> /D <sub>n</sub> <sup>d</sup>	D <sub>z</sub> (nm) <sup>d</sup>	SC <sub>sep</sub> <sup>e</sup> (%)	f <sub>sep</sub> (%) <sup>f</sup>
TRG139	33/16	5.62	319/0.20	96/2.75	502	2.21	94
TRG151	33/16	7.98	277/0.22	108/1.98	252	2.17	
TRG144	16/23	-	666/0.23	109/5.81	724	1.70	97
TRG148	16/23	-	177/0.08	91/1.53	167	2.45	96
TRG158	16/23	7.4	218/0.21	222/0.20	179	1.90	97
TRG143	10/39	7.4	137/0.07	77/1.4	124	2.45	98

<sup>a</sup> Theoretical solids contents; <sup>b</sup> Yield of cluster formation calculated from Equation 1 of Chapter 3; <sup>c</sup> Determined by DLS; <sup>d</sup> Determined by statistical analysis of 800-1200 particles from TEM images; <sup>e</sup> Experimental solids contents after magnetic separation; <sup>f</sup> Yield of cluster separation calculated using Equation 3 in Chapter 3;

The first experiment was carried out with the experimental conditions developed for TRG131 (*i.e.* PC<sub>th</sub> = 2.6%, 80% of DVB in the initial load and 20% in the feed, ADIBA at 60°C, Table 19), using the clusters stabilized by the macroRAFT agent containing the highest proportion of DMAEMA units (TRG139, Table 22). A stable latex was indeed obtained (TRG142, Table 23). However, the latex synthesized in the presence of the P(DMAEMA<sub>16</sub>-co-AA<sub>23</sub>)-b-PS<sub>11</sub>-TTC stabilized clusters was not stable (TRG146), with 45% of coagulum (based on total solids). The suspension pH was next decreased to 4.5 in order to protonate the amine groups of DMAEMA units and thus increase the stability, but the latex was still unstable (TRG153, Table 23). However at higher pH (9.5), the carboxylic acid group of the AA units was deprotonated,<sup>78</sup> resulting in a stable latex with a particle size of 313 nm (TRG159). It can be noted that ACPA initiator was used in this case. Similar conditions were also employed for

the encapsulation of the P(DMAEMA<sub>10-co-AA<sub>39</sub></sub>)-*b*-PS<sub>11</sub>-TTC stabilized clusters, and again, a stable latex was obtained (TRG160, Table 23).

**Table 23** – Experimental conditions and results for seeded semi-batch emulsion polymerization of styrene in the presence of DVB using P(DMAEMA-*co*-AA)-*b*-PS-TTC-stabilized IO clusters as seeds.

Ref.	Cluster	Initiator/T (°C)	pH <sub>0</sub> <sup>a</sup>	X (%) <sup>b</sup> /t (h) <sup>b</sup>	Z <sub>av</sub> (nm)/Poly <sup>c</sup>	ω <sub>free</sub> (%) <sup>d</sup>	IOC <sup>TGA</sup> (%) <sup>e</sup>	Y <sub>IO</sub> (%) <sup>f</sup>	Coag. (%) <sup>g</sup>
<i>PDMAEMA<sub>42-b-PS<sub>10</sub>-TTC</sub></i>									
<b>TRG131</b>	TRG119sep	ADIBA/60	5.3	53/7	353/0.23	6	54	85	0.21 (4.8)
<i>P(DMAEMA<sub>33-co-AA<sub>16</sub></sub>)-b-PS<sub>10</sub>-TTC</i>									
<b>TRG142</b>	TRG139sep	ADIBA/60	5.6	63/22	395/0.19	10	44	77	0.29 (6.8)
<i>P(DMAEMA<sub>16-co-AA<sub>23</sub></sub>)-b-PS<sub>11</sub>-TTC</i>									
<b>TRG146*</b>	TRG144sep	ADIBA/60	7.4	*	1351/0.80	-	-	-	1.02 (44.9)
<b>TRG153*</b>	TRG148sep	ADIBA/60	4.5	*	-	-	-	-	0.69 (15.4)
<b>TRG159</b>	TRG158sep	ACPA/80	9.5	31/6	313/0.26	6	54	89	0.15 (3.1)
<i>P(DMAEMA<sub>10-co-AA<sub>39</sub></sub>)-b-PS<sub>11</sub>-TTC</i>									
<b>TRG160</b>	TRG158sep	ACPA/80	9.5	30.7/6	176/0.08	0	59	75	0.01 (0.3)
<i>PAA<sub>50-b-PS<sub>10</sub>-TTC</sub></i>									
<b>TRG149</b>	TRG143sep	ACPA/80	9.5	47/21	650/0.43	3	59	100	0.16 (3.5)

\* *Unstable Latexes. 15 g of cluster dispersion; PC<sub>th</sub> ≈ 2.6 %; IO<sub>0</sub> (%) = 55; [Initiator] = 1.7 mM; 0.1 g of monomer introduced initially (30 wt% based on overall monomer mass), flow rate = 0.4 g h<sup>-1</sup>; Onset = 30 min; Endset = 80 min. S:DVB (all isomers including EVB) wt:wt ratio were 20:80 and 80:20 in the initial load and in the feed, respectively. <sup>a</sup>pH of reaction medium before polymerization; <sup>b</sup>Monomer conversion/reaction time; <sup>c</sup>Determined by DLS; <sup>d</sup>Determined using Equation 1 after 30 s of magnetic separation; <sup>e</sup>Iron oxide content in the magnetic fraction determined by TGA; <sup>f</sup>Yield of iron oxide incorporation in the magnetic fraction calculated using Equation 3; <sup>g</sup>Coagulum content based either on overall latex mass or on the total amount of solid (in brackets).*

The TEM micrographs of the amphoteric particles are shown in Figure 98. It can be seen that the composition of the hydrophilic block did not influence the hybrid particles morphology, with in all cases the formation of core-shell particles. So, magnetic carriers exhibiting a fully encapsulated morphology with controlled surface functionalization, were successfully obtained, *i.e.* the PAA-, the PDMAEMA- and the three P(DMAEMA-*co*-AA)-based systems.



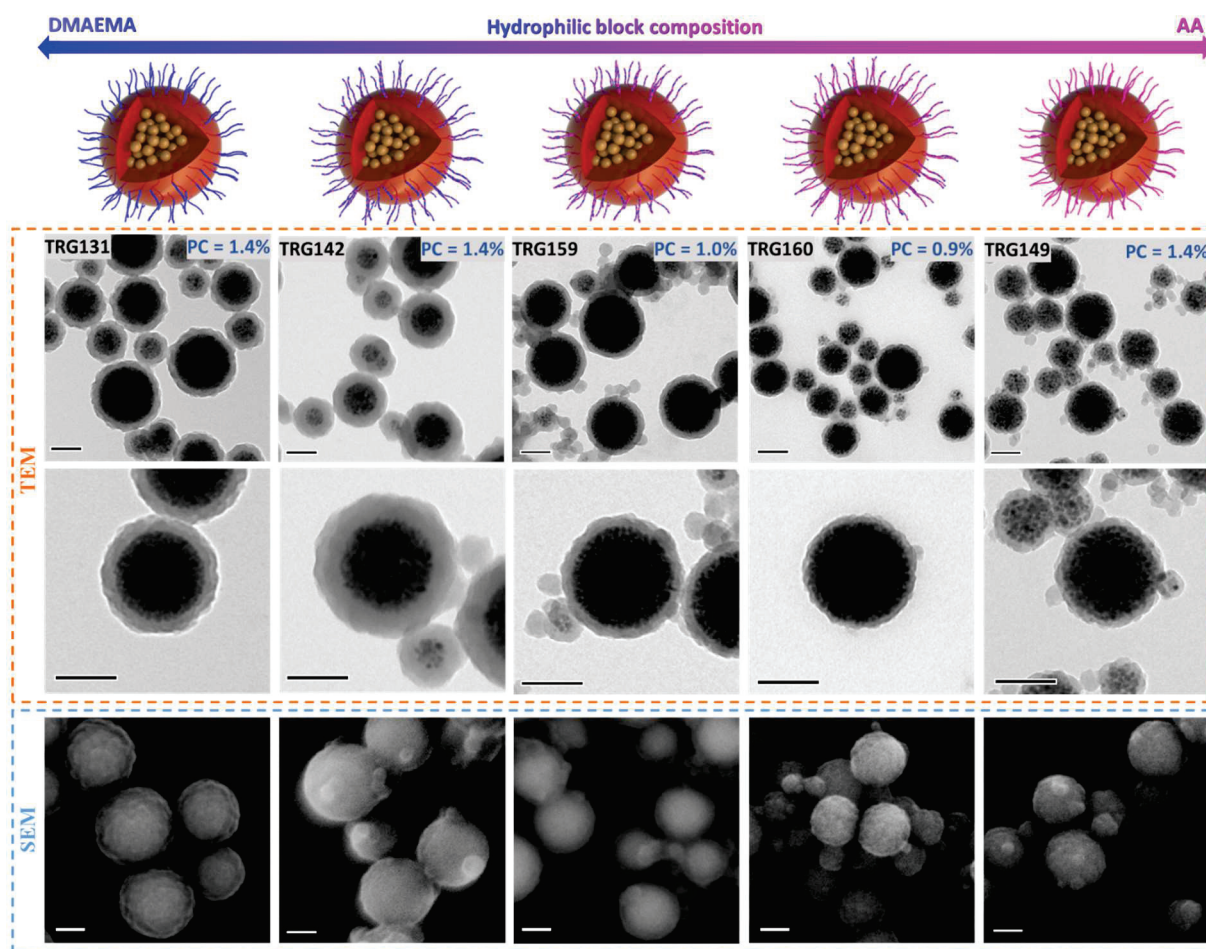


**Figure 98** – Schematic representation (*top*) and TEM or SEM images (*bottom*) of the composite latex particles synthesized in the presence of IO clusters stabilized by P(DMAEMA-*co*-AA)-TTC macroRAFT agents for various DMAEMA to AA ratios. .

### 3.4. Magnetic properties of the the composite IO/polymer latex particles

As mentioned in Chapter 1, magnetic separation is often used in life science for both analytical and sample preparation. To ensure a fast and efficient separation, the magnetic separation time and the magnetic bead loss have to be minimized. The rate of magnetic separation [ $v_x(x)$ ] is given by the equation:

$$v_x(x) = \frac{2r^2 \cdot M_s \cdot \nabla H}{9\eta} \quad (6)$$

where  $r$  is the radius of the composite particle,  $M_s$  the magnetization at saturation,  $\nabla H$  the magnetic gradient field, and  $\eta$  the viscosity of the medium. In order to obtain magnetic latex particles with a fast response to an external magnetic field, it is necessary to prepare relatively

large (> 100 nm) hybrid particles with high iron oxide contents. This also guarantees minimal bead loss.

The magnetic properties of the most interesting batches of the composite IO/polymer particles were investigated (Table 24). More specifically, only the impact of the time used for the magnetic separation was studied. Unfortunately, the saturation at magnetization have not been determined yet due to technical issues with the SQUID device.

**Table 24** – Characteristics of the magnetic latex particles used in the determination of magnetic separation time.

Ref.	macroRAFT	$D_n(nm)/D_w/D_n^a$	PC <sub>exp</sub> <sup>b</sup>	$\omega_{free}$ (%) <sup>c</sup>	IOC <sup>TGA</sup> (%) <sup>d</sup>	Y <sub>IO</sub> (%) <sup>e</sup>
<i>Polymer content</i>						
TRG119*	PDMAEMA <sub>42</sub> -b-PS <sub>10</sub> -TTC	71/1.58	-	-	82	-
TRG200	PDMAEMA <sub>42</sub> -b-PS <sub>10</sub> -TTC	81/1.82	1.7	12	47	91
TRG174	PDMAEMA <sub>42</sub> -b-PS <sub>10</sub> -TTC	81/1.82	4.6	30	32	87
<i>Particle morphology</i>						
TRG101	PDMAEMA <sub>42</sub> -b-PS <sub>10</sub> -TTC	82/1.61	3.4	11	44	89
TRG124	PDMAEMA <sub>42</sub> -b-PS <sub>10</sub> -TTC	71/1.58	1.6	6	46	95
TRG131	PDMAEMA <sub>42</sub> -b-PS <sub>10</sub> -TTC	71/1.58	1.4	6	54	85
<i>Surface functionalization</i>						
TRG131	PDMAEMA <sub>42</sub> -b-PS <sub>10</sub> -TTC	71/1.58	1.4	6	54	85
TRG142	P(DMAEMA <sub>33</sub> -co-AA <sub>16</sub> )-b-PS <sub>10</sub> -TTC	96/2.75	1.3	10	44	77
TRG159	P(DMAEMA <sub>16</sub> -co-AA <sub>23</sub> )-b-PS <sub>11</sub> -TTC	120/1.35	0.9	6	54	89
TRG160	P(DMAEMA <sub>10</sub> -co-AA <sub>39</sub> )-b-PS <sub>11</sub> -TTC	77/1.40	0.9	0	59	75
TRG149	PAA <sub>50</sub> -b-PS <sub>10</sub> -TTC	71/1.55	1.3	3	59	100

\* Cluster dispersion. <sup>a</sup> Cluster average diameter and dispersity determined before polymerization from statistical analysis of 800-1200 particles from TEM images; <sup>c</sup> Experimental polymer content determined by equation  $PC_{exp} = PC_{th} \cdot X$ ; <sup>d</sup> Determined using Equation 1 after 10 min of magnetic separation; <sup>e</sup> Iron oxide content in the magnetic fraction determined by TGA; <sup>e</sup> Yield of iron oxide incorporation in the magnetic fraction calculated based on Equation 3.

The fraction of magnetic particles ( $\omega_{mag}$ ) responding to an external magnetic field for both the clusters and the latex dispersions (TRG119, TRG174 and TRG200, Table 24) was determined for different magnetic separation times (Figure 99). These experiments were carried out in order to evaluate the time needed to separate the magnetic carriers from the medium. Figure



99 clearly indicates that the higher the fraction of IONP particles in the objects, the faster the separation. Indeed, the clusters, which contain the higher fraction of IONP, can be quantitatively separated in 10 s. As the initial amount of styrene increases, the fraction of hybrid particles that can be separated from the medium decreases. Actually, as discussed above, the formation of either unloaded polymer particles or hybrid particles with low iron oxide content is favored as the amount of styrene increases. This explains why the fraction of magnetic particles remains quite low for TRG174, even after 10 min. On the other hand, 90% of the particles were efficiently isolated by magnetic separation in only 30 s by decreasing the monomer content to 2.5% (TRG200).

Although the hybrid particles obtained from run TRG200 present a high magnetic response, hemispherical morphology was obtained from this polymerization. So, as explained in the previous sections, DVB was added to the polymerization recipes and the final morphology varied depending on the experimental conditions, resulting in core-shell hybrid particles (TRG101 and 131) or raspberry-like morphology (TRG124). As can be seen in Figure 100, the final morphology of the particles does not seem to affect the separation time, and high magnetic fraction was attained in all cases after 30 s of exposure. In addition the reaction carried out in the optimized experimental conditions for the PDMAEMA-*b*-PS system (*i.e.* thin shell and high IO content, TRG131) exhibit a very fast response to a magnetic field being separated in 10 s.

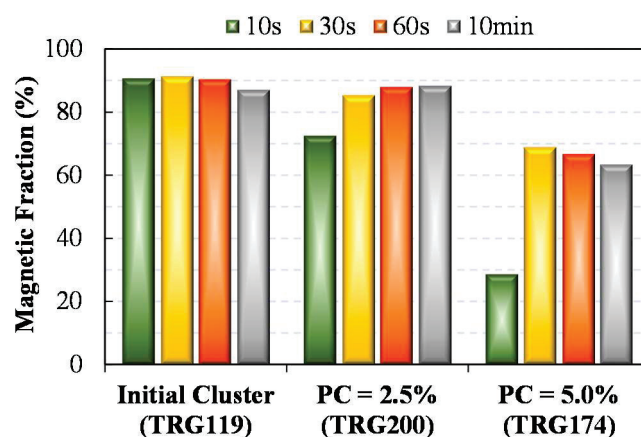


**Figure 99** – Magnetic fraction ( $\omega_{\text{mag}}$ ) obtained at different times of magnetic separation for PDMAEMA-stabilized clusters and IO/polymer composite particles prepared via semi-batch seeded emulsion polymerization using different initial amount of styrene in the presence of PDMAEMA-stabilized clusters as seeds.

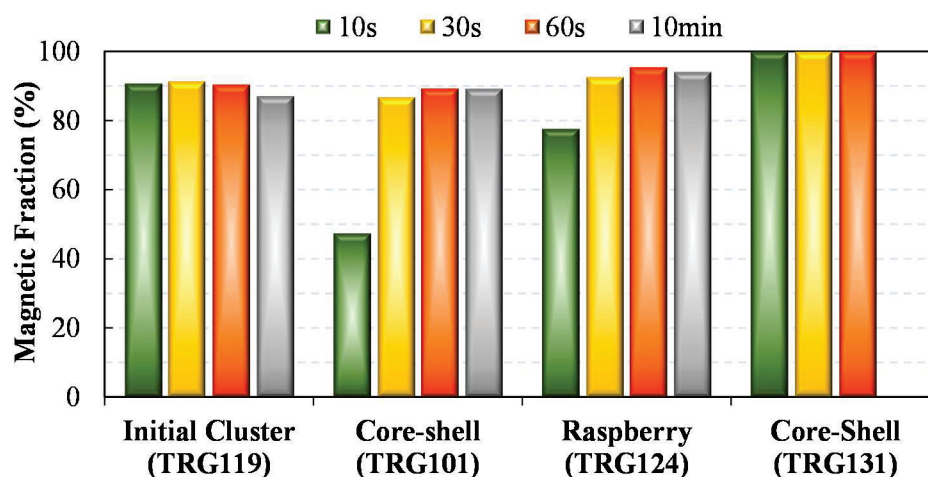


**Figure 100** – Magnetic fraction ( $\omega_{\text{mag}}$ ) obtained at different times of magnetic separation for PDMAEMA-stabilized clusters and IO/polymer composite particles presenting different morphologies prepared via semi-batch seeded emulsion polymerization of styrene in the presence of PDMAEMA-stabilized clusters as seeds.

Therefore, for the next series of experiments, the magnetic separation time was fixed at 30 s, which was considered to be a short separation time. Finally, Figure 101 shows the magnetic fractions of the particles prepared with different surface functionalization (Table 9). High magnetic fractions were obtained in all cases (often higher than 90%), making these iron oxide/polymer composite particles good candidates to be employed as carriers in magnetic separation protocols.

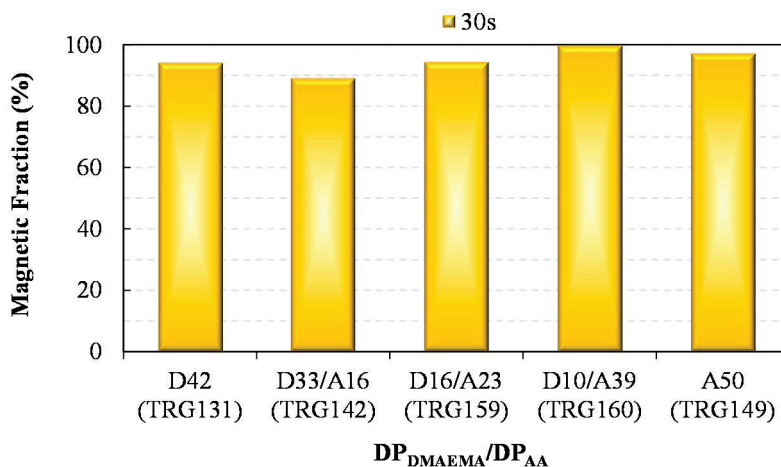


**Figure 101** - Magnetic fraction ( $\omega_{\text{mag}}$ ) obtained at different times of magnetic separation for IO/polymer composite particles prepared via semi-batch seeded emulsion polymerization of styrene/DVB, stabilized by hydrophilic segments with varied composition.

#### 4. CONCLUSIONS

The synthesis of magnetic latex particles decorated with well-defined polymer chains was presented in this chapter. The IO clusters with different surface functionalizations were prepared as described in Chapter 3, and used as seeds to form a polymer shell at their surface through seeded emulsion polymerization of styrene.

We first studied the influence of the polymerization process (batch *vs* semi-batch) on polymerization kinetics and particle morphology, working with PDMAEMA-stabilized clusters, 10 wt% of styrene and using ADIBA as initiator. The batch experiments led to the formation of free latex particles and a low fraction of magnetic particles. The elimination of the free macroRAFT present in water led to a meaningful increase of the amount of magnetic particles, also preventing the formation of unloaded particle via secondary nucleation. Lower polymerization rates were obtained in semi-batch due to a delayed particle nucleation. The investigation of the hybrid particle morphology showed in most cases some phase separation, due to an incompatibility between the polymer and the inorganic phase, even if the IONPs were homogeneously distributed in the polymeric matrix in some cases. Decreasing the initial amount of styrene (2 and 5 wt%) did not improve the situation, as the IONPs did not have the time to diffuse in the whole particle volume.

The addition of a crosslinking agent (DVB) in semi-batch conditions led to stable latexes. Moreover, for high DVB amounts (10 or 20 wt%), the targeted core-shell morphology was obtained, the iron oxide clusters being fully encapsulated in a polymeric shell. This positive result was likely linked to a restricted mobility of the IONPs in a highly crosslinked polymer matrix. The conversion was however limited to *ca.* 30% in these systems. The conversion was improved by using a concentration of DVB higher in the initial load than in the monomer feed. Furthermore, the shell thickness of the core-shell particles steadily increased with the polymer content demonstrating that it was possible to modulate the shell towards a desired morphology.

The optimized conditions of the PDMAEMA system were then extrapolated to the encapsulation of PAA-*b*-PS stabilized clusters. However, latex flocculation was initially observed, which was solved by changing the initiator nature and the initial pH (ACPA, pH 9.5). The optimized experimental conditions of either PAA-*b*-PS- or PDMAEMA-*b*-PS-based systems were then employed in the encapsulation of clusters stabilized with hydrophilic segments of different AA:DMAEMA composition. Fully encapsulated iron oxide clusters

were obtained for the five systems studied, *i.e.* the PAA-, the PDMAEMA- and the three P(DMAEMA-*co*-AA)-based systems.

The time required for an efficient magnetic separation of the obtained composite particles was finally studied and a very fast response to a magnetic field was observed for some samples: approximately 90% of the latex particles could be successfully separated in less than 30 s.

The five magnetic latex particles synthesized with controlled surface functionalization and presenting a strong response to a magnetic field will be tested as magnetic carriers for the capture and trigger release of bacteria aiming at increasing their concentration in a biological fluid for analytical purposes. These studies are detailed in Chapter 5.

## REFERENCES

1. Daniel, J.-C.; Pichot, C., *Les latex synthétiques: élaboration, propriétés, applications*. Lavoisier: 2006.
2. de Moraes, R. P. Pushing the Boundaries of Concentrated Dispersions: High Solids Content Bimodal Latex for Paper Coating Applications. Queen's University (Canada), 2012.
3. van Herk, A. M.; Landfester, K., *Hybrid latex particles: preparation with (mini) emulsion polymerization*. Springer: 2010; Vol. 233.
4. Bourgeat-Lami, E.; Lansalot, M., Organic/Inorganic Composite Latexes: The Marriage of Emulsion Polymerization and Inorganic Chemistry. In *Hybrid Latex Particles*, VanHerk, A. M.; Landfester, K., Eds. Springer-Verlag Berlin: Berlin, 2010; Vol. 233, pp 53-123.
5. Weiss, C. K.; Landfester, K., Miniemulsion polymerization as a means to encapsulate organic and inorganic materials. In *Hybrid Latex Particles*, Springer: 2010; pp 185-236.
6. Urban, D.; Schuler, B.; Schmidt-Thümmes, J., Large-Volume Applications of Latex Polymers. *Chemistry and Technology of Emulsion Polymerisation* **2005**, 226-256.
7. Rahman, M. M.; Elaissari, A., Organic–inorganic hybrid magnetic latex. In *Hybrid Latex Particles*, VanHerk, A. M.; Landfester, K., Eds. Springer-Verlag Berlin: Berlin, 2010; Vol. 233, pp 237-281.
8. Stuart, M. A. C.; Huck, W. T.; Genzer, J.; Müller, M.; Ober, C.; Stamm, M.; Sukhorukov, G. B.; Szleifer, I.; Tsukruk, V. V.; Urban, M., Emerging applications of stimuli-responsive polymer materials. *Nature Materials* **2010**, 9 (2), 101-113.
9. Zetterlund, P. B.; Thickett, S. C.; Perrier, S. b.; Bourgeat-Lami, E.; Lansalot, M., Controlled/living radical polymerization in dispersed systems: an update. *Chemical Reviews* **2015**, 115 (18), 9745-9800.
10. Chern, C., Emulsion polymerization mechanisms and kinetics. *Progress in Polymer Science* **2006**, 31 (5), 443-486.
11. Vanderhoff, J. W. In *Mechanism of emulsion polymerization*, Journal of Polymer Science: Polymer Symposia, Wiley Online Library: 1985; pp 161-198.
12. Harkins, W. D., A general theory of the mechanism of emulsion polymerization<sup>1</sup>. *Journal of the American Chemical Society* **1947**, 69 (6), 1428-1444.
13. Smith, W. V.; Ewart, R. H., Kinetics of emulsion polymerization. *The journal of chemical physics* **1948**, 16 (6), 592-599.
14. Roe, C. P., Surface chemistry aspects of emulsion polymerization. *Industrial & Engineering Chemistry* **1968**, 60 (9), 20-33.
15. Feeney, P. J.; Napper, D. H.; Gilbert, R. G., Coagulative nucleation and particle size distributions in emulsion polymerization. *Macromolecules* **1984**, 17 (12), 2520-2529.
16. Chern, C.-S., *Principles and applications of emulsion polymerization*. John Wiley & Sons: 2008.

17. Sundberg, D. C.; Durant, Y. G., Latex particle morphology, fundamental aspects: a review. *Polymer Reaction Engineering* **2003**, *11* (3), 379-432.
18. Ghosh Chaudhuri, R.; Paria, S., Core/shell nanoparticles: classes, properties, synthesis mechanisms, characterization, and applications. *Chemical Reviews* **2011**, *112* (4), 2373-2433.
19. Gawande, M. B.; Goswami, A.; Asefa, T.; Guo, H.; Biradar, A. V.; Peng, D.-L.; Zboril, R.; Varma, R. S., Core-shell nanoparticles: synthesis and applications in catalysis and electrocatalysis. *Chemical Society Reviews* **2015**, *44* (21), 7540-7590.
20. Xia, C.; Chen, W.; Wang, X.; Hedhili, M. N.; Wei, N.; Alshareef, H. N., Highly Stable Supercapacitors with Conducting Polymer Core-Shell Electrodes for Energy Storage Applications. *Advanced Energy Materials* **2015**, *5* (8).
21. Mandal, B.; Mittal, N. K.; Balabathula, P.; Thoma, L. A.; Wood, G. C., Development and in vitro evaluation of core-shell type lipid-polymer hybrid nanoparticles for the delivery of erlotinib in non-small cell lung cancer. *European Journal of Pharmaceutical Sciences* **2016**, *81*, 162-171.
22. Perro, A.; Duguet, E.; Lambert, O.; Taveau, J. C.; Bourgeat-Lami, E.; Ravaine, S., A chemical synthetic route towards “colloidal molecules”. *Angewandte Chemie International Edition* **2009**, *48* (2), 361-365.
23. Duguet, E.; Désert, A.; Perro, A.; Ravaine, S., Design and elaboration of colloidal molecules: an overview. *Chemical Society Reviews* **2011**, *40* (2), 941-960.
24. Qi, D.; Cao, Z.; Ziener, U., Recent advances in the preparation of hybrid nanoparticles in miniemulsions. *Advances in Colloid and Interface Science* **2014**, *211*, 47-62.
25. Bourgeat-Lami, E.; D’Agosto, F.; Lansalot, M., Synthesis of nanocapsules and polymer/inorganic nanoparticles through controlled radical polymerization at and near interfaces in heterogeneous media. In *Controlled Radical Polymerization at and from Solid Surfaces*, Springer: 2015; pp 123-161.
26. Asua, J. M., Challenges for industrialization of miniemulsion polymerization. *Progress in Polymer Science* **2014**, *39* (10), 1797-1826.
27. Zhang, S.-W.; Zhou, S.-X.; Weng, Y.-M.; Wu, L.-M., Synthesis of SiO<sub>2</sub>/polystyrene nanocomposite particles via miniemulsion polymerization. *Langmuir* **2005**, *21* (6), 2124-2128.
28. Tan, C. J.; Chua, H. G.; Ker, K. H.; Tong, Y. W., Preparation of bovine serum albumin surface-imprinted submicrometer particles with magnetic susceptibility through core-shell miniemulsion polymerization. *Analytical Chemistry* **2008**, *80* (3), 683-692.
29. Reyes, Y.; Peruzzo, P. J.; Fernández, M.; Paulis, M.; Leiza, J. R., Encapsulation of clay within polymer particles in a high-solids content aqueous dispersion. *Langmuir* **2013**, *29* (31), 9849-9856.
30. Van Berkel, K. Y.; Hawker, C. J., Tailored composite polymer-metal nanoparticles by miniemulsion polymerization and thiol-ene functionalization. *Journal of Polymer Science Part A: Polymer Chemistry* **2010**, *48* (7), 1594-1606.
31. Chen, T.; Cao, Z.; Guo, X.; Nie, J.; Xu, J.; Fan, Z.; Du, B., Preparation and characterization of thermosensitive organic-inorganic hybrid microgels with functional Fe<sub>3</sub>O<sub>4</sub> nanoparticles as crosslinker. *Polymer* **2011**, *52* (1), 172-179.



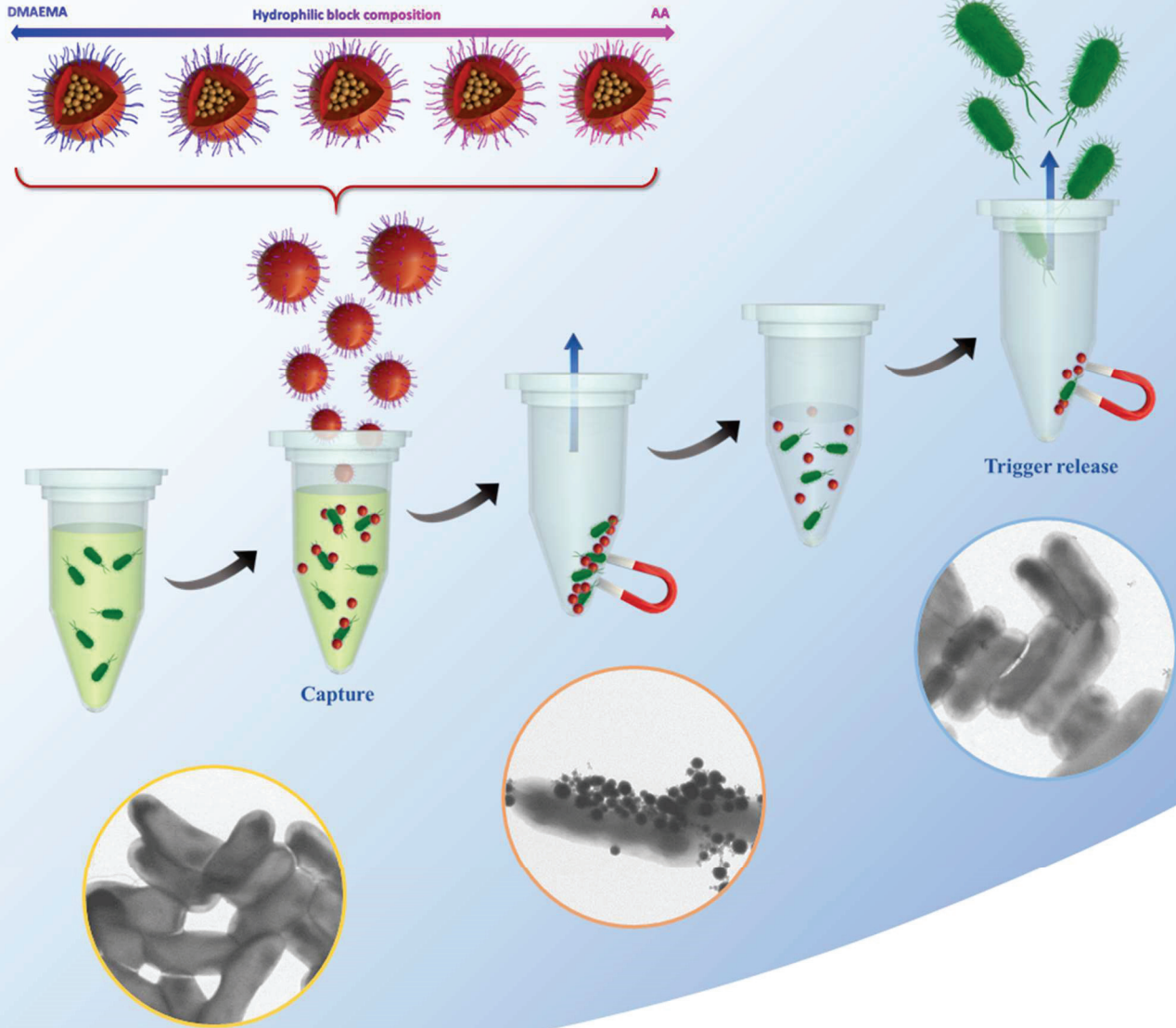
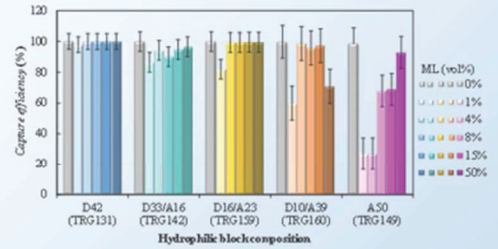
32. Li, Y.; Dong, M.; Kong, J.; Chai, Z.; Fu, G., Synthesis of Fe<sub>3</sub>O<sub>4</sub>@poly(methacrylic acid) core-shell submicrospheres via RAFT precipitation polymerization. *Journal of Colloid and Interface Science* **2013**, *394*, 199-207.
33. Macková, H.; Králová, D.; Horák, D., Magnetic poly (N-isopropylacrylamide) microspheres by dispersion and inverse emulsion polymerization. *Journal of Polymer Science Part A: Polymer Chemistry* **2007**, *45* (24), 5884-5898.
34. Niu, M.; Du, M.; Gao, Z.; Yang, C.; Lu, X.; Qiao, R.; Gao, M., Monodispersed magnetic polystyrene beads with excellent colloidal stability and strong magnetic response. *Macromolecular Rapid Communications* **2010**, *31* (20), 1805-1810.
35. Chen, Z.; Peng, K.; Mi, Y., Preparation and properties of magnetic polystyrene microspheres. *Journal of Applied Polymer Science* **2007**, *103* (6), 3660-3666.
36. Ozalp, V. C.; Bayramoglu, G.; Erdem, Z.; Arica, M. Y., Pathogen detection in complex samples by quartz crystal microbalance sensor coupled to aptamer functionalized core-shell type magnetic separation. *Analytica Chimica Acta* **2015**, *853*, 533-540.
37. Chen, K.; Zhu, Y.; Zhang, Y.; Li, L.; Lu, Y.; Guo, X., Synthesis of magnetic spherical polyelectrolyte brushes. *Macromolecules* **2011**, *44* (3), 632-639.
38. Joumaa, N.; Toussay, P.; Lansalot, M.; Elaissari, A., Surface modification of iron oxide nanoparticles by a phosphate-based macromonomer and further encapsulation into submicrometer polystyrene particles by miniemulsion polymerization. *Journal of Polymer Science Part A: Polymer Chemistry* **2008**, *46* (1), 327-340.
39. Kaewsaneha, C.; Tangboriboonrat, P.; Polpanich, D.; Eissa, M.; Elaissari, A., Anisotropic janus magnetic polymeric nanoparticles prepared via miniemulsion polymerization. *Journal of Polymer Science Part A: Polymer Chemistry* **2013**, *51* (22), 4779-4785.
40. Landfester, K.; Ramirez, L. P., Encapsulated magnetite particles for biomedical application. *Journal of Physics: Condensed Matter* **2003**, *15* (15), S1345.
41. Ramirez, L. P.; Landfester, K., Magnetic polystyrene nanoparticles with a high magnetite content obtained by miniemulsion processes. *Macromolecular Chemistry and Physics* **2003**, *204* (1), 22-31.
42. Ramos, J.; Forcada, J., Surfactant-free miniemulsion polymerization as a simple synthetic route to a successful encapsulation of magnetite nanoparticles. *Langmuir* **2011**, *27* (11), 7222-7230.
43. Teo, B. M.; Suh, S. K.; Hatton, T. A.; Ashokkumar, M.; Grieser, F., Sonochemical synthesis of magnetic Janus nanoparticles. *Langmuir* **2010**, *27* (1), 30-33.
44. Xu, Y.; Xu, H.; Gu, H., Controllable preparation of epoxy-functionalized magnetic polymer latexes with different morphologies by modified miniemulsion polymerization. *Journal of Polymer Science Part A: Polymer Chemistry* **2010**, *48* (11), 2284-2293.
45. Yoon, H.-J.; Lim, T. G.; Kim, J.-H.; Cho, Y. M.; Kim, Y. S.; Chung, U. S.; Kim, J. H.; Choi, B. W.; Koh, W.-G.; Jang, W.-D., Fabrication of multifunctional layer-by-layer nanocapsules toward the design of theragnostic nanoplatform. *Biomacromolecules* **2014**, *15* (4), 1382-1389.
46. Gong, T.; Yang, D.; Hu, J.; Yang, W.; Wang, C.; Lu, J. Q., Preparation of monodispersed hybrid nanospheres with high magnetite content from uniform Fe<sub>3</sub>O<sub>4</sub> clusters. *Colloids and Surfaces A: Physicochemical and Engineering Aspects* **2009**, *339* (1), 232-239.

47. Chakraborty, S.; Jähnichen, K.; Komber, H.; Basfar, A. A.; Voit, B., Synthesis of magnetic polystyrene nanoparticles using amphiphilic ionic liquid stabilized RAFT mediated miniemulsion polymerization. *Macromolecules* **2014**, *47* (13), 4186-4198.
48. Braconnot, S.; Eissa, M.; Elaissari, A., Morphology control of magnetic latex particles prepared from oil in water ferrofluid emulsion. *Colloid and Polymer Science* **2013**, *291* (1), 193-203.
49. Braconnot, S.; Hoang, C.; Fessi, H.; Elaissari, A., Elaboration of perfect core-shell submicronic magnetic latexes from oil in water ferrofluid droplets for bionanotechnology applications. *Materials Science and Engineering: C* **2009**, *29* (2), 624-630.
50. Feyen, M.; Weidenthaler, C.; Schüth, F.; Lu, A.-H., Synthesis of structurally stable colloidal composites as magnetically recyclable acid catalysts. *Chemistry of Materials* **2010**, *22* (9), 2955-2961.
51. Haladjova, E.; Rangelov, S.; Tsvetanov, C. B.; Posheva, V.; Peycheva, E.; Maximova, V.; Momekova, D.; Mountrichas, G.; Pispas, S.; Bakandritsos, A., Enhanced Gene Expression Promoted by Hybrid Magnetic/Cationic Block Copolymer Micelles. *Langmuir* **2014**, *30* (27), 8193-8200.
52. Li, K.; Dugas, P.-Y.; Lansalot, M.; Bourgeat-Lami, E., Surfactant-Free Emulsion Polymerization Stabilized by Ultrasmall Superparamagnetic Iron Oxide Particles Using Acrylic Acid or Methacrylic Acid as Auxiliary Comonomers. *Macromolecules* **2016**, *49* (20), 7609-7624.
53. Montagne, F.; Mondain-Monval, O.; Pichot, C.; Elaissari, A., Highly magnetic latexes from submicrometer oil in water ferrofluid emulsions. *Journal of Polymer Science Part A: Polymer Chemistry* **2006**, *44* (8), 2642-2656.
54. Paquet, C.; Page, L.; Kell, A.; Simard, B., Nanobeads highly loaded with superparamagnetic nanoparticles prepared by emulsification and seeded-emulsion polymerization. *Langmuir* **2010**, *26* (8), 5388-96.
55. Pibre, G.; Hakenholz, L.; Braconnot, S.; Mouaziz, H.; Elaissari, A., Elaboration of stimuli responsive core-shell magnetic latexes from oil in water ferrofluid emulsion. *e-Polymers* **2009**, *9* (1), 1652-1666.
56. Rahman, M. M.; Chehimi, M. M.; Fessi, H.; Elaissari, A., Highly temperature responsive core-shell magnetic particles: synthesis, characterization and colloidal properties. *Journal of Colloid and Interface Science* **2011**, *360* (2), 556-564.
57. Sacanna, S.; Philipse, A., Preparation and properties of monodisperse latex spheres with controlled magnetic moment for field-induced colloidal crystallization and (dipolar) chain formation. *Langmuir* **2006**, *22* (24), 10209-10216.
58. Xu, S.; Ma, W.-F.; You, L.-J.; Li, J.-M.; Guo, J.; Hu, J. J.; Wang, C.-C., Toward designer magnetite/polystyrene colloidal composite microspheres with controllable nanostructures and desirable surface functionalities. *Langmuir* **2012**, *28* (6), 3271-3278.
59. Zhang, F.; Yu, S.; Hou, G.; Xu, N.; Wu, Z.; Yue, L., Miniemulsion-based assembly of iron oxide nanoparticles and synthesis of magnetic polymer nanospheres. *Colloid and Polymer Science* **2015**, *293* (7), 1893-1902.
60. Montagne, F.; Mondain-Monval, O.; Pichot, C.; Mozzanega, H.; Elaissari, A., Preparation and characterization of narrow sized (o/w) magnetic emulsion. *Journal of Magnetism and Magnetic Materials* **2002**, *250*, 302-312.

61. Ge, J.; Hu, Y.; Yin, Y., Highly Tunable Superparamagnetic Colloidal Photonic Crystals. *Angewandte Chemie International Edition* **2007**, *46* (39), 7428-7431.
62. Chen, H.; Dong, M.; Li, Y.; Kong, J.; Chai, Z.; Fu, G., Facile synthesis of high-magnetization Fe<sub>3</sub>O<sub>4</sub>@polydivinylbenzene core-shell microspheres. *Reactive and Functional Polymers* **2013**, *73* (1), 18-22.
63. Nguyen, D.; Zondanos, H. S.; Farrugia, J. M.; Serelis, A. K.; Such, C. H.; Hawckett, B. S., Pigment encapsulation by emulsion polymerization using macro-RAFT copolymers. *Langmuir* **2008**, *24* (5), 2140-2150.
64. Ali, S. I.; Heuts, J. P.; Hawckett, B. S.; van Herk, A. M., Polymer encapsulated gibbsite nanoparticles: efficient preparation of anisotropic composite latex particles by RAFT-based starved feed emulsion polymerization. *Langmuir* **2009**, *25* (18), 10523-10533.
65. Zgheib, N.; Putaux, J.-L.; Thill, A.; Bourgeat-Lami, E.; D'Agosto, F.; Lansalot, M., Cerium oxide encapsulation by emulsion polymerization using hydrophilic macroRAFT agents. *Polymer Chemistry* **2013**, *4* (3), 607-614.
66. Bourgeat-Lami, E.; França, A.; Chaparro, T.; Silva, R. D.; Dugas, P.-Y.; Alves, G.; Santos, A., Synthesis of Polymer/Silica Hybrid Latexes by Surfactant-Free RAFT-Mediated Emulsion Polymerization. *Macromolecules* **2016**, *49* (12), 4431-4440.
67. Pereira, A. M. C. Synthesis of anisotropic polymer/inorganic composite particles via RAFT-mediated emulsion polymerization. Université Claude Bernard-Lyon I, 2014.
68. Cenacchi, A.; Pearson, S.; Kostadinova, D.; Leroux, F.; D'Agosto, F.; Lansalot, M.; Bourgeat-Lami, E.; Prevot, V., Nanocomposite latexes containing layered double hydroxides via RAFT-assisted encapsulating emulsion polymerization. *Polymer Chemistry* **2017**.
69. Li, K.; Dugas, P.-Y.; Bourgeat-Lami, E.; Lansalot, M., Polymer-encapsulated  $\gamma$ -Fe<sub>2</sub>O<sub>3</sub> nanoparticles prepared via RAFT-mediated emulsion polymerization. *Polymer* **2016**, *106*, 249-260.
70. Nguyen, D.; Pham, B. T.; Huynh, V.; Kim, B. J.; Pham, N. T.; Bickley, S. A.; Jones, S. K.; Serelis, A.; Davey, T.; Such, C., Monodispersed polymer encapsulated superparamagnetic iron oxide nanoparticles for cell labeling. *Polymer* **2016**, *106*, 238-248.
71. Asua, J. M., Mapping the morphology of polymer-inorganic nanocomposites synthesized by miniemulsion polymerization. *Macromolecular Chemistry and Physics* **2014**, *215* (5), 458-464.
72. Texter, J., *Reactions and synthesis in surfactant systems*. CRC Press: 2001.
73. Morton, M.; Kaizerman, S.; Altier, M. W., Swelling of latex particles. *Journal of Colloid Science* **1954**, *9* (4), 300-312.
74. Flory, P. J., *Principles of polymer chemistry*. Cornell University Press: 1953.
75. Errede, L., Polymer swelling 2: A restudy of poly (styrene-co-divinylbenzene) swelling in terms of the cross-link density. *Journal of Applied Polymer Science* **1986**, *31* (6), 1749-1761.
76. Minami, H.; Wang, Z.; Yamashita, T.; Okubo, M., Thermodynamic analysis of the morphology of monomer-adsorbed, cross-linked polymer particles prepared by the dynamic swelling method and seeded polymerization. *Colloid and Polymer Science* **2003**, *281* (3), 246-252.

77. Ge, J.; Hu, Y.; Zhang, T.; Yin, Y., Superparamagnetic Composite Colloids with Anisotropic Structures. *Journal of the American Chemical Society* **2007**, *129* (29), 8974-8975.

78. Bajomo, M.; Robb, I.; Steinke, J. H.; Bismarck, A., Fully Reversible pH-Triggered Network Formation of Amphoteric Polyelectrolyte Hydrogels. *Advanced Functional Materials* **2011**, *21* (1), 172-176.



# Chapter V

## USE OF MAGNETIC CARRIERS FOR BACTERIA CAPTURE AND TRIGGER RELEASE

**TABLE OF CONTENTS**

<b>1. INTRODUCTION.....</b>	<b>231</b>
<b>2. BIBLIOGRAPHIC REVIEW .....</b>	<b>231</b>
<b>2.1. Magnetic separation .....</b>	<b>231</b>
<b>2.2. Bacteria .....</b>	<b>234</b>
2.2.1. <i>Structure.....</i>	238
<b>3. EXPERIMENTAL SECTION .....</b>	<b>240</b>
<b>3.1. Materials .....</b>	<b>240</b>
<b>3.2. Methods .....</b>	<b>242</b>
3.2.1. <i>Preparation of bacteria samples.....</i>	242
3.2.2. <i>Magnetic separation.....</i>	242
<b>3.3. Characterizations .....</b>	<b>245</b>
3.3.1. <i>Optical microscopy .....</i>	245
3.3.2. <i>Electron microscopy.....</i>	246
<b>4. RESULTS AND DISCUSSION .....</b>	<b>246</b>
<b>4.1. High bacteria concentrations.....</b>	<b>247</b>
4.1.1. <i>Effect of PDMAEMA-based magnetic latex particles and E. coli concentrations .....</i>	247
4.1.2. <i>Effect of PAA-based magnetic latex particles and E. coli concentrations .....</i>	249
4.1.3. <i>Effect of MLP surface composition on E. coli separation.....</i>	250
4.1.4. <i>Effect of MLP surface composition on Bs separation .....</i>	252
<b>4.2. Low bacteria concentrations .....</b>	<b>254</b>
4.2.1. <i>Use of amphoteric magnetic latex particle to increase the microbial cell concentration..</i>	254
<b>4.3. Electron microscopy.....</b>	<b>255</b>
<b>5. CONCLUSIONS .....</b>	<b>258</b>



## **1. INTRODUCTION**

Sample preparation is a fundamental and essential step in almost all analytical procedures especially for biological and environmental samples. Usually, these steps are required due to the low concentration of the analytes or the presence of contaminants in the sample.<sup>1</sup> Conventional techniques such as extraction, electrophoresis, ultrafiltration, precipitation or solid-phase extraction, can present some limitations such as long time procedures with poor repeatability, non reversible adsorption of the analyte onto the stationary phase, no selective separation and inactivation of biological macromolecules. In addition, most of these techniques are not adapted to small volume samples. Nonetheless, magnetic separation can be employed as an alternative to these conventional techniques. For instance, magnetic separations can be successfully used in isolation/enrichment of DNA/RNA,<sup>2-5</sup> proteins,<sup>6, 7</sup> peptides,<sup>8, 9</sup> virus<sup>10, 11</sup> and bacteria.<sup>12-16</sup> Indeed, the characteristics of magnetic carriers such as their size, surface functionalization and ability to be magnetized are directly associated to successful separation of biotargets from a biological media. In this chapter the magnetic separation of different bio-compounds will be first reviewed. Then, the magnetic latex particles (MLPs) prepared during this project will be tested in the magnetic separation of different strains of bacteria. These tests were conducted in the *Laboratoire de Biologie et Architectures Microfluidiques* (LBAM) at *Commissariat à l'énergie atomique et aux énergies alternatives* (CEA) in Grenoble, France, with the collaboration of Dr. Dorothée Jary.

## **2. BIBLIOGRAPHIC REVIEW**

### **2.1. Magnetic separation**

As mentioned in the previous chapters, magnetic particles composed of Fe, Co and Ni, the well-known ferromagnetic metal elements in the periodic table, have been largely exploited for biomedical purposes. Among them, oxides based on iron metals, specially magnetite and maghemite, have received special attention due to their low toxicity, controllable magnetization, simple preparation and the superparamagnetic properties presented by small nanoparticles (< 20-15 nm).<sup>17-23</sup> In the field of sample preparation for biomedical diagnostics, magnetic nanoparticles can be used as carriers for magnetic separation. However, this protocol must be fast to be advantageous compared to conventional separation

methods. The time needed for the magnetic separation to be efficient mainly depends on the magnetic separation rate of the carriers, as extensively discussed in the previous chapters. Besides, the magnetic particles are usually encapsulated into a protective coating that avoids the undesirable and irreversible interactions between the analytes and the iron oxide nanoparticles.<sup>20</sup>

Depending on the mechanism of capture, magnetic separation methods can be classified into direct and indirect methods, as schematically represented in Figure 102. The direct method is used when the surface of the magnetic particle has a direct affinity (e.g. electrostatic interaction, phosphate complexation or hydrophobic interactions) with the biotargets. On the other hand, the indirect method is based on the use of an intermediary ligand to promote interaction between the biological target and the magnetic carrier. Oligonucleotides can be used for instance as ligand molecule for the separation and purification of nucleic acids through specific base pairing. Generally, the direct separation method has the advantages of being faster and easily controlled while the indirect method is more efficient, especially in the separation of biotargets that present poor affinity with the magnetic carrier.

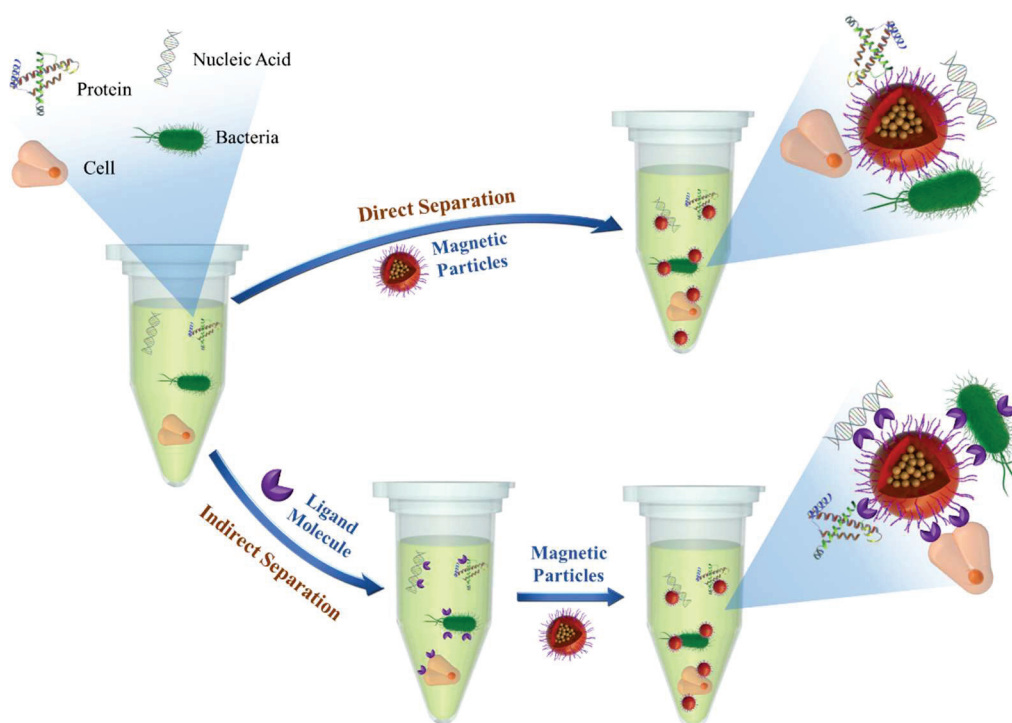


**Figure 102** – Scheme of biotarget capture step in either direct or indirect magnetic separation methods.

After the capture process of the analyte by the magnetic carriers, additional steps are involved in the magnetic separation process, as illustrated in Figure 103. A magnetic field is applied to isolate the magnetic beads/biological species complexes and, then the supernatant is collected. Depending on whether the magnetic carrier interacts or not with the biotarget, the magnetic separation can be classified into positive and negative sorting. Magnetic particles can be used to interact with non-desired species from the medium. In this case the biotarget will be found in the supernatant of the first separation, and the sorting process is known as negative. On the other hand, when the biotargets of interest are captured by the magnetic particles, the sorting is known as positive and the analyte is recovered after the elution process.<sup>24</sup> Indeed, the elution step occurs after re-dispersion of the magnetic particles/biotargets complex either in a different medium or by the variation of the temperature, shaking or ultrasonic waves. The variation of such conditions leads to the elution of the biotarget, which will be further analyzed.

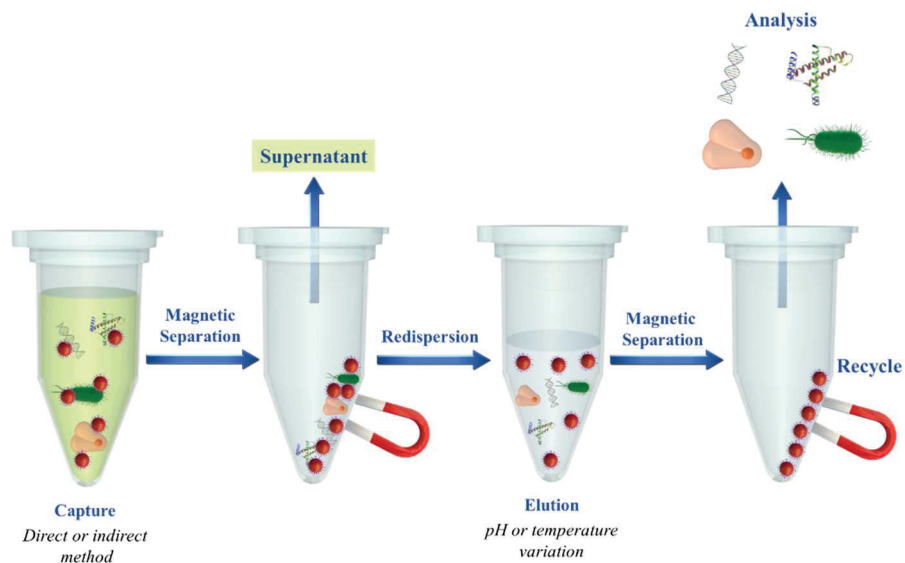


**Figure 103** - Scheme of magnetic separation using carriers able to capture and trigger release biotargets.

Magnetic separation processes can be also classified as specific or non-specific. Non-specific separations are based on the general capture of microorganisms via electrostatic interaction, phosphate complexation or hydrophobic interactions. Usually, the surface of the biotargets is negatively charged due to the presence of phosphate or hydroxyl groups, for instance. In order to have a good affinity with these biocompounds, the surface of the magnetic particles can carry metal cations, which allows the complexation with proteins,<sup>25</sup> or positive charges from (macro)molecules allowing electrostatic interactions.<sup>12, 24</sup> For

example, functionalized magnetic particles containing quaternized tertiary amino groups at the surface have been used for the separation of negatively charged *E. coli*.<sup>12</sup>

On the other hand, specific magnetic separation can be employed in systems based on “lock and key” interactions. Antibody/antigen, nucleic acid base-pairing and molecularly imprinted polymers (MIP) are some examples in which selective magnetic separation processes can be employed.<sup>1</sup> The MIP method consists in the adsorption of a target molecule at the surface of a particle followed by the formation of a surrounding polymer shell. Then, this molecule is desorbed or degraded from the particle surface resulting in an imprinted surface. The MIP particles can be next used in the selective separation and enrichment of analytes.<sup>26, 27</sup>

Table 25 summarizes some examples of magnetic separation of different biotargets and presents the main characteristics of the magnetic carriers.

## **2.2. Bacteria**

Since the pioneer work of Louis Pasteur, known as father of microbiology, in the 19<sup>th</sup> century,<sup>36</sup> bacteria have been discovered in many habitats such as soil, water, air, animal skin and gastrointestinal tract, and even in the most extreme habitats in the earth such as acidic hot springs, radioactive waste and Deep Ocean.<sup>37</sup> The relation between these microorganisms and more complex living organisms can be beneficial for both organisms. The class of *Ruminantia* (e.g. cattle, goats, sheep, deer, antelope), for example, depends on the digestion of cellulose fiber promoted by the bacteria present in their gastrointestinal tract to generate small sugars.<sup>38</sup> On the other hand, bacteria can also be the vector of infectious diseases, e.g. plague, tuberculosis, Hensen’s disease (leprosy) and cholera caused by bacteria *Yersinia pestis*,<sup>39</sup> *Mycobacterium tuberculosis*,<sup>40</sup> *Mycobacterium leprae*<sup>41</sup> or *Vibrio cholerae*,<sup>42</sup> respectively.

Bacteria display a wide diversity of morphologies, as illustrated in Figure 104. Generally, the bacteria shape can be classified in three main groups: coccus (spherical), bacillus (rods) and spiral (twisted). These individual units can also create rearrangements forming irregular aggregates, regular cubic/square form or linear chains generating different morphologies.



## Chapter V – Use of magnetic carriers for bacteria capture and trigger release

**Table 25** – Examples of magnetic separation of different biotargets.

Author	Magnetic Particle	Particle size	$M_s$ (emu g <sup>-1</sup> ) or IOC (%)	Surface Function	Biomolecule immobilized	Biotarget
<i>Bacteria and cells</i>						
Dong <i>et al.</i>	Fe <sub>3</sub> O <sub>4</sub> /qPDMAEMA	20-100 nm	39% <sup>IOC</sup>	Quaternary ammonium	Non specific	<i>E. coli</i>
El-Boubbou <i>et al.</i>	Fe <sub>3</sub> O <sub>4</sub> /SiO <sub>2</sub> @N <sub>3</sub> Fe <sub>3</sub> O <sub>4</sub> /SiO <sub>2</sub> @NH <sub>3</sub>	10 nm	≈ 90% <sup>a</sup>	Azide or primary amine	Carbohydrates	<i>E. coli</i> (two strains)
Liu <i>et al.</i> <sup>16</sup>	Fe <sub>3</sub> O <sub>4</sub> /Al <sub>2</sub> O <sub>3</sub>	-	-	Hydroxyls	Pigeon ovalbumin	Uropathogenic <i>E. coli</i>
Ozalp <i>et al.</i> <sup>28</sup>	Fe <sub>3</sub> O <sub>4</sub> /P(HPMA-co-EGDMA)-g-GMA	75-150 μm	7.1 emu g <sup>-1</sup>	Epoxy	Salmonella specific aptamer	Salmonella
Yang <i>et al.</i> <sup>13</sup>	SiMAG-DEAE FluidMAG-DEAE <sup>b</sup>	500 nm 100 nm	-	-	Non specific	<i>E. coli</i> BL21 Agrobacterium Tumefaciens C58Cl
<i>Virus</i>						
Veyret <i>et al.</i> <sup>10,29</sup>	Fe <sub>3</sub> O <sub>4</sub> /PEI-PMAMVE	150 nm	≈ 75% <sup>c</sup>	Primary amine	Non specific	Yellow fever virus
<i>Proteins</i>						
Gai <i>et al.</i> <sup>30</sup>	Fe <sub>3</sub> O <sub>4</sub> /SiO <sub>2</sub> /P(AAm-co-MBA)	120 nm	57 emu g <sup>-1</sup>	Bromine	MIP-P(AAm-co-MBAA)	Lysozyme
Li <i>et al.</i> <sup>31,32</sup>	Fe <sub>3</sub> O <sub>4</sub>	50 nm	45 emu g <sup>-1</sup>	Primary amine	Trypsin	Bovine serum albumin, myoglobin and cytochrome
Shao <i>et al.</i> <sup>7</sup>	Fe <sub>3</sub> O <sub>4</sub> /SiO <sub>2</sub> /LDH	300 nm	35 emu g <sup>-1</sup>	Ni <sup>2+</sup>	Non specific	Histidine protein
Zhou <i>et al.</i> <sup>26</sup>	Fe <sub>3</sub> O <sub>4</sub> /PDA	150 nm	73 emu g <sup>-1</sup>	Primary amine and hydroxyls	MIP-P(AAm-co-MBAA)	Hemoglobin



Table 25 (continued)

Peptides						
Chen <i>et al.</i> <sup>33,34</sup>	Fe <sub>3</sub> O <sub>4</sub> /SiO <sub>2</sub> /mSiO <sub>2</sub>	400 nm	53 emu g <sup>-1</sup>	Hydroxyls	-	Peptides
Liu <i>et al.</i> <sup>6</sup>	Fe <sub>3</sub> O <sub>4</sub> /SiO <sub>2</sub> /G	400 nm	21 emu g <sup>-1</sup>	Hydroxyls	-	Peptides
Ma <i>et al.</i> <sup>8</sup>	Fe <sub>3</sub> O <sub>4</sub> /mTiO <sub>2</sub>	280 nm	21 emu g <sup>-1</sup>	Hydroxyls	-	Peptides
Xiong <i>et al.</i> <sup>35</sup>	Fe <sub>3</sub> O <sub>4</sub> /SiO <sub>2</sub> /PEG-N <sub>3</sub>	240 nm	36 emu g <sup>-1</sup>	Azide	Maltose	Glycopeptides
Nucleic acids (DNA and RNA)						
Majewski <i>et al.</i> <sup>3</sup>	γ-Fe <sub>2</sub> O <sub>3</sub> /SiO <sub>2</sub> /PDMAEMA	100 nm	-	Tertiary amine	Non specific	Plasmid DNA
Rahman <i>et al.</i> <sup>2</sup>	IO/PDVB/P(NIPAM/AEMH/MBA)	250 nm	45%	Secondary amine	Non specific	Double stranded DNA
Drugs						
Li <i>et al.</i> <sup>27</sup>	Fe <sub>3</sub> O <sub>4</sub> /SiO <sub>2</sub> /P(TFMAA-co-EGDMA)	500 nm	42 emu g <sup>-1</sup>	Carboxylic acid and fluorine	MIP-P(TFMAA-co-EGDMA)	Tadalafil

<sup>a</sup>Iron oxide + silica content; <sup>b</sup>Commercial particles supplied by Chemicell with a amine functionalized surface. qPDMAEMA: quaternized PDMAEMA. HPMA: Hydroxypropyl methacrylate. EGDMA: ethyleneglycol dimethacrylate. GMA: glycidyl methacrylate. PEI: polyethyleneimine. PMAMVE: Poly(maleic anhydride-alt-methyl vinyl ether). PAAm = poly(N-Isopropylacrylamide). MBA: N,N-methylenebisacrylamide. LDH: Layered double hydroxide. PDA: polydopamine. G: Graphene. PDVB poly(divinyl benzene). PNIPAM: poly(N-isopropylacrylamide). AEMH: aminoethylmethacrylate. TFMAA: 2-(trifluoromethyl) acrylic acid.

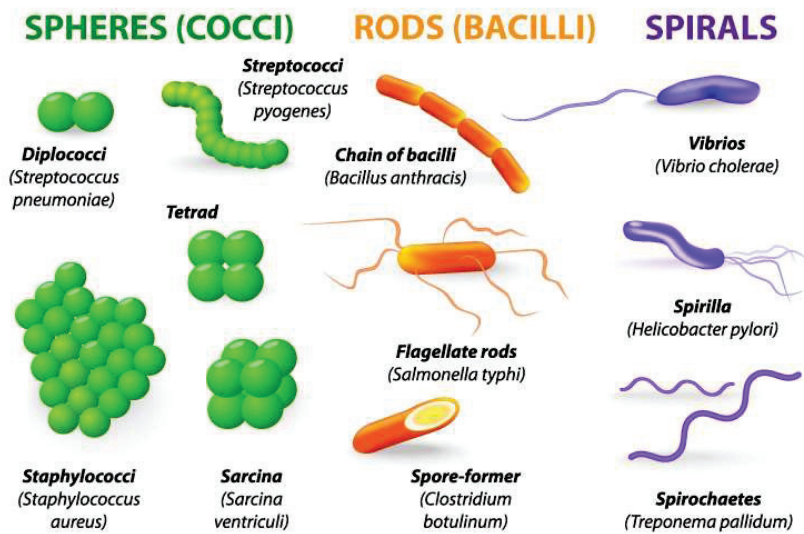


Figure 104 – Morphologies (shapes) and arrangements of bacterial cells. Adapted from <sup>43</sup>

### 2.2.1. Structure

Bacteria are prokaryotes, lacking well-defined nuclei and membrane-bound organelles, and with chromosomes composed of a single closed DNA circle. A scheme of bacteria structure is presented in Figure 105.

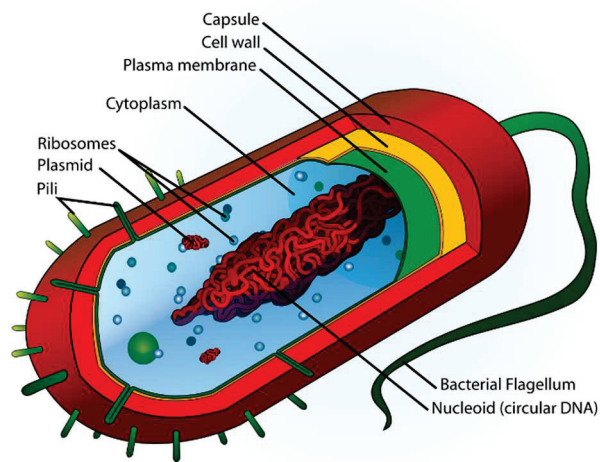


Figure 105 – Bacterial cell structure. Reproduced from <sup>44</sup>

The main cellular structures of bacteria are:

*Nucleoid*: is the region where the chromosomal DNA is located. The nucleoid is not isolated from the cytoplasm by a membrane (prokaryotic cell) and consists of an area

where the DNA strands are gathered. In addition some additional smaller circular auxiliary DNA strands (plasmids) can be also found in the cytoplasm.<sup>45</sup>

*Cytoplasm:* is composed of water, enzymes, nutrients, waste and gases containing also some cell structures as ribosomes, chromosomes and plasmids. The cytoplasm is the medium in which functions for cell growth, metabolism and replication are carried out.

*Ribosomes:* are responsible to translate the genetic code from nucleic acids to synthesize proteins, which is essential for all functions in a living organism.

*Plasma membrane:* is the more internal layer of the cell formed of phospholipids and proteins.

*Cell wall:* most of the bacteria is enclosed by a rigid cell wall composed of peptidoglycan, a peptide-sugar molecule.<sup>46</sup> It is responsible to protect the cell against the large differences in the osmotic pressure, which can burst the cell. Cell wall also helps to anchor appendages like the pili and flagella. Furthermore the thickness of this extracellular structure is one of most important parameter on bacteria classification, which can be divided in Gram positive (G+) and Gram negative (G-). In this classification, which was proposed by Gram,<sup>47</sup> a protocol based on a staining and washing technique is employed to differentiate the two forms. When exposed to a gram stain, G+ bacteria retain the purple color of the stain because the structure of their cell walls traps the dye. In G- bacteria, the cell wall is thin and releases the dye readily when washed with an alcohol or acetone solution.

*Capsule:* some species of bacteria have a third protective covering, a capsule made up of polysaccharides. The capsule is a major virulence factor in the major disease-causing bacteria. Nonetheless by removing their capsules the organisms become nonpathogenic, *i.e.* they don't cause disease.

It is worth mentioning that the surface properties of bacteria will be of prime importance for magnetic separation processes. Generally bacteria present negative charges at their surface, which can be associated to the presence of phosphate groups from biomolecules present in their outer membrane.<sup>32, 48</sup> Kubota *et al.*<sup>15</sup> measured the zeta potential of fourteen species of bacteria, including G+ and G- species, and obtained in all cases negative values of  $\zeta$  from -8 up to -30 mV. Based on this concept, the development of magnetic particles decorated with

cationic polymer have been reported in the literature as a successful strategy to capture bacteria based on electrostatic interactions.<sup>12, 15</sup>

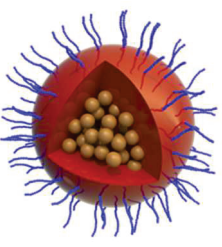
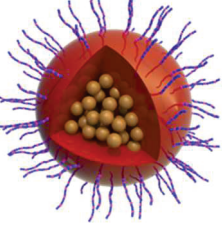
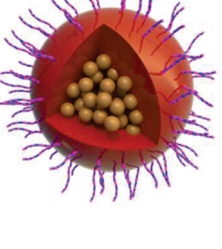
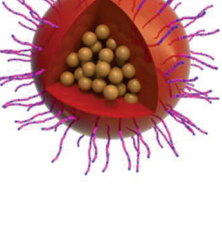
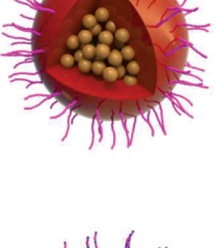
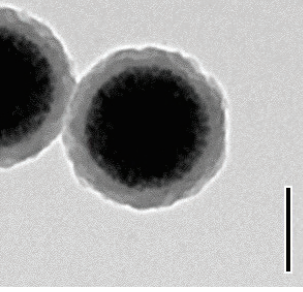
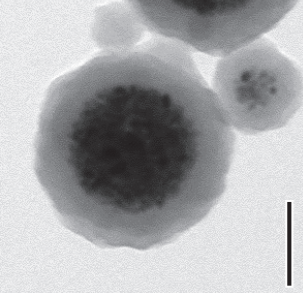
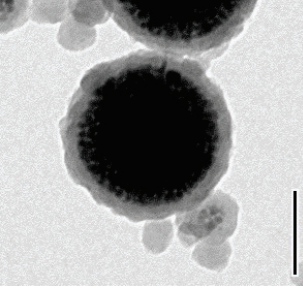
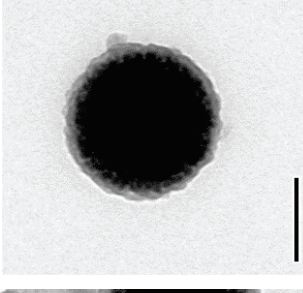
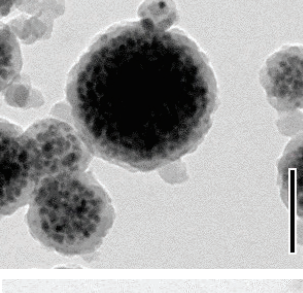
In this chapter, magnetic latex particles decorated with pH responsive polymers, namely PAA, PDMAEMA and copolymers of DMAEMA and AA, were employed for the capture and triggered release of bacteria, using different strains of bacteria as targets. It is expected that in acidic conditions, the amino groups from DMAEMA and/or the COOH function from AA will be protonated favoring the capture of bacteria via electrostatic interaction in the case of DMAEMA, and/or weak intermolecular interactions (H-bonding or hydrophobic interactions) in the case of AA. Then, during the elution step, a solution at basic pH will be used leading to deprotonation of AA and/or DMAEMA units, which should promote electrostatic repulsion between the bacteria and the magnetic particles, leading to cell release.

### **3. EXPERIMENTAL SECTION**

#### **3.1. Materials**

The magnetic carriers used in magnetic separation were prepared via seeded emulsion polymerization as previously described in Chapter 4. The magnetic latex particles were magnetically separated and redispersed in water adjusting the concentration to 10 g mL<sup>-1</sup> for all samples prior to use. Table 26 summarizes the characteristics of the MLPs. Trizma<sup>®</sup> saline solutions at pH 9 and pH 8 ( $\geq 99\%$ , Sigma-Aldrich) and acetic acid (AcOH, Sigma-Aldrich) were used as received. Glutaraldehyde, sodium cacodylate (p.a., Electron Microscopy Sciences) and phosphotungstic acid (PTA, p.a., Merk) were used without further purification.

**Table 26** – Summary of the main properties of the magnetic latex particles synthesized by seeded emulsion polymerization of styrene using DVB as crosslinker and amphiphilic macroRAFT agents as stabilizers.

Reference	TRG131	TRG142	TRG159	TRG160	TRG149
Scheme of MLPs					
Amphiphilic macroRAFT <sup>a</sup>	P(DMAEMA <sub>42</sub> - <i>b</i> -PS <sub>10</sub> )	P(DMAEMA <sub>33</sub> - <i>co</i> -AA <sub>16</sub> )- <i>b</i> -PS <sub>11</sub>	P(DMAEMA <sub>16</sub> - <i>co</i> -AA <sub>23</sub> )- <i>b</i> -PS <sub>11</sub>	P(DMAEMA <sub>10</sub> - <i>co</i> -AA <sub>39</sub> )- <i>b</i> -PS <sub>11</sub>	PAA <sub>40</sub> - <i>b</i> -PS <sub>13</sub>
TEM <sup>b</sup>					
<i>X</i> (%) <sup>c</sup>	53	63	31	30	47
<i>Z</i> <sub>av</sub> (nm)/Poly <sup>d</sup>	353 [0.23]	395 [0.19]	314 [0.26]	176 [0.09]	650 [0.43]
$\omega_{mag}$ (%) / IOC (%) <sup>e</sup>	94/54	90/44	94/54	100/59	97/59
Cluster Ref <sup>f</sup>	TRG119sep	TRG139sep	TRG158sep	TRG143sep	TRG140sep

<sup>a</sup>Chemical nature and composition of the macroRAFT agents used to stabilize the magnetic latex particles; <sup>b</sup>Scale bar: 100 nm; <sup>c</sup>Monomer conversion; <sup>d</sup>Determined by DLS; <sup>e</sup> $\omega_{mag}$ : Magnetic fraction of latex particles isolated after 30 s under a magnetic field and IOC: Iron oxide content of the magnetic fraction determined by TGA; <sup>f</sup>Reference of the IO clusters used as seeds in the emulsion polymerization reaction.



## **3.2. Methods**

### *3.2.1. Preparation of bacteria samples*

Six strains of bacteria, *Escherichia coli*: ATCC 11775 (*Ec*, G-), *Bacillus subtilis*: ATCC 11774 (*Bs* 134, G+), *Staphylococcus epidermidis*: ATCC 14990 (*Se* 09, G+) and ATCC 12228 (*Se* 26, G+), *Yersinia ruckeri*: ATCC 29473 (*Yr*, G-), *Pseudomonas putida*: ATCC 12633 (*Pp* 6, G-), *Bacillus thuringiensis*: ATCC 10792 (*Bt* 133, G+) were grown overnight in LB media at 37 °C. 2 mL of cultures were then centrifuged at 3500 rpm during 3 min and washed with 2 mL of water. A second centrifugation was carried out and the obtained precipitate was re-suspended in 50  $\mu$ L of water to form stock solutions ( $10^9$ - $10^{10}$  cells mL<sup>-1</sup>). An aliquot of 1  $\mu$ L was collected and diluted in 1 mL of water for the determination of bacteria concentration via optical microscopy.

### *3.2.2. Magnetic separation*

Five magnetic latex particles (the characteristics of the particles are summarized in Table 26) were employed in magnetic separation as schematically illustrated in Figure 106. Initially, different bacteria solutions (0.1 to 5.0 vol%) were prepared by diluting a stock solution ( $V_{\text{stock}}$ ) in acetic acid ( $V_{\text{AcOH}}$ , 0.01 vol%, pH 3.8) as indicated in Table 27 and the number of bacteria per mL ( $\bar{b}_0$ ) was determined via optical microscopy. Then, 1 mL (unless otherwise stated) of the freshly prepared suspensions of bacteria was transferred to a 1.5 mL Eppendorf vial, to which varying volumes of the magnetic latex ( $V_{\text{ML}}$ ) were added. After 5 min of incubation, the vials were placed in a spot of a magnetic rack (Dynamag–2 from ThermoFisher Scientific) and exposed during 2 min to permanent magnetic field. The supernatant was carefully removed by pipetting and the number of cells per mL was also determined via optical microscopy ( $\bar{b}_{\text{SNC}}$ ). The resulting particles were re-suspended in 250  $\mu$ L of Trizma solution (unless otherwise stated) at pH 8 or 9 (Table 27) and the vial was gently shaken at  $T_{\text{room}}$  or 40 °C (Table 26) during 5 min to allow cell elution. The vial was next placed in the magnetic rack and the supernatant was carefully collected to determine the concentration of cells released ( $\bar{b}_{\text{elu}}$ ). The efficiency of MLPs for the capture and elution of bacteria was then determined as follows:



$$\text{Capture efficiency} = \left( 1 - \frac{\bar{b}_{\text{SNC}}}{\bar{b}_0} \right) \cdot 100 \quad (1)$$

$$\text{Release efficiency} = \left( \frac{\bar{b}_{\text{elu}} \cdot V_{\text{el}}}{\bar{b}_0 \cdot V_{\bar{b}+\text{AcOH}}} \right) \cdot 100 \quad (2)$$

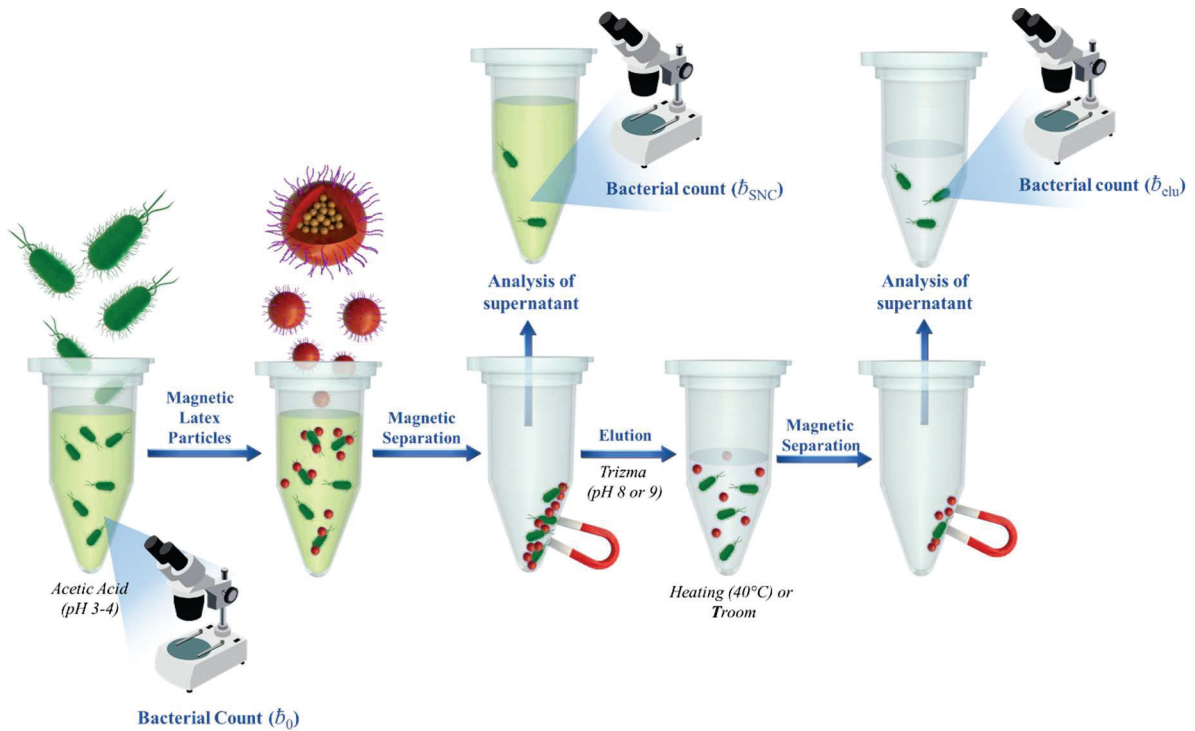


Figure 106 – Scheme of the protocol employed for magnetic separation of microbial cells.

The experimental conditions used during magnetic separation are summarized in Table 27.

**Table 27** – Experimental conditions of bacteria isolation by magnetic separation using magnetic latex particles stabilized with macroRAFT agents.

Ref.	Bacterial Strain	Capture			MLP <sup>a</sup>	V <sub>ML</sub> (μL)	Elution		
		V <sub>stock</sub> (μL)	Solution	V <sub>AcOH</sub> (μL)			Solution	V <sub>el</sub> (μL)	T
<i>Effect of cationic MLP (TRG131) and Ec concentrations</i>									
TRG175	<i>Ec</i>	0.5	0.01	500	TRG131	0-5-20- 40-90-250	Trizma (pH 9)	250	T <sub>room</sub>
TRG176		2	vol%	500					
TRG177		7	AcOH	500					
TRG178		25	(pH 4)	475					
<i>Effect of anionic MLP (TRG149) and Ec concentrations</i>									
TRG179	<i>Ec</i>	0.5	0.01	500	TRG149	0-5-20- 40-90-250	Trizma (pH 9)	250	T <sub>room</sub>
TRG180		2	vol%	500					
TRG181		7	AcOH	500					
TRG182		25	(pH 4)	475					
<i>Effect of amphoteric MLP concentration – Ec</i>									
TRG183	<i>Ec</i>	7	0.01	500	TRG159	0-5-20- 40-90-250	Trizma (pH 9)	250	T <sub>room</sub>
TRG184			vol%		TRG160				
TRG185			AcOH (pH 4)		TRG142				
<i>Effect of amphoteric MLP concentration – Bs</i>									
TRG186	<i>Bs</i>	7	0.01	500	TRG159	0-5-20- 40-90-250	Trizma (pH 9)	250	T <sub>room</sub>
TRG187			vol%		TRG160				
TRG188			AcOH (pH 4)		TRG142				
<i>Variation of bacterial strain</i>									
TRG198	<i>Ec</i>	2	0.01 vol% AcOH (pH 4)	1000	TRG159	40	10 mM Trizma (pH 9) + Twin 0.01%	50	T <sub>room</sub> - 40°C
	<i>Se 26</i>								
	<i>Se 08</i>								
	<i>Pp</i>								
	<i>Yr</i>								
<i>Bs</i>									
	<i>Bt</i>	10							
<i>Samples prepared for TEM observations</i>									
TRG169	<i>Ec 28</i>	0.5	0.01	500	TRG159	250	10 mM Trizma (pH 9)	250	T <sub>room</sub>
TRG170		25	vol%						
TRG170a			AcOH (pH 4)						

<sup>a</sup> The characteristics of the magnetic latex particles are given in Table 26.

### 3.3. Characterizations

#### 3.3.1. Optical microscopy

The number of cells per mL was determined via observations in an optical microscope Axioplan 2 imaging Zeiss. The bacterial suspensions were deposited in disposable slides (Fast Read 102<sup>®</sup>) containing 10 counting chambers (Figure 107A). Each chamber has a grid divided in 10 squares of 0.1  $\mu\text{L}$  which is subdivided in 16 sectors of  $6.25 \cdot 10^{-6}$  mL each (Figure 107B). After a 10- to 20-minute interval to bacteria deposition, observations were carried out at 20 000x of magnification using a Hg lamp operating in a dark field mode. An example of micrograph is shown in Figure 107C. It is worth mentioning that the concentration of bacterial suspensions was adjusted until the counting of the cells was possible. Image treatment for cells counting was made by using Image J free software.

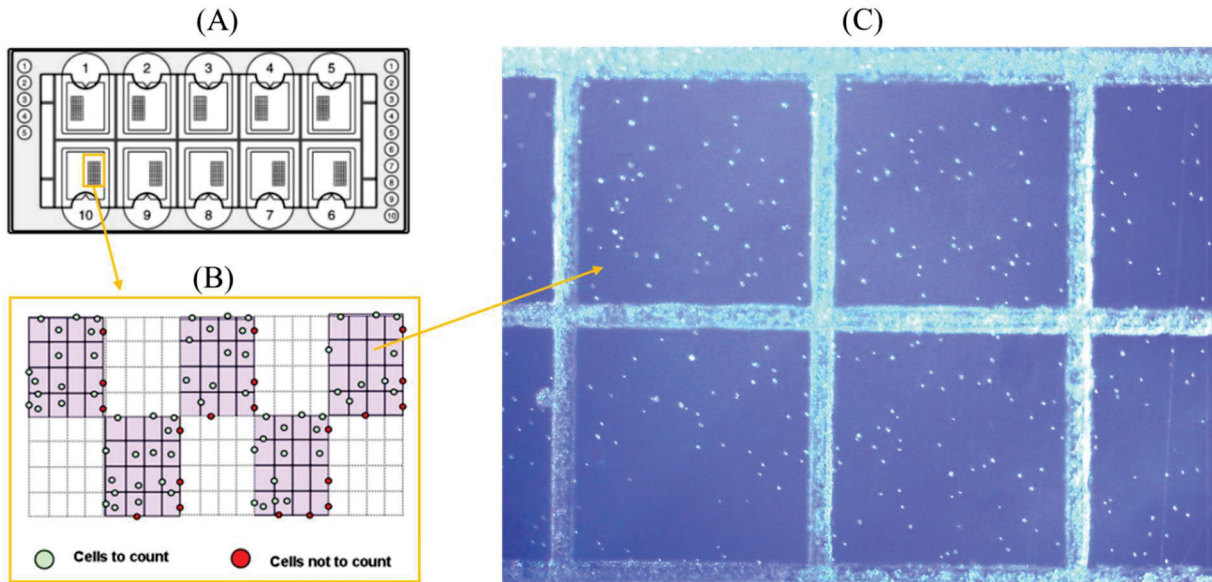


**Figure 107** – Disposable slides used for cell counting: (A) slide, (B) detail of counting chamber and (C) micrograph of a bacterial suspension, showing 4 sectors of counting ( $6.25 \cdot 10^{-6}$  mL each). (A,B) Adapted from Fast Read 102<sup>®</sup> datasheet (Biosigma<sup>®</sup>).

Individual cells were quantified by counting randomly at least 6 sectors for each run. With this information, the average number of cells per sector ( $\overline{n_b}$ ) and the sample standard deviation were calculated. The cell concentration ( $\hat{b}$ ) was then calculated as follows:

$$\hat{b} = \left( \frac{\overline{n_b}}{6.25 \cdot 10^{-6}} \right) \cdot f_{obs} \quad (3)$$

where  $f_{obs}$  is the dilution factor used to adjust the cell concentration for proper microscope observation, calculated as follows:

$$f_{\text{obs}} = \frac{V_0}{V_{\text{obs}}} \quad (4)$$

where  $V_0$  is the volume of the initial cell suspension and  $V_{\text{obs}}$  is the volume of solution used during the dilution for proper observation.

### 3.3.2. *Electron microscopy*

TEM observations were carried out for each step of the magnetic separation process. To do so, the magnetic separation of *E. coli* was carried out using the amphoteric MLPs (TRG159, Table 26) and the experimental conditions are presented in Table 27 (entry TRG169-TRG170a). Samples were withdrawn in each step of magnetic separation. Then, a previously reported protocol of bacterial fixation,<sup>49</sup> using glutaraldehyde 2.5 vol% and sodium cacodylate 0.2 M, was applied for each sample. Moreover, TEM grids were also prepared from non-fixed suspensions, to evaluate the effect of fixation on micrographs quality. The grid was prepared by dropping 5  $\mu\text{L}$  of each suspension, fixed and non-fixed ones, in a 200 mesh copper-grid. After 2 min (unless otherwise stated) of deposition, the samples were negatively stained during 10 s (unless otherwise stated) with 1% phosphotungstic acid solution (PTA). Excess solution was removed using filter paper. After drying, the stained samples were observed under a Philips CM120 microscope operating at an accelerating voltage of 120 kV (Centre Technologique des Microstructures (CT $\mu$ ), Claude Bernard University, Villeurbanne, France).

## 4. RESULTS AND DISCUSSION

Magnetic latex particles were employed as magnetic carriers for the separation of different bacterial strains. Initially the effect of MLP concentration on the capture and elution process was evaluated using *E. coli* (G-) as microbial model. The magnetic latex particles used in these preliminary studies were decorated with pH-responsive homopolymers, either PDMAEMA or PAA. Then, MLPs decorated with amphoteric copolymers composed of DMAEMA/AA at different molar ratios were used for the magnetic separation of two bacterial species: *E. coli* and *Bs*. Furthermore, the amphoteric MLPs stabilized by P(DMAEMA<sub>16-co-AA</sub><sub>23</sub>)-*b*-PS<sub>11</sub> were employed in a protocol to increase sample concentration of six bacterial strains. Finally, TEM observations of each step of the magnetic separation were carried out.

#### 4.1. High bacteria concentrations

##### 4.1.1. Effect of PDMAEMA-based magnetic latex particles and *E. coli* concentrations

PDMAEMA-decorated magnetic latex particles were used as carrier at different concentrations (from 1 up to 50 vol%) in the magnetic separation of *E. coli* suspensions. The cell concentration in the bacterial suspension was also varied from 0.1 up to 5 vol% resulting in a range of  $1 \cdot 10^7$  up to  $6 \cdot 10^8$  cells  $\text{mL}^{-1}$ . Hence, the effect of both parameters could be evaluated in the capture process as can be seen in Figure 108.

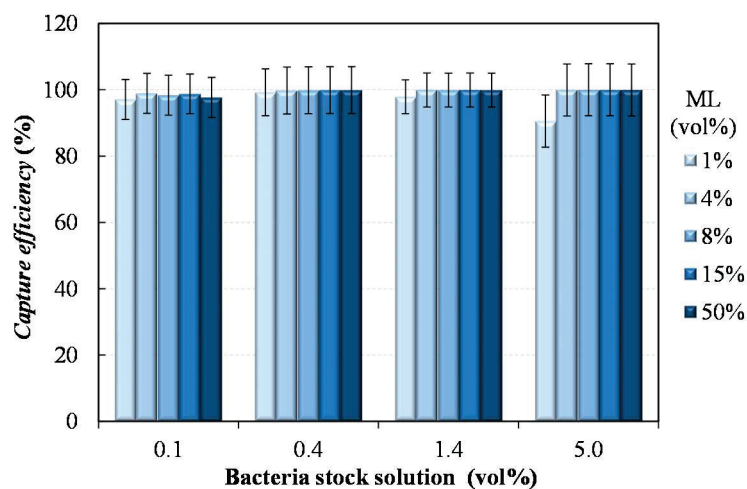


**Figure 108** – Effect of bacteria stock solution and magnetic latex particles (ML) concentrations on cell capture efficiency via magnetic separation. PDMAEMA-stabilized MLPs (TRG131, Table 26) were used as carrier and *E. coli* was employed as microbial model (entries TRG175-178 in Table 27).

As evidenced in Figure 108, capture efficiencies higher than 90% were obtained for all conditions tested, usually higher than 99%. Even for the highest concentration of bacteria, only 1 vol% of ML was enough to capture 90% of the initial cell amount in the medium, which represents  $6 \cdot 10^9$  cells captured per mg of magnetic latex particle. Yang *et al.*<sup>13</sup> studied the magnetic separation of *E. coli* using commercial magnetic particles SiMag DEAE, surface functionalized with a quaternized amine. The authors determined the adsorption isotherm and showed that the results fitted well with the Langmuir model, with a maximum cell adsorption of around  $7 \cdot 10^9$  cells  $\text{mg}^{-1}$ . The obtained values are in good agreement with this previous literature data, which indicates that our particles have adsorption properties equivalent to commercial magnetic particles.

On the other hand, as shown in Figure 109, low release efficiencies (often lower than 20%) were obtained using MLPs decorated with PDMAEMA brushes. This can be explained by the

composition of the polymer at the particle surface. In acidic conditions employed during the capture step, the DMAEMA units are protonated, which leads to a high capture efficiency due to strong electrostatic interactions between the bacteria and the magnetic particles. However, when the complex is re-suspended in the Trizma solution at pH 9, bacteria desorption did not take place and the cells stayed attached to the magnetic carrier. This could be associated to hydrophobic interactions generated under basic conditions between the uncharged PDMAEMA chains and the cell wall of the bacteria, formed by peptidoglycan and polysaccharides. It can also be observed in Figure 109 that at high cell concentration (5 vol%), higher release efficiency was obtained. This can be associated to an excessive cell concentration during the capture step. A fraction of bacteria captured was probably only physically entrapped into the aggregates formed, and not complexed via electrostatic interactions. Therefore, during the elution process, these non-interacted cells could be easily re-suspended.

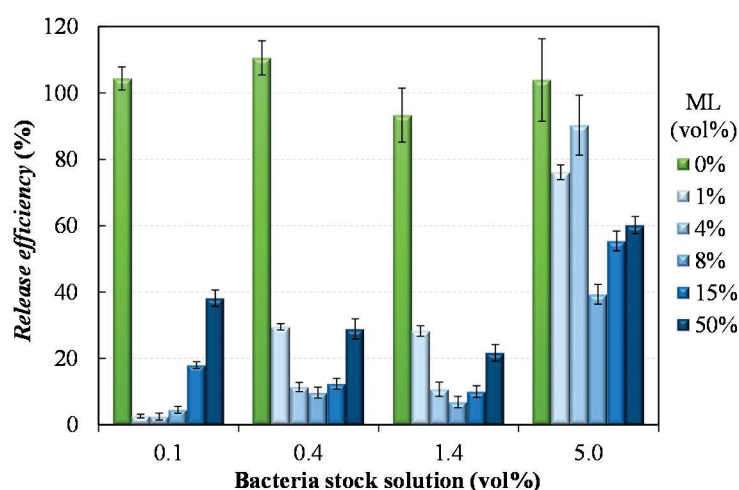


**Figure 109** – Effect of bacteria stock solution and magnetic latex (ML) concentrations on cell release efficiency via magnetic separation. PDMAEMA-stabilized MLPs (TRG131, Table 26) were used as carrier and *E. coli* was employed as microbial model (entries TRG175-178 in Table 27).

It is important to point out that, in the protocol employed, the elution step was carried out for only 5 min. It is possible that if a longer elution time had been applied, the system could have reached a desorption equilibrium, resulting in a higher release efficiency. Nonetheless, our strategy is based on the development of a fast method to increase the cell concentration in a biological medium and, for this reason, magnetic carriers that are able to trigger a fast release of the bacteria are needed. Hence, the elution time of 5 min was kept for the next series of experiments.



4.1.2. Effect of PAA-based magnetic latex particles and *E. coli* concentrations

Magnetic latex particles decorated with PAA chains were also employed as carrier for the magnetic separation of *E. coli* microbial cells. Initially, cells and MLP concentrations were varied in the same range as before for PDMAEMA-based MLPs. As can be seen in Figure 110, for all conditions tested, the capture efficiencies of PAA-based MLPs were lower than those obtained for the PDMAEMA-stabilized latexes (Figure 109). Indeed, one can consider that in the case of PDMAEMA, the magnetic particles can display strong electrostatic interactions with the bacteria cells. PAA-based MLPs are expected on the contrary to only weakly interact with the cell surface via hydrophobic interactions between the uncharged COOH (pH 4) and the surface of the bacteria, or/and by H-bonding between the COOH groups from the AA units and the hydroxyl or amine groups from the peptidoglycans biomolecules present in the cell's outer membrane. It is important to point out that a fraction of cells can also be physically entrapped into bacteria/MLPs aggregates. Indeed, the acidic conditions employed in the capture step are unfavorable to the colloidal stability of the PAA-stabilized particles. This can lead to the formation of big aggregates, which can increase the fraction of bacteria captured by physical entrapment. In summary, all interactions proposed, H-bonding, hydrophobic interaction or physical entrapment, can be considered as weak forces between the particles and the targets, resulting in a low capture efficiency.

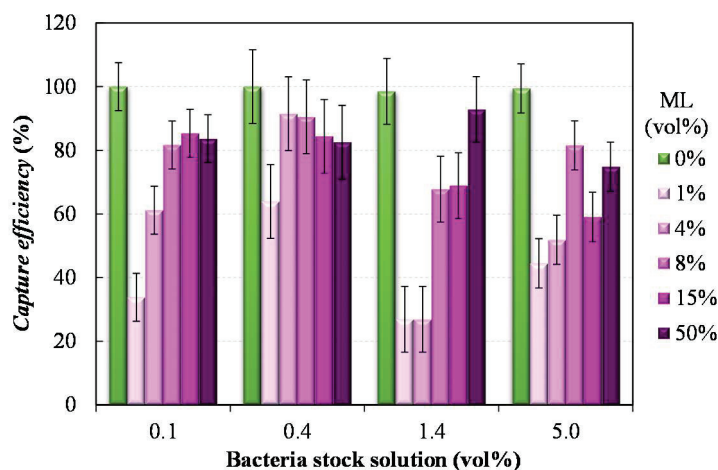


**Figure 110** – Effect of bacteria stock solution and magnetic latex (ML) concentrations on cell capture efficiency via magnetic separation. PAA-stabilized MLPs (TRG149, Table 26) were used as carrier and *E. coli* was employed as microbial model (entries TRG179-182 in Table 27).

The evolution of the release efficiency of the magnetic particles as a function of bacteria and particle concentrations is plotted in Figure 10. As expected, higher bacterial release efficiencies were obtained for the PAA-based particles (up to 75%, Figure 111), as compared

to PDMAEMA under the same conditions (Figure 109). This can be attributed to two factors: (1) weak interactions between the magnetic carrier and the bacteria, which can favor bacteria desorption during the elution step, and (2) repulsive electrostatic forces between the negatively charged surface of the bacteria and the deprotonated carboxylic groups of AA considering that the elution step was carried out at pH 9.

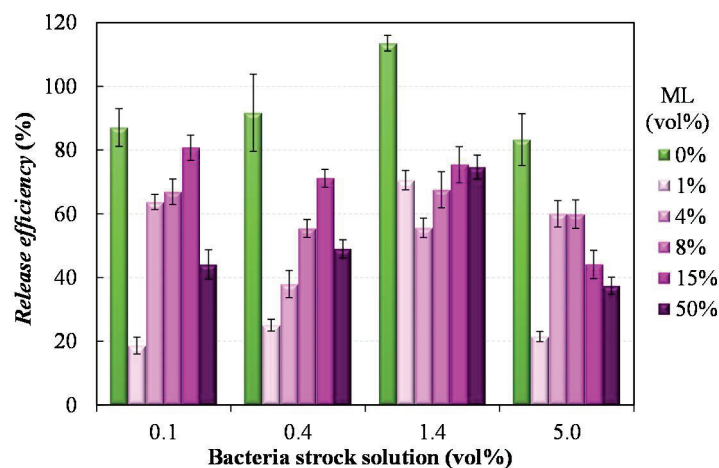


**Figure 111** – Effect of bacteria stock solution and magnetic latex (ML) concentrations on cell release efficiency via magnetic separation. PAA-stabilized MLPs (TRG149, Table 26) were used as carrier and *E. coli* was employed as microbial model (entries TRG179-182 in Table 27).

#### 4.1.3. Effect of MLP surface composition on *E. coli* separation

As demonstrated above, magnetic carriers decorated with PDMAEMA chains exhibit a high capture efficiency but a poor triggered cell release. On the other hand, the capture efficiency with PAA-stabilized MLPs is relatively low, and the release efficiency during the elution step is limited by the low cell capture efficiency.

To take advantage of the benefits of both systems, magnetic latex particles stabilized by AA/DMAEMA copolymers of different compositions were thus used as carriers for the magnetic separation of *E. coli*. The experimental conditions applied for these magnetic separations are presented in Table 27 (entries TRG183-185) and the efficiency of the capture step is shown in Figure 112.

Figure 112 clearly shows that the composition of the stabilizing hydrophilic block, which is decorating the MLP surface, plays an important role in the capture efficiency of *E. coli* microbial cells. The higher the DMAEMA content in the copolymer chains, the higher was the capture efficiency. This is an expected result due to the strong electrostatic interaction between the negatively charged bacteria and the positively charged MLPs in acidic conditions, mentioned above. Furthermore, an important result was obtained for the

P(DMAEMA<sub>16-co-AA</sub><sub>23</sub>)-*b*-PS<sub>11</sub> system, in which high values of capture efficiency were attained, often higher than 98%, even if this copolymer contains more AA (59 mol%) than DMAEMA units (41 mol%).

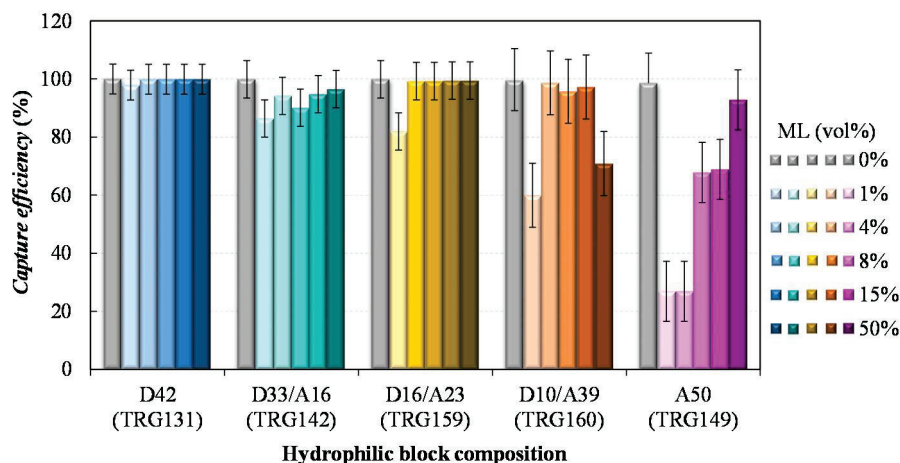


**Figure 112** – Effect of magnetic latex (ML) concentration and surface composition on cell capture efficiency via magnetic separation. The MLPs used as carriers (entries TRG131, TRG142, TRG159, TRG160 and TRG149, Table 26) were decorated with hydrophilic moiety of amphiphilic macroRAFT agents with different DMAEMA/AA compositions (D<sub>xx</sub>/A<sub>yy</sub>, where *xx* and *yy* represent the number of DMAEMA and AA units, respectively). *E. coli* was employed as microbial model (entries TRG183-185 in Table 27).

The opposite trend was observed for the elution step (Figure 113): the higher the amount of DMAMEA in the copolymer, the lower was the release efficiency. Besides, the amphoteric macroRAFT copolymers containing only 16 AA units (TRG142) did not generate enough repulsion to allow efficient desorption of the magnetic particles from the surface of *E. coli*, resulting in a low release efficiency. The release efficiency increased significantly when the number of AA units was increased further (TRG159 with 23 AA units) indicating that a minimum amount of COOH groups at the surface of the carrier is necessary to generate enough repulsive forces leading to a successful elution of the microbial cells. One should however keep in mind that the amount of DMAEMA units also decreases in this copolymer, reducing the extent of hydrophobic interactions, which, as mentioned above, can negatively impact the elution process.

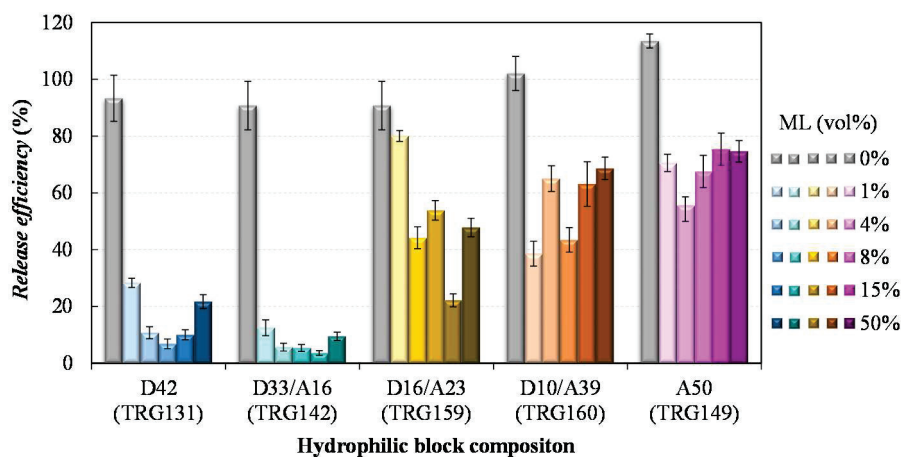


**Figure 113** – Effect of magnetic latex (ML) concentration and surface composition on cell release efficiency via magnetic separation. The MLPs used as carriers (Table 26) were decorated with hydrophilic moiety of amphiphilic macroRAFT agents with different DMAEMA/AA compositions (Dxx/Ayy, where xx and yy represent the number of DMAEMA and AA units, respectively). *E. coli* was employed as microbial model (entries TRG183-185 in Table 27).

#### 4.1.4. Effect of MLP surface composition on *Bs* separation

The amphoteric magnetic latex particles decorated with the AA/DMAEMA copolymers were also employed for the magnetic separation of a gram-positive bacteria, *Bacillus subtilis*. The results obtained during the capture step are shown in Figure 114. The capture efficiencies were in all cases lower than those obtained during the magnetic separation of *E. coli* (Figure 112), indicating a lower affinity between the MLPs and *Bs*. This may be related to the different zeta potential values of these two cells,  $\zeta = -20$  mV and  $-10$  mV for *E. coli* and *Bs*,<sup>15</sup> respectively, resulting in a weaker electrostatic interaction between the positively charged MLPs particles and the negatively charged *Bs* surface in acidic conditions.

The release efficiencies of the magnetic latex particles in the elution step using *Bs* cells (Figure 115A) were also lower than those observed for *E. coli* elution (Figure 113). This can be also associated to the lower zeta potential value of *Bs* compared to *E. coli* generating a lower repulsive electrostatic force between the cells and the negatively charged particles during the elution step.

Although no phase transition was evidenced in Chapter 2 for the amphoteric macroRAFT agents, these copolymers are composed of thermoresponsive DMAEMA units, and their conformation in water can thus be influenced by the temperature. Hence, the effect of temperature on the release efficiency was also evaluated during the elution step of *Bs* cells (Figure 115B). For the magnetic particles decorated with the copolymer containing the lowest DMAEMA content (TRG160), no effect of temperature was observed (see Figure 115A and 252

B). On the other hand, by increasing the content of DMAEMA in the copolymer chains an increase of release efficiency at 40°C was observed compared to release at room temperature (TRG159 and TRG142 in Figure 115A and B) suggesting that the chains have adopted a less extended conformation in water promoting cell release.

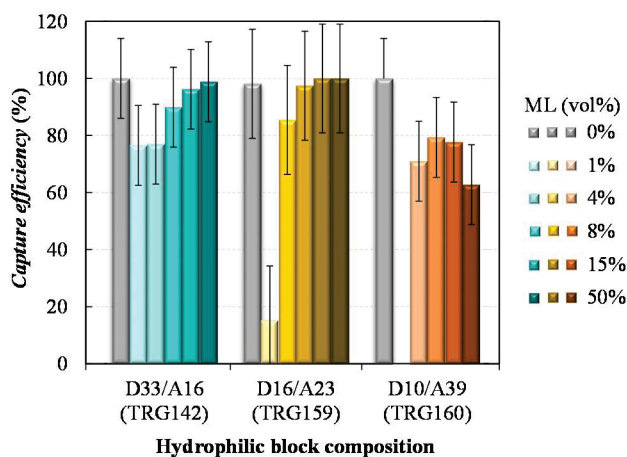


**Figure 114** – Effect of magnetic latex (ML) concentration and surface composition on cell capture efficiency via magnetic separation. MLP used as carriers (entries TRG142, TRG159 and TRG160, Table 26) were decorated with hydrophilic moiety of amphiphilic macroRAFT agents with different DMAEMA/AA compositions (Dxx/Ayy, where xx and yy represent the number of DMAEMA and AA units, respectively). *Bs* was employed as microbial model (entries TRG179-182 in Table 27).

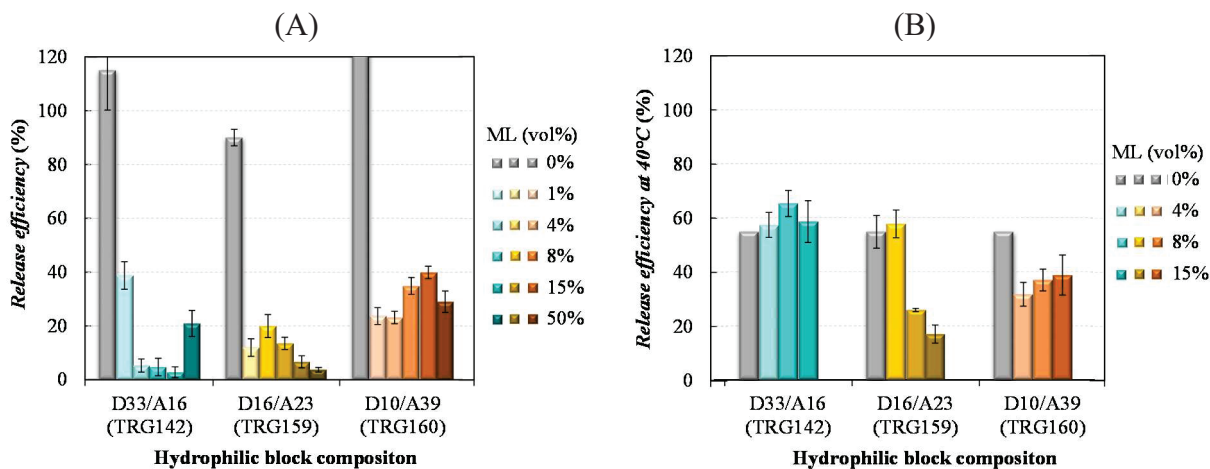


**Figure 115** – Effect of magnetic latex (ML) concentration and surface composition on cell release efficiency at (A) room temperature and (B) at 40 °C. The MLPs used as carriers (entries TRG142, TRG159 and TRG160, Table 26) were decorated with hydrophilic moiety of amphiphilic macroRAFT agents with different DMAEMA/AA compositions (Dxx/Ayy, where xx and yy represent the number of DMAEMA and AA units, respectively). *Bs* was employed as microbial model (entries TRG179-182 in Table 27).

Briefly, based on the studies of the capture and elution steps during the magnetic separation of *E. coli* and *Bs* using MLPs with variable surface compositions, the P(DMAEMA<sub>16-co</sub>-AA<sub>23</sub>)-*b*-PS<sub>11</sub>-stabilized MLPs (TRG159, Table 26) seem to be the best magnetic carriers prepared

during this project. Indeed, this system showed a high efficiency of capture for both microbial cells tested, *i.e.* G- (*E. coli*) and G+ (*Bs*) bacteria. In addition, the release efficiencies obtained for this system were close to the value obtained for the amphoteric particles with the highest AA content (TRG160). Therefore, for the next series of experiment, the amphoteric particles decorated with P(DMAEMA<sub>16-co-AA</sub><sub>23</sub>) (TRG159) will be used as magnetic carrier.

## 4.2. Low bacteria concentrations

### 4.2.1. Use of amphoteric magnetic latex particle to increase the microbial cell concentration

The low concentration of analytes in a biological medium is usually a limitation for their direct analysis via polymerase chain reaction (PCR) or mass spectroscopy (MS), for example. Therefore, the amphoteric magnetic latex particles (entry TRG159, Table 26) were evaluated as magnetic carrier to increase the microbial cell concentration in a biological medium. Six strains of bacteria were used as microorganism models in these runs (Table 27, entry TRG198). As shown in Figure 116, the magnetic carrier was successfully employed for cell concentration of different bacterial strains, leading to 5- up to 25-fold increases in cell concentration. In addition, for the two strains of *Se*, the temperature had a positive effect further increasing the concentration factor. However for *Pp* a negative effect was observed which could indicate a lower resistance to temperature of this bioorganism. It is worth mentioning that only one concentration cycle was performed, but if more cycles of separation and dispersion were carried out, maybe the cell concentration could be further increased.

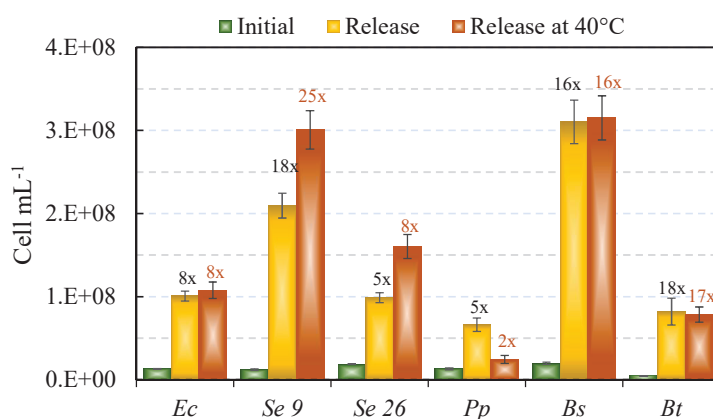


**Figure 116** – Employing magnetic separation method to increase the cell concentration in bacterial samples. Magnetic separation was carried out using MLPs (entry TRG159, Table 26) decorated with P(DMAEMA<sub>16-co-AA</sub><sub>23</sub>) chains and six different strains of bacteria as models (entry TRG198 in Table 27).



### 4.3. Electron microscopy

TEM observations during the various steps of the magnetic separation process were carried out. First, a magnetic separation of *E. coli* using the P(DMAEMA<sub>16</sub>-*co*-AA<sub>23</sub>)-stabilized MLPs (TRG159, Table 26) as carrier was carried out following the experimental conditions presented in Table 27 (entry TRG169). Samples were collected after each step of the magnetic separation (steps A to F illustrated in the scheme of Figure 117) and a protocol of cell fixation and staining was employed for each sample. However, the cell concentration was too low (0.1 vol%) in the grid resulting in poor images. Then, a second run was carried out (Table 27, entry TRG170) in which the initial concentration of cells was increased (5 vol%). All samples were also fixed and staining tests were carried out by varying the time of contact between the APT solution and the sample (TRG170, sample A, Figure 117, in which the best image quality was obtained after 10 s of staining). Moreover, the time of sample deposition on the TEM grid was also varied (1, 2, 5 and 10 min), and the best concentration was obtained after 2 min of deposition (for longer deposition period, too many objects were observed on the grid). It is important to point out that the bacteria fixation involves a laborious protocol with successive centrifugation and washing steps, which increases the grid preparation time. In general the fixation step is recommended in order to prevent the cells from bursting during the drying step keeping their original morphology.<sup>50</sup> Indeed the glutaraldehyde added to the bacteria suspension will generate crosslinked covalent bounds between the proteins, which increases the resistance of microbial cells.<sup>51</sup> Nonetheless some authors<sup>52, 53</sup> reported the successful TEM observation of *E. coli* without any fixation, which can avoid this additional time-consuming protocol. Thus, a third magnetic separation was carried out (TRG170a, Table 27) using the same conditions as for TRG170 but without the fixation protocol. The grids were prepared by using the optimized conditions, *i.e.* 2 min of sample deposition and 10 s of staining with APT, resulting in the micrographs shown in Figure 117.

The sequential micrographs of Figure 117-*bottom* (additional micrographs are presented in ANNEX 5.1.) show each step of the magnetic separation schematically represented in Figure 117-*top*. Sample A represents the initial bacterial sample in which the characteristic bacilli morphology of *E. coli* can be observed, with its typical dimensions of *ca.* 0.5  $\mu\text{m}$  width and 1-3  $\mu\text{m}$  length (Figure 117A and zoom of Figure 118A).<sup>16, 53-55</sup> Then, during the step of bacteria capture, the MLPs are surrounding the bacteria (Sample B, Figure 117B and Figure 118B), indicating successful interaction between the cells and the magnetic particles. In Sample C, as expected only very few objects could be found on the TEM grid due to the high capture

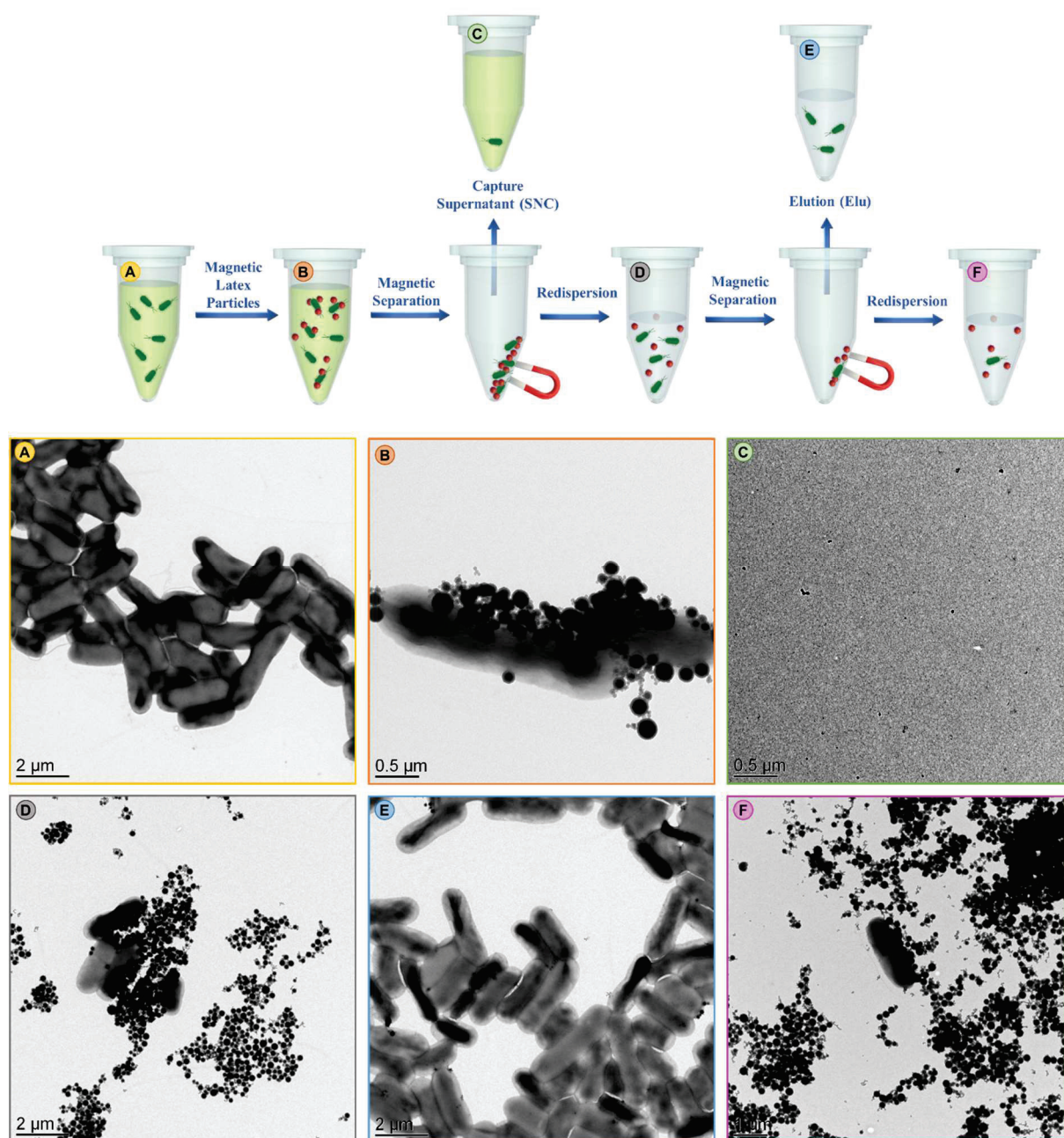


**Figure 117** – *Top* Scheme of magnetic separation and *bottom* TEM observations of samples withdrawn at each step of the magnetic separation using *E. coli* as model (TRG70a, Table 27): (A) initial bacteria suspension, (B) bacteria + MLPs during the capture step, (C) supernatant of capture, (D) bacteria + MLPs after dispersion during the elution step, (E) bacteria recovered after the elution step and (F) recycled MLPs.

efficiency of the magnetic carrier (TRG159, Table 26). Then, in Sample D, particles and bacteria with no variation in their morphology could be observed. Sample E is the *E. coli* recovered after the elution step in which a negligible amount of magnetic particles stay entrapped among the cells, indicating reversible interaction between the magnetic carrier and

the microbial cells. Moreover, no change in the bacteria morphology was noticed when comparing the initial bacterial sample (Figure 118A) and the cells recovered after the elution step (Figure 118E). Finally, the magnetic carriers could be recycled after elution as shown in Figure 117F.

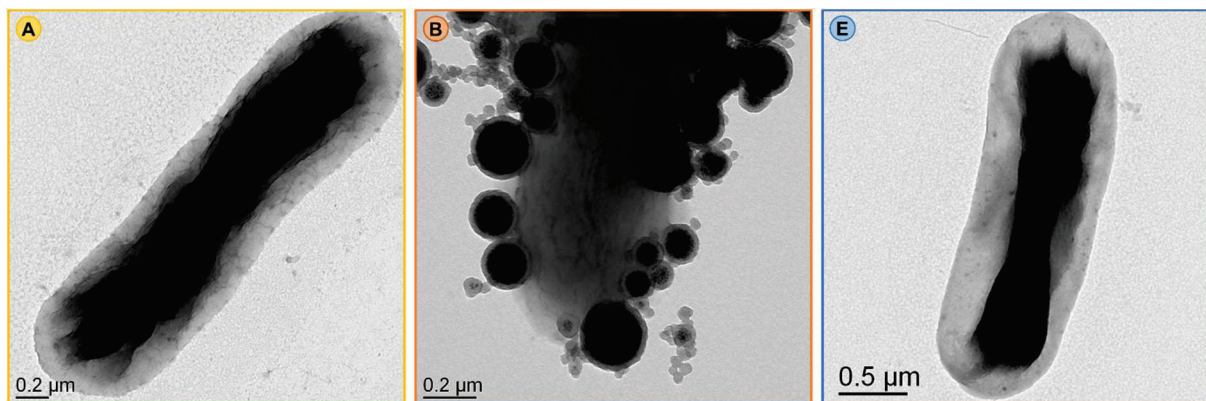


**Figure 118** – TEM observations of samples withdrawn at different steps of magnetic separation of *E. coli* (TRG70a, Table 27): (A) initial bacteria suspension, (B) bacteria + MLPs during the capture step and (E) bacteria recovered after the elution step.

Samples B and D of TRG170a were also observed by *cryo*-TEM to better understand the mechanism of cell capture and release by using the amphoteric MLPs (TRG159, Table 26). However, micrographs of low quality were obtained (Figure 119), as the bacterium was too big to be observed by using the grids available in our lab. On the other hand, when using grids with larger holes, a thicker frozen film will be generated and, consequently, a more energetic electron beam will be necessary to generate images of good quality. Unfortunately, we are not equipped with a microscope able to carry out this kind of *cryo*-TEM observation.

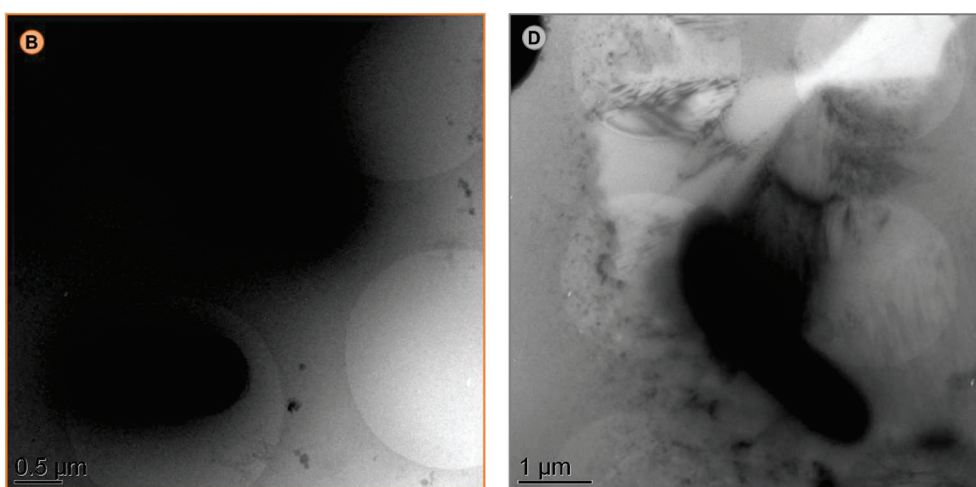


**Figure 119** – *Cryo*TEM observations of samples withdrawn from some specific steps of magnetic separation of *E. coli* (TRG170a, Table 27): bacteria + MLPs during either (B) the capture step or (D) the elution step.



## 5. CONCLUSIONS

Magnetic latex particles decorated with different pH-responsive polymers prepared during this project were tested as carriers for the magnetic separation of different strains of bacteria. The effects of the initial concentration of the cells and of the magnetic carriers, namely PAA- and PDMAEMA-stabilized MLPs, were first evaluated. Magnetic particles decorated with PDMAEMA chains exhibit high efficiencies in the capture of *E. coli* due to the electrostatic interaction generated from the positive charges at the particle surface (amine protonation from DMAEMA units in acidic conditions) and the negative charges from the bacteria surface. In contrast, the PAA-stabilized MLPs present a lower capture efficiency due to weak interactions (hydrophobic interactions, H-bonding) generated with the surface of *E. coli*. On the other hand, high release efficiencies were observed for PAA-systems during the elution step due to repulsive forces generated between the AA units (negatively charged at the basic conditions of the elution step) and the negatively charged bacteria. For PDMAEMA-systems poor release efficiency was always observed.

In a second study, magnetic latex particles decorated with hydrophilic copolymers with various DMAEMA/AA compositions were used as carriers in the magnetic separation of gram-positive and gram-negative bacteria. For both bacterial systems, *E. coli* (G-) and *Bs* (G+), the MLP surface composition was shown to play an important role in the capture and elution steps. The higher the DMAEMA content in the hydrophilic part of the copolymer, the higher were the efficiencies of cell capture. However, the higher was the DMAEMA content, the lower were the release efficiencies. Hence, the magnetic latex particles decorated with a copolymer of intermediate composition, *i.e.* P(DMAEMA<sub>16-co-AA</sub><sub>23</sub>)-*b*-PS<sub>11</sub> (TRG159), showed the better performance as magnetic carrier, as high capture efficiencies were obtained while the release efficiencies were close to the highest values obtained for other amphoteric systems. The thermoresponsive properties of the DMAEMA units were also exploited. For the MLPs decorated with the copolymer the richest in DMAEMA units, higher release efficiencies were obtained compared to the values attained at room temperature suggesting a contribution of temperature to desorption likely due a change of conformation of the copolymer chains at the MLP surface promoting bacteria cell release.

Furthermore, the MLPs exhibiting the best performances, namely the P(DMAEMA<sub>16-co-AA</sub><sub>23</sub>)-stabilized particles (TRG159), were successfully employed to increase the concentration of six different strains of bacteria in a biological medium leading to 5- up to 20-fold increases in cell concentration. This is an important outcome of this work.

The magnetic carrier developed during this project indeed appears to be a promising candidate to concentrate a wide variety of negatively charged biotargets such as phosphopeptides, nucleic acids, bacteria or proteins.

Transmission electron microscopy was employed to evaluate each step of the magnetic separation. Preliminary studies focusing on the time of sample deposition and the staining time during the grid preparation were first carried out to optimize these parameters. Then, the effect of sample fixation was also evaluated and both methods (with and without fixation) gave similar results. TEM observations also showed that the magnetic separation process did not affect the size or morphology of the bacteria. Furthermore, the recovered cells present a negligible amount of residual magnetic particles, which stay entrapped among the cells, indicating a totally reversible interaction between the magnetic carriers and the microbial cells. Finally *cryo*-TEM was employed to see how the particles interact with the bacteria, but unfortunately not clear images were obtained.

## REFERENCES

1. He, J. C.; Huang, M. Y.; Wang, D. M.; Zhang, Z. M.; Li, G. K., Magnetic separation techniques in sample preparation for biological analysis: A review. *Journal of Pharmaceutical and Biomedical Analysis* **2014**, *101*, 84-101.
2. Rahman, M. M.; Elaissari, A., Temperature and magnetic dual responsive microparticles for DNA separation. *Separation and Purification Technology* **2011**, *81* (3), 286-294.
3. Majewski, A. P.; Stahlschmidt, U.; Jérôme, V. r.; Freitag, R.; Müller, A. H.; Schmalz, H., PDMAEMA-grafted core-shell-corona particles for nonviral gene delivery and magnetic cell separation. *Biomacromolecules* **2013**, *14* (9), 3081-3090.
4. Bigall, N. C.; Curcio, A.; Leal, M. P.; Falqui, A.; Palumberi, D.; Di Corato, R.; Albanesi, E.; Cingolani, R.; Pellegrino, T., Magnetic nanocarriers with tunable pH dependence for controlled loading and release of cationic and anionic payloads. *Advanced Materials* **2011**, *23* (47), 5645-5650.
5. Chen, Z.; Yin, J.-J.; Zhou, Y.-T.; Zhang, Y.; Song, L.; Song, M.; Hu, S.; Gu, N., Dual enzyme-like activities of iron oxide nanoparticles and their implication for diminishing cytotoxicity. *Acs Nano* **2012**, *6* (5), 4001-4012.
6. Liu, Q.; Shi, J.; Cheng, M.; Li, G.; Cao, D.; Jiang, G., Preparation of graphene-encapsulated magnetic microspheres for protein/peptide enrichment and MALDI-TOF MS analysis. *Chemical Communications* **2012**, *48* (13), 1874-1876.
7. Shao, M.; Ning, F.; Zhao, J.; Wei, M.; Evans, D. G.; Duan, X., Preparation of Fe<sub>3</sub>O<sub>4</sub>@ SiO<sub>2</sub>@ layered double hydroxide core-shell microspheres for magnetic separation of proteins. *Journal of the American Chemical Society* **2012**, *134* (2), 1071-1077.
8. Ma, W.-F.; Zhang, Y.; Li, L.-L.; You, L.-J.; Zhang, P.; Zhang, Y.-T.; Li, J.-M.; Yu, M.; Guo, J.; Lu, H.-J., Tailor-made magnetic Fe<sub>3</sub>O<sub>4</sub>@ mTiO<sub>2</sub> microspheres with a tunable mesoporous anatase shell for highly selective and effective enrichment of phosphopeptides. *Acs Nano* **2012**, *6* (4), 3179-3188.
9. Zou, Z.; Ibisate, M.; Zhou, Y.; Aebersold, R.; Xia, Y.; Zhang, H., Synthesis and evaluation of superparamagnetic silica particles for extraction of glycopeptides in the microtiter plate format. *Analytical Chemistry* **2008**, *80* (4), 1228-1234.
10. Veyret, R.; Elaissari, A.; Marianneau, P.; Sall, A. A.; Delair, T., Magnetic colloids for the generic capture of viruses. *Analytical Biochemistry* **2005**, *346* (1), 59-68.
11. Arkhis, A.; Elaissari, A.; Delair, T.; Verrier, B.; Mandrand, B., Capture of enveloped viruses using polymer tentacles containing magnetic latex particles. *Journal of Biomedical Nanotechnology* **2010**, *6* (1), 28-36.
12. Dong, H.; Huang, J.; Koepsel, R. R.; Ye, P.; Russell, A. J.; Matyjaszewski, K., Recyclable antibacterial magnetic nanoparticles grafted with quaternized poly (2-(dimethylamino) ethyl methacrylate) brushes. *Biomacromolecules* **2011**, *12* (4), 1305-1311.
13. Yang, K.; Jenkins, D. M.; Su, W. W., Rapid concentration of bacteria using submicron magnetic anion exchangers for improving PCR-based multiplex pathogen detection. *Journal of Microbiological Methods* **2011**, *86* (1), 69-77.



14. El-Boubbou, K.; Gruden, C.; Huang, X., Magnetic glyco-nanoparticles: a unique tool for rapid pathogen detection, decontamination, and strain differentiation. *Journal of the American Chemical Society* **2007**, *129* (44), 13392-13393.
15. Kubota, M.; Matsui, M.; Chiku, H.; Kasashima, N.; Shimojoh, M.; Sakaguchi, K., Cell adsorption and selective desorption for separation of microbial cells by using chitosan-immobilized silica. *Applied and Environmental Microbiology* **2005**, *71* (12), 8895-8902.
16. Liu, J.-C.; Tsai, P.-J.; Lee, Y. C.; Chen, Y.-C., Affinity capture of uropathogenic *Escherichia coli* using pigeon ovalbumin-bound Fe<sub>3</sub>O<sub>4</sub>@ Al<sub>2</sub>O<sub>3</sub> magnetic nanoparticles. *Analytical Chemistry* **2008**, *80* (14), 5425-5432.
17. Cornell, R. M.; Schwertmann, U., *The iron oxides: structure, properties, reactions, occurrences and uses*. John Wiley & Sons: 2003.
18. Demirer, G. S.; Okur, A. C.; Kizilel, S., Synthesis and design of biologically inspired biocompatible iron oxide nanoparticles for biomedical applications. *Journal of Materials Chemistry B* **2015**, *3* (40), 7831-7849.
19. Gupta, A. K.; Gupta, M., Synthesis and surface engineering of iron oxide nanoparticles for biomedical applications. *Biomaterials* **2005**, *26* (18), 3995-4021.
20. Kalia, S.; Kango, S.; Kumar, A.; Haldorai, Y.; Kumari, B.; Kumar, R., Magnetic polymer nanocomposites for environmental and biomedical applications. *Colloid and Polymer Science* **2014**, *292* (9), 2025-2052.
21. Laurent, S.; Forge, D.; Port, M.; Roch, A.; Robic, C.; Vander Elst, L.; Muller, R. N., Magnetic iron oxide nanoparticles: synthesis, stabilization, vectorization, physicochemical characterizations, and biological applications. *Chemical Reviews* **2008**, *108* (6), 2064-2110.
22. Teja, A. S.; Koh, P.-Y., Synthesis, properties, and applications of magnetic iron oxide nanoparticles. *Progress in Crystal Growth and Characterization of Materials* **2009**, *55* (1), 22-45.
23. Wu, W.; Wu, Z.; Yu, T.; Jiang, C.; Kim, W.-S., Recent progress on magnetic iron oxide nanoparticles: synthesis, surface functional strategies and biomedical applications. *Science and Technology of Advanced Materials* **2016**.
24. Chong, C. Élaboration de particules de polymère magnétiques multifonctionnelles pour la préparation d'échantillons biologiques. Université Claude Bernard-Lyon I, 2013.
25. Elaissari, A.; Delair, T.; Pichot, C., Thermally sensitive, hydrophilic, and reactive latex particles as versatile supports for biomolecules immobilization. In *Aqueous Polymer Dispersions*, Springer: 2004; pp 82-87.
26. Zhou, W.-H.; Lu, C.-H.; Guo, X.-C.; Chen, F.-R.; Yang, H.-H.; Wang, X.-R., Mussel-inspired molecularly imprinted polymer coating superparamagnetic nanoparticles for protein recognition. *Journal of Materials Chemistry* **2010**, *20* (5), 880-883.
27. Li, Y.; Ding, M.-j.; Wang, S.; Wang, R.-y.; Wu, X.-l.; Wen, T.-t.; Yuan, L.-h.; Dai, P.; Lin, Y.-h.; Zhou, X.-m., Preparation of imprinted polymers at surface of magnetic nanoparticles for the selective extraction of tadalafil from medicines. *ACS Applied Materials & Interfaces* **2011**, *3* (9), 3308-3315.
28. Ozalp, V. C.; Bayramoglu, G.; Erdem, Z.; Arica, M. Y., Pathogen detection in complex samples by quartz crystal microbalance sensor coupled to aptamer functionalized core-shell type magnetic separation. *Analytica Chimica Acta* **2015**, *853*, 533-540.

29. Veyret, R.; Delair, T.; Pichot, C.; Elaissari, A., Amino-containing magnetic nanoemulsions: elaboration and nucleic acid extraction. *Journal of Magnetism and Magnetic Materials* **2005**, 295 (2), 155-163.
30. Gai, Q.-Q.; Qu, F.; Liu, Z.-J.; Dai, R.-J.; Zhang, Y.-K., Superparamagnetic lysozyme surface-imprinted polymer prepared by atom transfer radical polymerization and its application for protein separation. *Journal of Chromatography A* **2010**, 1217 (31), 5035-5042.
31. Li, Y.; Xu, X.; Deng, C.; Yang, P.; Zhang, X., Immobilization of trypsin on superparamagnetic nanoparticles for rapid and effective proteolysis. *Journal of Proteome Research* **2007**, 6 (9), 3849-3855.
32. Lin, S.; Yun, D.; Qi, D.; Deng, C.; Li, Y.; Zhang, X., Novel microwave-assisted digestion by trypsin-immobilized magnetic nanoparticles for proteomic analysis. *Journal of Proteome Research* **2008**, 7 (3), 1297-1307.
33. Deng, Y.; Qi, D.; Deng, C.; Zhang, X.; Zhao, D., Superparamagnetic high-magnetization microspheres with an Fe<sub>3</sub>O<sub>4</sub>@SiO<sub>2</sub> core and perpendicularly aligned mesoporous SiO<sub>2</sub> shell for removal of microcystins. *Journal of the American Chemical Society* **2008**, 130 (1), 28-29.
34. Chen, H.; Liu, S.; Yang, H.; Mao, Y.; Deng, C.; Zhang, X.; Yang, P., Selective separation and enrichment of peptides for MS analysis using the microspheres composed of Fe<sub>3</sub>O<sub>4</sub>@mSiO<sub>2</sub> core and perpendicularly aligned mesoporous SiO<sub>2</sub> shell. *Proteomics* **2010**, 10 (5), 930-939.
35. Xiong, Z.; Zhao, L.; Wang, F.; Zhu, J.; Qin, H.; Wu, R. a.; Zhang, W.; Zou, H., Synthesis of branched PEG brushes hybrid hydrophilic magnetic nanoparticles for the selective enrichment of N-linked glycopeptides. *Chemical Communications* **2012**, 48 (65), 8138-8140.
36. Pasteur, L., *Mémoire sur la fermentation appliquée lactique. Mémoire sur la fermentation alcoolique*. Mallet-Bachelier: 1857.
37. Fredrickson, J. K.; Zachara, J. M.; Balkwill, D. L.; Kennedy, D.; Shu-mei, W. L.; Kostandarithes, H. M.; Daly, M. J.; Romine, M. F.; Brockman, F. J., Geomicrobiology of high-level nuclear waste-contaminated vadose sediments at the Hanford Site, Washington State. *Applied and Environmental Microbiology* **2004**, 70 (7), 4230-4241.
38. Prothero, D. R., *The Princeton Field Guide to Prehistoric Mammals*. Princeton University Press: 2016.
39. Parkhill, J.; Wren, B.; Thomson, N.; Titball, R.; Holden, M.; Prentice, M.; Sebahia, M.; James, K.; Churcher, C.; Mungall, K., Genome sequence of *Yersinia pestis*, the causative agent of plague. *Nature* **2001**, 413 (6855), 523-527.
40. Brennan, P. J., Structure, function, and biogenesis of the cell wall of *Mycobacterium tuberculosis*. *Tuberculosis* **2003**, 83 (1), 91-97.
41. Young, R. A.; Mehra, V.; Sweetser, D., leprosy parasite *Mycobacterium leprae*. *Nature* **1985**, 316, 65K.
42. Finkelstein, R. A., Cholera, *Vibrio cholerae* O1 and O139, and other pathogenic vibrios. **1996**.
43. Various shapes and arrangements of Bacterial cells. <http://laboratoryinfo.com/various-shapes-and-arrangements-of-bacterial-cells/> (accessed 18/04/2017).
44. <https://pixabay.com/> (free database) (accessed 18/04/2017).

45. Thanbichler, M.; Wang, S. C.; Shapiro, L., The bacterial nucleoid: a highly organized and dynamic structure. *Journal of Cellular Biochemistry* **2005**, *96* (3), 506-521.
46. van Heijenoort, J., Formation of the glycan chains in the synthesis of bacterial peptidoglycan. *Glycobiology* **2001**, *11* (3), 25R-36R.
47. Gram, H. C. J.; Friedlaender, C., *Ueber die isolirte Färbung der Schizomyceten: in Schnitt- und Trockenpräparaten*. Theodor Fischer's medicinischer Buchhandlung: 1884.
48. Raetz, C. R.; Whitfield, C., Lipopolysaccharide endotoxins. *Annual review of biochemistry* **2002**, *71* (1), 635-700.
49. Liu, Y.; He, L.; Mustapha, A.; Li, H.; Hu, Z.; Lin, M., Antibacterial activities of zinc oxide nanoparticles against *Escherichia coli* O157: H7. *Journal of applied microbiology* **2009**, *107* (4), 1193-1201.
50. Chao, Y.; Zhang, T., Optimization of fixation methods for observation of bacterial cell morphology and surface ultrastructures by atomic force microscopy. *Applied Microbiology and Biotechnology* **2011**, *92* (2), 381.
51. Dapson, R., Macromolecular changes caused by formalin fixation and antigen retrieval. *Biotechnic & Histochemistry* **2007**, *82* (3), 133-140.
52. Niu, C.; Robbins, C. M.; Pittman, K. J.; Stubblefield, B. A.; Simmons, R. B.; Gilbert, E. S., LuxS influences *Escherichia coli* biofilm formation through autoinducer-2-dependent and autoinducer-2-independent modalities. *FEMS Microbiology Ecology* **2013**, *83* (3), 778-791.
53. Pal, S.; Mitra, K.; Azmi, S.; Ghosh, J. K.; Chakraborty, T. K., Towards the synthesis of sugar amino acid containing antimicrobial noncytotoxic CAP conjugates with gold nanoparticles and a mechanistic study of cell disruption. *Organic & Biomolecular Chemistry* **2011**, *9* (13), 4806-4810.
54. Sondi, I.; Salopek-Sondi, B., Silver nanoparticles as antimicrobial agent: a case study on *E. coli* as a model for Gram-negative bacteria. *Journal of Colloid and Interface Science* **2004**, *275* (1), 177-182.
55. Luef, B.; Fakra, S. C.; Csencsits, R.; Wrighton, K. C.; Williams, K. H.; Wilkins, M. J.; Downing, K. H.; Long, P. E.; Comolli, L. R.; Banfield, J. F., Iron-reducing bacteria accumulate ferric oxyhydroxide nanoparticle aggregates that may support planktonic growth. *The ISME Journal* **2013**, *7* (2), 338-350.

### **GENERAL CONCLUSION**

The development of magnetic latex particles using iron oxide nanoparticles as magnetic material has attracted an extensive interest aiming at specific applications in biomedical, environment and optics fields. In biomedical fields, many efforts have been devoted to the elaboration of smart and multifunctional particles combining properties of different inorganic/organic composite materials. For instance, these smart particles can be used as contrast agent in magnetic resonance imaging or as carriers in drug delivery systems assisted by a magnetic field. Magnetic particles can also be employed as carriers in magnetic separation of biocompounds, which can save time during the step of sample preparation in diagnostics. Nonetheless these particles must present some intrinsic characteristics to be successfully employed as magnetic carriers such as:

- Encapsulated iron oxide
- High iron oxide content
- Superparamagnetism
- Large particle size (> 100 nm)
- Control of surface chemistry

The superparamagnetism is an important characteristic of magnetic particles to facilitate their re-dispersion after field removal. This property is directly associated to the size of the iron oxide nanoparticles, and is usually observed for IONP smaller than 15-20 nm in diameter. However, magnetic carriers with low separation rate are generally obtained for particles in this size range, which limits the direct use of superparamagnetic IONP as carriers. In addition the hydrophilic surface of IONP can promote irreversible interaction with the living organisms or tissues in the biological medium. Thus, strategies based on multiple encapsulation of iron oxide nanoparticles into a protective outer shell, which results in composite particles, have been reported in the literature. The multi-encapsulation approach can prevent the undesirable interactions with organisms and, in addition, magnetic carriers with large particle sizes (*ca.* 200 nm) can be obtained. Besides, the surface functionalization of the magnetic polymer particles is obviously a key parameter, not only to afford suitable interactions with the biological targets, but also to allow the release of the biotargets during the elution step of magnetic separation.

Our synthetic strategy in order to develop magnetic carriers that fulfill all the aforementioned criteria was divided into three parts: (1) synthesis of amphiphilic block copolymers via RAFT mediated solution polymerization, (2) iron oxide cluster formation via an

emulsification/solvent evaporation process and (3) encapsulation of iron oxide clusters via seeded emulsion polymerization.

First, RAFT polymerization was successfully employed to synthesize amphiphilic block copolymers with a precise control of their composition. Initially, two hydrophilic macroRAFT agents, PAA-TTC and PDMAEMA-TTC, were synthesized carrying a reactivatable trithiocarbonate group (-TTC). SEC analysis showed an excellent agreement between the theoretical and experimental molar masses for both polymers. Moreover, chain-end functionalization was evaluated by using UV detection during the SEC analysis showing that most of the polymer chains were carrying the TTC end-group. This end-functionalization provided a living character to the macroRAFT agents as demonstrated by chain extension experiments. Amphiphilic block copolymers were then synthesized by chain extension reaction of PAA-TTC and PDMAEMA-TTC with styrene and well-defined block copolymers with narrow molar mass distributions ( $D < 1.25$ ) were formed.

Amphoteric macroRAFTs were also successfully synthesized by RAFT copolymerization of AA and DMAEMA at different molar ratios. Amphiphilic block copolymers were then prepared via chain extension reaction of the amphoteric macroRAFTs with a PS segment. However, only the synthesis of P(DMAEMA<sub>10-co-AA</sub><sub>39</sub>)-*b*-PS<sub>11</sub>-TTC was unambiguously demonstrated. Indeed, the SEC characterization of the other two amphiphilic macroRAFTs, richer in DMAEMA, was not possible due to solubility issues and/or undesirable interactions with the columns.

The thermoresponsive properties of the PDMAEMA-based macroRAFTs were then evaluated. In good agreement with the literature, the cloud point temperature shifted from *ca.* 45 °C at pH > 9 to around 70 °C at pH = 8 and it was completely absent at pH lower than 7.5 in the range of temperature studied (*i.e.* from 15 to 90 °C). However, no phase transition was observed for the amphoteric macroRAFT agents composed of AA and DMAEMA, both in basic and acidic conditions. This can be associated to antagonistic effects of pH on the solubility of AA and DMAEMA. Indeed, the macroRAFT will be charged over a wide range of pH values leading to a higher hydrophilicity, hindering the phase transition.

The second part of this thesis focused on the preparation of iron oxide clusters stabilized by the amphiphilic block copolymers previously described. As mentioned above, the composition of both blocks was controlled via RAFT polymerization, allowing in particular a fine control of the composition of the hydrophilic moiety. Commercial iron oxide

nanoparticles modified with fatty acids were used during the process of cluster formation. In a first step, these commercial nanoparticles were extensively characterized. RAMAN spectroscopy indicated that the nanoparticles were mainly composed of maghemite ( $\gamma\text{-Fe}_2\text{O}_3$ ). FTIR and RAMAN spectroscopy combined with TGA showed that some fatty acid molecules (15-20 wt%) were effectively chemically bonded to the inorganic surface. Moreover, the morphology of the IONP was investigated by TEM, showing an irregular shape of the nanoparticles with a number-average diameter  $D_n$  of 10 nm, in good agreement with the particle size determined by XRD. Finally, as expected for such small particle sizes, the IONP displayed superparamagnetic properties as evidenced by SQUID measurements.

Iron oxide clusters were then prepared via an emulsification/solvent evaporation process. The effect of sonication time, sonication power and macroRAFT concentration was studied using PDMAEMA<sub>43</sub>-*b*-PS<sub>9</sub>-TTC as stabilizer. The macroRAFT concentration was shown to have a strong influence on the droplet size and hence, on the cluster size. The higher the amount of macroRAFT, the lower was the cluster diameter. In addition, high yields were obtained (> 80%) for macroRAFT concentrations higher than  $1.5 \cdot 10^{-4}$  M. The HCl concentration in the macroRAFT solution was also varied, demonstrating an important effect on cluster stabilization, and clusters bigger than 300 nm could be obtained for  $[\text{HCl}]/[\text{macroRAFT}] = 10$  or 20. The best conditions ( $t = 240$  s and  $[\text{PDMAEMA}_{43}\text{-}b\text{-PS}_9\text{-TTC}] = 2.5 \cdot 10^{-4}$  M) were then applied in scale-up experiments. Clusters stabilized by PAA<sub>50</sub>-*b*-PS<sub>10</sub> were also prepared and a similar effect of the macroRAFT concentration was evidenced, showing that a minimum concentration of PAA<sub>50</sub>-*b*-PS<sub>10</sub>-TTC was needed (*ca.*  $2.5 \cdot 10^{-4}$  M) to ensure the formation of clusters with a high yield. In addition, PAA-TTC and PDMAEMA-TTC macroRAFTs were also evaluated for cluster formation showing that the lone hydrophilic block could also lead to stable iron oxide clusters. Furthermore amphiphilic macroRAFT agents presenting different AA/DMAEMA molar ratios were used in the formation of pH-responsive iron oxide clusters as demonstrated by the evolution of  $\zeta$ -potential as a function of pH.

The third part of the thesis was devoted to the synthesis of magnetic latex particles decorated with well-defined responsive polymer chains using the iron oxide clusters as seeds in emulsion polymerization of styrene.

The polymerization process (batch *vs* semi-continuous) was the first parameter studied using PDMAEMA<sub>45</sub>-*b*-PS<sub>9</sub>-TTC-stabilized clusters. The semi-batch system led to lower initial polymerization rates, which was attributed to the low monomer concentration. The



elimination of the free macroRAFT present in water led to a meaningful increase of the amount of magnetic particles, which also prevented the formation of unloaded particles via a secondary nucleation. Unlikely, hybrid particles exhibiting hemispherical morphology was often observed due to an incompatibility between the polymer and inorganic phases.

The addition of a crosslinking agent (DVB) (10 or 20 wt%) conduct to formation of the targeted core-shell morphology, the iron oxide clusters being fully encapsulated into a polymeric shell. The conversion was however limited to *ca.* 30% in these highly crosslinked systems. This limited conversion was mitigated by adding a concentration of DVB higher in the initial charge than in the monomer feed. TEM investigations of samples collected at intermediate conversions revealed that the shell thickness of the core-shell particles gradually increased with the polymer content, showing that is possible to finely control the shell thickness, and hence the iron oxide content.

The same strategy was exploited for the encapsulation of PAA-stabilized clusters. After some experimental adjustments, including changing the initiator and initial pH, stable systems were obtained and the expected encapsulated morphology was observed for the resulting hybrid particles. Moreover, magnetic particles decorated with hydrophilic segments of different AA/DMAEMA compositions were also successfully prepared. The iron oxide content of the hybrid particles was determined via thermogravimetric analysis. Composite latex particles with high iron oxide content were obtained, containing from 44 up to 59 wt% of magnetic material. This composition associated with their relative large particle size (> 100 nm) led to the formation of magnetic carriers with a very fast response to a magnetic field, as approximately 90% of the particles could be separated by a magnetic field in less than 30 s.

In the last part of our work, five types of magnetic latex particles surface-functionalized with different hydrophilic chains and presenting a strong response to a magnetic field were tested as carriers in the magnetic separation of different strains of bacteria. The effect of the initial cell and magnetic carrier (namely PAA- or PDMAEMA-stabilized MLPs) concentrations was first evaluated. Magnetic particles decorated with PDMAEMA chains revealed high efficiencies in the capture of *E. coli* (performed under acidic conditions) due to the electrostatic interaction between the positive charges at the particle surface and the negatively charged bacteria. In contrast, the PAA-stabilized MLPs presented a lower capture efficiency due to the weak interactions generated with the surface of *E. coli* at acidic pH. On the other hand, high release efficiencies were observed for PAA-systems during the elution step due to

repulsive electrostatic interactions. Consistently poor release efficiency was observed for the PDMAEMA-stabilized particles

In a second study, magnetic latex particles decorated with (co)polymers were evaluated in the magnetic separation of either gram positive (*Bs*) or gram negative bacteria (*E. coli*). For both bacterial systems, the surface composition of the MLPs was shown to play an important role in the capture and elution steps. The higher the DMAEMA content in the copolymer, the higher was the efficiency of cell capture. On the other hand, the higher was the DMAEMA content, the lower were the release efficiencies. Hence, the magnetic latex particles decorated with the copolymer with an intermediate composition, *i.e.* P(DMAEMA<sub>16-co-AA</sub><sub>23</sub>)-*b*-PS<sub>11</sub>, presented the best performance as magnetic carriers, as high capture efficiencies were obtained while the release efficiencies were close to the highest values obtained for the other carriers. Furthermore, the same MLP were successfully used as carriers to increase the concentration of six different strains of bacteria in a biological medium, leading to 5- up to 20-fold increase in cell concentration. These are important results showing that this specific magnetic carrier developed during this project is a promising candidate to concentrate a wide range of negatively charged biotargets such as phosphopeptides, nucleic acids, bacteria or proteins.

Transmission electron microscopy was employed to evaluate each step of the magnetic separation process. Preliminary studies comprising the time of sample deposition and staining time during the grid preparation were first carried out to optimize these conditions. TEM observations showed that neither the morphology nor the size of the bacteria changed during all steps of the magnetic separation process. Furthermore, TEM images also showed that the recovered cells contained a negligible amount of residual magnetic particles, which were entrapped among the cells, indicating a totally reversible interaction between the magnetic carriers and the microbial cells.

In summary, ten macroRAFT agents were synthesized via RAFT polymerization. Five hydrophilic macroRAFTs with various AA to DMAEMA ratios were successfully synthesized. Chain extension experiments of these hydrophilic macroRAFTs with styrene led to the formation of five amphiphilic block copolymers completing our macroRAFT library. The amphiphilic macroRAFT agents were then employed as stabilizers during the preparation of iron oxide cluster with different surface functionalization. Completing the third part of our strategy, fully encapsulated iron oxide cluster were prepared via seeded emulsion polymerization in the presence of a crosslinking agent. Finally, the five resulting magnetic

latex particles decorated with different pH-responsive polymer chains were tested as magnetic carriers on magnetic separation of bacteria. It was concluded that the precise control of surface functionalization achieved by RAFT polymerization, was of fundamental importance to generate magnetic carriers with pH tunable properties able to capture and release bacteria with high efficiencies.

## **PERSPECTIVES**

This study has demonstrated that our magnetic carriers seem to be promising candidates for an efficient magnetic separation process. Of course, there is room for improvement and different aspects of the project would deserve a deeper investigation and/or could be the topic of further studies:

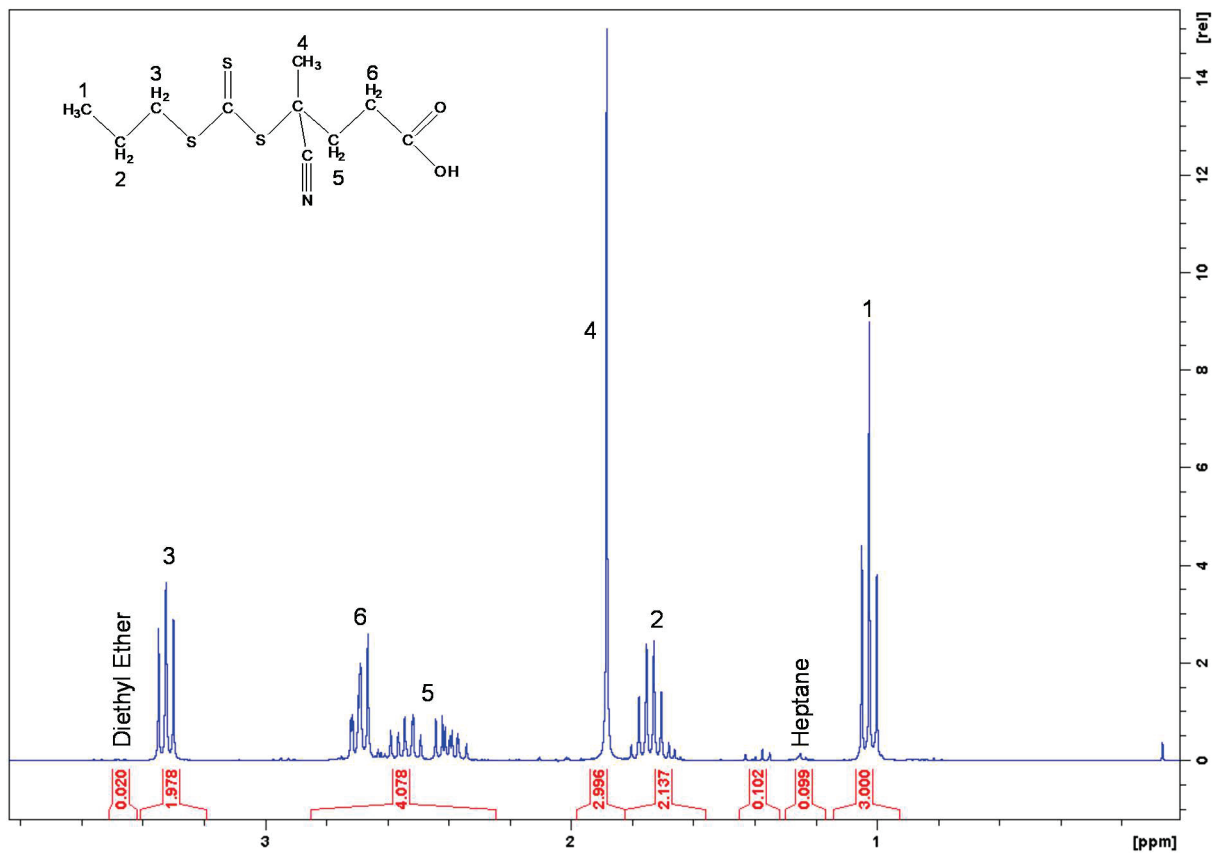
- Effect of fine control pH on cloud point temperature of amphoteric copolymers P(DMAEMA-*co*-AA).
- Synthesis of amphiphilic block copolymers via RAFT polymerization with different block lengths and their effect on cluster and particle stabilization.
- Synthesis of amphiphilic block copolymers via RAFT polymerization with hydrophilic block based on PEG segments.
- Study of the protonation degree of amphoteric macroRAFT P(DMAEMA-*co*-AA) on IO cluster formation.
- Encapsulation of iron oxide clusters via seeded emulsion polymerization with polymer(s) of different composition (*e.g.* MMA).
- Preparation of iron oxide clusters by a solvent displacement process via controlled precipitation of cationic/anionic polymers complexes (PDMAEMA/PAA).
- Encapsulation of iron oxide clusters with an inorganic silica shell.
- Evaluation of the magnetic carriers presenting different particle morphology prepared during this thesis for the magnetic separation of biotargets.
- Use of our magnetic carriers with different surface functionalization (PAA/PDMAEMA) on capture and trigger release of different biotargets such as nucleic acid, proteins and so on.
- Test our magnetic carriers with different surface functionalization (PAA/PDMAEMA) in process of DNA transfection into eukaryotic cells.



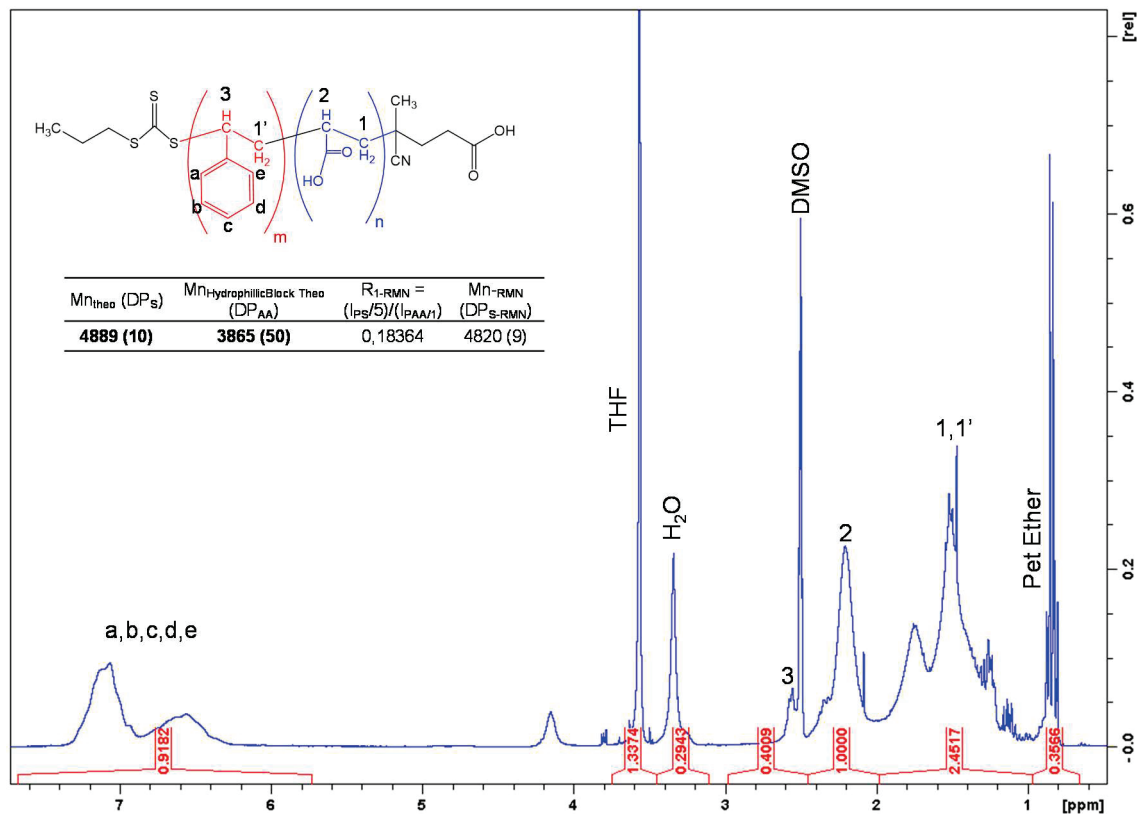
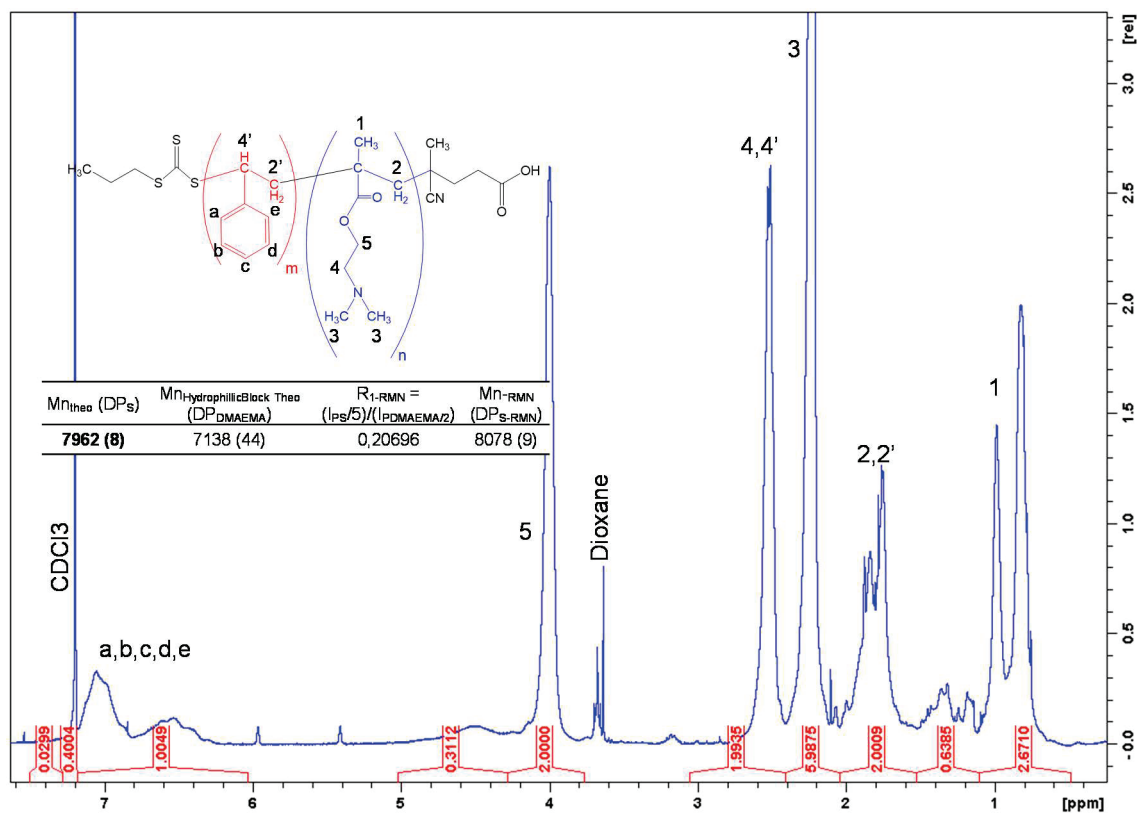
## ANNEXES

\_Toc482637556

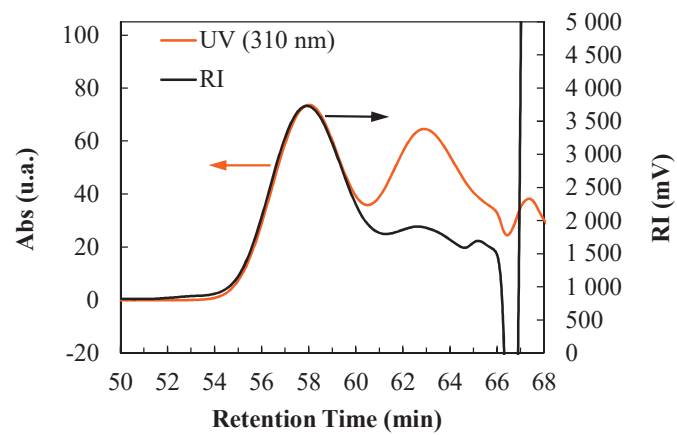
ANNEX 2. 1. – <sup>1</sup> H NMR spectrum of the CTPPA RAFT agent.....	272
ANNEX 2. 2 – Determination of the degree of polymerization of styrene by <sup>1</sup> H NMR.....	273
ANNEX 2. 3. – SEC Chromatogram of P(DMAEMA <sub>16-co-AA</sub> <sub>23</sub> )-TTC (TRG126) with UV-signal at wavelength of 310 nm .....	274
ANNEX 3. 1. – FTIR and GC analyses confirming the complete evaporation of toluene during the formation of IO clusters .....	275
ANNEX 3. 2. –Intensity and number frequency size distribution histograms obtained by statistical analysis of the cluster diameter from TEM images and comparaisn with the DLS particle size distribution .....	276
ANNEX 3. 3. – <i>Cryo</i> -TEM micrographs of toluene droplets loaded with FA@IONPs.....	277
ANNEX 3. 4. – Determination of free macroRAFT concentration.....	278
ANNEX 3. 5. – Number frequency size distribution histograms of the IO clusters prepared at a larger scale using PDMAEMA-b-PS-TTC as stabilizer.....	281
ANNEX 4. 1 – Gas chromatograms of Divinyl benzene.....	282
ANNEX 4. 2 – TEM micrographs of TRG90.....	283
ANNEX 5. 1 - TEM Images (TRG170).....	284

ANNEX 2. 1. –  $^1\text{H}$  NMR spectrum of the CTPPA RAFT agent



ANNEX 2.2 – Determination of the degree of polymerization of styrene by  $^1\text{H}$  NMR- PAA<sub>50</sub>-*b*-PS<sub>9</sub>-TTC (TRG66)- PDMAEMA<sub>44</sub>-*b*-PS<sub>9</sub>-TTC (TRG68)

ANNEX 2. 3. – SEC Chromatogram of P(DMAEMA<sub>16</sub>-*co*-AA<sub>23</sub>)-TTC (TRG126) with UV-signal at wavelength of 310 nm



### ANNEX 3. 1. – FTIR and GC analyses confirming the complete evaporation of toluene during the formation of IO clusters

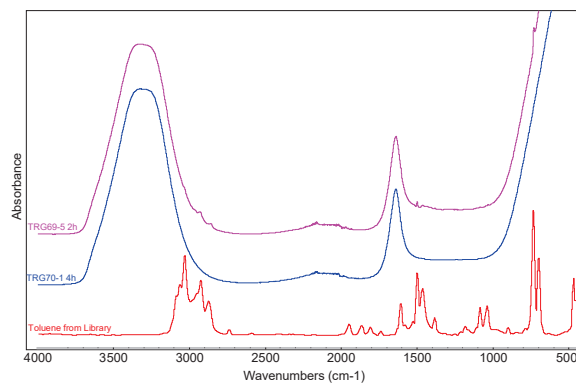


**Figure 120** – FTIR spectra of IO clusters after 2h and 4h of toluene evaporation. The spectra were recorded in ATR mode by depositing a drop of the suspension directly onto the crystal.

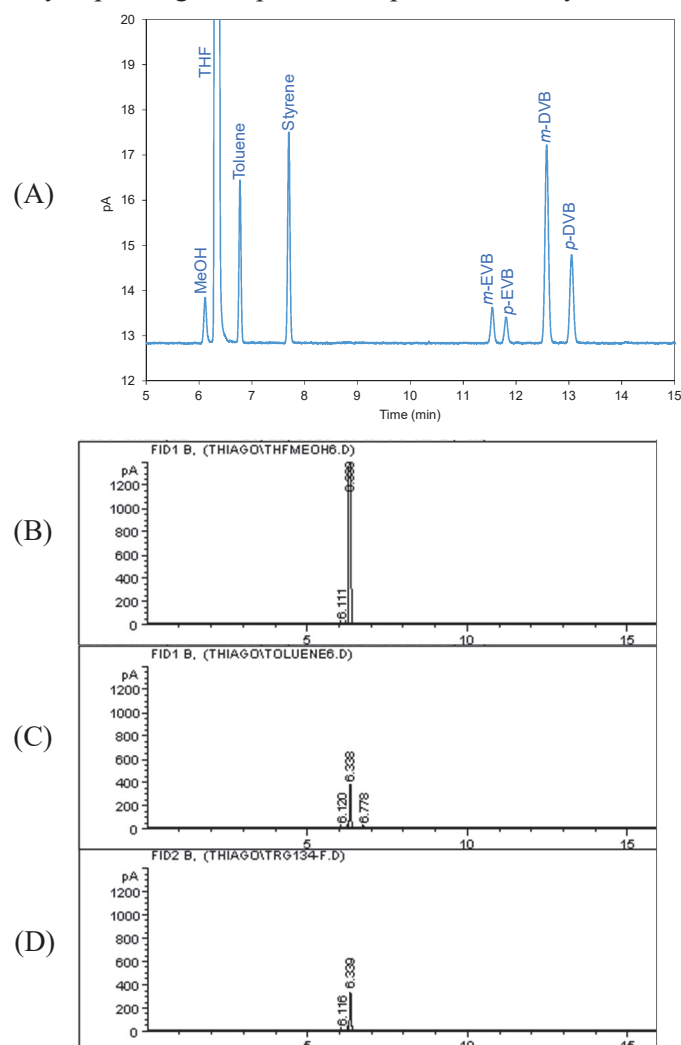


**Figure 121** – GC spectra of THF solutions with 0.05% methanol as internal standard. (A) Mixture of the chemicals to assess the separation efficiency, (B) THF solution with 0.05% methanol, (C) toluene and (D) a mixture of THF and iron oxide suspension in toluene (1:4 vol:vol).

ANNEX 3. 2. –Intensity and number frequency size distribution histograms obtained by statistical analysis of the cluster diameter from TEM images and comparison with the DLS particle size distribution

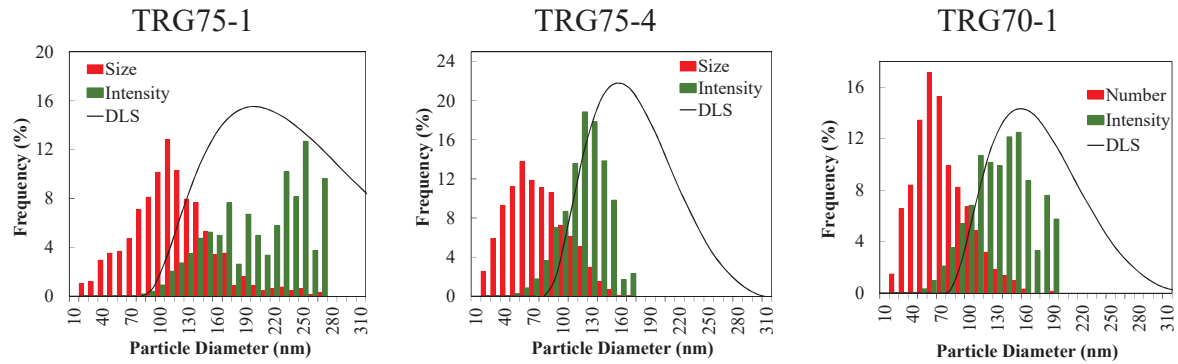
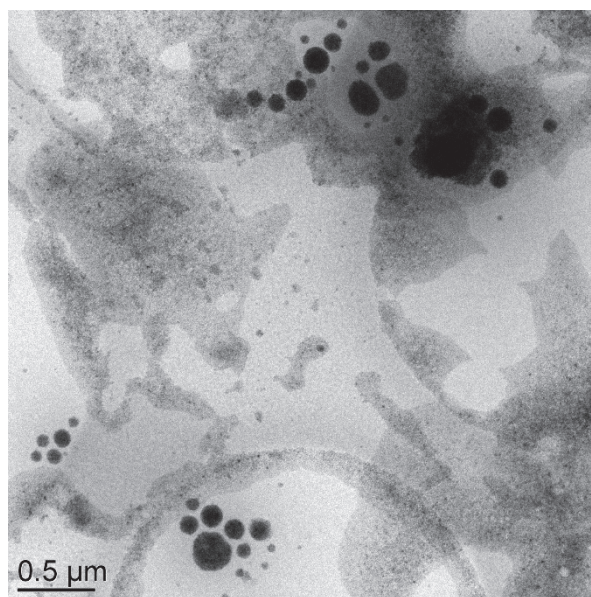
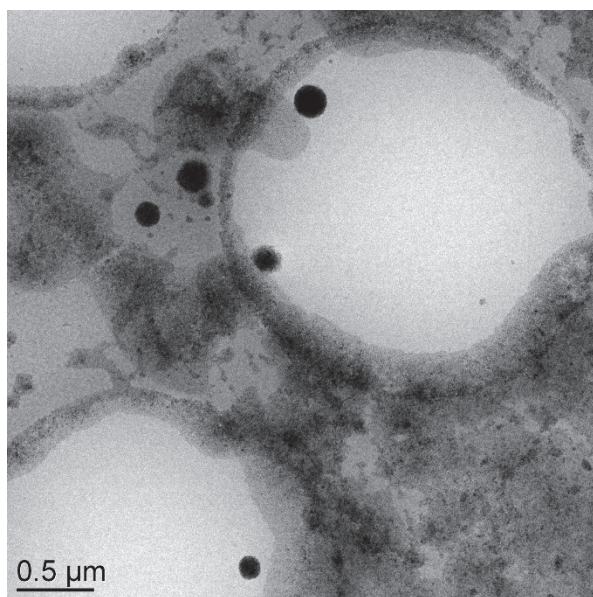
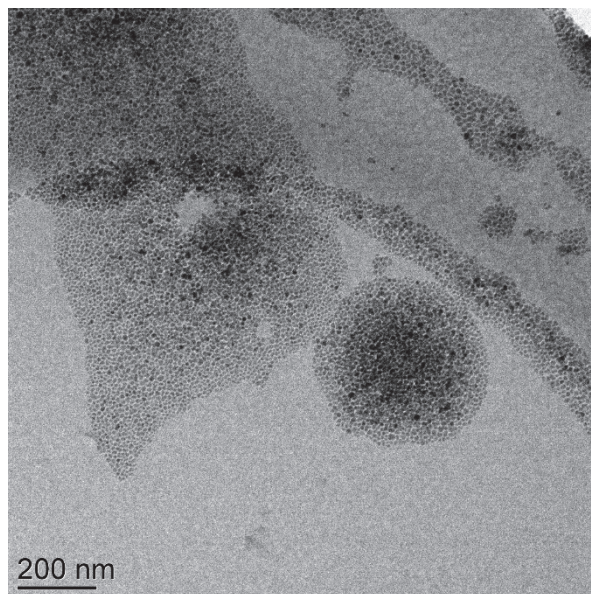
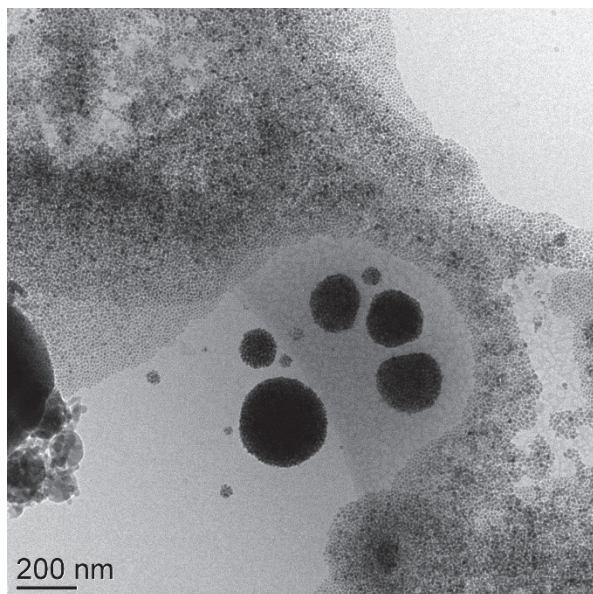


**Figure 122** – Determination of cluster size distributions. Comparison between the number (in red) and intensity (in green) frequency size distribution histograms determined from TEM images and the DLS size distribution (black trace).

ANNEX 3. 3. – Cryo-TEM micrographs of toluene droplets loaded with FA@IONPs





## ANNEX 3. 4. – Determination of free macroRAFT concentration

The amount of amphiphilic PDMAEMA-*b*-PS-TTC macroRAFT (entry TRG68) not adsorbed on iron oxide nanoparticles was estimated by UV-visible analyses using the maximum of absorbance of the TTC function ( $\lambda_{\text{max}} = 312 \text{ nm}$ ). A calibration curve was first established (Figure 123), that could be very well fitted to a straight line, according (following?) the Beer-Lambert law ( $\xi = 9118 \text{ L mol}^{-1} \text{ cm}^{-1}$ ).

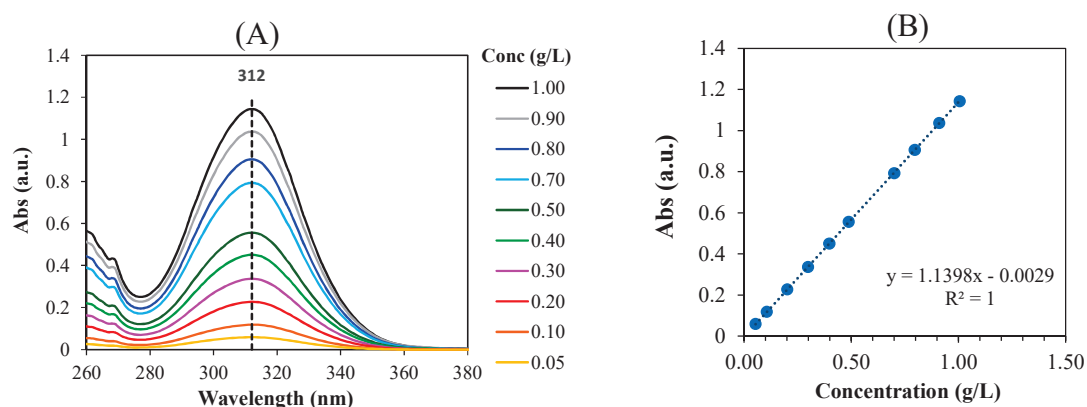


**Figure 123** – UV-vis calibration curve of PDMAEMA-*b*-PS-TTC: (A) UV spectra and (B) graph of absorbance at 312 nm vs. concentration.

To determine the amount of free macroRAFT in the aqueous phase, the iron oxide clusters were first separated from the aqueous solution by using a magnet and then the supernatant was carefully collected to analyze the macroRAFT concentration, as schematically represented in Figure 124. However, some iron oxide nanoparticles and small cluster still remained individually dispersed in the supernatant solution (*i.e.* nanoparticles not contained in the clusters), and their presence could disturb the UV-visible analysis (TEM images of the supernatant are shown in Figure 125). In order to separate them from the macroRAFT solutions, the resulting supernatant after magnetic separation was submitted to centrifugation at different rotation speeds. As can be seen in Figure 126B, a speed of 60 000 rpm was necessary to have a good separation, *i.e.* the spectrum of the supernatant is similar to that of the pure macroRAFT in solution. In parallel, solutions of the pure macroRAFT agent (*i.e.* without IO particles) were also submitted to centrifugation at different speeds. As can be seen in Figure 126A, when the conditions to have enough separation of iron oxide were applied (*i.e.*, 60 000 rpm), the macroRAFT agent also precipitated, which will disturb the quantification. Therefore, the quantification of free macroRAFT was not possible due to partial precipitation of macroRAFT during the centrifugation step. We also tried to separate



the residual IO particles by using a strong magnet. However, the magnet did not produce a magnetic field strong enough to separate the entire amount of iron oxide.

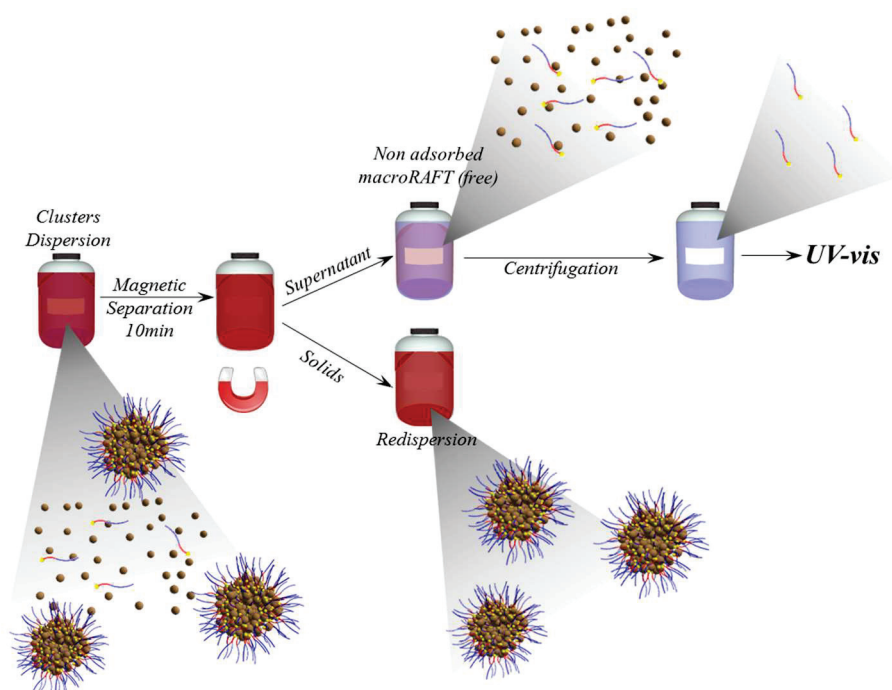


**Figure 124** – Schematic representation of the cluster purification in order to determine the free macroRAFT concentration in the aqueous phase.

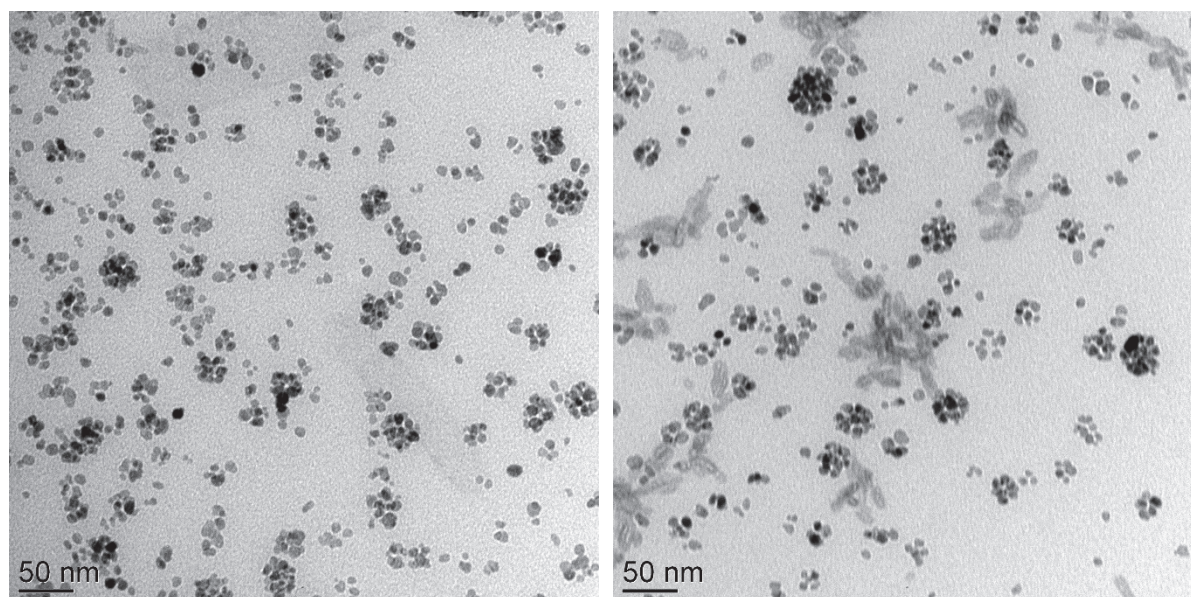


**Figure 125** – TEM micrographs of the supernatant collected after magnetic separation of the iron oxide clusters.

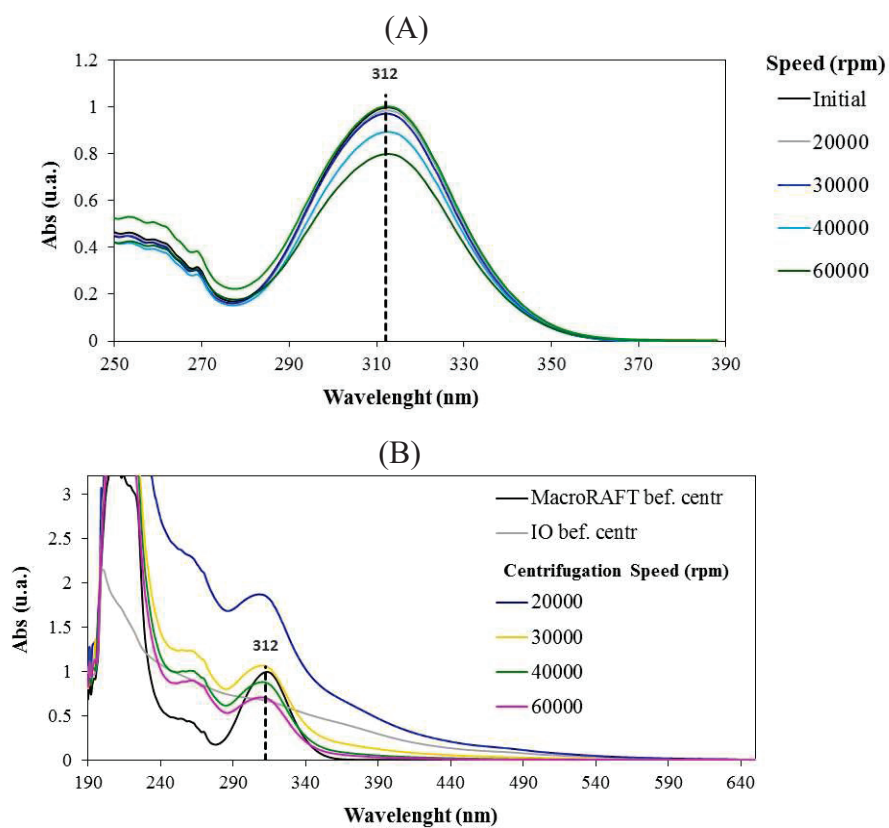
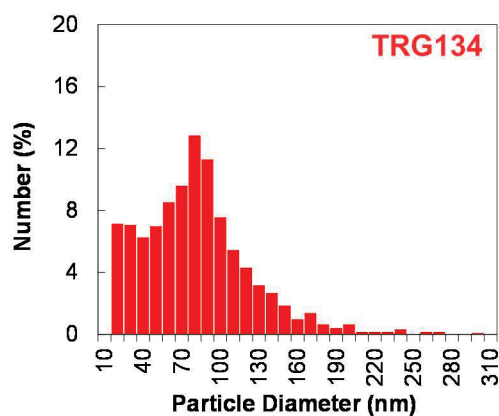
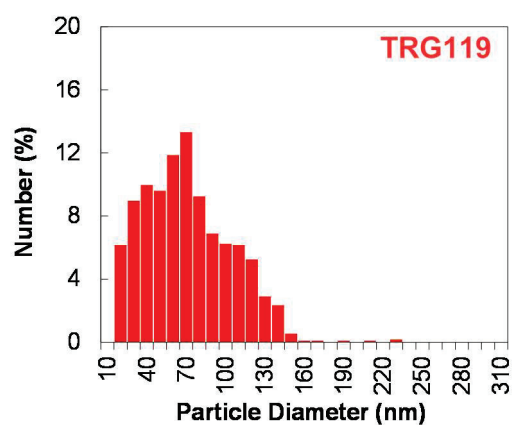
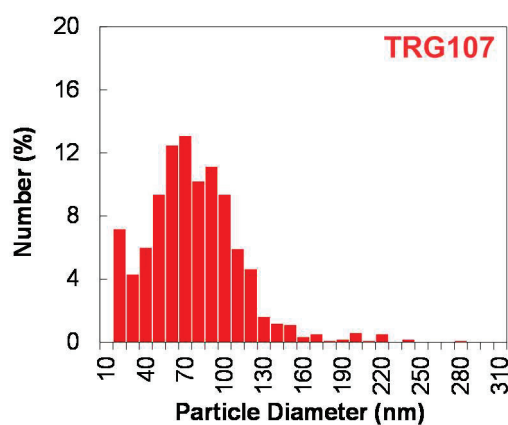
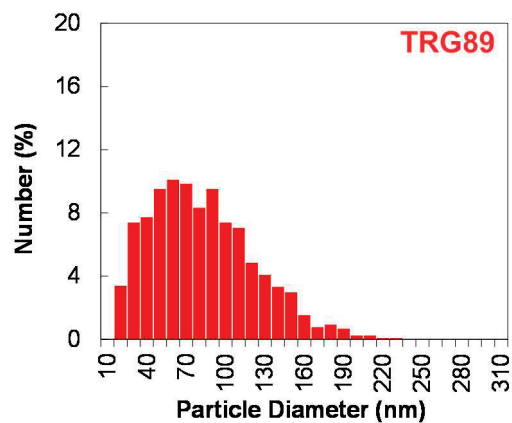
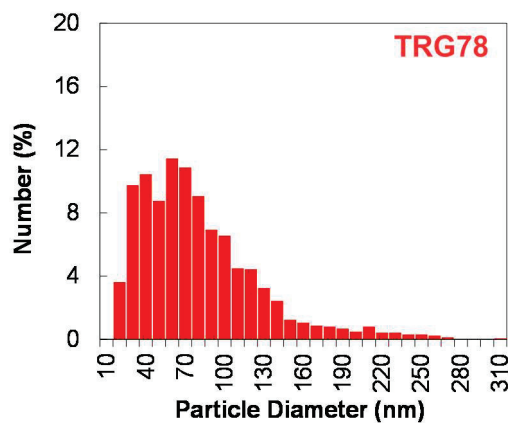


**Figure 126** – UV-vis spectra of the supernatant solutions after centrifugation of: (A) pure macroRAFT solutions and (B) macroRAFT agent + iron oxide nanoparticles at different centrifugation speeds.

ANNEX 3. 5. – Number frequency size distribution histograms of the IO clusters prepared at a larger scale using PDMAEMA-b-PS-TTC as stabilizer.



## ANNEX 4.1 – Gas chromatograms of Divinyl benzene

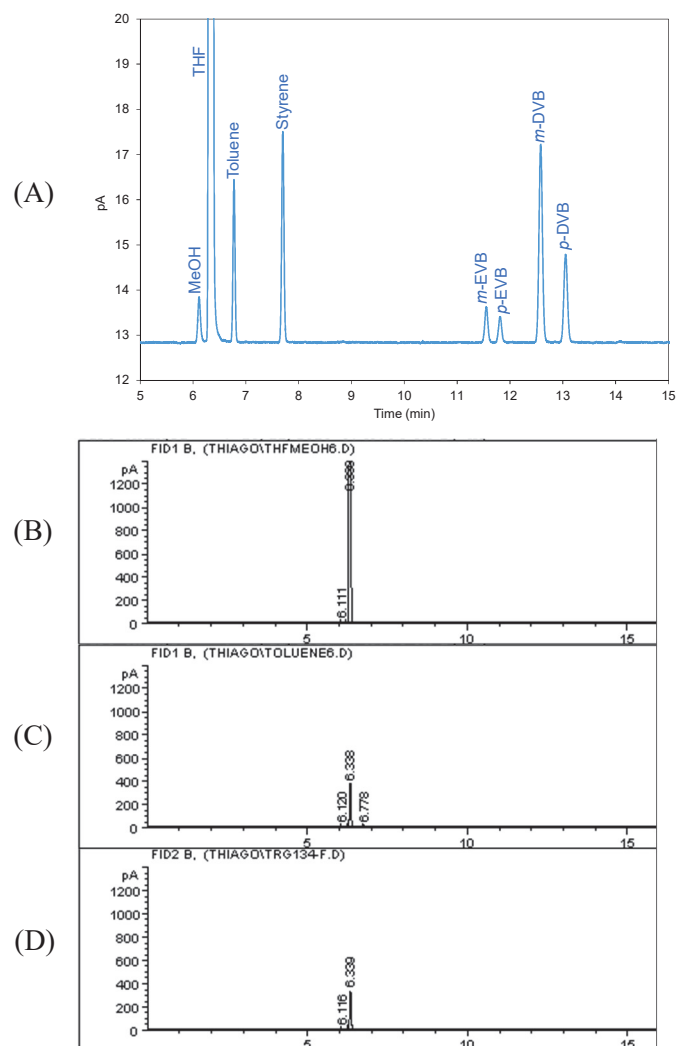
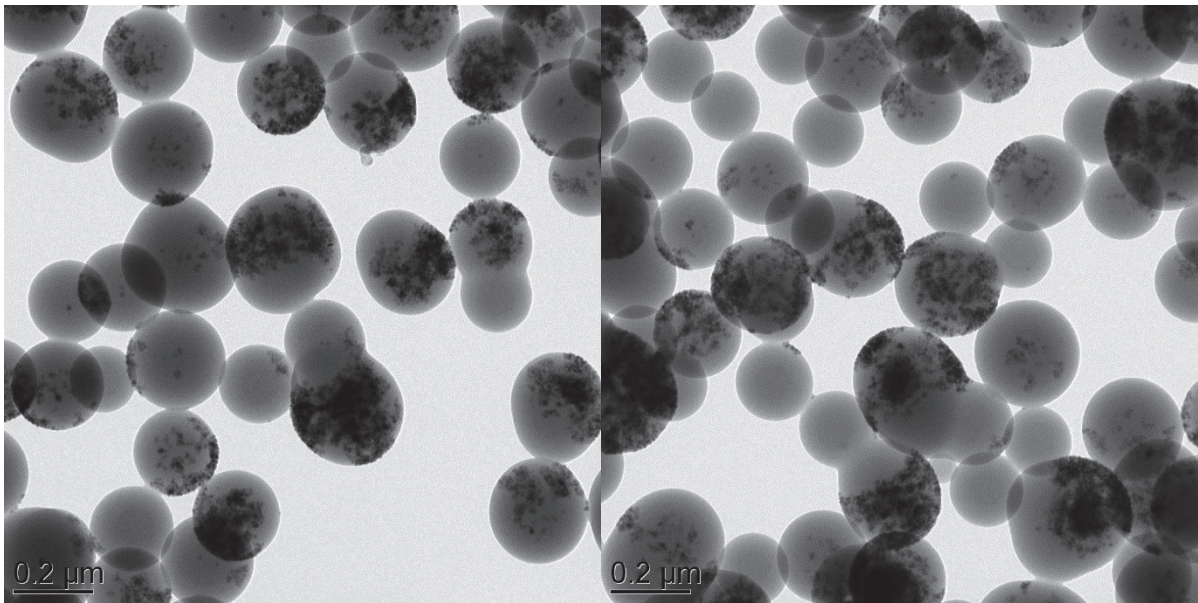


**Figure 127** – GC spectra of THF solutions with 0.05% methanol as internal standard of (A) mixture of the chemicals to check the separation efficiency of the method employed, (B) THF solutions with 0.05% methanol (C) Toluene and (D) mixture 1:4 of THF:Iron oxide dispersion (vol:vol).

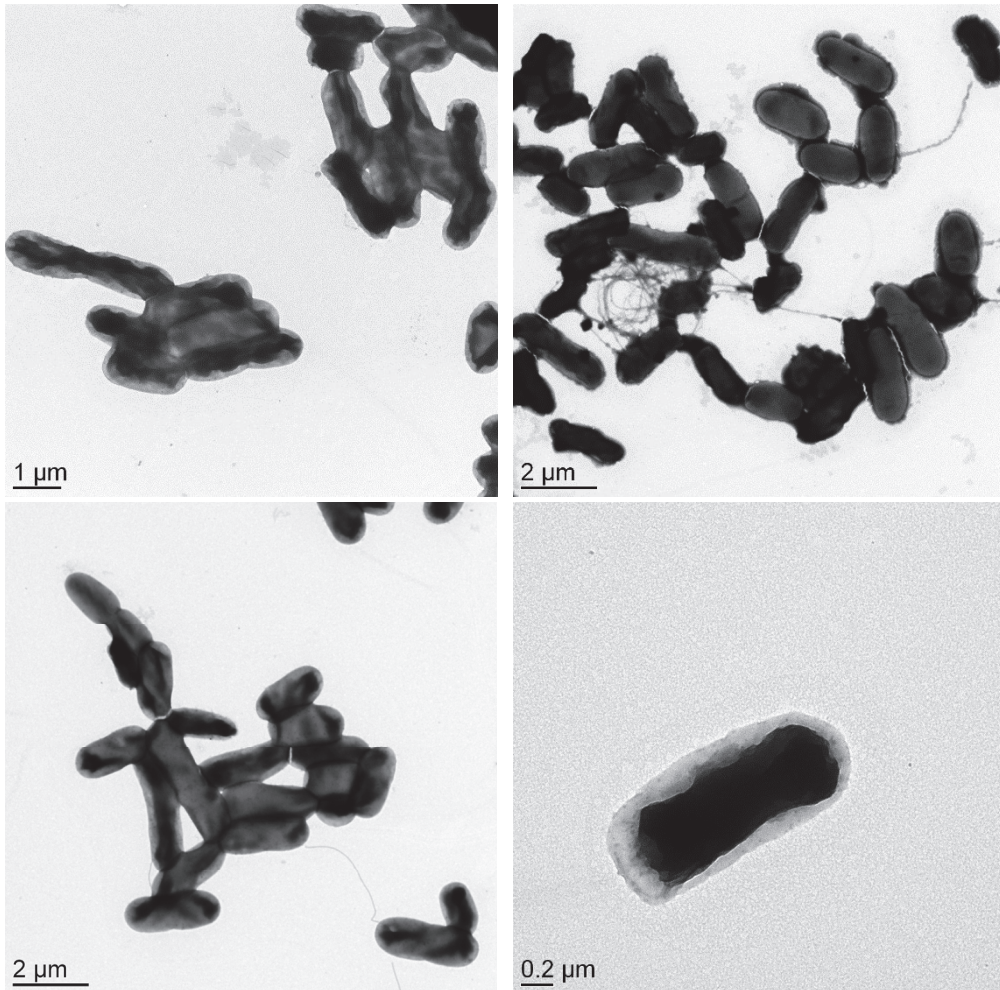
ANNEX 4. 2 – TEM micrographs of TRG90



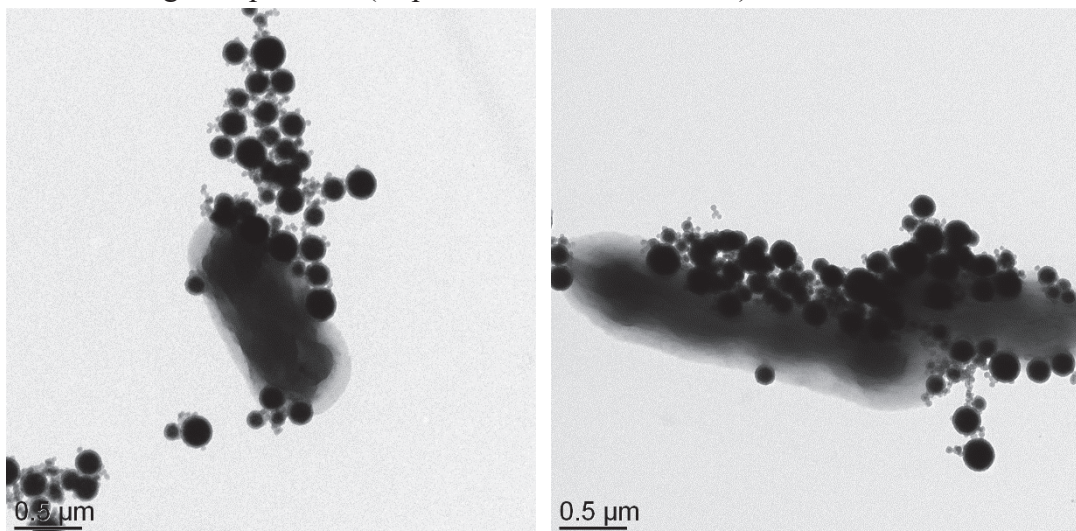


ANNEX 5. 1 - TEM Images (TRG170)

**A** Bacteria (*E. coli*)

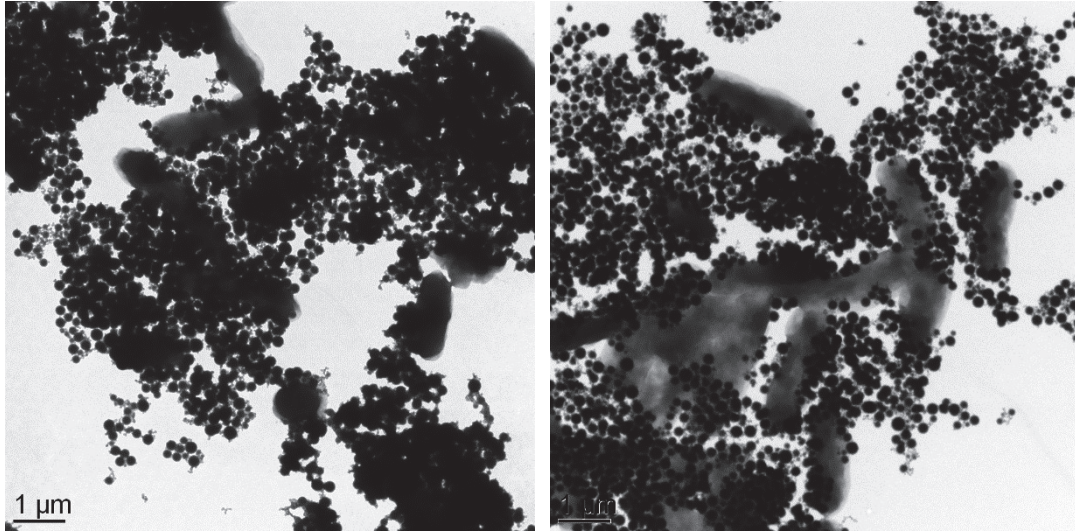


**B** Bacteria + magnetic particles (Capture – Acetic Acid 0.1%)

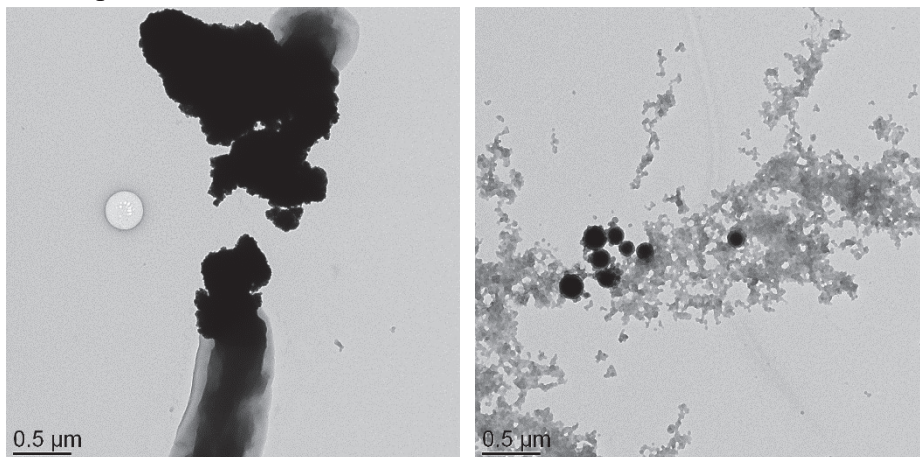




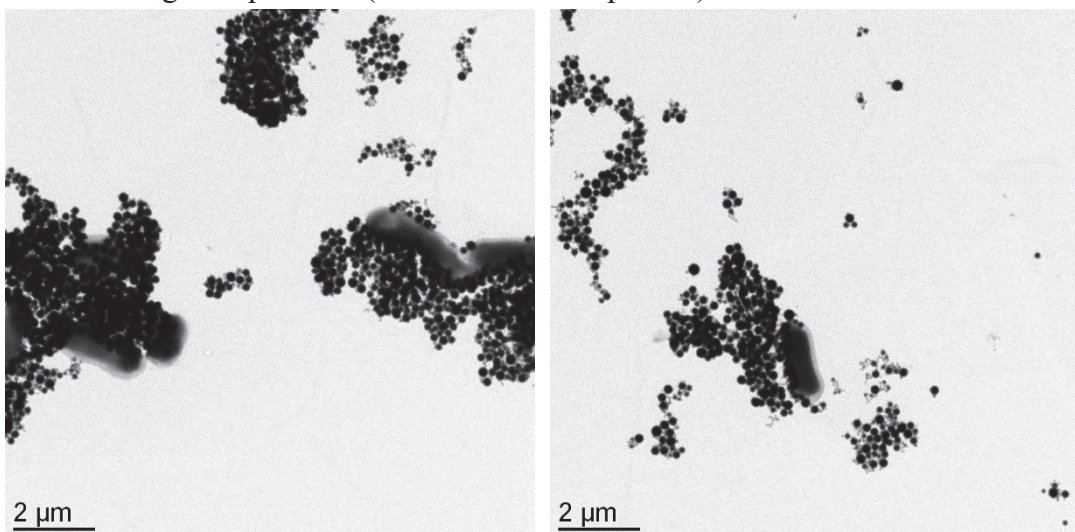
**B** Bacteria + magnetic particles (Capture – Acetic Acid 0.1%)



**C** Supernatant capture (*Nothing on TEM grids, only few objects due to possible sample contamination*)

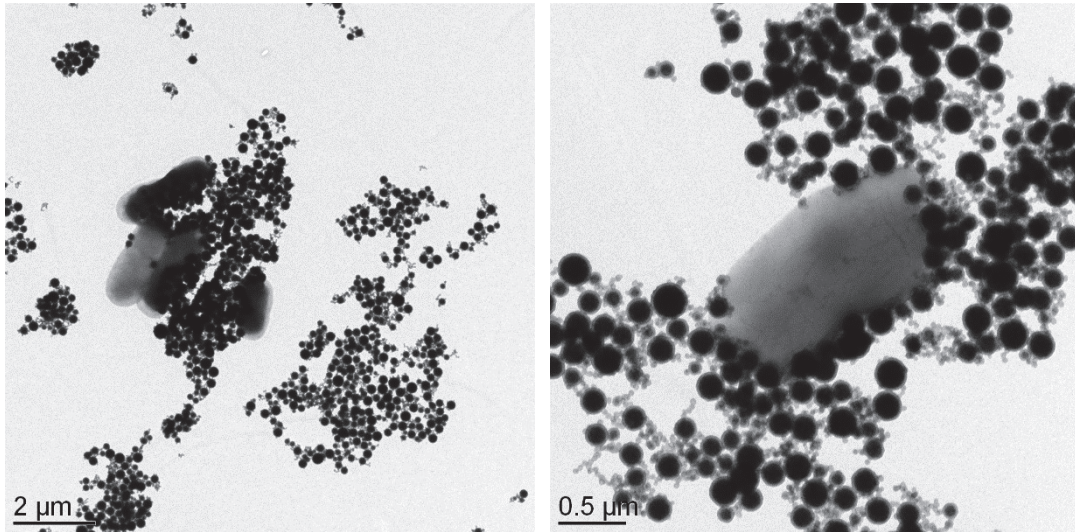


**D** Bacteria + magnetic particles (Release – Trizma pH = 9)

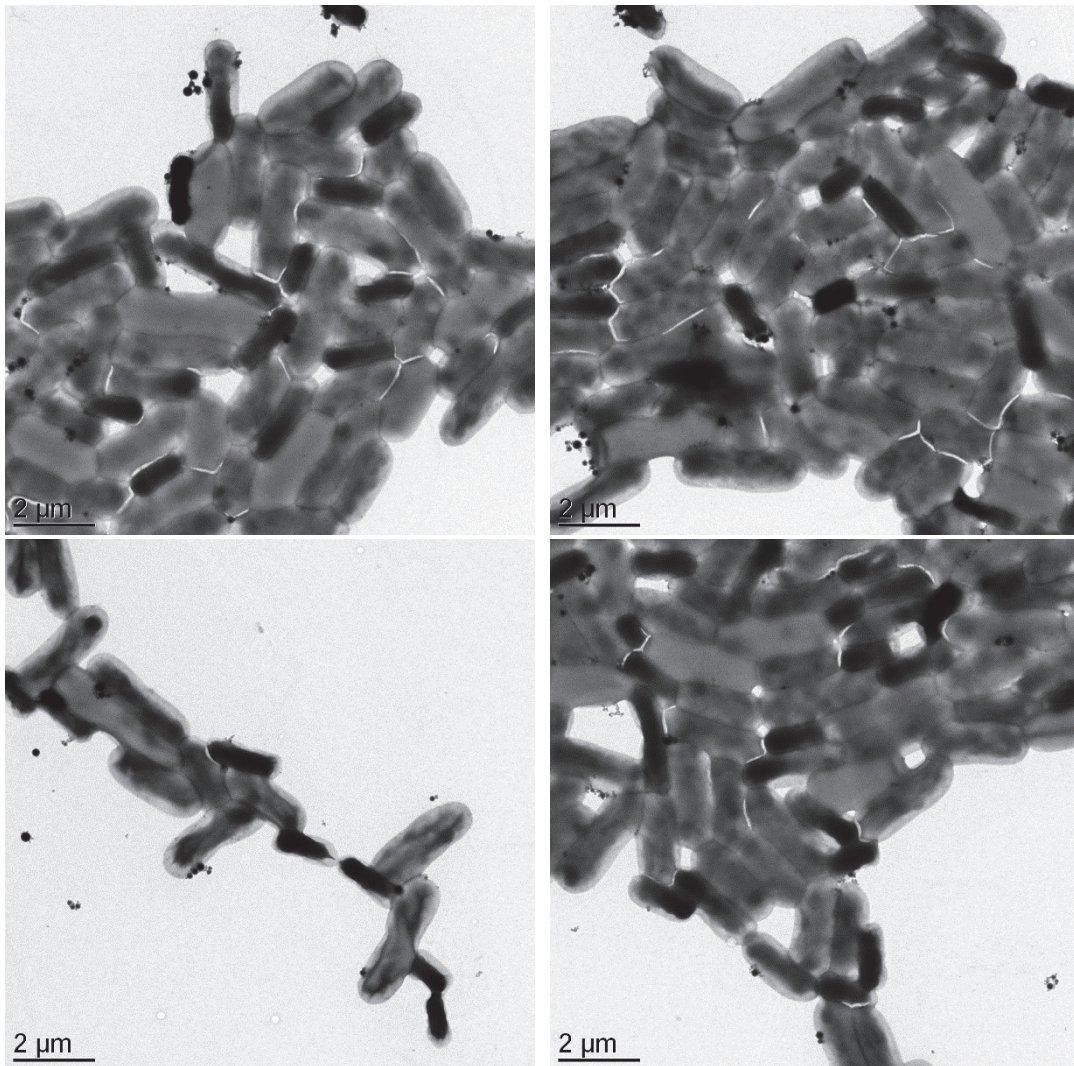




Ⓓ Bacteria + magnetic particles (Release – Trizma pH = 9)



Ⓔ Bacteria eluted (Supernatant after releasing step)





F Magnetic particles re-dispersed (Trizma pH = 9)

